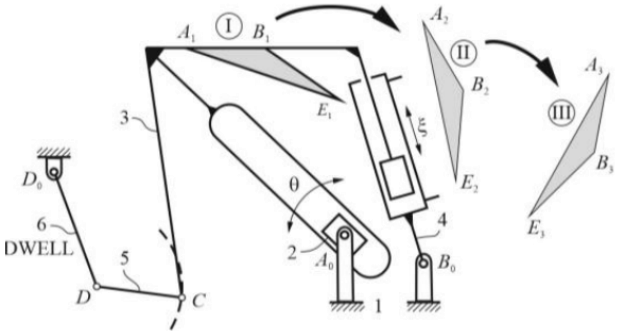
ISSN 1590-8844
Vol. 26 No. 01
2025

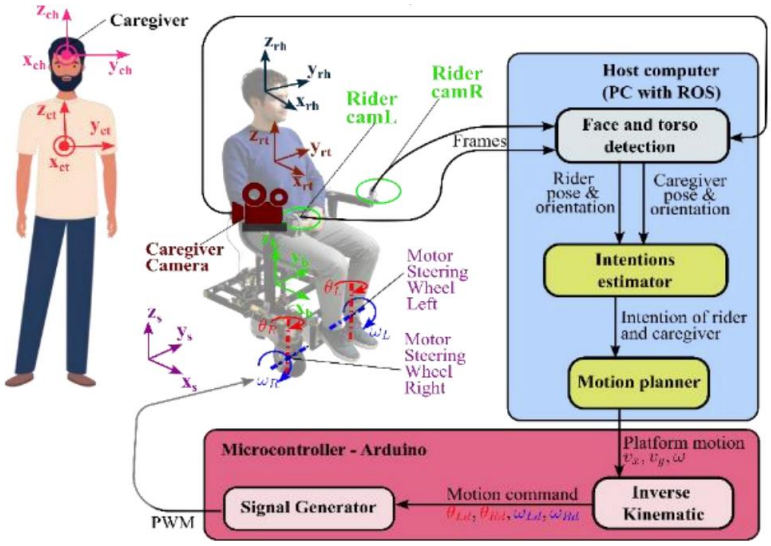
International Journal of Mechanics and Control

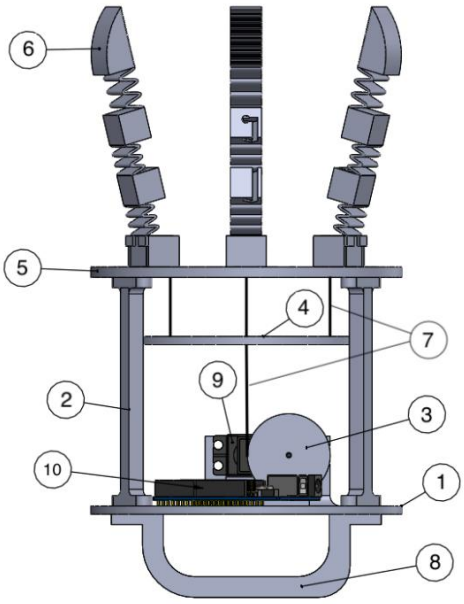
Editor: Andrea Manuello Bertetto

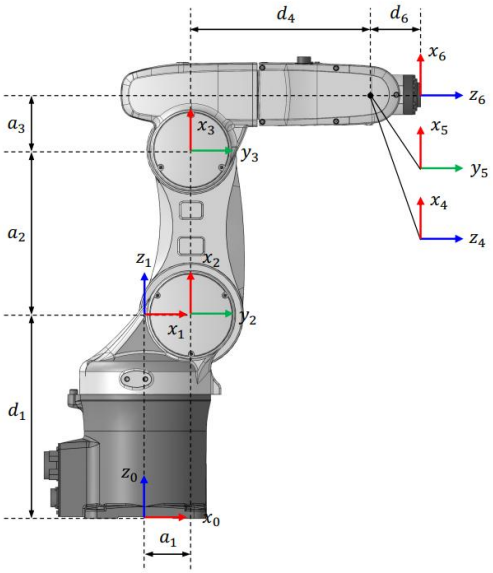
Scopus Indexed Journal

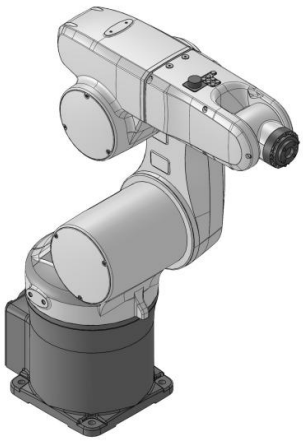
Reference Journal of IFToMM Italy
International Federation for the Promotion of Mechanism and Machine Science











Published by ASTRA M B S.R.L.
Via Febo, 22 – 10133 – Torino (Italy)

International Journal of Mechanics and Control

Associate Editors

Published by ASTRA M B S.R.L. – Torino – Italy E.C.

Honorary editors
Guido Belforte **Kazuo Yamafuji**

Editor: **Andrea Manuello Bertetto**

General Secretariat: **Matteo D. L. Dalla Vedova**
Simone Venturini
Alessandro Aimasso

Mario Acevedo
Universidad Panamericana
Mexico City – Mexico

Giovanni Boschetti
University of Padova
Vicenza – Italy

Luca Bruzzone
Università degli Studi di Genova
Genova – Italy

Giuseppe Carbone
Università della Calabria
Rende – Italy

Marco Ceccarelli
Università degli Studi di Roma Tor Vergata
Roma – Italy

Alberto Concu
AC Technologies S.r.l.s., Italy

Matteo Davide Lorenzo Dalla Vedova
Politecnico di Torino
Torino – Italy

Francesca Di Puccio
University of Pisa
Pisa – Italy

Carlo Ferraresi
Politecnico di Torino
Torino – Italy

Alexey Fomin
Mechanical Engineering Research Institute of the Russian Academy of Sciences (IMASH RAN)
Moscow – Russia

Walter Franco
Politecnico di Torino
Torino – Italy

Rafael Lopez Garcia
University of Jaen
Jaen – Spain

Viktor Glazunov
Mechanical Engineering Research Institute of the Russian Academy of Sciences (IMASH RAN)
Moscow – Russia

Rogério Sales Gonçalves
Federal University of Uberlândia
Uberlândia – Brazil.

Kenji Hashimoto
Waseda University
Tokyo – Japan

Giovanni Jacazio
Politecnico di Torino
Torino – Italy

Juan Carlos Jauregui Correa
Universidad Autonoma de Queretaro
Queretaro – Mexico

Med Amine Laribi
University of Poitiers
Poitiers – France.

Paolo Maggiore
Politecnico di Torino
Torino – Italy

Amedeo Manuello Bertetto
Politecnico di Torino
Torino – Italy

Mingfeng Wang
Brunel University
London – United Kingdom

Massimiliano Pau
University of Cagliari
Cagliari – Italy

Paolo Emilio Lino Maria Pennacchi
Politecnico di Milano
Milano – Italy

Giuseppe Quaglia
Politecnico di Torino
Torino – Italy

Roberto Ricciu
Università di Cagliari
Cagliari – Italy

Aleksandar Rodic
Institute Mihajlo Pupin
Belgrade – Serbia

Shuangji Yao
Yanshan University
Qinhuangdao – China

Patrizia Trovalusci
Sapienza - University of Rome
Roma – Italy

Mauro Velardocchia
Politecnico di Torino
Torino – Italy

Simone Venturini
Politecnico di Torino
Torino – Italy

Renato Vidoni
Free University of Bolzano
Bolzano – Italy

Ion Visa
Transilvania University of Brasov
Brasov – Romania

Yu-Hsun Chen
National Taiwan University of Science and Technology
Taipei City – Taiwan

Jaroslav Zapomel
VSB - Technical University of Ostrava
Ostrava - Czech Republic

Leon Zlajpah
Jozef Stefan Institute
Ljubljana – Slovenia

Official Torino Italy Court Registration
n. 5390, 5th May 2000
Deposito presso il Tribunale di Torino
n. 5390 del 5 maggio 2000
Direttore responsabile:
Andrea Manuello Bertetto

International Journal of Mechanics and Control

Editor: **Andrea Manuello Bertetto**

Honorary editors: **Guido Belforte**
Kazuo Yamafuji

General Secretariat: **Matteo D. L. Dalla Vedova**
Simone Venturini
Alessandro Aimasso

The Journal is addressed to scientists and engineers who work in the fields of mechanics (mechanics, machines, systems, control, structures). It is edited in Turin (Northern Italy) by ASTRA M B S.R.L., with an international board of editors. It will have not advertising. Turin has a great and long tradition in mechanics and automation of mechanical systems. The journal would will to satisfy the needs of young research workers of having their work published on a qualified paper in a short time, and of the public need to read the results of researches as fast as possible.
Interested parties will be University Departments, Private or Public Research Centres, Innovative Industries.

Aims and scope

The *International Journal of Mechanics and Control* publishes as rapidly as possible manuscripts of high standards. It aims at providing a fast means of exchange of ideas among workers in Mechanics, at offering an effective method of bringing new results quickly to the public and at establishing an informal vehicle for the discussion of ideas that may still in the formative stages.

Language: English

International Journal of Mechanics and Control will publish both scientific and applied contributions. The scope of the journal includes theoretical and computational methods, their applications and experimental procedures used to validate the theoretical foundations. The research reported in the journal will address the issues of new formulations, solution, algorithms, computational efficiency, analytical and computational kinematics synthesis, system dynamics, structures, flexibility effects, control, optimisation, real-time simulation, reliability and durability. Fields such as vehicle dynamics, aerospace technology, robotics and mechatronics, machine dynamics, crashworthiness, biomechanics, computer graphics, or system identification are also covered by the journal.

Please address contributions to

Prof. Andrea Manuello Bertetto
PhD Eng. Matteo D. L. Dalla Vedova

Dept. of Mechanical and Aerospace Engineering
Politecnico di Torino
C.so Duca degli Abruzzi, 24
10129 - Torino - Italy

www.jomac.it
e_mail: jomac@polito.it

Subscription information

Subscription order must be sent to
the publisher:

ASTRA M B S.R.L.
Via Febo, 22
10133 - Torino - Italy

e_mail: astra.mb.srl@gmail.com
mob.: +39 347 490 2080

International Journal of Mechanics and Control

Scientific Board

Published by ASTRA M B S.R.L.– Torino – Italy

Alessandro Aimasso
Politecnico di Torino
Torino – Italy

Atlas Akhmetzyanov
V.A. Trapeznikov Institute of Control Sciences
of Russian Academy of Sciences
Moscow – Russia

Domenico Appendino
Prima Industrie
Torino – Italy

Kenji Araki
Saitama University
Saitama – Japan

Amalia Ercoli Finzi
Politecnico di Milano
Milano – Italy

Anindya Ghoshal
Arizona State University
Tempe – Arizona – USA

Nunziatino Gualtieri
Space System Group, Alenia Spazio
Torino – Italy

Alexandre Ivanov
Politecnico di Torino
Torino – Italy

Roberto Ricciu
Università di Cagliari
Cagliari – Italy

Matteo Davide Lorenzo Dalla Vedova
Politecnico di Torino
Torino - Italy

Takashi Kawamura
Shinshu University
Nagano – Japan

Kin Huat Low
School of Mechanical and Aerospace Engineering
Nanyang Technological University
Singapore

Stamos Papastergiou
Jet Joint Undertaking
Abingdon – United Kingdom

Mihailo Ristic
Imperial College
London – United Kingdom

Jànos Somlò
Technical University of Budapest
Budapest – Hungary

Jozef Suchy
Faculty of Natural Science
Banska Bystrica – Slovakia

Federico Thomas
Instituto de Robótica e Informática Industrial
Barcelona – Espana

Simone Venturini
Politecnico di Torino
Torino – Italy

Vladimir Viktorov
Politecnico di Torino
Torino – Italy

Official Torino Italy Court Registration
n. 5390, 5th May 2000

Deposito presso il Tribunale di Torino
n. 5390 del 5 maggio 2000

Editor in Chief

Direttore responsabile:
Andrea Manuello Bertetto

ISSN 1590-8844
International Journal of Mechanics and Control, Vol. 26, No. 01, 2025
https://doi.org/10.69076/jomac.2025.0000

PREFACE FOR THE SPECIAL ISSUE OF THE INTERNATIONAL JOURNAL OF MECHANICS AND CONTROL (JOMAC) DEDICATED TO THE 5TH INTERNATIONAL CONFERENCE OF THE IFTOMM ITALY, IFIT 2024

Maria Cristina Valigi* Carmen Visconte**

* Dept. of Engineering
University of Perugia, Perugia, Italy

** Dept. of Mechanical and Aerospace Engineering – DIMEAS
Politecnico di Torino, Turin, Italy

GUEST EDITORIAL

Mechanical engineering is a multi-faceted discipline, encompassing a broad range of specialization and application. Due to the increasing complexity of engineering problems, a more and more multidisciplinary approach and a stronger connection among researchers with shared background but different expertise is becoming fundamental. On the base of this premise, the International Federation for the Promotion of Machine and Mechanism Science (IFToMM) organizes a series of international conferences, the IFIT ones, giving researchers from the Italian community, and not only, the opportunity to meet, learn about the latest innovation and discuss challenges. The last conference of this series, the 5th International Conference of the IFToMM ITALY - IFIT 2024, has been held at Politecnico di Torino in Turin, Italy, from 11th to 13th September 2024. It has hosted more than 160 researchers from different geographical areas, working in the field of applied mechanics and machine theory. This Special Issue collects the extended revised versions of some of the contributions that were presented at the IFIT 2024, which are representative of most of the topics covered in this conference. The papers have been evaluated again with a blind peer-review process to confirm the high quality of the works.

Contact author: Valigi M.C. [1], Visconte C. [2]

[1] Via G. Duranti, 93, 06125, Perugia (PG), Italy.
[2] Corso Duca degli Abruzzi, 24, 10129, Torino (TO), Italy.
E-mail: mariacristina.valigi@unipg.it, carmen.visconte@polito.it

In particular, the first paper is an example of research work in the field of mechanism design.
Giorgio Figliolini, Chiara Lanni and Luciano Tomassi present the kinematic synthesis of Oldham chain based six-bar dwell mechanisms for three-pose rigid-body guidance. The authors propose a general algorithm for designing these mechanisms, including an initial synthesis of the Oldham coupling and a subsequent addition of RR (revolute-revolute) or RP (revolute-prismatic) dyads to achieve a dwell output [1].
In the second paper, Stefan Leitner, Lorenzo Maccioni, Giovanni Carabin, Raffaele Spinelli and Renato Vidoni focus on the energy recovery potential of a hybrid self-propelled carriage called HULK, for the alpine logging operation. The authors present and discuss results of experimental tests on the engine-generator set, the energy dissipation unit and the battery pack [2].
The remaining papers concern the field of robotics.
In the third paper, Federico Neri, Giacomo Palmieri, Daniele Costa and Massimo Callegari present and compare two distinct strategies of obstacle avoidance tailored to differential wheeled mobile robots. In the first case, both translational and rotational repulsive velocities are considered while in the second case only repulsive rotational velocity is applied [3].
The fourth paper, authored by Domenico Donà, Paolo Boscariol, Matteo Bottin, Basilio Lenzo and Giulio Rosati, presents the use of a model identification technique for a serial robot, augmented with a regularization procedure, applied to the Mitsubishi RV-5AS-D-S01 industrial robot. The aim is to support the development of advanced control strategies for planning time-efficient or energy efficient tasks [4].

In the fifth paper, Lorenzo Baglieri, Daisuke Matsuura, Tsune Kobayashi and Giuseppe Quaglia present the development of a hands-free human-machine interface for electric wheelchair control, utilizing vision-based tracking of face and torso movements. The proposed system processes head and torso movements to generate control commands, enabling shared control between the rider and the caregiver [5].

The sixth paper deals with soft actuation and soft robotics applications. Monica Tiboni and Davide Loda describe the design, simulation, and characterization of a force-optimized, monolithic, soft actuator, called PneuNets. The actuator's geometry is optimized through FEM simulation, and the new design is experimentally validated [6].

In the seventh paper, Giovanni Boschetti and Teresa Sinico proposes a comparison between different calibration methodologies for a robot based on simulated data: within a multibody simulation environment manufacturing and measuring errors are artificially introduced, to obtain a set of data affected by statistical errors. These data are then used to test different approaches to robot calibration [7].

The eighth and last paper, authored by Silvia Logozzo and Maria Cristina Valigi, presents a novel prototype of robotic gripper for precision grasping. The gripper employs three monolithic soft-rigid fingers, each actuated with a tendon-driven mechanism, and integrates a differential system to adjust the gripping force based on object shape and size. Experimental tests are presented [8].

We would like to express our sincere appreciation to all researchers having contributed to this special issue and to the Editorial Board of JoMaC for giving us this Guest Editorial opportunity.

REFERENCES

[1] Figliolini G., Lanni C. and Tomassi L., Synthesis of Oldham chain based six-bar dwell mechanisms for three-pose rigid-body guidance. *International Journal of Mechanics and Control,* Vol. 26, No. 1, pp. 03-12, 2025.

[2] Leitner S., Maccioni L., Carabin G., Spinelli R. and Vidoni R., Performance and Efficiency of a Hybrid Self-Propelled Cable Logging Carriage: an Experimental Study. *International Journal of Mechanics and Control,* Vol. 26, No. 1, pp. 13-22, 2025.

[3] Neri F., Palmieri G., Costa D. and Callegari M., Obstacle avoidance methods for differential drive robots. *International Journal of Mechanics and Control,* Vol. 26, No. 1, pp. 23-36, 2025.

[4] Donà D., Boscariol P., Bottin M., Lenzo B. and Rosati G., Regularized Dynamic Parameter Identification for the Mitsubishi RV-5AS-D-S01 Robot. *International Journal of Mechanics and Control,* Vol. 26, No. 1, pp. 37-48, 2025.

[5] Baglieri L., Matsuura D., Kobayashi T. and Quaglia G., A hands-free human-machine interface for electric wheelchair control based on face and torso movement. *International Journal of Mechanics and Control,* Vol. 26, No. 1, pp. 49-56, 2025.

[6] Tiboni M. and Loda D., Force-optimized monolithic PneuNets soft actuators: design, simulation and characterization. *International Journal of Mechanics and Control,* Vol. 26, No. 1, pp. 57-66, 2025.

[7] Boschetti G. and Sinico T., Improving accuracy and robustness in robot kinematic calibration using a single draw-wire encoder: a comparative analysis. *International Journal of Mechanics and Control,* Vol. 26, No. 1, pp. 67-78, 2025.

[8] Logozzo S. and Valigi M.C., Design and characterization of a new soft robotic tendon driven gripper for precision grasping. *International Journal of Mechanics and Control,* Vol. 26, No. 1, pp. 79-86, 2025.

ISSN 1590-8844
International Journal of Mechanics and Control, Vol. 26, No. 01, 2025
https://doi.org/10.69076/jomac.2025.0001

SYNTHESIS OF OLDHAM CHAIN BASED SIX-BAR DWELL MECHANISMS FOR THREE-POSE RIGID-BODY GUIDANCE

Giorgio Figliolini* Chiara Lanni* Luciano Tomassi*

* University of Cassino and Southern Lazio

ABSTRACT

This paper deals with the kinematic synthesis of Oldham chain based six-bar dwell mechanisms for three-pose rigid-body guidance. In particular, a general algorithm is formulated to firstly synthesize a general Oldham mechanism with inclined or orthogonal slots, in order to reach three finitely separated and assigned positions, and secondly, to give a dwell output link of the whole six-bar mechanism by adding suitable RR or RP dyads. This second step is obtained by applying infinitesimal displacements synthesis methods, which make use of the coupler link centrodes of the Oldham mechanism, along with geometric loci, such as, the inflection and return circles, the circling-points curve and center-points curve, Ball's point. This dwell can be designed for any Oldham mechanism configuration, which could be coinciding with one of the three assigned poses. The proposed algorithm has been implemented in Matlab and validated by several examples and analysing the corresponding numerical and graphical results.

Keywords: Kinematic synthesis, six-bar linkages, three-pose rigid-body guidance, Oldham mechanisms, dwell mechanisms.

1 INTRODUCTION

The kinematic synthesis of planar mechanisms for rigid-body guidance through three finitely separated positions is a fundamental problem in mechanism design. In many practical applications, only the initial, intermediate, and final positions of a rigid body are prescribed to ensure the desired motion. This topic has been extensively addressed in the literature using various analytical and graphical approaches [1–4]. However, several contributions have explored different strategies for integrating type and dimensional synthesis in rigid-body guidance problems [5]. Furthermore, previous work by the authors has applied three-pose synthesis to the design of knee exoskeleton mechanisms, employing a four-bar linkage as the base kinematic chain [6]. One key difference is that the Oldham-based chains incorporate an additional prismatic pair, a feature that is less frequently employed in conventional rigid-body guidance mechanisms.

Contact author: Giorgio Figliolini[1], Chiara Lanni[2], Luciano Tomassi[3]

Viale dell'Università, Loc. Folcara, 03043 Cassino (FR)

E-mail: figliolini@unicas.it, lanni@unicas.it, luciano.tomassi@unicas.it

Nevertheless, recent studies have explored the introduction of prismatic joints into the design space of rigid-body synthesis, demonstrating their potential advantages in specific applications [7–8]. The Oldham coupling is a well-established mechanism used for torque transmission between parallel but non-collinear shafts, and its generalized formulations have been extensively studied to enhance its performance and adaptability in various mechanical applications [9–11]. The coupler link motion of the Oldham mechanism corresponds to an inverse Cardan motion, in which the centrodes take the form of the Cardan circles, generating an epi-trochoidal motion. Trochoidal-type mechanisms are widely used in applications such as pumps, compressors, and rotary machines due to their simplicity, reliability, and efficiency. One of the earliest studies on trochoidal profiles in pumping systems was conducted by Hill [12], followed by further geometric analyses on trochoidal envelopes [13]. More recent research has explored the kinematic synthesis of rotary mechanisms based on regular curve-polygons [14]. The synthesis of mechanisms based on infinitesimal displacements represents an alternative approach to rigid body-guidance methods [15]. This design strategy relies on geometric loci, such as the inflection circle and the circling-points curve, whose algebraic properties have been deeply investigated in [16]. Infinitesimal displacements are particularly useful in

the synthesis of mechanisms featuring dwells, where the output link remains stationary for part of the cycle while the input link moves continuously. Such mechanisms are widely employed in the processing industry and have been studied in the context of adjustable six-bar linkages and dwell-based six-bar mechanisms [17–18]. Similarly, infinitesimal displacements play a key role in the design of indexing mechanisms, where controlled intermittent motion is required, as seen in the synthesis of Geneva mechanisms with extended dwell periods and in the geometry design of indexing cam mechanisms [19–20]. In addition, functional design studies have demonstrated the application of parallel kinematics in high-precision biomedical manipulators, highlighting the relevance of customized synthesis approaches in performance-critical tasks [21]. As proposed by the authors in [22], the synthesis and analysis of Stephenson III six-bar mechanisms with instantaneous stop links have been explored, along with the investigation of first- and second-order centrodes of both coupler links in six-bar linkages that present an output member with dwell [23]. Hybrid synthesis approaches combining finite and infinitesimal displacements enable mechanisms to achieve both prescribed finite poses and controlled infinitesimal motion.

Foundational studies established a generalized framework for multiple finitely and infinitesimally separated positions [24–25], such as those with three infinitesimally and one finitely separated position [26]. In this paper, the kinematic synthesis of Oldham chain based six-bar dwell mechanisms for three-pose rigid-body guidance is proposed. In particular, a general algorithm is formulated to firstly synthesize a general Oldham mechanism with inclined or orthogonal slots, in order to reach three finitely separated and assigned positions, and secondly, to give a dwell output link of the whole six-bar mechanism by adding suitable RR or RP dyads. The paper is organized by firstly describing the kinematic structure of the proposed Oldham chain based six-bar dwell mechanism of 2R2P-3R and 2R2P-2RP types for three-pose rigid-body guidance, then formulating the synthesize of a general Oldham mechanism with inclined or orthogonal slots to reach three finitely separated and assigned positions, and in sequence, by developing the position analysis and achieving the coupler curves equations.

Thus, in the next, the whole six-bar dwell mechanism is synthesized by adding suitable RR or RP dyads to the previously synthesised Oldham mechanism. This second synthesis step is based on the coupler link centrodes of the Oldham mechanism, along with geometric loci, such as, the inflection and return circles, the circling-points curve and center-points curve, Ball's point. Finally, the proposed synthesis algorithm of Oldham chain based six-bar dwell mechanisms for three-pose rigid-body guidance is validated by means of several examples and analysing the corresponding numerical and graphical results for different mechanism configurations.

2 OLDHAM CHAIN BASED SIX-BAR DWELL MECHANISMS FOR THREE-POSE RIGID-BODY GUIDANCE

A general Oldham mechanism with inclined slots is firstly synthesized by referring to the three poses I, II and III of the triangular laminae with vertices A_i, B_i and E_i for i = 1, 2, 3, as sketched in Fig. 1. Then, choosing the first configuration of pose I, the synthesis of two types of six-bar dwell mechanisms is developed by adding a RR or a RP dyad, as shown in Figs. 1a and 1b, respectively. Moreover, these types of six-bar dwell mechanisms can be operated indifferently by choosing the piston 2 or the linear cylinder 3/4, which take the role of driving members with absolute rotation θ or relative translation ξ between 3 and 4. In particular, the Oldham rigid-body guidance mechanism of 2R2P type is composed by the piston 2 that is able to rotate around the fixed revolute joint A_0 and by the coupler link 3 and the glyph 4 that rotates around B_0. Instead, referring to the left side of both Figs. 1a and 1b, the RR and RP dyads are added and joined to the Oldham coupler link 3 through the moving revolute joint C and thus, they are composed by the links 5 and 6. Therefore, the kinematic synthesis of Oldham chain based six-bar dwell mechanisms for three-pose rigid-body guidance is formulated in two main steps: 1) the synthesis of a general Oldham mechanism with inclined slots to reach three given and finitely separated poses; 2) the infinitesimal synthesis of circular and straight path generators of Oldham type, by using geometrical loci, such as, the inflection and return circles, along with the circling-points and center-points curves, in order to find a suitable C point for adding the RR and RP dyads, as shown in Fig. 1a and 1b.

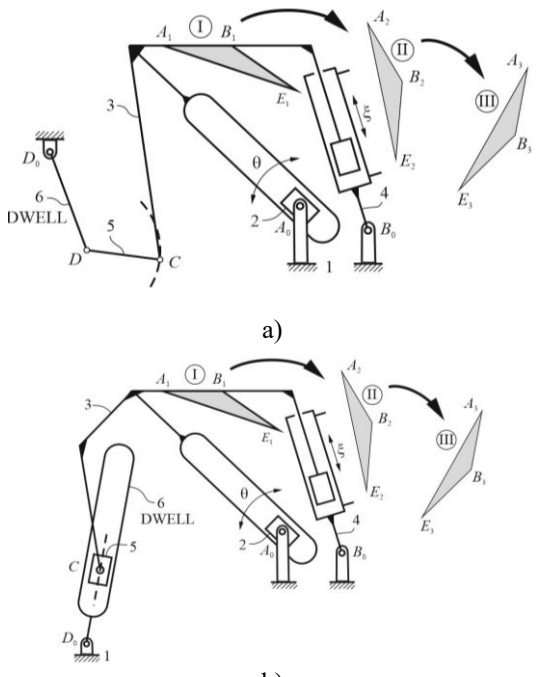


Figure 1 Oldham chain based six-bar dwell mechanisms: a) RR dyad; b) RP dyad.

2.1 SYNTHESIS OF OLDHAM MECHANISMS FOR THREE-FINITELY SEPARATED POSES

Referring to Fig. 2, supposed assigned the three finitely separated positions A_1B_1, A_2B_2 and A_3B_3, the pole triangle P_{12}, P_{23} and P_{13}, its circumcircle Cp, along with the three mirror circles Γ_1, Γ_2 and Γ_3 passing through the cardinal point H_C, which is also the orthocenter of the pole triangle, have been determined for synthesis purposes. As reported in [2], the kinematic synthesis of linkages for three-poses rigid-body can be formulated by applying the Suh & Radcliffe method, which makes use of displacement matrices. In fact, a rigid body displacement from a first *i*-pose to the second *j*-pose that can be sketched through the segments $A_i - B_i$ and $A_j - B_j$, respectively, is carried out through the homogeneous displacement matrix:

$$\mathbf{D}_{ij} = \begin{bmatrix} \cos\vartheta_{ij} & -\sin\vartheta_{ij} & x_j - x_i\cos\vartheta_{ij} + y_i\sin\vartheta_{ij} \\ \sin\vartheta_{ij} & \cos\vartheta_{ij} & y_j - x_i\sin\vartheta_{ij} - y_i\cos\vartheta_{ij} \\ 0 & 0 & 1 \end{bmatrix} \tag{1}$$

which is obtained by two basic displacement matrices, a rotation matrix of the counter-clockwise angle ϑ_{ij} about the origin O of the fixed frame OXY, and a translation matrix from point A_{iR} that is the image of $A_i = (x_i, y_i)$ after the rotation, up to the point $A_j(x_j, y_j)$. Assigning the position vectors $\mathbf{r}_{Ai}$ and $\mathbf{r}_{Aj}$ of point A, as follows

$$\mathbf{r}_{Ai} = \begin{bmatrix} x_{Ai} & y_{Ai} & 1 \end{bmatrix}^T \text{ and } \mathbf{r}_{Aj} = \begin{bmatrix} x_{Aj} & y_{Aj} & 1 \end{bmatrix}^T \tag{2}$$

along with the relative rotation angle ϑ_{ij}, the displacement matrix $\mathbf{D}_{ij}$ can be obtained by the Eq. (1). Symbol T of Eq. (2) indicates the transpose matrix.

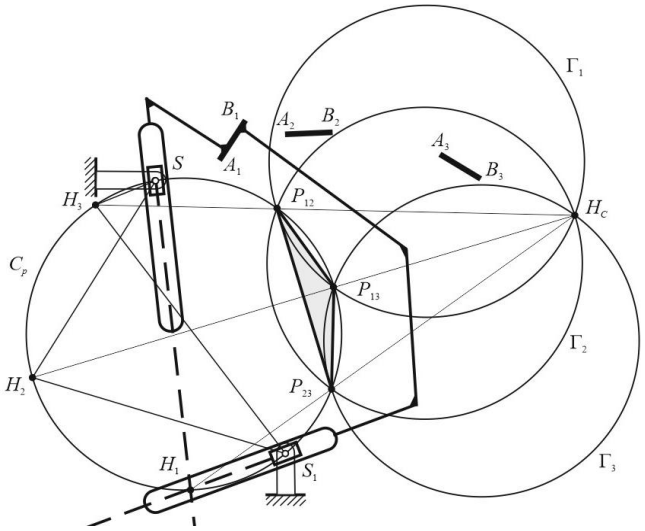


Figure 2 Graphical synthesis procedure of an Oldham mechanism with inclined slots.

Consequently, the position vector $\mathbf{r}_{Ej}$ of any point E of the rigid body at the *j*-pose can be determined through the matrix equation:

$$\mathbf{r}_{Ej} = \mathbf{D}_{ij}\,\mathbf{r}_{Ei} \tag{3}$$

where $\mathbf{r}_{Ei}$ is the position vector of E at E_i starting position. Of course, the same can be done for the point B, when $\mathbf{r}_{Bi}$ is assigned.

Moreover, the same finite displacement of the rigid body from the *i*- to the *j*-pose can be also performed through a pure rotation of the angle ϑ_{ij} about the rotation pole P_{ij}, which position vector $\mathbf{r}_{ij}$ can be expressed in homogeneous coordinates as

$$\mathbf{r}_{ij} = \begin{bmatrix} x_{ij} & y_{ij} & 1 \end{bmatrix}^T \tag{4}$$

where the Cartesian components x_{ij} and y_{ij} are given by

$$x_{ij} = \frac{x_i + x_j}{2} + (y_i - y_j)\frac{\sin\vartheta_{ij}}{2(1-\cos\vartheta_{ij})} \tag{5}$$

$$y_{ij} = \frac{y_i + y_j}{2} + (x_j - x_i)\frac{\sin\vartheta_{ij}}{2(1-\cos\vartheta_{ij})} \tag{6}$$

Thus, a suitable formulation to determine the pole triangle that is made by the rotation poles P_{12}, P_{23} and P_{13}, its circumcircle, along with the three mirror images of it with respect to each edge of the pole triangle, which also intersect each other at the cardinal point H_C (orthocenter), is developed. In particular, each side of the pole triangle and the position of H_C are obtained by applying the analytical geometry. The circumcircle Cp of the pole triangle can be formulated by imposing at the circle to pass through the rotation poles $P_{12} = (x_{12}, y_{12})$, $P_{23} = (x_{23}, y_{23})$ and $P_{13} = (x_{13}, y_{13})$, which gives the following linear system of three equations in three unknowns:

$$\mathbf{C}\mathbf{X} = \mathbf{G} \tag{7}$$

where $\mathbf{C}$ and $\mathbf{G}$ are given by

$$\mathbf{C} = \begin{bmatrix} x_{12} & y_{12} & 1 \\ x_{23} & y_{23} & 1 \\ x_{13} & y_{13} & 1 \end{bmatrix} \qquad \mathbf{G} = \begin{bmatrix} -(x_{12}^2 + y_{12}^2) \\ -(x_{23}^2 + y_{23}^2) \\ -(x_{13}^2 + y_{13}^2) \end{bmatrix} \tag{8}$$

while the column vector $\mathbf{X}$ takes the form

$$\mathbf{X} = \begin{bmatrix} a & b & c \end{bmatrix}^T \tag{9}$$

where a, b and c are the coefficient of the following algebraic equation of Cp

$$y^2 + x^2 + ax + by + c = 0 \tag{10}$$

Thus, the linear algebraic system of Eq. (6) can be solved by applying the Cramer method, as follows:

$$a = \frac{1}{\det\mathbf{C}} \det \begin{bmatrix} -(x_{12}^2 + y_{12}^2) & y_{12} & 1 \\ -(x_{23}^2 + y_{23}^2) & y_{23} & 1 \\ -(x_{13}^2 + y_{13}^2) & y_{13} & 1 \end{bmatrix} \tag{11}$$

$$b=\frac{1}{\det \mathbf{C}}\det\begin{bmatrix} x_{12} & -\left(x_{12}^2+y_{12}^2\right) & 1 \\ x_{23} & -\left(x_{23}^2+y_{23}^2\right) & 1 \\ x_{13} & -\left(x_{13}^2+y_{13}^2\right) & 1 \end{bmatrix} \tag{12}$$

$$c=\frac{1}{\det \mathbf{C}}\det\begin{bmatrix} x_{12} & y_{12} & -\left(x_{12}^2+y_{12}^2\right) \\ x_{23} & y_{23} & -\left(x_{23}^2+y_{23}^2\right) \\ x_{13} & y_{13} & -\left(x_{13}^2+y_{13}^2\right) \end{bmatrix} \tag{13}$$

Similarly, still referring to Fig. 2, the equations of the three mirror circles Γ_1, Γ_2 and Γ_3, which pass through the orthocenter H_C of the pole triangle, are determined in the same way by applying the analytical geometry. Thus, the kinematic synthesis of Oldham mechanisms is carried out by choosing the two arbitrary points S and S_1 on the circumcircle Cp, which represent respectively the fixed revolute joints A_0 and B_0 of the two pistons sketched in Fig.1, in order to guide with a one d.o.f., the coupler rigid body by means of the slots of the two prismatic pairs.

Referring to Figs. 2 and 3, the three successive poses I, II and III of the coupler rigid body, which correspond to the three assigned finitely separated positions A_1-B_1, A_2-B_2 and A_3-B_3, are achieved by tracing the three lines passing through H_C and that are normal to each side of the pole triangle, by giving the points H_1, H_2 and H_3, respectively, as intersections of these straight lines with the circumcircle Cp. Consequently, referring to Fig. 3a, the axes of the two straight slots pass through the points S and H_1, and S_1 and H_1, for the starting pose I and likewise, through S-H_2 and S_1-H_2 for the pose II, and finally, through S-H_3 and S_1-H_3 for the pose III. Of course, even this graphical synthesis procedure has been formulated in the form of algorithm by applying the analytical geometry with the aim to obtain a whole synthesis algorithm of Oldham mechanisms for three-finitely separated positions. The coupler curves of both points S and S_1, that are considered as belonging to the coupler rigid body with two slots, are determined in vector and matrix form. In particular, taking into account that this rigid body motion can be considered as the inverse motion of the Cardan mechanism, the centrodes are represented by the same Cardan circles, where the internal circle is fixed and having a diameter that is equal to the radius of the external moving circle, by giving a typical epitrochoid motion. Referring to Fig. 3b, the position vector $\mathbf{c}$ of the center C of Cp is expressed as:

$$\mathbf{c}=\begin{bmatrix} -a/2 & -b/2 & 1 \end{bmatrix}^T \tag{14}$$

while the position vector $\mathbf{h}_1^*$ of point H_1^* can be obtained by the vector-loop equation:

$$\mathbf{h}_1^*=\mathbf{c}+\mathbf{r} \tag{15}$$

where the position vector $\mathbf{r}$ is given by

$$\mathbf{r}=\begin{bmatrix} r\cos(2\theta+\alpha) & r\sin(2\theta+\alpha) & 1 \end{bmatrix}^T \tag{16}$$

Thus, substituting Eqs. (14) and (16) into Eq. (15), one has

$$\mathbf{h}_1^*=\begin{bmatrix} -\frac{a}{2}+r\cos(2\theta+\alpha) & -\frac{b}{2}+r\sin(2\theta+\alpha) & 1 \end{bmatrix}^T \tag{17}$$

where θ is the counterclockwise angle shown in Fig. 3.

The position vectors $\mathbf{s}^*$ and $\mathbf{s}_1^*$ of points S^* and S_1^* are obtained by the following loop-closure equations

$$\mathbf{s}^*=\mathbf{c}+\mathbf{r}+\mathbf{h}_S \tag{18}$$

$$\mathbf{s}_1^*=\mathbf{c}+\mathbf{r}+\mathbf{h}_{S1} \tag{19}$$

where the position vectors $\mathbf{h}_S$ and $\mathbf{h}_{S1}$ of points S^* and S_1^* with respect to H_1^* are given by

$$\mathbf{h}_S=\begin{bmatrix} -h_S\cos(\theta-\varphi_1) & -h_S\sin(\theta-\varphi_1) & 1 \end{bmatrix}^T \tag{20}$$

$$\mathbf{h}_{S1}=\begin{bmatrix} -h_{S1}\cos(\theta-\varphi_2) & -h_{S1}\sin(\theta-\varphi_2) & 1 \end{bmatrix}^T \tag{21}$$

Therefore, the coupler curves of both points S^* and S_1^* are obtained in vector function form by substituting the Eqs. (14), (16), (20) and (21) into Eqs. (18) and (19), respectively, as follows

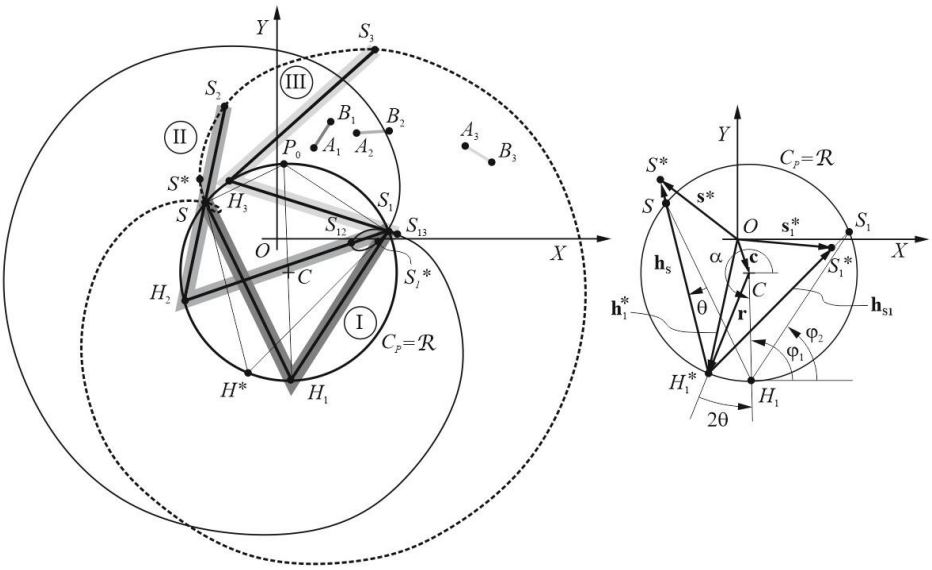
$$\mathbf{s}^*=\begin{bmatrix} -a/2+r\cos(2\theta+\alpha)-h_S\cos(\theta-\varphi_1) \\ -b/2+r\sin(2\theta+\alpha)-h_S\sin(\theta-\varphi_1) \\ 1 \end{bmatrix} \tag{22}$$

$$\mathbf{s}_1^*=\begin{bmatrix} -a/2+r\cos(2\theta+\alpha)-h_{S1}\cos(\theta-\varphi_2) \\ -b/2+r\sin(2\theta+\alpha)-h_{S1}\sin(\theta-\varphi_2) \\ 1 \end{bmatrix} \tag{23}$$

where the angles α, φ_1, φ_2 are shown in Fig. 3b as depending by points H_1, S and S_1. These trajectories of points S^* and S_1^* are sketched in Fig.3 by showing the typical shape of two epitrochoids, since obtained by rolling the external circle on the internal one of the inverse Cardan centrodes.

2.2 GENERAL OLDHAM MECHANISM: CENTRODES AND GEOMETRIC LOCI

The general Oldham mechanism with inclined slots is of 2R2P type and thus, shows a coupler link with two glyphs, which are coupled with the two corresponding pistons, each rotating around their fixed revolute joints. Thus, the instantaneous center of rotation IC of the coupler link traces the fixed and moving centrodes on the corresponding fixed and moving planes by remaining tangent each other at the IC. As it is well known, the coupler motion can be replaced by the pure-rolling of the moving centrode on the fixed one. The inflection and return circles are the mirror image of each other, with respect to the common tangent to both centrodes at the IC. In particular, the first is the locus of all coupler points showing an inflection at their paths, while the second is the locus of all center of curvature of all points at infinity. Finally, the circling-points and center-points curves are the geometric loci of all points showing a stationary curvature and their corresponding centers of curvature, respectively. The fixed and moving centrodes, the inflection and return circles, along with the circling-points and center-points curves, are geometric loci, which exchange their role under a kinematic inversion, which means that these loci are the same of those regarding the Cardan mechanism.



a) b)

Figure 3 General Oldham mechanism with inclined slots: a) epitrochoid coupler curves of points S and S_1 with cusps; b) position vectors and corresponding vector loops.

Therefore, these loci are now formulated by starting with the fixed and moving centrodes, and thus, referring to Fig.4, the Cartesian-coordinates of the instantaneous center of rotation P_0 are determined by using the analytical geometry and according to Chasles theorem, as follows

$$y-y_S=-(1/m_1)(x-x_S) \quad y-y_{S1}=-(1/m_2)(x-x_{S1}) \tag{24}$$

where the angular coefficients m_1 and m_2, are given by

$$m_1=\frac{y_S-y_{H1}}{x_S-x_{H1}} \quad m_2=\frac{y_{S1}-y_{H1}}{x_{S1}-x_{H1}} \tag{25}$$

Points S and S_1 are the fixed revolute joints and H_1 is the moving intersecting point of both glyph axes.

Consequently, the position vector $\mathbf{r}_{P0}$ of P_0 with respect the fixed frame OXY and as function of the motion parameter θ, represents the fixed centrode λ, which takes the form

$$\mathbf{r}_{P0}=\frac{1}{m_1-m_2}\begin{bmatrix}(m_1x_{S1}-m_2x_S)-m_1m_2(y_S-y_{S1})\\ x_S-x_{S1}+m_1y_S-m_2y_{S1}\\ 1\end{bmatrix} \tag{26}$$

The moving centrode can be expressed with respect the moving frame $\Omega x\,y$ by the following equation

$$\mathbf{r}_{P0}^*=\delta\begin{bmatrix}\cos\phi & \sin\phi & 1\end{bmatrix}^T \tag{27}$$

where δ is the diameter of both inflection and the return circles, while the angle ϕ is given by

$$\phi=\tan^{-1}\left[m_1-(y_{P0}-y_{H1})/(x_{P0}-x_{H1})\right] \tag{28}$$

In order to express both moving centrode $\mathbf{r}_{P0}^*$ of the coupler link with respect to the fixed frame OXY, the position vectors $\mathbf{r}_{P0}$ and $\mathbf{r}_{P0*}$ are multiplied for the corresponding transformation matrix $\mathbf{T}$, that can be in expressed by:

$$\mathbf{T}=\begin{bmatrix}\cos\beta & -\sin\beta & x_\Omega\\ \sin\beta & \cos\beta & y_\Omega\\ 0 & 0 & 1\end{bmatrix} \tag{29}$$

where β is the counterclockwise rotation angle of $\Omega x\,y$ with respect to OXY, while x_Ω and y_Ω are the Cartesian coordinates of the origin Ω in the same fixed frame. The return circle $\mathcal{R}$ for the pose I coincides with Cp and the cross center H_1 of the slots moves along Cp as opposite point of P_0 and thus, representing the return or cuspidal pole R. The inflection circle $\mathcal{I}$ can be obtained by mirroring the return circle $\mathcal{R}$ with respect the tangent line t_{P0} at point P_0. Thus, the inflection pole I_0 is located diametrically opposite to P_0 on $\mathcal{I}$. Both centers of $\mathcal{I}$ and $\mathcal{R}$ circles lies on the line n_{P0} that is perpendicular to the tangent line $t_{P0.}$ Regarding the circling-points and center-points curves, it noteworthy that some points on the moving plane have stationary curvature, i.e. the rate of change of their curvature radius with respect to reference position is zero. At this aim, the canonical reference frame of Fig. 4 has the origin in P_0, the abscissa axis coinciding with the tangent t to both centrodes l and λ at the P_0 point and the n-axis orthogonal to t and oriented toward the moving centrode l. In particular, the circling-points curve C_{SC} is the locus of the coupler points whose paths have, at least, four contact points with their osculating circles, which means to have a stationary curvature. Moreover, this geometric locus is represented by a third order algebraic curve, as in [16]. Thus, the equation of the circling-points curve C_{SC} can be expressed in the canonical frame as follows:

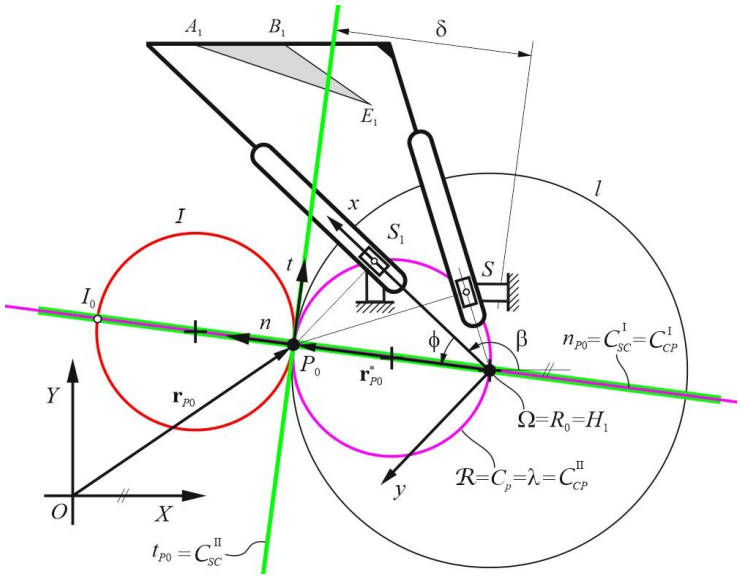


Figure 4 General Oldham mechanism: centrodes, inflection and return circles, circling-points and center-points curves.

$$\left(x^2+y^2\right)\left(\frac{x}{M}+\frac{y}{N}\right)-xy=0 \tag{30}$$

where M and N are the instantaneous geometric invariants and the x and y Cartesian-coordinates are supposed in this case to be coincident with the t and n axes, respectively.

In order to analyse the eventual degenerate forms, the Eq.(30) can be conveniently expressed in the homogeneous coordinates x_0, x_1 and x_2 as follows

$$x=\frac{x_1}{x_0} \qquad y=\frac{x_2}{x_0} \tag{31}$$

where x_0 in equal to 0 or 1 for proper and improper points, respectively. Thus, one has

$$\left(\frac{x_1^2}{x_0^2}+\frac{x_2^2}{x_0^2}\right)\left(\frac{x_1}{M\,x_0}+\frac{x_2}{N\,x_0}\right)-\frac{x_1x_2}{x_0^2}=0 \tag{32}$$

and, in turn

$$\left(x_1^2+x_2^2\right)+\left(\frac{x_1}{M}+\frac{x_2}{N}\right)-x_0x_1x_2=0 \tag{33}$$

The instantaneous geometric invariants M and N can be expressed with respect to the diameter δ of the inflection circle $\mathcal{I}$ and the radii of curvature r_λ and r_l of both centrodes λ and l, as follows

$$M=-\frac{3\delta}{\dfrac{\mathrm{d}\delta}{\mathrm{d}s}} \tag{34}$$

$$N=\frac{3r_\lambda r_l}{2r_\lambda-r_l} \tag{35}$$

However, in the case of the general Oldham mechanism, the centrodes are two circles and consequently, the diameter δ is constant, by which $M \rightarrow \infty$, along with N, since $r_l=2r_\lambda$ that substituted in Eq. (35), gives $N \rightarrow \infty$.

As a consequence, Eq. (33) takes the form

$$x_0\,x_1\,x_2=0 \tag{36}$$

which means that the circling-points curve C_{SC} degenerates into three straight lines of equations:

$$x_1=0\,,\quad x_2=0 \quad \text{and} \quad x_0=0 \tag{37}$$

where the first two corresponds to the abscissa and ordinate axes of the canonical frame, respectively, while $x_0=0$ is the line at infinity. In particular, these two real straight lines are indicated into Fig. 4, along with the next figures, with the symbols C_{SC}^{I} and C_{SC}^{II}.

Of course, these equations of the degenerate circling-points curve are then referred to the fixed frame OXY.

Similarly, the equation of the center-points curve C_{CP} is still expressed into the canonical frame with the origin in P_0 by considering that the novel instantaneous geometric invariants $\overline{M}$ and $\overline{N}$ are given by

$$\frac{1}{\overline{N}}=\frac{1}{\delta}-\frac{1}{N} \qquad \overline{N}=\delta \tag{38}$$

$$\frac{1}{\overline{M}}=-\frac{1}{M} \qquad \overline{M}\rightarrow\infty \tag{39}$$

Thus, substituting $\overline{M}$ and $\overline{N}$ of Eqs. (38) and (39), respectively, into the Eq. (30), one has

$$\begin{aligned}&\left(x^2+y^2-\delta x\right)=0\\ &y=0\end{aligned} \tag{40}$$

which means that the center-points curve degenerates into a ϕ-curve, i.e. the return circle $\mathcal{R}$ and the common normal to the centrodes at the P_0 point.

In particular, these two branches of the center-points curve are indicated into Fig. 4, along with the next figures, with the symbols C_{CP}^{I} (straight-line) and C_{CP}^{II} (circle).

Moreover, the intersection point of the circling-points curve C_{SC} and the infection circle $\mathcal{I}$ gives Ball's point, that is a

particular point of the moving plane, which traces a straight line with a third order approximation. These geometric loci and in particular, the circling-points and center-points curves, along with Ball's point, are fundamental tools to synthesize six-bar dwell mechanisms, as based on the three-poses rigid-body guidance of general Oldham type. In fact, any point laying on the circling-points curve, which consists in two straight lines coinciding with the canonical frame axes, is characterized by a coupler curve that has a stationary curvature and a center of curvature lying on the corresponding center-points curve. These two points are related each other by the Euler-Savary equation by using the centrodes or the inflection circle. Therefore, referring to Fig. 5a and choosing, for example, the point C on the C_{SC}^{I}, the center of curvature Ω_C is calculated by using the Euler-Savary equation, as follows

$$\Omega_C C = \left(P_0 C\right)^2 / C'C \tag{41}$$

where C' is the corresponding point of C laying on $\boldsymbol{I}$.

Thus, the RR dyad can be added by joining C and D with the link 5 and this last with D_0 of the fixed plane with the dwell link 6.

The RP dyad can be added to the three-poses rigid-body guidance of general Oldham type, by using Ball's point at the intersection between $\boldsymbol{I}$ and C_{SC}^{I}, and installing there the moving revolute joint in C, along with the prismatic pair that is composed by the piston 5 and the dwell glyph 6.

3 GRAPHICAL AND NUMERICAL RESULTS

The proposed general algorithm for the synthesis of Oldham six-bar dwell mechanisms for three-pose rigid-body guidance with inclined and/or orthogonal slots for three-finitely separated positions has been implemented in Matlab, in order to run significant examples for validation purposes. In particular, referring to Figs. 6 and 7, the first two examples of Figs. 6a and 6b show the pole triangle and its circumcircle, along with the three mirror circles and the orthocenter, by starting with the knowledge of the three poses A_1B_1, A_2B_2 and A_3B_3, while Figs. 7a and 7b refer to the case of inclined slots and Figs. 7c and 7d refer to the case of orthogonal slots. The corresponding input data are: A_1 = (30, 120) mm, B_1 = (60, 120) mm, A_2 = (120, 130) mm, B_2 = (135, 104.02) mm, A_3 = (190, 110) mm, B_3 = (184.8, 80.5) mm, θ_{12} = − 60°; θ_{23} = − 40°; θ_{13} = −100°; Case 1: S = (90, 48.9) mm, S_1 = (120, 38.6) mm; Case 2: S = (100, 49.2) mm, S_1 = (91.7, −15.08) mm. Regarding the synthesis of mechanisms with oscillating glyph, as shown in Fig. 7, the homologous points H_1, H_2 and H_3 of the cardinal point H_C must be determined as the symmetric points of H_C with respect to the first, second and third edge of the pole triangle, respectively. For example, H_1 is the symmetric point of H_C with respect to the straight line passing through the rotation poles P_{12} and P_{13}, which have in common the subscript 1, and so on for H_2 and H_3. These points are important because when a suitable point S is chosen on the circumcircle, in order to install the oscillating glyph, a moving straight-line passing through the points S and H_1 at the first pose, will pass through S and H_2 at the second pose, and through S and H_3 at the third pose of the moving plane. In particular, the trajectories of three-finitely separated positions I, II and III along with the epitrochoid coupler curves are shown in Figs.7c and 7d, respectively.

Figures 8 and 9 show the obtained six-bar dwell mechanisms for three-pose rigid body guidance along with the geometric loci for the case of inclined and orthogonal slots, respectively. The circling-points curve degenerates in two real and orthogonal straight lines, which coincide with the canonical frame axes. Similarly, the center-points curve C_{CP} degenerates into a ϕ-curve, where the circle C_{CP}^{II} coincides with both the return circle $\mathcal{R}$ and the fixed centrode λ, while the straight-line C_{CP}^{I} coincides with the common normal to centrodes at P_0.

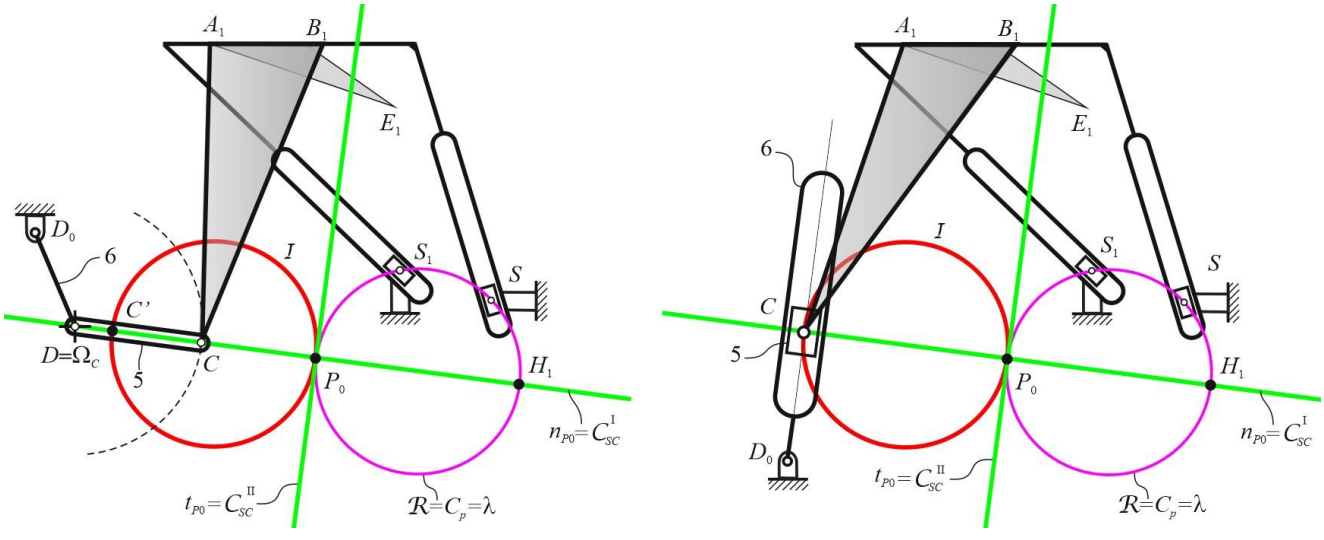


Figure 5 Dwell part synthesis of Oldham chain based six-bar dwell mechanisms: a) RR dyad; b) RP dyad.

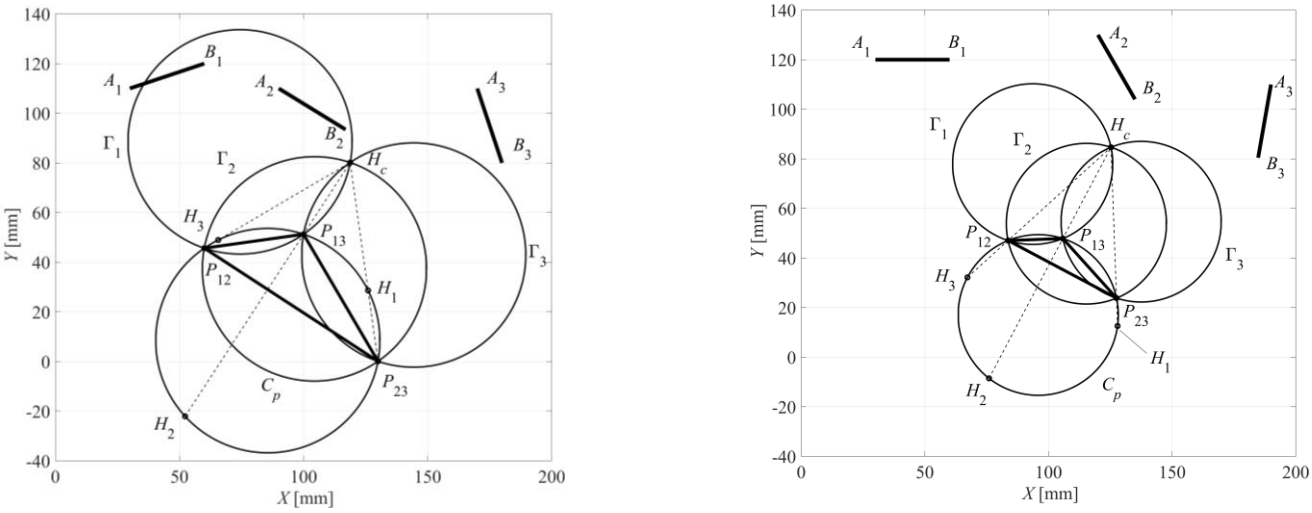


Figure 6 Synthesis of Oldham mechanisms for three-pose rigid-body guidance: a) & b) pole triangle and circles.

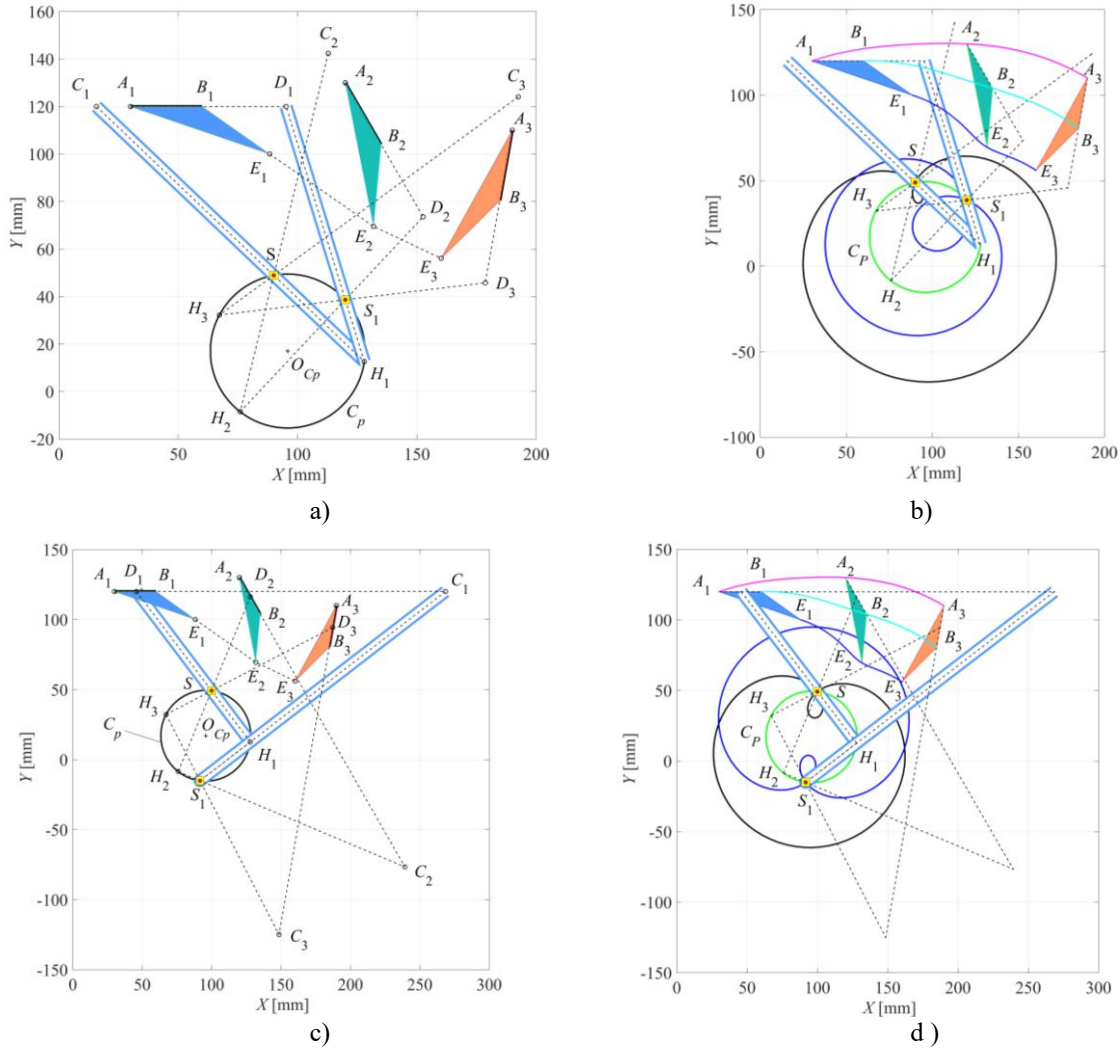
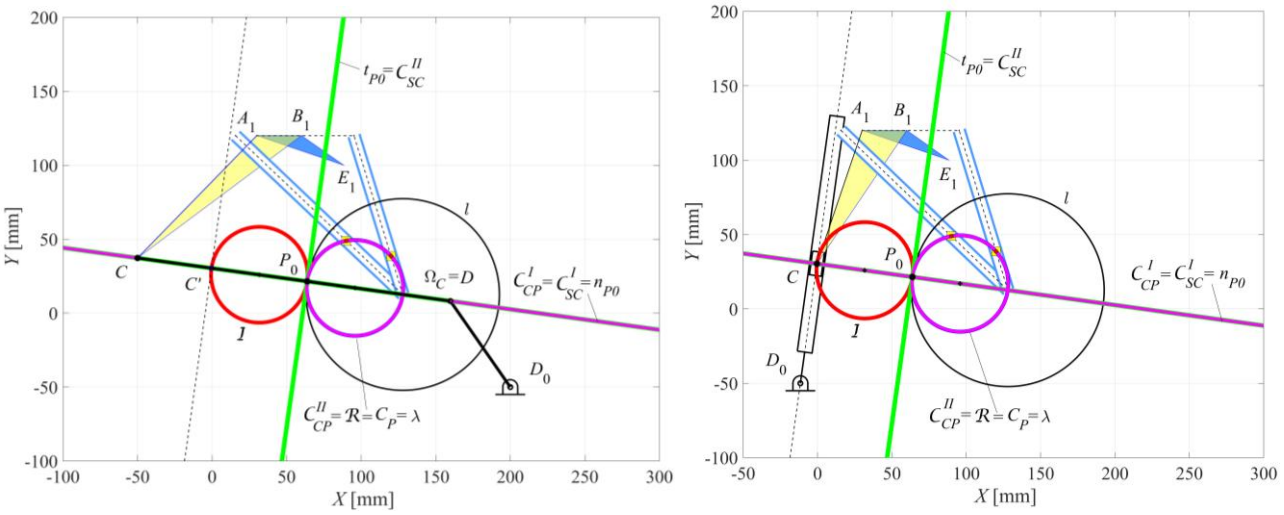
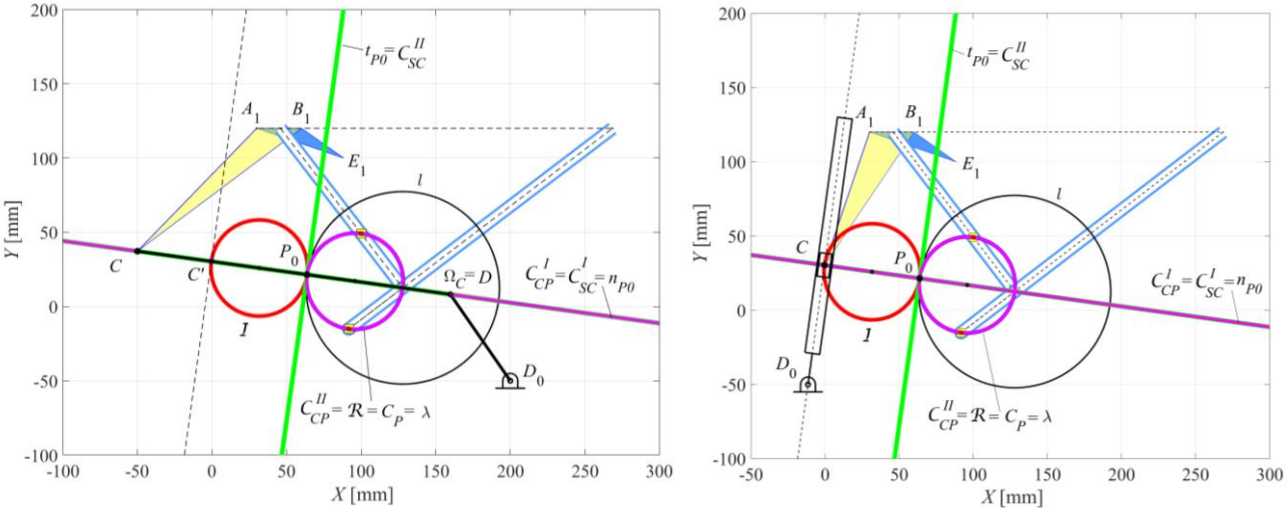


Figure 7 Synthesis of Oldham mechanisms for three-pose rigid-body guidance: Case 1: a) inclined slots; b) epitrochoid coupler curves; Case 2: c) orthogonal slots; d) epitrochoid coupler curves.



a) b)

Figure 8 Oldham chain based six-bar dwell mechanisms (case of inclined slots): a) RR dyad; b) RP dyad.



a) b)

Figure 9 Oldham chain based six-bar dwell mechanisms (case of orthogonal slots): a) RR dyad; b) RP dyad.

In the case of RR dyad, the chosen point on the circling-points curve is C = (–50, 37.27) mm, while in the case of the RP dyad, the Ball point that is still indicated with C has coordinates C = (–0.41, 30.39) mm. The fixed revolute joint D_0 for the RR case, has coordinates D_0 = (200, –50) mm, while for the RP dyad one has D_0 = (–11.55, –50) mm.

4. CONCLUSIONS

The kinematic synthesis of six-bar dwell mechanisms based on the Oldham kinematic chain for three-pose rigid-body guidance has been developed.

The proposed approach extends the classical three-pose synthesis problem by adding a RR and/or a RP dyad to the Oldham base chain, introducing a dwell in the output link. Unlike conventional design approaches, where the same link undergoes both finite and infinitesimal displacements, in the proposed mechanism, the coupler link of the Oldham mechanism exactly passes through the three prescribed poses, while the output link of the obtained six-bar linkage presents a dwell. A mathematical formulation of the problem has been carried out, along with a general synthesis algorithm, in order to design the three-pose guidance for the Oldham mechanism coupler link and to allow the output link dwell to occur at any desired configuration. The proposed algorithm has been implemented in Matlab and validated through several graphical and numerical examples. Further developments may focus on increasing the number of prescribed finite positions, extending the method to four or more poses, or enhancing the dwell duration by exploring the design of long-dwell mechanisms.

REFERENCES

[1] Beyer R., *The kinematic synthesis of mechanisms. London*. Chapman & Hall, 1963.

[2] Chiang C.H., *Kinematics and design of planar mechanisms*. Malabar, FL: Krieger, 2004.

[3] Hall A.S., *Kinematics and linkage design*. Prospect Heights, IL, Waveland Press, 1986.

[4] Hartenberg R.S. and Denavit J., *Kinematic synthesis of linkages*. McGraw-Hill, 1964.

[5] Hayes M. and Zsombor-Murray P., Towards integrated type and dimensional synthesis of mechanisms for rigid body guidance. *Proc. of the 2004 CSME Forum*, University of Western Ontario, London, ON, Canada, pp. 53-61, 2004.

[6] Tomassi L., Lanni C. and Figliolini G. A novel design method of four-bar linkages mimicking the human knee joint in the sagittal plane. *Niola, V., Gasparetto, A., Quaglia, G., Carbone, G. (eds) Advances in Italian Mechanism Science. IFToMM Italy 2022. Mechanisms and Machine Science*, Springer, Cham, Vol. 122, pp 586–592, 2022.

[7] Myszka D.H., and Murray A.P., Pole arrangements that introduce prismatic joints into the design space of four- and five-position rigid-body synthesis. *Mechanism and Machine Theory*, Vol. 45, No. 9, pp. 1314-1325, 2010.

[8] Zhao K., Schmiedeler, J.P., and Murray A.P., Kinematic synthesis of planar, shape-changing rigid-body mechanisms with prismatic joints. *Proc. of the ASME 2011 International Design Engineering Technical Conferences and Computers and Information in Engineering Conference - 35th Mechanisms and Robotics Conference, Parts A and B*. Washington, DC, USA, Vol. 6, pp. 523-533, 2011.

[9] Freudenstein F., Tsai L.W. and Maki E.R., The generalized Oldham coupling. *Journal of Mechanisms, Transmissions, and Automation in Design*, Vol. 106, No. 4, pp. 475–481, 1984.

[10] Hsieh W.H. and Tsai C.H., On the kinematic of generalized Oldham couplings. *Key Engineering Materials*, Vol. 661, pp. 10–15, 2015.

[11] Zhu Y., Yuan W. Guo, Q. Wang W., Zhang L. and Zhu S., Kinematic characteristics analysis of orbiting scroll and structural optimization of Oldham's coupling in scroll compression. *Machines* **2022**, Vol. 10, paper number 623.

[12] Hill M.F., *Kinematics of gerotors*. The Peter Reilly Company, Philadelphia, PA, 1927.

[13] Colbourne J.R., The geometry of trochoid envelopes and their application in rotary pumps. *Mechanism and Machine Theory*, Vol. 9, No. 3–4, pp. 421–435, 1974.

[14] Figliolini G., Rea P., and Grande S., Kinematic synthesis of rotary machines generated by regular curve-polygons. ASME *Journal of Mechanical Design,* Vol. 138, No. 2, 022301 (9 pages), 2016.

[15] Pennestrì E., *Engineering kinematics: mechanisms design for finitely separated positions*. Amazon. Roma, 2020.

[16] Stachel H., Strophoids, a family of cubic curves with remarkable properties. *Journal of Industrial Design and Engineering Graphics*, Vol. 10, No. 1, pp. 65–72, 2015.

[17] Gordon R. Pennock G.R. and Israr A., Kinematic analysis and synthesis of an adjustable six-bar linkage, *Mechanism and Machine Theory*, Vol. 44, No. 2, pp. 306-323, 2009.

[18] Čavić M., Penčić M., Rackov M., Dorić J. and Lu Z. Graphical synthesis of 6-bar dwell linkage mechanism. *FME Transactions*. Vol. 47, No. 2, pp. 226-233, 2019.

[19] Pasika V., Nosko P., Nosko O., Bashta O., Heletiy V. and Melnyk V., A method to synthesise groove cam Geneva mechanisms with increased dwell period. *Proc. of the Institution of Mechanical Engineers, Part C: Journal of Mechanical Engineering Science*. Vol. 238, No. 15, pp.7544-7555, 2024.

[20] Chang Z., Xu C., Pan T., Wang L. and Zhang X., A general framework for geometry design of indexing cam mechanism, *Mechanism and Machine Theory*, Vol. 44, No. 11, pp. 2079-2084, 2009.

[21] Callegari M., Luca Carbonari L., Palmieri G., Palpacelli M.-C., Functional Design of a Manipulator for the Automation of Laboratory Precision Tasks, *International Journal of Mechanics and Control*, Vol. 21, No. 02, pp. 29-37, 2020.

[22] Figliolini G., Lanni C., and Tomassi, L., Synthesis and analysis of Stephenson III six-bar motion generators with an instantaneous stop link. ASME. *Journal of Mechanisms and Robotics*, Vol. 17, No. 4, 044510 (7 pages), 2025**.**

[23] Figliolini G. Lanni C. and Tomassi L., First- and second-order centrodes of both coupler links of Stephenson III six-bar mechanisms. *Machines*, Vol. 13, No. 2, paper number 93, 2025.

[24] Tesar D., The generalized concept of three multiply separated positions in coplanar motion. *Journal of Mechanisms*, Vol. 2, No. 4, pp. 461-474, 1967;

[25] Tesar D., The generalized concept of four multiply separated positions in coplanar motion. *Journal of Mechanisms*. Vol. 3, No. 1, pp.11-23, 1968.

[26] Dijksman E.A., Geometrical treatment of the PPP-P case in coplanar motion (three infinitesimally and one finitely separated positions of a plane). *Journal of Mechanisms,* Vol. 4, No. 4, pp. 375-389, 1969.

ISSN 1590-8844
International Journal of Mechanics and Control, Vol. 26, No. 02, 2025
https://doi.org/10.69076/jomac.2025.0002

PERFORMANCE AND EFFICIENCY PF A HYBRID SELF-PROPELLED CABLE LOGGING CARRIAGE: AN EXPERIMENTAL STUDY

Stefan Leitner[*,**] Lorenzo Maccioni[*] Giovanni Carabin [*] Raffaele Spinelli [***] Renato Vidoni[*,****]

[*] Free University of Bozen-Bolzano, Bolzano (Italy)
[**] LeitAlpin GmbH, Bolzano (Italy) - https://www.leitalpin.com/en
[***] Consiglio Nazionale delle Ricerche, Istituto per la Bioeconomia (CNR IBE), Sesto Fiorentino (Italy)
[****] Polytechnic Department of Engineering and Architecture, University of Udine, Udine (Italy)

ABSTRACT

Global warming and the dependance on expensive fossil fuels in uncertain times are two main drivers for the development of alternative drivetrains. The alpine logging sector is no exception. Indeed, electrification has demonstrated significant potential for fuel savings in cable logging applications, particularly due to the high capacity for energy recovery in cyclic operations involving variations in potential energy. This work presents results of a study involving several key sub-systems as well as the roundtrip efficiency of a hybrid self-propelled carriage called HULK. In addition to performance and efficiency studies of the engine-generator unit, energy dissipation unit and battery system, its two main drive systems, i.e., the dropline winch and the propulsion module, have been evaluated. The tests enabled the performance mapping of key components, identification of optimal operating points, and confirmation of the substantial energy recovery potential. Furthermore, the results highlight the feasibility of energy-autarkic operation in real-world transport applications.

Keywords: Drivetrain electrification, mechatronics, modelling, energy recovery, smart forestry

1 INTRODUCTION

Mechanization and automation are key to competing in today's fast-moving industries that demand ever higher productivity, product quality, traceability, reduced or safer personnel involvement and environmentally friendly operation. Moreover, to realize more environmentally-friendly vehicles and machines, promising solutions involve improving efficiency as well as energy recovery and regeneration, e.g. [1, 2, 3, 4]. This is also the case in the logging industry, especially in locations unsuitable for ground-based machinery operation where, thanks to the availability of new mechatronic and IoT technologies, smart and precision forestry concepts are gaining attention.

Cable logging solutions have a long history as the solution of choice to extract timber from difficult terrain, inaccessible to ground based vehicles. First cable logging solutions, primitive steam-powered apparatus, date back over 150 years [5]. Since then, yarders and carriages have undergone dramatic changes in multiple waves of innovation. Internal combustion engines, stepless hydraulic transmissions, and electronic control represent the most obvious major breakthroughs [6, 7]. The latest wave of innovation started around 10 years ago, with the introduction of the first electrified cable logging solutions [8, 9, 10]. The transition started with slack-pulling carriages, followed by tower yarders, dropline carriages and now also Self-Propelled Carriages (SPCs). A major challenge to overcome in the design of electrified cable logging equipment is to ensure reliable energy supply, given the inability to connect

Contact authors: S. Leitner[*], G. Carabin[*], Renato Vidoni[**],
[*] FiRST Lab, Free University of Bozen-Bolzano, 39100, Bolzano (I)
[**] Polytechnic Department of Engineering and Architecture, University of Udine, Via delle Scienze, 33100, Udine (I)
E-mail: stefan.leitner@unibz.it , giovanni.carabin@unibz.it , renato.vidoni@uniud.it

the equipment to the power grid. The first electric semi-automated carriages were presented in 2015 [11]. A more recent development is presented by the hybrid tower yarder K507e-H by Koller, i.e. series hybrid drivetrain, that stores recovered energy in an on-board high-voltage super-capacitor to be employed for the subsequent duty cycle [14]. Regenerative energy is complemented by an on-board engine-generator unit in start-stop control. Fuel savings have been shown to be almost 60 % compared to a conventional Diesel-hydraulic yarder in common cable yarding uphill setups. Fully electric models could be envisioned with large battery packs, to be charged by an external energy source when not in operation [15]. Energy supply to carriages offers more options. In the literature, a total of six energy supply concepts have been proposed for slack-pulling carriages, dropline carriages and SPCs [16]. Slack-pulling and dropline carriages require relatively little energy per cycle. Carriage-internal storage systems can be charged during lateral yarding, when lowering the payload, and/or while traveling along the cableway. SPCs need to also power the energy-hungry propulsion during out- and in-hauling, therefore requiring more extensive means of energy supply.
The latest development in the European cable yarding equipment sector is related to SPCs, i.e. fully motorized remote-controlled carriages capable of powering the extraction process without any additional equipment, with the presentation of an advanced prototype of a hybrid SPC by Leitalpin (Leitalpin GmbH, Bozen, Italy) named HULK [12]. So far, few studies have been presented on electrified cable logging equipment, and the existing literature provides insufficient knowledge about the performance and efficiency of these systems both in their main-subsystems and in actual applications.
This paper, starting from the preliminary results presented in [13], aims to provide an in-depth understanding of the performance and potential of energy recovery by the novel hybrid SPC prototype HULK, which in turn provides a better understanding of the amount of energy to be supplied by external means, i.e., via fuel.
The work is organized as follows: Section 2 describes the hybrid SPC HULK and its main subsystems. After that, data acquisition as well as test and simulation setup for the experimental evaluation are reported in Section 3. Results are presented and discussed in Section 4 together with considerations on their meaning for actual transport applications. This work is then concluded with an outlook on ongoing and future studies on this subject (Section 5).

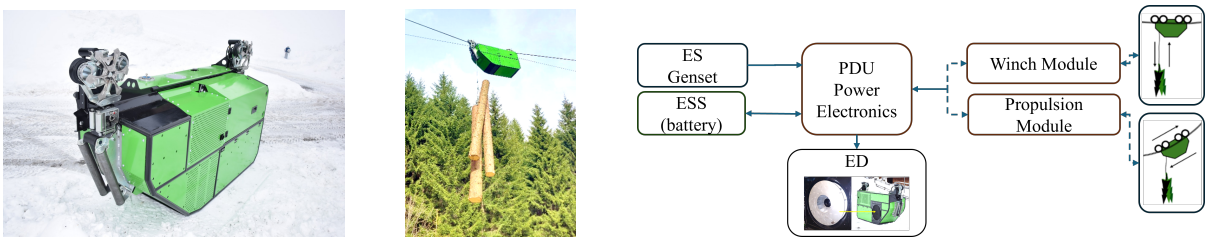
2 THE HYBRID SELF-PROPELLED CARRIAGE: HULK

The hybrid SPC HULK, depicted in Fig.s 1a, 1b, is the main subject studied in this work. Its key features and technical specifications are reported in Table I.

Table I - Key Features and Specifications of the SPC HULK

Dimensions LxWxH	2.4 x 0.75 x 1.5 m
Max Power	150 kW
Propulsion Speed	0.1 - 11 m/s
Propulsion Force	2 - 50 kN
Winch Speed	0.1 - 5 m/s
Winch Force	2 - 45 kN
Max Skyline Slope	$\pm$ 120 %
Hybrid Series Configuration	
Adaptive Energy Management	
Target Control (automated skyline support crossing)	
Long Range Remote Control	
Twin-Cable Configuration	

The drivetrain architecture is a series hybrid concept with independent drives for the dropline winch and for carriage propulsion, see Fig. 1. The Power Distribution Unit (PDU) is at the center of this setup and serves as the interconnection between all drivetrain parts. The Energy Source (ES), made up of a gasoline engine, mechanical transmission parts and a generator-inverter set, supplies energy to the carriage if the regenerative energy is not sufficient to cover the energy needs of the machine cycle. An Energy Storage System (ESS) with discharging/charging efficiency $\eta_{ESS_{C/DC}}$ is connected to the PDU and stabilizes the system voltage by providing and drawing energy at a rate of $P_{PDU_{ESS}}$ as needed. $P_{PDU_{ESS}}$ can be estimated as the sum of the power of all connected devices. ES power ($P_{PDU_{ES}}$) is determined by the fuel consumption rate (Q_{FUEL}) and overall ES efficiency (η_{ES}). Since handling heavy loads from a higher to a lower elevation can lead to overcome the limit of recoverable energy, an Energy Dissipation (ED) system, realized in the form of a high performance fan and depicted in Fig. 1c, is installed to generate energy dissipation power ($P_{PDU_{ED}}$).
The power drawn from or supplied to the PDU by the drives ($P_{PDU_{DR}}$), i.e. winch and propulsion modules, is a function of: instantaneous drive force (F_{DR}) and speed (v_{DR}); and total drive module efficiency in motoring (η_{MOT}) or regeneration (η_{GEN}) mode. Motoring mode is typically associated with lifting a load and moving the carriage uphill, while regenerative mode corresponds to lowering a load and traversing versus the lower end of the cableway. Performance and efficiency studies are to be performed both on single modules, i.e. ES, ED and ESS units, as well as on roundtrip tests for both the winch ($\eta_{W_{RT}}$) and propulsion modules ($\eta_{P_{RT}}$).
For the former, i.e. single modules, both the ES and ED are independent systems, which can be tested at machine standstill. During regular operation of the SPC, generator torque is controlled based on the engine's load factor to optimize its efficiency at every operating point. The engine, in turn, is speed controlled based on a power set-point



(a) (b) (c)

Figure 1 The HULK SPC: (a) and (b) the SPC advanced prototype; (c) Hulk main building blocks

computed within the energy management logic. For the ED, the fan is spun by a high-performance electric drive in power control, with cascading underlying torque and current control loops, respectively. The ED is activated by the SPC energy management logic to dissipate energy directly as it is generated at the drives, ensuring it occurs only during operation. The ESS employed in the SPCe is a power-density high-performance pack in the 800 V voltage range. Its power performance and efficiency are mainly determined by its impedance, which is highly dependent on the pack temperature and State-Of-Charge (SOC).

For the latter, i.e., roundtrip tests, the roundtrip efficiency analyzed in this study is defined as the percentage of energy recharged into the battery system during regeneration phases relative to the energy drawn from the battery during motoring phases. This is evaluated under the condition that the same mechanical work is performed on the carriage and/or payload during both motoring and regeneration phases.

3 EXPERIMENTAL SET-UP AND ROUNDTRIP TESTS SCENARIO

3.1 *Efficiency tests for ES, ED and ESS modules*

In this study, for the ES, the machine controller of the SPC was programmed in such a way that engine speed and generator torque could be controlled independently in predefined small steps. This allowed to set multiple speed-torque combinations.

For the ED, since the SPC offers an operational mode that allows direct control via the remote controller for testing and maintenance purposes, this mode was utilized to test the ED and gather performance data. Since the sole purpose of the ED is to remove excess energy from the system, its efficiency is mostly irrelevant. Still, it is desirable that the energy is dissipated directly at the fan, rather than converted to heat in the inverter-motor drive. In this study, the performance of the dissipation system drive components has been evaluated.

For the ESS, since pack impedance can only be determined indirectly by monitoring its voltage response to a change in current (or vice versa), to obtain responses at different cell temperatures and distinct SOC levels both for discharging and charging, an ad-hoc study has been performed: the pack was tested subjected to 10 kW of charging power (via the ES) and 25 kW of discharging power (via the ED) at various temperature-SOC operating points.

The data acquisition chain employed to obtain data during these tests is depicted in Fig. 2. CAN loggers, specifically of type CANedge1 of CSS Electronics were connected to the three CAN buses of the SPC to log and store the data. Every CANedge1 provides two independent channels, thus only two loggers were required. CAN bus data was stored in raw encrypted format on SD cards in the logging devices. The data were then converted and scaled to physical values via specifically developed Matlab code.

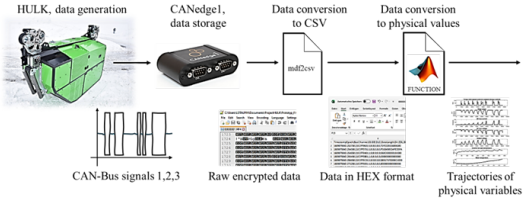


Figure 2 Data acquisition/conversion chain to obtain SPCe performance and efficiency data

3.2 *Roundtrip Efficiency Tests*

In 2024, a test campaign of the second prototype of HULK, an optimized version with respect to an earlier model tested after 2021, was performed by Leitalpin. Tests were carried out on a cableway installed by Leitalpin in the forests near Vipiteno, BZ, Italy. The installation concerned a standard standing skyline configuration, with a cableway length of about 400 m. The skyline had close to zero inclination at the lower end of the cableway, gradually rising to about 50 % slope versus the upper end of the installation. The objective of the tests were to obtain results of the roundtrip efficiencies of the winch and propulsion modules. Separate studies are carried out for the winch and the propulsion modules, evaluated via a combination of field tests and simulations.

Winch field tests consist of logging the winch motor torque during lifting ($T_{W_{LIFT}}(m_L)$) and lowering ($T_{W_{LOW}}(m_L)$) with various payloads, i.e, m_L between 0 kg and 2800 kg in steps of 700 kg.

Similarly, propulsion module field tests provide motor torque information for driving uphill ($T_{P_{UP}}$ (m_L,α_{SL})) and

downhill ($T_{P_{DOWN}}$ (m_L,α_{SL})) for the same set of payloads, and for skyline inclinations α_{SL} in the range of 0 % to 50 %. Assuming constant efficiencies for the electric drives, consisting of the power electronics and the electric motors (η_{DR}) and the battery system (η_{BAT}), both during charging and discharging, drive torque in motoring and regeneration phases becomes proportional to the energy needed and recovered, respectively. In addition, since the roundtrip efficiency is a ratio-based measure, variables such as the distances covered or the drive speeds during the field studies are canceled out, simplifying the estimation of the roundtrip efficiencies in (1) for the winch and (2) for the propulsion module, respectively.

$$\eta_{W_{RT}} = \frac{T_{W_{LOW}}(m_L) \cdot (\eta_{DR} \cdot \eta_{BAT})^2}{T_{W_{LIFT}}(m_L)} \tag{1}$$

$$\eta_{P_{RT}} = \frac{T_{P_{DOWN}}(m_L, \alpha_{SL}) \cdot (\eta_{DR} \cdot \eta_{BAT})^2}{T_{P_{UP}}(m_L, \alpha_{SL})} \tag{2}$$

η_{DR} and η_{BAT} were estimated thanks to the results of the single modules efficiency tests reported in the next section.

4 RESULTS AND DISCUSSION

4.1 ES, ED, ESS Modules

4.1.1 ES: Energy Source

A total of 120 engine speed-generator-torque combinations has been tested and engine speed, engine fuel consumption and ES power data collected. By setting the genset electrical output power in relation to the input power equivalent of the fuel consumption rate, the total genset efficiency can be determined through Eq. (3):

$$\eta_{ES} = \frac{P_{PDU_{ES}}}{Q_{FUEL} \cdot \gamma_{FUEL}} \tag{3}$$

where γ_{FUEL} is the specific energy density of gasoline (approx. 34.2 MJ/l or 9.5 kWh/l [18]).
In Table II the estimated results η_{ES} across the operating points given by Eq. (2) are reported while in Fig. 3 a visual representation is given.
As can be appreciated, the η_{ES} generally increases with the generator torque. Moreover, around 1800 rpm (close to minimum/idling speed) and 3000 rpm (engine nominal speed), (local) efficiency maxima are computed. While the former results in the largest η_{ES} of about 33.9 % at 45 Nm torque, the latter appears to be an ideal trade-off for power and efficiency, with an η_{ES} of about 25.6 % at 45 Nm torque.

4.1.2 Energy Dissipation System

To test the ED system, nine power levels from 5 kW up to a maximum of 50 kW were evaluated. The data have been collected by manually controlling the dissipation system. At peak performance, the dissipation system could reach about 100 kW of power at a speed of 7000 rpm, with the tangential speed of the dissipation system reaching Mach 0.55. Fig. 4 reports the trends of seven key dissipation system performance variables that are:

1. Torque-limit and set-point: The torque limit in speed control and the torque set-point in torque control sent to the inverter, given in Nm;
2. Motor speed: The motor speed driving the fan, given in rpm. Based on an arbitrary convention by Leitalpin, the propeller rotates in the negative direction;
3. DC bus current: The current flowing into the inverter at the HV DC terminals. This corresponds to the battery discharge current if no other loads are active;
4. DC bus voltage: The voltage at the inverter HV input DC terminals. This voltage follows the battery terminal voltage very closely;
5. Output voltage: The output voltage corresponds to the RMS voltage of the three-phase sinusoidal inverter output (motor input) voltage;
6. Inverter hot spot temperature: The temperature measured at the highest temperature point within the inverter. It corresponds to a measure close to the power semiconductors;
7. Motor temperature: The temperature measured within the stator windings of the PMSM machine.

Table II - ES efficiency as a function of engine speed and generator torque

Engine Speed [rpm]	*Generator Torque [Nm]*									
	0	5.0	10.0	15.0	20.0	25.0	30.0	35.0	40.0	45.0
1750	0.0	5.5	12.9	17.5	25.3	24.0	29.7	27.1	28.2	27.6
1800	0.0	4.3	15.4	18.5	21.4	28.0	31.1	30.7	31.8	33.9
1900	0.0	13.8	15.0	15.3	25.1	25.8	28.9	29.2	30.2	30.5
2000	0.0	7.6	8.8	11.3	13.9	17.8	19.6	20.1	22.5	21.7
2200	0.0	4.5	8.4	10.7	16.7	15.3	15.8	18.5	18.2	19.3
2400	0.0	7.2	7.7	14.4	14.4	16.5	17.3	18.9	19.3	19.3
2600	0.0	6.4	14.7	18.9	17.1	20.0	18.9	21.8	21.6	19.6
2800	0.0	6.2	14.9	18.0	19.6	22.3	21.4	21.6	21.5	20.0
3000	0.0	7.1	14.4	18.1	20.6	25.9	24.4	24.9	25.2	25.6
3200	0.0	4.7	9.4	14.1	19.2	22.2	23.1	23.6	23.9	20.2
3400	0.0	2.8	6.6	9.7	11.6	16.4	15.0	17.8	18.4	18.1
3600	0.0	3.8	6.9	10.8	11.8	17.1	17.3	18.4	17.8	17.2

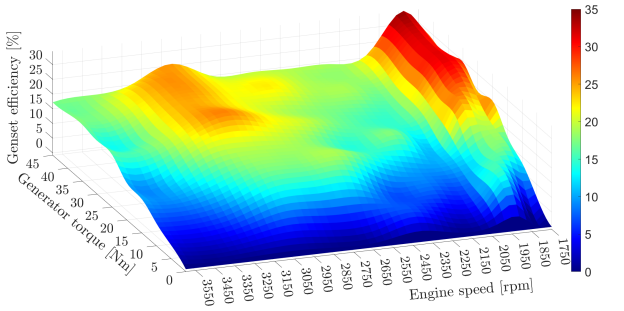


Figure 3 ES efficiency as a function of engine speed and generator torque: visual representation

The shape of the curves during operation, controlled by the energy management logic, depends on many operation variables and, while transitory data may only serve as an example, steady state data represent commonly expected operating points.

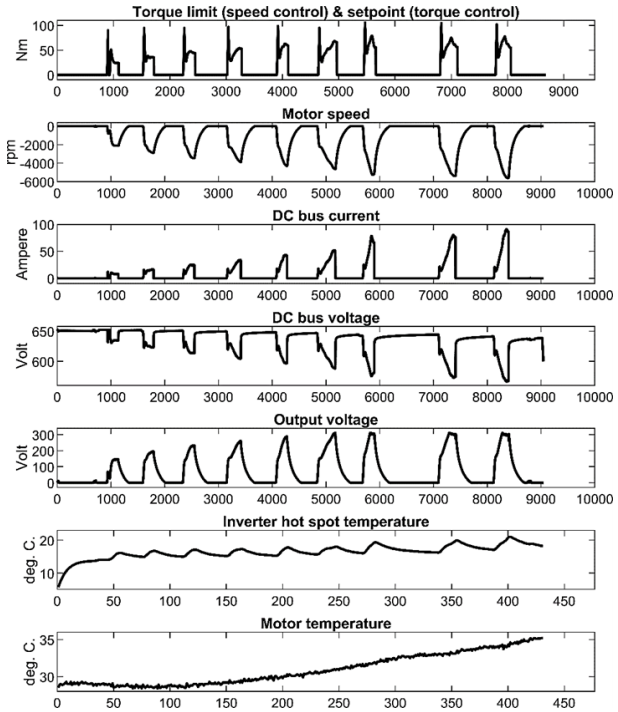


Figure 4 ED system: 7 key dissipation system performance variables during a test involving a tot. of 9 power levels (5 kW- 50 kW). X-axis: n° of samples during data acquisition

For each of the nine operating points, the product of the steady state values of DC bus current and voltage results in the electrical power input into the inverter. Similarly, the final steady state values of fan speed and torque define the mechanical output power of the motor. This provides nine independent propeller drive efficiency estimates at nine distinct operating points, as computed and reported in Table III. Through the inverter, current, voltage and speed are accurately measured. Motor torque is indirectly estimated by the inverter based on motor stator current measurements exploiting a simple linear model and the motor torque constant K_T [Nm/A]. Slight discrepancies between the K_T setting and actual motor properties, as well as nonlinear effects such as magnetic saturation can cause considerable deviations in the estimated vs. the generated torque. From the estimations, it clearly resulted that the K_T setting is too large since the inverter-motor efficiency will never reach 100 %. At the optimal operating point, the efficiency should reach about 95 %. A good approximation to the actual performance can thus be accomplished by down-scaling motor torque by a factor of 0.95 and re-estimating the motor output power and efficiency, accordingly. In Tab. III, data on which this compensation has been applied are labeled by (*). Looking at the electrical power draw from the dissipation system with respect to the motor speed, a non linear relationship (as foreseeable) can be appreciated, see Fig. 5. Indeed, while axial fans tend to have a somewhat torque-

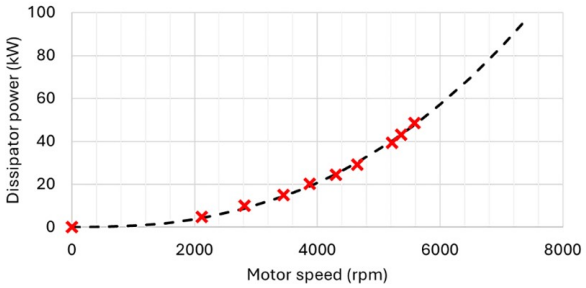


Figure 5 ED system: power drawn as a function of dissipation system motor speed n_{ED}

speed linear relationship, centrifugal fans typically follow a quadratic behavior. The dissipation system of the SPCe resembles a centrifugal fan but since there is limited space within the machine and the air flow is significantly restricted by the protective cover, torque does not rise in a quadratic way with speed but the dissipation system power $P_{PDU_{ED}}$ follows the following approximated behavior:

$$P_{PDU_{ED}} = k_{PDU_{UP}} \cdot n_{ED}^{2.5} \tag{4}$$

where n_{ED} is the fan speed in (rpm), $k_{PDU_{UP}}$ the estimated coefficient = $2.05 \cdot 10^{-8}$ and $P_{PDU_{ED}}$ is the dissipation system power in (kW).

From the curves shown in Fig. 4, looking at inverter hot spot and motor temperatures, their overall temperature rise is very similar. This indicates that they match well from a thermal (performance) standpoint. The thermal time constant (and capacity) is larger in the motor with respect to the inverter, such that its temperature does not respond swiftly to load changes. The power semiconductor in the inverter cannot absorb a lot of thermal energy and thus responds swiftly to current changes.

4.1.3 ESS: Energy Storage System

Tests were performed to characterize the ESS at different temperatures and distinct SOC levels both for charging (10 kW) and discharging (25 kW). Tested cell temperature levels are 5.5 °C (corresponding to air temperature), 11.4 °C and 16.6 °C. % SOC levels of 32 %, 45 %, 58 % and 71 % were evaluated. In Tab. IV the pack voltage rise and drop test results are reported together with the Open Circuit Voltages (OCV) at each of the SOC levels. Negative results report the pack voltage drop (ΔV_{ESS}) in response to 25 kW of power (drawn by the dissipation system), whereas positive results indicate a pack voltage rise (ΔV_{ESS}) in response to

Table III - ED system: electrical and mechanical performance and efficiency (torque corrected by a factor of 0.95

Operating point	1	2	3	4	5	6	7	8	9
DC Bus Current [A]	7.8	16.1	24.3	33.3	41.1	49.2	67.3	75.2	85.1
DC Bus Voltage [V]	634.9	623.2	613.3	605.8	597.4	591.8	583.9	573.8	569.5
IN-Electric Power [kW]	5	10	14.9	20.2	24.6	29.1	39.3	43.2	48.5
Motor Speed [rpm]	2114	2812	3449	3877	4303	4654	5219	5363	5584
Motor Torque [Nm]	21	33	41	50	54	58	69	73	78
Motor Torque*[Nm]	20	31	39	47	51	55	65	69	74
OUT-Mech Power*[kW]	4.4	9.2	14.1	19.3	23.1	26.9	35.8	38.9	43.3
Efficiency [%]	88	92	94	95	94	92	91	90	89

10 kW charging power. After completing the tests at the first temperature level, the pack was heated up to the other temperatures of interest with the help of the onboard thermal management system. Voltage responses were obtained at four SOC levels, by discharging the pack consecutively to the previously established levels. The DC impedance Z_{ESS}

Table IV - ESS system: measured battery pack terminal voltage drop and rise [V] with respect to the battery SOC and average cell temperature

		Discharging (25 kW)				Charging (10 kW)			
	SOC [%]	32	45	58	71	32	45	58	71
	OCV [V]	626	668	702	732	626	668	702	732
	5.5	-52	-39	-33	-30	19	20	20	21
	11.4	-43	-32	-28	-25	15	15	16	17
	16.6	-34	-25	-20	-16	11	13	12	13
Av. cell. temp	22.3	-25	-18	-14	-12	8	9	9	10
(°C)	28.5	-20	-15	-12	-10	5	5	6	8

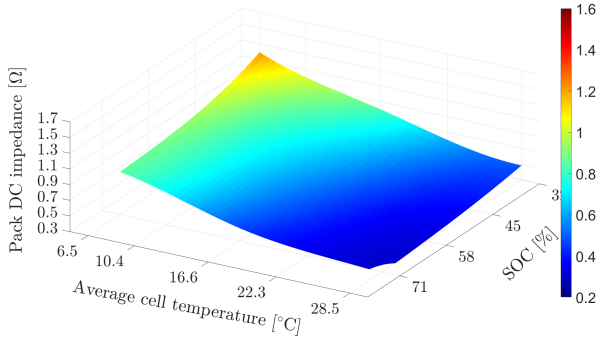
of the battery pack can be computed for each operating point through the Eq. (5):

$$Z_{ESS} = \frac{(OCV + \Delta V_{ESS}) \cdot \Delta V_{ESS}}{P_{PDU_{ESS}}} \tag{5}$$

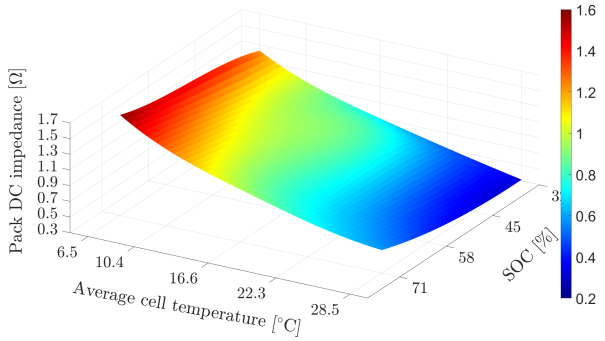
and the pack efficiency can be obtained through the following:

$$\eta_{ESS_{C/DC}} = \frac{P_{PDU_{ESS}} - \frac{\Delta V_{ESS}^2}{Z_{ESS}}}{P_{PDU_{ESS}}} \tag{6}$$

In Fig. 6, Z_{ESS} is shown through 3D surface plots with respect to SOC and cell temperature levels for discharging (Fig. 6a) and charging (Fig. 6b). As could be expected, cell temperature has a large impact on Z_{ESS} both during charging and discharging: the estimated pack DC impedance is 2.5 to 4 times higher than at the maximum tested temperature. As a consequence, at low temperatures the battery responds to load changes with large voltage changes. Moreover, as it can be expected, the pack impedance increases with the discharging of the battery. Looking at the estimations with respect to the SOC, larger discharge power can be better handled by a well charged than by a near depletion battery. Estimations show that at 28.5 °C, the Z_{ESS} increases by



(a)



(b)

Figure 6 ESS: battery pack DC impedance in charging (a) and discharging (b) wrt SOC and average cell temperature

68 % when discharging between 71 % and 32 % SOC. The reverse is true when charging: indeed, still at 28.5 °C, Z_{ESS} shows the maximum increase of 88 % between 32 % and 71 % SOC. The minimum estimated Z_{ESS} value is 290 mΩ (discharging at 28.5 °C and 71 % SOC) while the maximum is 1.59 Ω (charging at 5.5 °C and 71 % SOC). From these data and charts, the target operating point for the battery pack within the SPC to perform a large number of high-power micro-cycles can be selected at 58 % SOC and 28.5 °C, that correspond also to 702 V OCV, 330 mΩ and 430 mΩ Z_{ESS} for discharging and charging, respectively.

Given the selected operating point, $\eta_{ESS_{C/DC}}$ can be evaluated through Eq. (6). For an ESS of -120 kW, $\eta_{ESS_{C/DC}}$ results in 90.3 % and increases through the lowering of the power (discharging) up to the theoretical value of 100 % at 0 kW. Then, while increasing the power from o to 120 kW (charging), $\eta_{ESS_{C/DC}}$ decreases up to 86.5 %. In general, increasing power (i.e. current), leads to an increase of losses.

4.2 Roundtrip Tests

4.2.1 Winch Module

As reported, winch field tests consisted of logging the winch motor torque during lifting and lowering with various payloads. In Fig. 7, the field measurements results are shown. The motor torque trends follow almost straight lines when plotted against varying payload mass, both when lowering and lifting the payload. They can be respectively

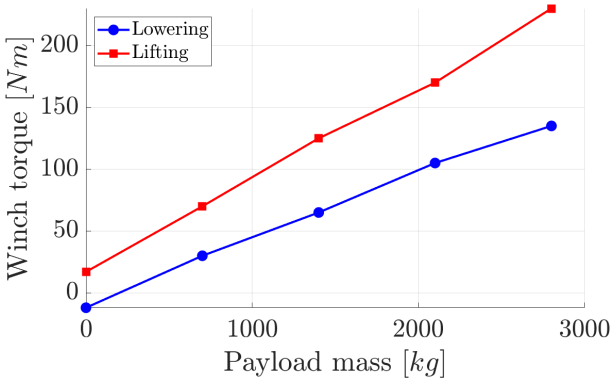


Figure 7 Winch motor torque during lifting and lowering as a function of the payload mass

approximated by Eq.s (7) and (8), where $T_{W_{LOW}}$ and $T_{W_{LIFT}}$ are expressed in Nm and m_L is expressed in kg:

$$T_{W_{LOW}}(m_L) = k_{W_{LOW}} \cdot m_L + T_{W_{LOW_0}} \quad (7)$$

$$T_{W_{LIFT}}(m_L) = k_{W_{LIFT}} \cdot m_L + T_{W_{LIFT_0}} \quad (8)$$

with $T_{W_{LOW_0}}$ = - 9.2 Nm, $k_{W_{LOW}}$ = 0.0527 m^2/s^2, $T_{W_{LIFT_0}}$ = 17.2 Nm and $k_{W_{LIFT}}$ = 0.0751 m^2/s^2. The maximum error between the measured and the estimated result is less than 4.9 Nm. Substituting Eq.s (7), and (8) into Eq. (1) yields an explicit solution of the approximate winch roundtrip efficiency of HULK as a function of payload mass. The estimations are plotted in Fig. 8. It shows that approximately 180 kg of payload is required to overcome mechanical losses in the system, enabling the winch drive to enter regeneration mode when lowering the payload. Up to this loading condition, the roundtrip efficiency is zero. The efficiency then continues to rise with an increasing payload, reaching 47.5 % at the maximum tested payload of 2800 kg. It

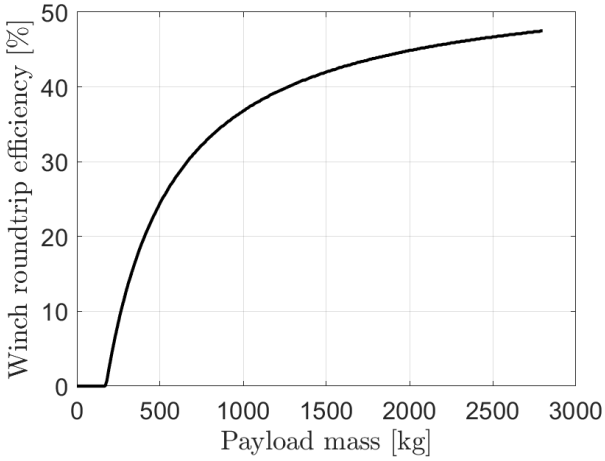


Figure 8 Roundtrip efficiency of the hybrid SPC when operating the winch, as a function of the payload mass

appears to asymptotically approach about 50 % at a very large payload. The winch roundtrip efficiency can also be interpreted as the ratio of lifting over lowering distance required to maintain a constant state of charge level of the battery system, i.e. at a payload of 800 kg, where the efficiency reaches 1/3 or 33 %, recovering the energy invested to lift the load by X meters requires it to be lowered by 3X meters.

4.2.2 Propulsion Module

Propulsion module field tests provide motor torque information for driving uphill and downhill for the same set of payloads previously reported, and for skyline inclinations in the range of 0 % to 50 %. Test results are reported in Fig. 9 and 10 Motor torque curves are provided for five different loading conditions, both when driving uphill and downhill. Given that the maximum skyline inclination at the test installation was 50 %, results have been extended to slopes of 100 % via mathematical extrapolation, depicted via dashed lines. The gradient and offset coefficients describing each of these extrapolations can in turn be approximated via linear expressions, yielding explicit solutions for the propulsion torque in uphill $T_{P_{UP}}$ (Nm) and downhill $T_{P_{DOWN}}$ (Nm) transport as a function of payload mass and skyline inclination α_{SL} (in %) respectively as given by Eq.s (9) and (10):

$$T_{P_{UP}}(m_L, \alpha_{SL}) = (k_{P_{UP_{0\%}}} \cdot m_L + T_{P_{UP_{0\%}}}) \cdot \alpha_{SL} + k_{P_{UP_0}} \cdot m_L + \\ + T_{P_{UP_0}} \quad (9)$$

where $T_{P_{UP_0}}$ = 37.857 Nm, $k_{P_{UP_0}}$ = 0.028 m^2/s^2, $T_{P_{UP_{0\%}}}$ = 1.774 Nm/% and $k_{P_{UP_{0\%}}}$ = 0.0009 m^2/s^2%;

$$T_{P_{DOWN}}(m_L, \alpha_{SL}) = (k_{P_{DOWN_{0\%}}} \cdot m_L + T_{P_{DOWN_{0\%}}}) \cdot \alpha_{SL} + \\ + k_{P_{DOWN_0}} \cdot m_L + T_{P_{DOWN_0}} \quad (10)$$

where $T_{P_{DOWN_0}}$ = 24.095 Nm, $k_{P_{DOWN_0}}$ = - 0.013 m^2/s^2, $T_{P_{DOWN_{0\%}}}$ = 0.583 Nm/% and $k_{P_{DOWN_{0\%}}}$ = 0.0016 m^2/s^2%.

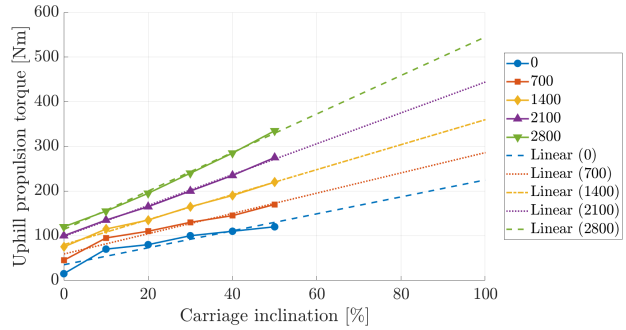


Figure 9 Propulsion motor torque when driving uphill, as a function of the payload mass and carriage inclination.

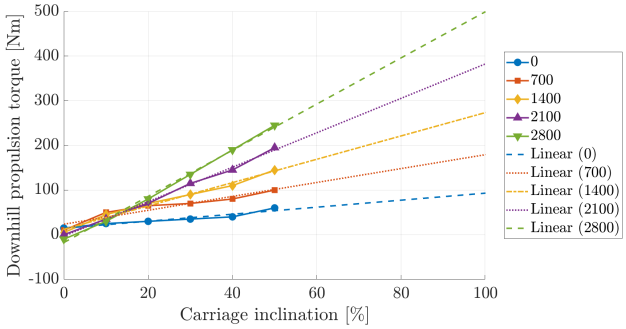


Figure 10 Propulsion motor torque when driving downhill, as a function of the payload mass and carriage inclination.

The average approximation error across the entire input range is 2.2 Nm for Eq. (9) and 0.6 Nm for Eq. (10). Substituting Eq.s (10) and (9) into Eq. (2) yields an explicit solution of the approximate propulsion module roundtrip efficiency of HULK as a function of payload mass and skyline inclination. The estimated results are presented in Fig. 11. With no skyline inclination ($\alpha_{SL} = 0\%$), the result of Eq. (2) can be negative, in which case it is kept at zero. With low payloads or small inclinations, there is only little potential for energy recovery. However, the weight of the carriage when moving uphill still draws

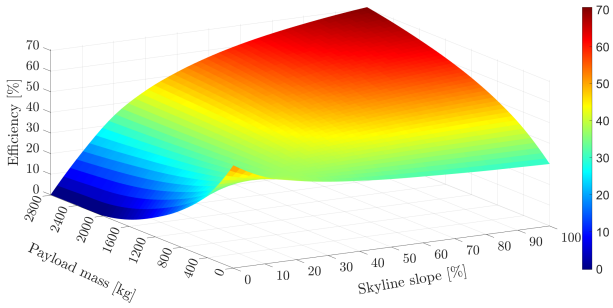


Figure 11 Roundtrip efficiency of the hybrid SPC when operating the propulsion module.

significant power. Consequently, in these cases, the roundtrip efficiency is only as high as 1/3 or lower. As expected, the efficiency rises with increasing payload and slope, ultimately reaching a maximum of 70.6 % when both these variables are maximized. The operating condition where both the payload and the slope are simultaneously very small results in an anomaly in terms of the expected result. Fig. 11 indicates an efficiency rise to 49.7 % at the (0,0) point. This effect can be explained with the help of Fig. 12.



(a) (b)

Figure 12 Impact of the skyline curvature on the propulsion force of HULK

The skyline slope in this work pertains to the slope of the skyline at the current carriage location, which is equivalent to the inclination of the carriage itself. As can be seen from the picture (Fig. 12a), the skyline (highlighted by the black dashed line) is significantly deflected by HULK. While the section of skyline behind HULK is close to horizontal, the section in front of it is rising at a considerable rate. As indicated by the sketch in Fig. 12b, this leads to a horizontal force component F_x, tending to force HULK in the downward direction, despite it resting on the (close to) horizontal skyline. Force F_x provides potential for energy recovery when moving downhill/backward on the flat skyline, consequently yielding increased efficiency. With rising payload, F_x becomes less relevant with respect to other forces, leading to a drop of the roundtrip efficiency.

Overall, results have shown substantial potential for energy recovery. However, unless the load is lowered much further at the landing site than it is yarded laterally and lifted in the felling area, the winch system cannot be self-sufficient. Its large gear reduction ratio leads to relatively low efficiency during the lowering phase, approaching 50 % at high loads. The reduction ratio in the propulsion module is significantly smaller, its maximum roundtrip efficiency therefore substantially higher. Moreover, in downhill transport, the carriage drives uphill unloaded. Results clearly show that the regeneration torque when moving downhill loaded can be much higher than the torque required to move uphill un-loaded. Computing the roundtrip efficiency with such different loading conditions would yield values significantly beyond 100 %. It is therefore reasonable to expect that the surplus of recovered energy from retarding the loaded carriage downhill can also compensate for the

lack of energy to complete the winching cycle. Thus, energy autarkic operation appears possible.

5 CONCLUSIONS

Alpine logging operations can benefit from hybridization or electrification of the equipment. In the recent past, the first hybrid and fully electric solutions emerged. The aim of this paper was to study several key sub-systems as well as the roundtrip efficiency of a hybrid self-propelled carriage, i.e. one of the latest innovations of this industry. In particular, engine-generator set, energy dissipation unit and battery pack were firstly tested with the machine at standstill. Results show that the engine-generator set can achieve an overall efficiency of up to 33.9 %, the battery system can supply a power of 120 kW with less than 10 % of losses, the winch a maximum roundtrip efficiency of 47.5 %, while the propulsion module an efficiency of up to 70.6%. All these results confirm the large potential for energy recovery and the potential of energy-autarkic operation in real-world transport applications. Future work will focus on extended fuel consumption studies, as well as studies of the fuel saving potential with respect to conventional SPCs and tower yarders. Another area of interest is to draw out the boundaries of transport characteristics in downhill setups to ensure HULK can operate energy autarkic.

Acknowledgments

This study was carried out within the Agritech National Research Center (Task 4.1.4) and received funding from the European Union Next-GenerationEU (PIANO NAZIONALE DI RIPRESA E RESILIENZA (PNRR) – MISSIONE 4 COMPONENTE 2, INVESTIMENTO 1.4 – D.D. 1032 17/06/2022, CN00000022).

REFERENCES

[1] Sholanov K., Omarov A., Ceccarelli M., Improving efficiency of converting wind energy in modified sail wind power station, *Int. Journal of Mechanics and Control*, ISSN 1590-8844, 23, 02, pp. 101-110, 2022.

[2] Castellano A., Cammalleri M., Optimal operation of power-split hybrid electric powertrain: comparison between two performance indices, *Int. Journal of Mechanics and Control*, ISSN 1590-8844, 23, 01, pp. 3-14, 2022.

[3] Logozzo S., Valigi M.C., Green tribology: wear evaluation methods for sustainability purposes, *Int. Journal of Mechanics and Control*, ISSN 1590-8844, 23, 01, pp. 23-34, 2022.

[4] Scalera L., Carabin, G., Vidoni, R., Wongratanaphisan, T., Energy Efficiency in a 4-DOF Parallel Robot Featuring Compliant Elements, *Int. Journal of Mechanics and Control*, ISSN 1590-8844, 20, 02, pp. 49-57, 2019.

[5] Visser R., Harrill H., Cable yarding in North America and New Zealand: A review of developments and practices. *In Croatian Journal of Forest Engineering*, 38-2, pp. 209–217, 2017.

[6] Harrill H., Visser R., A review of cable logging literature. *Rotorua, New Zealand: Future Forests Research Ltd.*, Report No.: H019. 17, 2014.

[7] Heinimann H.R., Stampfer K., Loschek J., Caminada L., Perspectives on Central European Cable Yarding Systems. *Austrian Journal of Forest Science*, 123-3, pp. 121-139, 2006.

[8] Varch T., et al., Advances in Cable Yarding: A Review of Recent Developments in Skyline Carriage Technology. *Current Forestry Reports*, 7, pp. 181–194, 2021.

[9] Vorraber M., Produktivität bei der Holzrückung mit dem Mast-seilgerät Koller K 307C-H und dem energierückgewinnenden Laufwagen ESK 2.0. [Productivity of timber extraction with the tower yarder Koller K 307C-H and the energy-recuperating carriage ESK 2.0]. *MS Thesis*, Vienna (Austria): University of Natural Resources and Life Sciences Vienna, 47 p., 2020.

[10] Varch T., et al., Productivity, fuel consumption and cost in whole tree cable yarding: conventional diesel carriage versus electrical energy-recuperating carriage. *International Journal of Forest Engineering*, 32(sup1), 20–30, 2020.

[11] Raymond K., Visser R., Harvesting technology watch, Future Forest Research Ltd., HTW-016, fgr.nz/documents/download/3763, 2015.

[12] Leitner S., et al.,Technical, Safety and Environmental Challenges in the Electrification of Cable Yarding Equipment. *Current Forestry Reports*, Vol.9, pp.263-275, 2023.

[13] Leitner S., Vidoni R., Performance and Efficiency Study of a Hybrid Self-Propelled Cable Logging Carriage – Preliminary Results. *Advances in Italian Mechanism Science*, pp.171-182, 2024.

[14] Cadei A., et al.,Energy Efficiency of a Hybrid Cable Yarding System: A Case Study in the North-Eastern Italian Alps under Real Working Conditions. *Journal of Agricultural Engineering*, 52, no. 3, 2021.

[15] Leitner S., Renzi M., Spinelli R., Vidoni R., On the Design of Hybrid Tower Yarder Drivetrains: A Case Study. *Forests*, 13, 1520, 2022.

[16] Leitner S., et al., Requirements and Challenges in the Design and Potential of Smart and Efficient Winch Assisted Forestry Machinery. *Lecture Notes in Civil Engineering*, vol 337. Springer, Cham., 2022.

[17] Leitalpin GmbH.; Projects. September 2024, [Online]. Available: http://www.leitalpin.com/en

[18] IOR energy, "Engineering Conversion Factors", https://web.archive.org/web/20100825042309/... http://www.ior.com.au/ecflist.html, accessed 01.04.2024

ISSN 1590-8844
International Journal of Mechanics and Control, Vol. 26, No. 02, 2025
https://doi.org/10.69076/jomac.2025.0003

OBSTACLE AVOIDANCE METHODS FOR DIFFERENTIAL DRIVE ROBOTS

Federico Neri* Giacomo Palmieri* Daniele Costa* Massimo Callegari*

* Department of Industrial Engineering and Mathematical Sciences (DIISM), Università Politecnica delle Marche, Ancona, Italy.

ABSTRACT

This paper presents an extended obstacle avoidance approach for non-holonomic mobile robots with differential drive transmission, focusing on collaborative environments where human operators and robots share the workspace. Two distinct avoidance strategies are evaluated: one combining translational and rotational movements for greater flexibility, and the other relying solely on rotational maneuvers to ensure smoother trajectory adjustments. The performance of these strategies is assessed through simulations in scenarios involving both static and dynamic obstacles. The first test shows a mobile robot navigating along a path where an obstacle is located, while in the second the mobile robot is fixed at a target position and an obstacle interferes. The robot's direction only changes when the obstacle enters the zone of influence. The possibility of using a rectangular kinematic structure with a tip at the front of the robot is introduced. Future developments will focus on implementing these strategies within a mobile manipulator system, comprising a differential drive base and a 6-DOF robotic arm, to expand the algorithm's applicability to advanced robotic configurations.

Keywords: obstacle avoidance; differential drive; non-holonomic; motion planning

1 INTRODUCTION

The increasing adoption of autonomous mobile robots (AMRs) in industrial environments has necessitated the development of advanced navigation strategies that can ensure safety and maintain efficiency without reducing cycle times. Unlike automated guided vehicles (AGVs), which rely on fixed routes and external infrastructure [1], AMRs use perception systems to dynamically adapt to their surroundings. This capability is particularly important in shared workspaces between humans and robots, where obstacle avoidance helps prevent collisions [2]. In recent years, significant advancements have been made in the development of mobile robots capable of operating in various environments [3]. These systems have been widely adopted not only in industrial and healthcare settings, where they navigate flat and structured surfaces [4], but also in more challenging terrains such as agricultural fields, where rough and uneven surfaces require advanced locomotion strategies [5]. The ability to adapt to different working conditions is important for expanding the applicability of mobile robots beyond controlled environments, enabling their deployment in outdoor and unstructured scenarios.

Another critical aspect of mobile robotics research is localization, which ensures precise positioning within a given workspace. The most commonly employed method relies on an initial environmental mapping performed at the time of installation. While this approach is widely adopted, it has notable limitations, particularly in modular or frequently changing environments such as warehouses or dynamic industrial settings. Structural modifications or temporary obstacles can compromise the accuracy of the map-matching algorithm, leading to localization failures and reduced navigation reliability [6].

To address these challenges, alternative localization strategies have been explored. One promising solution involves Ultra-Wideband (UWB) positioning systems, which provide

E-mail: federico.neri@staff.univpm.it, g.palmieri@univpm.it, d.costa@staff.univpm.it, m.callegari@staff.univpm.it

high-accuracy localization even in dynamic environments by leveraging time-of-flight measurements [7]. Another effective approach is the use of motion capture systems based on marker detection, such as OptiTrack, which enables real-time tracking with sub-millimeter precision [8]. These technologies, when integrated with onboard sensor fusion techniques, can significantly enhance the robustness and adaptability of mobile robot navigation, ensuring reliable performance even in highly dynamic and unstructured environments.

The reliance on predefined paths in mobile robot navigation presents significant challenges in dynamic environments. When obstacles suddenly appear or the workspace layout changes, a precomputed trajectory may become invalid, requiring the robot to stop and recalculate a new path. This process not only introduces inefficiencies but also increases the risk of navigation failures if real-time updates are not feasible. To address these issues, it is crucial to develop advanced algorithms capable of real-time obstacle avoidance [9], allowing robots to dynamically adjust their trajectories and ensure continuous, collision-free operation without the constraints of static path planning [10, 11].

Obstacle avoidance strategies in mobile robotics have been extensively studied [12, 13], with numerous approaches attempting to balance computational efficiency and real-time responsiveness. Global planning methods, such as A* and Dijkstra's algorithms, are widely used for generating optimal trajectories in static environments by computing the shortest path from a given start point to a goal while accounting for known obstacles [14]. However, their effectiveness is significantly reduced in dynamic environments, where obstacles can change over time, requiring more adaptive strategies to ensure safe and efficient navigation. In contrast, reactive methods, such as artificial potential fields [15] and vector field histogram, offer an immediate response to obstacles, but may suffer from problems such as local minima or oscillatory behaviour. Hybrid approaches attempt to combine the advantages of both solutions, providing a balance between long-term planning and immediate responsiveness. However, their application to non-holonomic robots with differential transmission presents a challenge, as these systems impose kinematic constraints that limit their manoeuvrability compared to omnidirectional platforms [16]. In current studies of obstacle avoidance techniques for mobile robots, it is often assumed that the robotic platform has almost unlimited mobility [17], neglecting the kinematic restrictions imposed by non-holonomic systems, such as those with differential drive. This leads to solutions that are effective in ideal simulations or on omnidirectional platforms, but may be difficult to apply to differential mobile robots in the real world. This research addresses this limitation in more detail than the existing literature by developing obstacle avoidance strategies that incorporate the robot's actual kinematic constraints. This approach allows for more effective and applicable solutions in real-world scenarios, improving navigation and safety in complex operational environments.

Regarding the kinematics of mobile robots, two main macrocategories can be identified: omnidirectional wheel systems and differential drive systems. Omnidirectional robots are equipped with specialized wheels, such as Mecanum or omnidirectional rollers, which allow movement in any direction without requiring rotation of the robot's body. This capability provides high maneuverability, making these robots particularly suitable for constrained environments where precise positioning is required, such as warehouses, medical facilities, and assembly lines [18, 19].

In contrast, differential drive robots rely on two independently controlled wheels to achieve movement [20, 21, 22]. By varying the relative speed of each wheel, the robot can translate forwards, backwards and rotate around an axis. However, due to their non-holonomic constraints, these robots cannot move laterally, which can limit their maneuverability in tight spaces [23]. Despite this, differential drive systems remain widely used due to their mechanical simplicity, cost-effectiveness, and robustness, making them ideal for applications in structured environments such as industrial automation and service robotics. The absence of lateral movements imposes constraints on path planning and requires advanced strategies to ensure efficient and smooth obstacle avoidance. To overcome these challenges, this study presents an advanced obstacle avoidance algorithm tailored for differential wheeled mobile robots operating in dynamic environments. The proposed approach effectively manages both static and moving obstacles, with its performance evaluated through simulations that incorporate various motion strategies. A strategy is developed that allows the robot to temporarily reposition itself to avoid interference, ensuring smooth collaboration without operational interruptions. This approach improves the flexibility of the system, allowing the robot to resume its position autonomously once the work area is free, without the need for external intervention.

The paper is structured as follows: Section 2 provides a detailed description of the proposed algorithm, outlining the developed avoidance strategies and the criteria employed for their evaluation. Section 3 presents the simulation results, comparing the effectiveness of the different strategies and analyzing their performance in terms of efficiency, safety, and adaptability to dynamic environments. In Section 4, the findings are critically examined, highlighting the strengths and limitations of the proposed approach and discussing its applicability in real-world scenarios. Finally, Section 5 summarizes the key contributions of this work and outlines potential future developments.

2 OBSTACLE AVOIDANCE ALGORITHM

In a planar representation, the mobile robot can be modeled as a rectangular chassis with two wheels symmetrically

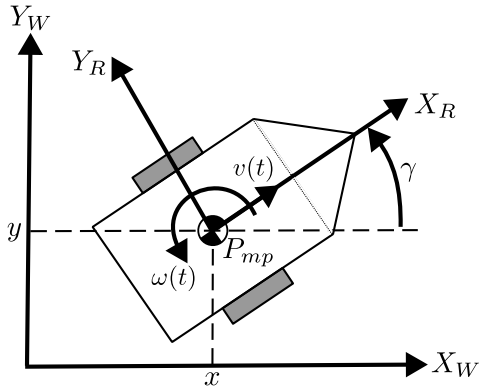


Figure 1 World and local reference frames.

positioned on either side. To simplify the analysis of the system, a local reference frame is defined, with the origin located at the center of the chassis, denoted as $\mathbf{P}_{mp}$. The axes X_R and Y_R are oriented as shown in Fig. 1. In relation to the world reference frame, the pose of the mobile platform is represented by the vector $\mathbf{x} = \begin{bmatrix} x & y & \gamma \end{bmatrix}^T$, where (x, y) denote the coordinates of the robot's position in the world frame, and γ represents the orientation of the robot, measured as the angle between the X_R axis and the global X_W axis.

Given the non-holonomic nature of the robot's locomotion, a constraint arises that prohibits motion along the Y_R direction. Consequently, the velocity of the mobile robot can only be expressed as a function of two variables: the linear velocity v along the X_R axis, and the angular velocity ω. Therefore, the robot's velocity vector in the local frame of reference is given by $\dot{\mathbf{q}} = \begin{bmatrix} v & \omega \end{bmatrix}^T$.

The velocity vector in the world reference frame can be obtained from the local velocity vector using a transformation matrix, known as the Jacobian matrix $\mathbf{J}$. This 3×2 matrix converts the local velocity components to the global frame and is given by

$$\mathbf{J} = \begin{bmatrix} \cos\gamma & 0 \\ \sin\gamma & 0 \\ 0 & 1 \end{bmatrix} \tag{1}$$

The velocity vector in the world reference frame can thus be obtained as $\dot{\mathbf{x}} = \mathbf{J}\dot{\mathbf{q}}$.

In order to generate a smooth and feasible point-to-point trajectory for a mobile robot with differential drive, a parametric cubic polynomial approach is utilized. Let the initial pose of the robot be $\mathbf{x}_i = \begin{bmatrix} x_i & y_i & \gamma_i \end{bmatrix}^T$ and the final pose be $\mathbf{x}_f = \begin{bmatrix} x_f & y_f & \gamma_f \end{bmatrix}^T$. The path between these two points is then expressed as:

$$\begin{bmatrix} x(s) \\ y(s) \end{bmatrix} = \\ = \begin{bmatrix} -(s-1)^3 x_i + s^3 x_f + \alpha_x s^2 (s-1) + \beta_x s (s-1)^2 \\ -(s-1)^3 y_i + s^3 y_f + \alpha_y s^2 (s-1) + \beta_y s (s-1)^2 \end{bmatrix} \tag{2}$$

where the parameter $s \in [0, 1]$ represents the normalized progression along the trajectory, and is defined as a function of time using a 5^{th} polynomial. The coefficients $\alpha_x, \alpha_y, \beta_x, \beta_y$ are introduced to further refine the shape of the trajectory, and are calculated as:

$$\begin{bmatrix} \alpha_x \\ \alpha_y \end{bmatrix} = \begin{bmatrix} k\cos\gamma_f - 3x_f \\ k\sin\gamma_f - 3y_f \end{bmatrix} \quad \begin{bmatrix} \beta_x \\ \beta_y \end{bmatrix} = \begin{bmatrix} k\cos\gamma_i + 3x_i \\ k\sin\gamma_i + 3y_i \end{bmatrix} \tag{3}$$

In these equations, the parameter k is a tuning variable that allows for adjusting the curvature radius of the path. The orientation along the trajectory, denoted by $\gamma(s)$, is computed by enforcing the condition that the local X_R axis remains tangent to the path at each point. Once the trajectory has been established, the reference velocity profile is derived from the velocity components in the world frame. The forward velocity v_r is given by the magnitude of the velocity vector $\sqrt{\dot{x}^2 + \dot{y}^2}$, while the angular velocity ω_r is simply the time derivative of the orientation $\dot{\gamma}$.

The proposed motion control system is designed to dynamically adjust the robot's trajectory in real time in response to obstacles that obstruct the platform's movement. A repulsive velocity vector is activated when the distance between the robot and the obstacle falls below a predefined threshold, represented by a safety radius r. This safety radius surrounds the robot and forms a protection zone on each side of the platform. This zone is modelled as a rectangular area, with rounded corners, in which the two semicircles share a common radius r.

The repulsive velocity vector $\dot{\mathbf{x}}_0$ is applied at the point $\mathbf{P}_r = \begin{bmatrix} p_x & p_y \end{bmatrix}^T$, which corresponds to a location on the segments of the robot's footprint that is closest to the obstacle. The position of the obstacle is denoted by $\mathbf{P}_o$, as shown in Fig. 2. The magnitude of the repulsive velocity, denoted by $\dot{x}_0$, is considered a control parameter and can be adjusted to modulate the strength of the repulsion. On the other hand, the direction of the repulsive velocity vector is determined by the unit vector along the distance vector $\mathbf{d}_o = \mathbf{P}_r - \mathbf{P}_o$, such that the repulsive velocity is expressed as $\dot{\mathbf{x}}_0 = \dot{x}_0 \hat{\mathbf{d}}_o$.

To describe the kinematics of the repulsive velocity vector, the Jacobian matrix $\mathbf{J}_0$ related to the point $\mathbf{P}_r$ is defined. This matrix relates the velocity components of the robot in the local frame of reference to the required velocity to avoid the obstacle. The kinematic expression of the repulsive velocity vector is derived as:

$$\dot{\mathbf{x}}_0 = \begin{bmatrix} \cos\gamma & -p_y\cos\gamma - p_x\sin\gamma \\ \sin\gamma & p_x\cos\gamma - p_y\sin\gamma \end{bmatrix} \begin{bmatrix} v \\ \omega \end{bmatrix} = \mathbf{J}_0 \begin{bmatrix} v \\ \omega \end{bmatrix} \tag{4}$$

In this expression, the Jacobian matrix $\mathbf{J}_0$ is used to transform the velocity components (v, ω) in the robot's local reference frame to the appropriate repulsive velocity $\dot{\mathbf{x}}_0$. The Jacobian depends on the configuration of the robot and the point of application of the repulsive force, allowing the robot to adjust its motion direction and speed in response to the obstacle's position and distance.

The strategy is designed to identify the link with the highest risk of collision by calculating the distance of each obstacle from each segment of the robot. As a result, the point $\mathbf{P}_r$ of minimum distance from the obstacle and the distance vector $\mathbf{d}_o$ can be obtained [24].

As illustrated in Fig. 2a, a significant problem can emerge when an obstacle interacts with the front edge of the moving platform. In such cases, the repulsive velocity generated may result solely from the translational movement of the platform without any rotational adjustment, causing the robot to move backwards along a straight path. Once the obstacle leaves the platform's area of influence, the control system orders the platform to return to its previous position, resulting in a repetitive stall scenario.

To overcome this limitation, a new strategy is proposed whereby a safety region is defined by dividing the frontal area of the platform into five segments that converge to form a tip, as illustrated in Fig. 2b. This configuration facilitates the simultaneous generation of rotational and translational velocities, allowing the robot to circumvent obstacles more effectively.

The proposed control strategy integrates two primary objectives: the primary task of following a predefined trajectory and a secondary task that is activated when the obstacle avoidance mechanism is triggered. The control law governing this behaviour can be expressed as follows:

$$\dot{\mathbf{q}} = \mathbf{v}_f + \mathbf{J}_0^{-1}\dot{\mathbf{x}}_0 \tag{5}$$

In this formulation, $\mathbf{v}_f$ represents the planned velocity profile with error compensation, as described by Maalouf et al. [25] and Kanayama et al. [26]. The expression for $\mathbf{v}_f$ is given by:

$$\mathbf{v}_f = \begin{bmatrix} v_f \\ \omega_f \end{bmatrix} = \begin{bmatrix} v_r\cos e_\gamma + k_x e_x \\ \omega_r + v_r k_y e_y + k_\gamma \sin e_\gamma \end{bmatrix} \tag{6}$$

Here, e_x, e_y, and e_γ denote the positional and orientation errors between the planned and actual poses in the robot's local reference frame. The terms k_x, k_y and k_γ are control gain parameters.

The parameters used in the proposed control strategy, such as the repulsive velocity $\dot{\mathbf{x}}_0$ and the recovery parameters k_x, k_y and k_γ, are essential for balancing obstacle avoidance and point-to-point trajectory tracking. The repulsive velocity $\dot{\mathbf{x}}_0$ directly influences the robot's responsiveness when an obstacle is detected, determining how quickly the robot will alter its path to avoid a collision. In contrast, the recovery parameters k_x, k_y and k_γ control how effectively the robot returns to its planned point-to-point trajectory after successfully avoiding the obstacle. A balance must be found between more aggressive avoidance behaviour, which increases safety but may compromise trajectory accuracy, and smoother trajectory tracking, which may reduce the robot's ability to react quickly to obstacles. Furthermore, these parameters depend on the maximum speeds that the robot can reach, which influence its ability to adapt to dynamic changes in the environment.

An alternative method of generating repulsive motion involves the imposition of purely rotational adjustments. In this scenario, only the component of the repulsive velocity perpendicular to the front edge of the platform is defined, with a fixed magnitude $v_{0n} = \dot{x}_0$, while the tangential component v_{0t} remains free. By imposing a zero velocity at the centre point of the platform $\mathbf{P}_{mp}$, the angular velocity required to produce the desired repulsive effect can be found as $\omega = \dot{x}_0/(p_y\cos\alpha_{mp} - p_x\sin\alpha_{mp})$, where the geometric variables are defined in Fig. 3. Thus the control law becomes:

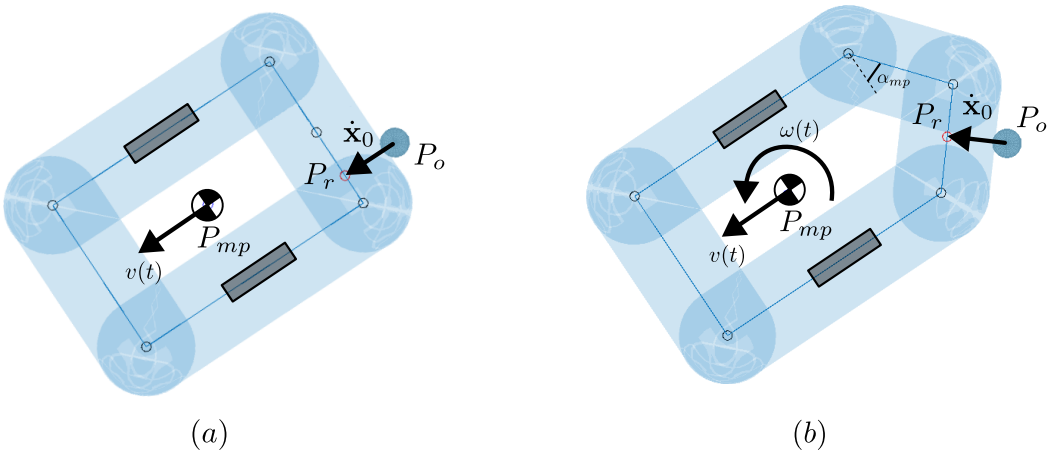
$$\dot{\mathbf{q}} = \mathbf{v}_f + \begin{bmatrix} 0 \\ \dfrac{\dot{x}_0}{p_y\cos\alpha_{mp} - p_x\sin\alpha_{mp}} \end{bmatrix} \tag{7}$$

In this equation, the geometric parameters p_x, p_y, and α_{mp} are illustrated in Fig. 3. To ensure that the platform rotates in the correct direction, the following geometric condition must be satisfied:

$$\alpha_{mp} > \tan^{-1}\left(\frac{D}{L}\right) \tag{8}$$

where D represents the distance between the wheels, L is the length of the robot, and α_{mp} is the angle of the tip. For the specific case study presented in this paper, $L = 890\,\mathrm{mm}$ and $D = 580\,\mathrm{mm}$, yielding a geometric constraint of $\alpha_{mp} > 33^\circ$.

A larger value of the angle α_{mp} results in a greater contribution from the angular velocity, leading to more pronounced rotational movement. However, if the angle becomes too large, the tip of the robot may become excessively large, potentially affecting the robot's ability to navigate efficiently. Consequently, an angle of $\alpha_{mp} = 40^\circ$ was selected for the control model, as it represents a suitable compromise, slightly above the minimum value considered optimal.



(a) (b)

Figure 2 Safety region delimiting the robot's footprint, with 4 segments (**a**) and 5 segments (**b**).

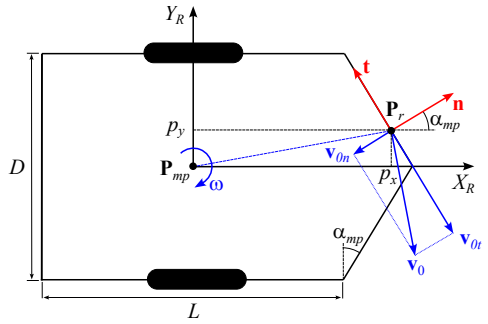


Figure 3 Geometric parameters for Eq. 7

3 RESULTS

Through Matlab simulations, the proposed algorithm was rigorously tested, demonstrating the response of the mobile robot when it encounters an obstacle along its planned trajectory.

To define the safety area around the segments of the robot, the radius r is increased compared to the r_{min} taken as reference. In particular, $r = \frac{4}{3} r_{min}$ and the radius r_{min} is set as a linear function of the velocity v_o of the obstacle, with lower and upper limits ($r_{min} = r_{inf} = 0.17\,\mathrm{m}$ for $v_o \leq v_{inf} = 0.1\,\mathrm{m/s}$, $r_{min} = r_{sup} = 0.23\,\mathrm{m}$ for $v_o \geq v_{sup} = 0.5\,\mathrm{m/s}$). For the examples shown the speed of the obstacle is zero or lower than the imposed limit, so only the minimum safety value will be taken into consideration.

In the experimental tests presented in the next sections, the following two methods will be used for obstacle avoidance:

- **Method 1** (Eq. 5): combines translational and rotational repulsive velocities. This method is suitable for static or semi-static environments, where the robot may need to maintain a specific position while adjusting its pose to avoid obstacles.
- **Method 2** (Eq. 7): applies only a repulsive rotational velocity to avoid obstacles. This approach ensures stable and smooth maneuvers, making it ideal for dynamic environments where the platform is continuously moving.

3.1 TEST CASE 1

In the simulated scenario, a stationary obstacle is positioned along the robot's trajectory. The point-to-point motion planning method facilitates the generation of a trajectory that respects the constraints inherent to a mobile robot with differential wheels, allowing the robot to reach the target position with the desired orientation. For this specific simulation, a curvature parameter of $k = 5\,\mathrm{m}$ was selected to ensure an adequate radius of curvature.

The figure 4 illustrates six frames ranging from $t = 0$ to $t = 15\,\mathrm{s}$, depicting the movement of the robot. The obstacle is represented as a circle. When the robot's influence region intersects with the obstacle, the algorithm kicks in, imposing a repulsive velocity term $\dot{x}_0 = 10\,\mathrm{m/s}$. Each frame includes the planned trajectory and the actual trajectory derived from the collision check based on Eq. 5, while the solid line represents the trajectory obtained using the control strategy defined by Eq. 7.

Once the robot overcomes the obstacle, the positioning error is incrementally corrected through a proportional correction term. The recovery parameters utilized in the simulation are $k_x = 9\,\mathrm{s}^{-1}$, $k_y = 9\,\mathrm{rad/m^2}$ and $k_\gamma = 5\,\mathrm{rad/s}$.

In Fig. 4, the point $\mathbf{P}_r$ closest to the obstacle is marked with a small red circle on the respective segment. In the images, a small blue circle indicates the point on the planned trajectory that the mobile robot must reach.

In the frames shown, it is possible to observe how, in the sections where the obstacle is not present or does not interfere with the robot's safety zone, the robot manages

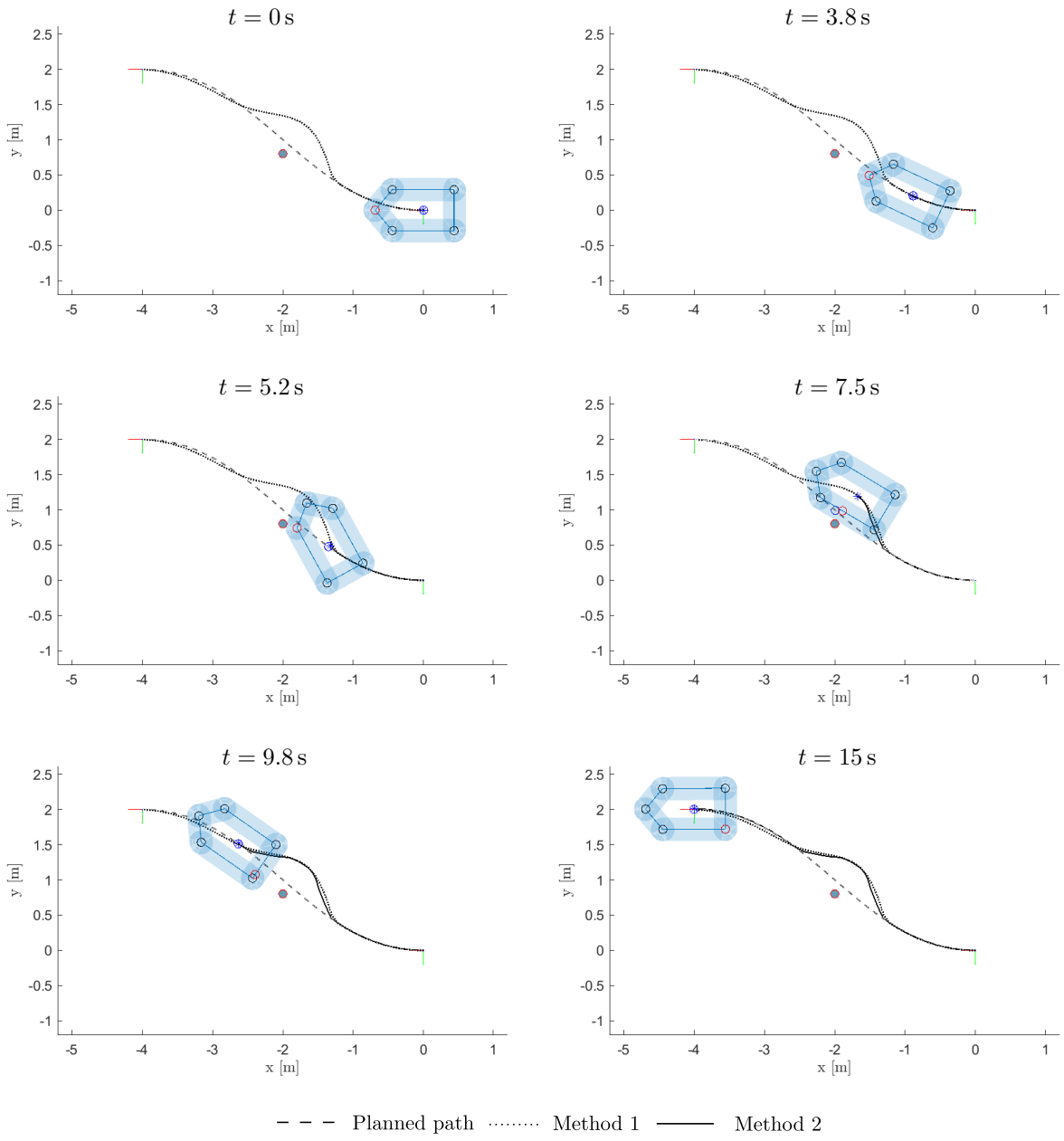


Figure 4 Avoidance of a fixed obstacle while the mobile robot moves along a path.

to faithfully follow the desired trajectory. Under these conditions, the mobile robot maintains an orientation tangent to the trajectory at every point, ensuring smooth movement in accordance with the initial planning.
However, when the distance between the obstacle and the robot's closest point reaches a predetermined limit value, the control system activates a repulsive velocity term that induces a deviation from the planned trajectory. This behaviour is essential to avoid a collision, allowing the robot to dynamically modify its path in response to the presence of the obstacle. It is important to emphasise that the robot's speed is generated moment by moment based on the information available in real time, and not through a predefined alternative path. This allows the system to continuously adapt to its surroundings, reacting immediately to any changes in the position of obstacles.
The effect of repulsive velocity manifests itself in a temporary alteration of the robot's motion, which deviates from its original trajectory in order to safely circumvent the obstacle. Once the obstacle has been overcome, the control system intervenes again to progressively correct the positioning error accumulated during the avoidance manoeuvre. This correction takes place through a proportional action, which gradually returns the robot to its initially planned trajectory, ensuring that the destination is reached with the correct final orientation.
The analysis of the frames makes it possible to appreciate the robot's behaviour in the different phases of the trajectory: initially, the movement occurs without interference, then the deviation induced by the repulsive velocity is observed, and finally the recovery phase that brings the robot back to the desired trajectory.
The comparative analysis of the planned and updated trajectories is presented in Fig. 5, while Fig. 6 illustrates the velocity components v and ω in the local reference frame of the robot.
Between $t = 5\,\mathrm{s}$ to $t = 10\,\mathrm{s}$, near the obstacle, a deviation of the trajectory from the planned path is observed.
Furthermore, Fig. 6a illustrates the velocity components generated by Eq. 5. In this context, a negative translational component emerges for the repulsive segment, resulting in a total velocity v that occasionally becomes negative. In contrast, Figure 6b shows the velocity derived from Eq. 7, in which only the rotational velocity is used for the repulsive action.
In both cases, the trends of the velocity components v and ω aim to closely follow the expected trajectory, indicated with a dotted line in the absence of obstacles.
From the analysis of the two methods, it is observed that method 2, based exclusively on rotation, allows to bypass and subsequently recover the trajectory more quickly than method 1. This behavior is due to the fact that, in method 1, when the robot reaches the minimum safety distance from the obstacle, a repulsive velocity is generated which, in some

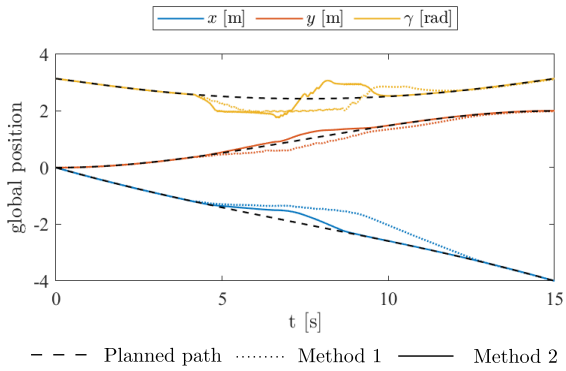


Figure 5 Test case 1: comparison between the planned path and the trajectories obtained using Eq.5 and Eq.7.

instants, induces a backward motion with a negative local translational component. This temporary inversion of motion leads to an increase in the time needed to recover the planned trajectory.
The graph in Fig. 7 shows the trend of the minimum distance between the robot and the obstacle for the two methods analyzed. In the interval between 5 and 10 seconds, the robot approaches the obstacle until it reaches a minimum distance. It can be observed that method 1 allows to maintain a slightly greater distance than method 2, avoiding to significantly fall below the safety margin.
The areas highlighted in the graph indicate critical safety thresholds: the gray band represents the safety margin within which the robot can operate without high risks, while the red zone identifies the minimum limit, beyond which the probability of collision increases considerably. Compared to method 2, method 1 shows a tendency to reach lower distances, suggesting a greater difficulty in ensuring a safe trajectory.
Despite that, method 2 proves more effective in avoiding the obstacle, while still limiting excessive approach and allowing for a quicker recovery of the desired trajectory.

3.2 TEST CASE 2

In the second test case analyzed, a moving obstacle interferes with a stationary robot. The robot is initially in a fix position, but when the obstacle approaches and enters its influence region, it temporarily moves to avoid a collision. Once the obstacle has passed, the robot returns to its original position. Figures 8 and 9 illustrate three frames for each method, from $t = 0$ to $t = 15\,\mathrm{s}$, depicting the movement of the obstacle and the robot's reaction. The obstacle, represented as a circle, moves along a predefined linear path. When the obstacle enters the robot's influence region, a repulsive velocity term $\dot{x}_0 = 10\,\mathrm{m/s}$ is imposed.
Once the obstacle moves past the robot, a proportional correction term incrementally adjusts the positioning error.

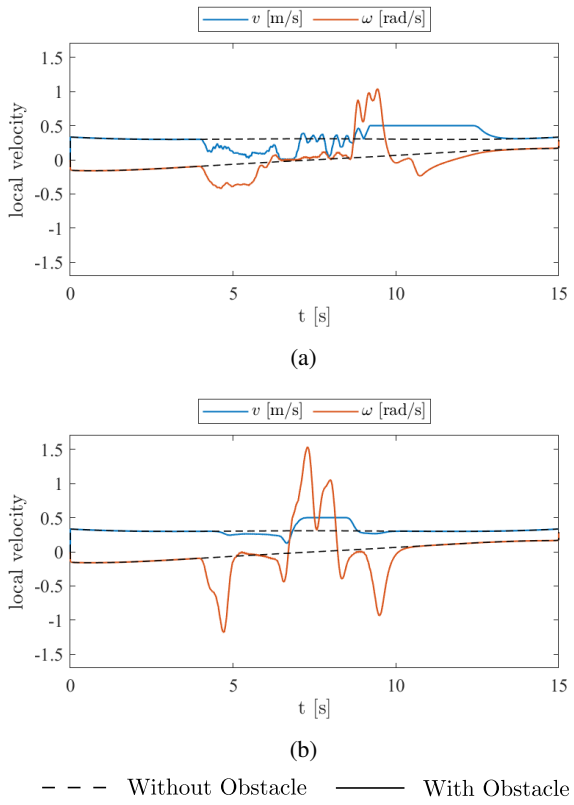


Figure 6 Test case 1: local velocities using Eq.5 (a) and Eq.7 (b).

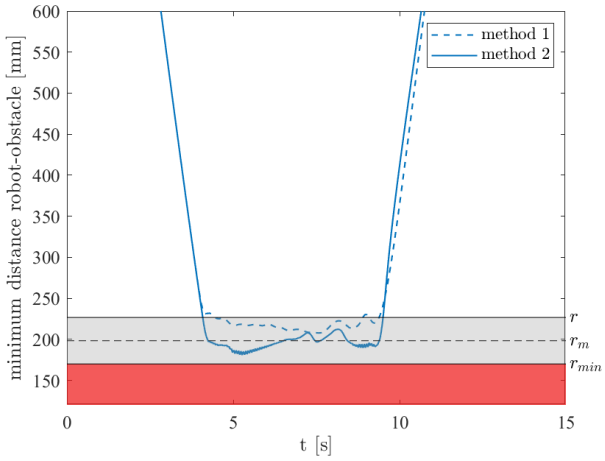


Figure 7 Test case 1: evolution of the minimum distance between the robot and the obstacle for the two methods considered, using Eq.5 and Eq.7.

The recovery parameters utilized in the simulation are $k_x = 1\,\mathrm{s}^{-1}$, $k_y = 1\,\mathrm{rad/m}^2$, and $k_\gamma = 2\,\mathrm{rad/s}$.

Figures 8 illustrate the test case frames using method 1, which avoids obstacles by allowing the robot to move backwards, exploiting the translational repulsive component of Eq.5. In contrast, Figure 9 depicts the scenario with method 2, where the mobile robot relies exclusively on rotational motion to avoid the obstacle with Eq.7. This constraint limits the effectiveness of the algorithm, making it unable to avoid obstacles that pass close to the center of the robot base. In this specific case, where the robot is in the desired position from the beginning, method 2 proves to be less effective, while method 1 provides a more efficient and reliable avoidance maneuver.

This scenario can occur when the robot is positioned in a desired work position and an operator needs to perform a task in the same area or wants to manually move the robot away. In such cases, the robot temporarily moves to avoid interference. Once the operator has left the workspace, the robot autonomously returns to its original position without requiring explicit commands or external communication. This capability enhances flexibility in collaborative environments, ensuring smooth human-robot interaction without disrupting workflow.

Figure 10 illustrates the comparison between the planned path and the actual trajectories obtained using the two different avoidance methods. The graph represents the global position of the robot over time, with the x-axis denoting time in seconds and the y-axis showing the position components x (blue), y (orange), and orientation γ (yellow). The dashed black line represents the planned trajectory, which the robot should ideally follow in the absence of obstacles. The dotted line corresponds to the trajectory obtained using method 1 (Eq.5), which allows for translational repulsion, including backward motion when necessary. Conversely, the solid black line depicts the trajectory using method 2 (Eq.7), which relies solely on rotational adjustments for avoidance.

From the graph, it is evident that during the interaction phase (between $t = 3$ s and $t = 12$ s), both methods result in deviations from the planned path due to the obstacle interference. However, the nature of these deviations differs significantly: method 1, benefiting from translational adjustments, enables the robot to maintain a trajectory closer to the planned one. method 2, limited to rotational avoidance, exhibits a larger deviation, especially when the obstacle passes near the robot's center, making it difficult to maintain a stable avoidance maneuver. After the obstacle exits the interaction region, both methods allow the robot to return to its original trajectory, with method 1 achieving a smoother and quicker recovery.

Figure 11 presents the local velocity profiles of the robot during test case 2, comparing the performance of the two obstacle avoidance methods. The plots illustrate the linear velocity v (blue) and the angular velocity ω (orange) over

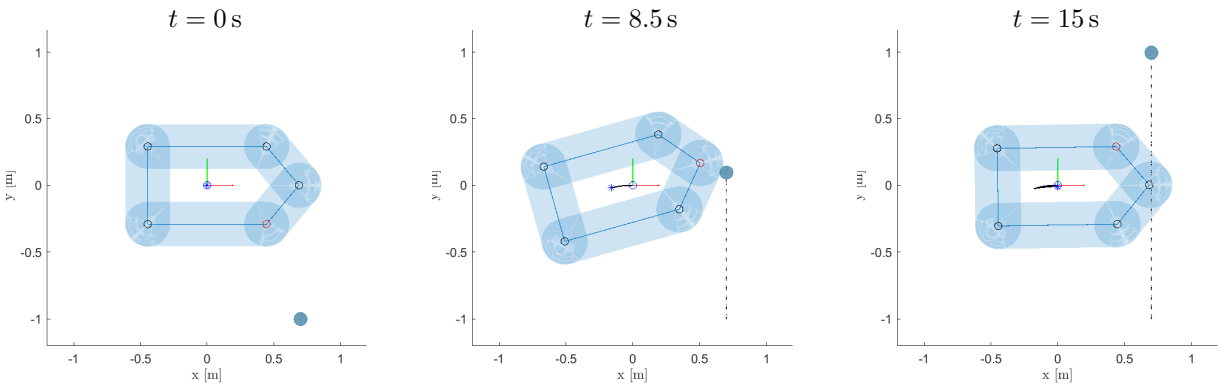


Figure 8 Avoidance of a dynamic obstacle that interferes with the mobile robot in a stationary position using Eq.5.

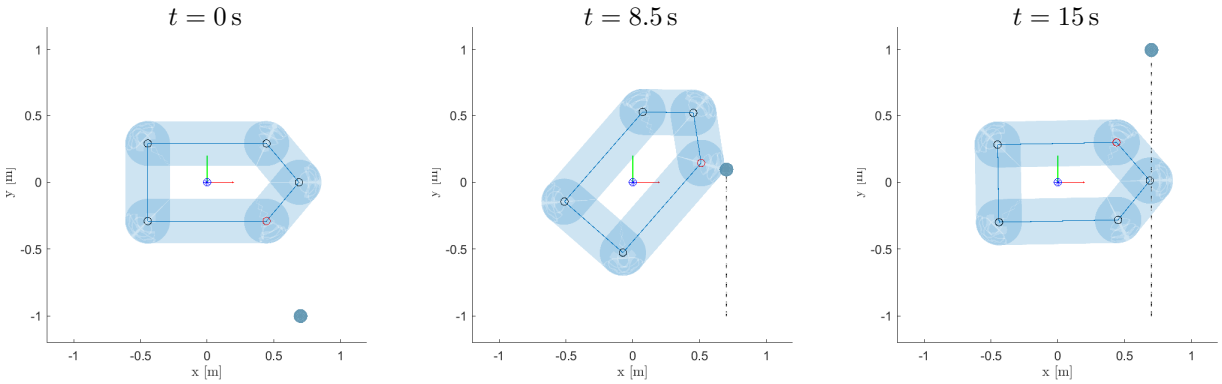


Figure 9 Avoidance of a dynamic obstacle that interferes with the mobile robot in a stationary position using Eq.7.

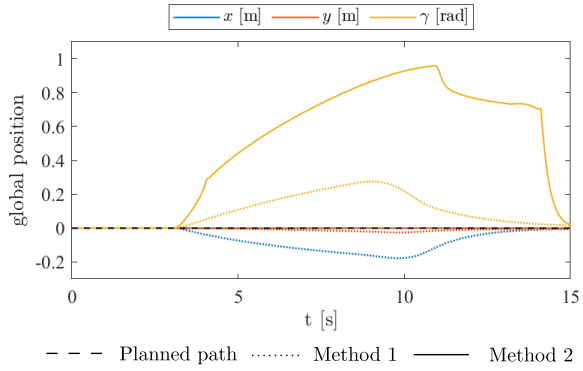


Figure 10 Test case 2: comparison between the planned path and the trajectories obtained using Eq.5 and Eq.7.

time. Subfigure 11a corresponds to the method based on Eq.5, which allows for translational repulsion, while subfigure 11b represents the method using Eq.7, which relies solely on rotational avoidance.

In subfigure (a), the velocity profile remains smooth throughout the trajectory, with minor deviations in both linear and angular velocities when the robot interacts with the obstacle (around $t = 3$ s). Since this method permits backward motion, the adjustments in velocity remain limited, ensuring a stable and efficient avoidance maneuver.

Conversely, in subfigure (b), the avoidance method relying only on rotational motion exhibits significant fluctuations in angular velocity ω. When the obstacle interferes with the robot's path, large spikes in ω indicate abrupt rotational adjustments to maintain a collision-free trajectory. This behavior results in less stable motion.

These results further highlight the advantages of incorporating translational motion for obstacle avoidance, as it allows the robot to maintain smoother and more controlled velocity profiles while ensuring effective maneuverability in dynamic environments.

Figure 12 illustrates the evolution of the minimum distance between the robot and the obstacle, comparing the two avoidance methods. The dashed line represents the distance profile for the method 1, which allows translational motion,

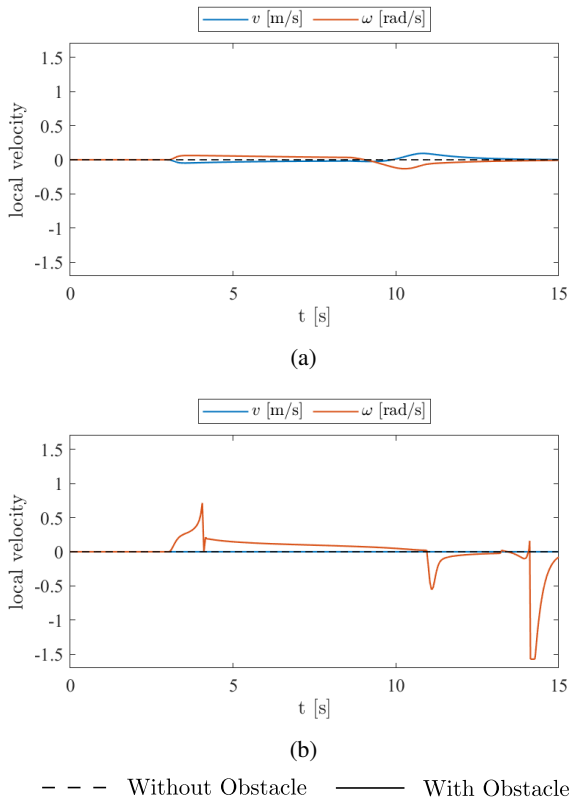


Figure 11 Test case 2: local velocities using Eq.5 (a) and Eq.7 (b).

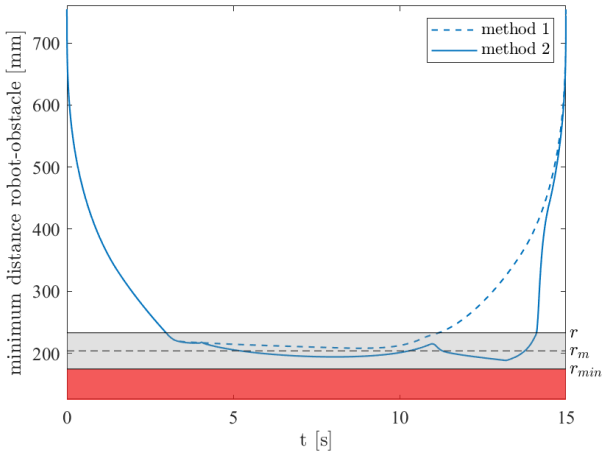


Figure 12 Test case 2: evolution of the minimum distance between the robot and the obstacle for the two methods considered, using Eq.5 and Eq.7.

while the solid line corresponds to the method 2, which relies solely on rotational avoidance.

The graph shows that, for both methods, the minimum distance between the robot and the obstacle decreases as the obstacle approaches. However, a significant difference can be observed in how each method handles proximity constraints. The method allowing translational motion (dashed line) maintains a greater separation from the obstacle throughout the interaction, ensuring a safer avoidance maneuver. Conversely, the purely rotational method (solid line) results in a much closer interaction, particularly around the minimum distance threshold. Both methods detect the obstacle at the same time, at $2.9\,\mathrm{s}$, but diverge in the times for exiting the safety beam: method 1 exits at $11.1\,\mathrm{s}$, with an overall duration of $8.2\,\mathrm{s}$, while method 2 exits at $14.1\,\mathrm{s}$, with an overall duration of $11.2\,\mathrm{s}$.

The shaded regions in the plot highlight critical safety zones: the red area represents distances below the minimum safety threshold r_{min}, where collision risk is high, while the gray region corresponds to a cautionary zone near the safety limit. The rotational method brings the robot close to the obstacle, whereas the translational method consistently maintains a safer distance.

4 DISCUSSION OF RESULTS

Two different methods are employed to enable obstacle avoidance. The first method allows the robot to move both translationally and rotationally, granting greater flexibility in avoiding obstacles, including the ability to temporarily move backward if necessary. The second method relies solely on rotational maneuvers, which can be effective in certain scenarios in which the robot has to move along a path where obstacles are present.

The obstacles considered in this study include both static objects unintentionally left within the workspace and dynamic elements, such as human operators moving within the shared area. The proposed algorithm is not constrained by the type of obstacle detection system used, as long as it can accurately provide the spatial coordinates of the detected object.

The comparative evaluation between the two avoidance strategies revealed significant performance differences. method 1, based on a classical reactive approach, showed stable behaviour, but with some limitations, especially in scenarios where speed of adaptation is crucial. In particular, its ability to avoid obstacles is less smooth, with more marked deviations from the desired path.

In contrast, method 2 demonstrated greater efficiency, allowing more progressive and smooth adjustments of the trajectory, reducing sudden deviations and improving continuity of motion. This approach proved to be more robust and flexible, being particularly suitable for contexts

in which the robot must follow a predetermined path in the presence of fixed or dynamic obstacles.
Test case 2 analysed the behaviour of the robot in a situation where it is already in the desired position and a moving obstacle is approaching. In this scenario, method 1 demonstrated superior performance compared to method 2, as it allows the robot to make a temporary deviation from its position without losing its main objective.
The analysis of local velocities shows that method 1, based on reactive control, allows the robot to move in a rapid and controlled manner to avoid interference with the obstacle, and then autonomously return to its initial position once the area is clear. This behaviour is particularly advantageous in collaborative applications, where human operators may have to work in the same area as the robot or move it temporarily without the need for explicit commands.
On the other hand, method 2, designed to generate more fluid and continuous trajectories, proved less effective in this specific context. Since the robot does not have to follow a predefined path, but simply maintain the desired position while avoiding collisions.
One limitation of the proposed approach is that it does not explicitly account for the relative velocity between the robot and the obstacle, which may lead to unnecessary deviations or delayed reactions depending on the scenario. A possible enhancement involves dynamically adjusting the safety radius based on the approaching speed: if the relative velocity is high, the safety region expands, activating the repulsive velocity earlier. This approach helps prevent excessive reactions to slow-moving obstacles while ensuring a timely response to fast-approaching ones.

5 CONCLUSIONS

This study presented a new approach for obstacle avoidance in non-holonomic mobile robots equipped with differential transmission. The proposed methodology was tested in complex dynamic environments, demonstrating its ability to improve manoeuvrability and reduce the risk of sudden stops, while maintaining real-time response. The simulations presented in the previous section are aimed at verifying the correctness of the algorithm. In fact, the final objective of this research is to transfer the control framework to a real system, currently under construction in the laboratory, where a vision system composed of three Intel RealSense depth cameras is able to capture the presence of people or objects within the work space [27].
A particularly relevant scenario arises when the robot is stationed in a designated work position, and an operator needs to perform a task in the same area or manually reposition the robot. In such cases, the robot temporarily relocates to prevent interference, ensuring seamless human-robot collaboration. Once the operator has vacated the workspace, the robot autonomously returns to its original position without requiring explicit commands or external communication. This adaptive behavior significantly enhances flexibility in collaborative environments, enabling uninterrupted workflows while maintaining operational efficiency and safety.
These results show that the choice of avoidance method depends not only on the nature of the obstacles (static or dynamic), but also on the specific task of the robot. When the main objective is to maintain a position and ensure flexibility in interaction with operators or other dynamic elements of the environment, method 1 is a more effective solution.
From a practical point of view, the integration of these methods in industrial mobile platforms can lead to significant benefits in terms of operational efficiency. The ability to maintain a safe minimum distance by dynamically adjusting the trajectory is particularly relevant for applications involving collaborative robots (cobots), where human-robot interaction is coupled with high-throughput industrial contexts.
A key contribution of this work lies in the integration of an optimised influence zone, which allows the robot to proactively adjust its path before entering critical proximity regions. This innovation reduces the risk of emergency stops and ensures continuous movement, solving one of the main limitations of conventional obstacle avoidance methods. The introduction of the tip into the model further refines trajectory planning in confined environments, demonstrating a clear advantage over conventional circular models, which tend to overestimate safety margins.
The study has some limitations due to the simplifications of the simulation, which does not consider real-life factors such as uneven surfaces, variable friction or errors in the vision sensors. To improve the robustness of the algorithm, future developments could include systems for predicting the trajectory of obstacles through machine learning, integration with advanced sensors and testing on a physical system to refine the model.
In future work, an exploration of the possibility of using variable coefficients for repulsive velocity and recovery parameters to further optimise robot performance is planned. By allowing these coefficients to adapt according to the robot's current state, environment and task requirements, expect to improve both the efficiency of obstacle avoidance and the accuracy of point-to-point trajectory tracking.
Future research will focus on extending the proposed algorithm to multi-robot coordination scenarios, where avoidance strategies will have to consider not only static and dynamic obstacles, but also the interaction between multiple agents operating in the same workspace. Furthermore, an experimental validation will be conducted on a fully autonomous mobile manipulator, combining a 6 degrees of freedom robotic arm with a differential transmission base. In this way, the additional degrees of freedom of the system can be exploited to improve collision avoidance and confer

the robot an optimal motion in terms of smoothness and dexterity. The integration of advanced perception systems, such as LiDAR and depth cameras, will further improve the accuracy of obstacle detection, enhancing situational awareness and decision-making capabilities.

REFERENCES

[1] Dimitrios Bechtsis, Naoum Tsolakis, Menippos Vouzas, and Dimitrios Vlachos. Industry 4.0: Sustainable material handling processes in industrial environments. In *Computer aided chemical engineering*, volume 40, pages 2281–2286. Elsevier, 2017.

[2] Mohd Nayab Zafar and JC Mohanta. Methodology for path planning and optimization of mobile robots: A review. *Procedia computer science*, 133:141–152, 2018.

[3] D Costa et al. A novel class of bio-inspired underwater robots. *INTERNATIONAL JOURNAL OF MECHANICS AND CONTROL*, 23(2):23–35, 2022.

[4] Luca Carbonari, Luigi Tagliavini, Andrea Botta, Paride Cavallone, and Giuseppe Quaglia. Preliminary observations for functional design of a mobile robotic manipulator. In *International Conference on Robotics in Alpe-Adria Danube Region*, pages 39–46. Springer, 2021.

[5] Carmen Visconte, Paride Cavallone, Luca Carbonari, Andrea Botta, and Giuseppe Quaglia. Design of a mechanism with embedded suspension to reconfigure the agri_q locomotion layout. *Robotics*, 10(1):15, 2021.

[6] Piotr Skrzypczyński. Mobile robot localization: where we are and what are the challenges? *Automation 2017: Innovations in Automation, Robotics and Measurement Techniques 1*, pages 249–267, 2017.

[7] Federico Neri, Luca Alfredo Annoni, Giacomo Palmieri, Matteo-Claudio Palpacelli, and Massimo Callegari. Localisation of mobile robots via ultra-wideband systems. In *International Design Engineering Technical Conferences and Computers and Information in Engineering Conference*, volume 87356, page V007T07A008. American Society of Mechanical Engineers, 2023.

[8] Bo Tao, Xingwei Zhao, Sijie Yan, and Han Ding. Kinematic modeling and control of mobile robot for large-scale workpiece machining. *Proceedings of the Institution of Mechanical Engineers, Part B: Journal of Engineering Manufacture*, 236(1-2):29–38, 2022.

[9] Oussama Khatib. Real-time obstacle avoidance for manipulators and mobile robots. *The international journal of robotics research*, 5(1):90–98, 1986.

[10] Gregor Klancar, Drago Matko, and Saso Blazic. Mobile robot control on a reference path. In *Proceedings of the 2005 IEEE International Symposium on, Mediterrean Conference on Control and Automation Intelligent Control, 2005.*, pages 1343–1348. IEEE, 2005.

[11] Lixing Liu, Xu Wang, Xin Yang, Hongjie Liu, Jianping Li, and Pengfei Wang. Path planning techniques for mobile robots: Review and prospect. *Expert Systems with Applications*, 227:120254, 2023.

[12] Antonio Sgorbissa and Renato Zaccaria. Planning and obstacle avoidance in mobile robotics. *Robotics and Autonomous Systems*, 60(4):628–638, 2012.

[13] Yunchao Tang, Shaojun Qi, Lixue Zhu, Xianrong Zhuo, Yunqi Zhang, and Fan Meng. Obstacle avoidance motion in mobile robotics. *Journal of System Simulation*, 36(1):1–26, 2024.

[14] Anish Pandey, Shalini Pandey, and D Parhi. Mobile robot navigation and obstacle avoidance techniques: A review. *Int Rob Auto J*, 2(3):00022, 2017.

[15] Shuzhi Sam Ge and Yun J Cui. Dynamic motion planning for mobile robots using potential field method. *Autonomous robots*, 13:207–222, 2002.

[16] Rocco Galati, Giacomo Mantriota, and Giulio Reina. An eco-friendly and sustainable route planning for a floor-marking omnidirectional robot. *International Journal of Mechanics and Control*, 23(2):73 – 83, 2022. Cited by: 2.

[17] Johann Borenstein and Yoram Koren. Real-time obstacle avoidance for fast mobile robots. *IEEE Transactions on systems, Man, and Cybernetics*, 19(5):1179–1187, 1989.

[18] Weihao Li, Chenguang Yang, Yiming Jiang, Xiaofeng Liu, Chun-Yi Su, et al. Motion planning for omnidirectional wheeled mobile robot by potential field method. *Journal of Advanced Transportation*, 2017, 2017.

[19] Patrick F Muir and Charles P Neuman. Kinematic modeling for feedback control of an omnidirectional wheeled mobile robot. *Autonomous robot vehicles*, pages 25–31, 1990.

[20] Sheha Ame Mnubi. Motion planning and trajectory for wheeled mobile robot. *International Journal of Science and Research*, 5(1):1064–1068, 2016.

[21] Soonshin Han, ByoungSuk Choi, and JangMyung Lee. A precise curved motion planning for a differential driving mobile robot. *Mechatronics*, 18(9):486–494, 2008.

[22] Martín Velasco-Villa, Raúl Dalí Cruz-Morales, Alejandro Rodriguez-Angeles, and Carlos A Domínguez-Ortega. Observer-based time-variant spacing policy for a platoon of non-holonomic mobile robots. *Sensors*, 21(11):3824, 2021.

[23] Ksenia Shabalina, Artur Sagitov, and Evgeni Magid. Comparative analysis of mobile robot wheels design. In *2018 11th International Conference on Developments in esystems Engineering (dese)*, pages 175–179. IEEE, 2018.

[24] Federico Neri, Matteo Forlini, Cecilia Scoccia, Giacomo Palmieri, and Massimo Callegari. Experimental evaluation of collision avoidance techniques for collaborative robots. *Applied Sciences*, 13(5):2944, 2023.

[25] Elie Maalouf, Maarouf Saad, and Hamadou Saliah. A higher level path tracking controller for a four-wheel differentially steered mobile robot. *Robotics and autonomous systems*, 54(1):23–33, 2006.

[26] Yutaka Kanayama, Yoshihiko Kimura, Fumio Miyazaki, and Tetsuo Noguchi. A stable tracking control method for an autonomous mobile robot. In *Proceedings., IEEE International Conference on Robotics and Automation*, pages 384–389. IEEE, 1990.

[27] Matteo Forlini, Federico Neri, Cecilia Scoccia, Luca Carbonari, and Giacomo Palmieri. Collision avoidance in collaborative robotics based on real-time skeleton tracking. In *International Conference on Robotics in Alpe-Adria Danube Region*, pages 81–88. Springer, 2023.

ISSN 1590-8844
International Journal of Mechanics and Control, Vol. 26, No. 02, 2025
https://doi.org/10.69076/jomac.2025.0004

REGULARIZED DYNAMIC PARAMETER IDENTIFICATION FOR THE MITSUBISHI RV-5AS-D-S01 ROBOT

D. Dona' [*] P. Boscariol [*] M. Bottin [**] B. Lenzo [**] G. Rosati [**]

[*] Department of Management and Engineering (DTG), University of Padua, 36100 Vicenza, Italy

[**] Department of Industrial Engineering (DII), University of Padua, 35131 Padova, Italy

ABSTRACT

The use of accurate dynamic models plays a role of paramount importance in the development of efficient and accurate robotic applications. Model-based techniques are at the heart of the development of advanced control strategies, and are extremely useful for planning time-efficient or energy efficient tasks, or to control the interaction with humans in a collaborative framework. The availability of accurate dynamic models for industrial robots is however often limited due to the fact that manufacturers rarely disclose sufficient technical data to build a reliable dynamic model, hence the need to use model identification techniques. This paper presents the results of the use of a model identification technique for a serial robot, augmented with a regularization procedure, applied to the Mitsubishi RV-5AS-D-S01 industrial robot.

Keywords: Identification, Serial robot, Dynamical parameters, regularization

1 INTRODUCTION

The execution of advanced robotic tasks requires the evaluation of not only the kinematic properties of the system but also of the forces and torques needed for the robot's operation. In this context, an accurate dynamic model is crucial for predicting the robot's interaction with the environment and to determine the control forces required to successfully accomplish the desired tasks.

The dynamic model of a serial robot is typically formulated using either the Lagrange equations or the Newton-Euler formulation [1]. However, regardless of the specific choice of the analytic formulation, the dynamic model depends on the robot's dynamical parameters, such as link masses, inertia terms, centers of mass, and friction parameters [2]. These parameters are almost never provided in manufacturer datasheets, which usually include only basic nominal kinematic specifications. A common approach that provides a partial solution to the estimation of the inertial parameters relies on the use of CAD models of the manipulator under investigation to extract the inertial parameters of each robot link [3]. This however requires to assume a known mass density of the robot links - generally a uniform one - which is rather unrealistic and potentially very detrimental to the modeling accuracy. By this approach, in particular, the mass concentration in the motors is neglected. An accurate model is essential for various applications, particularly for model-based control [4] and optimal control [5, 6] of robotic manipulators. The need for accurate dynamic parameters has driven extensive research in dynamic identification for decades, focusing on the estimation of inertial parameters [7, 8, 9, 10, 11, 12] and on the identification of friction forces [13, 14, 15].

A common approach is to design a regressor that maps unknown parameters to the required torques, with the parameters that best fit the data being the desired ones. The first instance of this idea can be found in [7], which, in addition to proposing identification from raw torque data, introduced the concept of *identifiable parameters*. Not all dynamical parameters can be determined through identification procedures, as some parameters may not contribute to the equations that originate the regressor. Consequently, it is necessary to establish a minimal set of

Contact author: Domenico Dona'[1]
[1] Stradella S. Nicola 3, 36100 Vicenza, Italy .
E-mail: domenico.dona@unipd.it

independent parameters, known as *base parameters* [16] and to express the dynamic model using just those.

The identification of dynamical parameters involves two main research directions: (i) optimization strategies for solving the regression problem and (ii) selection of excitation trajectories.

Once the regressor is defined, an optimization problem must be solved to estimate the parameters. If the regressor is linear in the unknown parameters, the problem reduces to a Least Squares Problem (LSP). This is the case for common serial manipulators as long as the set of parameters is chosen properly [17]. The solution of the LSP can however lead to poor results if the used data are numerically ill conditioned. This issue if often solved by a regularization of the LSP [18]. A common approach is to ensure that the estimated parameters should not deviate excessively from prior CAD-based estimates, by means of a regularizer that penalizes large discrepancies between the two. Enforcing physical consistency is essential, as naive optimization may yield unrealistic parameters, such as negative masses.

Beyond the proper formulation of the optimization problem, the choice of the trajectory used to collect the experimental data is also critical. The excitation trajectory should improve parameter identifiability, often by minimizing the condition number of the regressor matrix. In [19], various optimization objectives for trajectory selection are explored. Typically, parametric trajectories are defined using splines [20] or harmonic functions [21]. Harmonic functions are particularly advantageous because they allow a precise control over the excitation frequency content, thereby avoiding unwanted vibrations that can jeopardize the parameter estimation.

In this work, we employ optimized harmonic trajectories to identify the dynamic parameters of a Mitsubishi RV-5AS-D-S01 serial robot. We first synthesize the excitation trajectory using a genetic algorithm and then regularize the least-squares problem using CAD-based. This paper extends our previous work presented at the IFIT 2024 Conference [22] by including an extended identification technique and a more detailed analysis of the experimental results. Additional experimental results have been included too, so that one experimental trial will be devoted to the identification procedure, and one trial is devoted to the validation of the model.

The main contribution of this paper is the application of a regularized identification procedure based on CAD priors for the Mitsubishi RV-5AS-D-S01, and the reporting of the identified dynamic parameters and friction coefficients. To the best of Authors' knowledge, the only other work in literature concerning the identification of this specific manipulator is the already mentioned [22], which contains only partial data that are revised and expanded here.

The paper is organized as follows: the method for identifying the robot parameters is presented in Section 2, while the results are reported in Section 3. Conclusions are drawn in Section 4.

Table I - Modified Denavit-Hartenberg parameters for the Mitsubishi RV-5AS-D-S01.

$\mathbf{T}_{i,i-1}$	α_{i-1} (°)	a_{i-1} (mm)	ϑ_i (°)	d_i (mm)
10	0	0	q_1	254
21	-90	0	$q_2 - 90$	0
32	0	410	q_3	0
43	-90	0	q_4	500
54	90	0	q_5	0
65	-90	0	q_6	138.5

2 METHOD

2.1 ROBOT KINEMATICS

The manipulator under investigation is the Mitsubishi RV-5AS-D-S01, a six-axis serial manipulator with a spherical wrist. The Modified Denavit-Hartenberg (MDH) parameters are listed in Table I. This notation is the one made popular by JJ Craig in the classic textbook [23].

The transformation matrix $\mathbf{T}_{i,i-1}$ represents the homogeneous transformation (i.e., the combined rotation and translation) from the $(i-1)$-th frame to the i-th frame. Each matrix $\mathbf{T}_{i,i-1}$ can be expressed as:

$$\mathbf{T}_{i,i-1} = \mathbf{T}_{\mathrm{Rx}}(\alpha_{i-1})\,\mathbf{T}_{\mathrm{Tx}}(a_{i-1})\,\mathbf{T}_{\mathrm{Rz}}(\vartheta_i)\,\mathbf{T}_{\mathrm{Tz}}(d_i) \tag{1}$$

where $\mathbf{T}_{\mathrm{Rx}}(\cdot)$ and $\mathbf{T}_{\mathrm{Rz}}(\cdot)$ denote pure rotation matrices about the x-axis and z-axis, respectively, and $\mathbf{T}_{\mathrm{Tx}}(\cdot)$ and $\mathbf{T}_{\mathrm{Tz}}(\cdot)$ denote pure translation matrices along the x-axis and z-axis, respectively.

In particular, the transformation matrix can be decomposed as:

$${}^{i-1}\mathbf{T}_i = \begin{bmatrix} {}^{i-1}\mathbf{R}_i & {}^{i-1}\mathbf{r}_i \\ \mathbf{0}_3^\intercal & 1 \end{bmatrix}, \tag{2}$$

where ${}^{i}\mathbf{R}_{i-1}$ is the rotation matrix from frame $(i-1)$ to frame i, and ${}^{i-1}\mathbf{r}_i$ is the translation vector from the origin of frame $(i-1)$ to the origin of frame i, expressed in frame $(i-1)$.

The linear and angular velocities of the i-th frame (assuming only revolute joints) can be computed as:

$$\begin{aligned} {}^{i}\boldsymbol{\omega}_i &= {}^{i-1}\mathbf{R}_i^\intercal\, {}^{i-1}\boldsymbol{\omega}_{i-1} + {}^{i}\mathbf{k}_i\,\dot{q}_i, \\ {}^{i}\mathbf{v}_i &= {}^{i-1}\mathbf{R}_i^\intercal \left({}^{i-1}\mathbf{v}_{i-1} + {}^{i-1}\boldsymbol{\omega}_{i-1} \times {}^{i-1}\mathbf{r}_i\right) \end{aligned} \tag{3}$$

where the left superscript indicates the frame in which the quantities are expressed. The unit vector ${}^{i}\mathbf{k}_i = [0,\, 0,\, 1]^\intercal$ denotes the direction of the i-th z axis in the i-th frame.

The velocities of the global frame (frame 0) are given by:

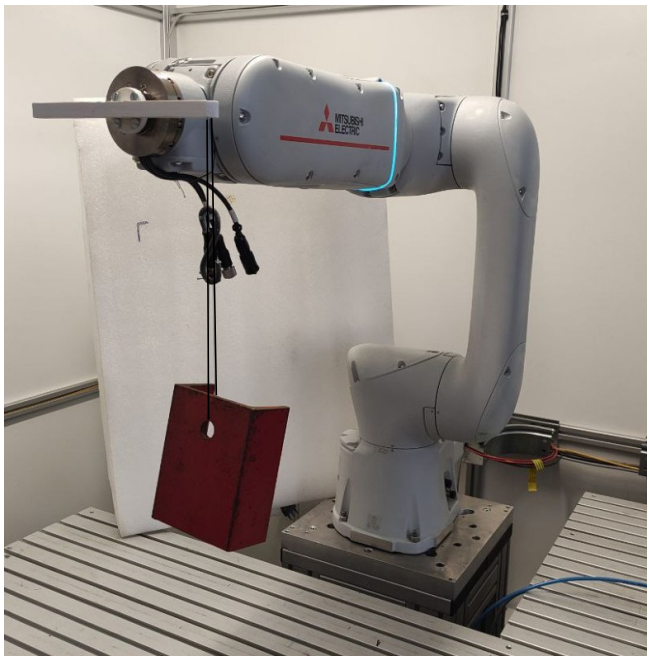


Figure 1 The experimental setup used for the static identification

$$^0\boldsymbol{\omega}_0 = \mathbf{0}_3, \qquad ^0\mathbf{v}_0 = \mathbf{0}_3 \tag{4}$$

since this frame is fixed to the ground link.

2.2 ROBOT STATICS

The proprietary software that is needed to program and execute the motion of the robot allows does not provide any direct measurement of the motor or joint torques. Motor torques can be estimated from motor currents, however this evaluation requires to use the motor torque constants k_t, which are, again, undisclosed by the manufacturer. An estimation of the latter can be achieved by applying a known external force to the robot in a convenient configuration, and then by measuring the change in the current caused by the external solicitation.

The gravity forces acting on the robot can then be formulated by means of the static balance equations of the system. Referring to Fig. 1, which shows the robot the home position $\mathbf{q}_h = \mathbf{0}_6$, it is possible to write the following relationships:

$$\begin{aligned} \tau_2 = \tau_3 &= -mg(d_4 + d_6) \\ \tau_5 &= -mg\, d_6 \\ \tau_4 = \tau_6 &= mg\, a_6 \end{aligned} \tag{5}$$

in which τ_j is the j-th joint torque due to the mass m added to the end-effector of the robot. The torque balance is represented graphically in figure 2.

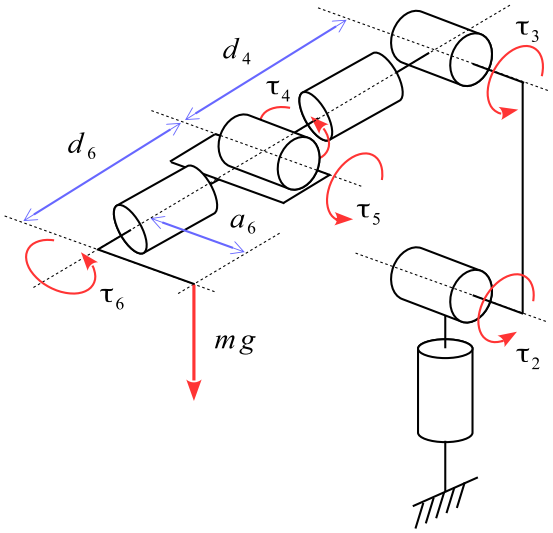


Figure 2 Torque balance due to the additional mass m

Mass m is offset from the tool center point by means of a plastic bar of length a_6. Given that the base of the robot is mounted horizontally, it is impossible to excite the first joint without any other additional implement. However, according to the manufacturer's datasheet, the first and second motors are identical to each other, hence it is assumed that they both share the same torque constant. The torque produced by the i-th motor can be computed as:

$$\tau_{\mathrm{m},i} = \frac{\tau_i}{k_{r,i}} \tag{6}$$

being $k_{r,i}$ the reduction ratio for joint i. Finally the i-th torque constant $k_{t,i}$ can be computed as:

$$k_{t,i} = \frac{\tau_{\mathrm{m},i}}{i_{a,i}} \tag{7}$$

where $i_{a,i}$ is the i-th armature current.

2.3 ROBOT DYNAMICS

The dynamics of the robot can be formulated using the Euler-Lagrange equations. The kinetic energy of the robot, written with quantities referred to the i-th frame, which is integral to the i-th link, is given by:

$$\mathcal{T} = \sum_{i=1}^{n} \left(\frac{1}{2} m_i \, {}^i\mathbf{v}_i{}^\intercal \, {}^i\mathbf{v}_i + \frac{1}{2} {}^i\boldsymbol{\omega}_i{}^\intercal \, \mathbf{I}_i \, {}^i\boldsymbol{\omega}_i - {}^i\mathbf{v}_i{}^\intercal \left({}^i\mathbf{s}_i \times {}^i\boldsymbol{\omega}_i \right) \right), \tag{8}$$

where m_i, ${}^i\mathbf{s}_i$, and $\mathbf{I}_i$ denote the i-th link mass, its first mass moment vector, and the inertia tensor expressed in the i-th

frame, respectively. The first mass moment vector is defined as:

$$ {}^{i}\mathbf{s}_i = {}^{i}\begin{bmatrix} s_{x,i} \\ s_{y,i} \\ s_{z,i} \end{bmatrix} = m_i^i \boldsymbol{\ell}_i = m_i \, {}^{i}\begin{bmatrix} \ell_{x,i} \\ \ell_{y,i} \\ \ell_{z,i} \end{bmatrix} \tag{9} $$

in which ${}^{i}\boldsymbol{\ell}_i$ is the position of the i-th CoM in the i-th reference frame. The number of degrees-of-freedom is denoted by n. The potential energy of the robot is due to gravity:

$$ \mathcal{U} = \sum_{i=1}^{n} \begin{bmatrix} 0 & 0 & -g \end{bmatrix} {}^{0}\mathbf{s}_i, \tag{10} $$

where ${}^{0}\mathbf{s}_i$ is the the first mass moment vector for the i-th link in the global frame. It can be computed using homogeneous coordinates as:

$$ \begin{bmatrix} {}^{0}\mathbf{s}_i \\ m_i \end{bmatrix} = m_i \begin{bmatrix} {}^{0}\boldsymbol{\ell}_i \\ 1 \end{bmatrix} = m_i \, {}^{0}\mathbf{T}_i \begin{bmatrix} {}^{i}\boldsymbol{\ell}_i \\ 1 \end{bmatrix} = {}^{0}\mathbf{T}_i \begin{bmatrix} {}^{i}\mathbf{s}_i \\ m_i \end{bmatrix}. \tag{11} $$

Thus, the Lagrangian of the system is:

$$ \mathcal{L} = \mathcal{T} - \mathcal{U}, \tag{12} $$

and the equations of motion are given by:

$$ \frac{\mathrm{d}}{\mathrm{d}t} \frac{\partial \mathcal{L}}{\partial \dot{\mathbf{q}}} - \frac{\partial \mathcal{L}}{\partial \mathbf{q}} = \boldsymbol{\tau} - \boldsymbol{\tau}_{\mathrm{f}}, \tag{13} $$

where $\boldsymbol{\tau}$ represents the joint torques and $\boldsymbol{\tau}_{\mathrm{f}}$ denotes the torques due to friction. In particular, we use the following model:

$$ \boldsymbol{\tau}_{\mathrm{f}} = \mathbf{F}_v \, \dot{\mathbf{q}} + \mathbf{F}_c \, \mathrm{sign}(\dot{\mathbf{q}}), \tag{14} $$

where $\mathbf{F}_v$ and $\mathbf{F}_c$ are diagonal matrices whose i-th entries are the i-th viscous and dry friction coefficients, respectively.
Since we measure the motor current (and therefore the torque), it is convenient to re-formulate equation (13) in terms of motor torque, by adding also the inertial terms associated with the motors:

$$ \tau_{\mathrm{m},i} = \frac{1}{k_{r,i}} \tau_i + k_{r,i} I_{m,i} \ddot{q}_i, \quad i = 1, \ldots, n, \tag{15} $$

where $k_{r,i}$ denote the gear ratio of the i-th gearbox, $\tau_{\mathrm{m},i}$ is the torque exerted by the i-th motor, and $I_{m,i}$ is the corresponding motor inertia. The inertia of the motor is known from the datasheets of the manufacturer. Now, the motor torque vector can be written in the following compact form:

$$ \boldsymbol{\tau}_{\mathrm{m}} = \boldsymbol{\Gamma}(\mathbf{q}, \dot{\mathbf{q}}, \ddot{\mathbf{q}}) \, \boldsymbol{\pi} + \mathbf{b}(\mathbf{q}, \dot{\mathbf{q}}, \ddot{\mathbf{q}}) \tag{16} $$

where $\boldsymbol{\Gamma}$ is the regression matrix and $\mathbf{b}$ is a term that does not depend on $\boldsymbol{\pi}$. The vector of unknown parameters, $\boldsymbol{\pi} = [\boldsymbol{\pi}_1, \ldots, \boldsymbol{\pi}_n]$, is defined as:

$$ \boldsymbol{\pi}_i = \big[m_i, \, {}^{i}\mathbf{s}_i^{\intercal}, \, I_{xx,i}, \, I_{yy,i}, \, I_{zz,i}, \, I_{xy,i}, \, I_{yz,i}, \, I_{xz,i}, \, f_{c,i}, \, f_{v,i}\big]^{\intercal} \in \mathbb{R}^{12} \tag{17} $$

The vector $\boldsymbol{\pi}$ includes the set of inertial and friction parameters to be estimated by means of the procedure which is outlined in the next section.

2.4 BASE PARAMETERS

Owing to the structure of the robot, not all the 72 parameters in π_i are identifiable [8]. For example, some of them do not appear in the equations of motion (16), i.e.:

$$ \exists \, \pi_i \quad \text{such that} \quad \frac{\partial \boldsymbol{\tau}_{\mathrm{m}}}{\partial \pi_i} = 0 \tag{18} $$

so they can be removed from $\boldsymbol{\pi}$, as well as from the corresponding columns of $\boldsymbol{\Gamma}$. Even after excluding these parameters, some parameters may still be linearly dependent on others. To separate the two sets, it is sufficient to apply the QR decomposition [8]:

$$ \boldsymbol{\Gamma} = \mathbf{Q}\mathbf{R} \tag{19} $$

The linearly independent parameters, denoted by $\boldsymbol{\pi}_{\mathrm{li}}$, are those corresponding to nonzero diagonal entries in $\mathbf{R}$. In the case of the studied robot, 48 independent parameters can be identified. Therefore, it is possible to rewrite (16) as:

$$ \boldsymbol{\tau}_{\mathrm{m}} = \begin{bmatrix} \boldsymbol{\Gamma}_{\mathrm{li}} & \boldsymbol{\Gamma}_{\mathrm{ld}} \end{bmatrix} \begin{bmatrix} \boldsymbol{\pi}_{\mathrm{li}} \\ \boldsymbol{\pi}_{\mathrm{ld}} \end{bmatrix} + \mathbf{b} \tag{20} $$

by reordering the entries according to $\mathbf{R}$, where $\boldsymbol{\Gamma}_{\mathrm{li}}$ and $\boldsymbol{\Gamma}_{\mathrm{ld}}$ are the regressor columns related to the linear independent and linear dependent parameters . Using the definition of linear dependency:

$$ \boldsymbol{\Gamma}_{\mathrm{ld}} = \boldsymbol{\Gamma}_{\mathrm{li}} \boldsymbol{\Psi} \tag{21} $$

the matrix $\boldsymbol{\Psi}$ can be obtained by applying the QR decomposition to both $\boldsymbol{\Gamma}_{\mathrm{li}}$ and $\boldsymbol{\Gamma}_{\mathrm{ld}}$, i.e.:

$$ \boldsymbol{\Gamma}_{\mathrm{li}} = \mathbf{Q}_{\mathrm{li}} \mathbf{R}_{\mathrm{li}} \quad \text{and} \quad \boldsymbol{\Gamma}_{\mathrm{ld}} = \mathbf{Q}_{\mathrm{ld}} \mathbf{R}_{\mathrm{ld}} \tag{22} $$

so that:

$$ \boldsymbol{\Psi} = \mathbf{R}_{\mathrm{li}}^{-1} \mathbf{R}_{\mathrm{ld}} \tag{23} $$

Thus, equation (20) can be written as:

$$ \boldsymbol{\tau}_{\mathrm{m}} = \begin{bmatrix} \boldsymbol{\Gamma}_{\mathrm{li}} & \boldsymbol{\Gamma}_{\mathrm{li}} \boldsymbol{\Psi} \end{bmatrix} \begin{bmatrix} \boldsymbol{\pi}_{\mathrm{li}} \\ \boldsymbol{\pi}_{\mathrm{ld}} \end{bmatrix} + \mathbf{b} = \boldsymbol{\Gamma}_{\mathrm{li}} \left(\boldsymbol{\pi}_{\mathrm{li}} + \boldsymbol{\Psi} \boldsymbol{\pi}_{\mathrm{ld}} \right) + \mathbf{b} = \boldsymbol{\Gamma}_{\mathrm{li}} \boldsymbol{\pi}_{\mathrm{bp}} + \mathbf{b} \tag{24} $$

where $\boldsymbol{\pi}_{\mathrm{bp}}$ is the vector of the so-called *base parameters*. The base parameters are the values that can be identified by means of the regression procedure that is explained in the next section. We will refer to $\boldsymbol{\Gamma}_{\mathrm{li}}$ as the reduced regressor.

2.5 IDENTIFICATION

After collecting data in the following form:

$$\{\boldsymbol{\tau}_{\mathrm{m},i},\, \mathbf{q}_i,\, \dot{\mathbf{q}}_i,\, \ddot{\mathbf{q}}_i\}_{i=1}^{s} \tag{25}$$

it is possible to solve the identification problem by addressing (24). A simple but effective approach is to compute the least squares (LS) solution, given by:

$$\boldsymbol{\pi}_{\mathrm{bp}}^{\star} = \arg\min_{\boldsymbol{\pi}_{\mathrm{bp}}} \|(\underline{\boldsymbol{\Gamma}}\boldsymbol{\pi}_{\mathrm{bp}} + \underline{\mathbf{b}}) - \underline{\boldsymbol{\tau}}_{\mathrm{m}}\|_2^2 \tag{26}$$

where $\underline{\boldsymbol{\Gamma}}$ and $\underline{\mathbf{b}}$ are the (reduced) regressor and constant term, stacked along a trajectory.

The quality of the LS solution depends on the condition number of $\boldsymbol{\Gamma}$, since the estimation is based on measured data which can be substantially affected by measurement noise; the higher the condition number, the higher is the sensibility of the solution to noise. The inaccuracy of the LS solution (26) can even lead to the determination of physically meaningless values, such as negative masses, negative diagonal terms in the inertia tensor, or negative friction parameters.

To mitigate this issue, a regularization approach [24, 25] can be adopted, penalizing deviations from a set of prior estimates $\boldsymbol{\pi}_{\mathrm{bp}}^{0}$ as, for example, estimates derived from CAD data under the assumption of uniform mass distribution. The modified problem then becomes:

$$\boldsymbol{\pi}_{\mathrm{bp}}^{\star} = \arg\min_{\boldsymbol{\pi}_{\mathrm{bp}}} \|(\underline{\boldsymbol{\Gamma}}\boldsymbol{\pi}_{\mathrm{bp}} + \underline{\mathbf{b}}) - \underline{\boldsymbol{\tau}}_{\mathrm{m}}\|_2^2 + \gamma\|\boldsymbol{\pi}_{\mathrm{bp}} - \boldsymbol{\pi}_{\mathrm{bp}}^{0}\|_2^2 \tag{27}$$

where γ is the regularization factor, which can be tuned to balance estimation accuracy and physical plausibility. The value of the parameter γ biases the adherence of the inertial parameters to the CAD estimates: it can be set to a high value only if the CAD estimates are reputed to be highly accurate. Setting a too low value of γ, on the other hand, defeats the purpose of the regularization. For the case under investigation here, an iterative tuning process has been performed starting with $\gamma = 0$ and increasing it until physical meaningfulness of the identified model has been achieved.

2.6 EXCITATION TRAJECTORIES

As discussed in Sect. 2.5, the condition number $\kappa = \mathrm{cond}(\boldsymbol{\Gamma})$ plays an important role in the quality of the identified parameters. In this context, it is desirable to select trajectories that minimize κ. We use a 5th-order Fourier basis to parametrize the trajectories, as it allows us to select frequency content of the planned motion. The approach used here reflects the choice discussed in the seminal work [21] and used in countless others works for robot identification. The motion law for the i-th joint is given by:

$$q_i(t) = q_{i,0} + \sum_{j=1}^{N} \left(a_{i,j}\sin(j\omega_f t) - b_{i,j}\cos(j\omega_f t)\right) \tag{28}$$

$$\dot{q}_i(t) = \sum_{j=1}^{N} \left(a_{i,j}\omega_f j\cos(j\omega_f t) + b_{i,j}\omega_f j\sin(j\omega_f t)\right) \tag{29}$$

$$\ddot{q}_i(t) = \textstyle\sum_{j=1}^{N} \left(-a_{i,j}(\omega_f j)^2\sin(j\omega_f t) + b_{i,j}(\omega_f j)^2\cos(j\omega_f t)\right) \tag{30}$$

where N is the order of the series (set to 5), $q_{i,0}$ is the initial position of the i-th joint, and $a_{i,j}$ and $b_{i,j}$ are the series coefficients. The base frequency ω_f is defined as $2\pi/t_f$ to ensure the periodicity of the motion, where t_f is the total time of the trajectory. Having composed the motion as a linear combination of harmonic signals allows total control over the frequency spectrum of the excitation. In particular, the limitation of the excitation trajectory frequency spectrum minimizes the excitation of second-order effects such as those associated with the joint flexibility. The latter are not included in the rigid model assumed throughout this work, so any motion-induced oscillation would appear as an unmodeled disturbance in eq. (27). The motion laws must be bounded to ensure its feasibility by limiting joint positions, velocities and accelerations. Using the Parseval identity, the limits can be simply imposed, in a conservative manner as:

$$\sum_{j=1}^{N} \sqrt{a_{i,j}^2 + b_{i,j}^2} + |q_{i,0}| < q_{i,\mathrm{lim}} \tag{31}$$

$$\sum_{j=1}^{N} \omega_f j \sqrt{a_{i,j}^2 + b_{i,j}^2} < \dot{q}_{i,\mathrm{lim}} \tag{32}$$

$$\sum_{j=1}^{N} (\omega_f j)^2 \sqrt{a_{i,j}^2 + b_{i,j}^2} < \ddot{q}_{i,\mathrm{lim}} \tag{33}$$

where $q_{i,\mathrm{lim}}$, $\dot{q}_{i,\mathrm{lim}}$, and $\ddot{q}_{i,\mathrm{lim}}$ are the joint limits for position, velocity, and acceleration, respectively. Furthermore, zero velocity and acceleration are enforced at the boundaries to ensure a rest-to-rest operation:

$$\dot{q}_i(0) = \sum_{j=1}^{N} a_{i,j}\omega_f j = 0 \tag{34}$$

$$\ddot{q}_i(0) = \sum_{j=1}^{N} b_{i,j}(\omega_f j)^2 = 0 \tag{35}$$

with the conditions at t_f met by construction. Finally, the optimization problem can be stated as:

$$\begin{aligned} \boldsymbol{\alpha}^{\star} &= \arg\min_{\boldsymbol{\alpha}} \mathrm{cond}\big(\boldsymbol{\Gamma}(\mathbf{q}, \dot{\mathbf{q}}, \ddot{\mathbf{q}})\big) \\ &\text{s.t.} \quad (31) - (35) \end{aligned} \tag{36}$$

where the vector $\boldsymbol{\alpha}$ contains all the coefficients $a_{i,j}$ and $b_{i,j}$, and the superscript $\star$ indicates optimality. Due to the strongly nonlinear nature of the problem, a genetic algorithm is used for its solution.
Finally, the identification process can be summarized by the following procedure:

Static identification
1. Attach a load to the end-effector
2. Measure the torques
3. Remove the load and re-do points 1-2 for all the different loads
4. Calculate the torques required at the joints using (5).
5. Calculate the torques required by the motors using (6).
6. Compute the torque constant by linear regression using (7).

Dynamic identification
1. Determine the independent parameters using the QR decomposition (19)
2. Once that the least-square problem (26) is defined, find the excitation trajectories by solving (36).
3. Execute the excitation trajectory and collect data in the form (25)
4. Solve the regularized LS square problem (27)

3 RESULTS

3.1 STATIC IDENTIFICATION

As mentioned in section 2 an off-center weight was attached to the end-effector of the robot to introduce an external static force (and the corresponding joint torques) with the aim of estimating the motor torque constants. The distance at which the weights are applied from the TCP, denoted as a_6, is set to 100 mm. The torques referenced in equations (5) are then normalized by their respective gearbox ratios.
A total of four different weights, specifically 1.334 kg, 2.2418 kg, 3.5758 kg, and 4.5369 kg, were applied to the end-effector. A linear regression was subsequently conducted to estimate the torque constants. The results of this identification process are summarized in Table II. Both the experimental data and the linear regression results are depicted in Figure 3, where the slope of the interpolated segments represents the identified torque constants $k_{t,i}$.

Table II - Identified torque constants of the Mitsubishi RV-5AS-D-S01. The first motor is the same as the second.

Joint #	2	3	4	5	6
k_t (Nm/A)	0.68	0.72	0.34	0.22	0.28

3.2 Dynamic Identification

Figure 4 illustrates the excitation trajectories described in Sect. 2.6 for the manipulator under investigation. The torques required to follow the prescribed trajectory are

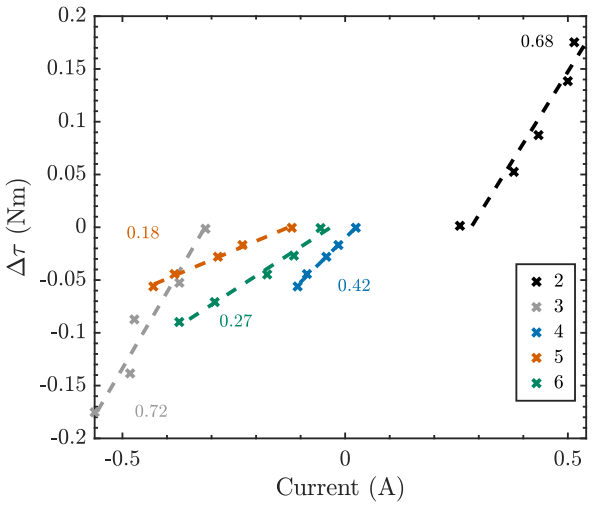


Figure 3 Experimental data from the torque constant identification process alongside their corresponding linear regressions.

Table III - Limits of the excitation trajectory.

Joint #	1	2	3	4	5	6
$q_{i,\text{lim}}$ (°)	240	148	150	200	120	200
$\dot{q}_{i,\text{lim}}$ (°/s)	124	124	124	297	356	360
$\ddot{q}_{i,\text{lim}}$ (°/s^2)	/	/	/	/	/	/

used to identify the dynamical parameters by solving the regression problem in Eq. (27). The identified parameters are summarized in Table V. The kinematic limits of the planned trajectory are presented in Table III: they reflect the joint motion limitations as provided by the robot manufacturer. The trajectory duration, t_f, is set to 60 s. The trajectory was repeated 10 times, and the results were time-averaged to mitigate measurement noise. The sample time is $\Delta t = 3.6$ ms. Figure 5 also shows the effects of relying just on CAD priors, which introduces a major modeling error that results in a very unreliable torque prediction. The experimental torques are shown, alongside the predicted joint torques from the identified model, in Fig. 5, which shows that the torque values predicted using the observed set of base parameters matches very closely the experimental data.For a quantitative assessment of the accuracy of the identified model, the root mean square errors ϵ_{rms} of the predicted motor torques are reported in Table IV. The results associated with the identification are the one in the first four rows of the table. The application of the proposed technique, i.e. of the regularized model identification procedure, provides a noticeable increase of the model accuracy over the CAD-based estimation, as the RMS errors for the torque of the first three joints, which are the most solicited ones, is reduced by one order of magnitude. In a similar manner, the R^2 values are close the ideal unitary value for all joints,

Table IV - Root mean square errors and correlation factor R^2 of the predicted torques using the identified parameters and using the CAD estimates, for the identification and validation trajectory.

Quantity	Trajectory	Unit of measurement	Joint 1	Joint 2	Joint 3	Joint 4	Joint 5	Joint 6
ϵ_{rms}	Identification	Nm	2.393	2.145	2.521	0.117	0.022	0.020
R^2	Identification	/	0.992	0.987	0.937	0.978	0.982	0.958
$\epsilon_{\text{rms,CAD}}$	Identification	Nm	25.550	34.421	32.786	0.781	0.386	0.099
R^2_{CAD}	Identification	/	0.043	−2.471	−9.735	0.002	−4.555	−0.018
ϵ_{rms}	Validation	Nm	3.113	4.616	2.737	0.344	0.079	0.044
R^2	Validation	/	0.981	0.945	0.957	0.900	0.769	0.825
$\epsilon_{\text{rms,CAD}}$	Validation	Nm	22.328	20.911	26.727	1.094	0.226	0.105
R^2_{CAD}	Validation	/	0.001	−0.124	−3.144	−0.006	−0.918	−0.001

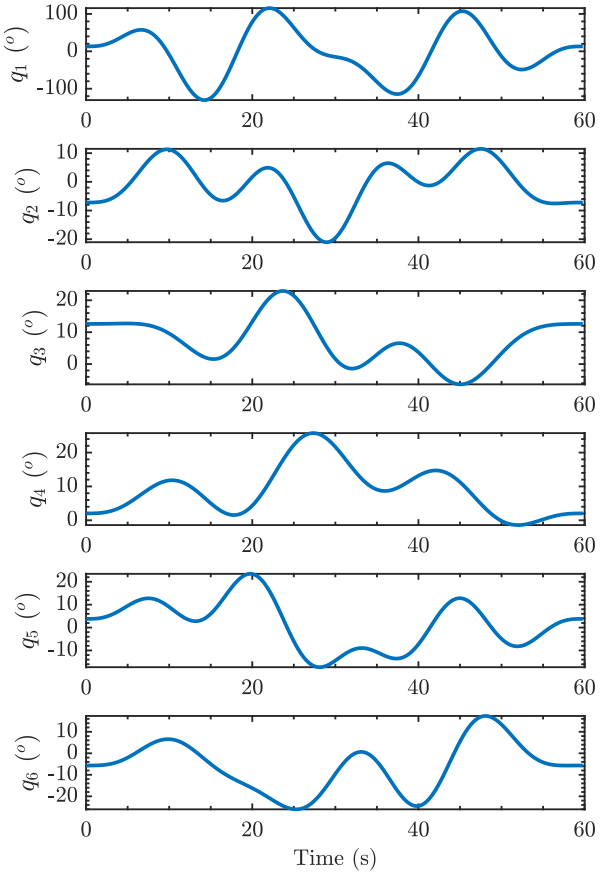


Figure 4 Identification trajectory: joint positions

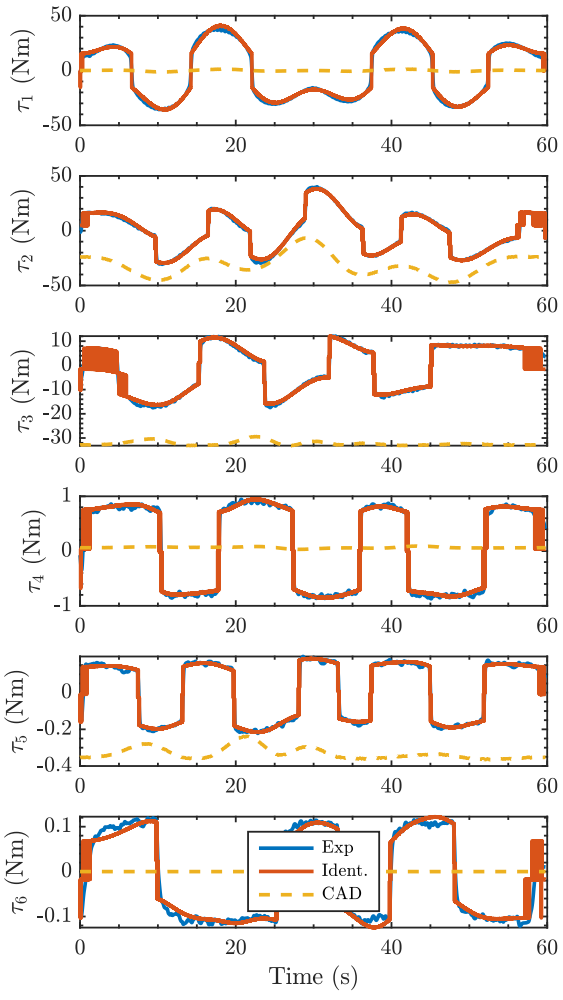


Figure 5 Identification trajectory: comparison of the experimental (blue) torques with the identified model (orange) and CAD model (yellow).

as far as the identified model is concerned. The same measure, when applied to the CAD-only based model, shows the significant inaccuracy of the latter, as the coefficients of correlation are close to zero or even negative in value. Nonetheless the CAD-based dynamic model, despite its low overall accuracy, can still be very effective in enforcing

Table V - Dynamical parameters identified in comparison with data from CAD with uniform mass density hypothesis. Mass are in [kg], first moments in [kg m], inertias are in [kg m^2], viscous friction in [Nms/rad], and dry friction in [Nm].

$\#\pi_{\text{bp},i}$	Exp.	Identified	CAD
$\pi_{\text{BP},1}$	$I_{yy,2} + I_{yy,3} + I_{zz,1} + 0.1681(m_3 + m_4 + m_5 + m_6)$	9.55576	3.02180
$\pi_{\text{BP},2}$	$0.41\, m_3 + 0.41\, m_4 + 0.41\, m_5 + 0.41\, m_6 + s_{x,2}$	5.30376	7.15908
$\pi_{\text{BP},3}$	$s_{y,2}$	0.02580	0.00033
$\pi_{\text{BP},4}$	$I_{xx,2} - I_{yy,2} - 0.1681(m_3 + m_4 + m_5 + m_6)$	0.85910	-2.82886
$\pi_{\text{BP},5}$	$I_{zz,2} + 0.1681(m_3 + m_4 + m_5 + m_6)$	8.98759	2.84213
$\pi_{\text{BP},6}$	$I_{xy,2}$	0.00154	0.00007
$\pi_{\text{BP},7}$	$I_{yz,2}$	0.02347	0.00005
$\pi_{\text{BP},8}$	$I_{xz,2} - 0.41\, s_{z,3}$	-0.08882	0.18549
$\pi_{\text{BP},9}$	$s_{x,3}$	1.70264	-0.01277
$\pi_{\text{BP},10}$	$0.5(m_4 + m_5 + m_6) + s_{y,3} + s_{z,4}$	-0.00046	3.32596
$\pi_{\text{BP},11}$	$I_{xx,3} - I_{yy,3} + I_{yy,4} + 0.25(m_4 + m_5 + m_6) + s_{z,4}$	0.00077	1.23174
$\pi_{\text{BP},12}$	$I_{yy,4} + I_{zz,3} + 0.25(m_4 + m_5 + m_6) + s_{z,4}$	0.10718	1.24939
$\pi_{\text{BP},13}$	$I_{xy,3}$	-0.20901	-0.00130
$\pi_{\text{BP},14}$	$I_{yz,3}$	-0.07813	-0.00113
$\pi_{\text{BP},15}$	$I_{xz,3}$	0.16095	-0.00036
$\pi_{\text{BP},16}$	$s_{x,4}$	-0.00591	-0.00350
$\pi_{\text{BP},17}$	$s_{y,4} - s_{z,5}$	-0.00603	-0.00592
$\pi_{\text{BP},18}$	$I_{xx,4} - I_{yy,4} + I_{yy,5}$	-0.31447	0.01009
$\pi_{\text{BP},19}$	$I_{yy,5} + I_{zz,4}$	1.00E-06	0.02696
$\pi_{\text{BP},20}$	$I_{xy,4}$	-0.03532	-2.50E-06
$\pi_{\text{BP},21}$	$I_{yz,4}$	0.09750	-5.16E-05
$\pi_{\text{BP},22}$	$I_{xz,4}$	0.05711	0.00074
$\pi_{\text{BP},23}$	$s_{x,5}$	0.01442	-0.00311
$\pi_{\text{BP},24}$	$0.1385\, m_6 + s_{y,5} + s_{z,6}$	0.00024	0.03698
$\pi_{\text{BP},25}$	$I_{xx,5} - I_{yy,5} + I_{yy,6} + 0.0192\, m_6 + 0.2770\, s_{z,6}$	0.03372	0.00331
$\pi_{\text{BP},26}$	$I_{yy,6} + I_{zz,5} + 0.0192\, m_6 + 0.2770\, s_{z,6}$	-0.00579	0.00664
$\pi_{\text{BP},27}$	$I_{xy,5}$	0.00685	-0.00023
$\pi_{\text{BP},28}$	$I_{yz,5}$	-0.04174	5.00E-07
$\pi_{\text{BP},29}$	$I_{xz,5}$	0.02402	2.00E-06
$\pi_{\text{BP},30}$	$s_{x,6}$	-0.01016	1.43E-05
$\pi_{\text{BP},31}$	$s_{y,6}$	0.00117	-1.63E-07
$\pi_{\text{BP},32}$	$I_{xx,6} - I_{yy,6}$	-0.01935	4.00E-07
$\pi_{\text{BP},33}$	$I_{zz,6}$	0.03807	5.64E-05
$\pi_{\text{BP},34}$	$I_{xy,6}$	0.02046	0
$\pi_{\text{BP},35}$	$I_{yz,6}$	-0.02131	0
$\pi_{\text{BP},36}$	$I_{xz,6}$	-0.00090	-2.00E-07
$\pi_{\text{BP},37}$	$f_{c,1}$	15.38560	/
$\pi_{\text{BP},38}$	$f_{c,2}$	11.18234	/
$\pi_{\text{BP},39}$	$f_{c,3}$	8.55444	/
$\pi_{\text{BP},40}$	$f_{c,4}$	0.71272	/
$\pi_{\text{BP},41}$	$f_{c,5}$	0.14961	/
$\pi_{\text{BP},42}$	$f_{c,6}$	0.08523	/
$\pi_{\text{BP},43}$	$f_{v,1}$	19.23173	/
$\pi_{\text{BP},44}$	$f_{v,2}$	82.22715	/
$\pi_{\text{BP},45}$	$f_{v,3}$	55.02575	/
$\pi_{\text{BP},46}$	$f_{v,4}$	3.15624	/
$\pi_{\text{BP},47}$	$f_{v,5}$	0.24428	/
$\pi_{\text{BP},48}$	$f_{v,6}$	0.10735	/

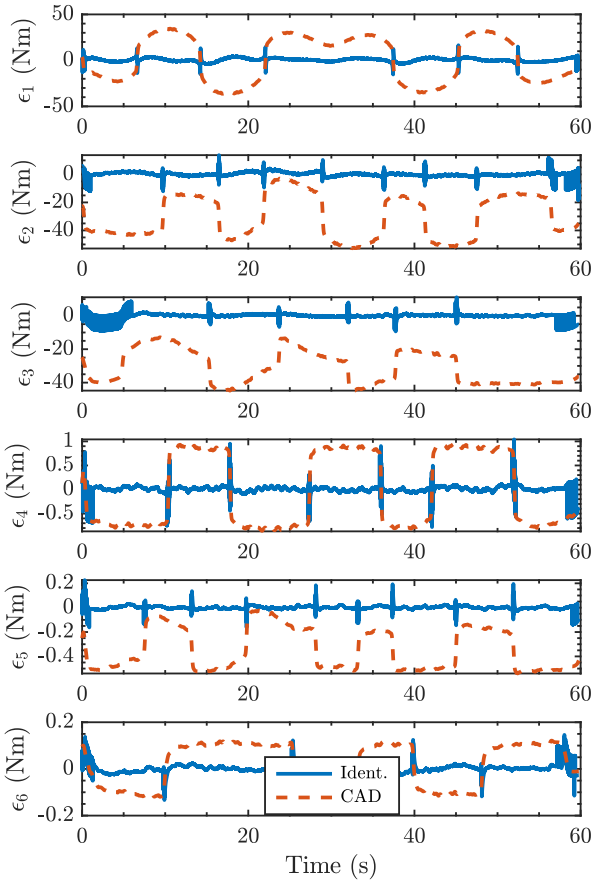


Figure 6 Identification trajectory: torque errors for each joint with respect to the experimental data.

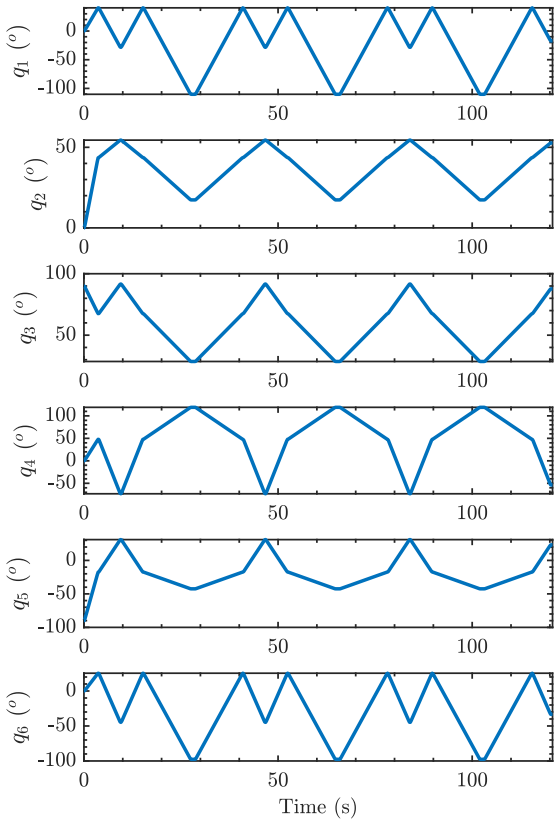


Figure 7 Validation trajectory: pick & place motion, joint positions

physical meaningfulness, owing to the careful choice of the regularization factor γ.

It must be also pointed out that the modeling based on just data gathered from CAD data do not include friction, which represents a major contribution in robot dynamics [26]. The error trend is reported in Fig. 6 by showing the time evolution of the torque modeling error, for each joint, when using the identification method or when using just CAD estimates.

As an additional validation of the procedure, and to better gauge the accuracy of the identified model, a test trajectory, referred to as 'validation trajectory', has been planned and then executed by the robot. The planned motion includes a sequence of pick-and-place motions, which is a typical task to be executed by industrial robots. The time evolution of the joint positions are reported in Fig.7. The data recorded during this test, and in particular the joint torques, are then compared with the joint torques estimated by the very same model identified during the previous test. Hence, the identification procedure is not repeated on the new data. The results of this comparison is reported in Fig.8, which contains also the output of the CAD based model. The closeness of the blue and red traces indicate that the modeling accuracy is minimally affected by the change in the motion profile. More details on the modeling error are reported in Fig.9 and in table IV: the measured accuracy, both in terms of torque RMS error and of correlation coefficients is slightly worsened over the results of the previous test, but nonetheless the overall accuracy of the model is very high.

4 CONCLUSIONS

This paper has presented the dynamic model identification of the Mitsubishi RV-5AS-D-S01 robotic arm.

The identification procedure consists of two stages. First, a static identification step is performed to characterize the motor torque constants. Then, a dynamic identification step is conducted to estimate the set of dynamic parameters.

Regularization with CAD-based estimates ensures physically meaningful parameters. This regularization is achieved by incorporating an L_2-norm penalty between the desired

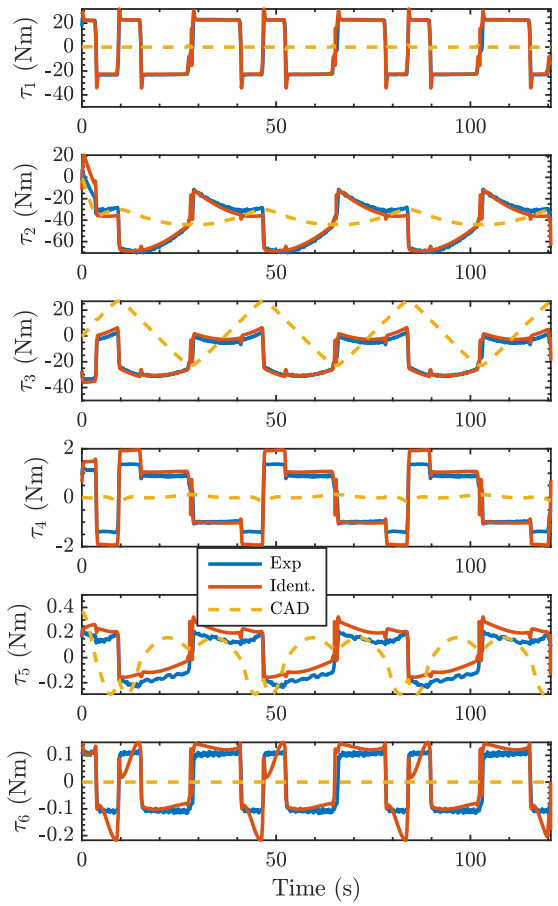


Figure 8 Validation trajectory: comparison of the experimental (blue) torques with the identified model (red)

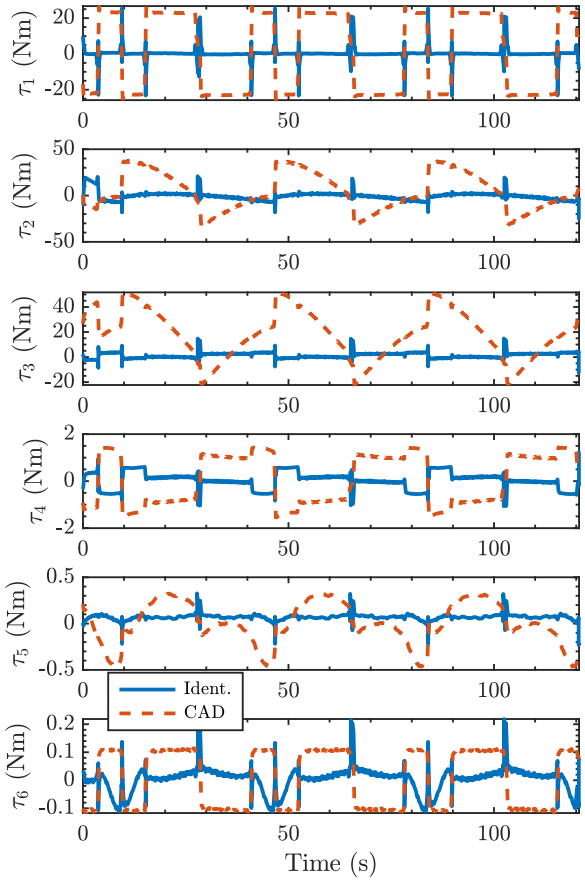


Figure 9 Validation trajectory: torque errors for each joint with respect to the experimental data.

parameters and the CAD-based estimates in the least squares formulation. The comparison between the experimental data and the identified model highlights that high level of accuracy of the identified model, showing a very good match between the two. The level of accuracy of the model based just on CAD-based priors is however unsuitable to properly describe the dynamic model of the robot under investigation. Future work will focus on further refining the parameter estimates by enforcing geometric constraints inherent to the mathematical structure of the dynamical parameters.

REFERENCES

[1] R. Featherstone, *Rigid body dynamics algorithms*. Springer, 2014.

[2] W. Khalil and E. Dombre, *Modeling, identification and control of robots*. Butterworth-Heinemann, 2004.

[3] J. Wu, J. Wang, and Z. You, "An overview of dynamic parameter identification of robots," *Robotics and computer-integrated manufacturing*, vol. 26, no. 5, pp. 414–419, 2010.

[4] J. Bettega, D. Richiedei, I. Tamellin, and A. Trevisani, "Stable inverse dynamics for feedforward control of nonminimum-phase underactuated systems," *Journal of Mechanisms and Robotics*, vol. 15, no. 3, p. 031002, 2023.

[5] D. Dona, B. Lenzo, P. Boscariol, and G. Rosati, "A real-time capable method for planning minimum energy trajectories for one degree-of-freedom mechatronic systems," *Control Engineering Practice*, vol. 142, p. 105766, 2024.

[6] D. Dona, G. Franzese, C. Della Santina, P. Boscariol, and B. Lenzo, "Real-time generation of near-minimum-energy trajectories via constraint-informed residual learning," *arXiv preprint arXiv:2501.09450*, 2025.

[7] C. H. An, C. G. Atkeson, and J. M. Hollerbach,

"Estimation of inertial parameters of rigid body links of manipulators," in *1985 24th IEEE Conference on Decision and Control*, pp. 990–995, IEEE, 1985.

[8] M. Gautier and G. Venture, "Identification of standard dynamic parameters of robots with positive definite inertia matrix," in *2013 IEEE/RSJ International Conference on Intelligent Robots and Systems*, pp. 5815–5820, IEEE, 2013.

[9] A. Bahloul, S. Tliba, and Y. Chitour, "Dynamic parameters identification of an industrial robot with and without payload," *Ifac-Papersonline*, vol. 51, no. 15, pp. 443–448, 2018.

[10] T. Lee and F. C. Park, "A geometric algorithm for robust multibody inertial parameter identification," *IEEE Robotics and Automation Letters*, vol. 3, no. 3, pp. 2455–2462, 2018.

[11] Q. Leboutet, J. Roux, A. Janot, J. R. Guadarrama-Olvera, and G. Cheng, "Inertial parameter identification in robotics: A survey," *Applied Sciences*, vol. 11, no. 9, p. 4303, 2021.

[12] C. Chen, W. Zhang, T. Liu, Z. Zhang, W. Lu, L. Wang, Y. Zheng, and Z. Lin, "Online identification of inertial parameters of a robot with partially combined links using IMU sensing," *Mechatronics*, vol. 94, p. 103023, 2023.

[13] M. Dalla Vedova, F. Di Fiore, *et al.*, "Proposal of a new simplified coulomb friction model applied to electrohydraulic servomechanisms," *INTERNATIONAL JOURNAL OF MECHANICS AND CONTROL*, vol. 21, no. 1, pp. 179–188, 2020.

[14] L. Hao, R. Pagani, M. Beschi, and G. Legnani, "Dynamic and friction parameters of an industrial robot: Identification, comparison and repetitiveness analysis," *Robotics*, vol. 10, no. 1, p. 49, 2021.

[15] G. Fabris, L. Scalera, P. Boscariol, and A. Gasparetto, "Experimental analysis and comparison of friction models applied to the UR5e robot," in *IFToMM Symposium on Mechanism Design for Robotics*, pp. 125–133, Springer, 2024.

[16] H. Mayeda, K. Yoshida, and K. Osuka, "Base parameters of manipulator dynamic models," in *Proceedings. 1988 IEEE International Conference on Robotics and Automation*, pp. 1367–1372, IEEE, 1988.

[17] M. Gabiccini, A. Bracci, D. De Carli, M. Fredianelli, A. Bicchi, *et al.*, "Explicit Lagrangian formulation of the dynamic regressors for serial manipulators," in *Proceedings of the XIX Aimeta Congress, Ancona, Italy*, pp. 14–17, 2009.

[18] T. Lee, P. M. Wensing, and F. C. Park, "Geometric robot dynamic identification: A convex programming approach," *IEEE Transactions on Robotics*, vol. 36, no. 2, pp. 348–365, 2019.

[19] J. Jia, M. Zhang, X. Zang, H. Zhang, and J. Zhao, "Dynamic parameter identification for a manipulator with joint torque sensors based on an improved experimental design," *Sensors*, vol. 19, no. 10, p. 2248, 2019.

[20] M. Gautier and W. Khalil, "Exciting trajectories for the identification of base inertial parameters of robots," *The International journal of robotics research*, vol. 11, no. 4, pp. 362–375, 1992.

[21] J. Swevers, C. Ganseman, D. B. Tukel, J. De Schutter, and H. Van Brussel, "Optimal robot excitation and identification," *IEEE transactions on robotics and automation*, vol. 13, no. 5, pp. 730–740, 1997.

[22] D. Dona', P. Boscariol, M. Bottin, B. Lenzo, and G. Rosati, "Static and dynamic identification of the Mitsubishi RV-5AS-D-S01 robot," in *The International Conference of IFToMM ITALY*, pp. 249–256, Springer, 2024.

[23] J. J. Craig, *Introduction to robotics: mechanics and control, 3/E*. Pearson Education India, 2009.

[24] J. Sjöberg, T. McKelvey, and L. Ljung, "On the use of regularization in system identification," *IFAC Proceedings Volumes*, vol. 26, no. 2, pp. 75–80, 1993.

[25] T. Lee, J. Kwon, P. M. Wensing, and F. C. Park, "Robot model identification and learning: A modern perspective," *Annual Review of Control, Robotics, and Autonomous Systems*, vol. 7, 2024.

[26] E. Clochiatti, L. Scalera, P. Boscariol, and A. Gasparetto, "Electro-mechanical modeling and identification of the UR5 e-series robot," *Robotica*, vol. 42, no. 7, p. 2430 – 2452, 2024.

ISSN 1590-8844
International Journal of Mechanics and Control, Vol. 26, No. 01, 2025
https://doi.org/10.69076/jomac.2025.0005

A HANDS-FREE HUMAN-MACHINE INTERFACE FOR ELECTRIC WHEELCHAIR CONTROL BASED ON FACE AND TORSO MOVEMENTS

Lorenzo Baglieri* Daisuke Matsuura** Tsune Kobayashi*** Giuseppe Quaglia*

* Politecnico di Torino, DIMEAS – Department of Mechanical and Aerospace Engineering[1]

** Institute of Science Tokyo - Department of Mechanical Engineering[2]

*** Institute of Science Tokyo[2] and JTEKT Corporation[3]

ABSTRACT

As the global population ages, mobility impairments are becoming a significant challenge, increasing the need for innovative assistive technologies. Traditional electric wheelchairs require manual input, which may not be feasible for users with severe disabilities. This paper presents a novel hands-free Human-Machine Interface (HMI) designed to enhance electric wheelchair control using face and torso movements. The proposed system integrates a vision-based motion capture method with a shared control strategy that considers both the rider's. A stereovision setup detects and tracks head and torso movements, which are then processed to generate control commands for the wheelchair. The experimental results demonstrate the feasibility of this system, highlighting its potential to improve wheelchair maneuverability in confined indoor environments while providing an intuitive and non-invasive control method. Challenges related to lighting conditions and system robustness are also discussed, with future work aimed at refining control accuracy and adaptability for different users.

Keywords: Human-Machine Interface (HMI), hands-free control, vision-based tracking, assistive technology, mobility assistance.

1 INTRODUCTION

The establishment of a highly aged society causes various and complex problems concerning welfare such as the rising number of people with walking diseases and the necessity of working-aged people for caregiving. In the European zone, the number of people with mobility limitations is over 120 million people by 2020 [1]. According to studies, up to 10% of people have difficulties or are unable e to use a traditional power wheelchair, another 10% have problems steering without help, and 40% struggle with steering [2].

Contact author: Lorenzo Baglieri

[1]Corso Duca degli Abruzzi 24, Torino, 10129, Italy.
[2]2-12-1 Ookayama, Meguro, Tokyo, 152-8550, Japan.
[3]1-1 Asahi, Kariya, Aichi, 448-8652, Japan.
E-mail: lorenzo.baglieri@polito.it, matsuura.d.aa@m.titech.ac.jp, kobayashi.t.cs@m.titech.ac.jp, giuseppe.quaglia@polito.it

To tackle this problem, some researchers have worked on a wheelchair with an alternative propulsion system [3] and mobility mechanism and haptic interface for electric wheelchairs to provide fine operability for riders and caregivers [4]. Although these researchers have contributed to improving the usability of manual- and electric wheelchairs, there was a common problem that the operation of those wheelchairs required manual input by the riders or caregivers. This research is thus going to develop an innovative human-machine interface (HMI) that allows the riders or caregivers to operate the electric wheelchair without occupying their hands, which results in the improvement of the users' daily activities. The developed HMI system will be implemented in an electric and omnidirectional wheelchair to perform better in narrow indoor environments [5] to demonstrate the feasibility of the proposed concept. Regarding the development of innovative Human-Machine Interfaces (HMI) to drive wheelchairs in a novelty way closer to the driver's need, especially the achievement of the free-hand interface, there are various ways such as EEG [6], eye gaze tracking [7], tactile sensation [8], IMU and visual information [9], and use of tongue [10]. The goal of the

above and other researchers is the development of a wheelchair that fits better with human life standards. For example, increasing the quality of life of users by allowing them to manage their mobility autonomously. From this point of view, the implementation of an HMI adapted to the user's disability while making assistance for the user in navigation possible is very important. The HMI system proposed by the authors estimates the intentions of the wheelchair users, the rider and the caregiver. The main objective is to obtain shared control of the wheelchair's movements between the two users' intentions. A set of different rules and various driving solutions divides the action priority of the two users, while one person can drive a wheelchair the other can make only some adjustments and vice-versa. To make the natural and non-invasive HMI system, a vision system to measure the movements of the face and torso of the rider and caregiver is desirable. Measured movements are used to generate commands for the wheelchair. Thanks to this it is possible to drive a wheelchair. Either of the rider's-, caregiver's intentions, or a combination of them is taken depending on the situation by a user's intention estimation and selection algorithm. This is the basis of our HMI that the authors are willing to achieve in the future. This aim also is addressed in the UN Sustainable Development Goals n. 3, Good Health and Well-Being.

1.1 COMPOSITION AND WORKING PRINCIPLE OF THE WHEELCHAIR

The proposed system is an electric wheelchair having omnidirectional capability and hands-free interface software aiming to enable a "side-by-side" style movement in which a wheelchair user and caregiver move around by side naturally, again, without using their hands for maneuvering. Figure 1 shows the subsystems that compose the wheelchair. The inputs come from different cameras (Rider camR, Rider camL and Caregiver Camera) that acquire the face and torso movements of the two persons, this movement are represented by the rider's head (rh) and rider torso (rt) reference frame. The acquisition phase and the elaboration of this information happens in a Host computer, that is a PC with an adequate GPU and an Ubuntu with ROS operating system. The elaboration phase is split into three different steps: Face and torso detection, Intention estimator and Motion Planner. The first step is identifying, from the acquired images, the movements of the face and torso of the rider and/or the caregiver. Once the movements are detected, the "Intention Estimator" chooses the overall direction of the wheelchair by overlapping the two inputs from the rider and caregiver. Finally, target motion is generated in the Motion Planner. In the Microcontroller the target motion is transformed into velocity commands for the traction motors and angular commands for the steering motors, to achieve the target motion. The following sections will focus on the Face and Torso Acquisition and the Intention Estimator, more specifically the case treated is the only one related to the rider.

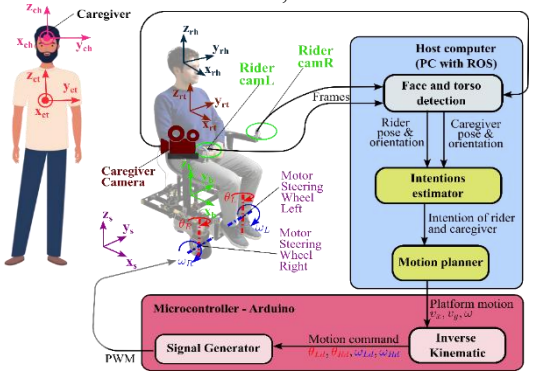


Figure 1 Description of all the hands-free side-by-side wheelchair subsystems.

2 FACE AND TORSO ACQUISITION

2.1 PROCESS VARIABLE

In this paragraph, it will be explained that all the variables used to explain the process of the acquisition of the face and torso movements (for brevity this process will be explained in detail only for the face variable, but the same concept can be applied for the shoulder or anything similar). Table I explains all the References Systems (R.F.s), the positions, the Rotation Matrix (R.M) and the Transformation Matrix (T.M.) that are taken into consideration for the calibration and for measuring the face pose. With the Reference System, it is intended that three axes are orthogonal respecting the right-hand rules for the crossing product among each other's. Regarding the position it is intended that a point in 3D-space in a certain R.F. is described with a 3x1 vector.

Table I - parameter for camera calibration process and of the acquisition of the rider landmarks for the calibration process

General variables	
$camL$	Reference System of the left camera
$camR$	Reference System of the right camera
T_{camL}^{camR}	Transformation matrix from $camR$ to $camL$
Calibration process variables	
M	Reference system of the calibration markers
p_{camL}^{M}	Position of the calibration marker from camL
p_{camR}^{M}	Position of the calibration marker from camR
Stereovision process variables	
$p_{camL}^{l,n}$	Position of a nth landmark from camL
$p_{camR}^{l,n}$	Position of a nth landmark from camR
A_{camL}	Projection matrix of rh in camL RF
A_{camR}	Projection matrix of rh in camR RF
$x_{camL}^{l,n}$	Pixel coordinates of a nth landmark in camL
$x_{camR}^{l,n}$	Pixel coordinates of a nth landmark in camR
T_{camL}^{rh}	Transformation matrix from rh to $camL$

With the Rotation Matrix, it is intended that the rotation around three coordinates to orient the origin R.F. like the measured R.F. and it is described with a 3x3 matrix. The Transformation Matrix is intended as a 4x4 matrix which includes a rotation matrix and a position matrix,

$$T = \begin{bmatrix} R & \boldsymbol{p} \\ \mathbf{0} & 1 \end{bmatrix} \quad (1)$$

Where R is the 3x3 R.M., $\boldsymbol{p}$ is the 3x1 position vector, $\mathbf{0}$ is a 1x3 zero vector and 1 is the scale factor

2.2 CALIBRATION PROCESS

Figure 2 shows how the calibration setup is made. The process includes two cameras (camL and camR) and a calibration target marker (M). The target is composed of a chessboard structure with 17 AruCo markers to make a unique pattern to be recognized and also an easy pattern to compare. In fact, the chessboard structure, with the real size of a square is uploaded in a software program to execute the calibration.

During several calibration trials, at least 20, coordinates of the target markers, ($\boldsymbol{p}^{\boldsymbol{M}}_{\boldsymbol{camL}}$ and $\boldsymbol{p}^{\boldsymbol{M}}_{\boldsymbol{camR}}$), are taken from the left- and right cameras. With the acquisition of the markers from the point of view of the cameras, it is possible to compare the single image to the expected, already uploaded in the software as mentioned above, to evaluate the intrinsic parameters of the camera, like focal length, f_x, f_y; principal point, c_x , c_y and skew factor, s . This parameter will constitute the intrinsic matrix of each camera

$$K = \begin{bmatrix} f_x & s & c_x \\ 0 & f_y & c_y \\ 0 & 0 & 1 \end{bmatrix} \quad (2)$$

In addition, fusing the two points of view from the two cameras on a common object and knowing the size of that object make it possible to perform triangulation for estimating the calibration matrix, namely, the transformation matrix from camR to camL, T^{camR}_{camL}. This matrix is calculated as the result of the minimum error optimization across the triangulation in all the measurements that are kept by the two cameras. The transformation matrix is useful to calculate the extrinsic matrix of the camera.

The extrinsic matrix is a 3x4 matrix composed of the rotation matrix, R, between the world reference frame and the camera reference frame. The last column has the position of the camera reference frame from the origin reference frame, $\boldsymbol{p}$:

$$E = [R \quad \boldsymbol{p}] \quad (3)$$

In this process, for simplicity, the world origin is put on the camL reference frame, so for the left camera the R matrix is the identity matrix and the $\boldsymbol{p}$ vector is a zero vector. For the right camera, the R and the $\boldsymbol{p}$ vector come out from the transformation matrix, from camR to camL, calculated during the calibration. Finally, it becomes possible to calculate the two projection matrices, A_{camR} and A_{camL}, multiplying the intrinsic matrices with the extrinsic one

$$\begin{aligned} A_{camR} &= K_{camR}E_{camR}, \\ A_{camL} &= K_{camL}E_{camL} \end{aligned} \quad (4)$$

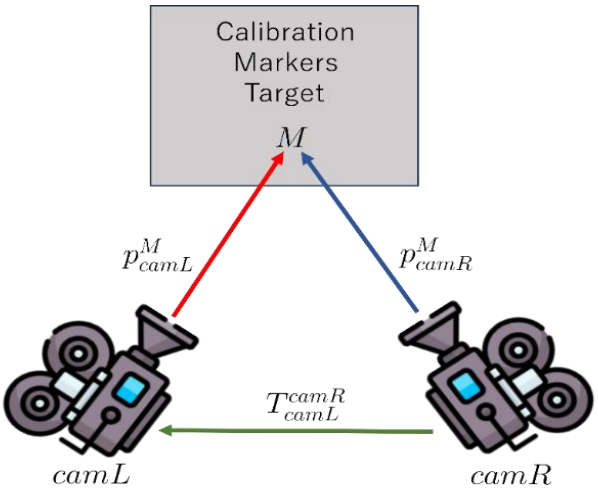


Figure 2 Calibration process.

2.3 FACE POSE AND ROTATION ESTIMATION

Figure 3 shows the configuration of cameras and riders when the system is used to collect the rider's movements. The five purple crosses on the face of the rider represent the landmarks that should be acquired: two eyes, a nose and two mouth corners. These five landmarks are useful to calculate the pose of the face with respect to a camera reference frame. This paragraph will only explain how to solve the triangulation problem and calculate the position of the landmarks from one of the two cameras.

The starting point is the pixel coordinates of the landmarks in each camera's viewpoint, $x^{l,n}_{camL}$ and $x^{l,n}_{camR}$. As shown in the Figure 3, the pixel coordinates of the landmarks are the projection of the 3D position of those landmarks on the camera's screen coordinate. This projection is calculated by multiplying the projection matrix by to position vector as

$$\begin{aligned} x^{l,n}_{canL} &= A_{camL}p^{l,n}_{camL}, \\ x^{l,n}_{canR} &= A_{camR}p^{l,n}_{camR} \end{aligned} \quad (5)$$

In eq. (6) there are two unknown vectors: $p^{l,n}_{camR}$ and $p^{l,n}_{camL}$. Using the transformation matrix between the two cameras it

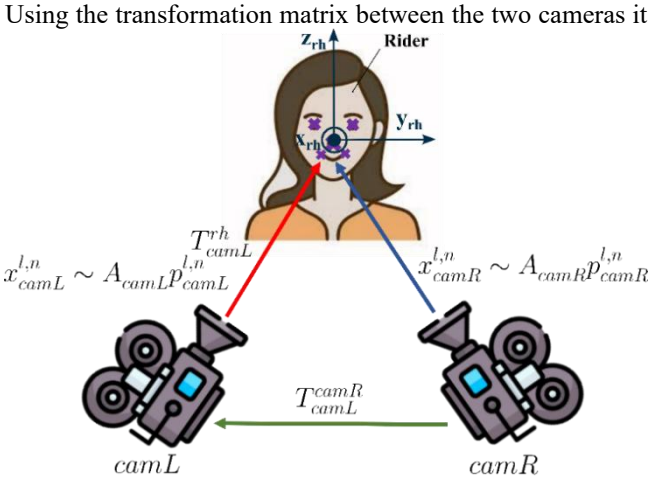


Figure 3 Stereovision working principle.

is possible to reduce the unknown vectors to only one that makes the system solvable

$$\begin{bmatrix} A_{camL} \\ A_{camR}T_{camR}^{camL} \end{bmatrix} p_{camL}^{l,n} = \begin{bmatrix} x_{canL}^{l,n} \\ x_{canR}^{l,n} \end{bmatrix} \quad (6)$$

This system contains a 4x3 matrix, which implies that the position vector is a 4-element vector and the pixel coordinate is a 3-element vector. The additional number in the pixel coordinate is the perspective division, which can be considered a scaling factor according to how close or far the object is from the camera. In the position coordinate vector, the 4th element is also a sort of scale factor but is always 1. From eq. (7) the position of the landmarks from the camL reference frame can be finally calculated. The position of the landmarks is used in the next section to calculate the position and orientation of the rider's head to estimate the one's intention.

3 INTENTION ESTIMATOR

3.1 FACE REFERENCE FRAME

This paragraph explains the use of the landmark position to calculate the reference frame of the rider's head. Figure 3 shows the landmark and how the reference frame should be placed accordingly. The first axis identified is the z-axis, it is placed from the nose marker and passing in the middle of the eyes' markers. The second marker identified is the y-axis, it starts from the nose landmark and the direction is between the left eye and the left corner of the mouth. The y-axis is depurated from any components on the z-axis to be sure that is perpendicular to the z-axis

$$\overrightarrow{y_{rh}} = \overrightarrow{y_{rh}} - (\overrightarrow{y_{rh}} \cdot \overrightarrow{z_{rh}})\overrightarrow{z_{rh}} \quad (7)$$

Finally, the x-axis is the axis that comes out from the nose landmark and it is calculated as the cross product of the y-axis and z-axis.

3.2 TRANSFORMING THE HEAD MOVEMENT IN RIDER MOTION INTENTION

The rider reference frame is the starting point to calculate the rider's motion intention. It is used to calculate the transformation matrix from rider's head (rh) to camL, T_{camL}^{rh}. This matrix represents the position and the orientation from the camL to the head reference but the most useful information is the movement of the rider's head from a customizable rest position. To acquire the movement of the rider head around a customizable rest position, it is important to choose a transformation matrix of a prompt rest position: $T_{camL}^{r,0}$. This transformation matrix will be settled as the origin of the rider's head translations and rotations. The rest position of the head, the one with the head aligned with the spinal column, is chosen as a rest position. Figure 4 shows how the rider movements are taken as input and then transformed into velocity commands. The rider's head's reference frame (*rh*) starts from the position *rh,0* which coincides with the reference frame with the same name. Here the rider moves at the *rh,a* position at which the polar coordinates can be calculated: distance, d_r, from the centre of the reference system and the angle, ϕ_r, of the direction w.r.t the $x_{rh,0}$ axes. The equations used to perform this calculation are below,

$$d_r = \sqrt{x_{rh,a}{}^2 + y_{rh,a}{}^2},$$
$$\Phi_r = \arcsin\left(y_{rh,a}/d_r\right) \text{ if } d_r \neq 0, \quad (8)$$
$$\Phi_r = 0 \text{ if } d_r = 0$$

With this formulation, a maximum and a minimum threshold can be set. All the velocities will have a constant behaviour regardless of the direction. Using a 5th-order polynomial function [11], explained in detail in the article written by *Taglaivini et al.*, it is possible to transform the d_r and $\theta_{z,rh}$ into linear velocity v, and angular velocity ω_z. The peculiarity of introducing the 5th-order polynomial function is to properly connect the deadband to the linear region of the input-output relationship to guarantee the achievement of comfortable behaviour of the wheelchair.

Table II summarizes all the variables that were used to transform the input signal into a command velocity signal ω_z. This can simply be done by using the direction Φ_{rt} as

$$v_x = v\cos(\Phi_r), v_y = v\sin(\Phi_r) \quad (9)$$

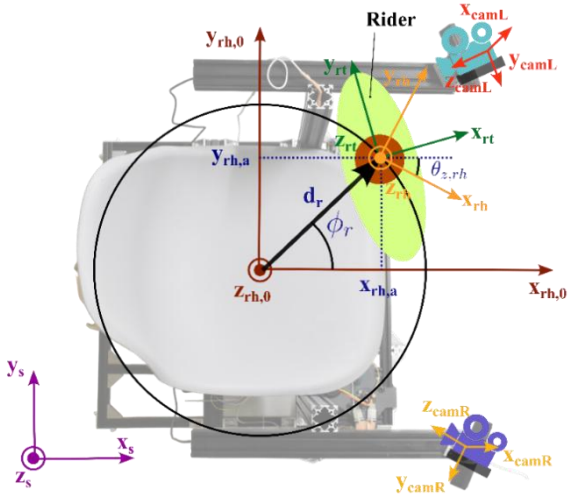


Figure 4 A rider moving from the rest position to generate a reference signal to move the wheelchair.

In the above, command velocities, v and ω_z, have been acquired in the polar coordinate. Then, they should be transformed into the reference velocities in the cartesian frame: two linear components, v_x and v_y. The deadband described in the Table are referred to the origin of the rider in the rest position (rh,0) Here, the three command velocities are obtained. Before the velocities are sent to the inverse kinematic routine they are elaborated by the Motion planner. It takes care to produce a unique velocity twist according to the rider and the caregiver's velocity intentions. In this case, the caregiver's intentions are not taken into consideration, so the only purpose of the motion planner is to add an exponential filter to smooth the velocity signal. The exponential filter used in this case considers the actual

velocity, the previous velocity and a smoothing factor. For a general variable it is possible to express it as:

$$s_t = \alpha x_t + (1-\alpha)x_{t-1}, \text{with } t > 0$$
$$s_t = x_t, \text{with } t = 0 \quad (10)$$

Where s_t is the smoothed variable, x_t is the actual variable, x_{t-1} is the previous variable and α the smoothing value (in this case 0.6)

Table II - Values and parameters that are involved in the velocity input generation

Variable	Value	Description
d_r	Obtained from measured data	Distance of the rider reference frame from the wheelchair reference frame in polar coordinates. Input of the polynomial function for linear velocity
Φ_r	Obtained from measured data	Direction of the rider reference frame from the wheelchair reference frame in polar coordinates.
$\theta_{z,rh}$	Obtained from measured data	Rotation of the head of the rider. Input of the polynomial function for angular velocity
v_{max}	0.3 m/s	Saturation for linear velocity.
$\omega_{z,max}$	0.5 rad/s	Saturation for angular velocity
d_{min}	4 cm	Dead band for the head motion to obtain a linear translation
θ_{min}	20°	Dead band for the head motion to obtain a linear translation
d_{change}	6 cm	Value for the head motion to change from polynomial to linear behavior
θ_{change}	40°	Value for the head rotation to change from polynomial to linear behavior
v_{change}	0.1 m/s	Linear velocity value to change from polynomial to linear behavior.
$\omega_{z,change}$	0.1 rad/s	Angular velocity value to change from polynomial to linear behavior.
d_{max}	10 cm	Maximum linear movements before entering the saturation zone
θ_{max}	90°	Maximum angular movements before entering the saturation zone

4 EXPERIMENTAL RESULTS

Figure 5 shows the experimental environment which is composed of an empty room with some cones that delimitates the area in which the experiment has been conducted. It is also possible to detect the monitor in which it was possible to overview the ongoing activity in the wheelchair's PC. The measurement of the wheelchair is conducted using a motion capture system. In the figure it is possible to see the tripod with two cameras and there were another two cameras symmetrically arranged on the other side of the room. The experiment aims to test the capabilities of going straight and rotating the system. During the experiment the rider was sitting on the wheelchair and was enabled the hands-free driving in order to follow a path in the perimetral lines of the cones. The experiment task was to drive around 90°-corners of the cone path. So there is an approaching phase to the cone path, until 5 s, then an approaching to the 90° corner at 13s, then the exit from the corner at 19s.

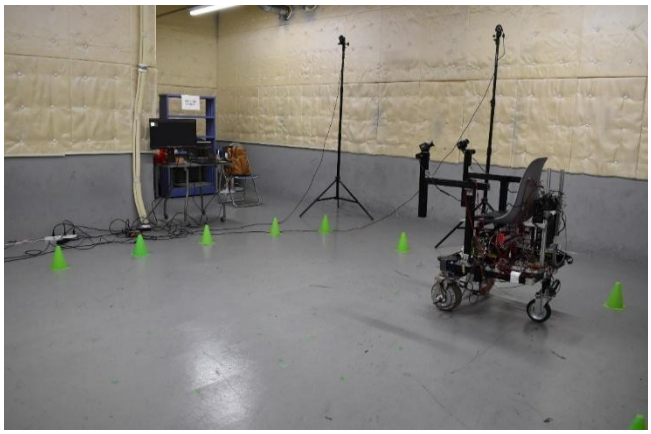


Figure 5 Experimental setup to test the hands-free driving wheelchair.

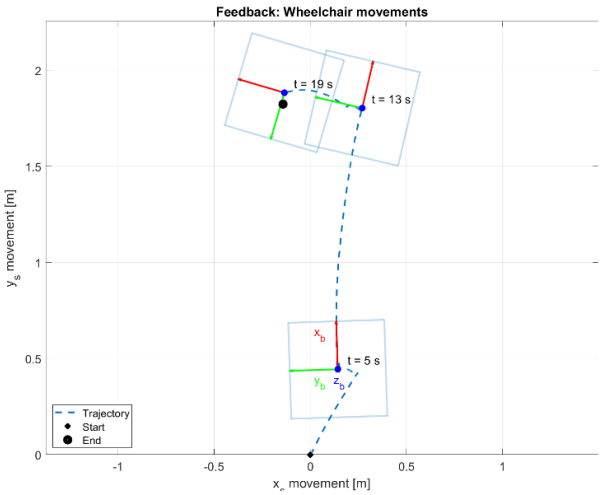


Figure 6 Trajectory and position followed by the wheelchair during the experiment.

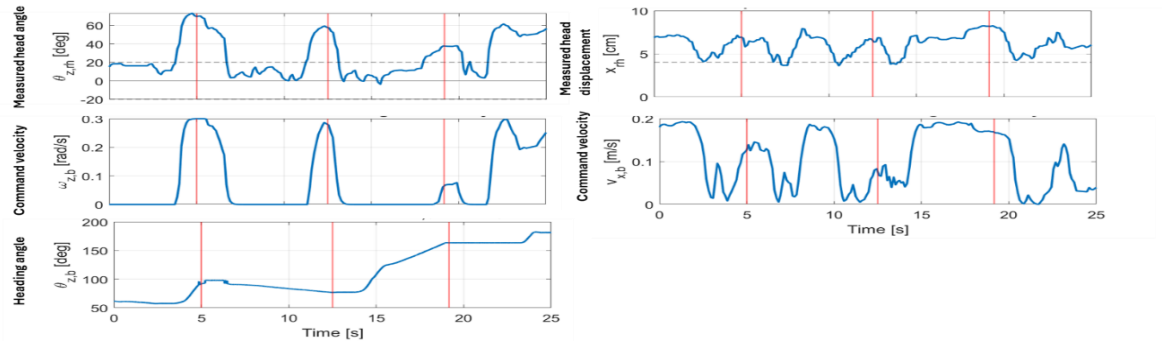


Figure 7 Head movements, velocity reference and rotation angle feedback during the experiment.

According to the user's experience, the driving method was enough satisfting although further calibration should be performed to increase the drivability of the system. Figure 6 and Figure 7 represent the results of the experiment. Figure 6 represents the head inputs, the generated velocity and the rotation angle feedback It is very interesting to notice that the control can be done in a very accurate way. The overall behaviour of the wheelchair was satisfactory; all the velocities are published according to the head movements as can be seen from the figure. The only problem is when the face is between a camera and a light, as Figure 7 represents the trajectory followed by the wheelchair during the experiment, there is a first phase, the first 5s, in which the wheelchair was approaching the perimetral line. Then the wheelchair turns to become parallel to the cone path and goes straight until it meets the corner at 13s, at this point start turning and complete another small straight trajectory. In the plot showing the wheelchair moving from the top point of view, it is possible to appreciate that the rotation and the linear velocity are not exactly as the input. The reasons for this misalignment are two. The difficulty is to put a marker in the exact center of rotation of the wheelchair so we are tracking a point that is close to the centre of rotation but not exactly the centre. Unfortunately in Figure 7 it is possible to see some accumulating delay between the input and the output, this is due to signal acquisition that happen with two different clock: motion capture clock and PC clock. In the real experience there wasn't such delay.

5 CONCLUSIONS

The papers explain how a hands-free interface is built from the head movements of the rider. The same approach can be used also for the rider's shoulder and for detecting some commands from the caregiver. Research activities are ongoing to define methods and strategies to share wheelchair control between two agents, i.e. the wheelchair rider and its caregiver and the results will provided in further papers. The results obtained in the experimental phase are interesting although some critical problems are still present. The most critical is the light position with respect to the rider and the camera because it can cause a complete loss of the rider landmarks detection and so an unexpected stop of the wheelchair motion. Future works will involve how to improve the overall drivability and, of course, how to solve the rider face illumination problems.

AKNOWLEDGEMENT

This publication is part of the project PNRR-NGEU which has received funding from the MUR – DM 351/2022 and has been supported by a joint research contract between JTEKT Corporation and Institute of Science Tokyo.

REFERENCES

[1] 'Persons with disabilities - Employment, Social Affairs & Inclusion - European Commission'. Accessed: Feb. 26, 2024. [Online]. Available: https://ec.europa.eu/social/main.jsp?catId=1137

[2] L. Fehr, W. E. Langbein, and S. B. Skaar, 'Adequacy of power wheelchair control i terfaces for persons with severe disabilities : A clinical survey', vol. Fehr, Linda, W. Edwin Langbein, and Steven B. Skaar. 'Adequacy of power wheelchair control interfaces for persons with severe disabilities: A clinical survey.' Journal of rehabilitation research and development, 2000.

[3] G. Quaglia, E. Bonisoli, and P. Cavallone, 'A proposal of alternative propulsion system for manual wheelchair', *International Journal of Mechanics and Control*, vol. 19, pp. 33–38, Jan. 2018.

[4] L. Tagliavini and G. Quaglia, 'On the Design of MoviWE.Q: An Omnidirectional Electric-Powered Wheelchair for Indoor Mobility', in *Advances in Mechanism and Machine Science*, M. Okada, Ed., Cham: Springer Nature Switzerland, 2023, pp. 311–321. doi: 10.1007/978-3-031-45770-8_31.

[5] L. Baglieri, D. Matsuura, T. Kobayashi, and G. Quaglia, 'Development of a Mobility Platform Aiming to Achieve User-Friendly Functionality', in *Proceedings of Jc-IFToMM International Symposium Vol. 7 (2024)*, Japanese Council of IFToMM, 2024, pp. 103–110. Accessed: Sep. 23, 2024. [Online]. Available: https://www.jstage.jst.go.jp/article/jciftomm/7/0/7_103/_article/-char/ja/

[6] I. Iturrate, J. Antelis, and J. Minguez, 'Synchronous EEG brain-actuated wheelchair with automated navigation', in *2009 IEEE International Conference on Robotics and Automation*, May 2009, pp. 2318–2325. doi: 10.1109/ROBOT.2009.5152580.

[7] Y. Matsumotot, T. Ino, and T. Ogsawara, 'Development of intelligent wheelchair system with face and gaze based interface', in *Proceedings 10th IEEE International Workshop on Robot and Human Interactive Communication. ROMAN 2001 (Cat. No.01TH8591)*, Sep. 2001, pp. 262–267. doi: 10.1109/ROMAN.2001.981912.

[8] D. Matsuura, K. Kiyomoto, and T. Kobayashi, 'Development of a simple human-cooperative transportation system based on tactile information', *ICPE2022*, vol. Proceedings of the 19th International Conference on Precision Engineering.

[9] L. Baglieri, D. Matsuura, T. Kobayashi, and G. Quaglia, 'Vision Systems and IMU Signals to Design a Hand-Free Driving HMI', in *Advances in Italian Mechanism Science*, vol. 163, G. Quaglia, G. Boschetti, and G. Carbone, Eds., in Mechanisms and Machine Science, vol. 163. , Cham: Springer Nature Switzerland, 2024, pp. 283–291. doi: 10.1007/978-3-031-64553-2_33.

[10] M. E. Lund, H. V. Christiensen, H. A. Caltenco, E. R. Lontis, B. Bentsen, and L. N. S. Andreasen Struijk, 'Inductive tongue control of powered wheelchairs', in *2010 Annual International Conference of the IEEE Engineering in Medicine and Biology*, Aug. 2010, pp. 3361–3364. doi: 10.1109/IEMBS.2010.5627923.

[11] L. Tagliavini, L. Baglieri, G. Colucci, A. Botta, C. Visconte, and G. Quaglia, 'D.O.T. PAQUITOP, an Autonomous Mobile Manipulator for Hospital Assistance', *Electronics*, vol. 12, no. 2, Art. no. 2, Jan. 2023, doi: 10.3390/electronics12020268.

ISSN 1590-8844
International Journal of Mechanics and Control, Vol. 26, No. 02, 2025
https://doi.org/10.69076/jomac.2025.0006

FORCE-OPTIMIZED MONOLITHIC PNEUNETS SOFT ACTUATORS: DESIGN, SIMULATION AND CHARACTERIZATION

Monica Tiboni[1] and Davide Loda[1]

[1] Department of Mechanical and Industrial Engineering, University of Brescia

ABSTRACT

This study investigates the design, simulation, and characterization of force-optimized, monolithic, PneuNets-based soft actuators for applications in robotics and rehabilitation. Building on previous work, the research explores the optimization of actuator geometry through Finite Element Method (FEM) simulations and experimental validation. By refining the actuator's geometry, particularly regarding chamber count and structural elements, the study aims to improve force output and efficiency while maintaining a simple, cost-effective design process. The elastomer Dragon Skin 30 was selected for its favorable mechanical properties, ensuring high deformation tolerance and efficient force control. The optimization process involved a detailed analysis of force and stress distribution using FEM, followed by actuator fabrication and testing. The results indicate that increasing the number of chambers enhances force output, with a maximum tip force of 1.2 N achieved in the final design. A comparison between the initial and final designs revealed significant improvements in force generation, thereby validating the FEM model as a reliable tool for actuator design. The study concludes that the optimized actuator design offers a promising solution for flexible and efficient soft actuators, suitable for rehabilitation and other delicate manipulation tasks.

Keywords: PneuNets, soft actuators, FEM simulation, force optimization, rehabilitation

1 INTRODUCTION

Soft pneumatic actuators, particularly PneuNets, have emerged as a promising solution for a wide range of applications, including soft robotics, biomedical devices [1, 2, 3], and industrial automation. These actuators, often characterized by their flexibility, lightweight structure, and ability to generate complex motions, have attracted significant research attention due to their potential for use in rehabilitation robots, prosthetics, and handling delicate objects [4, 5, 6, 7, 8, 9]. PneuNets actuators, which are formed by interconnected pneumatic chambers, offer advantages such as high bending speeds, large deformations, and low power consumption, making them well-suited for applications requiring dexterous manipulation.

Contact author: Monica Tiboni[1]
[1]Via Branze, 38, 25123 Brescia, Italy.
E-mail: monica.tiboni@unibs.it , davide.loda@unibs.it

In recent years, the development of monolithic PneuNets actuators, such as those presented in the work by Tiboni and Loda [10], has simplified the design and fabrication process. The authors propose an optimized approach to actuator design, production, and characterization, emphasizing simplicity and cost-effectiveness. By combining finite element method (FEM) simulations with a silicone-based molding process, they strike a balance between bending performance and structural compactness. Their experimental validation shows forces between 0.9 and 1N at 115 kPa, confirming the accuracy of their simulation-based design and highlighting the potential for low-cost, reliable actuator fabrication. This work serves as the foundation for the current study, where we enhance the design of PneuNet actuators to achieve greater force, through both FEM simulations and experimental validation.

Similarly, Zhong et al. [11] contribute to the modeling of soft pneumatic actuators by introducing an analytical model for predicting bending angles and tip contact forces. Their model, based on Neo-Hookean hyperelasticity theory,

offers a useful framework for understanding the relationship between input pressure, bending angle, and force. The study demonstrates a maximum force of 1N at 80 kPa, providing valuable insights into force prediction and actuator performance. Their approach complements our study by reinforcing the importance of accurate modeling for actuator optimization.

In a more complex design, Kim et al. [12] present a deployable soft pneumatic network (D-PneuNets) actuator with origami-inspired chambers aimed at enhancing compactness. Their actuators, made from Dragon Skin 10 and Dragon Skin 30 silicones, generate a maximum tip force of 2 to 2.5N at 12 kPa. This work is significant for our study, as it demonstrates the potential for optimizing actuation force through innovative geometric design, albeit with a more intricate fabrication process. While their focus is on compactness and force generation, the principles of geometry-driven performance improvements resonate with our objective of optimizing actuator force and bending capabilities.

Liu et al. [13] focus on the bending and force generation of soft pneumatic network actuators by developing an analytical model that accounts for parameters such as the gap between chambers, chamber thickness, and the number of chambers. Their work, validated with experimental data, reports a maximum tip force of 1.2N at 60 kPa. This study is particularly relevant as it reinforces the importance of geometric optimization in actuator design, an area we address in our work through the use of FEM simulations to fine-tune actuator geometry for optimal force output and bending performance.

Zhang et al. [14] introduce a new soft robotic gripper for rehabilitation that incorporates dual-modular soft actuators operating at different pressures. Their design, fabricated using Dragon Skin 30 and bonded with an extensible layer, achieves a maximum tip force of 3N at 80 kPa. This work highlights the advantages of multi-modular actuator designs, which complement our approach by providing a deeper understanding of how different actuator modules and pressure variations affect performance, especially in rehabilitation applications.

Wang et al. [15] explore a soft pneumatic glove that combines bidirectional bending actuators with variable chamber heights for rehabilitation and assisted grasping modes. Their experimental results show a bending angle of 261° at 100 kPa and a tip force of 1.59N at 130 kPa. This study is particularly relevant to our work, as it focuses on actuator performance in rehabilitation tasks, where both bending and force generation are critical. Their validation of FEM modeling and experimental data provides a robust comparison for our own actuator design and performance testing.

Xavier et al. [16] present an innovative 3D-printed omnidirectional soft pneumatic actuator designed for applications such as pipe inspection and biomedical devices. Their actuators, made using stereolithography (SLA) and fused deposition modeling (FDM), offer multimodal actuation, including bending, extension, and contraction. While their study primarily focuses on 3D printing techniques, the use of FEM for optimizing bending performance and their theoretical tip force prediction of 1.15N at 700 kPa provides valuable insights into optimizing actuator performance across various actuation modes. This highlights the potential of additive manufacturing in actuator design, offering future avenues for development in flexible, complex geometries.

Finally, Polygerinos et al. [17] present one of the earliest studies on soft pneumatic gloves for hand rehabilitation. Their design incorporates a multi-chamber actuator system made from Elastosil with extensible layers, validated by FEM simulations and experimental force measurements. The maximum tip force reported is 1.21N at 43 kPa. This pioneering work laid the foundation for soft robotic rehabilitation technologies and serves as a reference for our design considerations, particularly in terms of actuator fabrication and force prediction.

Building upon these insights, this paper presents a detailed study on the design, fabrication, and characterization of monolithic PneuNets actuators. By combining FEM simulations with experimental validation, we aim to optimize actuator performance by fine-tuning parameters such as chamber count and geometry. The goal is to provide insights into improving force output, and overall actuator efficiency, making them suitable for a range of applications while keeping the design and the production process as simple as possible.

2 MATERIALS AND METHODS

2.1 ACTUATOR MATERIAL

In this work, we adopt the same elastomer material as used in previous studies [1, 10], specifically the silicon rubber Dragon Skin 30 (Shore 30A). This material was chosen due to its favorable mechanical properties, which include high strain tolerance, low stress at high deformation, and the ability to recover its initial shape after deformation. As highlighted in previous works, elastomers are commonly used for pneumatic soft actuators due to their ability to withstand long, repetitive cycles while offering the necessary flexibility and force control. Dragon Skin 30 provides an effective balance between the need for soft materials that require lower input pressure and stiffer materials that demand more complex design considerations, ensuring both efficient performance and safety in actuator operation. Detailed material properties are reported in Table I.

2.2 ACTUATOR REVISED GEOMETRY

During the initial design phase (Figure 1a), geometric dimensions were selected according to Table II.

Table I - Material properties of Dragon Skin 30.

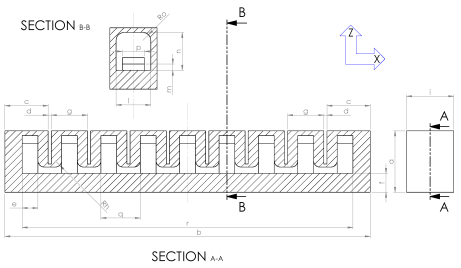
Property	Value
Mixed Viscosity (cps)	20,000
Specific Gravity (g/cc)	1.08
Specific Volume (cu.in./lb.)	25.7
Pot Life (min)	45
Cure Time (h)	16
Shore A Hardness (A)	30
Tensile Strength (psi)	500
100% Modulus (psi)	86
Elongation at Break (%)	364
Die B Tear Strength (pli)	108
Shrinkage (in./in.)	<0.001
Service Temperature Range (°C)	−53 ÷ 232

FEM analysis was then used to optimize the thickness of the actuator's bottom end (dimension f), with incremental increases of 1 mm per simulation. The base deformation under pressurization was used to determine the optimal value of f. Constraints were applied to the results, with a maximum allowable elongation of the bottom face set to 10% of its initial length and the total actuator height limited to 20 mm to avoid excessive bulk. Instead of using a strain-limiting layer, thicker walls were chosen for regions where deformation needed to be minimized (e.g., the bottom and ends of the actuator), while thinner walls were used in areas where more flexibility was required. However, thinner walls may lead to rupture during inflation, and larger chambers could slow down actuator movement due to increased air volume.

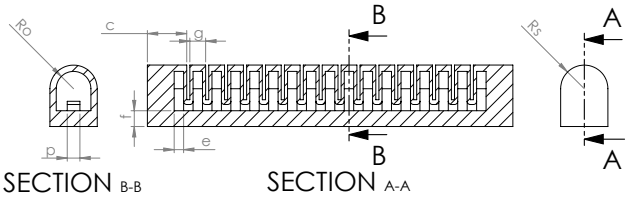
Table II - First geometric parameters.

Parameter	Value (mm)
a	19.50
b	116
c	13.75
d	1
e	5
f	2
g	11.5
Rh	2
i	15
l	11
m	2
n	12
Ro	2.5
p	7
q	12.5
r	105

With simulation and production methodologies tested and validated in [10], a revised actuator geometry is analyzed and proposed in this section. The main areas focused on



(a) First actuator geometry.



(b) Final actuator geometry.

Figure 1 Comparison of actuator geometries.

improving the footprint and making the bending effect more efficient.

To reduce the overall footprint, a junction radius was applied to the geometry of the chambers. Compared with the first version, the chambers wall thickness along the X-axis has been reduced to promote expansion in that direction, and more material has been added in the area overlying the inner connection channel (Table II: m) in order to decrease opportunities for rupture under pressure. The inner channel width (Table II: p) was reduced to minimize the capacitive effect. A parametric 3D CAD model was made to easily vary the number of chambers contained in the actuator while maintaining the same overall length as the first version. Once the outer radius of the chambers was defined as 7.5 mm, the outer thickness of the chambers as 1 mm, the measurement of the thickness overlying the inner channel as 1.5 mm and the channel width as 4 mm, tests were conducted increasing the number of chambers from 9 to 18.

These values were selected to favor feasibility on the basis of the experience gained from the implementation of the previous version. In fact, parts of internal actuator geometry described by "too small" values cannot be made by lost wax cores, as further described, since these cannot be produced with sufficient precision using the methods described in the previous sections. Additional and modified design

parameters, mentioned in Figure 1b, are reported in Table III.

Table III - Final geometric parameters.

Parameter	Value (mm)
c	12.5
e	3
f	5
g	5
Ro	5.5
p	4
Rs	7.5

2.3 FEM ANALYSIS FOR DESIGN OPTIMIZATION

Following the procedure presented in [10], FEM analysis is conducted in the ANSYS environment on a 3D model of the actuator created using solid modeling CAD. This preliminary analysis allows testing of the actuator's motion, forces, and stresses before physical production. For material modeling, a custom Yeoh hyperelastic model [18] as reported in Equation 1 is selected.

$$W = \sum_{i=1}^{n} C_i (I_1 - 3)^n \tag{1}$$

This type of model is commonly used to represent elastomer behavior under external forces. The adopted parameters, obtained from our previous study [10], are reported in Table IV.

Table IV - Yeoh hyperelastic model parameters.

Parameter	Value (MPa)
C_1	1.0744×10^{-1}
C_2	6.01×10^{-2}
C_3	3.02×10^{-4}

Meshing was optimized to obtain fast simulations, allowing for a large number of tests in a reasonable time. The main parameters used to define the meshing model are reported in Table V.

Each structure obtained from the parametric CAD, with chamber counts ranging from 9 to 18, was then exported to perform FEM analysis, adopting the same mesh model discussed above. The theoretical force was obtained in the same way as described in [10] and reported in Figure 2. In this case, the final pressure value was selected as 40 kPa to lighten the ANSYS solver's workload and get the result quickly. Data gathered from this test drove the selection of a 17-chamber design, as further described in Section 3.

Stress analysis (Figure 3b) was carried out in the same way as described in [10], but in order to obtain more accurate results, this time a dummy finger structure was bonded to the lower face of the actuator as shown in Figure 3a. The structural material is assigned as Dragon Skin 30 and features some gaps to represent the finger joints.

Table V - Mesh parameters.

Parameter	Value
Aspect ratio	AVG: 1.88, SD: 0.46
Jacobian ratio	AVG: 1, SD: 0
Skewness	AVG: 8.78×10^{-5}, SD: 0.13
Element quality	AVG: 0.83, SD: 9.64×10^{-2}
Element type	LINEAR
Capture curvature	YES
Capture proximity	YES
Nodes	21,962
Elements	99,592

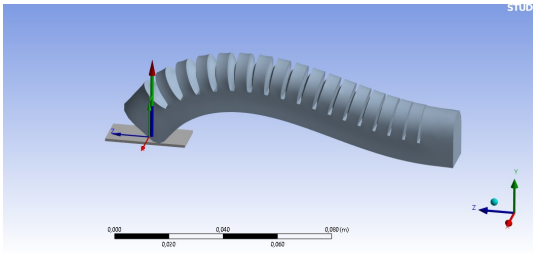
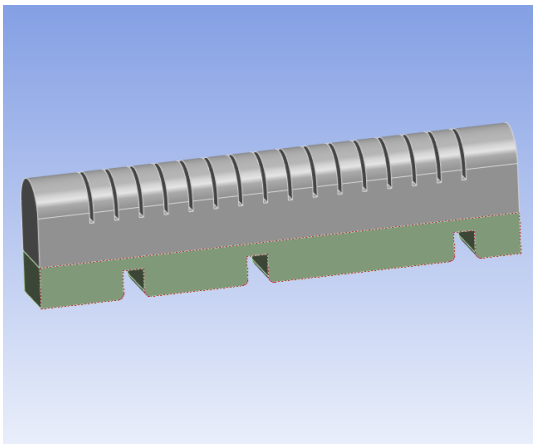


Figure 2 Tip force reaction.

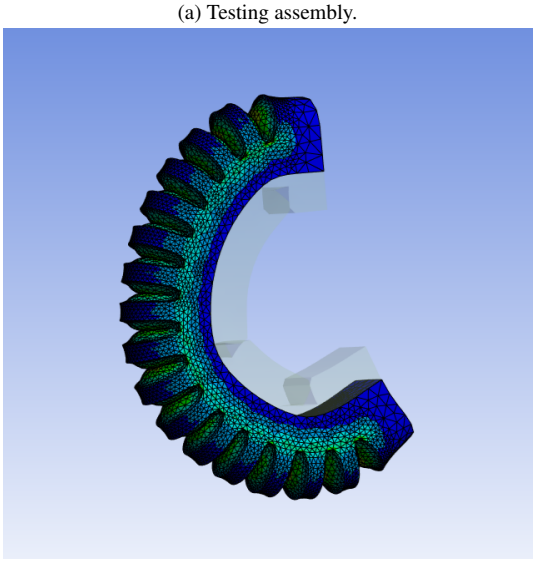
2.4 ACTUATOR PRODUCTION

The production process largely follows the one illustrated in our previous work, but with some modifications specific to the new geometry. The building procedure described in [10] involved several key steps, reported below.

1. Mold Production: A mold is created using ABS through 3D printing in two parts initially, which was later modified to a three-part design to facilitate easier extraction. The mold is designed to accommodate a wax core, ensuring a smooth and reliable extraction process.
2. Wax Core Casting: A wax core is produced by casting in a silicone mold. The silicone mold is created from a PLA hard mold, allowing for easy removal of the core once it has cooled.
3. Elastomer Preparation: Dragon Skin 30 silicone elastomer is mixed in equal parts (30 mL of Part A and Part B), then degassed in a vacuum chamber for 10 minutes to remove air bubbles.
4. Casting and Curing: The degassed silicone is then poured into the mold with the wax core, and the mold is allowed to cure for 24 hours.
5. Wax Core Removal: The actuator is heated in an oven at 70°C, causing the wax core to melt and be removed, leaving hollow cavities in the actuator.
6. Assembly: A tube is inserted into one of the hollow cavities, and a flange is added and secured with silicone



(a) Testing assembly.



(b) Stress distribution.

Figure 3 Stress distribution and testing assembly.

glue. The actuator's other end is sealed with silicone glue. Finally, to minimize air leaks, a kevlar wire may be wrapped around the cylindrical flange

2.4.1 Mold

A new mold was realized in just two parts since the final geometry allows for a simpler extraction compared to initial one. It is composed of two main bodies: an upper part and a lower part.

The lower part is needed to shape the outer surface of the chambers while the upper part is used to model the flat outer walls of the actuator and features some holes to hold in place two additional structures in charge of applying a light pressure on the wax core. This locking mechanism prevents the wax core from moving under the hydrostatic buoyancy provided by the silicone in its liquid state. The described assembly is reported in Figure 4.

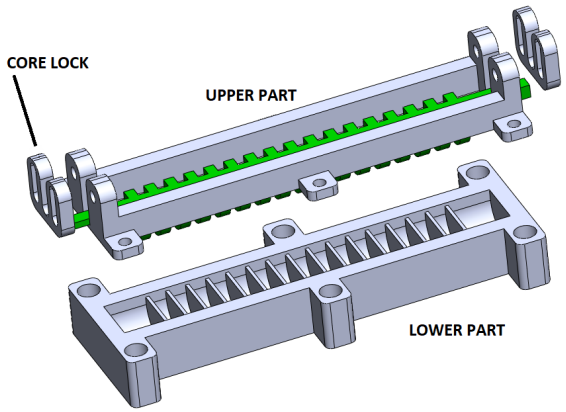


Figure 4 Mold assembly.

2.4.2 Wax core

In the same way described in [10], a soft Dragon Skin 30 mold is obtain by pouring the silicone in a 3D printed PLA one, whose assembly is reported in Figure 5.

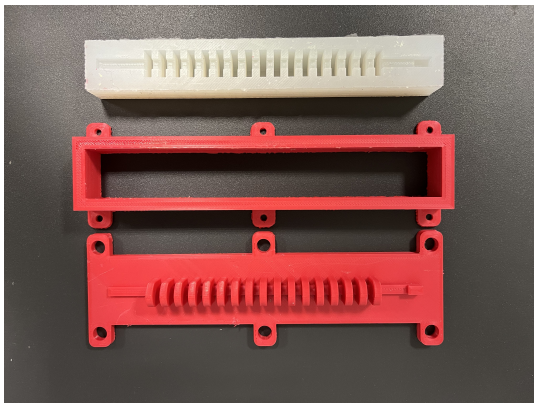


Figure 5 Wax core mold assembly.

However, the produced wax core was found to lack sufficient rigidity since the width of the chamber connection channel had been reduced compared to the first design. This could have caused the wax core to bend under the hydrostatic buoyancy provided by the liquid silicone, damaging the resulting actuator structure. To avoid this problem, it was decided to reinforce the wax core with some stiffer material: production tests were carried out by embedding in the wax cast a plastic and steel reinforcement core. Since the plastic one was still not stiff enough, the metal one was preferred: the final part was laser-cut from a 1 mm steel sheet and featured with some holes to allow the liquefied wax to properly surround the reinforcement as reported in Figure 6.

2.4.3 Final product

The production of the new version follows the same procedures adopted in [10]. Summing up:

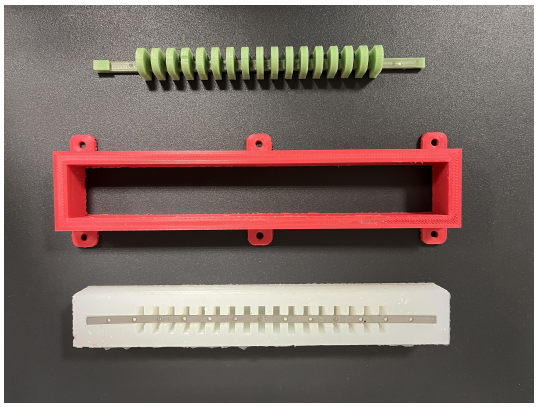


Figure 6 Wax core soft mold, steel reinforcement and de-molded part.

- A solution of 60 ml of liquid silicone is prepared and put under vacuum to reduce air presence in it;
- The solution is poured in the mold assembly (Figure 7) and left curing for 24 hours;
- The mold assembly is opened and the cast is extracted, as shown in Figure 8;
- The excess solidified material is cut off with a cutter, obtaining the final actuator;
- The cast is put in an oven in order to melt the wax core;
- A flange is glued to one of the inner channel ends while the other one is filled with Sil-Poxy silicon.

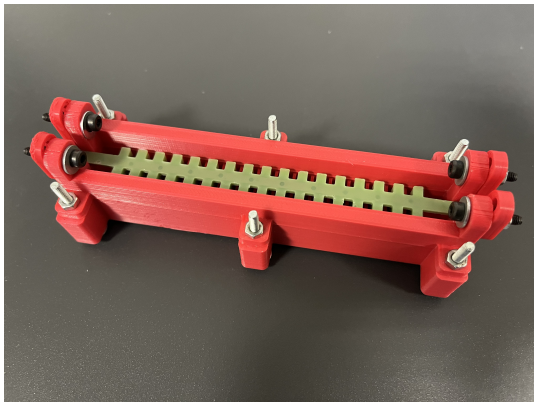


Figure 7 Actuator mold assembly.

Production tests were carried out using the wax cores with and without reinforcement. The results were then analyzed by observing the profile of the inner cavity in front of a light source: as expected, the hydrostatic buoyancy provided by the silicone causes the core without reinforcement to bend, whereas this does not occur if the metal reinforcement is adopted.

2.4.4 Chambers locking system

A chambers locking system was designed to be applied on the new version: it features 3D printed parts to prevent the first N-chambers from expanding, increasing overall performances and to provide a flat and hard surface to bond the actuator to the finger tip. A third part was realized, and its purpose will be later described. Part models and a CAD assembly are provided in Figure 9. The chamber locks are simply pressure mounted and held in place by the friction between the part and actuator materials.

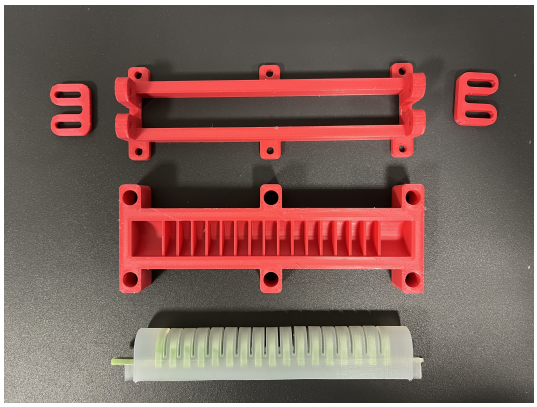


Figure 8 De-molded actuator.

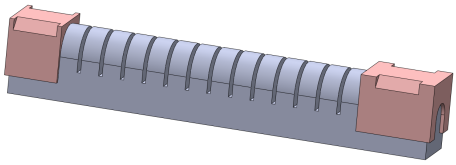


Figure 9 Chambers locking system.

2.4.5 Customizable inner geometry

Once the number and location of the chambers to be excluded is defined, it is reasonable to consider making a final structure specific to the actuator's use case. For example in finger rehabilitation discussed in [10], it could be reasonable to think of an exercise that involves PIP joint rotations exclusively. In this case, the chambers locking systems can be used to prevent the actuator bending on other joints to test the movement, but this could penalize the patient's comfort on long runs. Therefore, it was decided to investigate a solution that would adopt the same molds used for the production of actuator and core, but allowing "full" chambers to be made where expansion is not necessary. To achieve this, some parts obtained by laser cutting and provided with the same thickness as the inner chambers were made. These parts, referred to as "stoppers", can be inserted into the soft mold necessary for the production of the core, at the locations in which the chambers should be "filled". The liquid wax can therefore be poured into the mold as already shown in the previous sections and reported in Figure 10. The resulting

product will feature only the presence of the inner channel geometry where the stoppers are inserted.

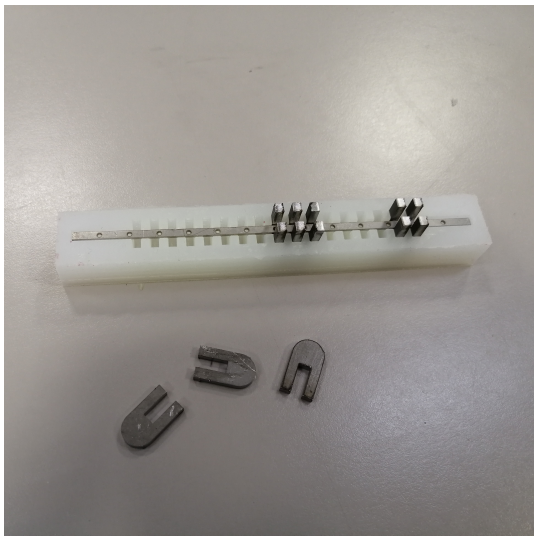


Figure 10 Core stoppers and steel core reinforcement.

3 RESULTS

3.1 TIP FORCE REACTION: FEM DESIGN ANALYSIS

Once the simulation described in 2.3, force reaction results were extracted and loaded into a MATLAB script for further analysis: results are presented in Figure 11.

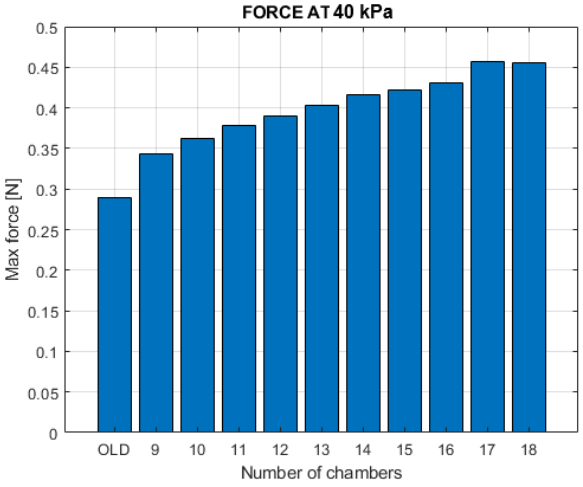


Figure 11 Force results for different geometries. OLD = first version.

From the graph above it can be seen that by increasing the number of chambers, the expressible force at 0.4 MPa increases considerably, with the maximum value recorded for the 17 chambers version. To verify the correctness of the collected data, the reaction force was probed along a complete work cycle, and the results are shown in Figure 12.

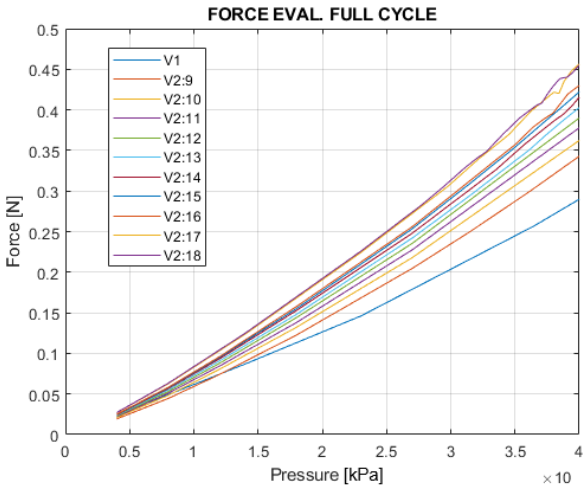


Figure 12 Force results for different geometries: complete cycle.

The 17-chambers version was adopted as the final one, since differences with the 18-chambers version are minimal and the lost-wax core is easier to make as the chambers are larger.

3.2 STRESS ANALYSIS

The minimum safety factor, computed for the final design with the FEM method, was in this case of value 2.8, while for the first geometry described in [10] was of value 2.4: even if the actuator was more constrained compared to the initial FEM analysis, the increased number of chambers allows for a better stress distribution resulting in a higher safety factor. Each sample (first and final design) was tested at a theoretical input pressure of 115 kPa and with the same meshing definition. Results are reported in Table VI.

Table VI - Stress analysis results.

Design	Safety Factor (at 115 kPa)
First version	2.4
Final version	2.8

3.3 TIP FORCE ANALYSIS

Force evaluation has been carried out by placing the actuator on a kitchen scale with 1g resolution while locked on a mechanical setup (off the scale). The actuator base was put on the same level of the scale in order to avoid tensions in the actuator due to misalignment between the two planes: to do this, a good method is to first weight the ”free” soft actuator and then to slowly lock the first chamber in place with a proper setup, as shown in Figure 13, until the weight is about the same. Data has been collected at given pressure steps, converted in Newtons and then compared to the theoretical FEM forces.



Figure 13 Tip force measurement.

Data are finally compared with the experimental ones: Figure 14 shows how the two datasets are comparable: small differences between the two curves are expected, as non-idealities are to be taken into account when moving from a simulation environment (FEM) to an experimental one. The FEM model can be trusted in predicting the tip force reaction of the actuator for various geometry as confirmed in [10].

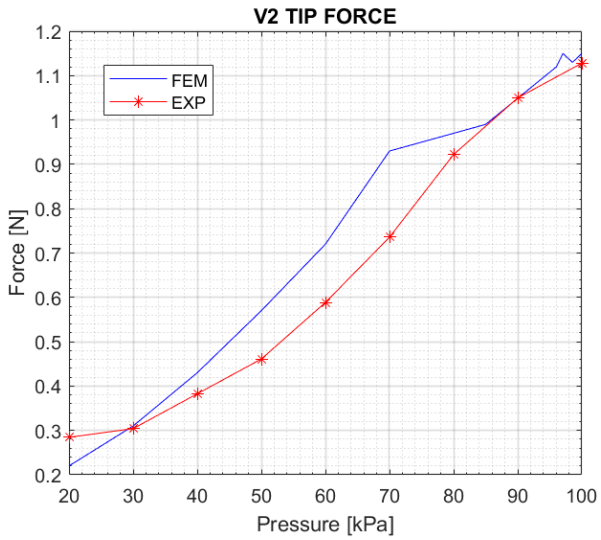


Figure 14 Tip force: FEM and experimental. V2 = final version.

In Figure 15 a comparison between the first and final version of the actuator is reported. The force profile of the new geometry shows significantly better results compared to the previous one, with a maximum force of 1.1N – 1.2N against 0.8N – 0.9N at an input pressure of 100 kPa.

3.4 DEFORMATION CONDITIONING

Building upon the deformation conditioning approach from previous studies [1], such a technique can be applied to the new actuator geometry (Figure 16a). In this case,

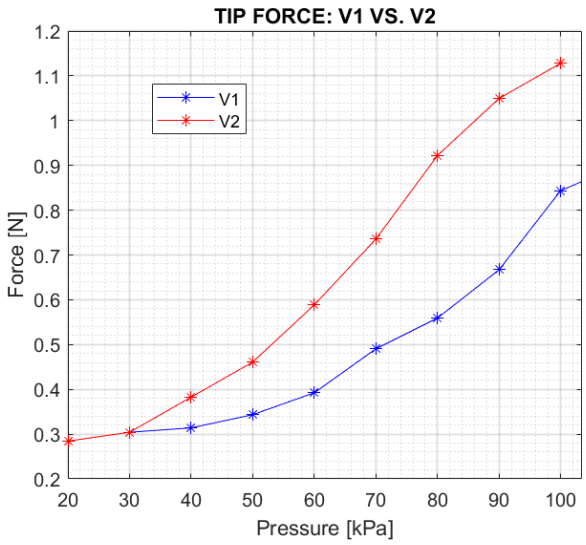


Figure 15 Tip force: First version vs. final version. V1 = first version, V2 = final version.

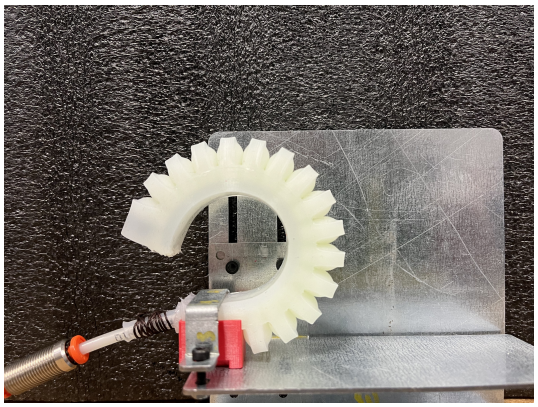
deformation conditioning is achieved by using a modified 3D printed part that interacts differently with the actuator's chambers (Figure 16b). This updated geometry aims to further refine the deformation control and improve the actuator's overall performance. As shown in the prior study, specific chambers are constrained to prevent expansion, allowing for a tailored deformation state validated through FEM analysis.

4 CONCLUSIONS

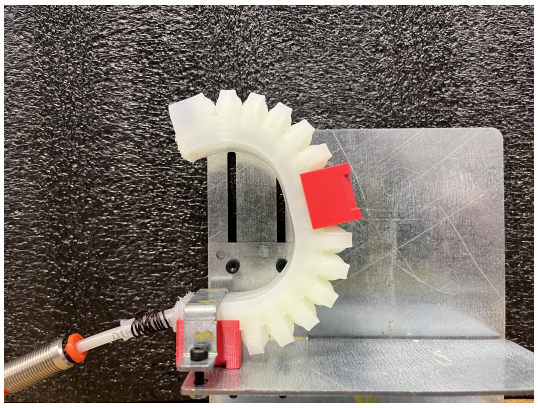
In this study, we have successfully explored the design, simulation, and experimental characterization of force-optimized monolithic PneuNets soft actuators. By combining finite element method (FEM) simulations with a detailed experimental validation process, we have demonstrated how optimizing actuator geometry—particularly chamber count, thickness variations, and inner channel design—can significantly enhance the force generation capabilities of PneuNets actuators.

The results obtained from FEM simulations and experimental force measurements reveal that increasing the number of chambers leads to a marked improvement in force output. Notably, the optimized 17-chamber actuator produced a maximum tip force of 1.1N–1.2N at 100 kPa input pressure, outperforming the earlier 9-chamber design, which showed a maximum force of 0.8N–0.9N at the same pressure. This confirms the efficacy of the proposed design modifications, particularly the reduction in wall thickness and the strategic reinforcement of key structural areas to avoid deformation under pressure.

Moreover, the stress analysis conducted via FEM showed that the revised design exhibits an improved safety factor



(a) Unconstrained deformation.



(b) Constrained deformation.

Figure 16 Deformation under constrained and unconstrained conditions.

of 2.8 compared to the earlier design's 2.4, ensuring better structural integrity and more efficient force distribution. These improvements highlight the balance achieved between flexibility and structural durability, which is crucial for ensuring reliable actuator performance in dynamic, real-world applications.

The successful validation of the FEM model in predicting the tip force further strengthens its role in actuator design and optimization. The agreement between experimental data and simulation results demonstrates the potential of FEM simulations to streamline actuator design processes, reducing the time and cost typically associated with prototyping.

In terms of practical applications, the optimized monolithic PneuNets actuators offer significant potential for a wide array of uses, including soft robotics, prosthetics, and rehabilitation devices, where both flexibility and force control are paramount. Future work could focus on extending this design framework to incorporate multi-modal actuators, as well as exploring additional materials and production techniques, to further enhance performance and expand the scope of applications.

Ultimately, this study lays a solid foundation for future advancements in the design and optimization of soft pneumatic actuators, reinforcing the value of combining simulation-driven design with experimental testing to achieve high-performance, cost-effective actuator solutions.

REFERENCES

[1] Loda D. and Tiboni M., PneuNets Soft Actuators: Characterization and Deformation Conditioning. In: Quaglia G., Boschetti G., Carbone G. (eds) *Advances in Italian Mechanism Science*. IFToMM Italy 2024. Mechanisms and Machine Science, vol 164. Springer, Cham, 2024.

[2] Achilli G.M., Amici C., Dragusanu M., Gobbo M., Logozzo S., Malvezzi M., Tiboni M., and Valigi M.C., Soft, Rigid, and Hybrid Robotic Exoskeletons for Hand Rehabilitation: Roadmap with Impairment-Oriented Rationale for Devices Design and Selection. *Appl. Sci.*, Vol. 13, No. 20, pp. 11287, 2023.

[3] Tiboni M. and Amici C., Soft Gloves: A Review on Recent Developments in Actuation, Sensing, Control and Applications. *Actuators*, Vol. 11, No. 8, pp. 232, 2022.

[4] Raparelli T., Eula G., Mazza L., Ivanov A., Pietrafesa F., Mala R. and Pontin M., A preliminar prototype of an industrial exoskeleton for the operator's trunk support. *International Journal of Mechanics and Control*, Vol. 23, No. 2, pp. 37-52, 2022.

[5] Costa D., A novel class of bio-inspired underwater robots. *International Journal of Mechanics and Control*, Vol. 23, No. 02, pp. 23-36, 2022.

[6] Amici C., Liu W., Pellegrini N., and Tiboni M., The Robot Selection Problem for Mini-Parallel Kinematic Machines: A Task-Driven Approach to the Selection Attributes Identification. *Micromachines*, Vol. 11, No. 8, 2020.

[7] Raparelli T., Eula G., Mazza L., Ivanov A., Pietrafesa F., Mala R. and Pontin M., The design of an innovative active exoskeleton prototype for industrial application with a pneumatic actuation. *International Journal of Mechanics and Control*, Vol. 23, No. 02, pp. 61-72, 2022.

[8] Bonafede G., Manuello Bertetto A., Fiorini P. and Muscolo G.G., Compliant legs in biped robots for running optimization. *International Journal of Mechanics and Control*, Vol. 23, No. 02, pp. 53-60, 2022.

[9] Park W., Seo S., and Bae J., A Hybrid Gripper With Soft Material and Rigid Structures. *IEEE Robotics and Automation Letters*, Vol. 4, No. 1, pp. 65-72, 2019.

[10] Tiboni M. and Loda D., Monolithic PneuNets Soft Actuators for Robotic Rehabilitation: Methodologies for Design, Production and Characterization. *Actuators*, Vol. 12, No. 7, pp. 299, 2023.

[11] Zhong G., Dou W., Zhang X., and Yi H., Bending

analysis and contact force modeling of soft pneumatic actuators with pleated structures. *International Journal of Mechanical Sciences*, Vol. 193, pp. 106150, 2021.

[12] Kim W., Seo B., Yu S.Y., and Cho K.J., Deployable Soft Pneumatic Networks (D-PneuNets) Actuator With Dual-Morphing Origami Chambers for High-Compactness. *IEEE Robotics and Automation Letters*, Vol. 7, No. 2, pp. 1262-1269, 2022.

[13] Liu Z., Wang F., Liu S., Tian Y., and Zhang D., Modeling and Analysis of Soft Pneumatic Network Bending Actuators. *IEEE/ASME Transactions on Mechatronics*, Vol. 26, No. 4, pp. 2195-2203, 2021.

[14] Zhang H., Liu W., Yu M., and Hou Y., Design, Fabrication, and Performance Test of a New Type of Soft-Robotic Gripper for Grasping. *Sensors*, Vol. 22, No. 14, pp. 5221, 2022.

[15] Wang F., Chen Y., Wang Y., Liu Z., Tian Y., and Zhang D., A soft pneumatic glove with multiple rehabilitation postures and assisted grasping modes. *Sensors and Actuators A: Physical*, Vol. 347, pp. 113978, 2022.

[16] Xavier M.S., Tawk C.D., Yong Y.K., and Fleming A.J., 3D-printed omnidirectional soft pneumatic actuators: Design, modeling and characterization. *Sensors and Actuators A: Physical*, Vol. 332, pp. 113199, 2021.

[17] Polygerinos P., Lyne S., Wang Z., Nicolini L.F., Mosadegh B., Whitesides G.M., and Walsh C.J., Towards a soft pneumatic glove for hand rehabilitation. *2013 IEEE/RSJ International Conference on Intelligent Robots and Systems*, pp. 1512-1517, 2013.

[18] Yeoh O.H., Some Forms of the Strain Energy Function for Rubber. *Rubber Chemistry and Technology*, Vol. 66, pp. 754-771, 1993.

ISSN 1590-8844
International Journal of Mechanics and Control, Vol. 26, No. 02, 2025
https://doi.org/10.69076/jomac.2025.0007

IMPROVING ACCURACY AND ROBUSTNESS IN ROBOT KINEMATIC CALIBRATION USING A SINGLE DRAW-WIRE ENCODER: A COMPARATIVE ANALYSIS

Giovanni Boschetti[*] Teresa Sinico[**]

[*] Department of Industrial Engineering (DII), University of Padova

[*] Department of Information Engineering (DEI), University of Padova

[**] Department of Management and Engineering (DTG), University of Padova

ABSTRACT

The demand for high-accuracy industrial manipulators has driven the development of affordable robot calibration procedures. This paper presents a critical comparison of kinematic calibration methods employing a single draw-wire encoder, focusing on the impact of measurement noise and encoder placement on calibration performance. We compare two distinct approaches: a standard optimization-based procedure, incorporating both fixed and estimated encoder location, and a recently proposed step-by-step method. Through simulation, we evaluate the sensitivity of each method to varying levels of measurement noise, demonstrating that the step-by-step method exhibits superior robustness to noise compared to the standard method when encoder location is estimated. Furthermore, we assess the influence of encoder location estimation on overall calibration accuracy, revealing that inaccurate encoder location estimation in the standard method can significantly degrade calibration results, particularly in noisy environments. Our findings provide valuable insights into the practical implementation of draw-wire encoder-based calibration, highlighting the trade-offs between computational complexity, robustness, and the required accuracy of the measurement system. Specifically, we demonstrate that achieving sub-millimeter accuracy requires encoder accuracy below $0.1\,\mathrm{mm}$, regardless of the calibration method employed. These results contribute to the advancement of cost-effective and reliable robot calibration techniques for industrial applications.

Keywords: Robot calibration, kinematic calibration, positioning accuracy, robot kinematics, draw-wire encoder

1 INTRODUCTION

The increasing demand for high-precision manufacturing tasks, encompassing applications such as laser cutting, visual servoing, assembly, and offline programming, has driven a continuous need for accurate and cost-effective calibration methods for industrial robots [1]. The ability to accurately position the robot's end-effector is critical for tasks requiring minimal deviation from pre-programmed paths or target locations. While industrial robots exhibit excellent repeatability – the ability to return to a previously taught point – their absolute positioning accuracy often falls short of the stringent requirements of modern manufacturing processes, typically exhibiting errors in the millimeter range. This discrepancy arises primarily from inaccuracies in the robot's kinematic model, which mathematically defines the relationship between joint angles and the resulting end-effector pose in Cartesian space [2, 3]. The model relies on nominal values for geometric parameters such as link lengths, joint offsets, and link twists. However,

Contact author: Giovanni Boschetti[1], Teresa Sinico[2]
[1]Via Venezia 1, Padova, 35131, Italy.
[2]Stradella S. Nicola 3, Vicenza, 36100, Italy.
E-mail: giovanni.boschetti@unipd.it,
teresa.sinico@phd.unipd.it

manufacturing tolerances and assembly errors inevitably lead to deviations from these nominal values, resulting in positioning errors. While other factors, such as deformation in mechanical components due to external loads and self-gravity, material degradation over time, thermal variations, sensor imprecision, friction, backlash, and other non-linearities can contribute to inaccuracy, the dominant source of error often lies in the geometric parameters. Therefore, kinematic calibration aims to enhance positioning accuracy by systematically identifying and compensating for deviations in the geometric parameters between the nominal and actual robot characteristics, addressing a primary cause of positioning errors [4].

Various calibration approaches have been developed to address this challenge. These approaches differ significantly in cost, complexity, the type of measurement system employed, and the specific parameter identification algorithm used. These systems can be broadly categorized into complete pose measurement systems and partial pose measurement systems. Complete pose measurement systems, such as laser trackers and coordinate measuring machines (CMMs), provide comprehensive measurements of the end-effector's position and orientation in three-dimensional space [5]. These systems offer high accuracy and are widely used in industrial settings. For instance, laser trackers have been successfully employed to achieve absolute calibration of industrial robots, demonstrating their ability to significantly reduce positioning errors [6, 7]. However, laser trackers are expensive, require specialized expertise, and can be time-consuming to set up, limiting their accessibility for smaller businesses or frequent recalibration. CMMs, while highly accurate, are typically stationary and unsuitable for in-situ calibration. Consequently, partial pose measurement systems, utilizing simpler and lower-cost sensors to capture limited aspects of the robot's pose, have gained traction as a more affordable alternative [8, 9, 10, 11].

Among partial pose measurement systems, methods based on single draw-wire encoders have emerged as a promising option for cost-effective robot calibration. A draw-wire encoder, also known as a string potentiometer or cable extension transducer, is a linear position sensor that measures distance by extending and retracting a tightly wound cable from a spool; the spool's rotation is directly coupled to a rotary encoder, allowing for precise determination of the cable extension based on the encoder's output. Draw-wire encoder-based calibration typically involves measuring the one-dimensional distance between the robot's end-effector and a fixed point using a draw-wire encoder for a number of robot poses. The unknown kinematic parameters and the coordinates of the encoder's fixed location are then estimated by minimizing the difference between the measured and predicted distances. Several studies have explored this approach, with slight variations in the implementation, including the choice of encoder location, the set of calibration points used, and the optimization algorithm employed. For example, a study investigated the use of simplified Denavit-Hartenberg (DH) models and Trust Region optimization to achieve computationally efficient and robust kinematic calibration, noting that calibrating only the joint encoder offsets – effectively correcting the robot's zero position for each joint without adjusting link lengths or other geometric parameters – can yield adequate results for many robotic applications [12]. Other works focused on the optimization algorithm, exploring hybrid identification methods combining a genetic algorithm for global search and a Levenberg-Marquardt algorithm for local refinement, rather than focusing on specific aspects of draw-wire encoder implementation [13, 14]. The use of a single draw-wire encoder has also been investigated for calibrating industrial robots with spherical wrist joints, presenting a cost-effective solution and analyzing the impact of the number of calibration points on accuracy [15], and for calibrating collaborative robots [16]. A key design choice in draw-wire encoder calibration is the selection of the encoder's fixed location: typically, existing approaches in the literature involve locating the sensor either inside or outside the manipulator's workspace, with the sensor location then needing to be simultaneously estimated during the calibration process, adding complexity due to the increased number of parameters. In contrast, a novel step-by-step calibration procedure was recently introduced, presenting an alternative approach that identifies each kinematic parameter sequentially by carefully selecting calibration poses to isolate parameter errors [17]. This eliminates the need to simultaneously estimate all parameters and the encoder location, potentially leading to improved robustness and reduced computational complexity.

Building on this research, the aim of this paper is to provide a comprehensive analysis of kinematic calibration procedures using a single draw-wire encoder. This work expands on the comparative analysis initially presented in our previous conference paper [18], and presents a critical comparison of the standard optimization-based approach, incorporating both fixed and estimated encoder location, with the recently proposed step-by-step calibration procedure. This work investigates: 1) Which procedure, the standard kinematic calibration procedure using a single draw-wire encoder or the step-by-step procedure, leads to the best estimation of robot kinematic parameters, taking into account noise in distance measurements; 2) To what extent the estimation of the three coordinates of the draw-wire encoder's exit point affect the estimation of robot kinematic parameters; 3) The required accuracy of the draw-wire encoder in order to obtain reliable results. Through extensive simulation studies, we aim to provide practical guidelines for selecting appropriate draw-wire encoder-based calibration techniques based on specific robot characteristics and application requirements.

2 KINEMATIC CALIBRATION PROCEDURES USING A SINGLE DRAW-WIRE ENCODER

2.1 KINEMATIC MODELING

While calibration procedures differ in their measurement systems and parameter identification strategies, a common requirement is the establishment of a suitable kinematic model that accurately represents the robot's geometry. This model serves as the foundation for relating joint variables to the end-effector pose, enabling the computation of predicted distances for comparison with measurements. The Denavit-Hartenberg (DH) convention is a widely adopted and standardized approach for establishing these kinematic models [19]. The DH convention uses a set of four parameters to describe each link in the robot's kinematic chain, providing a systematic way to define coordinate frames and transformations between them. However, the standard DH convention suffers from certain limitations. Notably, it exhibits a discontinuity when two consecutive joint axes are parallel, leading to singularities and potential numerical instability in the calibration process [20]. Alternative kinematic models, such as the Modified DH (MDH), S-model, or Product of Exponentials (POE) based models, have been proposed to address these limitations, offering alternative parameterizations that ensure continuity and completeness [21, 22, 23]. Regardless of the specific modeling approach, it is crucial that the chosen kinematic model for calibration be complete, continuous, and minimal [24]. Completeness ensures that all relevant geometric relationships are captured, continuity avoids singularities and numerical instabilities, and minimality prevents over-parameterization and redundancy in the model.

2.2 STANDARD CALIBRATION PROCEDURE (OPTIMIZATION-BASED)

The standard optimization-based kinematic calibration procedure, when adapted for use with a single draw-wire encoder, focuses on determining the optimal set of robot's geometric parameters $\boldsymbol{p} = (p_1, \ldots, p_j)$ and the encoder location $\boldsymbol{p}_e = (x_0, y_0, z_0)$ that minimizes the discrepancy between measured and predicted draw-wire distances.

Before starting data acquisition, it is necessary to address the placement of the draw-wire encoder, a key design choice impacting the calibration process. Different approaches exist regarding the encoder location: in some implementations, such as that described in [12], the encoder is deliberately placed outside the robot's workspace, while in other cases, as in [25], the encoder is positioned in an arbitrary location within the workspace. In yet other implementations [13, 14, 15, 26], the specific location of the encoder is not explicitly defined in the published description of the method. Regardless of the physical location, the precise coordinates $\boldsymbol{p}_e = (x_0, y_0, z_0)$ of the encoder's exit point are not known with sufficient accuracy a priori. Instead, the encoder location is treated as an additional set of parameters to be identified simultaneously with the robot's geometric parameters during the optimization process.

Following the encoder setup, a set of N robot calibration poses is selected. The selection, and more specifically the number and distribution of these target poses, influence the accuracy and robustness of the calibration. When calibrating a robot using measurement data that captures the full 3D pose of the end-effector, it is possible to employ observability indices to select the most informative robot poses, as mentioned in [27]. However, these indices, often based on singular value decomposition (SVD) of the Jacobian matrix,are not directly applicable when using only 1D distance measurements. This is because observability indices require knowledge of how changes in each kinematic parameter uniquely affect the robot's pose in multiple dimensions; with a single distance measurement, the information is limited to how the parameters affect the distance along a single line. In the absence of traditional observability metrics, alternative strategies must be considered for selecting the calibration poses. One approach is to record wire length data for the same robot position, but with different robot orientations and configurations. This can involve varying parameters such as the elbow configuration (above/below) or wrist orientation (lefty/righty). The underlying principle is that, in a well-calibrated robot, the measured draw-wire distance for a given end-effector position should ideally be invariant to changes in the robot's internal configuration. By comparing the distance measurements across these configurations, the sensitivity to various geometric parameters can be enhanced.

Once a set of N robot calibration poses has been selected, the robot is moved through them, and the distance data is recorded. For each target configuration i, the joint variables $\boldsymbol{\theta}_i = (\theta_i, \ldots, \theta_n)$ are precisely measured by the robot's joint encoders and recorded. Simultaneously, at each target configuration, the draw-wire's length $\tilde{d}_i$ measured is accurately recorded, representing the 1D distance between the end-effector and the encoder's exit point.

It is important to emphasize that the calibration procedure is typically restricted to a subset of the robot's geometric parameters. For example, the calibration might focus only on compensating for joint angle offsets, while other parameters, such as link lengths, are assumed to be known accurately. For this reason, it is useful to define a vector $\boldsymbol{e}$ containing only the parameters that are to be estimated:

$$\boldsymbol{e} = (e_1, e_2, ..., e_m), \tag{1}$$

where m is the number of parameters being estimated. Further, we define a vector $\delta\boldsymbol{e}$ representing the offsets from the nominal values of those parameters:

$$\delta\boldsymbol{e} = (\delta e_1, \delta e_2, ..., \delta e_m). \tag{2}$$

Next, a cost function, E, is defined to quantify the overall error between the measured and predicted distances across

the entire dataset. This cost function is commonly expressed as a sum of squared residuals:

$$E(\delta \boldsymbol{e}, \boldsymbol{p}_e) = \sum_{i=1}^{N} (d_i(\delta \boldsymbol{e}, \boldsymbol{p}_e) - \tilde{d}_i)^2, \tag{3}$$

where $d_i(\delta \boldsymbol{e}, \boldsymbol{p}_e)$ is the predicted draw-wire distance, calculated using the direct kinematic model with the recorded joint angles $\boldsymbol{\theta}_i$, nominal geometric parameters $\boldsymbol{p}$, encoder location $\boldsymbol{p}_e$ and unknown offsets $\delta \boldsymbol{e}$. The end-effector's coordinates can therefore be written as a function of the error vector $(x_i(\boldsymbol{\delta e}), y_i(\boldsymbol{\delta e}), z_i(\boldsymbol{\delta e}))$, and the predicted distance is expressed mathematically as follows:

$$d_i(\boldsymbol{\delta e}, \boldsymbol{p}_e) = \sqrt{(x_i(\boldsymbol{\delta e}) - x_0)^2 + (y_i(\boldsymbol{\delta e}) - y_0)^2 + (z_i(\boldsymbol{\delta e}) - z_0)^2}. \tag{4}$$

The primary goal is to find parameters to reduce the error, which consists in the minimization of the cost function using optimization algorithm. This involves selecting appropriate optimization parameters that minimize the aggregate error described in the error function:

$$(\boldsymbol{\delta e}^*, \boldsymbol{p}_e^*) = \arg \min_{\boldsymbol{\delta e} \in \boldsymbol{\Omega}, \boldsymbol{p}_e \in \boldsymbol{V}} \sum_{i=1}^{N} (d_i(\boldsymbol{\delta e}, \boldsymbol{p}_e) - \tilde{d}_i)^2, \tag{5}$$

where $\boldsymbol{\Omega}$ represents the set of allowable deviations for the error parameters $\delta \boldsymbol{e}$, and $\boldsymbol{V}$ denotes the permissible range of values for the encoder location $\boldsymbol{p}_e$. A zero-valued vector is commonly used as the initial estimate for the error parameter offsets, $\delta \boldsymbol{e}$. The initial guess for the encoder location $\boldsymbol{p}_e$ is derived through a preliminary optimization or measurement. Numerous optimization algorithms can be employed to solve this minimization problem. Given the inherent non-linearity of robot kinematics, global optimization algorithms are generally recommended. In particular, the Particle Swarm Optimization (PSO) algorithm has demonstrated particular effectiveness in robot calibration contexts [28, 29].

2.3 STEP-BY-STEP CALIBRATION PROCEDURE

An alternative approach to kinematic calibration with a single draw-wire encoder is to employ a step-by-step procedure, wherein the kinematic parameters are identified sequentially, rather than simultaneously. This method, detailed in [17], avoids the need for precise knowledge of the encoder's location and offers potential advantages in terms of computational efficiency and robustness to noise.

The process initiates with the robot placed in a specific initial configuration defined by a set of joint variables, $\boldsymbol{\theta}_0 = (\theta_{0,1}, \dots \theta_{0,n})$. The draw-wire encoder is then carefully mounted such that the two tips, the one attached to the end-effector and the other to the encoder, are coincident in this configuration. This ensures that the measured distance $\tilde{d}_0$, is essentially zero in this initial pose. This critical step eliminates the need to explicitly estimate the encoder location coordinates $\boldsymbol{p}_e = (x_0, y_0, z_0)$, as they are now implicitly defined by the robot's kinematics at $\boldsymbol{\theta}_0$.

The core of the step-by-step procedure is to identify each unknown kinematic parameter (e_j) in a sequential manner. For each parameter e_j, a specific set of N_j calibration poses, denoted as $S_j(\boldsymbol{\theta})$, is selected. A key requirement for $S_j(\boldsymbol{\theta})$ is that, within this specific set of poses, the discrepancy between the measured and predicted draw-wire distances depends primarily on the error in that single parameter e_j (and potentially on the errors in parameters that have already been identified in previous steps). In other words, the influence of all other unknown parameters should be minimized or eliminated in the cost function. This ensures that the identification process is as decoupled as possible, improving accuracy and reducing the complexity of the optimization. This targeted selection of calibration poses can be achieved by performing an analysis that considers the partial derivatives of the end-effector position with respect to the kinematic parameters, evaluated both at the encoder location and at the calibration location. By taking the difference of these derivatives and then computing the projection onto the direction of the theoretical draw-wire distance, one can quantify the influence of each parameter on the wire length. The joint coordinates are then chosen so that some terms in the influence is null.

For each pose $\boldsymbol{\theta}$ belonging to $S_j(\boldsymbol{\theta})$, the draw-wire length $\tilde{d}_i$ is measured and recorded. A cost function, $E_j(\delta e_j)$, is then formulated that depends only on the error parameter δe_j:

$$E_j(\delta e_j) = \sum_{i=1}^{N_j} (d_i(\delta e_j) - \tilde{d}_i)^2, \tag{6}$$

where $d_i(\delta e_j)$ is the predicted draw-wire distance for the $i-$th pose in the set $S_j(\boldsymbol{\theta})$, calculated using the direct kinematic model with the current estimate of all previously identified parameters (if any), and with the error parameter e_j offset by δe_j. The error parameter δe_j is then determined by minimizing the cost function $E_j(\delta e_j)$:

$$\delta e_j^* = \arg \min_{\delta e_j \in \Omega_j} E_j(\delta e_j), \tag{7}$$

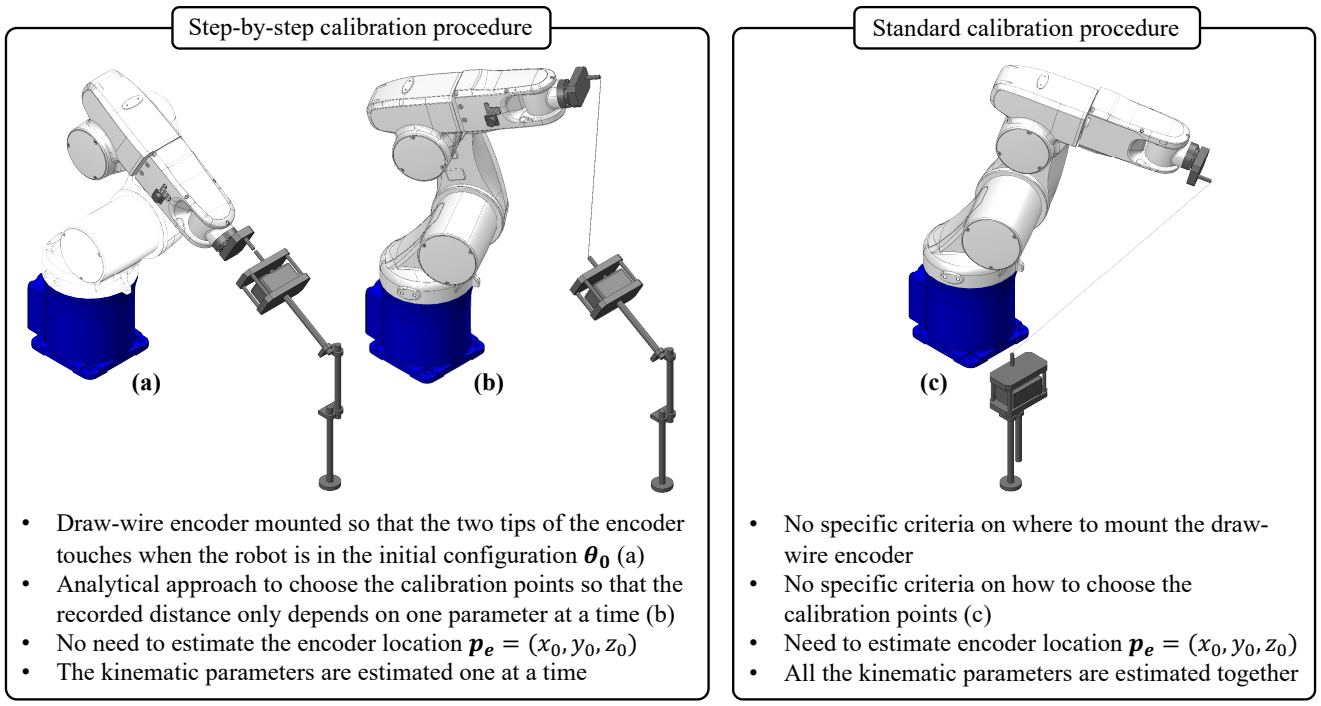


Figure 1 Summary of the step-by-step and standard calibration procedures with a single draw-wire encoder, illustrating key differences in setup and estimation strategies.

where Ω_j is the set of allowable deviations for the parameter e_j. The estimated offset, δe_j^*, is then used to update the value of the corresponding parameter e_j. The process is iterated sequentially for each of the m unknown kinematic parameters.

This step-by-step approach offers several advantages. By decoupling the parameter identification, the computational burden is significantly reduced, as only one parameter needs to be optimized at each step. Also, since the encoder location does not need to be explicitly estimated, the procedure becomes less sensitive to errors in identifying the encoder coordinates. Finally, the targeted selection of calibration points for each parameter helps to improve the accuracy and robustness of the calibration process.

To provide a clear overview of the key distinctions between these two approaches, Figure 1 illustrates the setup and estimation strategies of both the step-by-step and standard calibration procedures, highlighting the specific criteria for calibration points and the necessity of estimating the encoder location.

3 SIMULATION SETUP

This section outlines the simulation environment and procedures used to compare the standard and step-by-step kinematic calibration methods.

3.1 INDUSTRIAL MANIPULATOR

To conduct a comparative assessment of the standard and step-by-step calibration procedures, a simulated robot manipulator was used. Six-degree-of-freedom (6-DOF) articulated robots with a spherical wrist are the most common configuration in industrial applications; for this reason, this robot type was selected for the simulation. More in detail, the simulated manipulator is an Adept Viper S650 robot [30], depicted in Figure 2 along with attached DH frames and parameters. The nominal DH parameters are where nominal parameters value are $d_1 = 335\,\text{mm}$, $a_1 = 75\,\text{mm}$, $a_2 = 27\,\text{mm}$, $a_3 = 90\,\text{mm}$, $d_4 = 295\,\text{mm}$ and $d_6 = 80\,\text{mm}$. To develop the kinematic calibration model for this simulated Adept Viper S650 robot, we employed the methodology outlined in [12, 17], resulting in the DH(-) calibration model detailed in Table I, This model encompasses a set of ten parameters that can be grouped as:

$$\boldsymbol{\delta e} = (\delta\theta_2, \delta\theta_3, \delta\theta_4, \delta\theta_5, \delta\theta_6, \delta a_1, \delta a_2, \delta a_3, \delta d_4, \delta d_6). \quad (8)$$

3.2 SIMULATION ENVIRONMENT

The simulations comparing the standard optimization-based and step-by-step kinematic calibration procedures were conducted within the MATLAB environment. The simulations utilized the Simscape Multibody toolbox to model the robot's kinematic behavior and facilitate 3D visualization of the robot and measurement setup.

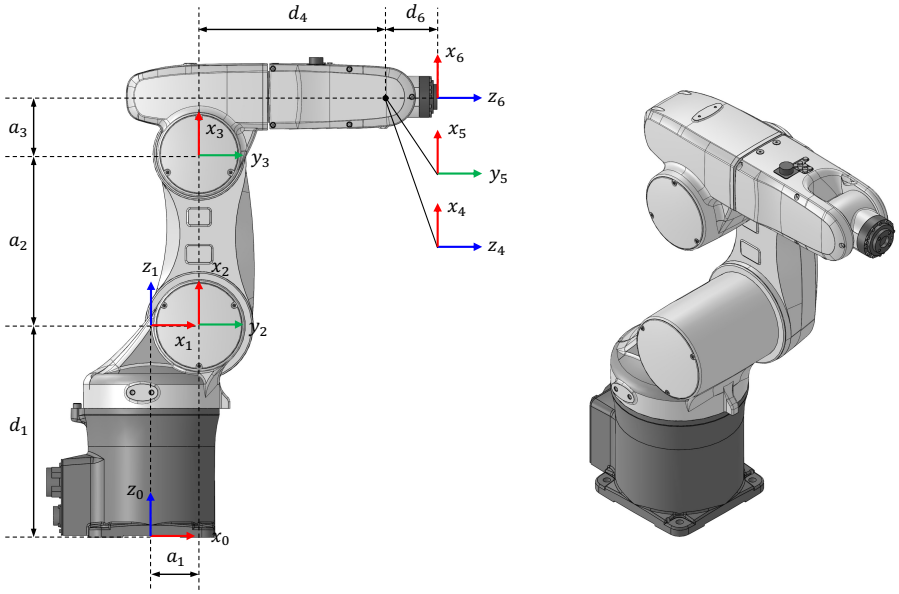


Figure 2 Adept Viper S650 six-degrees-of-freedom manipulator with attached DH frames and parameters.

Table I - DH(-) kinematic calibration model for the Adept Viper S650 manipulator.

i	α_{i-1} ($^\circ$)	a_{i-1} (mm)	θ_i ($^\circ$)	d_i (mm)
1	0	0	θ_1	d_1
2	-90	$a_1 + \delta a_1$	$\theta_2 + \delta\theta_2$	0
3	0	$a_2 + \delta a_2$	$\theta_3 + \delta\theta_3$	0
4	-90	$a_3 + \delta a_3$	$\theta_4 + \delta\theta_4$	$d_4 + \delta d_4$
5	90	0	$\theta_5 + \delta\theta_5$	0
6	-90	0	$\theta_6 + \delta\theta_6$	$d_6 + \delta d_6$

3.3 COMPARISON PROCEDURE

The performance of the two calibration procedures, considering both accuracy and robustness to measurement noise, was assessed through a simulation within the MATLAB environment, following the process described in the flowchart in Figure 3. The assessment consisted of simulating the robot's kinematic behavior and measurement process with perturbed parameters, applying both the standard optimization-based and step-by-step calibration procedures to the simulated data, and comparing the resulting parameter estimates to the original, perturbed parameter values using statistical analysis.

3.3.1 Parameter perturbation

The process begins by introducing errors into the nominal kinematic parameters of the simulated Adept Viper S650 robot. This is achieved by applying random offsets to each parameter, drawn from a uniform distribution within a specified range. The use of a uniform distribution reflects the unpredictable nature of manufacturing tolerances and assembly errors. Two distinct error levels are considered to evaluate the robustness of the calibration procedures to varying degrees of initial error; specifically, each angular parameter (e.g., joint angle offsets) is perturbed by an amount randomly selected from the interval $(-1^\circ, 1^\circ)$, while each length parameter (e.g., link lengths, offsets) is perturbed by an amount randomly selected from the interval $(-1\,\mathrm{mm}, 1\,\mathrm{mm})$.

3.3.2 Distance data perturbation and noise injection

To simulate realistic measurement inaccuracies inherent in draw-wire encoder systems, and to assess the required accuracy of the encoder for reliable kinematic calibration, a random noise component was introduced to each generated distance data point ($\tilde{d}_i$). This noise was modeled as a uniformly distributed random variable within a specified range, $\pm\delta d$. The selection of a uniform distribution reflects the assumption of unbiased sensor noise, where deviations from the true distance are equally likely to occur in either direction within the defined bounds.

Two distinct noise levels were investigated to understand the sensitivity of the calibration procedures to varying degrees of measurement uncertainty and to determine the minimum accuracy requirements for the draw-wire encoder. These levels, chosen to fall within the typical accuracy range of draw-wire encoders (0.1-0.2 mm), are a low noise condition and a high noise condition. Under the low noise condition, $\pm\delta d = \pm 0.1\,\mathrm{mm}$: this represents a scenario with relatively precise distance measurements, characteristic of high-quality draw-wire encoders or carefully controlled experimental conditions. On the other hand, the high noise condition, $\pm\delta d = \pm 0.2\,\mathrm{mm}$, simulates a more challenging environment, potentially arising from lower-grade encoders,

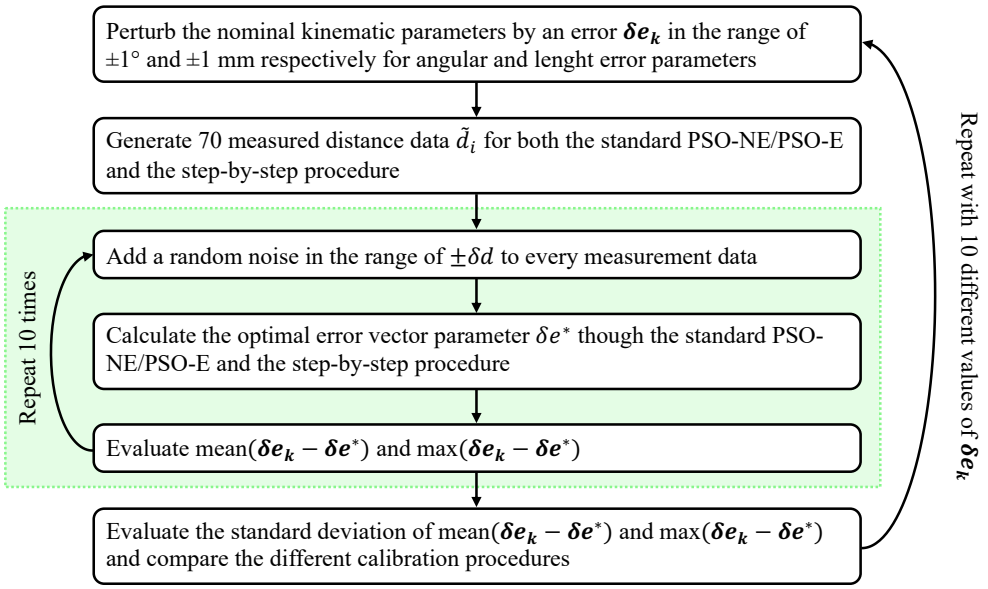


Figure 3 Flowchart of the comparison procedure.

environmental disturbances (e.g., vibrations), or less rigorous experimental setups. By analyzing the performance of the calibration algorithms under these different noise conditions, we can effectively evaluate the required accuracy of the draw-wire encoder to obtain reliable calibration results.

To simulate the inherent uncertainties present in real-world sensor readings, a random value within the specified $\pm\delta d$ range was added to each generated distance measurement $\tilde{d}_i$. This noise injection process was repeated for all 70 measured distance data points in each simulation run, ensuring the calibration algorithms were consistently challenged with noisy data and ultimately allowing us to assess the required encoder accuracy.

The use of 70 calibration points is a common practice in robot calibration studies, providing a balance between accuracy and experimental effort. Using fewer calibration points can lead to under-identification of parameters, while more can become computationally expensive. A minimum of 70 points has been proven to be sufficient to meet a certain degree of precision.

3.3.3 Calibration and evaluation

Following the generation of perturbed distance data, both the standard optimization-based and step-by-step calibration procedures were applied to estimate the kinematic parameters of the simulated Adept Viper S650 robot. Each calibration procedure was implemented as described in Sections 3.3.1 and 3.3.1, utilizing the same set of 70 calibration points and the same initial parameter values for a fair comparison. The standard optimization-based procedure was implemented in two variants to assess the influence of simultaneously estimating the draw-wire encoder's exit point coordinates along with the robot's kinematic parameters:

- PSO-NE (Particle Swarm Optimization - No Encoder Estimation): in this variant, the coordinates of the draw-wire encoder's exit point were assumed to be known a priori and were held constant during the optimization process. This simulates a scenario where the encoder is accurately positioned and its location is precisely measured using an external measurement system.
- PSO-E (Particle Swarm Optimization - Encoder Estimation): in this variant, the coordinates of the draw-wire encoder's exit point were treated as additional parameters to be estimated simultaneously with the robot's kinematic parameters during the optimization process. This simulates a scenario where the encoder's location is not precisely known and needs to be determined through the calibration procedure itself.

To ensure robust statistical analysis and to mitigate the influence of random variations in the noise injection process, each calibration scenario (defined by a specific noise level and calibration procedure) was repeated 10 times. In each repetition, a new set of perturbed distance data was generated, and the calibration algorithm was executed to obtain a new estimate of the kinematic parameters, $\boldsymbol{\delta e^*}$. The performance of each calibration procedure was assessed by comparing the estimated kinematic parameters, $\boldsymbol{\delta e^*}$, to the original, perturbed kinematic parameters, $\boldsymbol{\delta e_k}$ (introduced in Section 3.3.1). The assessment considered two primary performance metrics. The mean error was calculated for each kinematic parameter by averaging the absolute difference between the estimated value ($\boldsymbol{\delta e^*}$) and the true value ($\boldsymbol{\delta e_k}$) across the 10 repetitions: this metric provides an indication of the average accuracy of the parameter estimation. In addition, the maximum error was determined for each

kinematic parameter by identifying the largest absolute difference between the estimated value ($\boldsymbol{\delta e}^*$) and the true value ($\boldsymbol{\delta e_k}$) across the 10 repetitions: this metric reveals the worst-case accuracy of the parameter estimation. In addition to the mean and maximum errors, the standard deviation of both metrics was also computed across the 10 repetitions to quantify the repeatability and robustness of each calibration procedure. A low standard deviation indicates that the calibration procedure consistently produces similar results across different noisy datasets, while a high standard deviation suggests that the results are more sensitive to variations in the noise. The resulting mean errors, maximum errors, and their corresponding standard deviations were then compared across the different calibration procedures (PSO-NE, PSO-E, and Step-by-Step) and noise levels ($\pm 0.1\,\mathrm{mm}$ and $\pm 0.1\,\mathrm{mm}$) to evaluate their relative performance in terms of accuracy and robustness.

4 RESULTS AND DISCUSSION

The simulation tests revealed considerable differences in the performance of the step-by-step, PSO-NE, and PSO-E calibration procedures under varying noise conditions. The results are summarized in Figures 4 and 5, which depict the mean error and maximum error in the estimation of kinematic parameters, respectively, for each calibration procedure across 10 simulation runs.

4.1 IMPACT OF NOISE IN CALIBRATION ACCURACY

As shown in Figure 4, when the noise level was low ($\pm 0.1\,\mathrm{mm}$), all three calibration procedures exhibited comparable performance. The mean error in the estimation of kinematic parameters remained consistently low for all three algorithms, indicating that with highly accurate distance measurements, both the standard optimization-based approaches and the step-by-step procedure can effectively identify the robot's kinematic parameters. However, a significant divergence in performance was observed when the noise level increased to $\pm 0.2\,\mathrm{mm}$. As illustrated in Figure 4, the step-by-step procedure maintained a relatively stable mean error, demonstrating its robustness to measurement noise. In contrast, the mean error for both PSO-NE and PSO-E increased considerably, indicating a greater sensitivity to noise. This suggests that the step-by-step procedure is more resilient to inaccuracies in distance measurements, making it a more reliable option in environments where high-precision sensors are not available or where environmental noise is a concern.

4.2 INFLUENCE OF ENCODER LOCATION ESTIMATION

The results also highlight the impact of estimating the encoder's exit point coordinates on the accuracy of the standard optimization-based procedure. A comparison of PSO-NE and PSO-E in Figure 4 reveals that PSO-E, which estimates the encoder location, consistently exhibited higher mean errors compared to PSO-NE, particularly at the higher noise level. This indicates that simultaneously estimating the encoder location and the kinematic parameters can lead to a degradation in calibration accuracy, especially when the measurement data is noisy. The increased uncertainty in the encoder location estimate appears to propagate and negatively influence the estimation of the robot's kinematic parameters.

4.3 ANALYSIS OF MAXIMUM ERROR AND REPEATABILITY

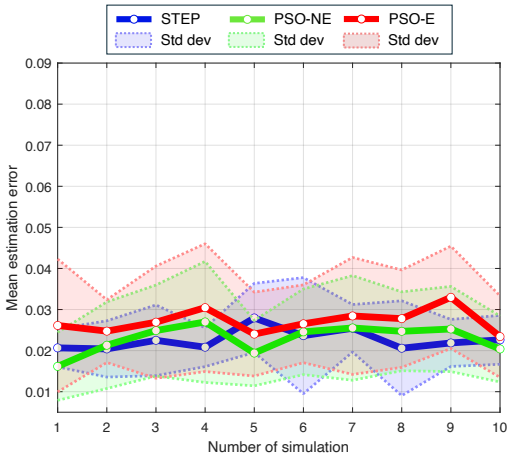
The analysis of maximum errors, presented in Figure 5, further reinforces these findings. The step-by-step procedure consistently yielded lower maximum errors compared to PSO-NE and PSO-E, indicating a better worst-case performance. Furthermore, the standard deviation of both mean and maximum errors was generally lower for the step-by-step procedure, suggesting greater repeatability and robustness. This implies that the step-by-step procedure is less susceptible to random variations in the noise and provides more consistent calibration results across multiple runs.

4.4 IMPLICATIONS FOR ENCODER ACCURACY REQUIREMENTS

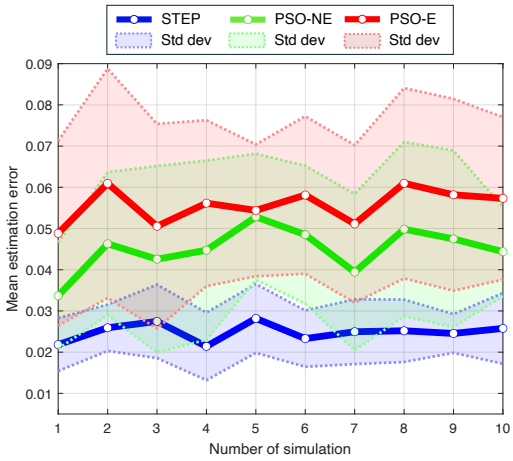
The observed performance trends underscore the importance of encoder accuracy for reliable robot kinematic calibration. The results suggest that to achieve sub-millimeter accuracy in robot positioning, the draw-wire encoder should exhibit an accuracy of at least $\pm 0.1\,\mathrm{mm}$. When the encoder accuracy falls below this threshold (i.e., noise level exceeds $\pm 0.1\,\mathrm{mm}$), the performance of the standard optimization-based procedures (particularly PSO-E) degrades significantly, while the step-by-step procedure offers a more robust alternative.

4.5 COMPUTATIONAL CONSIDERATIONS

Beyond accuracy and robustness, computational complexity is also a critical factor. The step-by-step procedure is inherently less computationally demanding than the standard optimization-based procedures, as it involves estimating only one parameter at a time. This allows for the implementation of a simple iterative process, which can be directly incorporated into the robot controller's programming environment. This simplicity is particularly advantageous for real-time calibration or for applications where computational resources are limited within the robot's control system. In contrast, the standard procedure requires a complex optimization algorithm, such as PSO, which is generally unsuitable for direct implementation within a robot controller. This is due to the significant computational resources needed by these algorithms, as well as the typical absence of embedded optimization software within robot

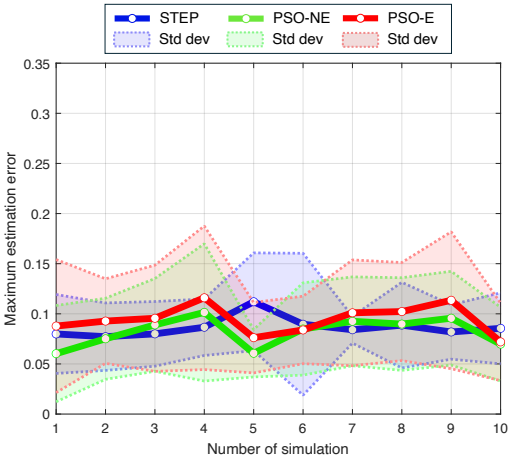


(a) Results with a random error of ± 0.1 mm on the measured length.

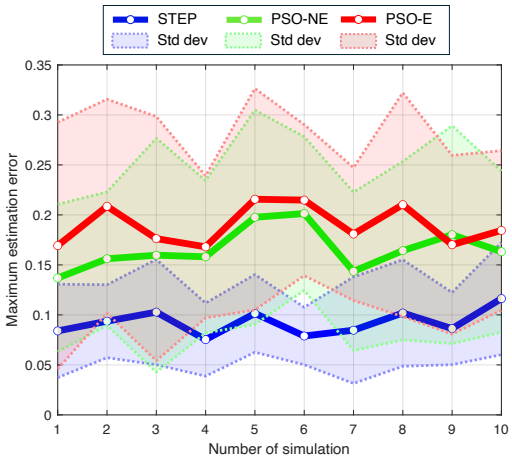


(b) Results with a random error of ± 0.2 mm on the measured length.

Figure 4 Mean error of the identified kinematic parameters using the STEP, PSO-NE and PSO-E algorithms.



(a) Results with a random error of ± 0.1 mm on the measured length.



(b) Results with a random error of ± 0.2 mm on the measured length.

Figure 5 Maximum error of the identified kinematic parameters using the STEP, PSO-NE and PSO-E algorithms.

control systems. The step-by-step procedure, by requiring the estimation of only a single parameter at each step via simple iterative algorithms, is much more readily deployable directly within the robot's control system.

In summary, the step-by-step calibration procedure offers a compelling alternative to the standard optimization-based approaches, particularly in scenarios where high-precision distance measurements are challenging to obtain or where computational resources are constrained. While the standard optimization-based procedures can achieve comparable performance with highly accurate encoder data, their sensitivity to noise and the added complexity of estimating the encoder location make them less robust and potentially less reliable in real-world applications.

5 CONCLUSIONS

This study compared standard optimization-based and step-by-step kinematic calibration procedures using a single draw-wire encoder. Simulations revealed that while standard methods can match the step-by-step procedure's performance with highly accurate encoder data (± 0.1 mm or better), they are more sensitive to measurement noise and encoder location uncertainty. Simultaneously estimating encoder location degraded accuracy (PSO-E). The step-by-step procedure proved more robust to noise, offering a compelling alternative when high-precision measurements or computational resources are limited. Encoder accuracy of at least ± 0.1 mm is crucial for achieving sub-millimeter robot positioning accuracy.

This research contributes valuable insights into the trade-offs between accuracy, robustness, and complexity in draw-wire encoder-based robot calibration, guiding practitioners in selecting appropriate strategies.

REFERENCES

[1] Dahu Zhu, Xiaozhi Feng, Xiaohu Xu, Zeyuan Yang, Wenlong Li, Sijie Yan, and Han Ding. Robotic grinding of complex components: A step towards efficient and intelligent machining – challenges, solutions, and applications. *Robotics and Computer-Integrated Manufacturing*, 65, 2020. doi: 10.1016/j.rcim.2019.101908.

[2] Ulrich Schneider, Manuel Drust, Matteo Ansaloni, Christian Lehmann, Marcello Pellicciari, Francesco Leali, Jan Willem Gunnink, and Alexander Verl. Improving robotic machining accuracy through experimental error investigation and modular compensation. *International Journal of Advanced Manufacturing Technology*, 85(1-4):3 – 15, 2016. doi: 10.1007/s00170-014-6021-2.

[3] Massimo Martorelli, Cesare Rossi, Sergio Savino, and Gabriele Staiano. A contactless robot kinematic calibration method by digital photogrammetry. *International Journal of Mechanics and Control*, 16(2):9 – 16, 2015.

[4] Kaiwei Ma, Fengyu Xu, Qingyu Xu, Shuang Gao, and Guo-Ping Jiang. Trajectory error compensation method for grinding robots based on kinematic calibration and joint variable prediction. *Robotics and Computer-Integrated Manufacturing*, 92, 2025. doi: 10.1016/j.rcim.2024.102889.

[5] Albert Nubiola, Mohamed Slamani, Ahmed Joubair, and Ilian A. Bonev. Comparison of two calibration methods for a small industrial robot based on an optical cmm and a laser tracker. *Robotica*, 32(3):447 – 466, 2014. doi: 10.1017/S0263574713000714.

[6] Albert Nubiola and Ilian A. Bonev. Absolute calibration of an abb irb 1600 robot using a laser tracker. *Robotics and Computer-Integrated Manufacturing*, 29(1):236 – 245, 2013. doi: 10.1016/j.rcim.2012.06.004.

[7] Theodor Borangiu, Anamaria Dogar, and Alexandru Dumitrache. Calibration of robot-mounted laser scanning probe based on a tool transformation. *International Journal of Mechanics and Control*, 11(1):39 – 43, 2010.

[8] Martin Gaudreault, Ahmed Joubair, and Ilian Bonev. Self-calibration of an industrial robot using a novel affordable 3d measuring device. *Sensors (Switzerland)*, 18(10), 2018. doi: 10.3390/s18103380.

[9] Temesguen Messay-Kebede, George Sutton, and Ouboti Djaneye-Boundjou. Geometry based self kinematic calibration method for industrial robots. *Proceedings - IEEE International Conference on Robotics and Automation*, page 4921 – 4926, 2018. doi: 10.1109/ICRA.2018.8460764.

[10] Juan S. Toquica and José Maurício S. T. Motta. A methodology for industrial robot calibration based on measurement sub-regions. *International Journal of Advanced Manufacturing Technology*, 119(1-2):1199 – 1216, 2022. doi: 10.1007/s00170-021-08308-4.

[11] Erika Ottaviano, Marco Ceccarelli, Maria Toti, and Carolina Avila Carrasco. Catrasys (cassino tracking system): A wire system for experimental evaluation of robot workspace. *Journal of Robotics and Mechatronics*, 14(1):78 – 87, 2002. doi: 10.20965/jrm.2002.p0078.

[12] Temesguen Messay, Raúl Ordóñez, and Eric Marcil. Computationally efficient and robust kinematic calibration methodologies and their application to industrial robots. *Robotics and Computer-Integrated Manufacturing*, 37:33 – 48, 2016. doi: 10.1016/j.rcim.2015.06.003.

[13] Zhibin Li, Shuai Li, and Hao Wu. A new variable step-size levenberg-marquardt algorithm for industrial robot calibration. In *2022 IEEE International Conference on Networking, Sensing and Control (ICNSC)*, pages 1–6, 2022. doi: 10.1109/ICNSC55942.2022.10004134.

[14] Zhibin Li, Shuai Li, and Xin Luo. Efficient industrial robot calibration via a novel unscented kalman filter-incorporated variable step-size levenberg–marquardt algorithm. *IEEE Transactions on Instrumentation and Measurement*, 72:1–12, 2023. doi: 10.1109/TIM.2023.3265744.

[15] Huitaek Yun, Heungki Jeon, Seunghan Yang, and Martin B.G. Jun. Calibration of industrial robots with spherical joint using single wire encoder. *Manufacturing Letters*, 33:46–50, 2022. ISSN 2213-8463. doi: https://doi.org/10.1016/j.mfglet.2022.07.120.

[16] Heungki Jeon, Martin B. G. Jun, Seung-Han Yang, and Huitaek Yun. Cost-effective calibration of collaborative robot arm with single wire encoder. *International Journal of Precision Engineering and Manufacturing*, 24(9):1615 – 1623, 2023. doi: 10.1007/s12541-023-00886-5.

[17] Giovanni Boschetti and Teresa Sinico. A novel step-by-step procedure for the kinematic calibration of robots using a single draw-wire encoder. *International Journal of Advanced Manufacturing Technology*, 2024. doi: 10.1007/s00170-024-13219-1.

[18] Giovanni Boschetti and Teresa Sinico. Kinematic calibration of robots using a single draw-wire encoder: A comparison. *Mechanisms and Machine Science*, 163 MMS:3 – 10, 2024. doi: 10.1007/978-3-031-64553-2_1.

[19] Bruno Siciliano and Oussama Khatib. *Springer handbook of robotics*. Springer, 2016. doi: 10.1007/978-3-319-32552-1.

[20] Samad A. Hayati. Robot arm geometric link parameter estimation. In *The 22nd IEEE Conference on Decision and Control*, pages 1477–1483, 1983. doi: 10.1109/cdc.1983.269783.

[21] Hanqi Zhuang, Zvi S. Roth, and Fumio Hamano. A complete and parametrically continuous kinematic model for robot manipulators. *IEEE Transactions on Robotics and Automation*, 8(4):451 – 463, 1992. doi: 10.1109/70.149944.

[22] H.W. Stone and A.C. Sanderson. Statistical performance evaluation of the s-model arm signature identification technique. In *Proceedings. 1988 IEEE International Conference on Robotics and Automation*, pages 939–946 vol.2, 1988. doi: 10.1109/ROBOT.1988.12180.

[23] Hanqi Zhuang, Luke K. Wang, and Zvi S. Roth. Error-model-based robot calibration using a modified cpc model. *Robotics and Computer Integrated Manufacturing*, 10(4):287 – 299, 1993. doi: 10.1016/0736-5845(93)90042-I.

[24] Klaus Schröer, Stephen L. Albright, and Michael Grethlein. Complete, minimal and model-continuous kinematic models for robot calibration. *Robotics and Computer-Integrated Manufacturing*, 13(1):73 – 85, 1997. doi: 10.1016/S0736-5845(96)00025-7.

[25] M.R. Driels and W.E. Swayze. Automated partial pose measurement system for manipulator calibration experiments. *IEEE Transactions on Robotics and Automation*, 10(4):430–440, 1994. doi: 10.1109/70.313094.

[26] Guanbin Gao, Yuan Li, Fei Liu, and Shichang Han. Kinematic calibration of industrial robots based on distance information using a hybrid identification method. *Complexity*, 2021, 2021. doi: 10.1155/2021/8874226.

[27] Morris R. Driels and Uday S. Pathre. Significance of observation strategy on the design of robot calibration experiments. *Journal of Robotic Systems*, 7(2):197 – 223, 1990. doi: 10.1002/rob.4620070206.

[28] Zafer Bingül and Ouzhan Karahan. Dynamic identification of staubli rx-60 robot using pso and ls methods. *Expert Systems with Applications*, 38(4):4136 – 4149, 2011. doi: 10.1016/j.eswa.2010.09.076.

[29] Russell C. Eberhart and Yuhui Shi. Comparison between genetic algorithms and particle swarm optimization. *Lecture Notes in Computer Science (including subseries Lecture Notes in Artificial Intelligence and Lecture Notes in Bioinformatics)*, 1447:611 – 616, 1998. doi: 10.1007/bfb0040812.

[30] Adept Omron. Viper 650/850 robot with emb-60r user's guide. URL `https://files.omron.eu/downloads/latest/manual/en/i599_viper_650,_850_robot_with_emb-60r_users_manual_en.pdf?v=1`. [Accessed: April 4, 2025].

ISSN 1590-8844
International Journal of Mechanics and Control, Vol. 26, No. 02, 2025
https://doi.org/10.69076/jomac.2025.0008

DESIGN AND CHARACTERIZATION OF A NEW SOFT ROBOTIC TENDON DRIVEN GRIPPER FOR PRECISION GRASPING

Silvia Logozzo* Maria Cristina Valigi*

ABSTRACT

The paper presents a new prototype of a robotic gripper for precision grasping which is a challenging task for artificial grippers. The grasping ability is crucial when interacting with the physical world besides in manipulation tasks. Precision grasping requires a high degree of control, involving factors such as contact friction, contact area, and object trajectories. The proposed gripper is novel in its design, featuring three monolithic fingers, a differential, and a control system. The monolithic fingers are conceived with soft, deformable materials and structures and are actuated by tendons, which allow them to conform to the shape of the object being grasped. The differential system is used to adjust the force applied by each finger, enabling the gripper to grasp objects with various shapes and sizes. The control system is responsible for coordinating the fingers' movements, allowing a secure grasp. The paper provides a detailed analysis of the proposed gripper design. A 3D printed prototype was used to characterize the trajectories of the fingers and discuss the ability of the gripper to grasp various objects. In addition, the vibration of the fingers was studied. Overall, the proposed gripper represents a significant advancement in the field of precision grasping.

Keywords: Robotic precision grasping; Underactuated gripper; Soft-rigid finger; hybrid gripper; tendon-driven actuation

1 INTRODUCTION

In recent decades, the use of robotic manipulation has become increasingly requested in many activities, especially related to the medical and industrial field and in a collaborative human-robot environment[1]. In fact, robotic manipulators and grippers can enhance many tasks that help human operators, improve their abilities [2, 3], or protect them from injuries, toxic environments, or hard/hazardous works [4, 5]. For these reasons, advances in robotic manipulation are increasingly required with the main purpose of developing robotic grippers and manipulators that can mimic the dexterity and precision of the human hand [6, 7].

Contact author: Maria Cristina Valigi[1], Silvia Logozzo[1]
[1]Department of Engineering - University of Perugia.
E-mail: mariacristina.valigi@unipg.it, silvia.logozzo@unipg.it

The human hand is capable of accomplishing even very complicated tasks by performing two specific grasping operations, i.e. power and precision grasping, with different characteristics in terms of compliance, trajectories of the fingers, contact surfaces, and applied forces. In power grasping, the forces exerted by the fingers and the contact areas are higher because the object is normally wrapped by the hand with a conformal contact [8]. In contrast, in precision grasping the objects are grasped between the fingertips, with small contact surfaces and applied forces [9, 10, 11]. Therefore, in power grasping the objects are usually big with respect to the dimensions of a hand, while in precision grasping the objects are generally small and sometimes fragile. In fact, precision grasping operations are often devoted to manipulating objects that must be grasped with care or placed precisely in specific small volumes [12]. In this scenario, the design of robotic grippers for precision grasping takes an important role, even because many different parameters and characteristics can be changed or tuned to obtain different grasping solutions, as in particular

the number of fingers, the actuation strategy and the main structural features [13].

Several research activities have recently focused on the study and development of grasping solutions, especially for precision grasping, employing different conceptualizations and designs [14]. Considering the structure of the grippers and the fingers, many soft robotic hands with different flexible fingers have been proposed [15, 16, 17]. The softness of fingers and/or joints can improve the grasping effectiveness and capability, promoting the design of compliant structures and conformal end-effectors, with an expected advantageous impact on several fields such as healthcare and manufacturing. Therefore, because of their increasing adaptability and versatility, soft manipulators are expected to be the future direction for complex grasping operations. Moving towards this direction, underactuation is a key feature of soft robotic grippers to increase the simplicity and task adaptability, maintaining robustness. The adaptability and efficiency of compliant underactuated grippers make them a highly promising solution for advanced robotic manipulation. To enhance the compliance of grasping in underactuated structures, the use of differential systems is crucial to allow fingers to move independently one to the other and secure the grip [18, 19].

Although deformable structures offer significant advantages in robotic finger design, they also introduce complex challenges in kinematic and dynamic modeling that must be addressed during both the design and control phases. This research presents the integration of Wave-joints as a fundamental component in the development of an underactuated robotic gripper [20]. The gripper features three tendon-driven fingers and a single differential system, enhancing its grasping capabilities. The project focuses on the gripper's design and includes promising experimental results demonstrating its grasping performance. While Wave-joint fingers have been explored previously, the prototype studied in this paper incorporates key modifications and innovations. These include adjustments to the positioning of the final joint — referred to as the last phalanx (or fingertip) — as well as refinements in the tendon housing, which influence the actuation of the phalanges. These design improvements contribute to enhanced precision grasping abilities, as demonstrated by the experiments presented in this work. In addition, the paper provides the characterization of the finger trajectories discussing the ability of the gripper to grasp various objects. Finally, the finger vibration after the object is released was studied.

The paper is structured as follows: Section 2 provides all the details of the finger and gripper design; Section 3 details the experimental campaigns focused on the evaluation of the grasping abilities, trajectories and release vibrations and results; Section 4 is devoted to conclusions and potential future developments.

2 DESIGN

2.1 THE WAVE-JOINT

The Wave-joint concept was previously introduced in [20] providing a flexible adjustable joint between phalanges. The Wave-joint consists of a sinusoidal wave structure, that can be properly parameterized to adjust the mechanical properties of the finger (Fig. 1(a)). This approach eliminates the need for multi-material elastic joints allowing for a monolithic finger design, as shown in Fig.1(b).

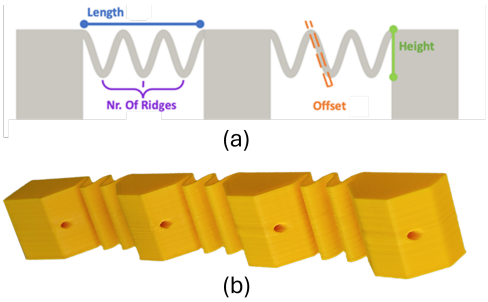


Figure 1 The Wave-joint: (a) structure; (b) a Wave-joint finger

Compared to traditional rectangular-section flexible joints, this wave-shaped joint offers greater flexibility while maintaining structural integrity. Additionally, using the same material for both rigid and flexible sections enhances durability and consistency in performance. In fact, previous studies on innovative grippers have highlighted the effectiveness of monolithic joints in balancing compliance and rigidity. By adjusting the sinusoidal wave parameters, a wide range of stiffness values can be achieved, making the design adaptable to various tasks. The rigorous characterization of this joint, as detailed in [21], includes both numerical simulations and experimental validation, confirming its versatility.

The Wave-joint finger prototype reported in Fig. 1(b) represents a previous version of this new monolithic tendon-driven finger structure. This type of finger structure enables the development of compliant underactuated grippers, which offer enhanced precision and control in object manipulation. By tuning the joint stiffness values, these grippers can be optimized for specific grasping tasks, achieving the desired postures efficiently. Another key benefit of this design is its ability to tune the directions in which contact forces increase by increasing the tendon tension to perform twisting tasks as explored in [20].

2.2 THE NEW WAVE-JOINT FINGERS

The proof-of-concept of the new Wave-joint finger design is based on an enhanced version of the previous structure and is specifically conceived for precision grasping tasks. This updated model maintains the fundamental concept of a tendon-driven, monolithic 3D-printed structure, featuring

rigid phalanges and flexible wave-joints. In the new configuration, reported in Fig. 2, the finger consists of three Wave-joints and four phalanges: the base phalanx, fixed at the palm, two intermediate phalanges, and a fingertip.

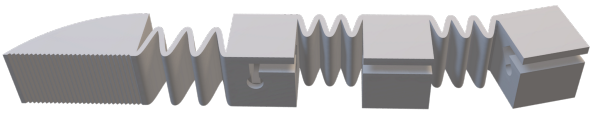


Figure 2 The new Wave-joint finger

The two joints closer to the palm have the same geometry, and their position makes them responsible for the flexion of the finger when the tendon is actuated by the motor. In contrast, the last Wave-joint that is connected to the fingertip differs from the other two ones both in terms of geometry, position and actuation. In fact, this last joint is not aligned with the other two joints and is positioned on the opposite side of the phalanx, allowing the fingertip to extend when the rest of the finger is flexed, as illustrated in Fig. 3. In addition, the fingertip and its Wave-joint are not actuated by tendons, as the tendons are configured to move just the two middle phalanges.

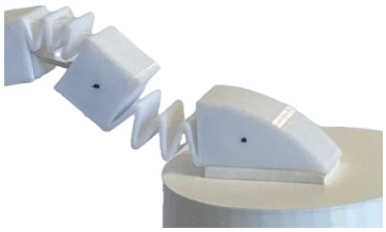


Figure 3 Fingertip extension for precision grasping

As shown in Fig. 3, precision grasping is achieved mainly by the stiffness of the last Wave-joint, as the fingertip itself is not actuated. In this finger configuration, the fingertip can extend even when the two middle phalanges are flexed due to the force exerted by the tendon. Although the tendon is responsible for the motion of the other joints, it has a minor influence on the position of the fingertip, as its primary movement is dictated by the interaction between the fingertip and the object. This arrangement ensures that contact occurs primarily at the tip of the fingertip, promoting precision grasping operations.

2.3 THE NEW GRIPPER DESIGN

The new proposed grasping device was conceived as a three-Wave-joint-finger gripper to perform precision grasping operations. This structure provides a good compromise between simplicity and grasping ability, as three is the minimum number of fingers to correctly perform different precision grasps of objects of different shapes. In particular, the gripper was designed with two different configurations to perform spherical and cylindrical precision grasping, as shown in Fig. 4, red where the three fingers were labeled with A,B,C.

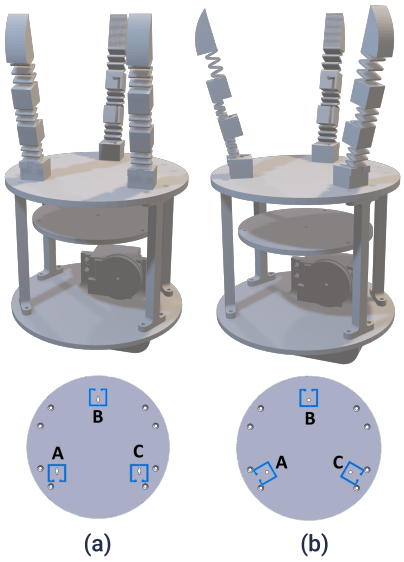


Figure 4 The new gripper configurations and fingers A,B,C: (a) cylindrical grasping; (b) spherical grasping

In the spherical grasping configuration, the fingers are evenly spaced along a circular path on the palm, as shown in Fig. 4(b). In this setup, all contact forces are directed toward the center of a sphere. In the cylindrical grasp configuration, the fingers are parallel, with two positioned opposite the third to generate forces directed toward the cylinder axis, as illustrated in Fig. 4(a). The gripper is an underactuated, tendon-driven device in which a single motor simultaneously controls all three fingers. However, a differential mechanism, based on the seesaw structure [19], allows the fingers to move independently, enabling them to continue moving even after some have made contact with the object, ensuring the compliance of grasping. The differential structure is represented in Fig. 5.

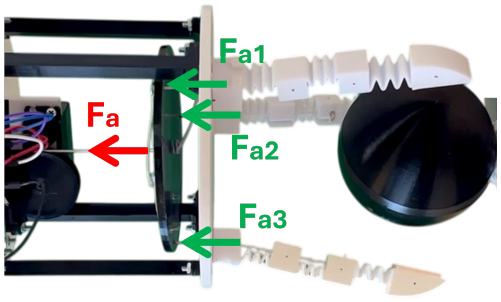


Figure 5 The differential disc structure and operation

The main components of the proposed gripper are represented in Fig. 6:

1. Base: provided with a handle and a table for the servo motor.

2. Structural supports
3. Pulley: to transmit the motion from the motor to the tendons.
4. Differential system: a disc that splits the actuation force F_a among the three tendons
5. Palm: where the fingers can be locked into proper snap seats and easily removed for replacement.
6. Wave-joint fingers actuated by tendons
7. Tendons
8. Handle
9. Servomotor: Hitec HSR-5980SG
10. Controller: Arduino UNO board.

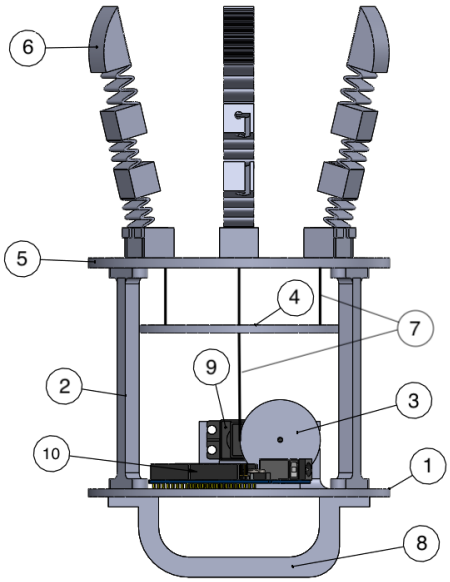


Figure 6 The new gripper design and components

All of the designed components of the gripper are prototyped in PETG (polyethylene tereph-thalate glycol) using a MEX (Material EXtrusion) 3D printer. The new gripper has a palm diameter of 150 mm, a total height of 300 mm and an overall weight of 370 g. The finger length is 130 mm and the pulley diameter is 40 mm.

The palm dimensions were selected to accommodate finger placement in both spherical and cylindrical configurations, even within the same palm if needed. In addition, the design ensures that the fingers remain sufficiently open in the resting position, allowing for an effective grasp of the chosen objects.

The total height of the gripper was chosen to ensure an adequate tendon stroke to flex all three fingers. In turn, the fingers are designed with a length that can balance precision and power grasping, allowing them to adapt to various object shapes.

3 SIMULATIONS, EXPERIMENTS AND RESULTS

3.1 PRECISION GRASPING TESTS AND RESULTS

Precision grasping tests were conducted to analyze the behavior of the robotic hand, both in the spherical and cylindrical configurations, when grasping objects of various shapes. Objects such as a cube and a sphere were grasped using the spherical configuration, and objects such as a prismatic box and a cylinder were gripped with the cylindrical configuration. The test setup, represented in Fig. 7, was arranged using an articulated arm to support the robotic gripper and some tripods were used to support different cameras to allow to record several videos from multiple perspectives for the three robotic fingers, allowing for a detailed analysis of the robotic hand's grasping behavior. Furthermore, the experimental setup was designed to ensure that the objects were grasped solely through contact with the three fingertips.



Figure 7 The test setup

The experiment aimed to evaluate the precision grasping capabilities of the new gripper using the following different objects: a plastic sphere, a dough cube, a prismatic paper box, an empty plastic bottle. Fig. 8 captures the gripper in action during the precision grasping process of the different objects. One can observe that although the fingertip and the last Wave-joint were not actively actuated, they were able to secure the objects due to the inherent stiffness. The grasping tasks were successfully completed, demonstrating satisfactory ability to perform precision grasping. Observations indicated that the fingertip's positioning during grasping was primarily influenced by its adaptation to the object's shape, a result of its stiffness, which effectively introduced an additional degree of underactuation.

During the gripping process, the object is secured by the friction generated at the contact points between the fingertips and the object. This friction could be quantified by integrating force sensors into the fingertips, as proposed in

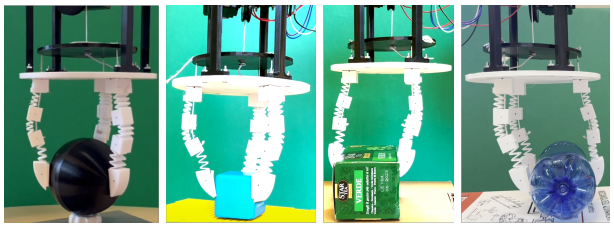


Figure 8 Precision grasping tests

[11]. Additionally, the contact is influenced by the stiffness of the terminal Wave-joint, which was evaluated in [21]. Understanding the relationship between joint stiffness and the normal force exchanged between the contacting surfaces could be beneficial during the design phase to estimate the maximum weight the gripper can support. For the tested joint, experimental results determined that the gripper, using three fingers, can support a maximum weight of 370 g.

3.2 TRAJECTORIES, STUDY OF RELEASE AND RESULTS

Motion tracking simulations were conducted to analyze the trajectories of the phalanges in all three fingers during precision grasping tests, using both spherical and cylindrical configurations. The motion tracking process involved recording three videos for each finger and grasp, followed by image analysis to extract movement data. One target for each phalanx was captured and tracked during the grasps. The resulting trajectories of the phalanges of the three fingers A,B,C for different grasps can be observed in Fig. 9 and 10.

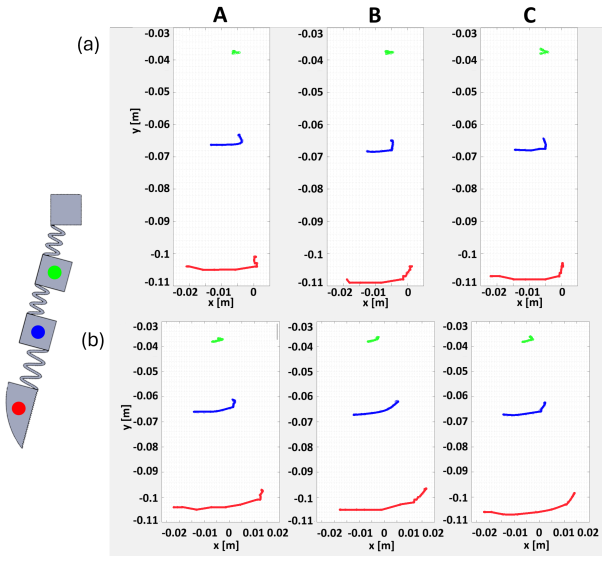


Figure 9 Trajectories of fingers A,B,C in spherical grasping: (a) sphere; (b) cube

From these figures one can observe that in the cylindrical grasp, the finger B (represented in the last column of Fig. 10), which is the mirror counterpart to the two fingers exerting

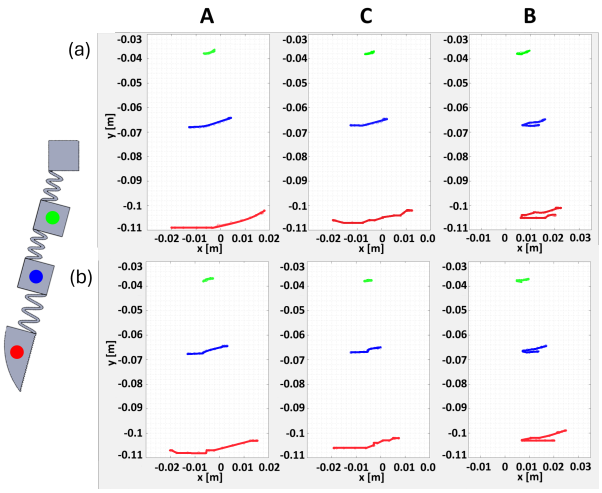


Figure 10 Trajectories of fingers A,B,C in cylindrical grasping: (a) bottle; (b) prismatic box

force in the same direction (fingers A,C), behaves entirely differently compared to the spherical grasp. Initially, when the single finger starts to move from its rest position, it follows its natural trajectory, remaining free, just like the other two fingers. However, once all three fingers come into contact with the target, the combined force exerted by the two fingers in the same direction is significantly greater than the opposing force applied by the single finger. As a result, the single finger B, overpowered by the other two, alters its trajectory, moving in the opposite direction during the second phase of its motion. This phenomenon can be attributed to the stiffness of the Wave-joint structures in the fingers. Since all three fingers have the same stiffness, they apply force with equal intensity. Consequently, when the single finger is counteracted by twice the force it exerts, its trajectory is inevitably modified, and the differential system contributes to modify the distribution of forces.

Other tests were performed in order to predict the vibrations of the fingers when the object is released; this study is useful to design a precise positioning of the fingers and to tune the joint stiffness depending on the task. For this purpose, the same motion tracking system was used as in the trajectory tests, and the dynamic parameters of the fingers were deduced from the video analysis. In particular, stiffness and damping were evaluated analyzing the videos of the oscillations and extracting the responses by tracking the target on the phalanges. The dynamic model of the finger was developed by approximating it as a vertical beam subjected to bending under a horizontal force, while also accounting for the presence of damping. Since the motion is approximately the same for all fingers, the analysis focuses on the damped oscillatory motion of just one finger, which is mounted on the palm in a spherical-grasp configuration, upon the release of the sphere. Experimental observations indicated that the system was underdamped. Therefore,

using well-established vibration dynamics equations, it was possible to identify the dynamic parameters of the system as the natural frequency ω_n=56.4 rad/s, and the damping ratio ξ=0.02. Thus, the theoretical system response was simulated considering the dynamic model of the finger, and compared to the experimental results, as reported in Fig. 11

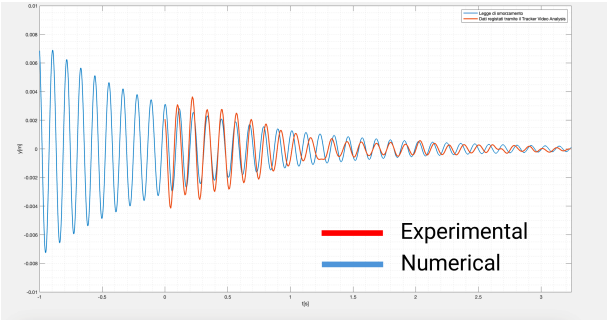


Figure 11 Comparison of experimental and numerical response.

The comparison confirms a highly accurate dynamic modeling of the finger, which in turn enables the characterization of the entire system stiffness, a parameter that is challenging to determine due to the inhomogeneity of the components produced by 3D printing.

4 CONCLUSIONS

In this paper, a new Wave-joint finger was proposed specifically for precision grasping where the last phalanx was not actuated. A new three-finger underactuated robotic gripper was designed and prototyped using the new finger conceptualization. The gripper was successfully tested and validated through precision grasping experiments, demonstrating that the maximum weight that the gripper can support with three fingers is 370 g. Precision grasping with both spherical and cylindrical configurations was satisfactory and the motion tracking allowed to trace the trajectories of the phalanges of all the fingers during the grasping of different objects. In addition, the dynamic behavior of the fingers when the object is released was determined. Future directions could lead to a correlation of joint stiffness with normal forces in the contact between the finger and an object, which would be useful to estimate the maximum weight of the object that can be supported by the gripper, during the design phase. Furthermore, the introduction of different fingertips could be explored for a softer contact, evaluating the contact conditions by using sensors on the fingertips. Additional improvements could also be oriented to reduce the gripper's overall footprint both in height and width reducing the modularity of the prototype and defining specific tasks to be accomplished by the gripper.

ACKNOWLEDGMENTS

This research was partially funded by "Fondazione CARIT 2022", grant "Progettazione e caratterizzazione sostenibile di materiali per applica-zioni industriali, agroalimentari e biomediche".

REFERENCES

[1] Imen Belhadj, Mahdi Aicha, Moncef Hammadi, and Nizar Aifaoui. Human-robot interoperability for end of life disassembly lines of mechatronic products. *International Journal of Mechanics and Control*, 25(2):3 – 8, 2024.

[2] Monica Malvezzi, Zubair Iqbal, Maria Cristina Valigi, Maria Pozzi, Domenico Prattichizzo, and Gionata Salvietti. Design of wearable robotic extra fingers for human hand augmentation. *Robotics*, 8(4), 2019.

[3] Min Wu, Yanhao He, and Steven Liu. Adaptive impedance control based on reinforcement learning in a human-robot collaboration task with human reference estimation. *International Journal of Mechanics and Control*, 21(1):21 – 31, 2020.

[4] G.M. Achilli, S. Logozzo, M.C. Valigi, G. Salvietti, D. Prattichizzo, and M. Malvezzi. Underactuated soft gripper for helping humans in harmful works. *Mechanisms and Machine Science*, 108 MMS:264 – 272, 2022.

[5] G.M. Achilli, S. Logozzo, M. Malvezzi, and M.C. Valigi. Underactuated embedded constraints gripper for grasping in toxic environments. *SN Applied Sciences*, 5(4), 2023.

[6] Stefano Rodinò, Francesco Lago, Dmitry Malyshev, and Giuseppe Carbone. Design of a movable palmfor a 3-fingers robotic hand. *International Journal of Mechanics and Control*, 24(1):177 – 188, 2023.

[7] F.J. Espinosa-Garcia, M. Arias-Montiel, E. Lugo González, R. Tapia-Herrera, and M. Ceccarelli. A review and classifiacation of robotic hands focused on palm structure. *International Journal of Mechanics and Control*, 23(1):45 – 59, 2022.

[8] F. Cordella, L. Zollo, A. Salerno, E. Guglielmelli, and B. Siciliano. Validation of a power grasping algorithm for an anthropomorphic robotic hand on the basis of human grasping action. *Latest Advances in Robot Kinematics*, page 91 – 98, 2012.

[9] Silvia Logozzo, Maria Cristina Valigi, and Monica Malvezzi. Modelling the human touch: A basic study for haptic technology. *Tribology International*, 166, 2022.

[10] Gabriele Maria Achilli, Silvia Logozzo, Monica Malvezzi, and Maria Cristina Valigi. Contact mechanics analysis of a soft robotic fingerpad. *Frontiers in Mechanical Engineering*, 8, 2022.

[11] Gabriele Maria Achilli, Virginia Burini, Silvia Logozzo, and Maria Cristina Valigi. Contact force recognition in robotic fingertips' interface. *Mechanisms and Machine Science*, 160 MMS:247 – 256, 2024.

[12] Liang Gong, Wenjie Wang, Tao Wang, and Chengliang Liu. Robotic harvesting of the occluded fruits with a precise shape and position reconstruction approach. *Journal of Field Robotics*, 39(1):69 – 84, 2022.

[13] Digby Chappell, Fernando Bello, Petar Kormushev, and Nicolas Rojas. The hydra hand: A mode-switching underactuated gripper with precision and power grasping modes. *IEEE Robotics and Automation Letters*, 8(11):7599 – 7606, 2023.

[14] Charalampos Valsamos, Nikolaos Stravopodis, and Vassilis C. Moulianitis. Mechatronic design and construction of a novel 1 dof link for the structuring of serial self-metamorphic manipulators. *International Journal of Mechanics and Control*, 22(2):181 – 193, 2021.

[15] Daniela Maffiodo and Terenziano Raparelli. Flexible fingers based on shape memory alloy actuated modules. *Machines*, 7(2), 2019.

[16] Daniela Maffiodo and Terenziano Raparelli. Comparison among different modular sma actuated flexible fingers. *Mechanisms and Machine Science*, 68:324 – 331, 2019.

[17] Massimiliano Mastrangelo and Vito Cacucciolo. High-force soft grippers with electroadhesion on curved objects. *2022 IEEE 5th International Conference on Soft Robotics, RoboSoft 2022*, page 384 – 389, 2022.

[18] Gabriele Maria Achilli, Silvia Logozzo, Maria Cristina Valigi, and Monica Malvezzi. Preliminary study on multibody modeling and simulation of an underactuated gripper with differential transmission. *Proceedings of the ASME Design Engineering Technical Conference*, 9, 2021.

[19] Gabriele Maria Achilli, Silvia Logozzo, and Maria Cristina Valigi. An educational test rig for kinesthetic learning of mechanisms for underactuated robotic hands. *Robotics*, 11(5), 2022.

[20] Mihai Dragusanu, Gabriele Maria Achilli, Maria Cristina Valigi, Domenico Prattichizzo, Monica Malvezzi, and Gionata Salvietti. The wavejoints: A novel methodology to design soft-rigid grippers made by monolithic 3d printed fingers with adjustable joint stiffness. *Proceedings - IEEE International Conference on Robotics and Automation*, page 6173 – 6179, 2022.

[21] Gabriele Maria Achilli, Silvia Logozzo, Maria Cristina Valigi, Mihai Dragusanu, and Monica Malvezzi. Theoretical and experimental characterization of a new robotic gripper's joint. *Mechanisms and Machine Science*, 122 MMS:738 – 745, 2022.

ISSN 1590-8844
International Journal of Mechanics and Control, Vol. 26, No. 01, 2025
https://doi.org/10.69076/jomac.2025.0009

AN INNOVATIVE PROTOTYPE OF AN AUTOMATIC DEVICE FOR MOVING FINGERS AND WRIST DURING fMRI ANALYSIS

Gabriella Eula*

* Department of Mechanical and Aerospace Engineering, Politecnico di Torino, Torino, Italy

ABSTRACT

The paper presents an innovative active device capable of moving the fingers and the wrist of the human hand during fMRI (functional Magnetic Resonance Imaging). The prototype can be used both for motor learning studies and for stroke analysis. Various possible configurations were investigated. The first was an active glove. The second was a box in which the subject's hand is inserted, and then moved by pneumatic actuators. The authors optimized this configuration, and also developed an interesting design procedure using data from the literature, experimental measurements, numerical simulations, and experimental videos. This configuration moves the wrist in addition to the fingers, a feature which is innovative, useful and commonly found in devices of this kind.

Keywords: automatic devices for fMRI analysis; automatic machine to move hand during fMRI analysis; automatic system moving fingers during fMRI analysis

1 INTRODUCTION

fMRI (functional Magnetic Resonance Imaging) is a biomedical technique that provides information on the brain activities involved in a particular cognitive process or motor action by exploiting the effect of an external magnetic field. To avoid altering the quality of the brain image and harming the patient, it is essential that only non-magnetic materials be present in the MRI chamber. Selecting an appropriate actuation system type and materials is thus crucial. This imaging technique is employed to evaluate how the brain metabolism reacts after performing an action such as speaking, moving a limb, reading or thinking. The first scientists who studied this technique [1,2] understood the importance of evaluating blood oxygenation level in order to capture brain images. In general, when a human being performs a certain action, a part of the blood flow circulates within a certain brain area: in particular, for each action that a human performs, a different area of the brain is activated.

Contact author: Gabriella Eula[1]

[1]Corso Duca Degli Abruzzi 24, Torino, TO, 100129, Italy
E-mail: gabriella.eula@polito.it

This area is supplied with blood so that the action can be transported to the rest of the body via muscles and nerves. When blood flow increases, the level of oxygen present in it also increases proportionally: this variation is recorded by magnetic resonance imaging thanks to the change in magnetism of the hemoglobin present in the blood. The use of technology in rehabilitation is a therapeutic opportunity for patients who have suffered a serious accident or people born with particular disabilities. Over the last 15 years, the use of rehabilitation technology has become much more common, while the quality of the devices employed has also increased considerably. A number of studies have addressed finger movements and mechanisms acting on the fingers [3,4]. Many devices used to move the fingers during fMRI imaging feature a glove structure using various kinds of actuation [5-13], based in particular on inflatable silicone pneumatic actuators [10,13]. Some devices also provide wrist movement [8,14,15]. In some systems, the fingers are actuated by external silicon pneumatic actuators [10] on the upper side of each finger and secured in a textile structure.
Other devices use a mechanism on the upper side of each finger to guide the finger movement from this point [16, 17], or employ cable drives [8,11,12]. Some systems were also designed to measure finger grasping force [15,18-20], to provide a better understanding of hand movements [21-27] or to be used both for rehabilitation purposes and for fMRI analysis [5-7, 22, 28-43]. Actuation is often pneumatic, as in the cases where inflatable actuators are

used [10,13]. In an application designed for use in the patient's home without supervision by a physiotherapist [35], the hand is inserted in a box where physiological finger positions are replicated and forces can be imposed to perform rehabilitation exercises for flexion and extension movements of the metacarpophalangeal joint (MP joint) and the proximal interphalangeal joint (PIP joint) of the index, middle, ring and little fingers. However, they are not specific applications for fMRI analysis. In a study conducted on primates [27] in which fingers were immobilized using a soft cast, a restriction "of the cortical areas corresponding to the distal part of the upper limb and an expansion of the most proximal areas of the arm that maintain active contact with the environment" was observed. This study found that when the fingers were immobilized their function decreased, but wrist and forearm function increased. These effects were reversed when the soft casts immobilizing the fingers were removed. The glove prototype presented in [5] was worn by a healthy human subject lying supine on the fMRI analysis table. During this test, the MRC-Glove was activated five times in 30-second blocks. During fMRI analysis carried out while moving the fingers of the human hand, a possible cycle time can be 3s for finger flexion and 3s for finger extension. This procedure is performed for a continuous period of 30s followed by a 21s rest [6]. This study was carried out at a supply pressure of 2 bar, analyzing the movements of all fingers except the thumb. Wrist movements were not analyzed. The pneumatic actuators whereby finger joints can be bent were operated non-simultaneously. In previous work, the present authors designed and constructed a prototype to move a subject's foot or feet during fMRI analysis [43,44]. The results obtained were good and demonstrated the prototype's reliability.

This article presents a study useful for the design of an innovative active device able to work in a magnetic resonance chamber during fMRI analysis, moving the subject's finger/fingers or his wrist according to physiological and non-physiological trajectories, so that the brain areas activated during this movement can be studied. The information thus obtained can be used to identify possible ways of recovering hand motor functions in patients with brain injuries so that they can engage in daily activities that would otherwise be impossible. The wrist motion for these analyses, both on healthy people and on patients, has been considered by our clinicians useful for the purposes of the analysis itself and constitutes an originality of the machine compared to the most frequent layouts of them. The non-glove structure of the machine was also judged to be more versatile. It also allows not only the imposition of certain trajectories to the fingers, but also to impose non-physiological trajectories, useful for motor learning studies.This machine can be useful in general: for motor learning studies; for rehabilitation training settings especially related to brain recovery; for fMRI analysis useful for preliminary evaluations for neurological surgical interventions.

2 PRESENTATION OF THE PROTOTYPE

The device must be designed to ensure that, during tests in the magnetic resonance chamber, the hand performs passive movements, i.e., thanks to the application of an external force, without actively contracting the muscles. Specifically, the subject's left hand must perform the following movements: complete flexion and extension of each finger individually while keeping the remaining fingers extended; complete and simultaneous flexion and extension of the index, middle, ring and little fingers; complete flexion and extension of the wrist. The term flexion refers to that movement of the body that decreases the angle between the structures or joints involved, bringing them further together. Extension is the opposite movement, in which the angle increases and the structures or joints move away from each other. Flexion of the fingers thus consists of bending the phalanges towards the palm of the hand, while extension consists of straightening the fingers.

Wrist flexion occurs when the wrist is bent towards the palm of the hand, while wrist extension occurs when the wrist is bent upwards. Given the particular nature of the application environment, selecting appropriate materials is of fundamental importance to guarantee correct device operation and patient safety, as no ferromagnetic materials can be introduced in the magnetic resonance (MR) chamber. The first stage of this study consisted of designing gloves where the fingers and the wrist were moved using silicon pneumatic actuators constructed in the laboratory.

Details of the first glove protype with silicon pneumatic actuators located atop each finger are shown in Figure 1.

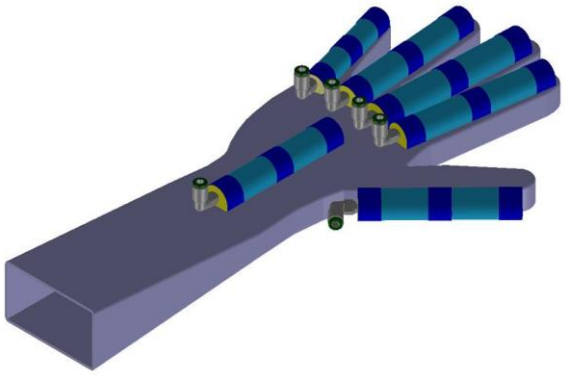


Figure 1 First prototype of an active glove controlled by means of silicon pneumatic actuators.

With this design, the correct physiological trajectory of the fingers cannot be readily controlled and monitored because of the deformability of the textile structure. In addition, the stiffness and the deformation of each silicon actuator make it difficult to determine whether or not the finger is moved through the natural physiological trajectory. However, this information is important in enabling the clinicians who move the fingers during fMRI analysis to understand brain function. Consequently, the design shown in Figure 2a was developed. In this case, the person places their hand in a box and the fingers are moved using standard external

ISSN 1590-8844
International Journal of Mechanics and Control, Vol. 26, No. 01, 2025
https://doi.org/10.69076/jomac.2025.0009

linear pneumatic cylinders. In this configuration, however, interference can occur between the moving cylinder and the finger, as shown in Figures 2b and c. Moreover, the finger's trajectory can differ from the physiological path and is difficult to check. In addition, this design features an actuator for each finger, thus increasing the number of components, costs, control system complexity, weight, and device bulk. Lastly, the authors developed the design illustrated in Figures 3a and 3b, which is the prototype presented here. This prototype can also move the wrist, as established in the beginning of this study. This can be useful for further studies of brain function. The prototype features a single linear actuator for all fingers, a pneumatic motor for the thumb, and a linear actuator for the wrist.
The design of this final prototype started from the analysis of each finger's movement during passive exercises performed with the assistance of a physiotherapist, a situation in which finger trajectories are well controlled.



Figure 2a The first prototype with a box geometry, showing the hand inside.

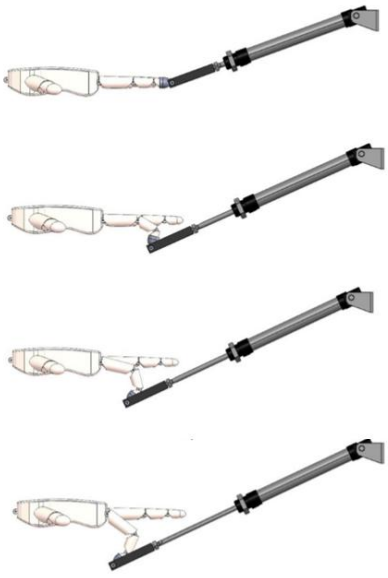


Figure 2b Finger movement in the first box prototype.

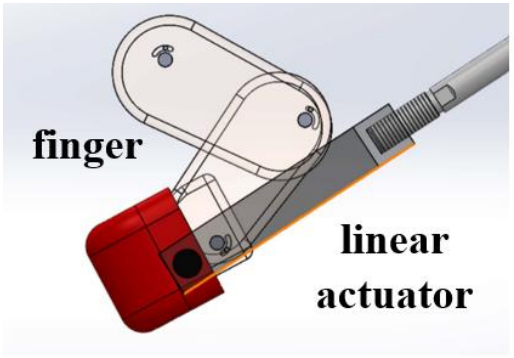


Figure 2c A detail of possible interference between the pneumatic cylinder and the finger.

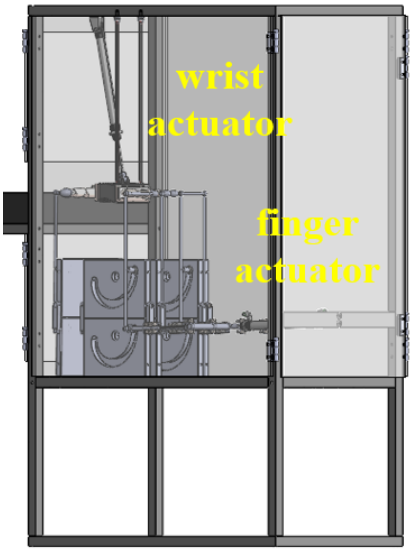


Figure 3a The final prototype structure.

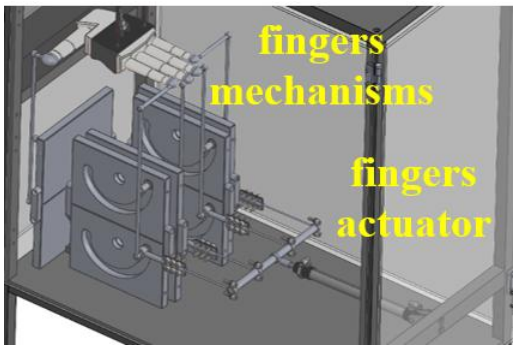


Figure 3b Detail of the single linear pneumatic actuator for all fingers.

The automatic machine must be capable of reproducing these trajectories, which are important for brain activation study during fMRI analysis. Various kinds of brain activation during finger movement can be investigated by using physiological and non-physiological fingers and wrist trajectories. This final layout connects each finger to a vertical link (Figures 4a) which is in turn connected to a non-driven pin moving in a crescent-shaped slot and mounted on a telescopic shaft (Figure 4b). The slot can reproduce a physiological trajectory or a non-physiological

trajectory in order to move the finger along a known path and investigate the resulting brain activation. The prototype foresees to use the compressed air as kind of actuation, as it is compatible with the RM chamber, safe, clean and easy to use in hospitals too. In particular this machine allows to move all fingers together or one or more than one, with the patient in a passive state. The Figure 4a shows the mechanisms for all the fingers and also for the thumb.
The Figure 4b shows some details of the system designed to move the subject's fingers. A non-driven pin is inserted in the slot and connected to a telescopic shaft rotating along a horizontal axis and each finger is connected to a link put between the finger and the non-driven pin. The subject's fingertips are inserted in thimbles on each link. Activating the telescopic shaft rotation, it is possible to move the link, and so the finger to it connected, and to obtain the required finger movement for the brain functioning study. Trajectories can be obtained experimentally by analyzing videos, and numerically from measurements of each finger's phalanges, as then here explained. They can be then compared with other trajectories from the applicable literature. They allow to design properly the slot. So this design is capable of moving each finger (or all fingers together) along known, accurate trajectories established by the clinicians and the trajectories may be physiological or non-physiological. In Figure 4c the movement C (then described in detail) is shown, as an example of movement to design the slot. Analysing the physiological trajectory of each finger in a healthy subject, the slot shown in Figure 4b can be designed.

2.1 FINGER MOVEMENT

The physiological Range of Movement (ROM) for the finger phalanges and wrist are: proximal phalanx 0°-90°; middle phalanx 0°-110°; distal phalanx 0°-90°; wrist 0°-85° [25,27]. Following the literature [39], finger trajectories are analyzed in plane [x,y], where x is directed along the finger and y is perpendicular to x, as shown in Figure 5.

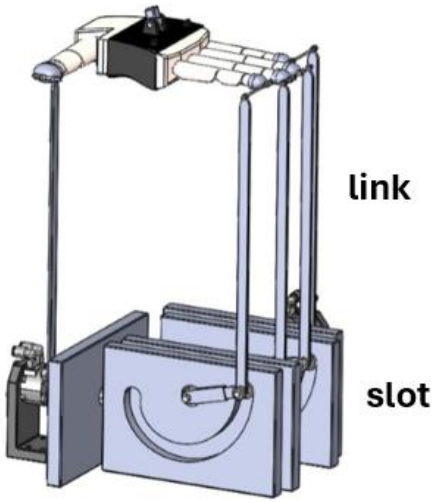


Figure 4a The mechanisms designed to move all the fingers and the thumb.

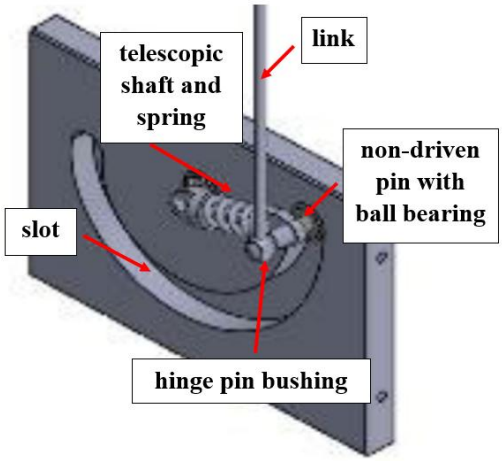


Figure 4b A detail of the slot and of the part of mechanism used to guide the finger.

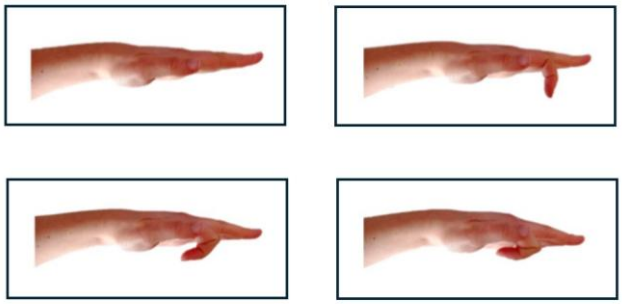


Figure 4c The movement (here C) imposed on the fingers.

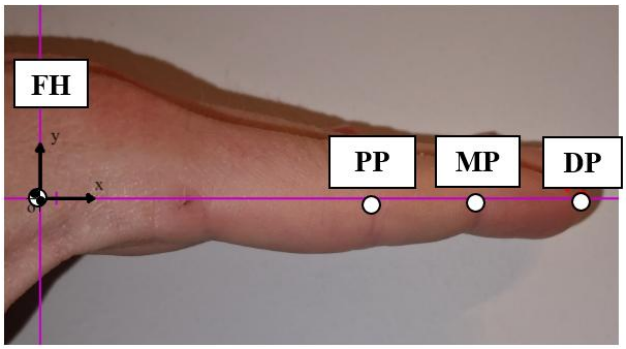


Figure 5 The reference system adopted for the index finger.

Figure 5 shows the phalanges and the reference system adopted for this study. FH is the base of the proximal phalanx, here considered fixed, PP is the head of the proximal phalanx, MP is the base of the middle phalanx, and DP is the head of the distal phalanx. In particular, three possible movements designated as A, B, C were investigated. Figure 6a shows the angles used for the phalanges trajectories [21], while Figures 6b, c, d illustrate the angles α, β, γ in each movement (A, B, C) considered and then used to model the finger movement in a calculation software. The angles α, β, γ are the main angles used to model finger movement with calculation software program. In movement A, only the distal and middle phalanges of the index finger are moved, and the proximal phalanx is kept stationary.

ISSN 1590-8844
International Journal of Mechanics and Control, Vol. 26, No. 01, 2025
https://doi.org/10.69076/jomac.2025.0009

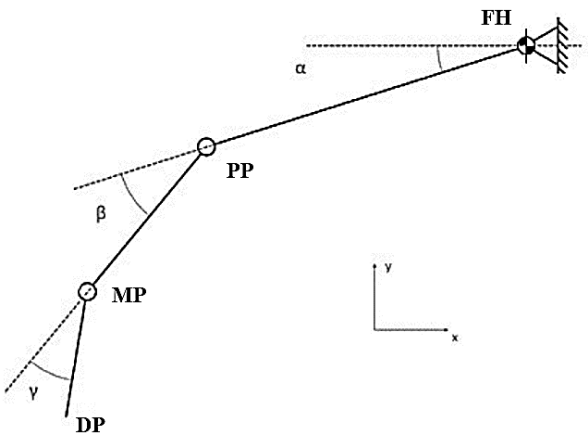


Figure 6a The angles involed in the study of the phalanges trajetories.

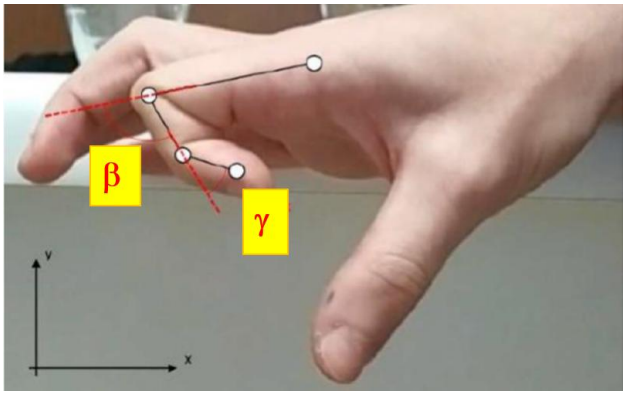


Figure 6b Details of movement A.

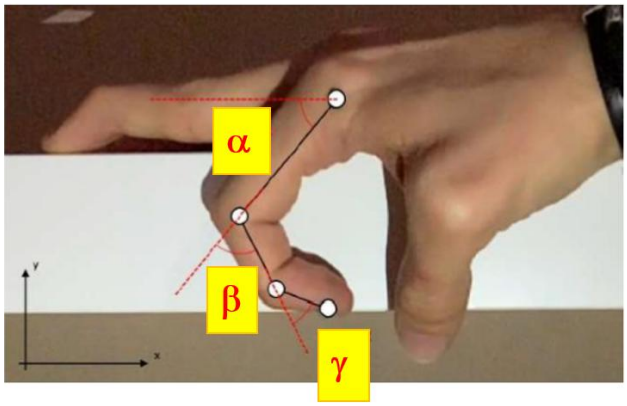


Figure 6c Details of movement B.

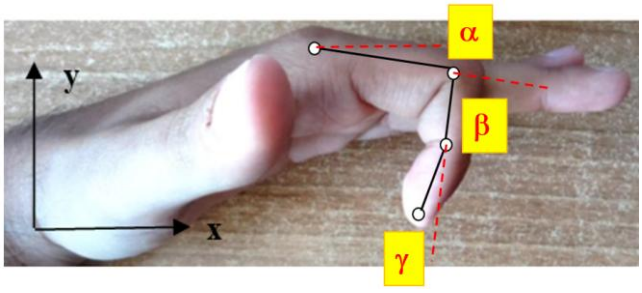


Figure 6d Details of movement C.

In movement B, all phalanges of the index finger are moved, while all other fingers are stationary, extended and resting on a rigid fixed support. In movement C, all the phalanges of the index finger are moved, while the other fingers are extended but not supported. As movement C yields the most physiological trajetories, it was selected for the subsequent studies and design stages.

2.2 WRIST MOVEMENT

In agreement with several clinicians, the authors decided to move the subject's wrist with this device. This can also be useful for fMRI analysis. Figure 7a shows the movement to be imposed on the subject's hand. Figure 7b shows the linear pneumatic actuator connected to the subject's hand in order to move it as shown in Figure 7a.

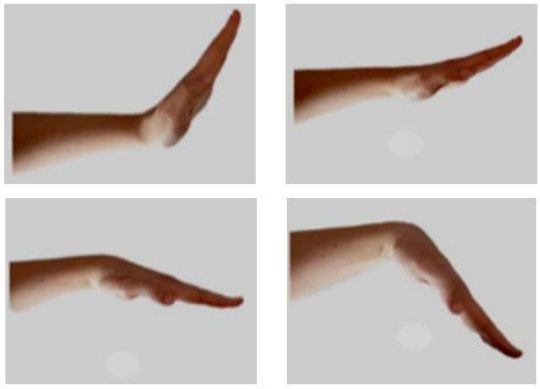


Figure 7a Details of the movement imposed on the wrist.

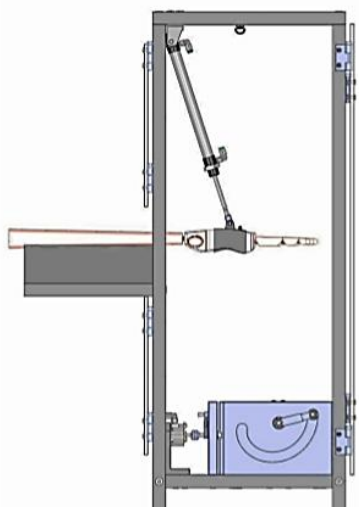


Figure 7b The linear pneumatic actuator to move the wrist.

3 STUDY FLOWCHART

The steps of the design process presented here realised are illustrated in Figure 8. The process involves: producing videos of finger movements, which are then analyzed using specific software to establish the experimental finger trajectories; reviewing the trajectories presented in the literature; carrying out experimental measurements on multiple subjects, determining the length of each phalanx of each finger and then calculating the finger trajectories for

the average male hand and the average female hand; comparing the trajectories presented in the literature (with similar subjects), the trajectories calculated from phalange measurements, and the trajectories from the experimental videos; transferring this information to CAD software in order to construct slots for the average male and average female hands.

4 FINGER MEASUREMENTS USED FOR SLOT DESIGN

The most important parts of this device are the slots that establish the movement of the fingers. Multiple measurements were taken of both hands of several subjects and using different kinds of caliper, in order to design slots for average male and female subjects. The number of subjects examined can already be considered useful for the design analyses for which it is intended.

In this paper the tests carried out analysing the index finger were illustrated, but the method can be applied also to the other fingers. Furthermore, for brevity sake, only some of the all measurements carried out on men and women are here presented, illustrating only male subjects. In all the tables presented, SD means Standard Deviation. The data collected by operator 1 for the right hands of 10 healthy right-handed subjects are shown in Table 1. Measurements were made with a digital caliper with the hand extended on a flat surface. Table II shows the data collected by operator 2 on 20 subjects. Measurements were made using standard caliper on the left hand extended on a flat surface. Table III shows data referring to movement C collected on two subjects by operator 3 using a standard caliper with the right hand on a flat surface. Figure 9 shows the index finger trajectory calculated by operator 2 for the left hand of a 23 year old male subject, body mass 60 kg, height 1.77 m, proximal phalanx 45 mm, medium phalanx 27 mm, distal phalanx 15 mm (also illustrated in Table I), using the reference system illustrated in Figure 5, with the same finger initial position. Measurements were taken by several different operators. For the sake of brevity, Tables I, II and III show only some of the measurements. The different operators' measurements can be readily compared by looking at the index finger dimensions: operator 1, right hand, subject height 1.78 m, digital caliper, index finger length 96.9 mm; operator 2 left hand, subject height 1.78 mm, standard caliper, index finger length 82.7 mm; operator 3, right hand, subject height 1.78 m, standard caliper, index finger length 84.5 mm; operator 1, left hand, subject height 1.82 m, digital caliper, index finger length 93.1 mm. The differences in these measurements stem from the use of both digital and standard calipers: the digital caliper gives better measurement results. In addition, the experimental results obtained from these measurements were analyzed by means of different techniques proposed in the literature: statistical parameters (average value, standard deviation); correlation between hand dimensions and subject height [45-50] considering the proportionality of these values and using different methods (Pearson linear correlation coefficient [51] with the Anderson-Darling test [52] and the Shapiro-Wilk test [53]); linear regression with the t-Student test [54]; the ratio between the length of the phalanges (average differences) [55,56]).

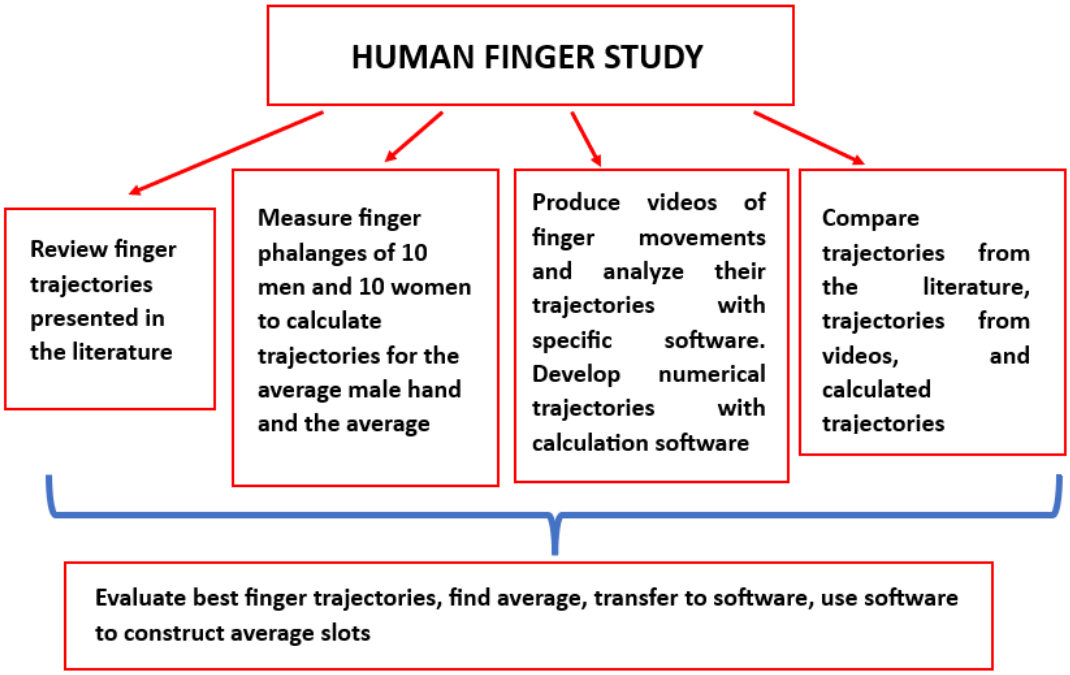


Figure 8 Steps of the slot design process.

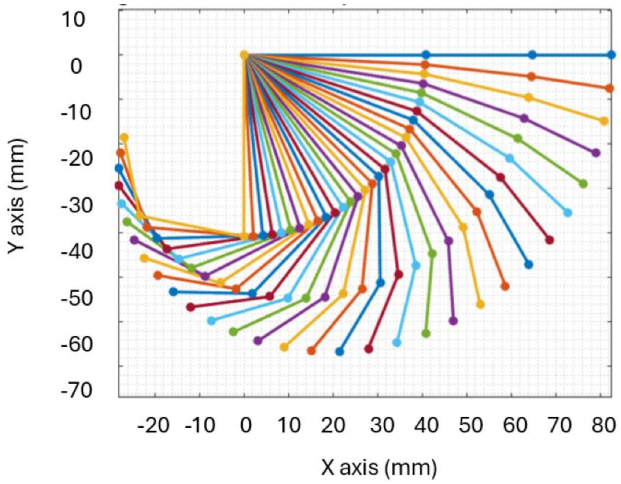


Figure 9 Preliminary example of a calculated trajectory of the index finger phalanges.

It should be noted that there are non-negligible differences of up to 11% between some of these calculations. These differences may be due to various factors. First, the study does not distinguish between sex and gender: values are calculated for both sexes and some studies cited earlier [48] highlight a difference in length relationships. Furthermore, an error may arise from the fact that the measurements were taken from the back of the finger in the joint halfway up the height of the finger (the free end), thus with a certain angle that increases the dimension. To obtain additional information, Student's t-test [54] was carried out (after passing the appropriate controls) on the values of ratios other than 1 (with $\alpha = 0.05$); p-values were 0.88 for the female gender and 0.77 for the male gender. The p-value is the probability that the results from the sample data occurred by chance; α is the threshold of statistical significance established by the operator, and represents the probability of type I error. On the basis of these considerations, average male hand and female hand dimensions were calculated and used to design the corresponding slots. By way of example, Table IV shows the characteristics of average male and female right hands from operator 1 measurements. The average fingers were obtained using operator 1 measurements as he used the digital caliper. In particular, phalange measurements were used to construct the index finger trajectory in the [x, y] plane using calculation software, to analyze the index finger trajectory obtained from experimental videos, and to construct the index finger geometry in a specific software program. All these results were then compared with each other and with similar trajectories obtained from the literature. Figure 10 shows experimental and numerical trajectories obtained by the authors with the subjects indicated in Table I from which average valves were calculated. Here h is the height of the subject. The trajectory shown in black in Figure 10 is from the literature [39,49] and it is the index finger trajectory with proximal phalanx 43 mm, medial phalanx 28 mm, distal phalanx 25 mm. The results obtained are good and demonstrate the study's reliability. The authors will carry out further experimental analyses using specific software to analyze finger movements and determine the corresponding trajectory. This is also important in developing a method for analyzing these movements precisely and to carry out accurately all these studies.

5 FINGER TRAJECTORIES

The procedures described above can be employed to design a slot for use by average adult male and female subjects. The slots are machined in interchangeable plates that can be installed on the device to reproduce different physiological and non-physiological trajectories. For the clinicians it is important to know the real trajectory imposed in order to analyse it together with the corresponding brain activation. The position of the links can be maintained exactly vertical or not, on the basis of the required finger movement.

Table I - Subjects examined by operator 1: right index finger

Subject	Age	Body mass (kg)	Height (m)	Proximal phalanx (mm)	Middle phalanx (mm)	Distal phalanx (mm)	Total length (mm)
M1	30	82.7	180.0	45.41	24.70	20.22	90.3
M2	26	64.0	174.7	44.75	24.29	24.09	93.1
M3	27	72.1	191.5	48.53	30.55	26.65	107
M4	26	79.1	177.5	49.74	28.82	23.03	101.6
M5	26	60.5	172.5	39.33	23.24	21.44	84.0
M6	25	67.0	174.2	39.51	24.59	24.02	88.1
M7	33	65.4	174.9	51.44	27.50	24.53	103.5
M8	30	79.1	183.5	55.36	27.94	25.19	108.5
M9	30	69.7	177.6	45.74	28,.79	24.64	99.2
M10	30	59.2	179.9	47.41	23.67	23.64	94.7
SD				4.98	2.59	1.84	8.1
Averages	28.3	69.88	178.63	46.72	26.41	23.75	96.9

Table II - Subjects examined by operator 2: right index finger

Subject	Age	Body Mass (kg)	Height (m)	Proximal phalanx (mm)	Middle phalanx (mm)	Distal phalanx (mm)	Total length (mm)
M1	23	69	181.5	43	23	16	82
M2	28	67	169.0	39	23	17	79
M3	32	82	189.0	44	26	19	89
M4	41	73	171.0	40	24	18	82
M5	59	100	182.0	39	26	19	84
M6	29	60	167.0	36	20	20	76
M7	23	87	185.0	41	23	21	85
M8	26	71	175.0	38	23	21	82
M9	26	69	178.0	38	25	18	81
M10	31	96	188.0	44	24	17	85
M11	27	74	172.0	41	21	19	81
M12	54	76	179.0	44	27	17	88
M13	33	80	180.0	42	21	18	81
M14	61	91	177.0	42	24	18	84
M15	39	85	185.0	40	27	18	85
M16	25	59	161.0	39	21	16	.6
M17	24	86	182.0	41	26	17	84
M18	24	85	189.0	41	24	19	84
M19	23	60	177.0	45	27	15	87
M20	27	76	181.0	40	24	15	79
SD				2.37	2.14	1.71	3.5
Averages	32.75	77.30	178.43	40.85	23.95	17.9	82.7

Table III - Subjects examined by operator 3: right index finger

Subject	Age	Body Mass (kg)	Height (cm)	Proximal phalanx (mm)	Middle phalanx (mm)	Distal phalanx (mm)	Total length (cm)
M1	23	69	182	43	23	16	82
M2	23	60	177	45	27	15	87
SD				1.42	2.83	0.71	3.5
Averages	23	64.5	179.5	44.0	25.0	15.5	84.5

Table IV - Average male and female right hands from operator 1 measurements

Subject	Average phalanges (dimensions in mm)													
	Thumb		Index			Middle			Ring			Pinkie		
	FP	FD	FP	FM	FD	FP	FM	FD	FP	FM	FD	FP	FM	FD
Average male	43.56	34.01	53.01	33.59	26.20	58.33	40.31	27.80	54.50	38.34	27.30	43.76	29.00	24.60
Average female	39.56	29.32	49.14	30.75	22.50	53.24	36.01	24.50	49.40	33.83	24.40	41.32	24.70	21.90
SD male	4.34	2.35	3.57	2.47	2.19	3.25	3.07	1.96	2.42	3.17	1.92	2.84	2.49	1.90
SD female	2.29	3.04	3.67	1.98	1.25	4.29	2,30	1.62	3.59	2.28	1.69	2.31	1.99	1.66

ISSN 1590-8844
International Journal of Mechanics and Control, Vol. 26, No. 01, 2025
https://doi.org/10.69076/jomac.2025.0009

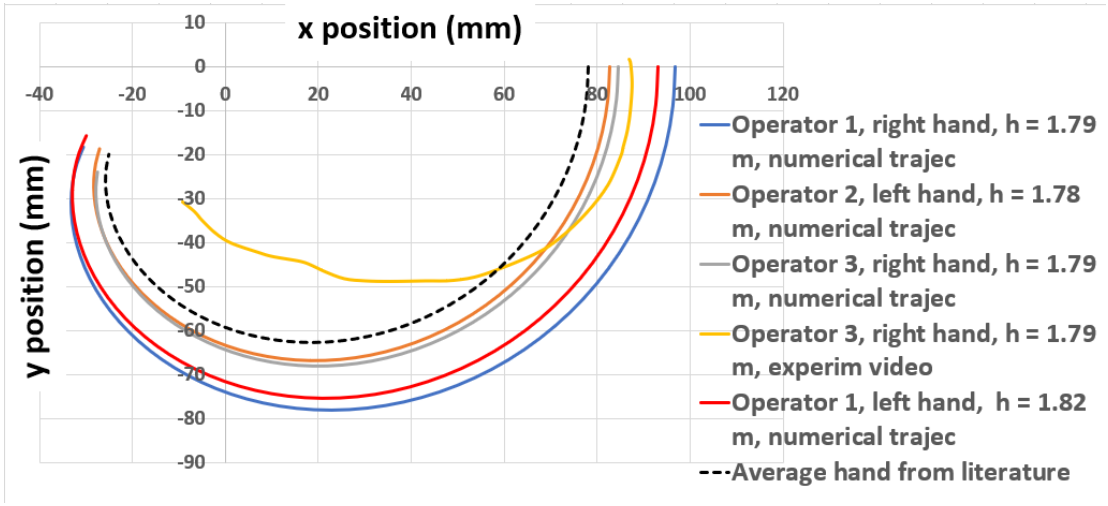


Figure 10 Index finger trajectories obtained in various conditions.

5.1 PHYSIOLOGICAL TRAJECTORIES

Many fMRI analyses, including those carried out for motor learning purposes, are performed while moving fingers along physiological paths. It is thus important to study and obtain these trajectories by means of a procedure such as that proposed above. Figure 11a shows the mechanism used to move the index finger along a physiological trajectory for an average male subject. The possibility of inclination of the link is very low, as the mechanism follows the finger trajectory in its same physiological cycle time and the condition of the subject has to be passive. A non verticality of the link means that the subject is not completely passive and this can be an important warning for the clinicians during the fMRI analysis. Anyway this possible inclination can be avoided as follows. The Figure 11b shows the mechanism where two identical slots are used together in order to maintain the link in a vertical position, if necessary. The non-circularity and the complexity of the slot shape favours the effect of this second slot also using a simple circular pin, fixed on the link. In this case it is important the choice of the materials in contact, in order to reduce the friction. The Figure 11c shows another solution where the possible inclination of the link is avoided using a cart type constraint, that also improves the sliding condition. However, the doctors' needs can be adequately met using the initial configuration with a single slot. Links can be connected to all fingers or to a single finger, thus moving all fingers simultaneously or one finger at a time. A reduction of the link length, compatible with the wrist movement, can also improve this aspect. This length reduction can be foreseen since the wrist movement can not be imposed together with the fingers motion. So the machine design can provide a horizontal flat bed to pull down the actuator and the fingers mechanisms when the wrist movement is activated. On the other hand, all these fingers mechanisms can be lifted up and positioned at an adequate distance for their motion, as shown in Figure 12.

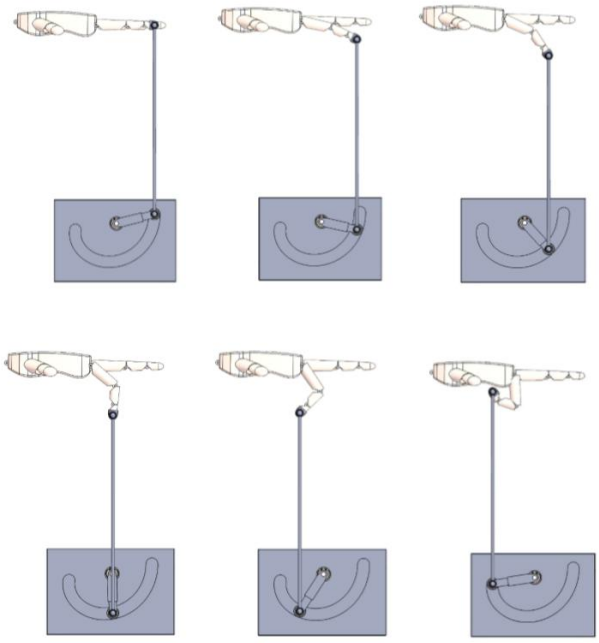


Figure 11a Finger movement along a physiological trajectory.

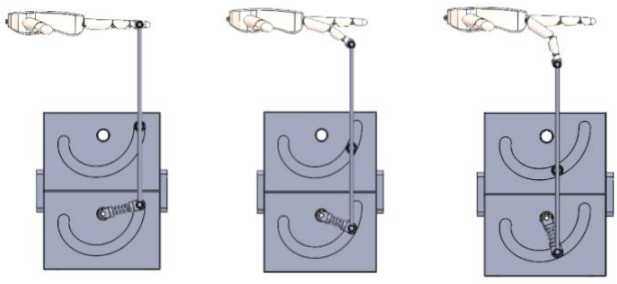


Figure11b Finger movement along a physiological trajectory (link maintained in the vertical position by using a second slot).

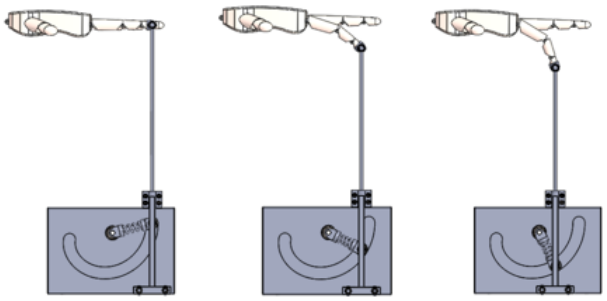


Figure11c Finger movement along a physiological trajectory (link maintained in the vertical position by using a cart type constraint).

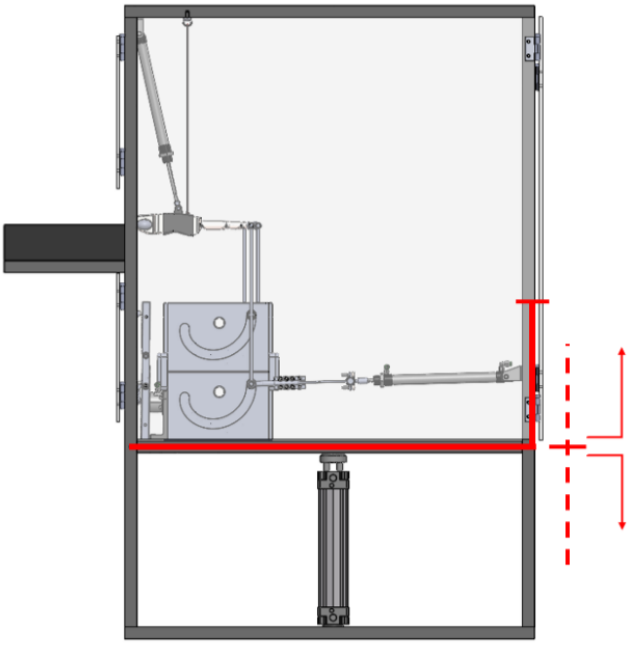


Figure 12 The possible system to move up and down vertically the platform with all the fingers mechanisms and actuators.

5.2 NON-PHYSIOLOGICAL TRAJECTORIES

The device's structure also makes it possible to move fingers and wrist along non-physiological paths. To this end, the trajectories are investigated experimentally and numerically in order to construct the corresponding slots. For clinicians, it is important to know the exact trajectory imposed by the device in order to analyse it together with the associated brain activation.

Depending on the type of movement required, links can be maintained in the vertical position or allowed to depart from it as the fingers are moved. Slots reproducing non-physiological trajectories can be designed after analyzing such movements experimentally and numerically. This can be useful for studies of brain function in healthy subjects and patients. Figure 13a shows the non-physiological movement considered here. The corresponding slot is shown in Figure 13b.

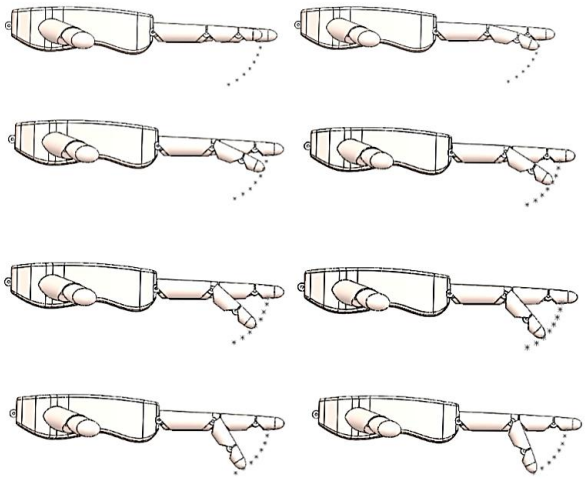


Figure 13a An example of a non-physiological finger trajectory.

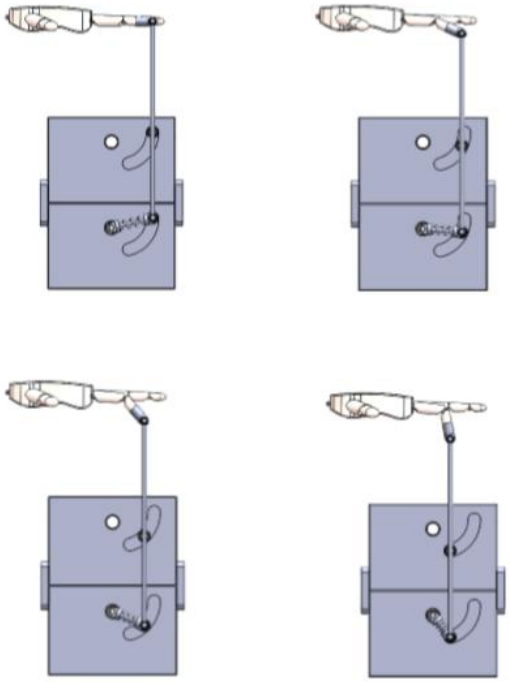


Figure 13b Non-physiological trajectory by clinicians.

6 SOME SOLUTIONS FOR FINGER MOVEMENT

Different kinds of drive or actuation can be used to move the telescopic shaft and hence the finger.

6.1 FIRST SOLUTION: BELT DRIVE

A belt drive can be connected to two fingers at the same time if necessary, as shown in Figure 14, where (1) are the pulleys and (2) are the belts. The same transmission structure is then used to move all the fingers. The pulleys are driven by pneumatic motors. Drawbacks of this configuration include its bulk, its large number of parts and motors, and the need to ensure correct belt tension at all times.

ISSN 1590-8844
International Journal of Mechanics and Control, Vol. 26, No. 01, 2025
https://doi.org/10.69076/jomac.2025.0009

6.2 SECOND SOLUTION: SINGLE PNEUMATIC ACTUATOR

In this configuration, a linear pneumatic actuator can be connected to one or all fingers. The mechanism is illustrated in Figure 15: the linear actuator, slots and vertical link are shown on the left, while the new geometry of the telescopic shaft is shown on the right. Here a spring is added to guarantee that the non-guided pin and the slot are in contact at all times. Further details of the single linear pneumatic actuator are shown in Figure 3b. The single linear pneumatic actuator is mounted facing the fingers to move one or all fingers together. A telescopic shaft drives the neutral pin along the slot. This configuration is an improvement over the belt drive, as it is smaller, lighter, and features simpler construction with fewer components.

6.3 THUMB MOVEMENT USING A PNEUMATIC MOTOR

The thumb is moved in the frontal plane (Figure 16) rather than the sagittal plane. Movement is imposed by a pneumatic motor connected directly to the telescopic shaft.

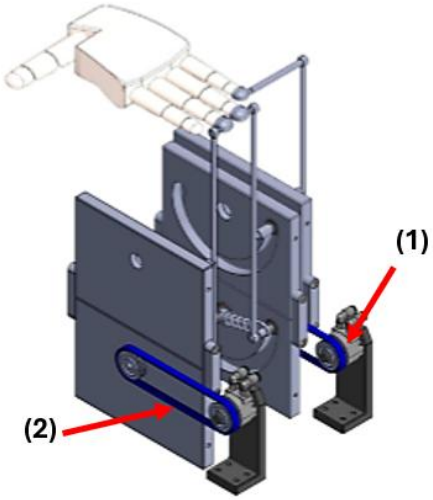


Figure 14 Finger mechanisms with belt drives.

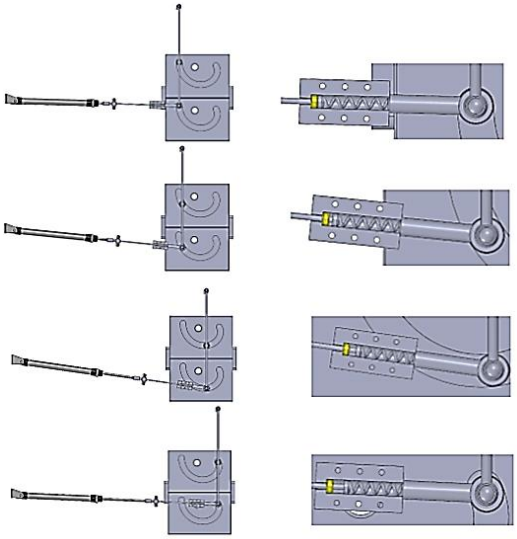


Figure 15 Fingers moved by a single pneumatic actuator.

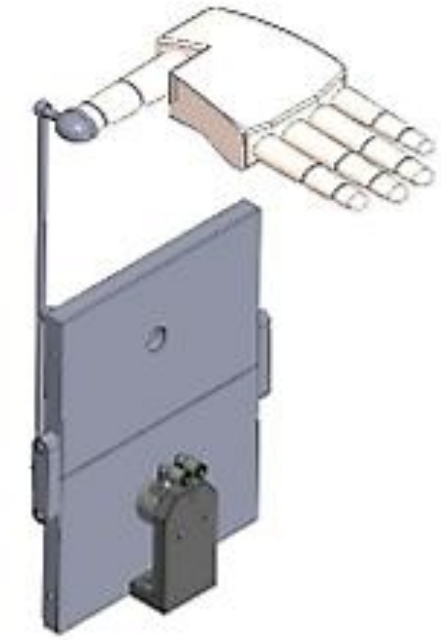


Figure 16 Pneumatic thumb motor.

7 OPERATION MODELING AND SIMULATION

Several models were constructed on a specific software platform to investigate finger movement mechanism kinematics. Simulations were carried out with various prototype geometries. In particular, the configuration where the fingers are actuated by a single linear pneumatic cylinder was analyzed. The study was carried out by operator 4. Figure 17a shows the left index finger geometry and its physiological trajectory (24 year old male subject, body mass 75 kg, height 1.85 m, proximal phalanx 45 mm, middle phalanx 30 mm, distal phalanx 20 mm). In this figure, FH is the point considered fixed on the hand, while PP, MP, DP are the extremities of each phalanx. In this finger model the geometry of each phalanx is cylindrical. Figures 17b, 17c, 17d show all the parts of the mechanism connected to this finger and moved by a single linear pneumatic actuator, analyzing its function in a succession of frames. Simulations were also carried out on the geometries for the configuration which maintains the link in the vertical position. All simulations results are good, demonstrating the study's reliability and the mechanism's ability to replicate the desired trajectory for each finger. In particular in the Figures 17b (1) is the index finger during the flexion, (2) is the vertical link, (3) is the first slot, (4) is the second slot, (5) are the trajectories of each finger phalanx, (6) are the trajectories of the slots, (7) is the telescopic shaft. During this simulation, the slots were simulated using the proper trajectories pathways. The Figure 17c shows the simulation using the cart type constraint in order to guarantee the exact vertical position of the link. Figure 18 shows the simulated trajectory of the index finger driven by the mechanism, compared with the other trajectories. A direct comparison of this trajectory

with the trajectory obtained with the same software by operator 3 (23 year old male subject, body mass 64 kg, height 179.5 cm, right index finger having 44 mm proximal phalanx, 25 mm middle phalanx, 15.5 mm distal phalanx) shows several similarities.

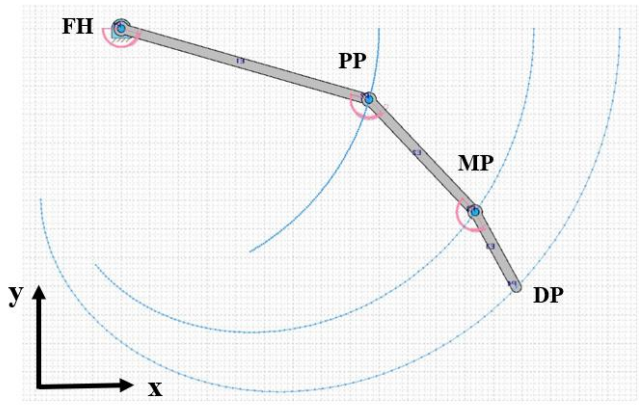


Figure 17a The index finger phalanges trajectories simulated in a specific software.

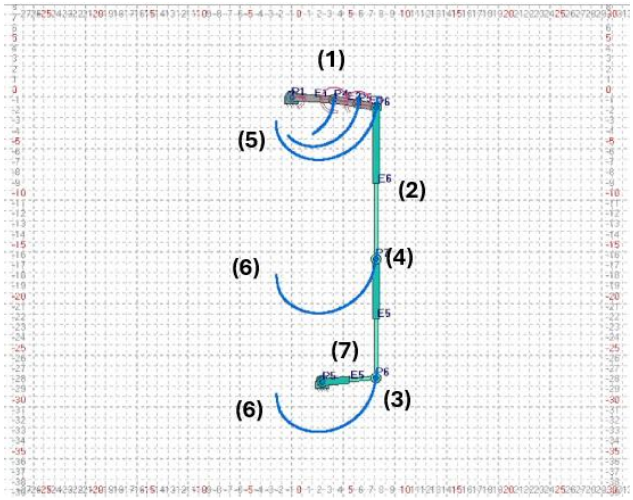


Figure 17b The index finger and its mechanism using two slots.

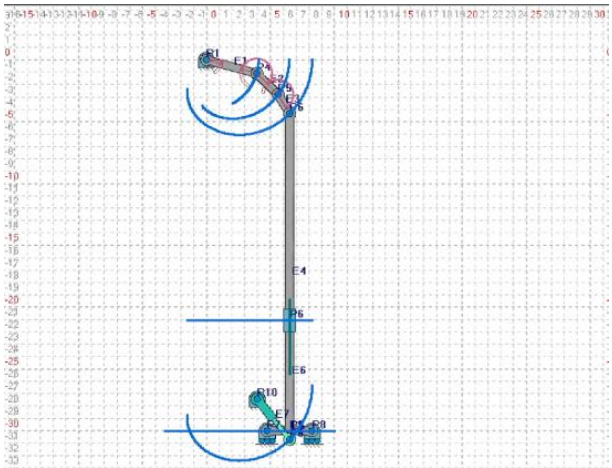


Figure 17c A simulation using the cart type constraint.

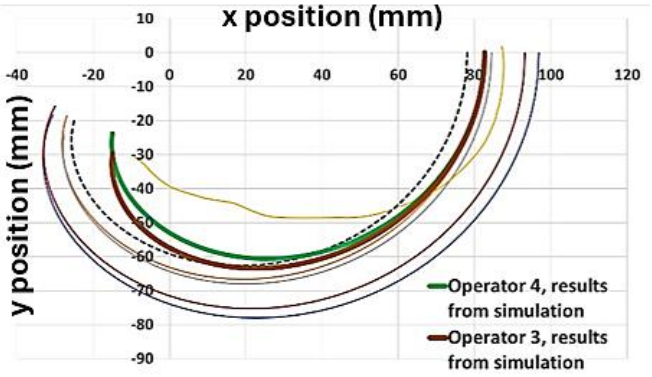


Figure 18 Comparison of simulation results and the other index finger trajectories.

The simulated trajectories show less extension than the trajectories obtained from calculations and from the experimental videos.

In fact, the simulation was influenced by the cylindrical shape of each phalanx (Figures 19a and 19b) [57], which can generate interference between the various parts of the phalanges in the finger model. It is also necessary to remember that the physiological shape of the fingers is not exactly a cylindrical one. Additional studies carried out moving the index finger (average male hand from operator 1 measurements, Table IV) manually in a CAD environment show that an imperfectly cylindrical shape (Figure 19c and 19d) of each phalanx can improve its movement and yields trajectories that are more similar to those produced from numerical considerations. With cylindrical phalanges, finger flexion (as shown by the length illustrated in the Figure 19b) is slightly less than in the case where each phalanx is modeled with a shape that is not perfectly cylindrical (Figures 19c and 19d). Further possible shapes, such as an equivalent trapezoidal shape (Figures 19e and 19f), can be analyzed to improve the finger model to avoid interference between the phalanges and to simulate full, correct finger flexion (Figure 19f). Each phalanx dimensions are here the same as those illustrated in Figures 19 a, b, c, d.

This is important in order to ensure that simulation yields realistic finger movements and trajectories in conformity with other numerical and experimental studies that can be used to investigate the articulated mechanism's kinematics.

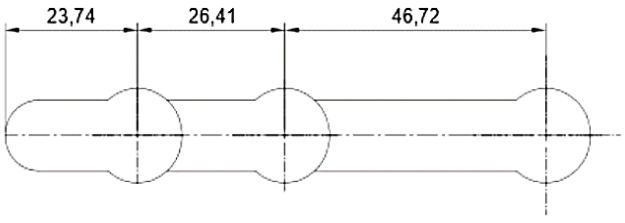


Figure 19a A CAD model of the extended index finger constructed using a cylindrical shape for each phalanx (dimensions in mm).

ISSN 1590-8844
International Journal of Mechanics and Control, Vol. 26, No. 01, 2025
https://doi.org/10.69076/jomac.2025.0009

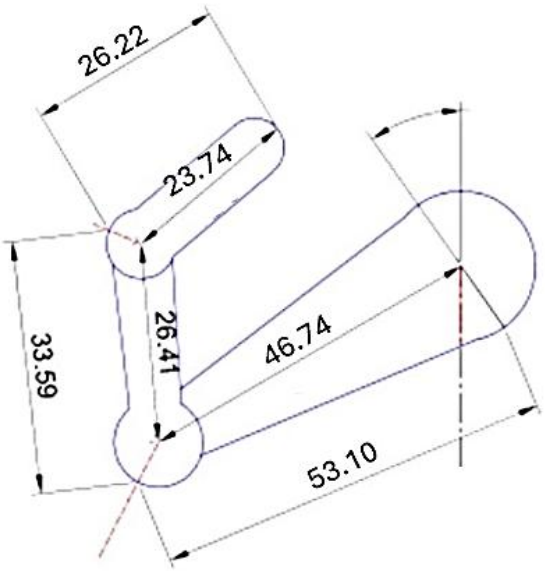


Figure 19b A CAD model of the flexed index finger constructed using a cylindrical shape for each phalanx.

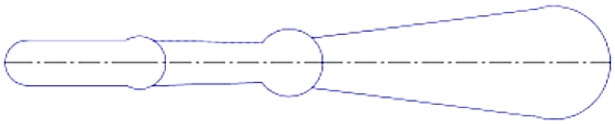


Figure 19c A CAD model of the extended index finger constructed using an imperfectly cylindrical shape for each phalanx.

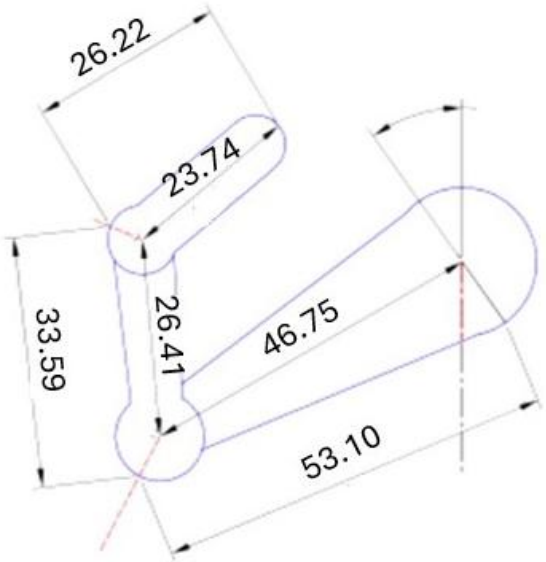


Figure 19d A CAD model of the flexed index finger constructed using an imperfectly cylindrical shape for each phalanx.

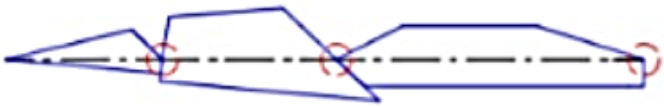


Figure 19e A further possible CAD model of the extended index finger constructed using a trapezoidal shape for each phalanx.

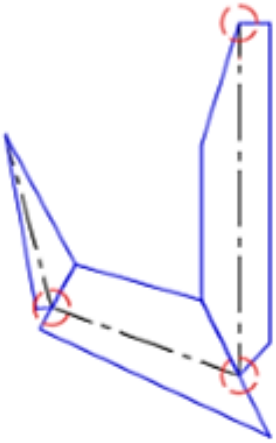


Figure 19f A further CAD model of the flexed index finger constructed using a trapezoidal shape for each phalanx.

It should be borne in mind that while the operation of the finger movement mechanism can be represented via simulation, the trajectory obtained for each finger can be influenced by the phalanx shape used in the simulation model. Assigning an appropriate geometrical shape to each phalanx during simulation is thus essential in evaluating the mechanism. The authors will address these issues in future work. The considerations presented above are useful for developing a methodology for analyzing and measuring finger trajectories, verifying the operation of the mechanism that guides them in the device presented here, and creating the slots along which each finger (or all fingers together) are guided through physiological and non-physiological motions.

8 COMPLETE PROTOTYPE: FOUR PNEUMATIC ACTUATORS

Figure 20 shows the complete prototype with its main dimensions. It has four pneumatic actuators: a pneumatic motor for thumb movement, a linear pneumatic actuator for the finger/fingers movement, a linear pneumatic actuator for the wrist movement, a linear pneumatic cylinder to move up and down all the fingers mechanisms and actuators platform. Wrist trajectories are determined using the same procedures as for the fingers. The Figure 20 shows the prototype put close to the cot in the magnetic resonance chamber. Some main dimensions of the prototype will can be improved.

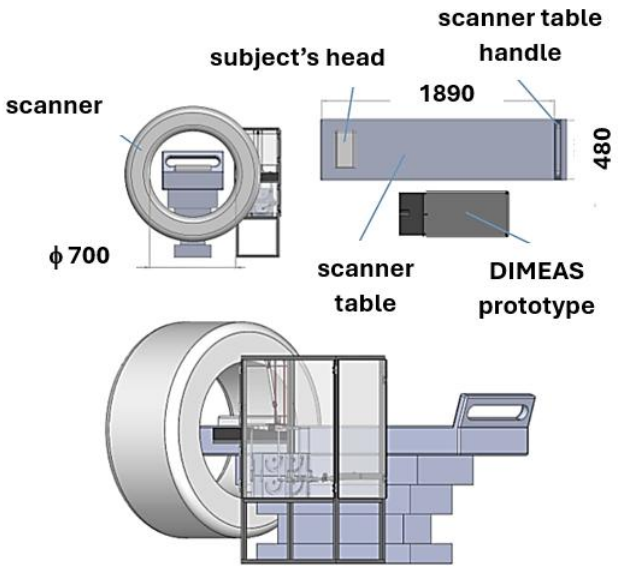


Figure 20 Some details of the prototype put inside the magnetic resonance chamber (dimensions in millimiter).

9 CONCLUSION

The paper illustrates the design process for an innovative active device capable of moving the fingers and wrist of one or both hands during fMRI analysis. The device can be used with healthy subjects and with patients. The whole structure of the machine will be improved using the movable platform to reduce the link length and removing the second slot. This is possible because the motion will never be imposed simultaneously on the wrist and fingers. For a correct use of the machine in the magnetic resonance chamber, a further check of all the materials constituting the various parts of the machine will be necessary. In any case any electronic/electrical device must be positioned outside the magnetic resonance chamber, including the electro-pneumatic control circuit. In future work, the authors plan to construct a model of the device's electropneumatic control system in order to analyze signal transaction times along 10 m long lines. The electropneumatic control system will be placed outside the magnetic resonance chamber, but the system must be able to function with the time cycle established by the clinicians. Supply pressure can be varied to impose different movement conditions on the fingers and hand, as well as to measure the subject's performance with varying levels of assistance from the device. Future construction of this device will start from development and testing of its main parts, i.e., the slots and finger movement mechanisms.The use of non-magnetic materials will necessarily lead to building many parts of the machine in plastic materials. This aspect obviously facilitates the parts in relative motion, reducing friction and improving the performance and duration of the machine itself.

AKNOWLEGEMENTS

The author thanks Prof. Katiuscia Sacco (Dept. of Psychology, University of Torino, Italy), engineers N. Ferrero, C. Gili, P. Ferrando, M. Tonaj, E. Castellaneta, M. Caddeo, and students G. Mano and A.G. Barone for their help in this study.

REFERENCES

[1] Thulborn K.R., Correlating BOLD functional magnetic resonance imaging with metabolic changes during neuronal activation should benefit the study of cognitive processing. *Nature Medicine*, Vol. 4, pp. 159-167, 1998.

[2] Ogawa S., Lee T.M., Kay A.R. and Tank D.W., Brain magnetic resonance imaging with contrast dependent on blood oxygenation. *Proc. Natl. Acad. Sci. USA*, *Biophysics*, December, Vol. 87, No. 24, pp. 9868-9872, 1990.

[3] Niola V., Penta F., Rossi C. and Savino S., An underactuated mechanical hand: Theoretical studies and prototyping. *International Journal of Mechanics and Control*, Vol. 16, No. 1, pp. 11-19, 2015.

[4] Savino S., Underactuated mechanical hand control by EMG sensors. *International Journal of Mechanics and Control*, Vol. 17, No. 1, 2016.

[5] Yap H.K., Lim J.H., Nasrallah F., Low F.Z., Goh J.C.H., Yeow R.C.H., MRC-glove: A fMRI compatible soft robotic glove for hand rehabilitation application. *2015 IEEE International Conference on Rehabilitation Robotics (ICORR)*, 11th-14th August 2015, Singapore, pp. 735-740, 2015.

[6] Yap H.K., Kamaldin N., Lim J.H., Cho Hong Goh J. and Yeow C.H., A magnetic resonance compatible soft wearable robotic glove for hand rehabilitation and brain imaging. *IEEE Transactions on Neural Systems and Rehabilitation Engineering*, Vol. 25, No. 6, pp. 782-793, 2016.

[7] Chen Y., Le S., Chu Tan Q., Lau O., Wan F. and Song C., A lobster-inspired robotic glove for hand rehabilitation. *IEEE International Conference on Robotics and Automation (ICRA)*, Singapore, 2017, pp. 4782-478, 2017.

[8] Hashida R., Matsuse H., Bekki M., Omoto M., Morimoto S., Hino T., Harano Y., Iwasa C., Miyamoto K., Haraguchi M., Nago T. and Shiba N., Evaluation of motor-assisted gloves (SEM Glove) for patients with functional finger disorders: a clinical pilot study. *Kurume Medical J.*, Vol. 65, No. 2, pp. 63-70, 2019.

[9] Chu C.Y. and Patterson R., Soft robotic devices for hand rehabilitation and assistance: a narrative review. *J. of NeuroEngineering and Rehabilitation*, Vol. 15, No. 9, pp. 1-14, 2018.

[10] Ahmed Y.S., Al-Neami A.Q. and Lateef S., Robotic glove for rehabilitation purpose: review. *Iraqi J. of*

Electrical and Electronic Eng. Conference article The 3rd Scientific Conference of Electrical and Electronic Eng., 15th-16th June 2020, Basrah Iraq, pp. 86-92, 2020.

[11] Serrano D., Copaci D., Arias J., Moreno L.E. and Blanco D., SMA-Based soft exo-glove. *IEEE Robotics and Automation Letters*, Vol. 8, No. 9, pp. 5448-5455, 2023.

[12] Liu H., Wu C., Lin S., Chen Y., Hu Y., Xu T., Yuan W. and Li Y., Finger flexion and extension driven by a single motor in robotic glove design. *Advanced Intelligent Systems*, Vol. 5, No. 5, pp. 1-10, 2023.

[13] Gorissen B., Reynaerts D., Konishi S., Yoshida K., wan Kim J. and De Volder M., Elastic inflatable actuators for soft robotic applications. *Advanced Materials*, Vol. 29, No. 43, pp. 1-14, 2017.

[14] Lambelet C., Lyu M., Wolley D., Gassert R. and Wenderoth N., The eWrist – A wearable wrist exoskeleton with sEMG-based force control for stroke rehabilitation. *Int. Conference on Rehabilitation Robotics (ICORR)*, 17th – 20th July 2017, QEII Centre, London UK, pp. 726-733, 2017.

[15] Alhamad R., Seth N. and Abdullah H.A., Initial testing of robotic exoskeleton hand device for stroke rehabilitation. *Sensors MDPI*, Vol. 23, No. 14, pp. 1-18, 2023.

[16] Jo I., Park Y., Lee J. and Bae J., A portable and spring-guided hand exoskeleton for exercising flexion/extension of the fingers. *Mechanism and Machine Theory*, Vol. 135, pp. 176-191, 2019.

[17] Aggogeri F., Mikolajczyk T. and O'Kane J., Robotics for rehabilitation of hand movement in stroke survivors. *Advances in Rehabilitation Eng. with Robotics and Mechatronics Devices*, Vol. 11, No. 4, pp. 1-14, 2019.

[18] Ratz R., Conti F., Muri R.M. and Marchal-Crespo L., A novel clinical-driven design of robotic hand rehabilitation: combining sensory training, effortless setup, and large range of motion in a palmar device. *Frontiers in Neurorobotics*, Vol. 15, pp. 1-22, 2021.

[19] Arbuckle S.A., Pruszynski J.A. and Diedrichsen J., Mapping the integration of sensory information across fingers in human sensorimotor cortex. *The Journal of Neuroscience*, Vol. 42, No. 26, pp. 5173-5185, 2022.

[20] Cobos S., Ferre M., Sanchèz Uràn M.A., Ortego J. and Pena C., Constraints for realistic hand manipulation. *10th Annual International Workshop on Presence (PRESENCE '07)*, October 2007, Barcelona Spain, pp. 369-388, 2007.

[21] Cobos S., Ferre M., Sanchèz Uràn M.A., Ortego J. and Pena C., Efficient human hand kinematics for manipulation tasks. *IEEE/RSJ International Conference on Intelligent Robots and Systems (IROS'08)*, September 2008, Nice France, pp. 2246-2251, 2008.

[22] Du Plessis T., Djouani K. and Oosthuizen C., A review of active hand exoskeletons for rehabilitation and assistance, *Robotics*, Vol. 10, No. 1, pp. 1- 42, 2021.

[23] Shimawaki, S. Nakamura Y., Nakabayashi M. and Sugimoto H., Flexion angles of finger joints in two-finger tip pinching using 3D bone models constructed from X-Ray Computed Tomography (CT) images. *Applied Bionics and Biomechanics*, pp. 1 – 6, 2020.

[24] Husaini H., Hasanuddin I., Zaqy S.Y.B. and Akhyar A., Stress analysis on mechanical hand prototype with kinematics model approach and performance tests. Disruptive Innovation in Mechanical Engineering for Industry, *Proceedings of the 3rd Int. Conference on Mechanical Eng. (ICOME 2017), published by American Institute of Physics*, 13th July 2018 Surabaya Indonesia, Vol. 1983, No. 1, pp. 1-6, 2018.

[25] Kamper D.G., Cruz E.G. and Siegel M.P., Stereotypical fingertip trajectories during grasp. *J. Neurophysiol*, Vol. 90, No. 6, pp. 3702-3710, 2003.

[26] Imbinto I., Montagnani F., Bacchereti M. and Cipriani C., The S-Finger: a synergetic externally powered digit with tactile sensing and feedback. *IEEE Transactions on Neural Systems and Rehabilitation Eng.*, Vol. 26, No. 6, pp. 1-9, 2018.

[27] Milliken G.W., Plantz E.J. and Nudo R.J., Distal forelimb representations in primary motor cortex are redistributed after forelimb restriction: a longitudinal study in adult squirrel monkeys. *J. Neurophysiol*., Vol. 109, No. 5, pp. 1268-1282, 2013.

[28] Hussain I., Santarnecchi E., Leo A., Ricciardi E., Rossi S. and Prattichizzo D., A magnetic compatible supernumerary robotic finger for functional magnetic resonance imaging (fMRI) acquisitions: device description and preliminary results. *International Conference on Rehabilitation Robotics (ICORR)*, 17th – 20th July 2017, QEII Centre, London UK, pp. 1177-1182, 2017.

[29] Carey J.R., Kimberley T.J., Lewis S.M., Auerbach E.J., Dorsey L., Rundquist P. and Ugurbil K., Analysis of fMRI and finger tracking training in subjects with chronic stroke. *Brain*, Vol. 125, pp. 773-788, 2002.

[30] De Luca C., Comani S., Di Donato L., Caulo M., Bertollo M. and Romani G.L., A-Magnetic Optic-Mechanical Device to Quantify Finger Kinematics for fMRI Studies of Bimanual Coordination. *Brain Topogr*, Vol. 19, No. 3, pp. 155–160, 2007.

[31] Lolli V., Rovai A., Trotta N., Bourguignon M., Goldman S., Sadeghi N., Jousmäki V and De Tiège X., MRI-compatible pneumatic stimulator for sensorimotor mapping. *J. of Neuroscience Methods*, Vol. 313, pp. 29-36, 2019.

[32] Pinter D., Pegritz S., Pargfrieder C., Reiter G., Wurm W., Gattringer T., Linderl-Madrutter R., Neuper C., Fazekas F., Grieshofer P. and Enzinger C., Exploratory Study on the Effects of a Robotic Hand Rehabilitation Device on Changes in Grip Strength and Brain Activity after Stroke. *Top Stroke Rehabil*, Vol. 20, No. 4, pp. 308-316, 2013.

[33] Schaechter J.D., Stokes C., Connell B.D., Perdue K and Bonmassar G., Finger motion sensors for fMRI motor studies. *NeuroImage*, Vol. 31, pp. 1549-1559, 2006.

[34] Menon S., Brantner G., Aholt C., Kay K. and Khatib O., Haptic fMRI: combining functional neuroimaging with haptics for studying the brain's motor control representation. *35th Annu Int. Conf. IEEE Eng. Med. Biol. Soc (EMBC)*, 3rd – 7th July 2013 Osaka Japan, pp. 4137-4142, 2013.

[35] Pawel L.M., *Designing of a hand rehabilitation robotic device for the post-stroke patients with flaccidity*. School of Industrial and Information Eng. Master of Science in Biomedical Eng. Master Thesis Politecnico di Milano Italy, supervisor Prof. Carlo Albino Frigo, 2019.

[36] Espinosa-Garcia F.J., Tapia-Herrera R., Lugo-Gonzalez E. and Aria-Montiel M., Design and simulation of a robotic hand with foldable palm based on mechanisms with variable topologies. *Memorias del XXI Congreso Mexicano de Robotica (XXI COMRob 2019)*, 13th-15th November 2019, Manzanito Colima Mexico, 13-15 de November, pp. 300-305, 2019.

[37] Byoung-Ho K., Analysis of coordinated motions of humanoid robot fingers using interphalangeal joint coordination. *Int. J. of Advanced Robotic Systems*, Vol. 11. No. 4, pp. 1-8, 2014.

[38] Tang Z., Sugano S. and Iwata H., A finger exoskeleton for rehabilitation and brain image study. *IEEE 13th Int. Conference on Rehabilitation Robotics*, 24th -26th June 2013 Seattle Washington USA, pp. 1-6, 2013.

[39] Carbone G., Gerding E-C., Corves B., Cafolla D., Russo M. and Ceccarelli, M., Design of a two-DOFs driving mechanism for a motion-assisted finger exoskeleton. *Applied Sciences MDPI*, Vol. 10, No. 7, pp. 1-23, 2020.

[40] Parida P.K. and Biswai B.B., Design and Analysis of a Multifingered Robot Hand. *International Journal of Robotics and Automation (IJRA)*, Vol. 1, No. 2, pp. 69-77, 2012.

[41] Liu C., Lu J., Yang H. and Guo K., Current State of Robotics in Hand Rehabilitation after Stroke: A Systematic Review. *Applied Sciences MDPI*, Vol. 12, No. 9, pp. 1-26, 2022.

[42] Vanoglio F., Bernocchi P., Mule' C., Garofali F., Mora C., Taveggia G., Scalvini S. and Luisa A., Feasibility and efficacy of a robotic device for hand rehabilitation in hemiplegic stroke patients: a randomized pilot controlled study. *Clinical Rehabilitation*, Vol. 31, No. 3, pp. 351-360, 2017.

[43] Sacco K., *Neuroimaging per lo studio del cervello umano*. II edition, Idelson Gnocchi Ed., 5th June 2020, pp. 1-260, 2020.

[44] Belforte G., Eula G., Sirolli S., Bois P., Geda E., D'Agata F., Cauda F., Duca S., Zettin M., Virgilio R., Geminiani G. and Sacco K., Bra.Di.P.O. and P.I.G.R.O.: Innovative devices for motor learning programs. *Journal of Robotics*, Vol. 2014, pp. 1-12, 2014.

[45] Agrawal J., Raichandani L., Sushma K. and Surbhi Raichandani S., Estimation of stature from hand length and length of phalanges. *Journal of Evolution of Medical and Dental Sciences*, Vol. 2, No. 50, pp. 9651-9656, 2013.

[46] Bures M., Gorner T. and Sediva B., Hand anthropometry of Czech population. *2015 IEEE Int. Conference on Industrial Eng. and Eng. Management* (IEEM), Singapore pp. 1-7, 2015.

[47] Guerra R.S., Fonseca I., Pichel F., Restivo M.T. and Amaral T.F., Hand length as an alternative measurement of height. *Eur J Clin Nutr*, Vol. 68, No. 2, pp. 229-233, 2014.

[48] Kondo M., Ogihara N., Shinoda K., Anada S., Ito K., Murata M., Tanaka T., Takai S. and Matsu'ura S., Sexual dimorphism in the human hand proportion: A radiographic study. *Bull. Natl. Mus. Nat. Sci*, Vol. 43, pp. 1-6, 2017.

[49] Buryanov A. and Kotuk V., Proportions of hand segments. *Int. J. Morphol*, Vol. 28, No. 3, pp. 755-758, 2010.

[50] Herman I.P., *Physics of the Human Body*. 2nd Edition, Springer Verlag, 2016.

[51] Penn State Eberly College of Science, 2.6 – (Pearson) Correlation coefficient r. *STAT 462 lesson Applied Regression Analysis*, Dept. of Statistics Online Programs, 2018.

[52] Anderson T.W. and Darling D.A., Asymptotic theory of certain "goodness-of-fit" criteria based on stochastic processes. *Annals of Mathematical Statistics*, Vol. 23, No. 2, pp. 193–212. 1952.

[53] Shapiro S.S. and Wilk M.B., An analysis of variance test for normality (complete samples). *Biometrika*, Vol. 52, No. 3 and 4, pp. 591-611, 1965.

[54] Blair R.C. and Higgins J.J., A Comparison of the Power of Wilcoxon's Rank-Sum Statistic to That of Student's t Statistic under Various Nonnormal Distributions. *Journal of Educational Statistics*, Vol. 5, No. 4 pp. 309-335, 1980.

[55] Conley T. and Taber C. Inference with "Difference in Differences" with a Small Number of Policy Changes. *NBER Technical Working Paper*, No. 312, pp. 1-51, 2005.

[56] Lane D., *Difference between two means*. LibreTexts Statistics Libraries, 2022.

[57] Lin J., Wu Y. and Huang T.S., Modeling the constraints of human hand motion. *Prodeedings Workshop on Human Motion*, 7th-8th December 2000, Austin Texas USA, pp. 121-126, 2000.

ISSN 1590-8844
International Journal of Mechanics and Control, Vol. 26, No. 01, 2025
https://doi.org/10.69076/jomac.2025.0010

MODELING A SUBJECT WEARING AN INDUSTRIAL TRUNK SUPPORT EXOSKELETON

Gabriella Eula*

* Department of Mechanical and Aerospace Engineering, Politecnico di Torino, Torino Italy

ABSTRACT

The paper presents a model of a human body wearing an industrial trunk support exoskeleton based on a pneumatically actuated prototype designed and constructed at the Politecnico of Turin Department of Mechanical and Aerospace Engineering (DIMEAS). Developed using commercial software, this innovative model was used to investigate the movement, mass and inertia parameters of the wearer's trunk with and without the exoskeleton. These considerations are always very important for control system design. Actuation units are located at each hip joint, consist of pneumatic motors and toothed belt drives, and feature a particular structure to respect the physiological difference between the hip joint and the lumbo-sacral joint. Preliminary simulation results are in good agreement with the results obtained from earlier numerical models. The simulation technique illustrated here is faster than previous approaches, as a CAD human body model can be imported directly into a software environment and then evaluated.

Keywords: industrial trunk support exoskeleton; operator wearing a trunk exoskeleton model; industrial trunk support exoskeleton with pneumatic actuation; active industrial exoskeleton

1 INTRODUCTION

Industrial exoskeletons continue to make progress in a wide range of applications [1, 3].They can be designed for full-body use [4], for lower limbs only [5-8], or for the upper body, i.e., trunk or upper limbs [9-14]. Functions can include assisting the wearer while working in a seated position or bending forward, while handing or moving loads, while holding demanding postures with raised arms for prolonged periods, etc. The structure of industrial exoskeletons must be robust and lightweight to ensure strength as well as wearer comfort. In most cases this is achieved by using aluminum alloys or composite materials. The structure includes joints so that the device can move smoothly and naturally along with the wearer's body. The force needed to perform the tasks for which industrial exoskeletons are designed is provided by pneumatic, hydraulic or electric actuators.

Contact author: Gabriella Eula[1]

[1] Corso Duca Degli Abruzzi 24, Torino, TO, 100129, Italy
E-mail: gabriella.eula@polito.it

Actuators are controlled by an electronic system which is based on special algorithms and interprets the data provided by sensors. Such exoskeletons feature a single battery power source. A major benefit of these exoskeletons is that they reduce musculoskeletal loading and fatigue, thus lowering the risk of injury to the wearer [15]. In designing exoskeleton control systems, it is essential to consider all parameters, inertia properties in particular [16,17]. Accordingly, this study included an analysis of the inertial aspects, whose findings were in full agreement with others presented in the literature for the human body shape and position considered here. A number of dynamic considerations must be borne in mind in assessing the motor torque applied to the human body joints. Often these dynamic actions influence the required torque numerical value, so it is better to examine a static equilibrium condition [11-14] during the design process of the actuation units and their power. Exoskeletons are used for a wide range of purposes, including military [3], rehabilitation/assistance training [2, 5, 6] and industrial applications [9, 11-14]. In many industrial operations, robotic devices can help workers improve performance and prevent musculoskeletal strain and fatigue. Many of these exoskeletons provide the wearer with a percentage of the maximum required muscle torque. In addition to the ability to deliver this percentage of the required maximum torque,

these machines must accommodate working conditions calling for total maximum torque or legs-free operation. The latter operating mode allows the wearer's legs to move freely in the event of an emergency or during tasks calling for independent leg movement [11-14]. This paper presents a simulation model constructed in a commercial software environment. The model was used first to analyze the wearer's entire body, and then to analyze the body together with the DIMEAS (Department of Mechanical and Aerospace Engineering, Politecnico of Turin, Italy) trunk exoskeleton. The exoskeleton was designed to support the wearer's trunk in tasks requiring flexion, extension, or bending forward while stationary for prolonged periods.

This study was conducted to develop a reliable model for use in analyzing how the wearer and exoskeleton systems function together. It was based on previous work by the authors on several types of exoskeleton [2, 5-7, 11-14]. In view of the importance of inertia parameters [18-29] for exoskeleton operation, the authors used a software environment to construct a model of the entire human body and then of the human body wearing the DIMEAS industrial trunk support exoskeleton. These models can be used to assess inertial actions and their influence while varying the main parameters. Comparison with the data presented in the literature [16, 17-29] confirmed the models' reliability. The models' operation was evaluated through a comparison with previous experimental tests on trunk flexion and with earlier numerical models developed by the authors using other software. These comparisons all yielded satisfactory results, and suggested a strategy for future exoskeleton design.

2 BRIEF DESCRIPTION OF THE DIMEAS EXOSKELETON PROTOTYPE

The exoskeleton considered here is an active industrial trunk support exoskeleton designed and constructed at DIMEAS [12,13]. Figure 1a shows the prototype as worn. The exoskeleton consists of two pneumatic actuation units on the hip joint axis (A) which assist the wearer during trunk movement; a rigid backframe structure (B) carried on the wearer's back to provide support; and two leg-links (C) worn in contact with the thigh to support part of the load. Figure 1b is a photograph of the DIMEAS prototype. Actuation unit details are shown in Figure 1c, where (1) is the pulley connected to the pneumatic motor; (2) is the pulley connected to the backframe and representing the actuation unit joint for the physiological lumbosacral joint; (3) is the first toothed belt; (4) is the hip joint pulley connected to the leg-link; (5) is the second toothed belt; and (6) is a detail of the backframe bar. Using two toothed belt drives enables the exoskeleton structure to reproduce the physiological difference between the hip joint and the lumbosacral joint. This is important in order to ensure physiological trunk movement on the part of the wearer. Figure 1d shows the main elements of the exoskeleton and the human body parts involved.

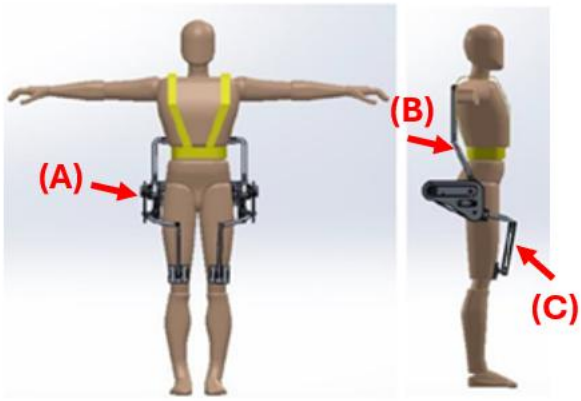


Figure 1a The exoskeleton prototype as worn.



Figure 1b The DIMEAS prototype.

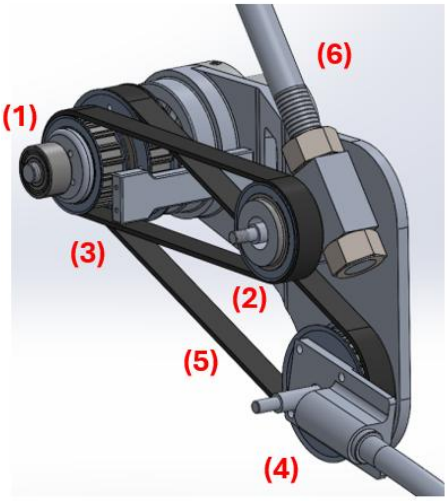


Figure 1c Hip actuation unit details.

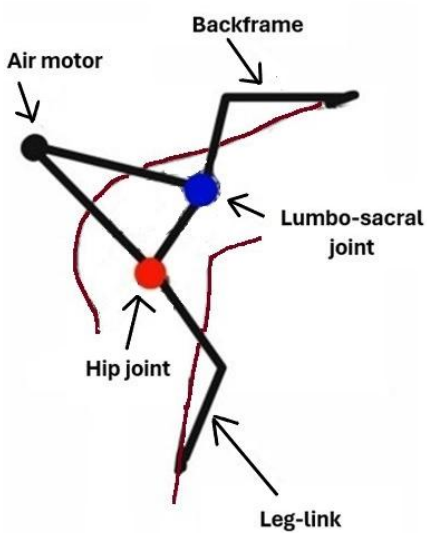


Figure 1d Schematic diagram of the main human and exoskeleton parts.

Pneumatic actuation was chosen for safety purposes. In addition, it makes it possible to control applied torque by varying air motor supply pressure, and to lock the exoskeleton in any trunk flexion position desired by the wearer by pressurizing both air motor chambers. The authors modeled the exoskeleton and the wearer's body in a commercial software environment (Simcenter Amesim [30]) which is often used to simulate mechanical systems. The actuation units were also analyzed.

3 THE MODELS

Using a specific software tool, the authors imported in Simcenter Amesim environment [30]: a model of the human body obtained from free web archives [31] (here called model A); a model of the human body constructed using a CAD software (SOLIDWORKS® 2023) and designed using physiological information from the literature [32] (here called model B). Figure 2 shows human body model A wearing the exoskeleton, as uploaded in Simcenter Amesim.

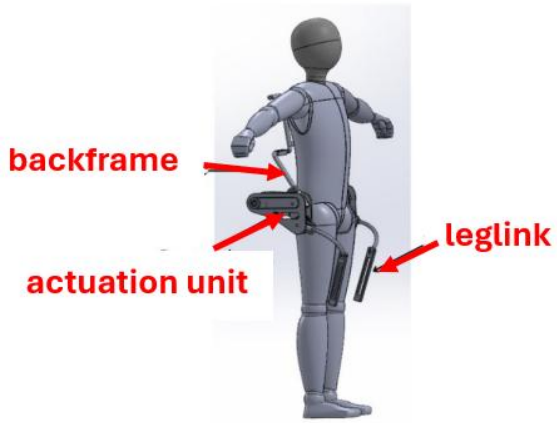


Figure 2 CAD human body model A wearing the exoskeleton.

These human bodies were analyzed alone and then wearing the exoskeleton. Choosing appropriate modeling parameters to ensure correct simulation was a key part of the study.

4 THE BODY MODEL

To simulate the "wearer + exoskeleton" system in the Simcenter Amesim environment, the human body model was first studied without the exoskeleton. This step was important in selecting the best simulation parameters, with particular attention to the inertial aspects. The properties shown in Table I were used to simulate body parts [32,33].

Table I - Density of the human parts considered here

Body part	Density (kg/m^3)
Forearm and hand	1140
Arm	1070
Foot and leg	1090
Thigh	1050
Head and neck	1110
Trunk	1030

Trunk mass was 59.43 kg. The other parameters used for the simulation are illustrated in the following paragraphs. Two models of the human body were developed and studied in the software environment, with particular attention to inertia properties. Both human body models represent a 95th percentile adult Italian male [32-35]. For all simulations in the Simcenter Amesim environment, both of the human body model's arms were in abduction. The human body model was separated into two subsystems, one for the upper body, and the other for the lower body. The sections were connected by means of the hip joint. Each subsystem has its own center of mass. The decision to model two subsections was motivated by the type of movement investigated, viz., trunk flexion followed by extension, with limited leg rotation. Accordingly, the movement of interest here is that of the trunk, not that of the entire body.

4.1 BODY MODEL A

Figure 3a shows CAD body model A [31]. In this figure and in the following description, the exoskeleton is not worn. This CAD model was imported in Simcenter Amesim. In particular, tools called "ports" were used. In Simcenter Amesim, ports are the points of connection between two subsystems using the same joint, which also enables them to move relative to each other. Figure 3b shows the ports set for the upper body: port A is the connection with the hip joint to move the trunk, and is also connected to port D on the legs; port B is the connection between the trunk and the backframe.

Figure 3c shows the ports set for the lower body: port D is the connection with the hip joint for trunk movement; ports B and C are the connections between the two leg-links and the exoskeleton; port A is the connection with the ankle joint.

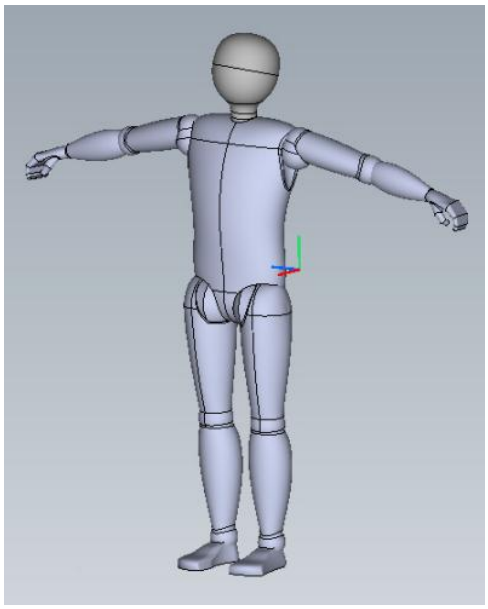


Figure 3a CAD human body model A.

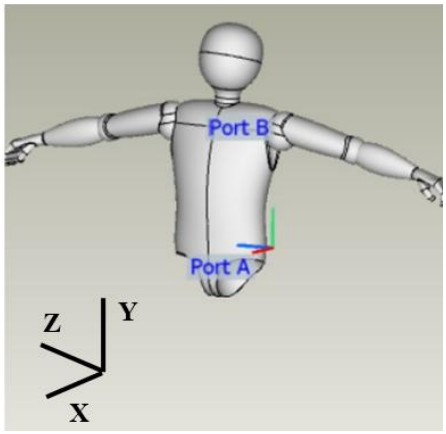


Figure 3b Upper body ports.

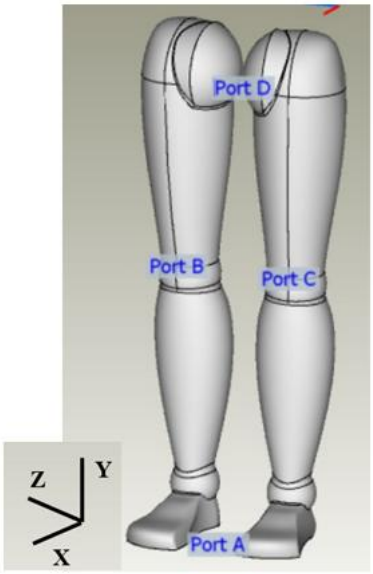


Figure 3c Lower body ports.

The upper and lower body were connected using a controlled hinge in each hip joint which receives an input torque that provides the control signal for the movement. A similar controlled hinge was also set between the legs and the ground in order to simulate leg movement relative to the trunk. The main purpose of this simulation is to assess total muscle torque on the hip joints. The assembly process is purely numerical and hidden from the user, but a sketch viewer in the icon can be used to see the result of this process, as shown in Figure 4. The two subsystems set in the software are as shown in Figure 4, where the two rigid bodies are connected by the hinge representing the hip joint and the second hinge is connected to the zero velocity source, i.e., to the ground. Each shape has its center of mass, yellow points in Figure 4.

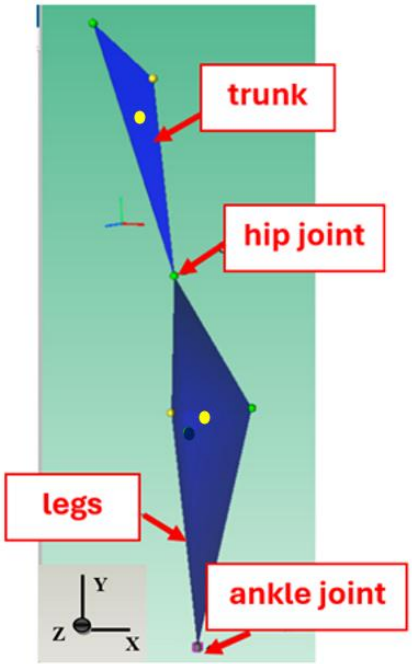


Figure 4 Visualization of the human body (model A) assembled in Simcenter Amesim.

The anomalous shape of the bodies is due to the fact that the assembly algorithm is based on the positions of the centers of mass (represented in Figure 4 as yellow points) and connection ports (represented here as green points). The legs protrude more at the height of the knee, as the body port coordinates were modified to make them coincide with those of the end of the leg-link. This was necessary because at this stage the CAD model does not include the leg strap that secures the leg-link to the wearer's legs, so the strap could not be imported to Simcenter Amesim. This does not affect the simulation, as the mass and the inertia matrix are still those of the CAD model, but it is important to simulate the effective contact between the two bodies. In the simulation with the body model alone, the only connection ports that can be used to simulate movement are those for the legs, those connected to the ground thanks to the zero velocity source (bottom of Figure 4) and those connecting with the torso through the hip joint

(bottom of Figure 4). For the trunk, the only port used is that which connects it to the legs through the hip joint. The uppermost port (green dot at the top in Figure 4) was used for connection to the exoskeleton backframe. In practice, the connection ports serve to obtain the geometry of the bodies, to understand how they are arranged in space, to evaluate the movement permitted by the joints, and to obtain a video simulation. These ports are inserted when a rigid body is added to the sketch (i.e., the schema in the software environment) and whose coordinates are added during parameterization.

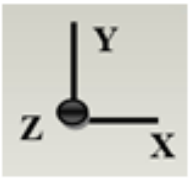
4.1.1 Inertia properties

The ports and associated parameters used to assess inertia properties are those from the CAD model. Characteristics are as follows:

• coordinate system orientation: this section presents the rotations according to the Euler decomposition (z, y, x), i.e., the first rotation around the z-axis, the second rotation around the intermediate y-axis and the third rotation around the target x-axis. In addition, these rotations can be blocked;

• position of the part considered: this window presents the coordinates of the reference system origin (designed by the letter O), the center of mass (designated by the letter G) and those of all the ports;

• inertia: values relating to the mass and the inertia matrix with respect to the body's center of mass, divided into moments of inertia around the x, y, z axes, designated as Gx, Gy and Gz respectively, representing the diagonal of the matrix, and in inertia products xy, xz, yz representing the values of the diagonal (Figure 5);



$$\begin{matrix} I_{xx} & I_{xy} & I_{xz} \\ I_{yx} & I_{yy} & I_{yz} \\ I_{zx} & I_{zy} & I_{zz} \end{matrix}$$

Figure 5 The general Simcenter Amesim inertia matrix.

• initial speeds: here, the three coordinates of initial values for absolute velocity of the center of mass and of angular velocity relative to the local orientation system can be entered. For both bodies in consideration, initial velocities were null, as the intention is to simulate movement starting from the rest position;

• advanced: in this section, the rotation mode for both rigid bodies was set to high in order to use the Euler angles and ensure faster calculation. As the axis of rotation during movement is known to be the z axis, it was chosen as the main axis of rotation. For the same reason, rotation of the center of mass along the x and y axes and its position along the z axis were limited. Numerical values for the rigid body representing the trunk with the coordinates of the two ports and the inertia values (referred to the center of gravity, trunk mass 59.43 kg) are shown together with the inertia matrix (values in kg/m^2) in Figures 13. As there are two separate subsystems connected through the hip joints, the software generates two inertia matrices, one for the upper body, and one for the lower body. The legs' mass is 35.61 kg and the inertia matrix, referred to the center of mass, is illustrated in Figures 13 (values in kg/m^2). These matrices were derived from the imported CAD geometry and automatically determined by Simcenter Simcenter Amesim after setting the correct density. At 3.29 kgm^2, the highest moment of inertia was Ixx, i.e., that along the Gx axis. This indicates that the body has greater resistance to rotation around this axis. The lowest moment of inertia was Iyy, equal to 0.53 kgm^2 in the lower body matrix. The off-diagonal moments of inertia are smaller than the diagonal moments: this indicates that mass is uniformly distributed or that the body has little tendency to rotate around two different axes simultaneously. This is also due to the movement considered here, viz., trunk flexion in the sagittal plane. It can thus be concluded that the matrix calculated by the software is consistent with the rigid body for the legs and the movements it performs.

4.1.2 The Simcenter Amesim body model

The sketch shown in Figure 6 represents the whole human body in the Simcenter Amesim environment.

From the bottom (i.e., the system ground connection), the main components are:

• zero velocity source: in Simcenter Amesim this is called zerospeedsource3D, and represents the system ground connection;

• pilot operated hinge: shown in Figure 6 with ankle joint and hip joint;

• table: this component, called dynamic time table in Simcenter Amesim, is used to interpolate data in the form of a table;

• sign inversion: in Simcenter Amesim, sign inversion reverses the sign of the data received as input;

• conversion into angular displacement and velocity signal: called null to rotary velocity and displacement units in Simcenter Amesim, this component converts a dimensionless signal into a dimensional signal;

• rotating damper spring: in Simcenter Amesim, this is called a rotary spring damper and is used to provide torque to the piloted hinges;

• zero force source: used to close the ports of the components that are not connected. As explained, analyzing model. A calls for the use of two subsystems, one for the legs and one for the upper body, from the trunk up to the head (hereinafter referred to as the trunk for convenience). The two subsystems are joined by a hinge corresponding to the hip joint, while the legs are connected to the floor through an additional point corresponding to the ankle.

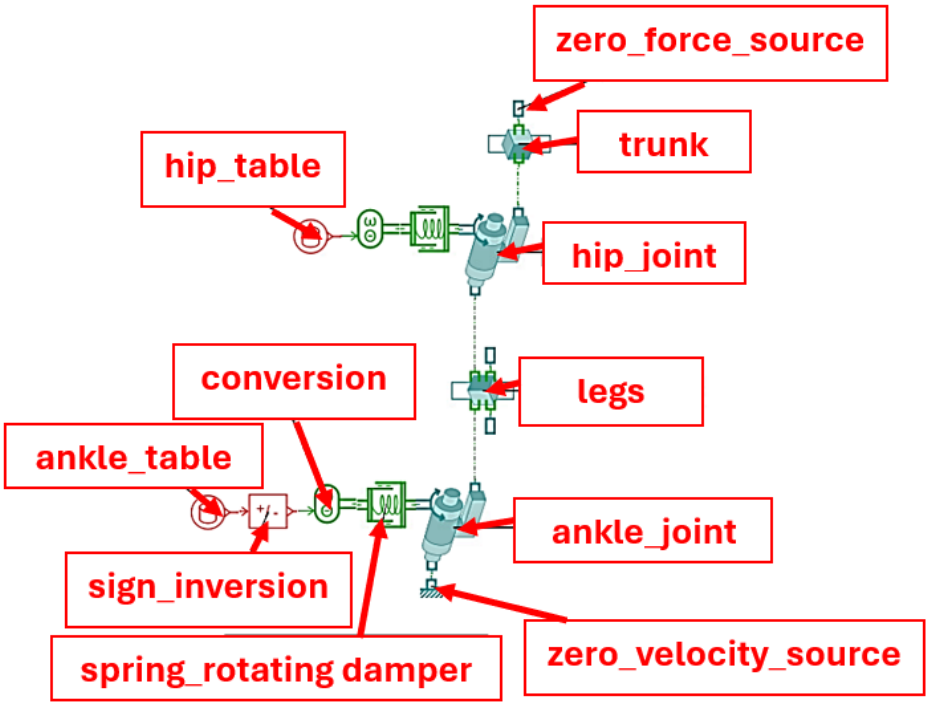
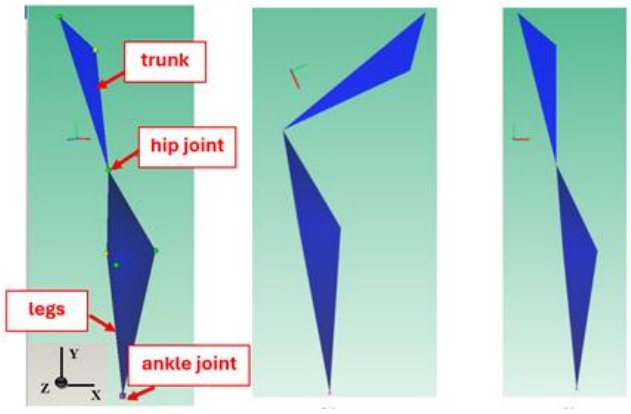


Figure 6 Sketch of the body simulated in Simcenter Amesim.

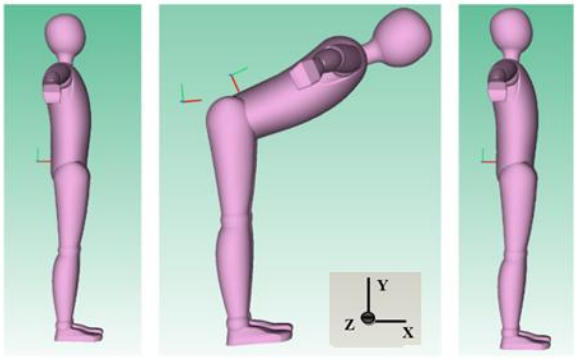
4.1.3 Trunk movement simulation

The body appears as two geometric figures, with the two rigid bodies for the legs and the trunk in blue. The geometric figures thus depend on the location of the center of mass and the location of the connecting ports (Figure 7a). Figures 7 show the video frames for the three main instants, showing how the body moves exactly as expected, i.e., with the trunk flexing forward and the legs bending backwards. The two joints that permit these movements also function correctly. The 3D body model provides a more realistic representation of body movements, as can be seen from the video frames for three different moments shown in Figure 7b.



a) b) c)

Figure 7a Trunk movement simulation in Simcenter Amesim (a) t = 0 s, b) t = 30 s, c) t = 60s) (model A).



a) b) c)

Figure 7b Trunk movement simulation with CAD human body model A (a) t = 0 s, b) t = 30 s, c) t = 60s).

In conclusion, simulations of the body model without the exoskeleton yielded the expected results, first because the body actually moves according to the setup, and also because total muscle torque at the hip is in line with the model. Torque is null when the body is upright, and reaches its maximum value when the trunk is in the position with the greatest bending angle. The hip joint was simulated using a rotary spring damper selected from the Simcenter Amesim library. In this simulation, the default values for the stiffness of the rotary spring in the ankle joint and the stiffness of the rotary spring in the hip joint were changed to 1010 Nm/degree, yielding acceptable torque values and trends for simulating muscle action. Figures 8a and 8b show trunk and leg joint angular displacements versus time. The graphs confirm that the body moves correctly in the right direction.

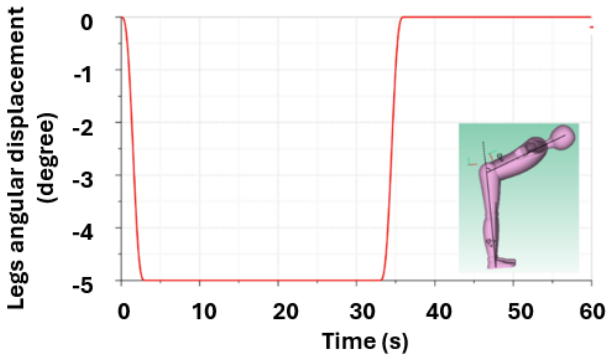


Figure 8a Leg angular displacement.

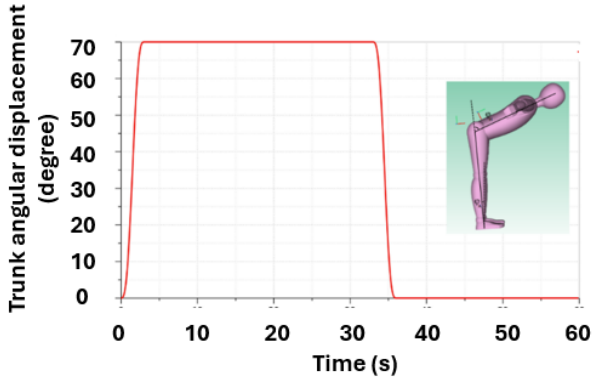


Figure 8b Trunk angular displacement.

The graphs for the trunk and the legs differ in the direction of the displacement and, consequently, the speed in order to simulate the fact that the legs bend backwards to balance body weight as the trunk bends forward. Figure 9a shows the main angles involved in these considerations. The angular displacement curves for the case where the modeled subject A is not wearing the exoskeleton are clear from Figure 9b, where it can be seen that the inflection point of the displacement occurs at x = 1.5s and y_1 = 35°, while the resulting maximum velocity at 1.5s is 7.8 rpm. These simulation results were compared with earlier theoretical and experimental results obtained by the authors on a subject without exoskeleton in the DIMEAS laboratory [12, 13] as shown in Figure 9c. Specifically, in this case the maximum bending angle of the trunk is 65° instead of 70°. The small difference between the simulation (Figure 9b) and theoretical/experimental results (Figure 9c) may be due to the different inertial properties of the human body involved. As can be seen, the two studies are in good agreement, as the angular values, behavior and time are quite similar. The graph of total muscle torque at the hip considers the z-axis torque at one of the hip ports. The hip joint was considered to be exactly centered between the two hips as shown in Figure 10, where an anatomical detail is overlaid on the body model. This location was chosen to simplify the simulation from the computational standpoint.

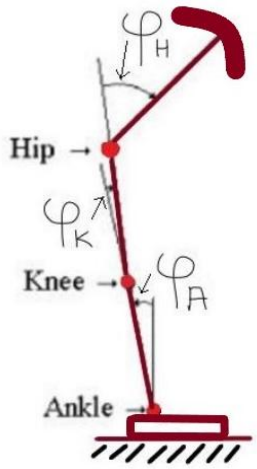


Figure 9a Details of the angles discussed in the text.

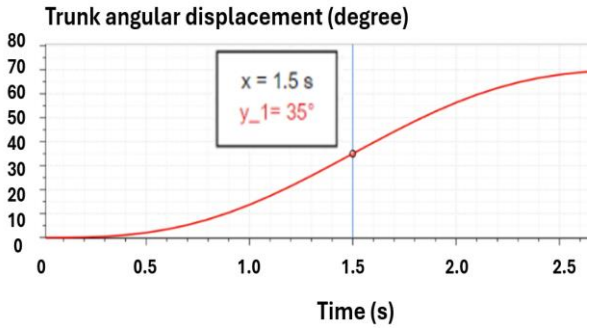


Figure 9b Trunk angular displacement obtained in Simcenter Amesim.

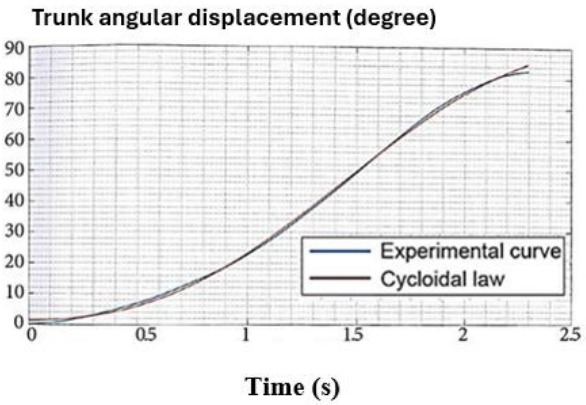


Figure 9c A previous comparison between the theoretical and the experimental cycloidal law of trunk flexion [12].

For this reason, the muscle torque at the hip is the total for both joints. This is also useful because the torque that must be input to the motor is the same for the two parts of the exoskeleton, so a single torque must also be calculated at the hip. Plotting total muscle torque at the hip was essential, as the simulation with the body model alone served specifically to visualize three-dimensional movement.

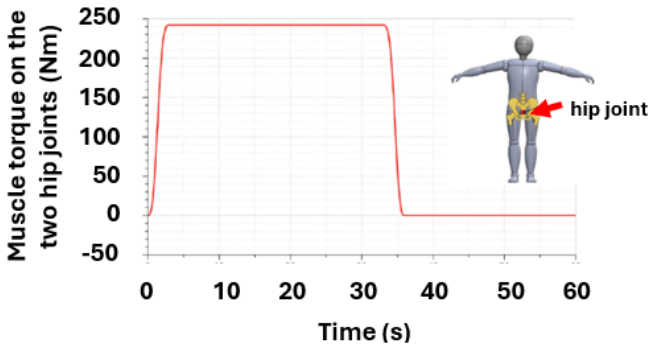


Figure 10 Simulated muscle torque on the two hip joints.

4.2 BODY MODEL B

Given the importance of the inertia matrix, the authors constructed a second human body model in a CAD environment (SolidWorks 2022) on the basis of data from the literature and ISO 7250-2 [33-35]. This model was then uploaded to Simcenter Amesim to compare its inertia matrices with those found with the first model. This second CAD human body model is shown in Figure 11a [30, 32-35], while its configuration in Simcenter Amesim is shown in Figure 11b.

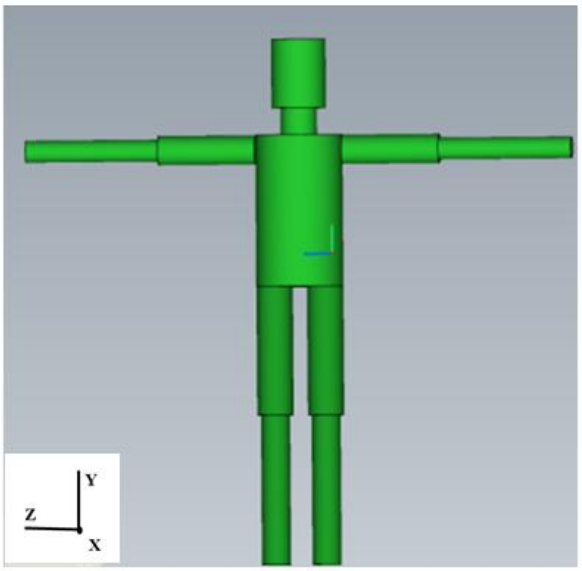


Figure 11a CAD human body model B imported into Simcenter Amesim [32, 33].

4.2.1 Inertia properties

Figure 12 shows the dynamic free body diagram of the wearer's trunk during movement. The arms are considered to be in abduction. It should be noted that the muscle torque on the hip joint is reduced by the inertial effects. During the trunk exoskeleton design process, it could thus be useful to analyze the static condition with the trunk flexed, as this makes it possible to examine a higher hip joint torque. The trunk and the leg matrices of the first and the second body models are shown in Figures 13a and 13b respectively. Values are expressed in kgm^2.

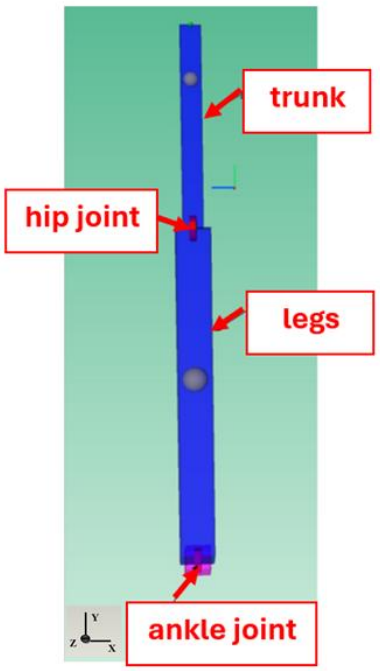


Figure 11b Human body model B in the Simcenter Amesim configuration.

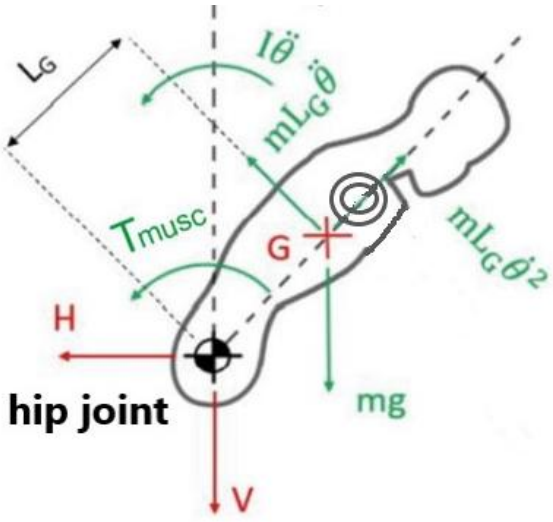


Figure 12 Dynamic free body diagram of the wearer's trunk [12].

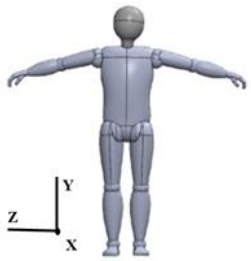
Table II shows the length of the main parts of this human body model (95%ile adult Italian male) [32-35].

Table II - Lengths of main model parts

Human part	Length (m)
Leg and foot	0.52
Thigh	0.45
Trunk	0.53
Head	0.24
Neck	0.09
Forearm	0.34
Arm and hand	0.46

The diagonal values are very similar because they are the body's main moments of inertia, which depend on the distribution of mass and shape which is very similar in the two cases.

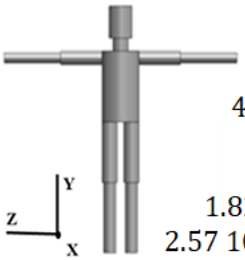
By contrast, the off-diagonal values are clearly different because they are moments of inertia of the products with respect to pairs of different axes and can vary depending on the distribution of the mass. For human body model B, products of inertia Ixy and Iyz are zero, meaning that there is no correlation between the distribution of mass along a certain axis and rotation around the other axis. This is to be expected because the mass distribution is symmetrical to the x and y axes and with respect to the y and z axes. The value of the inertia product Ixy is not exactly equal to 0, but is a very small infinitesimal (Figures 13b). In Figures 13, the diagonal values for the legs, unlike those for the trunk, differ for the two bodies. A further discrepancy between models A and B concerns the assembly. Model B features regular geometries, i.e., two cylindrical shapes respectively representing the trunk and leg subsystems, and connected by the hip joint hinge (Figure 11b). The legs' center of mass (grey dots in Figure 11b) is exactly in the center, as the legs are perfectly equal and symmetrical with no part having greater mass. For the body, the center of mass is somewhat higher because of the presence of the arms. A comparison was carried out between the model A and the model B, designed with regular shapes using the software SolidWorks 2022 and following the data provided by the standards [33-35]. The inertia matrices of this model's trunk, head, arms and legs were then compared with those for model A. The values, expressed in kgm^2, show similarities along the main diagonal of the matrices' trunk and significant differences off the diagonal. The leg matrices, however, are entirely different because of the discrepancies between the two models' volumes and masses. Moreover, unlike model A, in this case no connection ports were added at the knees because they need not be connected with the exoskeleton leg-links. To compare the total muscle torques at the hip for the two human body models, a sketch was also created for model B. As can be seen from the simulated torque curves in Figure 14, maximum torque with model B is lower than that obtained with the more realistic model, probably because of the different positions of the two models' centers of mass.



$$\begin{matrix} 5.77 & 0.14 & -0.12 \\ 0.14 & 3.29 & 0.02 \\ -0.12 & 0.02 & 2.87 \end{matrix}$$

$$\begin{matrix} 3.39 & -0.07 & -0.01 \\ -0.07 & 0.53 & 0.04 \\ -0.01 & 0.04 & 3.01 \end{matrix}$$

Figure 13a CAD human body model A and its inertia matrix in Simcenter Amesim [31].



$$\begin{matrix} 6.17 & 4.86\ 10^{-17} & 0.36 \\ 4.86\ 10^{-17} & 3.82 & 0 \\ 0.36 & 0 & 2.93 \end{matrix}$$

$$\begin{matrix} 1.82 & 2.57\ 10^{-16} & -0.02 \\ 2.57\ 10^{-16} & 0.2 & 2.77\ 10^{-17} \\ -0.02 & 2.77\ 10^{-17} & 1.66 \end{matrix}$$

Figure 13b CAD human body model B and its inertia matrix in Simcenter Amesim [32-35].

A further comparison can be based on the torque calculated from the free body diagram with the hip joint as the pole. Here the maximum total muscle torque at the hip was approximately 266 Nm [12]. This is very close to the approximately 240 Nm torque obtained with model A, and thus much lower than the theoretical value, due to the fact that the distance between the center of mass and the pole is probably different in the two cases, and also because in the theoretical case, the displacement of the center of mass during the movement was not considered to be flexion. In any case, the difference between the two maximum torques could be due to the different trunk inertia matrices for models A and B and how they interact with the muscle torque calculation, as shown in the dynamic free body diagram in Figure 12: a lower inertia effect (Figure 13a) yields a higher hip joint torque (Figure 14) referred to the model A. In the end of the paper the Table III illustrates a summary on the results and considerations obtainable about the maximum torque values.

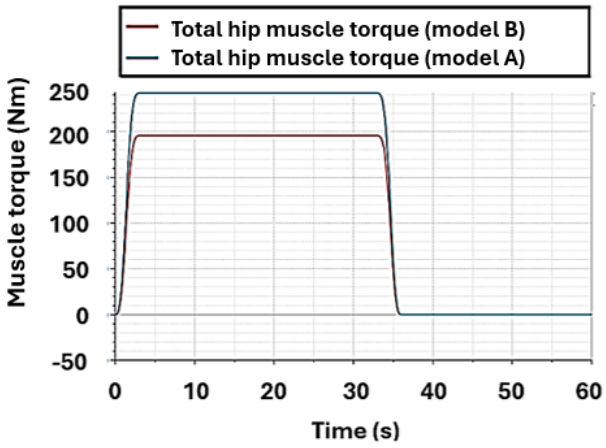


Figure 14 Some preliminary simulation results.

As inertial properties are very important for correct simulation and subsequent control system design, information for this purpose was gleaned from the literature [16, 18-29]. In [18], for example, a male subject with a height of 1.74 m, body mass of 74 kg and a trunk mass of 34.66 kg was analyzed. Mass moments of inertia were

calculated with the human body bending forward about the vertical axis with the arms extended. The trunk's moment of inertia calculated on a vertical axis passing through the chest was found to be 2.17 kgm^2, with a distance of 0.23 m between the trunk's center of mass and the shoulder joint. This value can be compared with the I_{yy} moment of inertia from the trunk matrices presented here, considering the vertical y axis and calculated during simulation (3.29 kgm^2 for body model A, 3.82 kgm^2 for model B). Taking the subjects' differing characteristics into account, the simulation result can be regarded as entirely satisfactory. In [19], a mathematical model of the human body was used to determine the mass inertial parameters of different body segments. Mass moments of inertial were calculated for a standing position with the arms hanging naturally at the sides. The model consists of 16 segments representing head + neck, upper, middle and lower torso, thigh, shank, foot, upper arm, lower arm and hand, all assumed to be relatively simple geometrical bodies. Full body symmetry with respect to the sagittal plane was assumed, and the geometrical data were taken from an anthropological investigation of the Bulgarian population [36] which measured a total of 2435 males. The average values were used to design a model representing the average Bulgarian male. For an average subject having a body mass of 98.5 kg and a height of 1.90 m, the trunk moment of inertial on the vertical axis was 1.37 kgm^2. As recent studies [16, 17] have used computer vision and techniques such as Human Mesh Recovery (HMR) in calculating the inertia properties of the upper body, the authors plan to investigate using these tools to verify the reliability of their human body models in the future. Several tasks were analyzed in the computer vision study [16]. In the first task, the person stood straight up, then flexed his elbows all the way up and then down, until returning to the neutral posture. The process was repeated three times. The second task was a shoulder rotation.
The participant stood with his upper arm abducted parallel to the ground and elbows flexed at 90° with the palms open. He then rotated his upper arm until his fingers were pointing upwards. Subsequently, the rotation was then reversed until the participant's fingers were pointing to the ground and then returned to the initial position. This task was repeated three times.

5 THE FULL MODEL

The exoskeleton model is a series of rigid bodies hinged to the two bodies representing the trunk and legs to simulate the device's interaction with the wearer's body. Input consists of the angular displacements at the hip hinge and ankles described in the previous section, plus the torque to be supplied to the motor, calculated as 30% of the total muscle torque and represented in Figure 14, where it is plotted versus time on the x-axis. This torque is transmitted to the two components that simulate the motor and divided between the two driving pulleys of the backframe and leg-link drive pulleys. For brevity only the case of the model A wearing the exoskeleton was here presented (Figure 15a). In the simulation with body model A, the stiffness of the rotary spring was 1010 Nm/degree; the stiffness of the rotary spring in the hip joint was also 1010 Nm/degree, while initial belt tension was 50 N, and belt stiffness per unit length was 17000 N/m. Tests carried out with model A wearing the simulated exoskeleton are described in detail below. The exoskeleton imported as assembled in CAD software was added to the human body model and the relative movements of all components were defined (Figure 15b). The imported CAD model features the ports described earlier, and all joined parts move together.

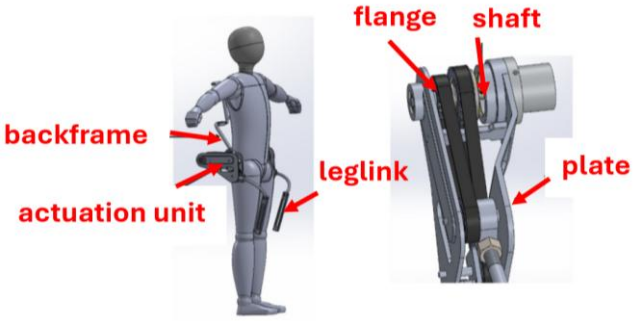


Figure 15a CAD model A and the exoskeleton with details of the actuation unit.

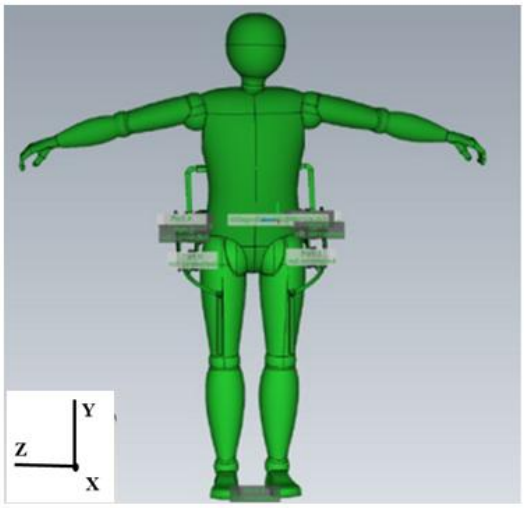


Figure 15b CAD model A with the exoskeleton (Simcenter Amesim environment).

Figure 16 shows the sketch of the operator wearing the exoskeleton. The actuation units were simulated by means of a sketch with the left and right actuation unit models. The exoskeleton model (Figure 16) consists of right/left flange, backframe drive pulley, backframe, reducer, counterplate, right/left shaft, right/left leg-link pulley, right/left plate, right/left leg-link, and right/left leg-link pulley. The two actuation units were connected by means of the wearer's trunk, the backframe, the legs, and the ankle joint. Each motor received 30% of the maximum hip muscle torque. Motor torque was reduced from maximum

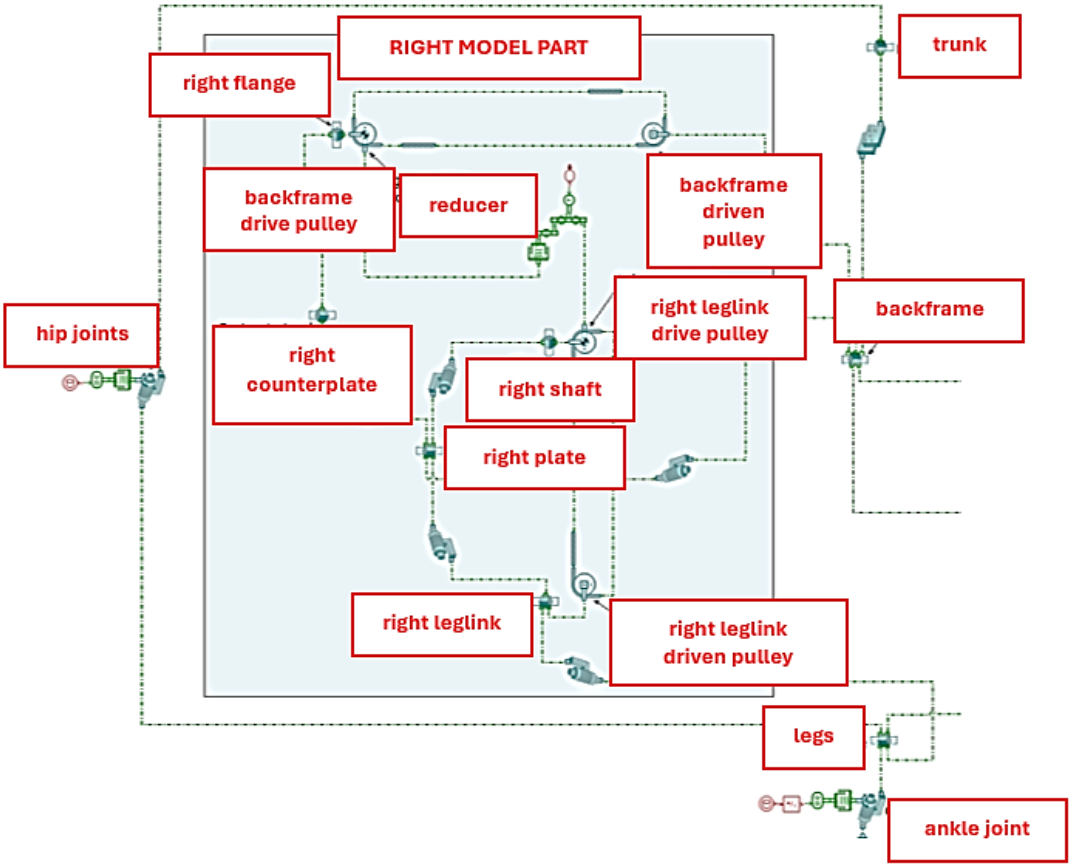


Figure 16 Simcenter Amesim sketch of the wearer and exoskeleton.

by a gain block, and delivered by a transmitter block. The main components simulating the motor include the reducer and a rotary spring providing torque to the backframe and leg-link drive pulley. The blocks representing the belt drives were then created. In these blocks, the drive pulleys have their own inertia parameters with a structure providing motor torque on the inlet port and the pulley velocity on the outlet port. The driven pulleys' angular velocity is delivered by the port connected to the backframe and the leg-link. As mentioned above, the main purpose of this simulation is to check that the total muscle torque at the hip is 70% of that calculated with the human body model alone, given that the exoskeleton serves to reduce muscle fatigue.

6 PRELIMINARY SIMULATION RESULTS

The assembled bodies can now be visualized to understand how they move relative to each other and whether the simulation leads to correct flexion as provided in input. The rigid bodies are seen as different geometric figures based on the location of the center of mass and ports (Figures 17 a, b, c). Total muscle torque at the hip, in this case, is influenced by the stiffnesses provided to the rotary spring component as well as by the drive belts' initial tension and stiffness. For example, increasing initial belt tension increases the maximum torque, which would thus exceed what it should be for the exoskeleton to actually reduce the wearer's muscle fatigue. An average value of the maximum torque on each hip joint in the case of the wearer (model A) with full exoskeleton is about 88 Nm. It is interesting to see what angles are assumed by the exoskeleton components as they move together with the wearer's body.

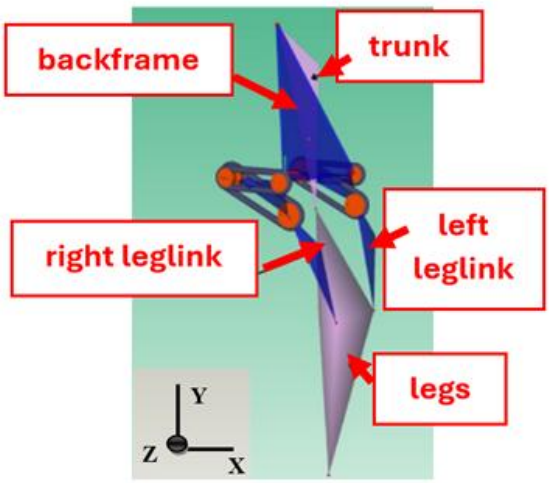


Figure 17a Simcenter Amesim model A of the wearer with exoskeleton and actuation units (side view).

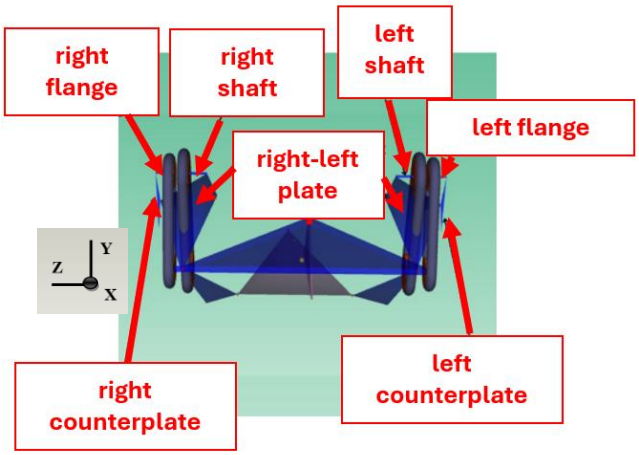


Figure 17b Simcenter Amesim model A of the wearer with exoskeleton and actuation units (top view).

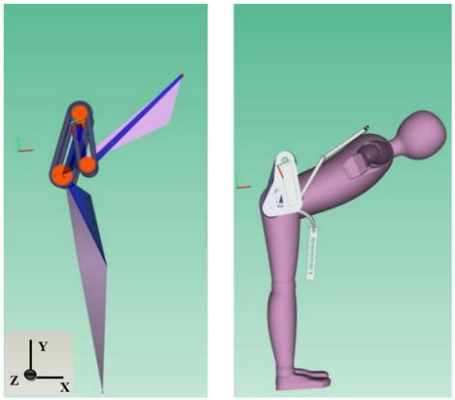


Figure 17c Simcenter Amesim model A of the wearer with full exoskeleton. Right: CAD representation.

Figure 18a shows leg-link angular displacement, while Figure 18b shows backframe angular displacement. The latter in particular is in good agreement with previous experimental studies [11, 12]. The negative sign is due to the clockwise rotation imposed to the motor. The backframe angular displacement curve takes into account instants with non-constant velocity, and thus with accelerations as shown in the dynamic free body diagram in Figure 12.

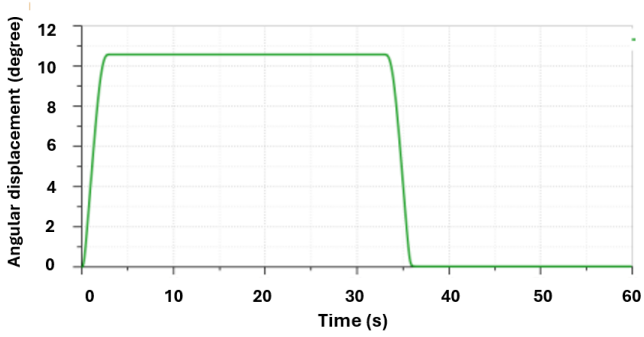


Figure 18a Leg-link angular displacement.

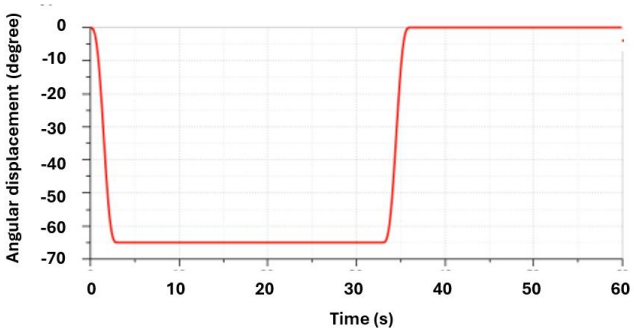


Figure 18b Backframe angular displacement.

7 COMPARISON WITH PREVIOUS MODELS BY THE AUTHORS

In earlier work, the authors modeled a human trunk wearing this exoskeleton using Matlab (2020 version) and Simulink (2020 version) software [12, 13]. This model was based on the trunk dynamic free body diagram (Figure 12) and its dynamic equilibrium. Figure 19a shows this model. The model consists of the wearer's trunk, the control system for each pneumatic motor with its proportional solenoid valve, and an angular position input for speed and acceleration. The control system must ensure correct exoskeleton function as the wearer's trunk bends forward, is held in the forward position, and returns upright. The control system is designed so that the motor delivers 30% of maximum muscle torque. Position and temperature sensors are also provided. The red circle indicates the pneumatic motor, whose extended model is illustrated in Figure 19b. In general, this control system must guarantee that the angular position, angular velocity and angular acceleration sensors are read correctly together with the physiological torque in play at all times, and that the motors for each hip joint are appropriately controlled. In addition, control logic must be simple and parts must be lightweight so as not to burden the wearer. Control logic covers the four stages of exoskeleton operation, which include a stage controlled by a position sensor in which the mechanism is locked to support the trunk while the wearer bends forward in a stationary position. If the operator's trunk flexes less than 20°, trunk movement is considered along with that of the pelvis, while for flexion exceeding 20° the pelvis is considered rotated 20° from its position when the operator is standing and the trunk continues to bend forward up to a maximum of 70° from the vertical. In this stage, a speed sensor senses when the wearer's trunk is bent forward and stationary, and activates the actuation group to generate the torque needed to support it. When the speed sensor senses that the wearer's trunk begins to return to the upright position, the control system acts to assist this movement. The model used in an earlier study to investigate the trunk flexion system is illustrated in Figure 19b, which shows the reducer i_rid, the motor characteristic, the correction factor, and torque feedback T_{FB}.

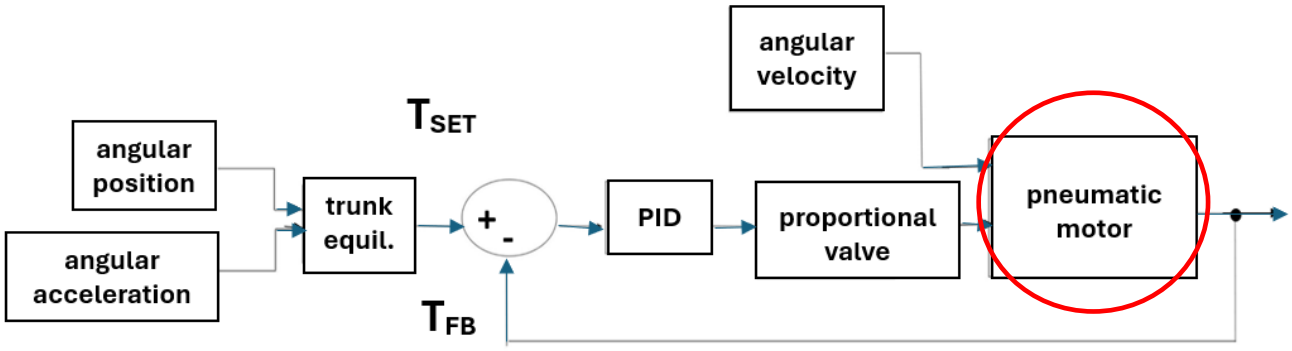


Figure 19a The authors' previous model of the entire "wearer + exoskeleton + pneumatic motor control" system [13].

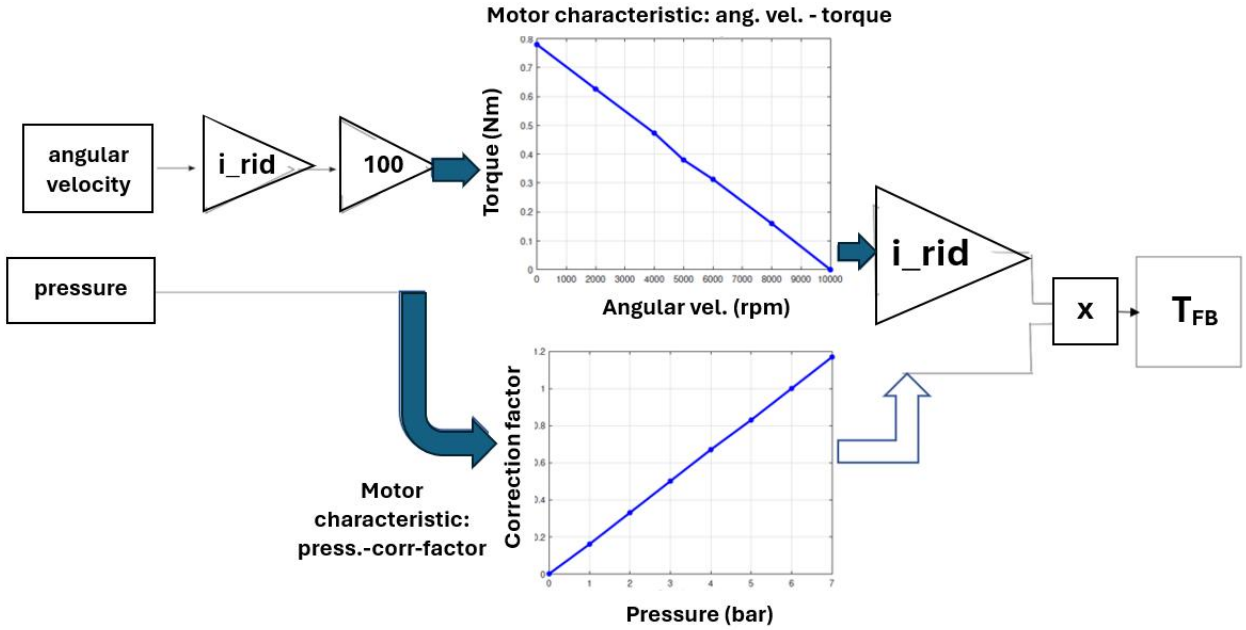


Figure 19b The authors' previous model of the exoskeleton actuation unit (pneumatic motor) [13].

As shown in the figure, this model controls the actuation unit using two graphs (supplied by the motor manufacturer) of motor torque versus angular velocity and of the motor correction factor versus pressure. The "i_rid" block shown before and after these characteristic curves simulates the harmonic drive used in each actuation unit, which reduces the angular velocity but increases torque by a factor of 100. Each pneumatic motor, which generates 30% of the maximum muscle torque to support the wearer's trunk, is controlled via an electro-pneumatic proportional valve.

As explained in [12,13] the pneumatic control circuit can be essentially made of a pneumatic source, a filter, a proportional valves, the air motor. The discharged of the air motor can be stopped during the operator's trunk flexion stable phase, in order to sustain it for all the time required. Figure 19c shows a possible layout of this pneumatic control system, where: (1) is the pneumatic source; (2) is the filter; (3) is a control direction flow valve 4/2; (4) is a manometer; (5) is a proportional valve; (6) is the air motor. In this scheme the components (3) and (4) are only useful for experimental tests carried out in laboratory. In it there are: source (1); a filter (2); a control direction flow valve 4/2 (3); a manometer (4); a proportional valves (5); the air motor (6).

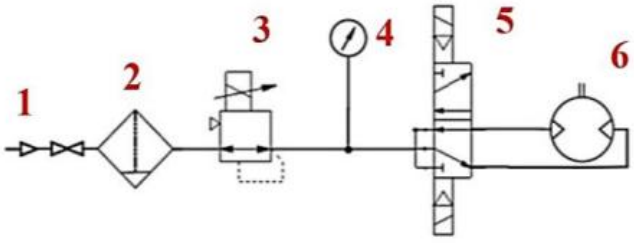


Figure 19c A possible layout of the pneumatic control system [12,13].

The choice of a pneumatic actuation has been made for the advantages it offers, such as: high power-to-weight ratio, possibility to work in dirty and explosive atmospheres, greater comfort and safety, linked to the compressibility of the air. The pressure output of the proportional valve is obtained by varying its input voltage from 0 to 10 V, producing a maximum pressure of 6 bar (1 bar = 10^5 Pa) to power the pneumatic motor. Each pneumatic motor is driven by a PID controller, where proportional (k_P) and integrative gains (k_I) equal to k_P = 0.8 and k_I = 5 ensure system stability and accuracy. Figures 20 show the torque on the total hip joints obtained in the various simulations.
Figure 20a shows the torque obtained through the simulation. The figure compares the feedback torque signal from the air motor (T_{FB}) and the set muscle torque (T_{SET}). The two curves are very similar, with practically negligible error. This error has two peaks as the wearer's trunk flexes forward and returns upright. In any case, error is minimal and causes no disturbance in system operation. In particular, proportional valve control voltage rises to a maximum when the trunk is at maximum flexion, when maximum torque is required. The supply pressure of each air motor also increases along with proportional valve control voltage. The torque designated as T_{SET} in Figure 20b was the torque on the hip joint obtained from the dynamic trunk equilibrium and equal to the 30% of maximum muscle torque. Its behavior and maximum value is in good agreement with the corresponding torque in Figure 20c, demonstrating that the two models using different structures and software packages function correctly. The few differences between maximum torques may be due to the inertia parameters used in the models, which were taken directly from the Simcenter Amesim inertia matrices in some cases, and from the trunk free body diagram and from the trunk dynamic equilibrium in others. As the hip joint torque value and curve demonstrate, the new models presented here and earlier ones are comparable. This is encouraging, both as a preliminary validation of the new model and in terms of being able to use two different but equally valid models.

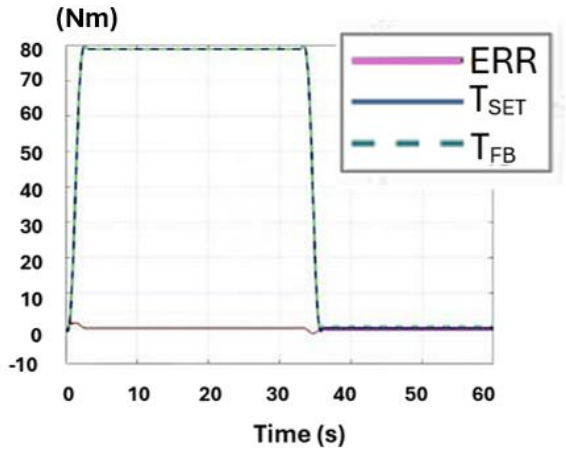


Figure 20a Torque curve and error obtained from the previous model [13].

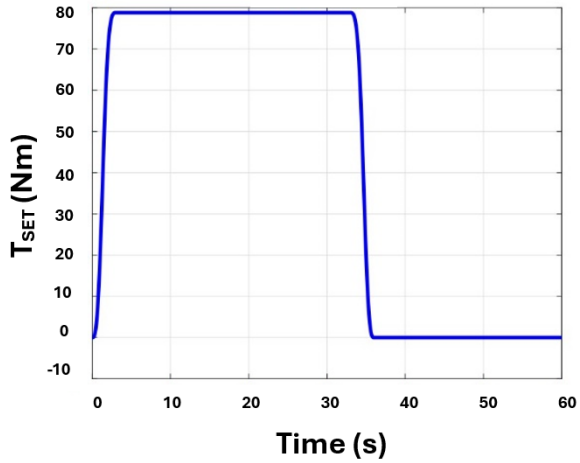


Figure 20b Motor torque curve from the previous model[13].

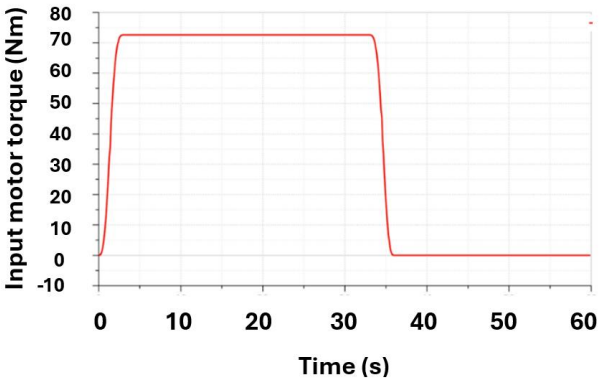


Figure 20c Motor torque curve from the Simcenter Amesim wearer and exoskeleton model.

Table III - A summary on the maximum torques values obtained on each hip joint

Maximum torque	Numerical value (Nm)
Operator without exoskeleton (human model A, Simcenter Amesim enviroment)	123
Operator without exoskeleton (human model B, Simcenter Amesim enviroment)	98
Wearer (model A) with full exoskeleton (Simcenter Amesim environment)	72
Wearer (equilibrium from free body diagram) with full exoskeleton (Matlab and Simulink 2020 environment)	79

Table III illustrates a useful comparison among the various maximum torques values obtained in the presented studies.The differences among the various maximum torque values could be attributed to the different inertial matrices constructed in Simcenter Amesim referring to the two human models (A and B) proposed in the literature [32] without exoskeleton. The addition of this one increased the

inertia torque in this phase of trunk flexion and acceleration downwards, reducing the torque required on each hip joint. A similar situation arises in the case of a model in Matlab-Simulink 2020 environment. This can precisely confirm the inertial effect linked to the presence of the exoskeleton.

8 CONCLUSIONS

The evaluation of inertias is a fundamental aspect in the design of exoskeletons and their control systems. In this paper the author aims to present a particular study on the inertias of the upper body, using various CAD models, made according to literature and examining the inertial aspects both in the case of the body alone and in the case of the operator wearing an exoskeleton. So the simulation presented here made it possible to evaluate the behavior of an exoskeleton in interaction with the human body during flexion and extension, and when standing while bent forward. The results verified that the exoskeleton performs its intended purpose by evaluating the total muscle torque at the hip, which was 30% less than that obtained during body flexion and extension without the device. The results obtained were appropriately compared with similar studies present in the literature and the comparison always gave satisfactory results. A comparison with earlier numerical models of the "wearer + exoskeleton" system yielded good results and shows that all the models are reliable. This also provides various types of models and simulation possibilities with different software also useful for future studies with other types of exoskeletons. The study carried out by the author can produce an interesting method of study on this argument. Such models and analyses can also be useful for ergonomic considerations. Future work will focus on optimizing the motor model, for example by using the Simcenter Amesim pneumatic library, designing the control system, optimizing the drive system through detailed studies of the friction coefficients between the belt and pulley, elongations and tensions, and on using new AI-based tools such as computer vision and Human Mesh Recovery for experimental inertia analysis. Currently, many studies on the topic are conducted with various AI software, also based on the human body pose estimation. Other work currently centers on calculating mass moments of inertia for comparison with those presented here in order to improve Simcenter Amesim simulations. In the future it may be possible to evaluate the possibility of setting up models that are also useful for understanding the actual interaction between the human body and the exoskeleton and the stresses that it produces on the body itself. Further studies are underway by the authors to deepen the calculation of the inertia matrix in SimCenter Amesim, analyzing various positions of the human body and comparing the results obtained with appropriate literature papers where similar subjects and positions are examined.

ACKNOWLEDGEMENTS

The author would like to thank Prof. Terenziano Raparelli, BSIM Italy (Turin, Italy) and Eng. M. Ancona for their help during this study.

REFERENCES

[1] Pons J.L., *Wearable robots: biomechatronic exoskeletons*. Vol. 70. Wiley Online Library, 2008.

[2] Belforte G., Eula G., Appendino S. and Sirolli S., Pneumatic Interactive Gait Rehabilitation Orthosis: design and preliminary testing. *Proc. of the Institution of Mechanical Engineers, Part H: Journal of Engineering in Medicine*, Vol. 225, No. 2, pp. 158-169, 2011.

[3] Harman E. A. and Frykman P. N., Heavy load carriage performance correlates: backpack vs individual towed trailer. *Medicine & Science in Sports & Exercise*, Vol. 27, No. 5, S136, 1995.

[4] Christensen S., Rafique S. and Bai S., Design of a powered full-body exoskeleton for physical assistance of elderly people. *International Journal of Advanced Robotic Systems*, Vol. 18, No. 6, pp. 1-15, 2021.

[5] Belforte G., Eula G., Sirolli S., Appendino S., Geda E., Geminiani G., Zettin M., Virgilio R. and Sacco K., Control curves for a new lower limbs robotic exoskeleton obtained from the study of joints angles during an unloaded human walking. *International Journal of Mechanics and Control (JoMac)*, Vol. 18, No. 01, pp. 3-14, 2017.

[6] Belforte G., Raparelli T., Eula G., Sirolli S., Appendino S., Geminiani G.C., Geda E., Zettin M., Virgilio R. and Sacco K., Study and realisation of a preliminary control system for the active exoskeleton called P.I.G.R.O., suitable for unloaded robotic neurorehabilitation treatments. *International Journal of Mechanics and Control (JoMac)*, Vol. 22, No. 01, pp. 125-142, 2021.

[7] Belforte G. and Eula G., Design of an active-passive device for human ankle movement during functional magnetic resonance imaging analysis. *Proc. of the Institution of Mechanical Engineers, Part H: Journal of Engineering in Medicine*, Vol. 226, No. 1, pp. 21-32, 2011.

[8] Wu Q., Wang X., Du F. and Zhang X., Design and control of a powered hip exoskeleton for walking assistance. *Int. Journal of Advanced Robotic Systems*, Vol. 12, No. 18, p. 1-12, 2015.

[9] Hara H. and Sankai Y., Development of HAL for lumbar support. *SCIS & ISIS 2010 - Joint 5th Int. Conf. on Soft Computing and Intelligent Systems and 11th International Symposium on Advanced Intelligent Systems*, December 8-12th Okayama Convention Center, Okayama Japan, pp. 416–421, 2010.

[10] Abane A., Guiatni M., Ababou N., Amine Alouane M. and Bouzid Y., Mechatronics Design and Control of a Transformed Upper Limb Rehabilitation Exoskeleton. *International Journal of Mechanics and Control (JoMac)*, Vol. 21, No. 01, pp. 75-90, 2020.

[11] Raparelli T., Eula G., Mazza L., Ivanov A., Pietrafesa F., Mala R. and Pontin M., A preliminary prototype of an industrial exoskeleton for the operator's trunk support. *International Journal of Mechanics and Control* (*JoMac)*, Vol. 23, No. 02, pp. 37-52, 2022.

[12] Raparelli T., Eula G., Mazza L., Ivanov A., Pietrafesa F., Mala R. and Pontin M., The design of an innovative active exoskeleton prototype for industrial application with a pneumatic actuation. *International Journal of Mechanics and Control*, Vol. 23, No. 02, pp. 61-72, 2022.

[13] Raparelli T., Mazza L., Eula G. and Pietrafesa F., Sistema di controllo per un esoscheletro industriale ad azionamento pneumatico. *Oleodinamica Pneumatica, ed. Tecniche Nuove Italia*, December 2022, pp. 24-29, 2022.

[14] Raparelli T., Mazza L. and Eula G., Study concerning design and optimization of a multifunction actuation group for an industrial exoskeleton. *IFIT 2024 Politecnico di Torino (IFToMM Italy 2024)*, Turin, Italy, Vol. II, Chapter 1, MMS 164, 2024.

[15] Huysamen K., Power V. and O'Sullivan L., Elongation of the surface of the spine during lifting and lowering, and implications for the design of an upper body industrial exoskeleton. *Applied Ergonomics*, Vol. 72, No. 4, pp. 10-16, 2018.

[16] Menychtas D., Glushkova A. and Manitsaris S., Extracting the Inertia Properties of the Human Upper Body Using Computer Vision. *Computer Vision Systems* 12th International Conference, ICVS 2019, Thessaloniki Greece, September 23–25, Vol. 11754, pp. 596-603, 2019.

[17] Muhammad Z.U.D., Huang Z. and Khan R., A review of 3D human body pose estimation and mesh recovery. *Digital Signal Processing*, Vol. 128, No C, pp. 1-22, 2022.

[18] Krishnan R.H., Devnandh V., Brahma A.K. and Pugazhenthi S., Estimation of mass moment of inertia of human body, when bending forward, for the design of self-transfer robotic facility. *J. of Eng. Science and Technology*, Vol. 11, No. 2, pp. 166-176, 2016.

[19] Nikolova G. Kotev V. and Dantchev D., CAD design of human male body for mass-inertial characteristics studies. *NCTAM 2017, MATEC Web of Conferences*, Vol. 145, 04006, pp. 1-6, 2018.

[20] Drillis R., Contini R. and Bluestein M, Body segment parameters: a survey of measurement techniques. *Digital Resource Foundation O&P Library Artificial Limbs*, Vol. 8, No. 1, pp. 44-66, 1964.

[21] Bova M., Massaro M. and Petrone N., A three-dimensional parametric biomechanical rider model for multibody applications. *Applied Sciences MDPI*, Vol. 10, No. 13, pp. 1-25, 2020.

[22] Bogovic S., Stjepanovic Z., Cupar A., Jevsnik B., Regina-Car B. and Rudolf A., The use of new technologies for the development of protective clothing: comparative analysis of body dimensions of static and dynamic postures and its application. AUTEX Research Journal, Vol. 19, No. 4, pp. 301-311, 2019.

[23] Fan Y., Li Z. and Lv C., Calculation of mass and inertia moment of human body in motion by means of transformation matrix. *Proc. of SPIE, The International Society for Optical Eng*., Vol. 7128, pp. 1-8, 2008.

[24] Liu L., Cooper J.L. and Ballard D.H., Computational modeling: human dynamic model. *Frontiers in Neurorobotics,* Vol. 15, pp. 1-36, 2021

[25] Ma Y., Kwon J., Mao Z., Lee K., Li Linlin and Chung H., Segment inertial parameters of Korean adults estimated from three-dimensional body laser scan data. *Int. J. of Industrial Ergonomics*, Vol. 41, No. 1, pp. 19-29, 2011.

[26] Dodig M., Models and modelling of dynamic moments of inertia of human body. *International Journal of Sprots Science*, Vol. 6, No. 6, pp. 249-256, 2016.

[27] Paletta L., Santner K, Fritz G., Hofmann A., Londron G., Thallinger G. and Mayer H., FACTS—A computer vision system for 3D recovery and semantic mapping of human factors. *In: Chen, M., Leibe, B., Neumann, B. (eds) Computer Vision Systems. ICVS 2013. Lecture Notes in Computer Science ed. Springer, Berlin, Heidelberg*, Vol. 7963, pp. 62-72, 2013.

[28] Liang W., Inertia parameters of human body identification by using the inequality constraints derived from the dynamic equations. *Proceedings of the 2018 IEEE, Int. Conf. on Cyborg and Bionic Systems (CBS)*, Shenzhen China, 25-27 October, pp. 549-553, 2018.

[29] Robert. T., Leborgne P., Abid M., Bonnet V., Venture G. and Dumas R., Whole body segment inertia parameters estimation from movement and ground reaction forces: a feasibility study. *Computer Methods in Biomechanics and Biomedical Eng.*, Vol. 20, No. s1, pp. 175-176, 2017.

[30] https://bsim-engineering.com/

[31] https://grabcad.com/

[32] Herman I.P., *Physics of the Human Body.* Springer 2nd Edition, pp. 1-980, 2016.

[33] ISO 7250-1:2017 (Main) Basic human body measurements for technological design—Part 1: Body measurement definitions and landmarks, 2017.

[34] UNI EN ISO 7250-1:2010. Basic human body measurements for technological design—Part 1: Body measurement definitions and landmarks, 2010.

[35] UNI EN ISO/TR 7250-2:2010. Basic human body measurements for technological design—Part 2: Statistical summaries of body measurements from individual ISO populations, 2010.

[36] Izdatelstvo A., *Anthropology of the Bulgarian population at the end of the 20th century (30-40 years old persons).* ed. Yordanov Yordan, pp. 1-431, 2006.

ISSN 1590-8844
International Journal of Mechanics and Control, Vol. 26, No. 02, 2025
https://doi.org/10.69076/jomac.2025.0011

SIMPLIFIED MODEL FOR DYNAMIC ANALYSIS OF ROBOTIC MANIPULATORS

Andrea Cesaro* Matteo Bottin* Michele Tonan* Alberto Doria* Giulio Rosati*

* Department of Industrial Engineering
University of Padova, Italy

ABSTRACT

The dynamic analysis of robotic manipulators is a well-known problem, but very often the inertia tensors of the links are unknown and the computational complexity is high. This paper introduces a simplified approach, based on the use of a limited set of lumped masses placed along the joint axes, which provides an efficient and sufficiently accurate estimation of joint torques, linear momentum, and kinetic energy along a given trajectory. One of the main advantages brought by this approach is that its implementation does not require the knowledge of the inertia tensors of the links. Compared to traditional methods, the proposed approach offers a good balance between accuracy and complexity, since the normalized root mean square error (NRMSE) in kinetic energy is lower than 3% with a consistent reduction in computation time (8%). Therefore, it is a valuable tool for the design and control of robotic manipulators in a wide range of industrial and service applications. Moreover, the quick calculation of linear momentum and kinetic energy is useful for the prediction of collision severity. The detailed description of the proposed method is completed with numerical simulations dealing with three different robotic manipulators.

Keywords: robotics, lumped parameters, simplified model, dynamic equivalence

1 INTRODUCTION

Although the dynamic analysis problem for robotic manipulators is a well-known problem [6, 14], the development of simplified models makes it possible to describe the dynamic behavior of such systems with reduced complexity, with a reasonable degree of approximation. The use of lumped masses is based on the principle of dynamic equivalence [13, 17], an approach that makes it possible to obtain a lumped element rigid body that moves like a continuous rigid body when subjected to the application of the same force system. More specifically, two rigid systems are dynamically equivalent if they possess the same mass, location of the center of mass (COM), and inertia tensor [9]. This principle is applicable to rigid bodies having both two-dimensional and three-dimensional motions [3]. Theory concerning the study of dynamically equivalent systems is quite well known and was established more than a century ago by Routh [12] and is now applied in various fields such as planar mechanisms [11, 4] or biomedical robotics [7].

In planar motion, a rigid body is described by four lumped parameters as four conditions must be met: one for mass equivalence, two for COM equivalence, and one for moment of inertia equivalence. Moreover, if the masses can be placed along an axis passing through the COM, the number of lumped parameters can be reduced to three. On the other hand, in three-dimensional motion, a rigid body is described by ten lumped parameters, as ten conditions must be met: one for mass equivalence, three for COM equivalence, and six for inertia tensor equivalence. If the masses can be placed along the principal axes passing through the COM, the number of lumped parameters is reduced to seven. Other particular cases have been treated by Laus and Selig in [10]. Therefore, the real challenge is to efficiently apply this principle to three-dimensional mechanisms such as 6 and 7-axis robotic manipulators [5]. The resulting dynamic models are valuable in the field of traditional industrial robotics, in the field of flexible robots [8, 1], and in collaborative robotics applications. Estimating joint torques, linear momentum,

Contact author: Andrea Cesaro* E-mail: andrea.cesaro@unipd.it

and kinetic energy is crucial to evaluating the potential effect of collisions between robots and human operators.
This paper proposes a simplified dynamic model for robotic manipulators, similar to the approach presented in [2] for planar manipulators. The model is based on the Denavit-Hartenberg notation and satisfies the conditions for mass equivalence and COM equivalence while neglecting the inertia tensor equivalence condition. The method consists of positioning a limited number of lumped masses at predetermined positions along the joint axes. In this way, a simple equivalent system and a good approximation compared to the full dynamic model are achieved at the same time. This method can be applied to any industrial robot, although some limitations may arise if a precise dynamic model is required [16].
The paper is structured as follows. Section 2 introduces the mathematical model at the basis of the simplified approach, both the general case and some particular cases are dealt with. Section 3 describes its application to three different robotic manipulators: a 6-axis robot with spherical wrist, a 6-axis robot with 3 parallel axes, and a 7-axis robot with spherical shoulder and wrist. Section 4 shows simulation results. First comparisons between joint torques, linear momentum and kinetic energy predicted by the full and simplified models for a sample trajectory are made. Then the comparison between the two models is extended considering a random sample of trajectories. Finally, conclusions are drawn in Section 5.

2 MATHEMATICAL MODEL

An open chain robot manipulator composed of n links connected to the base and to each other by n single degrees of freedom joints is considered. In the full model, the mass of each link is concentrated in the COM and the inertia tensor describes the spatial distribution of the mass. Therefore, the inverse dynamics can be calculated through the following three steps with the Newton-Euler formulation [6], knowing the inertia properties of the links:

- calculate the velocities and accelerations of each body in the kinematic chain;
- calculate the forces and torques needed to produce these accelerations;
- calculate the forces transmitted through the joints by the forces acting on the bodies.

The i-th link of the robotic arm depicted in Figure 1 is considered. In the simplified model, we propose to replace the rigid link with two lumped masses m_{1i} and m_{2i} arranged in such a way to guarantee the position of the COM ($\boldsymbol{C}_i$) and the total mass M_i of the link whereas the inertia tensor equivalence is not guaranteed. Let the frames of the link i and $i+1$ and their origins O_i and O_{i+1} be chosen according to the Denavit-Hartenberg notation, we propose to position the mass m_{1i} along the z_i axis at a distance L_{1i} from O_i and the mass m_{2i} along the z_{i+1} axis at a distance L_{2i} from the intersection point between the axis z_{i+1} and the axis x_i. Therefore, the position of the center of mass $\boldsymbol{C}_i$ and the total mass M_i are maintained only if:

$$\boldsymbol{C}_i = \frac{m_{1i}}{M_i}\boldsymbol{r}_{1i} + \frac{m_{2i}}{M_i}\boldsymbol{r}_{2i} \tag{1}$$

$$M_i = m_{1i} + m_{2i} \tag{2}$$

where $\boldsymbol{r}_{1i}$ and $\boldsymbol{r}_{2i}$ are the position vectors of the two lumped masses with respect to O_i. By projecting equation 1 in system i and normalizing equation 2 to M_i we get:

$$\left\{ \begin{array}{c} x_{Ci} \\ y_{Ci} \\ z_{Ci} \end{array} \right\}_i = \mu_{1i} \left\{ \begin{array}{c} 0 \\ 0 \\ L_{1i} \end{array} \right\}_i + \mu_{2i} \left\{ \begin{array}{c} a_i \\ -L_{2i}\sin\alpha_i \\ L_{2i}\cos\alpha_i \end{array} \right\}_i \tag{3}$$

$$\mu_{1i} + \mu_{2i} = 1 \tag{4}$$

where $\mu_{1i} = \frac{m_{1i}}{M_i}$ and $\mu_{2i} = \frac{m_{2i}}{M_i}$ are the two normalized lumped masses, a_i and α_i are two DH parameters (as shown in Figure 1) and x_{Ci}, y_{Ci} and z_{Ci} are the coordinates of $\boldsymbol{C}_i$ in the i-th reference frame. From equations 3 and 4 we obtain the following equations

$$\left\{ \begin{array}{l} x_{Ci} = \mu_{2i}\, a_i \\ y_{Ci} = -\mu_{2i}\, L_{2i}\sin\alpha_i \\ z_{Ci} = \mu_{1i}\, L_{1i} + \mu_{2i}\, L_{2i}\cos\alpha_i \\ \mu_{1i} + \mu_{2i} = 1 \end{array} \right. \tag{5}$$

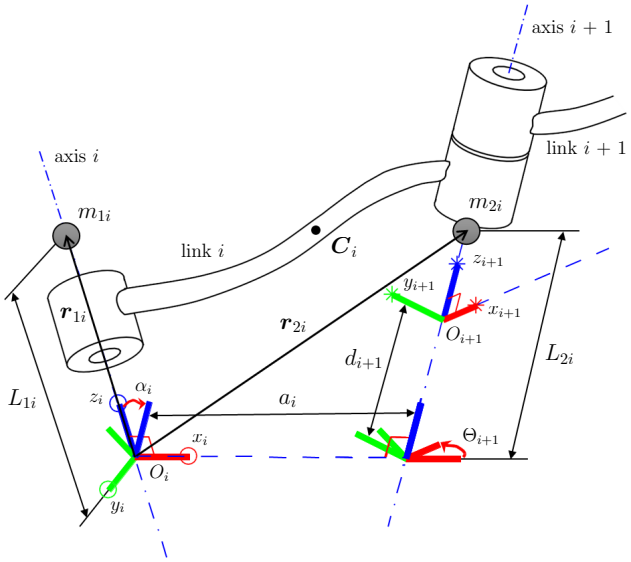


Figure 1 DH parameters of the i-th link of a robot manipulator and lumped masses m_{1i} and m_{2i}

which give the four unknowns (the position and the value of each lumped mass):

$$\begin{cases} \mu_{2i} = \frac{x_{Ci}}{a_i} \\ \mu_{1i} = 1 - \mu_{2i} \\ L_{2i} = -\frac{y_{Ci}}{\mu_{2i} \sin \alpha_i} \\ L_{1i} = (z_{Ci} - \mu_{2i}\, L_{2i} \cos \alpha_i)\, \frac{1}{\mu_{1i}} \end{cases} \tag{6}$$

This solution holds true only if $a_i \neq 0$ and $\alpha_i \neq k\pi$, where $k \in \mathbb{Z}$, i. e. the axes z_i and z_{i+1} are skew axes. Furthermore, since the parameters a_i and α_i reach up to $a_{n-1}$and α_{n-1} as per the DH notation, this solution can be applied up to the $(n-1)$-th link. Therefore, the lumped parameters of the n-th link, which includes the tool, must be calculated in a different way. For example, in the common case of a manipulator with a spherical wrist and axisymmetric tool, the first lumped mass can be positioned in the wrist center, the second at the tool tip.
Once the four unknowns have been assigned for each link, we can calculate the forces and moments applied on each link i of the system composed of the lumped masses:

$$\boldsymbol{F}_{1i} = \mu_{1i} M_i (\dot{\boldsymbol{v}}_{Oi} + \dot{\boldsymbol{\omega}}_i \times \boldsymbol{r}_{1i} + \boldsymbol{\omega}_i \times \boldsymbol{\omega}_i \times \boldsymbol{r}_{1i}) \tag{7}$$

$$\boldsymbol{F}_{2i} = \mu_{2i} M_i (\dot{\boldsymbol{v}}_{Oi} + \dot{\boldsymbol{\omega}}_i \times \boldsymbol{r}_{2i} + \boldsymbol{\omega}_i \times \boldsymbol{\omega}_i \times \boldsymbol{r}_{2i}) \tag{8}$$

$$\boldsymbol{f}_i = \boldsymbol{f}_{i+1} + \boldsymbol{F}_{1i} + \boldsymbol{F}_{2i} \tag{9}$$

$$\begin{aligned} \boldsymbol{n}_i = &\boldsymbol{n}_{i+1} + (O_{i+1} - O_i) \times \boldsymbol{f}_{i+1} + \\ &+ \boldsymbol{r}_{1i} \times \boldsymbol{F}_{1i} + \boldsymbol{r}_{2i} \times \boldsymbol{F}_{2i} \end{aligned} \tag{10}$$

where:

- $\boldsymbol{F}_{1i}$ and $\boldsymbol{F}_{2i}$ are the reaction forces applied by the link i on the lumped masses
- $\dot{\boldsymbol{v}}_{Oi}$ is the linear acceleration of the origin O_i
- $\boldsymbol{\omega}_i$ and $\dot{\boldsymbol{\omega}}_i$ are the angular velocity and acceleration of link i
- $\boldsymbol{f}_i$ and $\boldsymbol{n}_i$ are the force and the moment exerted on link i through joint i.

The joint torque τ_i of the link i can be calculated as follows:

$$\tau_i = \boldsymbol{z}_i \cdot \boldsymbol{n}_i \tag{11}$$

where $\boldsymbol{z}_i$ is the unit vector defining the direction of the i-th joint axis.
Estimating the linear momentum and the kinetic energy of the robot is important as well. The linear momentum $\boldsymbol{Q}$ of the system of lumped masses is given by:

$$\boldsymbol{Q} = \sum_{i=1}^{n} [\mu_{1i}(\boldsymbol{v}_{Oi} + \boldsymbol{\omega}_i \times \boldsymbol{r}_{1i}) + \mu_{2i}(\boldsymbol{v}_{Oi} + \boldsymbol{\omega}_i \times \boldsymbol{r}_{2i})] M_i \tag{12}$$

while the kinetic energy E_k is:

$$\begin{aligned} E_k = \sum_{i=1}^{n} \Big[&\mu_{1i} (\boldsymbol{v}_{Oi} + \boldsymbol{\omega}_i \times \boldsymbol{r}_{1i}) \cdot (\boldsymbol{v}_{Oi} + \boldsymbol{\omega}_i \times \boldsymbol{r}_{1i}) + \\ &+ \mu_{2i} (\boldsymbol{v}_{Oi} + \boldsymbol{\omega}_i \times \boldsymbol{r}_{2i}) \cdot (\boldsymbol{v}_{Oi} + \boldsymbol{\omega}_i \times \boldsymbol{r}_{2i}) \Big] \frac{M_i}{2} \end{aligned} \tag{13}$$

This model is approximated, because the inertia equivalence is not respected. Actually, the two lumped masses of each link generate an inertia tensor about the COM which is an approximation of the real inertia tensor. For this reason, the calculated linear momentum is equal in the full and simplified model, since it is independent of the inertia tensor, while the joint torques and the kinetic energy have a degree of approximation.

2.1 PARTICULAR CASES

When $a_i = 0$ and $\alpha_i = k\pi$ solution 6 is not valid. In this section, we address how the lumped parameters of the simplified model can be calculated in such cases.

2.1.1 Parallel axes

If $\alpha_i = k\pi$ the z_i and z_{i+1} axes are parallel and the COM of the lumped masses system belongs to the $x_i z_i$ plane. In this case, we rewrite the system 5 as follows:

$$\begin{cases} x_{Ci} = \mu_{2i}\, a_i \\ y_{Ci} = 0 \\ z_{Ci} = \mu_{1i}\, L_{1i} + \mu_{2i}\, L_{2i} \\ \mu_{1i} + \mu_{2i} = 1 \end{cases} \tag{14}$$

which gives

$$\begin{cases} \mu_{2i} = \frac{x_{Ci}}{a_i} \\ \mu_{1i} = 1 - \mu_{2i} \\ L_{1i} = (z_{Ci} - \mu_{2i}\, L_{2i})\, \frac{1}{\mu_{1i}} \end{cases} \tag{15}$$

where one of the unknowns L_{1i} and L_{2i} can be freely chosen. In this particular case, the equivalence in terms of COM is obtained only if $y_{Ci} = 0$, otherwise the simplified model introduces an approximation error on the y position of the COM.

2.1.2 Intersecting axes

If $a_i = 0$ the z_i and z_{i+1} axes intersect each other and the COM of the lumped masses system belongs to the $y_i z_i$ plane. In this case, we rewrite the system 5 as follows:

$$\begin{cases} x_{Ci} = 0 \\ y_{Ci} = -\mu_{2i}\, L_{2i} \sin \alpha_i \\ z_{Ci} = \mu_{1i}\, L_{1i} + \mu_{2i}\, L_{2i} \cos \alpha_i \\ \mu_{1i} + \mu_{2i} = 1 \end{cases} \tag{16}$$

which gives

$$\begin{cases} \mu_{1i} = 1 - \mu_{2i} \\ L_{2i} = -\frac{y_{Ci}}{\mu_{2i} \sin \alpha_i} \\ L_{1i} = (z_{Ci} - \mu_{2i}\, L_{2i} \cos \alpha_i)\, \frac{1}{\mu_{1i}} \end{cases} \tag{17}$$

where one of the four unknowns can be freely chosen. In this particular case, the equivalence in terms of COM is obtained only if $x_{Ci} = 0$, otherwise the simplified model introduces an approximation error on the x position of the COM.

2.1.3 Coincident axes

If $a_i = 0$ and $\alpha_i = k\pi$ the z_i and z_{i+1} axes are coincident axes and the COM of the lumped masses system belongs to the z_i axis. In this case, we rewrite the system 5 as follows:

$$\begin{cases} x_{Ci} = 0 \\ y_{Ci} = 0 \\ z_{Ci} = \mu_{1i}\, L_{1i} + \mu_{2i}\, L_{2i} \\ \mu_{1i} + \mu_{2i} = 1 \end{cases} \tag{18}$$

which gives

$$\begin{cases} \mu_{1i} = 1 - \mu_{2i} \\ L_{1i} = (z_{Ci} - \mu_{2i}\, L_{2i})\, \frac{1}{\mu_{1i}} \end{cases} \tag{19}$$

where two of the four unknowns can be freely chosen. In this particular case, the equivalence in terms of COM is obtained only if $x_{Ci} = 0$ and $y_{Ci} = 0$, otherwise the simplified model introduces an approximation error on the x and y position of the COM.

To summarize, in the cases where $a_i = 0$ or $\alpha_i = k\pi$ the position of the COM is not always maintained because the COM of the lumped masses system belongs to a specific plane or axis of frame i, while the COM of the actual link (point $\boldsymbol{C}_i$) may not. For this reason, in these cases, the simplified model introduces a further approximation. However, very often in industrial manipulators, the COM lies close to such planes/axes, therefore, the degree of approximation is acceptable. On the other hand, the possibility of choosing one or two unknowns makes it possible to simplify the lumped masses system, for example by making coincident the position of masses that belong to the same axis.

3 APPLICATION OF LUMPED MASS METHOD

The proposed simplified model substitutes each rigid link of the robotic manipulator with two lumped masses, so if the number of links is n then the total number of lumped masses is $2n$. But very often, when considering a real robot, further simplifications can be made thanks to the particular cases described above. Some lumped masses can be combined together by properly choosing their positions along the joint axes in order to create an even simpler lumped masses model. In this section, we present the positioning of the lumped masses of three different robotic manipulators having industrially used architectures: 6-axis robots with spherical wrist, 6-axis robots with 3 parallel axes, and 7-axis robots with spherical shoulder and wrist.

3.1 6-AXIS ROBOT WITH SPHERICAL WIRST

The Adept Viper s650 robotic manipulator is an example of a 6-axis industrial robot with spherical wrist. In Table I the DH parameters are presented. The mass M_i and the position of the COM of each link have been estimated by means of a CAD software [15]. Links 4-5-6 have been considered axisymmetric, with the introduction of a further simplification and a negligible approximation with respect to the real manipulator. In Table II the total mass M_i of each link and the values of the four parameters of the lumped mass model calculated according to the formulas of Section 2 are presented. Values marked with asterisks in Table II have been arbitrarily chosen according to the particular cases (Section 2.1), in order to aggregate some lumped masses into a single point.

link i	α_{i-1} (°)	a_{i-1} (mm)	θ_i (°)	d_i (mm)
1	0	0	q_1	335
2	−90	75	$q_2 - 90$	0
3	0	270	q_3	0
4	−90	90	q_4	295
5	90	0	q_5	0
6	−90	0	q_6	−80

Table I - DH parameters of the links of the Adept Viper s650

link i	M_i (kg)	L_{1i} (mm)	L_{2i} (mm)	μ_{1i} ()	μ_{2i} ()
1	6.59	−87	−15	0.502	0.498
2	5.38	210	−14*	0.575	0.425
3	5.01	−14	11	0.498	0.502
4	2.22	−284*	0	0.354	0.646
5	0.48	0	200*	0.919	0.081
6	0.77	−80*	120*	0.430	0.570

Table II - Lumped parameters of the links of the Adept Viper s650

After this operation, the aggregated lumped masses resulted:

$$m_1 = \mu_{11} M_1 \tag{20}$$
$$m_2 = \mu_{21} M_1 \tag{21}$$
$$m_3 = \mu_{12} M_2 \tag{22}$$
$$m_4 = \mu_{22} M_2 + \mu_{13} M_3 \tag{23}$$
$$m_5 = \mu_{23} M_3 + \mu_{14} M_4 \tag{24}$$
$$m_6 = \mu_{24} M_4 + \mu_{15} M_5 + \mu_{16} M_6 \tag{25}$$
$$m_7 = \mu_{25} M_5 + \mu_{26} M_6 \tag{26}$$

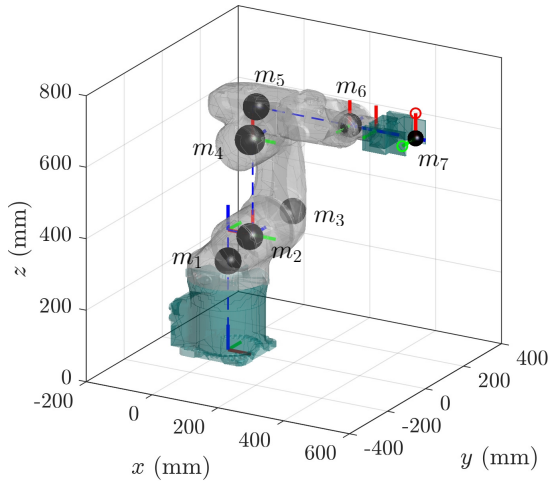


Figure 2 Adept Viper s650 with the aggregated lumped masses represented as black spheres

Overall, the simplified model consists of 7 aggregated lumped masses as shown in Fig. 2, the first of which is steady (as it belongs to the z_1 axis) and the other six are mobile. This is an important simplification because in this way the inertia model is now composed of only 7 aggregated lumped masses instead of 6 masses and 6 inertia tensors.

3.2 6-AXIS ROBOTS WITH 3 PARALLEL AXES

The TechMan TM5-700 robotic manipulator is an example of a 6-axis robot with 3 parallel axes. Owing to the particular structure of this robot it was possible to use the equations of Section 2.1 without making symmetry approximations. The DH parameters, total mass M_i of each link, and the values of the four parameters of the lumped mass model are summarized in Table III and IV. Values marked with asterisks in the table have been arbitrarily chosen according to the particular cases in order to aggregate some lumped masses into a single mass.

link i	α_{i-1} (°)	a_{i-1} (mm)	θ_i (°)	d_i (mm)
1	0	0	q_1	145.2
2	−90	0	$q_2 - 90$	0
3	0	329	q_3	0
4	0	311.5	$q_4 - 90$	−122.3
5	−90	0	q_5	106
6	−90	0	q_6	113.15

Table III - DH parameters of the links of the TechMan TM5-700

link i	M_i (kg)	L_{1i} (mm)	L_{2i} (mm)	μ_{1i} ()	μ_{2i} ()
1	3.20	3	−146*	0.962	0.038
2	9.14	−146*	−150	0.500	0.500
3	4.18	−150*	106	0.491	0.509
4	1.27	228*	−4	0.018	0.982
5	1.27	−110*	−4	0.037	0.963
6	2.31	−117*	120*	0.500	0.500

Table IV - Lumped parameters of the links of the TechMan TM5-700

After this operation, the aggregated lumped masses resulted:

$$m_1 = \mu_{11} M_1 \tag{27}$$
$$m_2 = \mu_{21} M_1 + \mu_{12} M_2 \tag{28}$$
$$m_3 = \mu_{22} M_2 + \mu_{13} M_3 \tag{29}$$
$$m_4 = \mu_{23} M_3 + \mu_{14} M_4 \tag{30}$$
$$m_5 = \mu_{24} M_4 + \mu_{15} M_5 \tag{31}$$
$$m_6 = \mu_{25} M_5 + \mu_{16} M_6 \tag{32}$$
$$m_7 = \mu_{26} M_6 \tag{33}$$

Overall, the simplified model consists again of 7 lumped masses as shown in Fig. 3.

3.3 7-AXIS ROBOTS WITH SPHERICAL SHOULDER AND WIRST

The Kuka LBR iiwa 14 R820 is one of the most common 7-axis robotic manipulators. In Table V the DH parameters are presented. In Table VI the total mass M_i of each link and the values of the four parameters of the lumped mass model are presented. In order to simplify the model as much as possible with the least number of aggregated masses, the individual

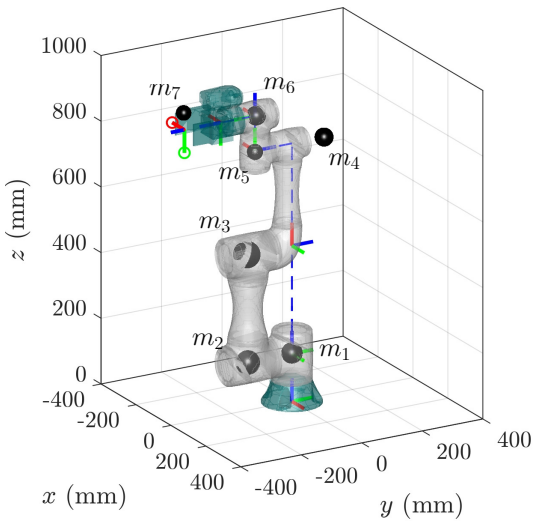


Figure 3 TechMan TM5-700 with the aggregated lumped masses represented as black spheres

links were considered axisymmetric and the two lumped masses of every link were located at one of the 4 particular points: shoulder, elbow, wrist, and gripper. Therefore, the parameters marked with asterisks are chosen arbitrarily, while the others are calculated accordingly, following the pertinent particular case.
The two lumped masses of the first link are steady since they have to lie along the z_1 axis. For this reason, they were moved to the shoulder (which is steady) to further simplify the model without affecting the dynamics of the system. For this reason L_{11} and L_{21} are both equal to zero.

link i	α_{i-1} (°)	a_{i-1} (mm)	θ_i (°)	d_i (mm)
1	0	0	q_1	358
2	-90	0	q_2	0
3	90	0	q_3	420
4	90	0	q_4	0
5	-90	0	q_5	400
6	-90	0	q_6	0
7	90	0	q_6	126

Table V - DH parameters of the links of the Kuka LBR iiwa 14 R820

link i	M_i (kg)	L_{1i} (mm)	L_{2i} (mm)	μ_{1i} ()	μ_{2i} ()
1	5.28	0*	0	0.500	0.500
2	5.08	0	420*	0.855	0.145
3	4.08	-420*	0	0.207	0.793
4	3.52	0	400*	0.826	0.174
5	2.18	-400*	0	0.345	0.655
6	2.72	0	246*	0.932	0.068
7	1.13	-126*	120*	0.350	0.650

Table VI - Lumped parameters of the links of the Kuka LBR iiwa 14 R820

After these operations, the aggregated lumped masses resulted:

$$m_1 = \mu_{11}M_1 + \mu_{21}M_1 + \mu_{12}M_2 + \mu_{13}M_3 \quad (34)$$
$$m_2 = \mu_{22}M_2 + \mu_{23}M_3 + \mu_{14}M_4 + \mu_{15}M_5 \quad (35)$$
$$m_3 = \mu_{24}M_4 + \mu_{25}M_5 + \mu_{16}M_6 + \mu_{17}M_7 \quad (36)$$
$$m_4 = \mu_{26}M_6 + \mu_{27}M_7 \quad (37)$$

Consequently, the actual massive links can be substituted with only 4 lumped masses: one is located in the shoulder (as it belongs to the z_1 axis), one is located in the elbow, one in the wrist, and one in the gripper tip as shown in Fig. 4.
It is worth noting that in all three cases, the first aggregate mass m_1 belongs to the z_1 axis, and consequently it does not move. This consideration provides a further simplification to the model since it is possible to neglect m_1 in calculations.

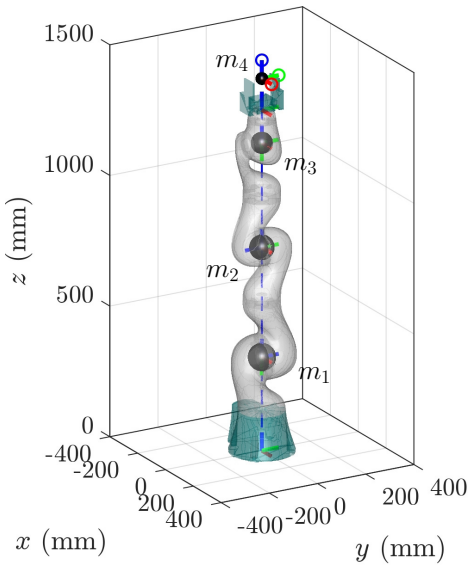


Figure 4 Kuka LBR iiwa 14 R820 with the aggregated lumped masses represented as black spheres

4 SIMULATION RESULTS

To compare the full dynamic model with the proposed simplified model, we consider the calculus of joint torques, linear momentum, and kinetic energy of the robot manipulators using both models. To evaluate these quantities in the Adept Viper s650, we utilize a sample trajectory of 2 seconds (represented in Fig. 5) where each joint performs a rotation of at least 60 degrees, using a 5-th degree polynomial time law for each joint. The starting and arrival pose with angles expressed in the Euler ZYZ convention are $(300, -100, 150, 0, 180, 180)$ and $(0, 500, 600, 30, -30, 90)$ respectively.
The results in terms of joint torques are summarized in Fig. 6. We observe that the difference in torques between the two models is very small for the first three joints, which are the

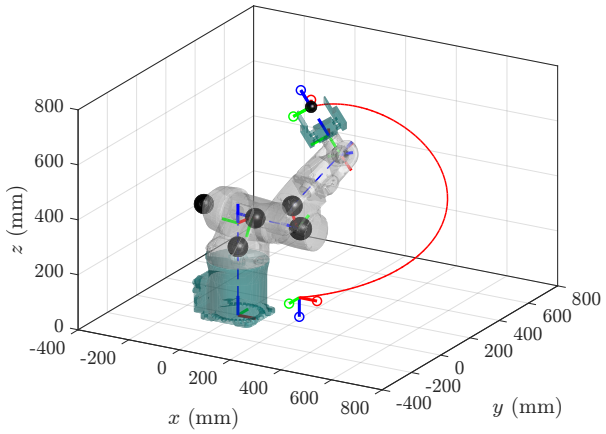


Figure 5 Sample trajectory of Adept Viper s650

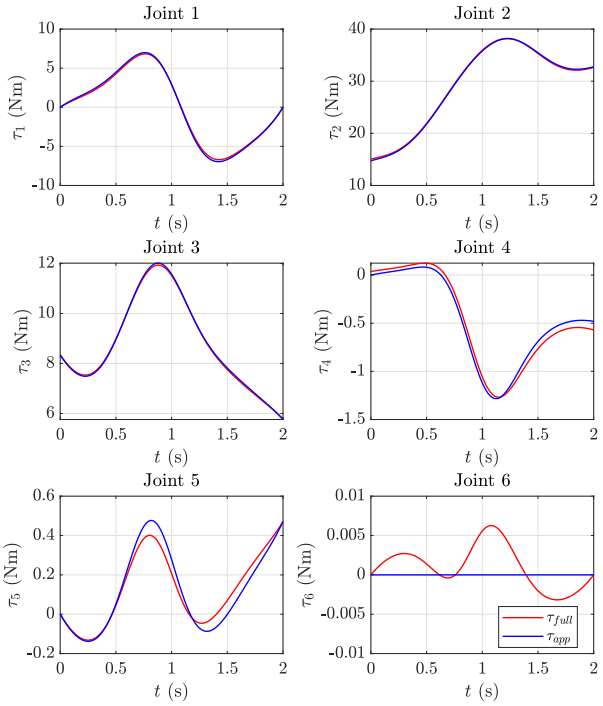


Figure 6 Joint torques of Adept Viper s650 for the sample trajectory: the red and blue lines are the torques provided by the full and simplified model, respectively

most relevant in terms of torques and have the largest effect on positioning precision. For joints 4 and 5, the difference is larger at some points of the trajectory, but it remains reasonably small. The torque of joint 6 in the simplified model remains zero since the corresponding lumped masses belong to the z_6 axes.

In Fig. 7 the linear momentum and kinetic energy of the two robots are presented. The small difference in linear momentum values between the two models derives from some approximations of the COM positions as described

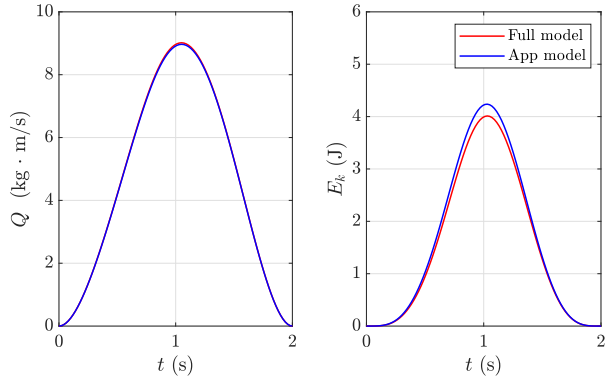


Figure 7 Magnitude of linear momentum and kinetic energy of Adept Viper s650 given by the two models for the sample trajectory (full model in red and simplified model in blue)

in Section 2.1. The more noticeable difference in kinetic energy, which appears at the center of the trajectory, is primarily attributed to the fact that the inertia tensor of the simplified model is an approximation of the real inertia tensor.

Since the lumped element model could give a better or worse approximation of the dynamics of the actual robot depending on the selected configuration and trajectory, specific simulations must be carried out to assess the model's accuracy for every application. Therefore, for every robot, 100 simulations of trajectories with random initial and final configurations within the joint space were performed, and for each simulation, the normalized root mean square error (NRMSE) for the torques, linear momentum, and kinetic energy was calculated. The $\text{NRMSE}(p)_k$ for a generic parameter p in the k-th simulation is calculated as follows:

$$\begin{aligned}\text{NRMSE}(p)_k &= \frac{\text{RMSE}(p)_k}{\Delta p_k} \cdot 100 = \\ &= \frac{\sqrt{\frac{1}{N}\sum_{i=1}^{N}(p_{full,ki} - p_{app,ki})^2}}{\Delta p_k} \cdot 100\end{aligned} \tag{38}$$

where $p_{full,ki}$ and $p_{app,ki}$ are the values of the parameter p in the k-th simulation calculated in the i-th simulation step by means of the full and approximate model respectively, N is the total number of simulations steps for every simulation, while Δp_k represents the difference between the maximum and minimum values of the parameter $p_{full,k}$ in the k-th simulation.

The results dealing with Adept Viper are summarized for the six torques in Figure 8 and for the linear momentum and kinetic energy in Figure 9. The NRMSE values for each simulation are shown with red circles, while the median values are represented with a blue line. We can observe that all median NRMSE errors for the first three torques - the most relevant in quantitative terms - are below 5%, indicating a good level of accuracy for the model in most cases.

On the other hand, the median NRMSE errors for the linear momentum and kinetic energy are even smaller.

Similar simulations were performed for the other two industrial robots: the TechMan TM5-700 and the Kuka LBR iiwa 14 R820. In Figure 10, the median NRMSE errors of the linear momentum and kinetic energy for the three robots are presented. It is evident that the median NRMSE errors are significantly low, especially for linear momentum, which is below 1% because the approximated inertia tensor does not affect linear momentum. The maximum error in the kinetic energy, which depends on the approximation of the inertia tensor, is about 3% for the three robots. The median NRMSE error of linear momentum for the Techman robot is almost zero, thanks to the specific arrangement of its centers of mass (COMs), which lie almost perfectly on the planes that are used to locate the lumped masses in the approximate model.

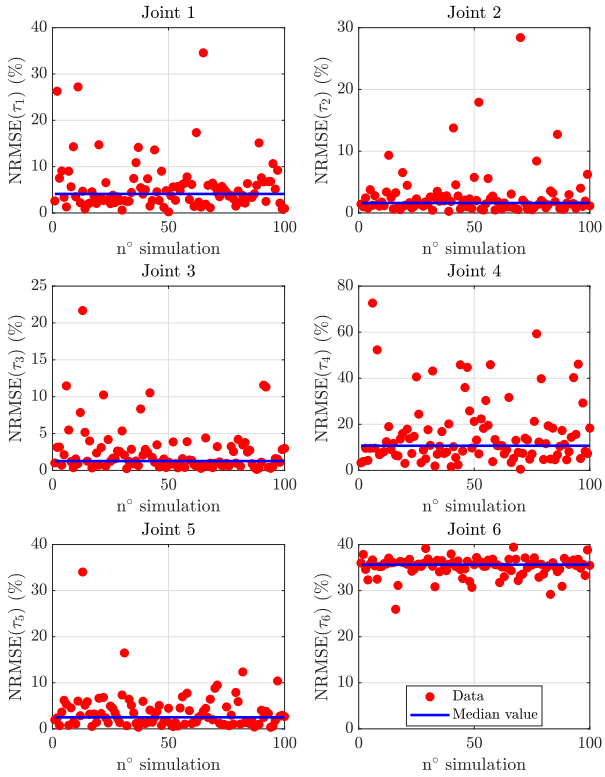


Figure 8 NRMSE for the torques of the links of Adept Viper s650 with the punctual value of the error for each simulation in red and the median value in blue

For each robot, the two models were run on the same computer, and the computational time required to calculate torques, linear momentum, and kinetic energy was recorded. Then, the mean percentage reduction in computation time was calculated, showing a consistent reduction of approximately 8% across all cases.

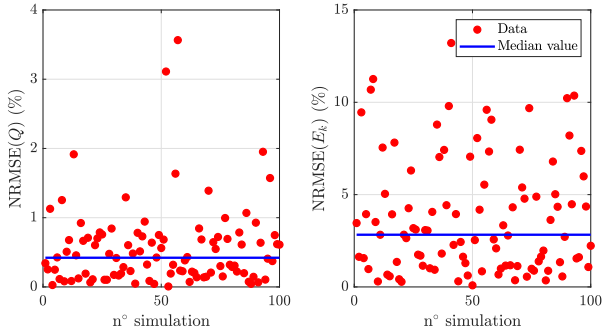


Figure 9 NRMSE for the linear momentum and kinetic energy of Adept Viper s650 with the punctual value of the error for each simulation in red and the median value in blue

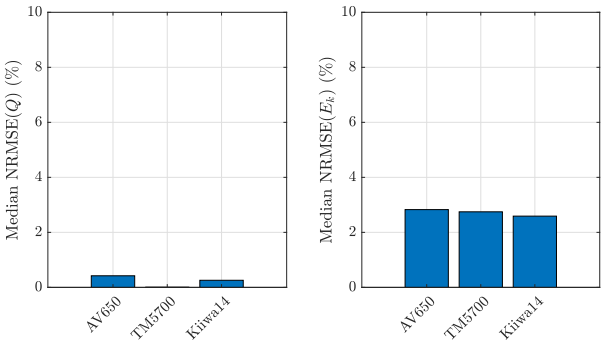


Figure 10 Median NRMSE errors for linear momentum (on the left) and kinetic energy (on the right) of the three robots

5 CONCLUSION

This paper presented a simplified method for the dynamic simulation of robotic manipulators, offering an alternative to the traditional full model approach. Unlike the conventional model, which requires the knowledge of all inertia parameters (such as masses, centers of mass, and inertia tensors of the links), the proposed simplified method makes it possible to obtain an approximated solution to the dynamic problem without the knowledge of the inertia tensors. This leads to a reduction in computational complexity, but also makes it possible to perform dynamic modeling in scenarios where inertia tensors may be unknown. Simulation results confirm the applicability of the simplified model to industrial manipulators and to service manipulators used for personal care. In particular, the good approximation in the calculation of linear momentum and kinetic energy paves the way for their use in the safety assessment of collaborative robotics applications. Future research will deal with the comparison between measured impact forces and numerical impact forces predicted by means of the model.

ACKNOWLEDGEMENT

This research was funded by the European Union - NextGenerationEU - PRIN 2022 - Project. no. 2022XXH9JZ_002 / ERC.

REFERENCES

[1] Z Arkouli, P Aivaliotis, and S Makris. Towards accurate robot modelling of flexible robotic manipulators. *Procedia CIRP*, 97:497–501, 2021. 10.1016/j.procir.2020.07.009.

[2] A. Caneschi, M. Bottin, A. Doria, A. Cesaro, and G. Rosati. Lumped parameters robot models to study impact dynamics. 165 Mechanisms and Machine Science:253–260, 2024. 10.1007/978-3-031-67295-8_28.

[3] Himanshu Chaudhary and Subir Kumar Saha. Equimomental system and its applications. In *Engineering Systems Design and Analysis*, volume 42509, pages 33–42, 2006. 10.1115/ESDA2006-95066.

[4] Jan de Jong, Johannes van Dijk, and Just Herder. On the dynamic equivalence of planar mechanisms, an inertia decomposition method. In *New Trends in Mechanism and Machine Science: Theory and Industrial Applications*, pages 51–59. Springer, 2017. 10.1007/978-3-319-44156-6_6.

[5] Mehdi Fazilat and Nadjet Zioui. The impact of simplifications of the dynamic model on the motion of a six-jointed industrial articulated robotic arm movement. *Journal of Robotics and Control (JRC)*, 5(1):173–186, 2024. 10.18196/jrc.v5i1.20263.

[6] Roy Featherstone. *Rigid body dynamics algorithms*. Springer, 2014.

[7] Bogdan Gherman, Doina Pisla, Calin Vaida, and Nicolae Plitea. Development of inverse dynamic model for a surgical hybrid parallel robot with equivalent lumped masses. *Robotics and Computer-Integrated Manufacturing*, 28(3):402–415, 2012. 10.1016/j.rcim.2011.11.003.

[8] Ivan Giorgio and Dionisio Del Vescovo. Non-linear lumped-parameter modeling of planar multi-link manipulators with highly flexible arms. *Robotics*, 7(4):60, 2018. 10.3390/robotics7040060.

[9] NC Huang. Equimomental system of rigidly connected equal particles. *Journal of guidance, control, and dynamics*, 16(6):1194–1196, 1993. 10.2514/3.21150.

[10] LP Laus and JM Selig. Rigid body dynamics using equimomental systems of point-masses. *Acta Mechanica*, 231(1):221–236, 2020. 10.1007/s00707-019-02543-3.

[11] Neider Nadid Romero Nuñez, Rodrigo S Vieira, and Daniel Martins. Equimomental systems representations of point-masses of planar rigid-bodies. *Acta Mechanica*, 234(11):5565–5580, 2023. 10.1007/s00707-023-03683-3.

[12] Edward John Routh. *A Treatise on the Dynamics of a System of Rigid Bodies...: Elemementary part*, volume 1. Macmillan and Company, 1905.

[13] W Seyferth. Massenersatz durch punktmassen in räumlichen getrieben. *Mechanism and Machine Theory*, 9(1):49–59, 1974. 10.1016/0094-114X(74)90007-X.

[14] Bruno Siciliano, Lorenzo Sciavicco, Luigi Villani, and Giuseppe Oriolo. *Robotics Modelling, Planning and Control*. Springer, 2009. 10.1007/978-1-84628-642-1_9.

[15] M. Tonan, M. Bottin, A. Doria, and G. Rosati. A modal approach for the identification of joint and link compliance of an industrial manipulator. 122 Mechanisms and Machine Science:628–636, 2022. 10.1007/978-3-031-10776-4_72.

[16] M. Tonan, A. Doria, M. Bottin, and G. Rosati. Oscillation-free point-to-point motions of planar differentially flat under-actuated robots: a laplace transform method. *Robotica*, 42(4):1262–1280, 2024. 10.1017/S0263574724000249.

[17] Yangnian Wu and Clément M Gosselin. On the dynamic balancing of multi-dof parallel mechanisms with multiple legs. *Journal of Mechanical Design*, 2007. 10.1115/1.2406093.

ISSN 1590-8844
International Journal of Mechanics and Control, Vol. 26, No. 01, 2025
https://doi.org/10.69076/jomac.2025.0012

DESIGN AND TESTING OF ALMATY ANKLE EXOSKELETON V.2

Nursultan Zhetenbayev* Marco Ceccarelli** Matteo Russo**

*Almaty University of Power Engineering and Telecommunications, Almaty, Kazakhstan

**LARM2 Laboratory of Robot Mechatronics, University of Rome Tor Vergata, Italy

ABSTRACT

This paper presents the development and testing of the passive Almaty Ankle Exoskeleton V.2. The device features a new design with three electric linear actuators, and the shin and foot platforms are connected by links with spherical and universal joints. Functional testing demonstrates the proto-type's ability to operate effectively within the natural range of ankle joint movements. Preliminary results indicate that the exoskeleton can reduce calf muscle activation in the work limb where the device is applied. In this the passive exoskeleton is designed for dorsiflexion and plantarflexion, whose operation with numerical results is highlighted by focusing on parameters such as angular velocity, linear acceleration, and angles. These measurements provide valuable information about the exoskeleton's performance and efficiency.

Keywords: Ankle Exoskeletons, Design, Performance, Experimental evaluation, Almaty Ankle Exoskeleton V.2

1 INTRODUCTION

The ankle joint is a complex joint that forms a kinematic link between the lower limb and the foot, allowing motions for daily tasks. It experiences high compressive and shifting forces during walking, but due to its structure it functions with a high degree of stability. Unfortunately, this joint is very susceptible to acute and long-term in-juries in physically active people. Thus, there is a need for rehabilitation to restore full function of the damaged joint [1-3]. To solve the above-mentioned problems, researchers have explored the field of robotics for the rehabilitation of the ankle. Traditional rehabilitation therapy is mainly based on individual treatment by rehabilitation trainers, which has such drawbacks as low efficiency and high labor intensity [4]. To counteract these aspects and to improve the quality of rehabilitation in recent years, rehabilitation therapy has been involving robotic system. These robots are de-signed to improve the locomotor function of the ankle joint. Robotic systems are used in clinics to recover from stroke and ankle injuries, but their use is limited, and they are very expensive.

Contact author: Nursultan Zhetenbayev

Almaty University of Power Engineering and Telecommunications, Almaty, Kazakhstan
E-mail: n.zhetenbayev@gmail.com

Prices range from $75,000 to $350,000. These high costs make people think that robots are too expensive for both healthcare systems and individuals [5, 6].

Platform robots are basic-stationary, and the foot is connected to a mobile platform and usually uses a parallel mechanism to perform ankle movements. Stationary systems have been developed for more than 20 years, starting in 1999 [7]. Most previous robotic designs are based on a static platform, where an immobile device requires the patient to keep their foot on a grounded platform (usually in a seated position) to perform rehabilitation, which is inconvenient for home use [8-19]. These devices are not only bulky but also fixed in place. As a result, patients must visit a hospital or facility where the rehabilitation equipment is installed, despite potential mobility impairments.

In [8] the authors developed an exoskeleton using 3D printing technology from a PLA material. Exoskeleton is intended to improve the rehabilitation of the ankle joint through three degrees of freedom. The design uses an Arduino Uno controller to control the motors and sensors. The exoskeleton is programmed to work at low speeds, which limits the range of movement compared to a normal human and can reduce the effectiveness of rehabilitation.

In the work [9], the authors presented a robotic platform for ankle rehabilitation, equipped with 6 actuators powered by IBL3605A motors from Tech Servo Co. Ltd., Shenzhen, China.

These actuators provide a semi-closed loop for position control and communicate with a PC-104-based personal computer via a CAN bus for efficient system management. The developed exercise modes, including constant speed, constant torque, and awareness, are suitable for various stages of rehabilitation and demonstrate an innovative approach to comprehensive body training. The current control system uses a mouse and keyboard for user input, but it lacks a more user-friendly interface that could improve overall user experience. The device described in [10] is characterized by complexity and high cost due to the use of mechanical transmissions for motion conversion. Additionally, a limitation is the need for external fluid sources for pneumatic or hydraulic actuators, which is not always feasible for home use. The control system uses linear and rotary actuators, along with additional mechanical transmissions to activate prismatic joints. The rehabilitation device is too complex and requires the presence of a physical therapist, as well as being too expensive for home use. Such a system can be tedious and exhausting, reducing patient motivation for regular use.

Described in [11] is the PKAnkle robot, whose controller includes a force and torque sensor installed under the sole and an EMG signal map with eight control channels. The position and alignment of the drives of wearable devices can create in-ternal forces in the ankle not directly related to real movements, that can mislead a patient's protraction during rehabilitation. The prototype causes unwanted internal forces in the ankle due to incorrect positioning and alignment of the drives, which can also mislead the coupling. PKAnkle wearables require precise ergonomic design be-sides to be lightweight, comfortable and suitable for a wide range of anatomical features. The exoskeleton designs in [12] and [13] present challenges: [12] highlights issues with increased inertia and limited motor placement in serial mechanisms, while [13] emphasizes difficulties in controlling force and position due to environmental variability, requiring advanced control strategies for effective ankle rehabilitation. The parallel mechanism of the exoskeleton [14] provides high load capacity and flexibility but has limited working space and complex constraints, which reduces effectiveness and accuracy during rehabilitation. One of the main drawbacks of rehabilitative robotics is the difficulty in teaching medical personnel how to work with a robot. Robot in [15] in rehabilitation clinics are very expensive and have limited functionality due to manufacturer's limitations. The exoskeleton control system is implemented using the component intermediate software Orocos. The prototype has a limited range of motion, allowing only two degrees of freedom and one progressive degree of freedom, that can limit the kinds of exercises for ankle rehabilitation. Although the software architecture is modular, it can create problems with programming and configuration for different patients or exercises. Reliance on component software such as Orocos [15] can lead to potential compatibility problems or limitations in the long run.

Exoskeleton design in [16] involve mechanical joint restrictions that limit the range of motion and require design adjustments for patient safety, with a drive system of linear drives and a stepper motor, but face challenges in movement range, weight, and cost.

The exoskeleton design in [17] faces issues with excessive strain on the patient's ankle, high development costs, and complexity, with limitations in personalized treatment and adaptability to various ankle conditions, potentially affecting service and durability.

Structures described in [18] may encounter maintenance and repair issues due to their complexity, with limitations in degrees of freedom affecting adaptability, precision, and stability. The exoskeleton uses a stepper motor and adaptive impedance control but faces challenges with movement flexibility, rotation centering, and overall operation.

In [19], the device P.I.G.R.O. (Pneumatic Interactive Gait Rehabilitation Orthosis) is described. This exoskeleton, based on pneumatic actuators, is designed to support patients in unloaded walking during the initial stages of neurorehabilitation. Its features include pneumatic actuators, adaptability to the patient's movements and muscle activity, and a structural strength analysis performed using the FEM method.

Moreover, this exoskeleton represents an innovative solution for early rehabilitation steps but still requires further improvement for clinical trials and commercial application.

From the described designs of robotic ankle rehabilitation platforms, the following significant deficiencies can be identified:

- Limited range of movements: Many prototypes have limited range of movements, which can negatively affect the effectiveness of rehabilitation. For ex-ample, parallel mechanisms often have limited workspace, which limits the types of exercise for patients.
- Complexity of management and learning: Systems require complex management and programming strategies that complicate the training of medical personnel and implementation into clinical practice. This creates a barrier to widespread use in rehabilitation institutions.
- High cost and complexity: Many robots are expensive and require complex engineering, making them inaccessible for home use and daily clinical practice due to budget constraints.
- Problems with proprioception and physiological aspects: Several designs may create unnatural sensations or strain the patient's foot, making rehabilitation difficult and may mislead proprioception.
- Individual anatomical and functional features: not all systems consider the in-dividual characteristics of patients, which reduces their effectiveness.
- Durability problems with regular use: Wearable designs face durability problems that require additional maintenance costs.

All these challenges require further efforts to improve the availability, efficiency and usability of robotic ankle rehabilitation platforms in both clinical and home settings.
They not only save money, but they also help to better use resources. Robotic exoskeletons can be an attractive means of rehabilitation, not only for restoring motor activity, but also to increase physical activity years after an injury [20]. Using robots at home brings many benefits, including saving money and time on treatment. The home-grown portable robotic exoskeleton can do all the movements that you get in a rehabilitation centre. The exoskeleton devices for the ankle joint are wearable human-machine integrated mechanical devices, which are usually anthropomorphically designed to pro-vide active and passive help to users [21].
Exoskeleton devices for ankle rehabilitation show significant promise in improving clinical evaluation, The United Nations High Commissioner for Human Rights has been working to ensure that the United Nations system is able to provide effective and timely rehabilitation.
However, problems such as size limitations, long-term efficiency, comfort issues, and mechanical complexity must be addressed through constant research and innovation. Future developments should be aimed at improving the usability of devices, Clinical applicability is extended through large-scale research and design optimization to improve patient comfort and safety. The aim of this work is to develop a compact device for rehabilitation of the hu-man ankle. A new of this work is the development of a device with a purely mechanical mechanism, made of materials available on the market. The proposed for rehabilitation of the ankle joint. It is designed for convenient use by patients and physiotherapists. The system is simple, reliable and easy to use. This paper reports experiences towards an improved version of Almaty Ankle Exoskeleton V.2.

2 MATERIALS AND METHODS

This section outlines the methodology used in the development of the proposed rehabilitation device. Initially, it was necessary to identify issues in the design of V1, with particular attention to the requirements for the Almaty Ankle Exoskeleton V.2. A CAD model with three degrees of freedom was then developed, and a prototype was created using 3D printing. The final stage involved testing the models of the Almaty Ankle Exoskeleton V.2 and conducting functional tests of the device, followed by a comprehensive discussion of the results obtained.

2.1 PROBLEMS IN DESIGN V1

Figure 1b shows the prototype of the Almaty Ankle Exoskeleton V.1, equipped with four electric linear actuators, while Figure 1a presents its kinematic design [22]. The system consists of two main platforms: the foot platform (AB) and the shank platform (CDE). These platforms are connected by a series of linkages and actuation elements arranged in a closed-loop mechanism. The primary rotation point of the exoskeleton is pointing A, which corresponds to the anatomical ankle joint of the human body. The rotation around this point is denoted by the angle φ, representing the plantarflexion and dorsiflexion movements of the foot. The system consists of three main linkages: BE and AC, which connect the foot platform to the shank platform. Their respective lengths are denoted as l_1 and l_2, and their angles with respect to the horizontal axis are α_1 and α_2. The link EF, driven by the linear actuator S_3, directly controls the motion of the foot platform.
There are three linear actuators in the system:

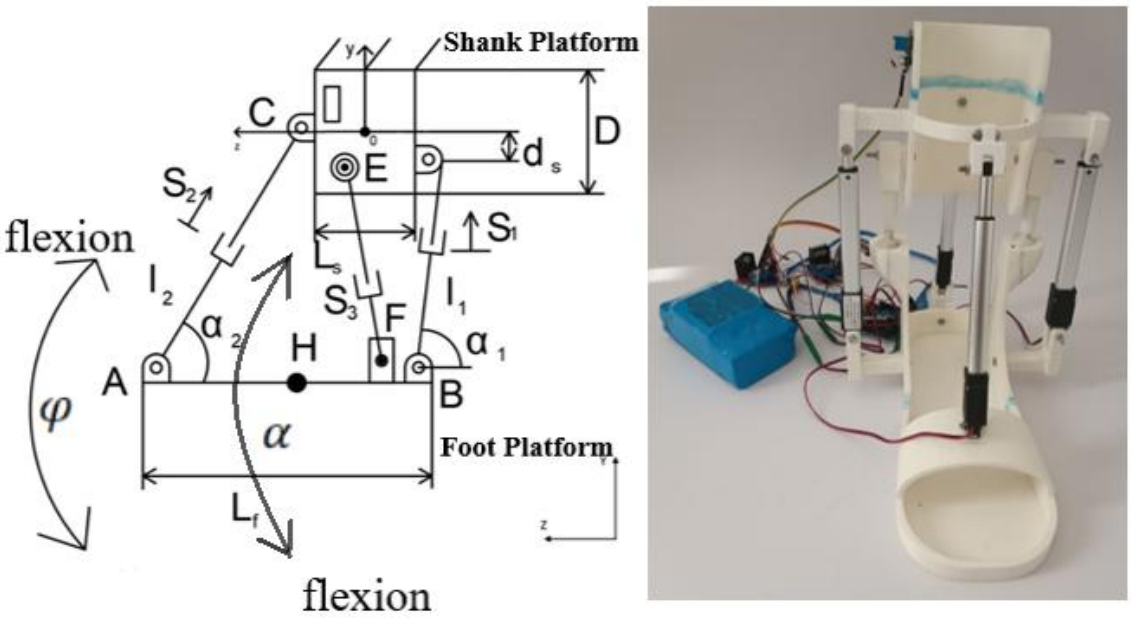
- S_1: A vertical actuator located between the upper section of the shank platform and point E, providing vertical displacement.
- S_2: Drives the linkage between points C and A.
- S_3: Positioned between points E and F, directly influencing the foot platform and controlling its rotation.

By varying the lengths and directions of these actuators, the foot platform rotates around point A according to the angle φ. This mechanism enables the exoskeleton to precisely match the desired motion trajectory and provide optimal assistance to the ankle joint.
The key parameters of the model are:

- L_f — length of the foot platform,
- D — vertical distance between the shank and foot platforms,
- D_s — vertical offset from point E to the top edge of the shank platform,
- S_1, S_2, S_3 — linear displacements of the actuators.

The use of these actuators increases the total weight and size of the exoskeleton, making it less convenient for long-term use for rehabilitation purposes. In addition, the four electric linear actuators require more power, which complicates the control system due to the need to control the engines and related electronics. In general, the main drawbacks of the Almaty Ankle Exoskeleton V.1 with four electric linear actuators are complex control system and large dimensions, which leads to inconvenience. The Actuonix L16 linear actuator [24] is a popular choice for various applications, including our exoskeleton. However, certain drawbacks were identified during experiments. These issues were particularly evident during ankle testing, where precision and reliability were critically important, as described in [24]. Some of the drawbacks and problems associated with the Actuonix L16 linear actuator were identified during the experiment. The Actuonix L16 linear actuator has several limitations:

1. Limited Load Capacity: The actuator's load capacity is insufficient for applications requiring higher output power, such as supporting and activating the ankle under dynamic conditions.
2. Speed: The speed of the L16 linear actuator is not high enough for applications that require quick and responsive movements, which is critical for effective rehabilitation.
3. Accuracy: The L16 linear actuator does not provide the necessary accuracy, impacting the effectiveness of the exoskeleton in delivering precise ankle care and support.
4. Power Consumption: The power consumption of the L16 is high, which affects the overall energy efficiency of the system.



a) b)

Figure 1 Almaty Ankle Exoskeleton V.1 [23]: a) kinematic design; b) a built prototype.

Fig. 2 shows the main components of the Almaty ankle exoskeleton version 1. The model has several potential drawbacks, including a power supply that requires connection to a personal computer (PC) to control all devices. The bulkiness and lack of portability of the device reduce the system's convenience and mobility. Managing multiple components complicates the setup of the exoskeleton. Users may encounter difficulties in assembling and operating the system without technical assistance, making it less accessible for non-specialists. The need for multiple connections between the power supply, personal computers, and control unit leads to tangled wires, increasing the risk of failures and reducing ease of use.

In the updated exoskeleton model, each actuator is functionally assigned to support specific anatomical movements of the ankle joint:

- Actuator S1 is responsible for dorsal and plantar flexion, which corresponds to the upward and downward rotation of the foot in the sagittal plane.
- Actuators S2 and S3 control inversion and eversion, which represent the tilting of the sole inward (medially) and outward (laterally) in the frontal plane.

This separation of function allows for precise assistance and control of individual degrees of freedom in ankle movement. By distributing the workload across multiple actuators, the system enhances movement accuracy, adaptability, and enables targeted rehabilitation protocols based on the patient's specific needs. Dependence on an external power source limits the mobility of the exoskeleton. Users will always need access to an electrical outlet, restricting its use to indoor environments or areas with a reliable power supply, which diminishes its practical utility in real-world applications. The presence of a power supply also poses potential safety risks, such as electric shock or short circuits, especially if the equipment is not properly insulated or maintained. Using multiple components increases the likelihood of system failure. A malfunction in just one component can render the entire system inoperative. Using a personal computer for control also leads to high energy consumption. This reduces the system's overall energy efficiency and can make it more expensive to operate over time due to increased power usage. Users will require specialized training to properly operate and maintain the exoskeleton, which could become a significant obstacle for individuals without a technical background. Fig. 3 shows the mechanical design of the prototype, which has several significant shortcomings that have affected its performance, usability, and safety. The rigid foot platform causes discomfort for the user. Insufficient adaptation to the natural move-ments of the ankle joint can lead to discomfort, inefficient support during movement, and even potential injuries. The thin plastic strap securing the foot in the exoskeleton would slip and shift, reducing control and increasing the risk of injury. The combination of a rigid platform and unreliable foot fixation increases the risk of falling due to inadequate support and possible slippage. The rigid design unevenly distributes pressure on the foot, which, as experiments have shown, causes discomfort during prolonged use. The foot platform does not allow for easy adjustment according to the individual needs of users. Each person may require different levels of fit or support, and the cur-rent design does not always accommodate these requirements.

2.2 REQUIREMENTS

The requirements for the Almaty ankle exoskeleton V.2 were developed based on the experience with version V.1: first, the design should use lightweight materials to reduce the overall weight of the exoskeleton and improve user comfort.

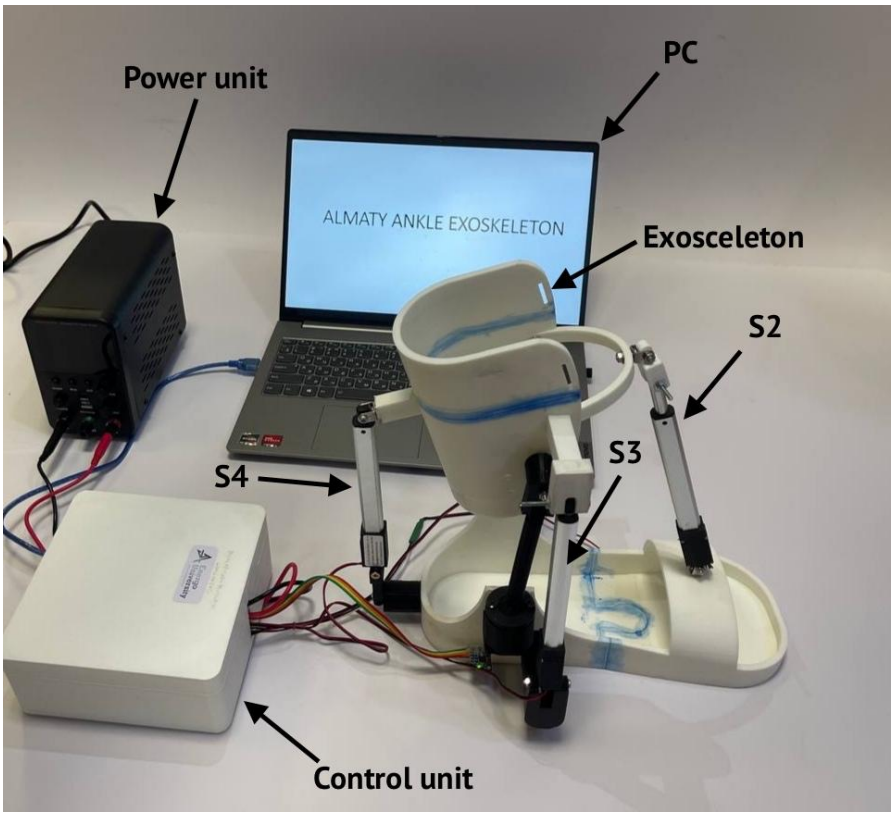
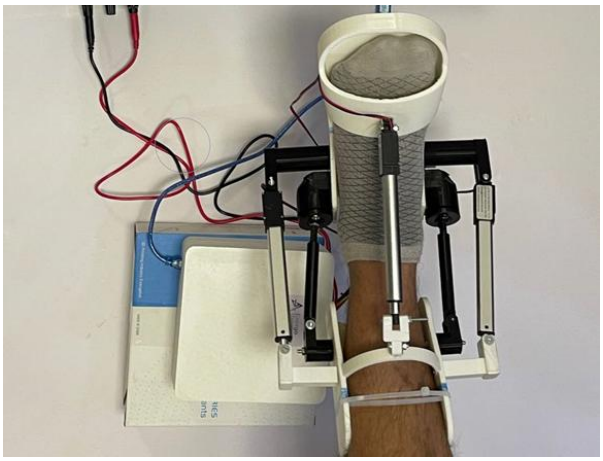


Figure 2 Almaty Ankle Exoskeleton V.1 with the main components [23].


Figure 3 Almaty Ankle Exoskeleton V.1 with the main components [23].

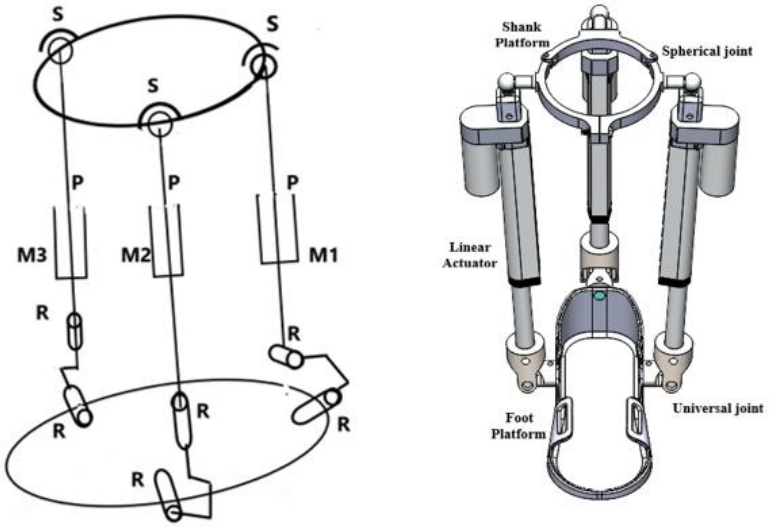
It is necessary to create a more compact and ergonomic design that minimizes bulkiness and enhances user mobility during rehabilitation.

- Improved degrees of freedom for better simulation of natural ankle movement, improving functionality.
- The exoskeleton should easily adapt to the different anatomical features of the user with minimal changes.
- Introduction of energy efficiency components and mechanisms to reduce energy consumption.
- Improved control system to ensure accuracy of movement and responsive-ness.
- Enable security mechanisms to protect the user in case of system failures or malfunctions.
- The design should be easy to maintain, with accessible components that can be quickly maintained or replaced.
- Development of an auxiliary device for movement with introduction of possibilities of monitoring the condition of the ankle during rehabilitation.
- Considering the limitations of the first prototype, the second version will be compact, and all components will be minimized.

Firstly, the use of actuators with higher load capacity and output power will be considered. This will ensure that the actuators can handle the dynamic loads encountered during rehabilitation. The actuators should offer greater speed and responsive-ness to improve the exoskeleton's performance.

It is important to choose actuators known for their reliability and long service life to reduce maintenance needs and ensure dependable operation over time. Additionally, actuators designed with energy efficiency in mind are essential since the V.2 exoskeleton will be powered by batteries. Addressing these aspects will help enhance the performance and reliability of the ankle exoskeleton, making it more effective and user-friendly. A more compact and integrated power solution, such as battery packs, will be developed to improve mobility and convenience. To increase durability and performance, more robust materials like lightweight PLA plastic will be used.

The platform will include flexible elements that better adapt to the natural movements of the ankles and enhance comfort.



a) b)

Figure 4 A CAD design of the ankle motion- assisting exoskeleton: a) kinematic design; b) CAD model.

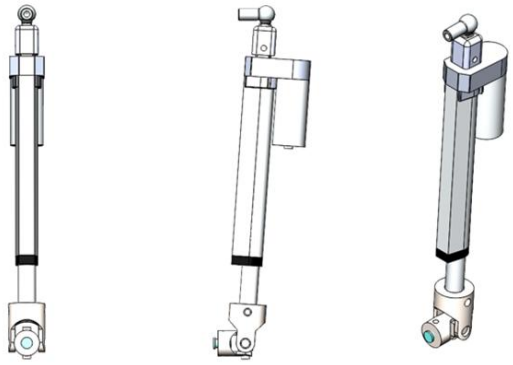


Figure 5 The actuator that connects the Shank Platform and Foot Platform in Fig. 4, [24].

A mounting mechanism with adjustable straps and foot supports will also be added to ensure a stable and snug fit. Addressing these issues will significantly improve the Almaty Ankle Exoskeleton V.2 in terms of durability, user comfort, safety, and overall effectiveness.

2.3 DESIGN SOLUTION

Figure 4a shows the kinematic design, and Fig. 4b presents the CAD model of the Almaty Ankle Exoskeleton V.2, a wearable device designed to support ankle joint movements. The proposed solution features a parallel mechanism with electric linear actuators, as the Almaty Ankle Exoskeleton V.2. The tibia platform is located below the knee and can be adjusted to fit the patient's leg size. A key feature of the device is the sole, made from PLA plastic, ensuring its durability during rehabilitation. The electric linear actuators are equipped with spherical and universal joints that connect the tibia platform to the sole, as shown in Figure 5.The Exoskeleton V.2 is designed to be attached to the tibia, facilitating ankle mobility.

Its design includes an electric linear servomotor, which converts linear motion into the force needed for the exoskeleton's operation. This force helps support the user's ankle during movement, enhancing mobility and reducing joint strain. Fig. 6 shows the view of the CAD project with the main components of Almaty Ankle Exoskeleton V.2:

- The tibia body 1 is a shank platform that is shaped to provide a reliable and convenient fit for the user, and at the same time serves as a basis for fixing components that contribute to the functionality of the exoskeleton.
- The angle joints 2 and 11 are designed to connect the actuator to tibia a platform that holds the tibia during movement in the ankle joint.
- The connection 4 is intended for fixing a linear actuator to angular hinge joints.
- The linear actuator 3, 5 and 12 provides controlled linear motion to perform certain movements that facilitate ankle function during rehabilitation.
- 6 is the internal contour of the Actuator, which provides the force to create movement in the actuator.

- The universal hinge 7, 8, and 13 is designed to connect the actuator to a platform that holds the feet together, allowing for smooth, rotational movement of the foot.
- The foot housing 9 is a foot platform designed to accommodate the foot of the us-er. It secures the foot in the exoskeleton, ensuring correct position and stability during exercise.
- The mounting brackets 10 for the shank platform are designed according to the specified size.
- 14 is a Velcro strap that effectively transfers the load to the ankle.

Fig. 7 shows the CAD design with dimensions of the mechanical solution for the Almaty Ankle Exoskeleton V.2. The ankle exoskeleton includes attachments between the foot (AB) and the thigh (CD) using ball and universal joint elements. Linear actuators S1, S2, and S3 are installed at the front and back of the ankle. The electric linear actuator features a system that synchronizes the movement of the two interconnected parts of the exoskeleton and moves the ankle along with the exoskeleton.
All dimensions of the Almaty Ankle Exoskeleton V.2 are listed in Table 1.

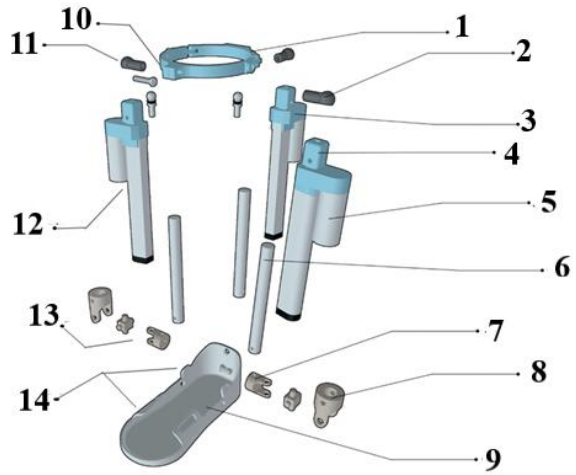


Figure 6 Exploded view of CAD model of exoskeleton ankle in Fig. 4 with structural elements.
1 - shank platform; 2, 11 - angle joints; 3, 5, 12 - linear electric actuator (S1, S2, S3); 4 - actuator attachment (S3); 6 - the internal circuit of the actuator; 7, 8, 13 - universal joint designed to connect the actuator to the platform; 9 - Foot platform; 10 - Shank platform fixture designed to fit the size; 14 - Foot platform attachment with ankle.

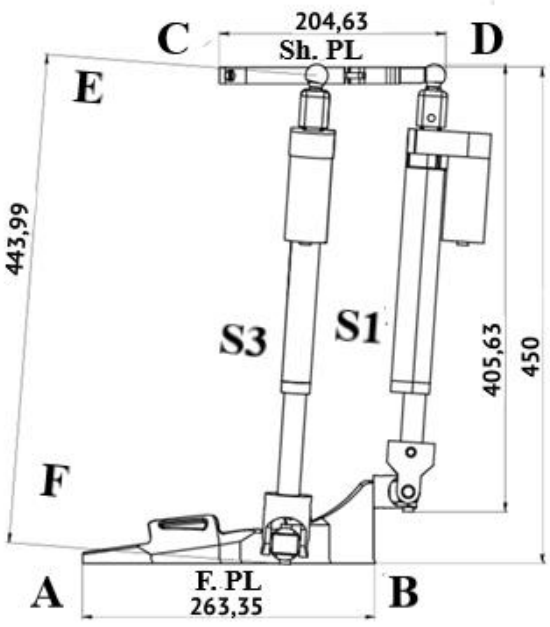


Figure 7 Technical design of the proposed Almaty Ankle Exoskeleton V.2.

Table I - Experimental values

Size (mm)	Sh.P	F.P	S_1	S_2	S_3	DB	Sh.P
	204,63	263,35	405,63	443,99	443,99	450	204,63

2.4 PROTOTYPE

The housings for the ankle exoskeleton were 3D printed using a Flash Forge Adventure 5 printer.

The foot and shank platforms, made from PLA plastic, are strong and rigid, making them suitable for use as structural components of the exoskeleton. The printing process is shown in Figure 8: the Foot platform was printed in 2 hours and the Shank platform in 45 minutes.

Fig. 9 shows an electric linear actuator that converts rotational motion into linear motion, allowing precise adjustment of distance and speed.

The electric linear actuator has the following specifications: IP54 protection class, 150 mm stroke length, 12 V operating voltage, 1.5 cm/s speed, and 50 kg load capacity [25].

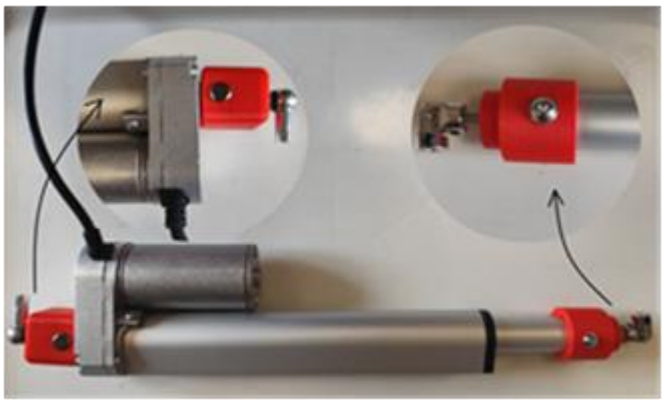
A spherical joint is attached to the upper part of the actuator to connect the rod with the support ring, while a universal joint is attached to the lower part, as shown in Figures 10a and 10b.

Advantages of using this linear actuator for the exoskeleton of the ankle joint:

- Precise motion actuator provides control over the movement of the ankle, which is necessary to achieve natural and smooth movement. This accuracy helps to mimic the natural cycle during rehabilitation.
- The adjustable drive speed of up to 1.5 cm/s ensures controlled and consistent movement, ensuring that the exoskeleton will respond adequately to user needs.
- Support and stability with a load capacity of 50 kg the actuator can with-stand weight and force applied by the user's foot and ankle, ensuring stability and strength. This ensures that the drive can cope with dynamic loads during rehabilitation.
- Working from 12 V DC: the drive running from 12 V DC is compatible with standard power sources and batteries, making it energy efficient and easy to integrate into exoskeleton design.
- Sensor integration: the actuator can be integrated with various sensors and control systems to create a responsive and adaptive exoskeleton.



Figure 8 Exploded view of CAD model of exoskeleton.



a) b)

Figure 9 Electric linear actuator with (a) universal joint connection (b) spherical joint connection.

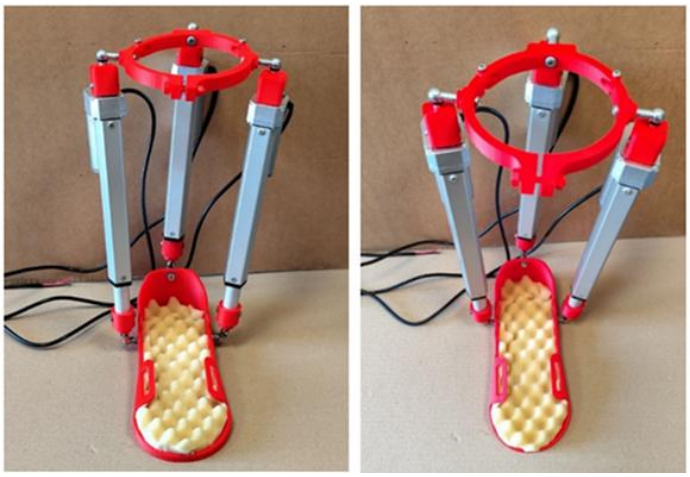


Figure 10 Almaty Ankle Exoskeleton V.2 the full prototype.

2.5 TESTING LAYOUT

This prototype includes a motor system that targets the anterior tibialis muscle, providing tactile stimulation during active movement. It supports key movements such as dorsiflexion and plantarflexion, abduction and adduction, as well as inversion and eversion, which are essential for walking and maintaining balance.

Fig. 11 shows a circuit design of a laboratory prototype of the ankle joint, which shows the connection of all the main components. The programming code for the prototype's command and control unit in Appendix A1 includes algorithms for control and monitoring, covering:

- Sensor data acquisition: Reading data from accelerometers and gyroscope sensors.
- Actuator control: Managing the movement of motors and servos based on input signals.
- System safety mechanisms: Implementing overvoltage protection and error detection to prevent malfunction.
- Memory and communication protocols: Storing data on an SD card and supports wireless communication for real-time monitoring.

The Arduino Nano is used as the control microcontroller, based on the ATmega328P processor [26]. It supports communication interfaces such as I²C, SPI, and UART. This controller processes data from the sensors and sends appropriate commands to the actuators. For motor control, the L298N Motor [27] is utilized. This module operates within a voltage range of 5V – 35V and provides up to 2A per channel. By adjusting the speed and direction of the motors, it enhances the precision of the exoskeleton's movements. The MPU-6050 sensor [28] is used to monitor movement and to determine angular parameters.

This sensor combines an accelerometer and gyroscope, enabling tracking of motion directions and angular changes. It measures acceleration in the range of ±2g – ±16g and angular velocity in the range of ±250°/s – ±2000°/s, ensuring the exoskeleton's responsiveness to user movements. A MicroSD Card Module is used for data collection and storage.

It communicates with the microcontroller via the SPI interface, allowing system performance data to be recorded for further analysis. The power supply consists of a 9V battery, ensuring stable operation. Additionally, an LED indicator is integrated into the system, connected via a 330 Ω resistor, providing visual feedback on the exoskeleton's operational status.

The exoskeleton is also equipped with additional wireless portable devices, as shown in Fig. 12. These devices include an IMU sensor, Arduino Nano, microSD card for data recording, and a 9V battery that powers all the components. The devices will be positioned below the knee and will capture precise data on ankle joint movements, providing effective assistance to users in performing these movements. All components of the device create a holistic system for monitoring and rehabilitation of the ankle. IMU collects detailed motion data, Arduino Nano processes this data and manages the system, the microSD card stores data for further analysis, and the switch and LED provide user interaction and feedback. Rechargeable battery ensures the device portability, allowing it to be used in a variety of circumstances: at home, in a clinic or during everyday activities. Such an approach makes it possible to effectively monitor the progress of rehabilitation, accompany patients during physical activity and provide valuable information to health workers. This ankle measuring device combines physical support and advanced sensory technology for effective rehabilitation. It is equipped with platforms attached to the top of the ankle and foot, which provides stability and flexibility. The elastic material of the ring provides a comfortable fit, ensuring natural movement of the ankle. During rehabilitation, the device accurately measures the movement of the ankle. These data help to assess progress, adjust rehabilitation plans and accelerate recovery. With a combination of support and technology, this device offers a comprehensive solution for ankle rehabilitation, improving recovery and function. The device is lightweight and easy to carry, which is crucial for patient comfort and ease of use during rehabilitation.

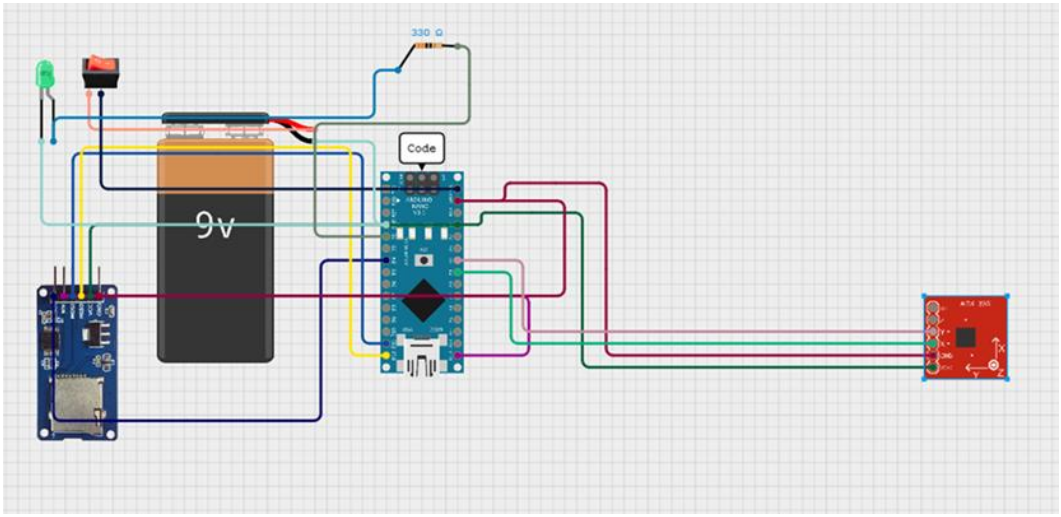


Figure 11 The circuit design for a lab prototype.

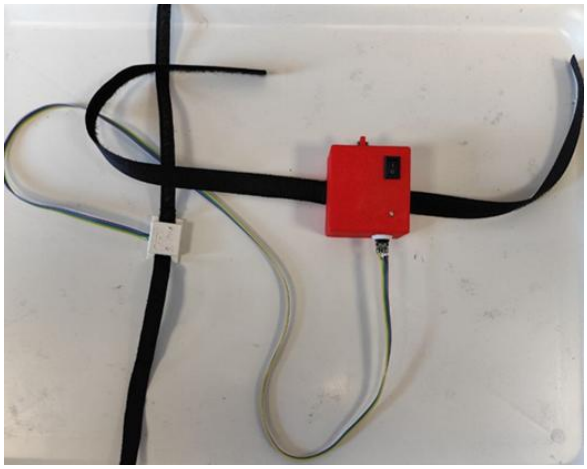


Figure 12 A device for reading the movement of the ankle joint during rehabilitation.

3 RESULTS

The following sections present the test models of the Almaty Ankle Exoskeleton V.2 and the results of the device's functional testing.

3.1 TESTING MODES

Rehabilitation of the human ankle joint primarily aims to restore mobility, strength, and stability to ensure normal functional movements. Among the various movements that the ankle joint can perform, the most important are dorsiflexion and plantarflexion. These movements are essential not only for basic walking but also for more complex actions such as running, jumping, and maintaining balance.

- Dorsiflexion is the movement of the foot upward toward the shin. The normal range of motion (ROM) for dorsiflexion in a healthy ankle typically ranges from 10 to 20 degrees.
- Plantarflexion involves pointing the foot downward, away from the shin. The normal range of motion for plantarflexion generally ranges from 40 to 50 degrees.

In ankle joint rehabilitation, dorsiflexion and plantarflexion are critical movements that help restore normal ankle function.

By focusing on these movements and their corresponding ranges, rehabilitation programs assist patients in regaining the mobility, strength, and stability needed to prevent reinjury and return to normal activities.

Effective training in dorsiflexion (10-20 degrees) and plantarflexion (40-50 degrees) leads to improved gait mechanics, better balance, and the ability to perform a wide range of functional actions. Testing of the models is shown in Figure 14.

In the Almaty Ankle Exoskeleton V.2, functional testing of the device was conducted for dorsiflexion and plantarflexion, with only one actuator (S1) in operation.

The S1 actuator in the exoskeleton provides the necessary force to support or enhance ankle movement. The actuator is controlled by a joystick, which adjusts the speed and direction of movement based on the user's actions. Fig. 14 shows the laboratory device designed to control the electric actuators of the exoskeleton during rehabilitation exercises, demonstrating how the device operates:

- Arduino Uno: This microcontroller acts as the main controller, sending control signals to the L298N motor driver based on programmed instructions.
- L298N Motor Driver: This component receives signals from the Arduino and controls the electric linear actuator. It manages the direction and speed of the actuator.
- Electric Linear Actuator: This device converts electrical energy into mechanical motion. Depending on the signals from the L298N driver, it extends or retracts.
- 12V Adapter: It provides the necessary power for both the L298N motor driver and the linear actuator.
- Joystick: It sends signals to the Arduino Uno, specifying the desired direction and speed of the actuator's movement.

Thus, the Arduino Uno sends commands to the L298N driver, which then controls the movement of the linear actuator powered by the 12V adapter. This setup can be used for precise control of linear motion in various applications.

The linear actuator is controlled by a joystick, which provides a comfortable and intuitive interface. This allows for easy control of the linear electric actuator. During the joystick manipulation experiments directly matched the desired drive movement, offering a simple control method.

Figure 15 illustrates the key ankle joint movements supported by the exoskeleton:

- Figure 15a shows the foot in a dorsal flexion position, where the toes are elevated upwards toward the shin. This movement is typically used during the swing phase of gait and is assisted by actuator S1.
- Figure 15b presents the neutral (resting) position, where the foot is aligned horizontally with no active flexion. This represents the default static alignment of the foot before or after movement initiation.
- Figure 15c demonstrates plantar flexion, in which the foot is extended downward, as in the push-off phase during walking. This movement is also driven by actuator S1, in the opposite direction to dorsal flexion.

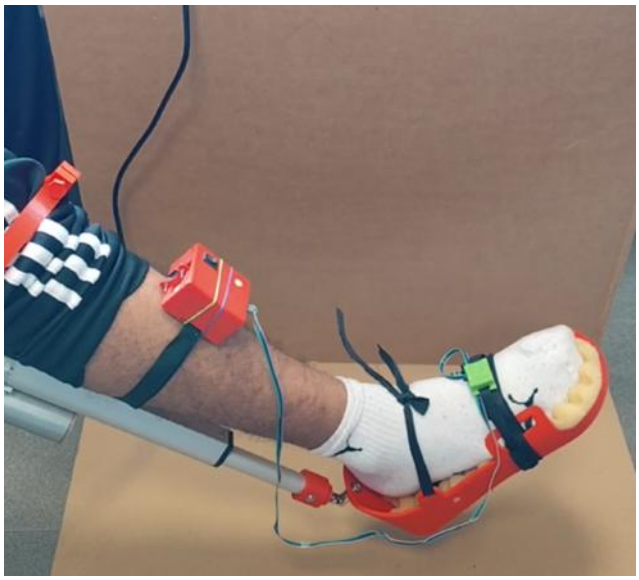


Figure 13 Testing models Almaty Ankle Exoskeleton V.2.

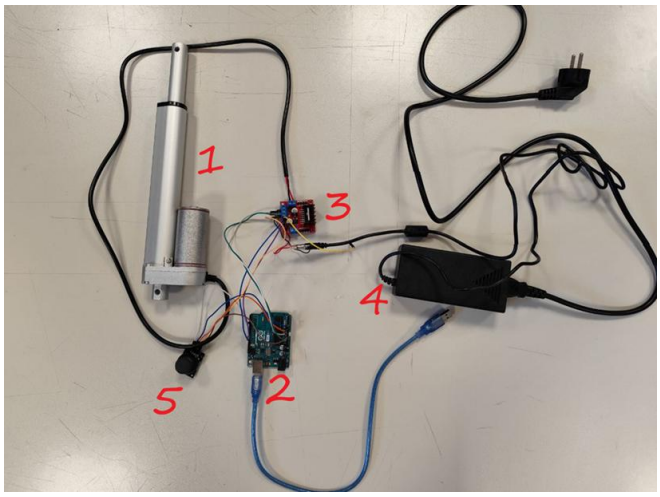
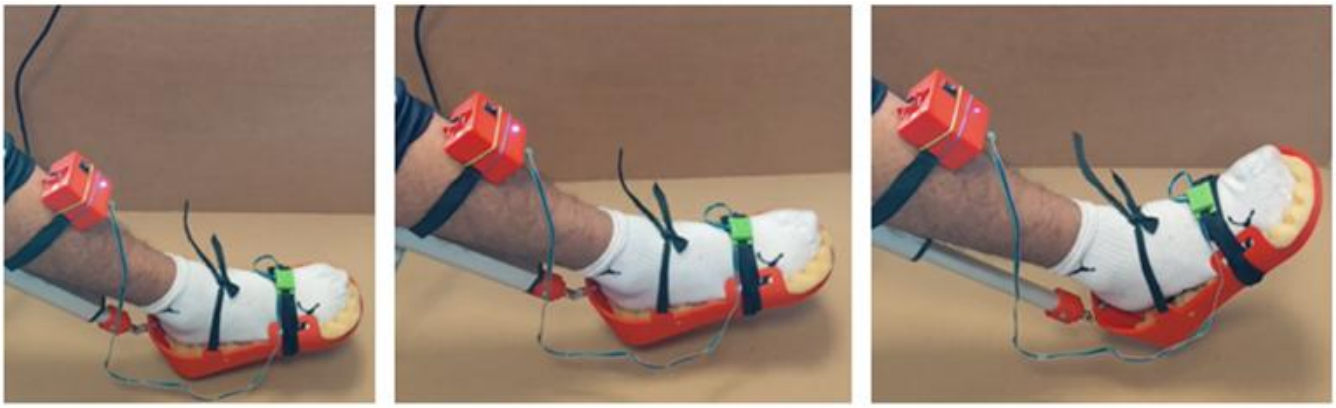


Figure 14 Lab setup. (1- Linear Actuator; 2- Arduino Uno; 3- L298N motor driver; 4- 12V DC; 5- joystick).



a) b) c)

Figure 15 Snapshot of a functional test of ankle joint movement: a) dorsal flexion b) neutral (resting) position c) plantar flexion.

The use of a joystick in the ankle exoskeleton is useful in rehabilitation institutions, as patients or therapists can easily control movements such as dorsiflexion and plantar fasciitis. This makes the process more accessible and less intimidating for those who are not familiar with complex controls. The joystick allows for instant correction of exoskeleton movements in real time, which is crucial in rehabilitation scenarios. Thus, the use of a joystick to control the linear actuator provides an accurate and responsive interface that is necessary for effective therapy.

3.2 TESTING RESULTS

The ankle motion sensor IMU of Fig. 15 allows you to accurately measure and record the angular velocity and direction of joint movements. This sensor, built into the device, provides high accuracy tracking of movement dynamics, making it an indispensable tool for analysis and rehabilitation of the ankle. Fig. 16 shows the angle velocity of the ankle joint for 90 seconds of back and sole flexion. Fig. 17 shows three components of angular velocity: ω_x ,ω_y ,ω_z. The angular velocity range is -15 to 15 degrees per second. The graph also shows changes in angular velocity as a function of time, which allows to evaluate the movement dynamics of the joint during the test. Changes in angular velocity are associated with movements of the foot. The high sensitivity of the IMU sensor detects even the slightest changes in angular velocity.

Figure 17 shows the linear acceleration of the ankle joint during dorsiflexion and plantarflexion over a period of 90 seconds.

The graph displays four components of linear acceleration: g_x,g_y,g_z and g. The linear acceleration of the foot platform ranges from -1 to 1.5 m/s².

Figure 18 shows the angles of ankle flexion in dorsal and plantar flexion. The graph shows three components of angular motion: Roll (blue line), Pitch (blue line) and Yaw (orange line). Angle range of angles ranges from -15 to 35 degrees. The Pitch line shows significant oscillations from about -5 to 30 degrees, indicating repeated flexing movements in the back (up) and sole (down). The human ankle performs three primary movements: dorsal/plantar flexion, inversion/eversion, and abduction/adduction.

These movements correspond to the Pitch, Roll, and Yaw coordinate systems as represented in Figure 18:

- Pitch-axis movement corresponds to dorsal and plantar flexion, which involves the forward and backward bending of the foot.
- Roll-axis movement corresponds to inversion and eversion, which refers to the inward and outward tilting of the foot.
- Yaw-axis movement corresponds to abduction and adduction, describing the foot's rotation in the transverse plane.

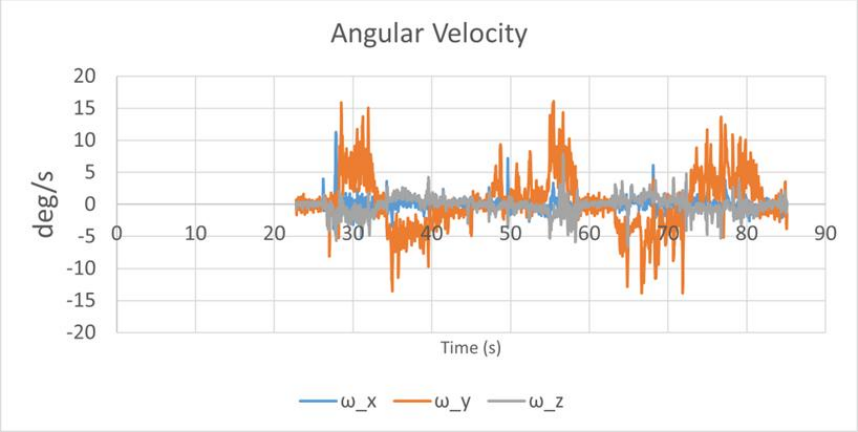


Figure 16 The results of the laboratory test, presented in Fig. 15, show the angular velocity measured by the IMU sensor.

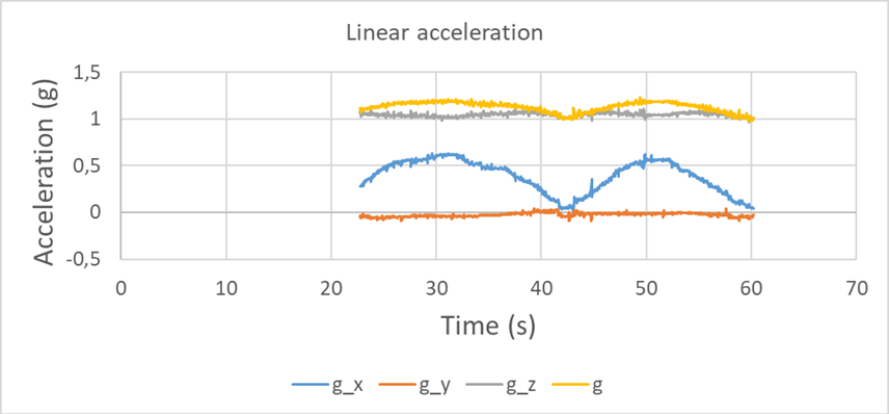


Figure 17 Results of linear acceleration movement with dorsal and plantar flexion in Fig. 15.

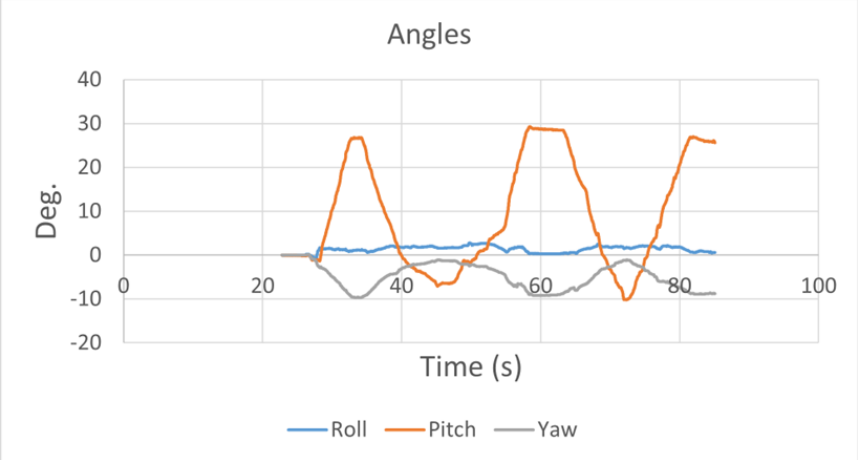


Figure 18 Acquired results of test like in Fig.16 in terms plots of angles Pitch and Roll, Yaw in Figure 15.

The second author decided to personally test the feasibility and effectiveness of the laboratory prototype by conducting laboratory tests using exercises for dorsal flexion of the ankle joint and plantar flexion, as shown in Fig. 19.



Figure 19 Snapshot of a second functional test of ankle joint movement dorsal and plantar flexion.

Figures 20, 21, 22 show graphs of the component's angular velocity, linear acceleration, angles recorded by an IMU sensor attached to the ankle.

The Figure 20 shows the angular velocity of the foot platform during ankle dorsiflexion and plantar flexion. The graph shows the changes in angular velocity over time and consists of three lines representing the different components of angular velocity: ω_x (blue), ω_y (orange), and ω_z (gray). The graph shows that the angular velocities fluctuate, with jumps in the ω_y component being noticeable. The range of angular velocities varies from -20 to 20 degrees per second.

Figure 21 shows the linear acceleration of the foot platform during dorsal and plantar flexion. The graph displays four lines representing different components of acceleration: a_x (blue), a_y (orange), a_z (grey), and a (yellow).

The components a_z and a fluctuate between 1 to 1.5 m/s² over a period of 70 seconds. The a_x component fluctuates around 0.5 m/s², while a_y shows more variability, fluctuating around 0 m/s². Figure 22 shows the angles of the foot platform. The graph consists of three lines: Pitch (orange line), Roll (blue line), and Yaw (gray line). Each line changes over time, indicating the fluctuations in these angles during the test. Pitch fluctuates between 15 degrees and -20 degrees, while Roll and Yaw values remain relatively stable at around 10 degrees and 0.5 degrees, respectively.

4 DISCUSSIONS

The Almaty Ankle Exoskeleton V.2 prototype, equipped with three actuators, is developed to assist and rehabilitate ankle joint movements, particularly focusing on dorsiflexion and plantar flexion. The functional testing of this device aimed to validate its operation by assessing the performance of the actuators and their ability to facilitate natural ankle movements. Functional testing is a crucial step to ensure that the device meets the required specifications and can be effectively used for ankle rehabilitation. The initial testing involved a volunteer using the exoskeleton to perform free ankle movements. During the test, the device provided a controlled rotation of the ankle joint, focusing on the dorsiflexion and plantar flexion movements. This preliminary test was essential to observe the functionality of the actuators and the overall device performance.

The functional testing results indicate that the Almaty Ankle Exoskeleton V.2 has the potential to be a valuable tool in rehabilitating the ankle joint. The device's ability to accurately track and control the critical movements of dorsiflexion and plantar flexion suggests that it can effectively assist in restoring mobility, strength, and stability to the ankle. These movements are essential for basic activities such as walking, running, and maintaining balance, making their rehabilitation critical for patients recovering from injuries or surgeries.

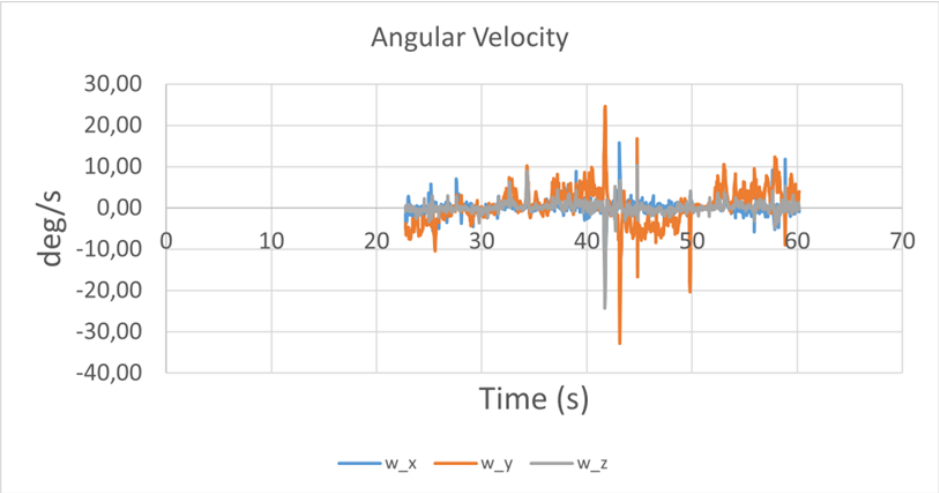


Figure 20 The results of investigations of the angular velocity of the ankle joint during dorsal and plantar flexion are presented.

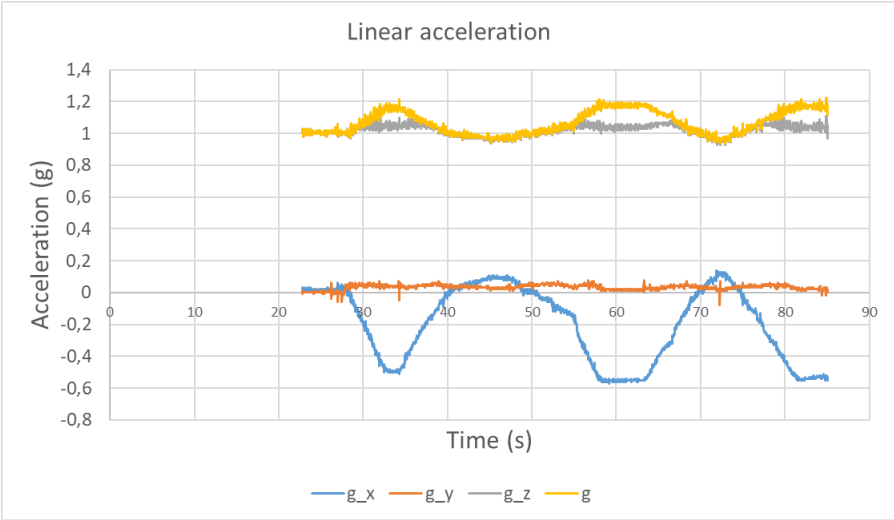


Figure 21 Results of linear acceleration movement with dorsal and plantar flexion.

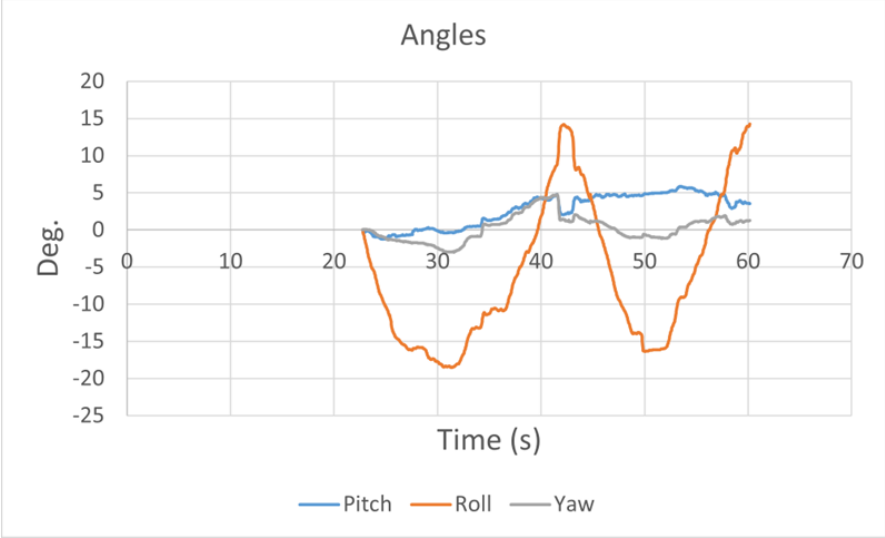


Figure 22 Acquired results of test like in Fig.20 in terms plots of angles Pitch and Roll, Yaw.

Table II - Summary of the test results data obtained, indicating the functional test of the ankle dorsiflexion exoskeleton- plantarflexion

Parameters	Angular Velocity	Linear Acceleration	Angles
1 Test	-15 to 15 deg.	-1 to 1.5 m/s².	-15 to 35 deg.
2 Test	-20 to 20 deg.	1 to 1.5 m/s²	15 to -20 deg.

Moreover, the precise measurement of angular velocity, linear acceleration, and flexion angles provided by the exoskeleton ensures that the rehabilitation process can be closely monitored and adjusted as needed. This level of control and feedback can lead to more effective rehabilitation outcomes, reducing the risk of re-injury and improving overall functional recovery. All the results of the Almaty ankle exoskeleton V.2 experiment are shown in Table II. The functional testing of the Almaty Ankle Exoskeleton V.2 prototype demonstrates its capability to facilitate and monitor the critical movements of the ankle joint. The positive results suggest that, with further refinement and testing, this exoskeleton could become a reliable device for ankle joint rehabilitation. Its ability to assist in dorsiflexion and plantar flexion, coupled with accurate tracking and feedback mechanisms, makes it a promising tool for improving patient outcomes in rehabilitation settings. Future work should focus on long-term testing and clinical trials to validate its efficacy in real-world rehabilitation scenarios.

5 CONCLUSIONS

The development of the Almaty Ankle Exoskeleton V.2 is in progress. By incorporating three linear electric actuators and a carefully design, meet the primary objective of assisting ankle physiotherapy exercises. The lightweight, compact design of the proposed exoskeleton V2 enhances user comfort and mobility of the previous design, while its precise control capabilities support natural ankle movements crucial for rehabilitation. The testing results indicate that the exoskeleton can accurately assist dorsiflexion and plantar flexion, movements essential for restoring normal gait and balance. The use of a joystick for actuator control adds an intuitive interface for users, making the rehabilitation process more accessible and manageable. Future enhancements of the device, including adjustments in the foot platform and improvements of the structural components, are expected to further optimize user comfort and device functionality. These refinements will increase the exoskeleton's versatility, making it suitable for a broader range of users and rehabilitation scenarios.

Funding: This research was funded by the Ministry of Science and Higher Education of the Republic of Kazakhstan, Grant No. AP14972221.

Acknowledgments: The first author expresses gratitude to the JSC «Center for International Pro-grams» Bolashak 2024 program, which provided him with the opportunity to conduct research at LARM2 in Rome in summer 2024.

REFERENCES

[1] Venkata Sai Prathyush I., Ceccarelli M., Russo, M., Control Design for CABLEankle, a Cable Driven Manipulator for Ankle Motion Assistance. *Actuators* 2022, 11, 63.

[2] Brockett C.L., Chapman G.J., Biomechanics of the ankle. *Orthop. Trauma* 2016, 30, 232-238.

[3] Hohl K., Giffhorn M., Jackson S., Jayaraman A., A framework for clinical utilization of robotic exoskeletons in rehabilitation. *J NeuroEngineering Rehabil* 19, 2022.

[4] Roy A. Krebs., Shawnna H., Patterson L., Judkins T., Khanna Ira., Forrester L., Macko R., Hogan N., Measurement of Human Ankle Stiffness Using the Anklebot, *IEEE 10th Int. Conference on Rehabilitation Robotics,* Noordwijk, Netherlands, 2007, pp. 356-363.

[5] Gonçalves R.S., Rodrigues L.A.O., Humbert R., Carbone G., A User-Friendly Nonmotorized Device for Ankle Rehabilitation. *Robotics* 2023, 12, 32.

[6] Rafal Khalid S., Wajdi Sadik A., Smart Robotic Exoskeleton: Constructing Using 3D Printer Technique for Ankle-Foot Rehabilitation, *Journal of Robotics and Control (JRC)* Volume 4, Issue 4, 2023.

[7] Zhetenbayev N., Zhauyt A., Balbayev G., Shingissov B., Robot device for ankle joint rehabilitation: A review. *Vibroengineering PROCEDIA* 2022, 41, 96–102.

[8] Liu Q., Wang C., Long JJ., Sun T., Duan L., Zhang X., Zhang B., Shen Y., Shang W., Lin Z., Wang Y., Xia J., Wei J., Li W., Wu Z., Development of a New Robotic Ankle Rehabilitation Platform for Hemiplegic Patients after Stroke. *J Healthc Eng.,* 2018.

[9] Ioan Doroftei., Cristina-Magda Cazacu., and Stelian Alaci., Design and Experimental Testing of an Ankle Rehabilitation, *Robot Actuators* 2023, 12, 238.

[10] Malosio M., Pio Negri., S Pedrocchi., N Vicentini., F Caimmi1., M Molinari., L Tosatti., A. Spherical Parallel Three Degrees-of-Freedom Robot for Ankle-Foot, *NeuroRehabilitation 34th Annual Int. Conf. of the IEEE EMBS* San Diego, California USA, 2012.

[11] Jingke S., Jun W., Bin Y., Chenglei L., Cunjin A., Jianjun Z., Configuration Design and Kinematic Performance Analysis of a Novel 4-DOF Parallel Ankle Rehabilitation Mechanism with Two Virtual Motion Centers. Chin. *J. Mech. Eng.* 36, 154, 2023.

[12] Tsoi Y., Xie S.Q., Graham A.E., Design, Modeling and Control of an Ankle Rehabilitation Robot. In: Liu, D., Wang, L., Tan, K.C. (eds) *Design and Control of Intelligent Robotic Systems. Studies in Computational Intelligence, vol 177. Springer, Berlin*, 2009.

[13] Congzhe W., Yuefa F., Sheng G., Yaqiong C., Design and Kinematical Performance Analysis of a 3-RUS/RRR Redundantly Actuated Parallel Mechanism for Ankle Rehabilitation J. *Mechanisms Robotics.* Nov 2013, 5(4): 041003 Paper No: JMR-12-1107.

[14] Vallés M., Cazalilla J., Valera Á., Mata V., Page Á., Díaz-Rodríguez M., A 3-PRS parallel manipulator for ankle rehabilitation: towards a low-cost robotic rehabilitation. *Robotica.* 2017, 35(10):1939-1957.

[15] Li J., Zuo S., Zhang L., Dong M., Zhang Z., Tao C., and Ji R., Mechanical Design and Performance Analysis of a Novel Parallel Robot for Ankle Rehabilitation. *ASME. J. Mechanisms Robotics.* October 2020; 12(5): 051007.

[16] Shiping Z., Jianfeng L., Mingjie D., Xiaodong Z., Wenpei F., Yuan K., Design and Performance Evaluation of a Novel Wearable Parallel Mechanism for Ankle Rehabilitation, *Frontiers in Neurorobotics,* 14, 2020.

[17] Roy A., Forrester LW., Macko RF., Short-term ankle motor performance with ankle robotics training in chronic hemiparetic stroke. *J Rehabil Res Dev.* 2011.

[18] Jungyoon K., Sungjae H., Ryanghee S., Younghee L., Youngho K., Development of an Active Ankle Foot Orthosis to Prevent Foot Drop and Toe Drag in Hemiplegic Patients: A Preliminary Study, *Applied Bionics and Biomechanics,* Vol. 8, 2011.

[19] Belforte G., Raparelli T., Eula G., Sirolli S., Appendino S., Geminiani G.C., Geda E., Zettin M., Virgilio R., Sacco K. Study and realisation of a preliminary control system for the active exoskeleton called P.I.G.R.O., suitable for unloaded robotic neurorehabilitation treatments, *International Journal of Mechanics and Control,* Vol. 22, No. 2, pp. 95-106, 2021.

[20] Nursultan Z., Marco C., Balbayev G., A Portable Robotic System for Ankle Joint Rehabilitation. *Electronics* 2023, 12, 4271.

[21] Nursultan Z., Ceccarelli M., Balbayev G., Experimental Characterization of Almaty Ankle Joint Exoskeleton. Okada, M. (eds) Advances in Mechanism and Machine Science. IFToMM WC 2023. *Mechanisms and Machine Science*, vol 147. Springer, Cham, 2023.

[22] Actuonix, Miniature Linear Actuators L16, user manual, 2024. URL: https://www.actuonix.com/linear-servos-for-rc, visited on 17/08/2024.

[23] Nursultan Z., Aidos S., Ceccarelli M., Sergazin G. An Experimental Characterization of Almaty Ankle Exoskeleton. In: Advances in Asian Mechanism and Machine Science. Asian MMS 2024. *Mechanisms and Machine Science,* vol 167. Springer, Cham. 2024.

[24] Linear actuator IP54 150mm 12V 1.5cm/s 50Kg, 2024. URL:https://www.robotstore.it/en/Attuatore-Lineare-IP54-150mm-12V-1-5cm-s-50Kg , visited on 17/03/2025.

[25] Adventurer 5M, user manual, 2024. URL:https://flashforge.com/products/adventurer5m?srsltid=AfmBOop4Z-vf1DfHV6eJKa9WRh13j6yAzHdhfrGYaQHHmi-lu3kKl4a, visited on 28/08/2024.

[26] Arduino Nano, user manual, 2025. URL: https://docs.arduino.cc/hardware/nano/, visited on 15/03/2025.

[27] L298N Motor Driver Module, user manual, 2025. URL: https://https://components101.com/modules/l293n-motor-driver-module/, visited on 15/03/2025.

[28] MPU-6050, user manual, 2025. URL: https://invensense.tdk.com/products/motion-tracking/6-axis/mpu-6050/, visited on 16/03/2025.

APPENDIX 1: Programming code for prototype operation

```
Programming Code for the Prototype's Command and
Control Unit:
#include <Wire.h>
#include <SPI.h>
#include <SD.h>
#include <Servo.h>
// Define pins
#define LED_PIN 6
#define SD_CS_PIN 10
#define SERVO_PIN 9
#define SENSOR_PIN A0
Servo actuator;
File logFile;
void setup() {
    Serial.begin(115200);
    pinMode(LED_PIN, OUTPUT);
    // Initialize SD card
    if (!SD.begin(SD_CS_PIN)) {
        Serial.println("SD   card   initialization
failed!");
    } else {
        Serial.println("SD    card    initialized
successfully.");
    }

    // Initialize actuator
    actuator.attach(SERVO_PIN);
    actuator.write(90);     //   Set   to   initial
position
     Serial.println("System started.");
}
void loop() {
    // Read sensor data
    int sensorValue = analogRead(SENSOR_PIN);
    float voltage = sensorValue * (5.0 / 1023.0);
    // Write to log file
    logFile = SD.open("log.txt", FILE_WRITE);
    if (logFile) {
        logFile.print("Sensor Voltage: ");
        logFile.println(voltage);
        logFile.close();
    }
    // Control the actuator based on sensor input
    if (voltage > 2.5) {
        actuator.write(120);  // Activate motion
        digitalWrite(LED_PIN, HIGH);
    } else {
        actuator.write(90);  // Return to initial
position
        digitalWrite(LED_PIN, LOW);
    }
    delay(500);
}
}
```

ISSN 1590-8844
International Journal of Mechanics and Control, Vol. 26, No. 01, 2025
https://doi.org/10.69076/jomac.2025.0013

DESIGN AND TESTING A SENSORED ROTATING CRANK FOR ARM EXERCISES OF ELDERLY PEOPLE

Susana Sanz* Matteo Russo** Maria Garrosa* Marco Ceccarelli**

* Institute for Vehicles Safety Assurance, Department of Mechanical Engineering, University Carlos III of Madrid

** Laboratory of Robot Mechatronics, Department of Industrial Engineering, University of Rome Tor Vergata

ABSTRACT

A portable device for arm exercise at home is presented with its peculiarities. The proposed device is suitable for performing exercises that improve the mobility of the upper limbs with feat uses in comfort, easy-operation, and low cost. Portability and motion exercise are ensured by a light sensored rotating crank that is installed on a light cubic frame. In this paper, the suitability of the device is tested with elderly people. A test protocol is defined and a comparison of the results obtained by a young person and an older person is discussed to prove the efficiency and to characterize performance. Values of force applied to the knob, acceleration, and angular velocity of the crank are discussed as a characterization of the device operation. The device detected the smaller movement capacity of an older person with respect to a younger person. This is reflected in the maximum acceleration, which is approximately half in the tests of an older person than in the tests of a younger person.

Keywords: Medical Devices, Biomechanics, Arm Exercises, Rehabilitation exercise, Elderly people

1 INTRODUCTION

Within the complexity of the human body, the upper limbs offer individual capabilities necessary for daily life. Bones, muscles, tendons, joints, make the arm a complex biomechanical element necessary for many daily tasks in manipulation and locomotion. Given importance, when the upper limbs diminish their functionality, they generate problems in the daily activity of the individual. Upper limb problems are caused by accidents, disabling injuries, surgical operations or mobility problems due to old age and lack of exercise. It has been reported that up to 30% of stroke patients suffer permanent disabilities and up to 20% require intensive rehabilitation programs [1]. Research has shown that, in postoperative treatment, the time between the operation and the start of exercise is decisive.

Contact author: Susana Sanz[1], Marco Ceccarelli[2]

[1]University Carlos III of Madrid, 28911 Madrid, Spain.
[2]Department of Industrial Engineering, University of Rome Tor Vergata, 00133 Rome, Italy
E-mail: ssanz@ing.uc3m.es, marco.ceccarelli@uniroma2.it

In interventions, such as lymph node dissection in breast cancer, the results of arm mobility improve markedly the earlier the exercises are started [2].
The authors of the paper [3] indicate the importance of confidence development in stroke survivors to support long-term self-care after stroke. This lack of confidence is the same as that suffered by older people who see their abilities decline. Health improvement with rehabilitation for people with upper limb disabilities has been studied by researchers [4-5]. They conclude that digital technologies used in post-stroke upper limb rehabilitation are multimodal and based on systems comprising telerehabilitation, gamification, virtual reality, mobile technology, sensors, and robotics.
The work [6] investigates the effects of arm pedaling exercise on cutaneous microcirculation in elderly and sedentary individuals. Cutaneous flow responses were measured in the upper and lower extremities. The results suggest that acute exercise can improve microvascular function, although adaptations may vary between upper and lower limbs. The study suggests that improved cutaneous microcirculation may facilitate better blood flow, which is crucial for vascular health and muscle function. As circulation is optimized, participants are likely to experience an increased ability to perform daily activities, which could translate into an overall improvement in mobility and quality of life.

Since the time lapse to start rehabilitation is so important after certain interventions, new telerehabilitation processes are designed. Telerehabilitation activities have been shown to be effective, being one of the most important ways to reduce rehabilitation costs and increase patients' quality of life. Telerehabilitation processes are increasing for different ailments, such as after breast cancer surgery with node dissection [7-8]. Also, home exercises after cardiovascular accidents [9]. Home cardiac telerehabilitation exercises are proposed in the research [10]. Home exercise helps people with lupus. The authors in [11] conclude that upper extremity exercise significantly improves hand function, pain, performance of daily activities, and quality of life with systemic lupus erythematosus.

The objective of the work [12] is to present the implementation of a wireless sensor system for upper limb rehabilitation, which serves as a complementary system to monitor the patient's progress during rehabilitation exercises. The main conclusion is that the proposed system offers accuracy comparable to that of a commercial sensor, with a very low error rate.

Work such as [13] aims to create a tele-rehabilitation platform to support remote rehabilitation of both upper and lower extremities. Artificial intelligence methods [13] are utilized to regulate the limb's movement angle around the joint. Another form of remote rehabilitation is robot-assisted therapy, which is discussed in various academic papers. The work [14] introduces a novel approach to bilateral upper limb training, emphasizing the coordination of both arms. Researchers in [15] investigate on a significant number of individuals who have suffered from cardiovascular events and observe that robotic rehabilitation enhances upper limb mobility. The authors of [16] provide an extensive overview of robotic solutions for upper limb rehabilitation. Additionally, the development of a mechanism for assisting upper limb movements in adults and children is detailed in [17].

Telerehabilitation serves to address waiting lists in medical centers and enhances health post-intervention where swift treatment is vital. However, its application isn't as widespread solely for improving mobility due to prolonged immobility, particularly among the elderly. Degeneration and/or sedentary lifestyles can lead to a loss of mobility in the upper extremities, resulting in a notable decline in daily life quality.

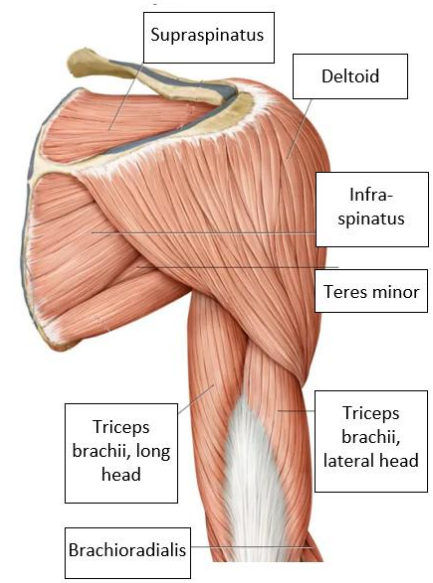
Work such as [18] highlights the necessity for tailored strength and balance exercises in multidisciplinary fall and injury prevention efforts. The primary aim of the work in [19] was to assess whether crank exercise elicited systemic or localized cutaneous microcirculatory effects in a healthy elderly population, comparing results with previous findings in patients with chronic venous disease. The work concludes that acute exercise involving arm lifting enhances microvascular endothelial function in the extremities. Furthermore, it is noted that elderly individuals often experience shoulder pain [20], and like other conditions, various at-home therapies exist to enhance mobility. For instance, a robotic system guides elderly individuals through a series of exercises while monitoring their movements [21]. In addition to home exercises to improve injuries, there is research activity that is reported for example in [22-25], that looks for the benefits of exercise in elderly people, even if they do not have a particular ailment and just suffer from normal aging effects. Individual, unsupervised home exercise programs have been shown to enhance muscle strength, physical function, gait, and balance in older people. The authors of [26] discuss the effectiveness of home exercise programs. They compare unsupervised versus supervised exercise and conclude that both are effective, although the results improve with some supervision. This work presents a patented device for exercise of upper limb mobility for elderly people with or without previous upper limb problems. It is a sensorized device easy with specific features for its use by elderly users. Its operation is discussed through the comparison of tests by two healthy people, young and one elderly.

2 REQUIREMENTS FOR ARM EXERCISES

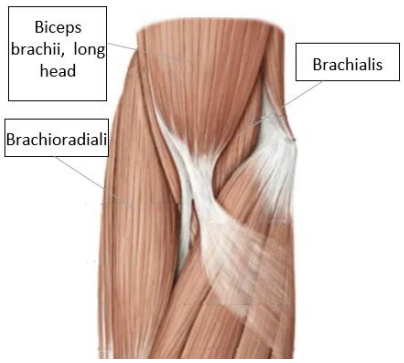
For the design of a device to exercise arm mobility, it is necessary to know the biomechanics of the upper limbs. The upper extremity has five elements: shoulder, arm, elbow, forearm and hand. Essential for movement are the shoulder and arm containing the glenohumeral joint, which allows a full range of motion. They are complemented by various ligaments that stabilize the joint.

Muscular anatomy of the upper limb in man is composed of anterior muscles of shoulder joint and arm (Figure 1a) and anterior muscles of foreman (Figure 1b). The upper limb is a complicated web of musculature that must be known in depth to be able to conduct the appropriate tests and obtain the right information to achieve the proposed purpose.

The muscular anatomy of the arm shown in Figure 1b is simpler than in the shoulder, being composed of four muscles grouped into two sets according to their behavior: biceps brachii, coracobrachialis and brachialis, allowing for anterior brachial behavior or flexion of the arm. The fourth muscle, triceps brachii, will allow posterior brachial behavior. Whatever the origin of the problem is, in the case of having injury or ailment in any of the exposed muscles, the movement of the upper limb is affected with mobility reduction. The upper limb has a total of 7 degrees of freedom (DOF). The shoulder joint has three degrees of freedom: two for flexion-extension and one for abduction-adduction as summarized in Figure 2. The elbow joint has one DOF for flexion-extension and the movement of the forearm with pronation-supination adds another DOF to the elbow. The wrist joint has two degrees of freedom, one for flexion-extension and another for abduction-adduction. However, also the pronation-supination adds another DOF to the wrist joint. Knowledge of the movements and muscles involved led to the design of a device that, by means of simple movements, exercises the arm musculature and can improve mobility [28].



a)



b)

Figure 1 The Muscles of [27]:
a) the Shoulder Joint and Arm b) Forearm.

Sarcopenia is the process of loss of muscle mass and strength that occurs naturally with aging [22]. The muscles most commonly affected by sarcopenia are the major muscle groups that are used in daily, functional activities. In this disease it affects the muscles of the arms, such as the deltoids (shoulders), biceps (front of the arm) and triceps (back of the arm). These muscle groups are important for maintaining mobility, stability and functional ability in daily life. Sarcopenia can affect the ability to perform simple tasks such as getting up from a chair, climbing stairs or carrying heavy objects, which can have a significant impact on the quality of life of older people. The weight and size of the device must be appropriate to make the device portable. Data can be ensured through a SD memory to monitor the evolution of the patient by possible supervision by medical operators. The components can be selected from the market and other parts can be 3D printed, making a device low-cost solution. The design should be oriented towards user operability with an assembly reconfigurable and adjustable depending on the user conditions.

Figure 3 summarizes design requirements in terms of main features of a low-cost user-oriented device for arm assisted exercise [29].

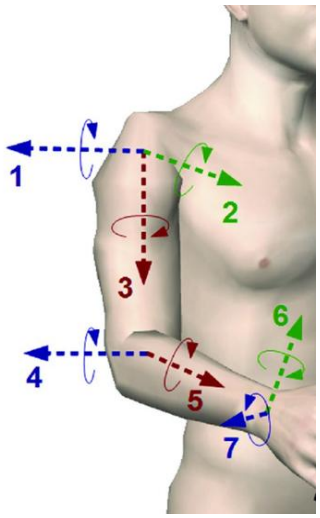


Figure 2 Motion axes of the human arm
1,7: Abduction-Adduction; 2,3,4,6: Flexion-Extension;
5: pronation-Supination.

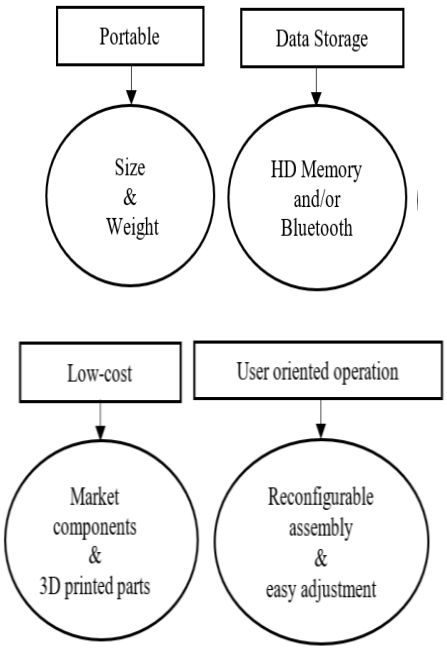


Figure 3: Requirements for design and operation of arm assisting devices

Table 1 lists the values of the main design features for a home assisting device. Device should be a size of 30x30x30 cm and a weight of 20 N to give a portable device. The crank should freely rotate with power assistance or production of about 100W with a battery or a dynamo, respectively. These values meet the objectives and are recommended for a portable device.

Table 1 - Values of reference for main aspects in Fig. 3

Size (cm)	30x30x30
Weight (N)	20.0
Range of motion (deg)	> 360
Power (W)	< 100

3 DESIGN OF ROTATING DEVICE

The sensored rotating device must meet the requirements summarized in Figure 3, [29]. It should be a lightweight, easy to assembly, easy to use, and low cost. With these requirements, a prototype is manufactured to perform upper limb exercises in different modalities. The principle of operation of the device will be controlled rotary movements with protocols that are designed according to the desired movement for individual's arm. Figure 4 shows a CAD design of the proposed sensored rotating device. The motor/dynamo is attached to the crank as a dynamo. The dynamo´s shaft is attached to one end of the crank, which allows rotational movement around the motor axis. On the opposite side of the crank is attached the drive knob of the device. This knob rotates freely around its axis, allowing a comfortable and ergonomic movement of the crank for user.

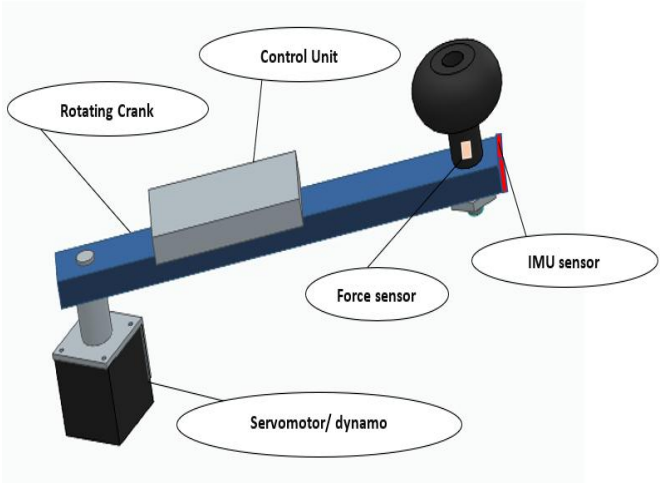
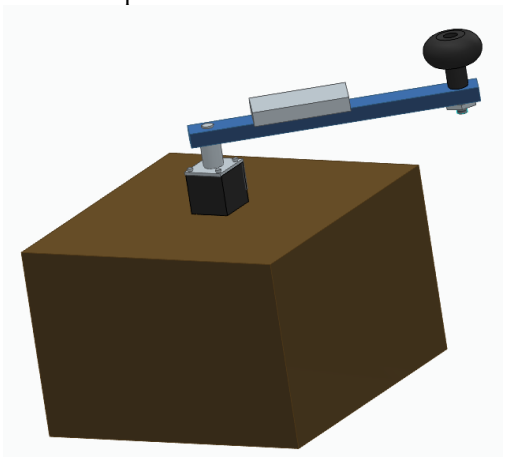


Figure 4 CAD design of sensored rotating device.

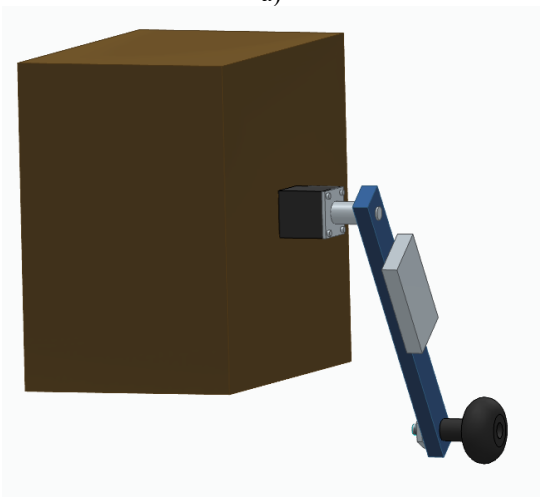
The designed rotating device in Figure 4 needs to be attached to a light test frame. This frame is designed as a cube volume with an aluminum profile for easy and quick assembly. The device weighs 1 kg and the frame weighs 1 kg. Being a total of 2 kg. It is light for transportation. The union between the volume and the table surface can be obtained by commercial clamps. These give enough support, are cheap and easy to use. The first prototype presented in a previous work [28] is redesigned to improve the functionality with features that are discussed in this paper. In the device, the necessary electronics is installed to process to the data acquisition in a wireless way, with no need of the computer and the cable. Since the data acquisition system is light, it is placed on the crank yet.

The designed device allows a multitude of exercises, when combining the positioning of the individual with the device itself. For example, exercise is possible standing in front of the device. Also, the individual can position to the device laterally. Both can use crank in the horizontal or vertical plane. In addition, it is possible to perform the exercise sitting, achieving full extension of the upper limb.

By placing the device on a cube structure, it is possible to perform exercises in two orthogonal planes. Depending on the placement of the cube, the device is placed in the horizontal plane (Figure 5a) or in the vertical plane (Figure 5b). Depending on the positioning, the movement will exercise different parts of the arm.



a)



b)

Figure 5 CAD Design with sensored rotating crank in: a) horizontal plane; b) vertical plane.

4 PROTOTYPE AND TESTING LAYOUT

With the requirements described above, the prototype is manufactured by using commercial components. Figure 6 shows the prototype of crank device according to the designed solution in Figure 4 and according to the patent [30]. This device can be divided into three elements, Figure 6. The motor (1), in this work is not powered, working as a dynamo.

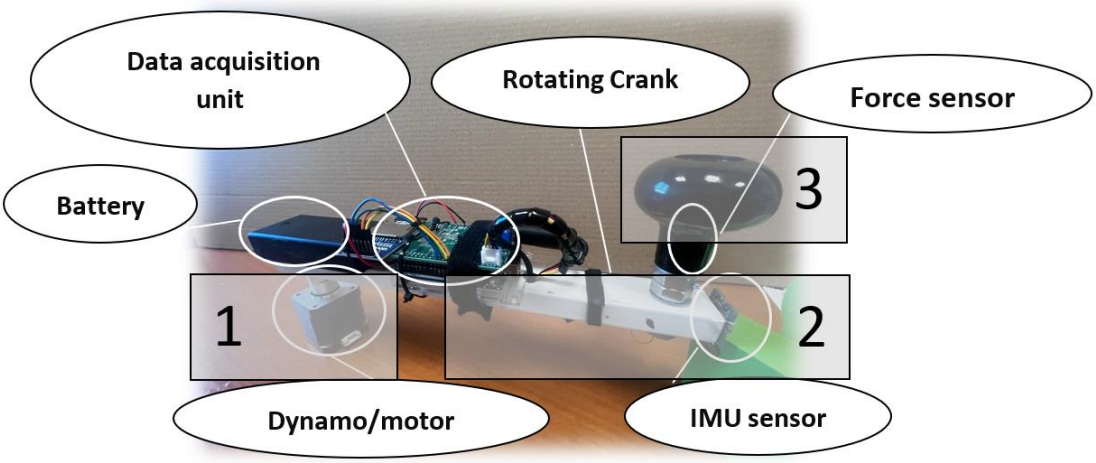


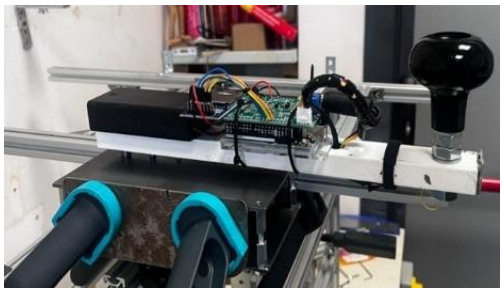
Figure 6 Prototype of the crank device (1: motor; 2: crank; 3: knob).

Table II - Device components of the prototype in Figure 6

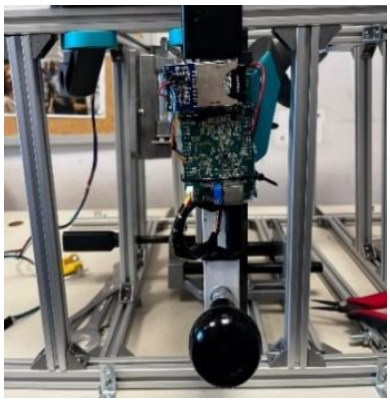
ITEM	PRODUCER	MODEL	SELLER	APPROXIMATE COST €
IMU [31]	Seeed	Sku 114020121	Mouser electronics	12€
FORCE SENSOR [32]	Tokyo sokkio kenkyujo	FLAB-2-11	EUROPAVIA	4,5€
BATTERY [33]	Zygy	B08K8DLHT6	Yihongtong technology	10 €
ARDUINO UNO [34]	Arduino	UNO	Digikey	20€
MOTOR/DYNAMO [35]	Osm technology CO. LTD	Nema 17 HS115-1504S1	Stepperonline	10€

A current sensor is installed in it to record the amount of energy generated in the experiment during arm exercise. The crank (2) is the element that allows the movement, containing the data acquisition system, battery and an IMU for recording speed and acceleration in the exercise. The knob (3) is a commercial element that is approved for the operation of car handwheels with a single hand, allowing smooth and ergonomic movement. Inside the knob, force sensors are installed to quantify the force applied to operate the crank. The device is designed to perform active and passive exercises, depending on whether the crank is driven by the arm (active) or by the motor (passive). In this work we show exercises in active mode, when the motor acting as a dynamo without being powered. Figure 7a shows the device positioned horizontally and Figure 7b shows it positioned vertically. Switching from one position to another is easy by rotating the cube. The connection of the device to the cube frame and the positioning of the individual allows the performance of exercises in different postures, sitting, standing, frontally or laterally. The efficacy of the prototype has been proven in previous tests [31] where the comparative use of both hands of the same individual was carried out.

Figure 8 shows a summary of the different configurations in which the device can be used. Exercises can be performed while uses is standing or sitting position. The device can be positioned horizontally or vertically. In addition, the position of the individual can also be varied, being frontal or lateral.
In this paper, a comparative experience is reported two healthy people, one young and one old. For all the tests, a protocol is established with the location of the individual and the performance sequence of the exercise. Both individuals are right-handed females of the same height and similar build. The exercises are performed in the vertical plane and with the individual facing the device.
For the location, the position of the individual should be seated in front of the device, with the shoulder aligned with the axis of rotation of the crank, as it in Figure 9a. The starting position of the exercise can be seen in Figure 9b. The distance to the device should be adequate to perform the complete rotation without difficulty without moving the upper trunk like Figure 9c shows. The test consisted of three turns clockwise and three counterclockwise, performed with both hands. Figure 10 lists the instructions given to the individual at the time of the informed consensus for the test.



a)



b)

Figure 7 A lab setup of the prototype for running the crank in: a) horizontal plane; b) vertical plane

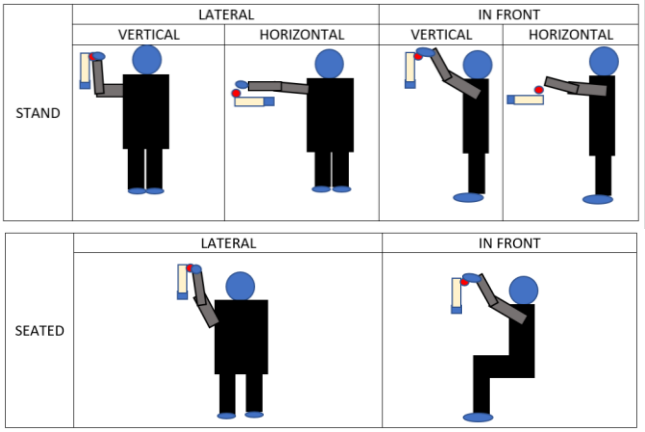


Figure 8 Description of protocol for testing modes.

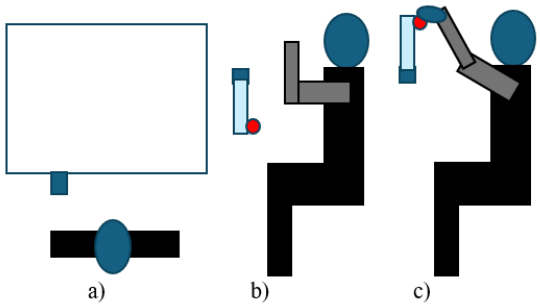
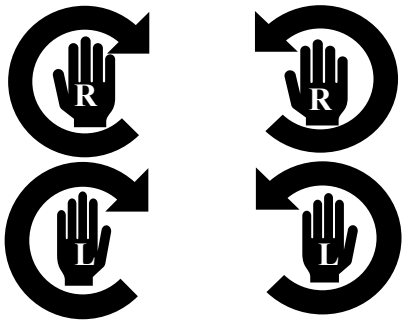


Figure 9 Scheme for position of volunteer: a) top view; b) lateral view; c) lateral view with full extension.

Motion sequence

1) Three complete clockwise rotations RIGHT ARM
2) Three complete counterclockwise rotations RIGHT ARM
3) Three complete clockwise rotations LEFT ARM
4) Three complete counterclockwise rotations LEFT ARM

a)



b)

Figure 10 Protocol for carrying out exercises: a) instructions; b) motion directions.

5 TEST RESULTS

Values of force applied on the knob and information about the movement of the crank are acquired during the exercise described in Figure 10. The exercise was performed with two people in the same position to ensure that the results are comparable. Figure 11 shows the first author performing the test with the left hand with proper positioning as shown in Figure 9. The axis of rotation of the device is between top of the head and shoulder. In the first image a rotational movement is complete and effortless. The exercise is performed with left arms to compare the results of use with young and older people. The author is a young person, of 46 years of age, without any injury throughout her life to the shoulders or arms. She has height and weight characteristics close to the Spanish normal one, being a height of 170 cm and weight 75 kg. She is a right-handed person, so her daily activities are mostly performed with her right hand.



Figure 11 Snapshot of a test by the first author with rotating crank in vertical configuration.

Figure 12 shows the positioning of both volunteers who are compared in this paper. Devices is configurated for vertical running of the crank. Figure 12a shows the first author whose completeness has been defined above. Figure 12b shows the older volunteer at 77 years of age with a height of 168 cm and a weight of 70 kg.

It can be seen that both configurations are similar, and the protocol defined in Figure 10 has been performed by both volunteers with their non-dominant hand.



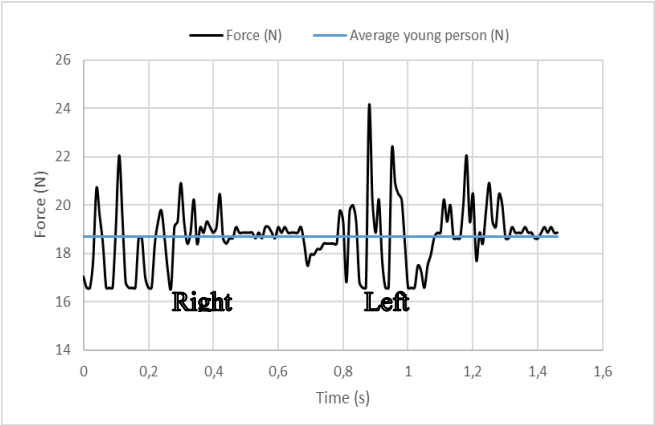
a)



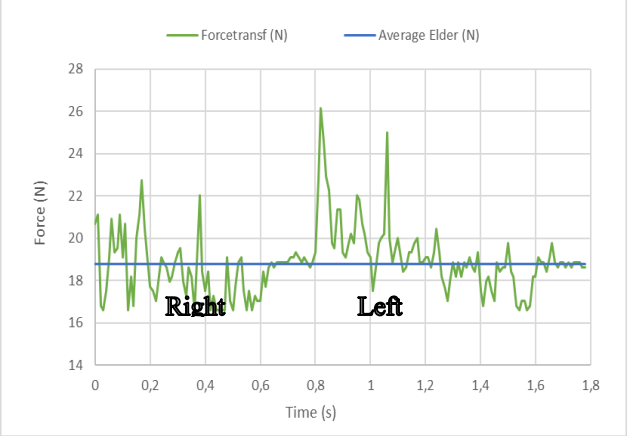
b)

Figure 12 Right-handed people during experiment: a) young author; b) older volunteer.

The comparison of a young person and an older person, both without ailments in their arms, has also been experimented in order to compare the force by which the handle knob has been operated. The results are shown in Figure 13. In addition, the average force during the experiments has been calculated as the average of the values during the experiment. The results of the right-hand movements, initially in clockwise and then in counterclockwise movements, are shown in Figure 13a and Figure 13b for a duration up to about 0.7 seconds. After 0.7 seconds the left-hand movements are acquired again. In Figure 13a the average force applied to the knob is 18.68N, with the average force in the right hand being 18.52N and in the left hand 18.84N. These values are very similar in both hands, coinciding with the studies carried out to evaluate fitness for healthy adults. It is observed that the maximum value of force is applied with the non-dominant hand having a value of 24.09N, being the maximum value of the dominant hand 22.04N. Both peaks recorded in clockwise motion. As well as the behaviour by both hands, these results agree with the results obtained in [29].



a)



b)

Figure 13 Acquired results in terms of force on the knob during test by a right-handed people of: a) young person; b) older person.

Figure 13b shows the values in terms of force applied by the older person when performing the same exercise. It is observed that the average force applied throughout the exercise is similar (18.77N), being 18.38N in the right hand and 19.16N in the left hand. It is observed that in an older person the difference between both hands is larger as due to the fact that the musculature is not exercised in the same way as the young person.

In Figure 13b for left hand clockwise, the maximum force value (26.14 N) is obtained compared to 22.72 N for the dominant hand in the clockwise direction. In elderly people, a more significant difference is observed between both hands.

Figure 13 shows that both individuals use the largest force with the non-dominant hand. In the case of the young person, Figure 13a, in a clockwise direction. In the case of the older person, Figure 13b, counterclockwise.

Figure 14 shows the acceleration module, free of gravity as

$$a = \sqrt{a_x^2 + a_y^2 + a_z^2} - g \quad (1)$$

The value of the acceleration module is clearly influenced by the acceleration in the z-axis.

The young person used 0.4 seconds less time to perform the exercise than the older person. This difference is significant, since it is 25% less of the total time.

Acceleration has much lower values in older people. In Figure 14a, corresponding to a young person, the maximum acceleration is 19.70 m/s^2 when compared to 15.24 m/s^2 in Figure 14b belonging to an older person. The acceleration used by a young person is similar in both hands, while for an older person it is significantly smaller in the non-dominant hand than in the dominant hand. Table 3 summarizes the values in terms of acceleration module obtained by both volunteers. The maximum, minimum and average values are listed for each phase of the exercise. The maximum difference between the two individuals is obtained on the left-hand side in a counterclockwise rotation.

Considering Figure 6, the working plane of the crank is ZX, vertical plane. Therefore, the results obtained in acceleration are greatly influenced by gravity. Figure 15 shows the acceleration in axis z, the points at which the crank is at its upper point (arm fully extended upwards) provide maximum acceleration values in each revolution. When the individual changes hands to do the exercise, the crank is at rest. It is observed that at that moment only the force of gravity acts, with the acceleration value in axis z is 9.81 m/s^2.

Figure 16 shows the acceleration in axis y, In Figure 16a, belonging to the young person, the movement is firmer. However, in Figure 15b the opposite is observed, with a slower motion and, therefore, a more variable plot.

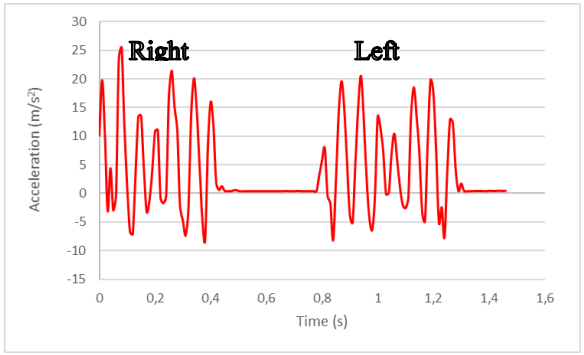
Figure 17 shows the values recorded in terms of angular velocity with respect to axis x (blue) and axis z (yellow). Considering that the axis y is the axis that has the direction of the axis of rotation, the angular velocity y is the predominant one. The angular acceleration in x and z must be close to zero. In Figure 18, it can be seen that the value of the angular velocity in the x and z axis is not zero. This is because the crank has vertical motion due to instability and/or lack of perpendicularityy of the platform.

It is observed that the values of angular velocity in x and angular acceleration in y for the young person (Figure 17a) are larger than for the older person (Figure 17b). This is due to the fact that the faster and more energetic movement increases the instability of the device in this plane of use.

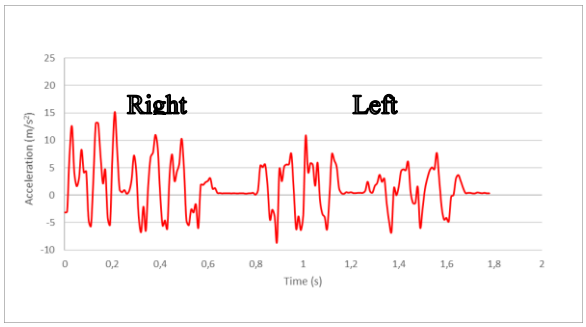
Figure 18 shows the predetermined angular velocity, Ω_y. The values are lower in the test performed by the elderly person. Being the maximum 6.52 rad/s versus 10.28 rad/s recorded in the young person. It is observed that the elderly person uses much more force with the left hand than with the right, that is, they are more affected by the non-mobility of the non-dominant hand. In the counterclockwise turn, 26.14 N is used with the left hand compared to 22.04 N with the right and 18.85 N with the average. This fact is observed in the young person but on a lower average, obtaining 24.09 N in a clockwise direction compared to 22.04 N for the right hand in the same direction of rotation and 18.69 N for its average.

Table III - Comparative results in terms of acceleration module

HAND	DIRECTION OF ROTATION	ACCELERATION	YOUNG PERSON (m/s^2)	OLDER PERSON (m/s^2)	DIFFERENCE (%)
RIGHT HAND	CLOCKWISE	MAXIMUN	25.43	15.24	40
		MININUM	-7.13	-5.62	21
		AVERAGE	6.10	3.57	41
	COUNTER CLOCKWISE	MAXIMUN	21.37	11.05	48
		MININUM	-8.16	-6.77	17
		AVERAGE	4.43	1.07	76
LEFT HAND	CLOCKWISE	MAXIMUN	20.47	10.80	47
		MININUM	-8.20	-8.47	-3
		AVERAGE	5.24	1.18	78
	COUNTER CLOCKWISE	MAXIMUN	19.70	7.74	61
		MININUM	-7.75	-6.66	14
		AVERAGE	3.13	0.95	70

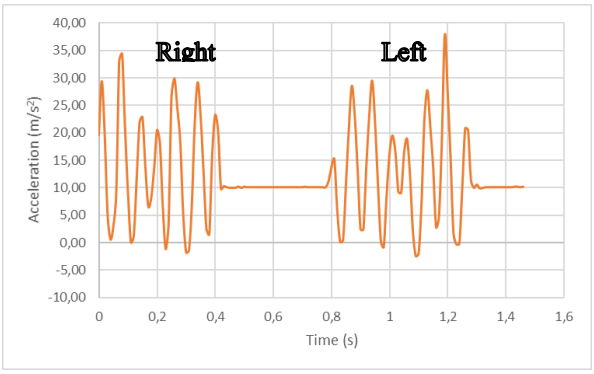


a)

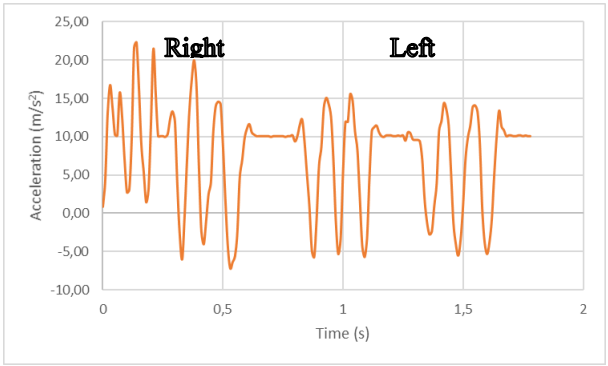


b)

Figure 14 Acquired results in terms of acceleration module during experiment of a right-handed people of: (a) young person; (b) older person.

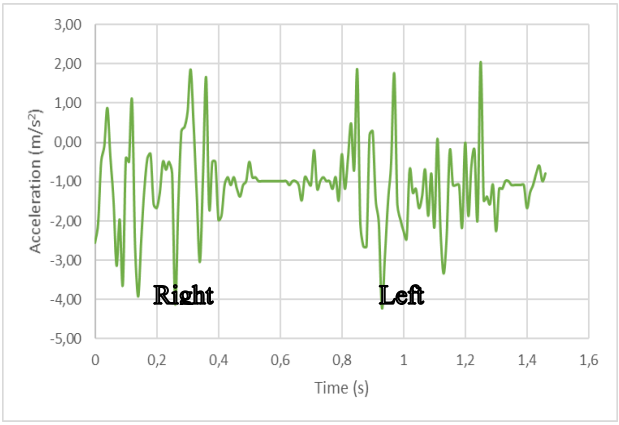


a)

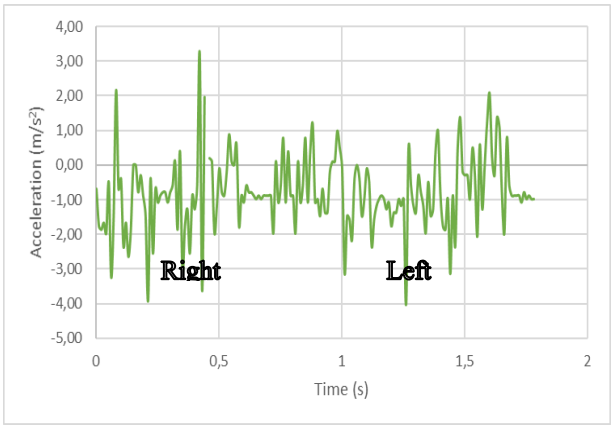


b)

Figure 15 Acquired results in terms of acceleration in axis z during experiment of a right-handed people of: (a) young person; (b) older person.



a)

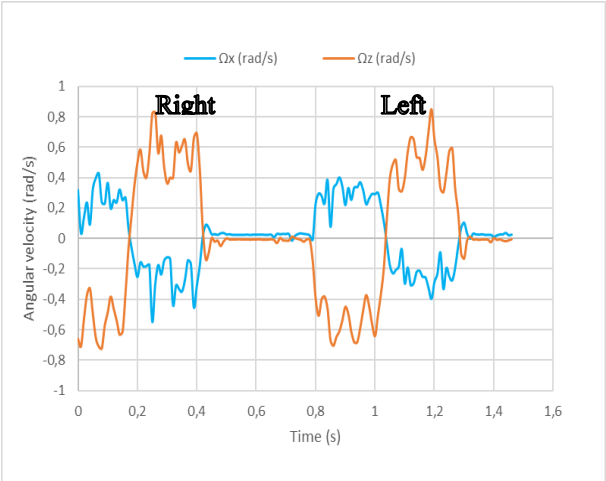


b)

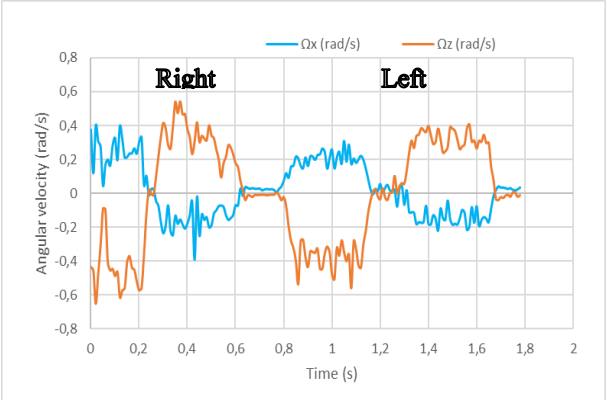
Figure 16 Acquired results in terms of acceleration in axis y during experiment of a right-handed people of: (a) young person; (b) older person.

The averages of the force applied by each individual are similar, with that applied by the older person being somewhat higher. It can be seen in the following plot that for equal force the acceleration registered by the person is much greater. Table 4 shows the highlighted values. The exercise is divided into four phases: clockwise and counterclockwise for right hand and left hand. For these four phases, the values of the acceleration modulus and angular velocity at the instant are reported when the force is maximum. In addition, the time taken for each phase is shown. Considering maximum force as indicative, the older person generally uses more force in the exercise than the younger person.

Table 4 shows that in the counterclockwise movement the older person uses slightly less force than the younger person. For the values of acceleration magnitude, the opposite occurs, and this is reflected also in the time spent by each volunteer doing the exercise. The older person in all phases spends more time than the younger one. The use of the prototype has been satisfactory, with satisfactory results so that it can be considered adequate in design and operation. The reported results in Figures 13-18 are illustrative to characterize the outcomes of the exercise with the proposed device.



a)



b)

Figure 17 Results acquired in terms of angular velocity in axis x and axis z during experiment of a right-handed people of: (a) young person; (b) older person.

In particular, the operation performance is characterized by:

- acceleration monitoring of the exercise with data showing the time evolution and the value variations, such as from -8 up to 25 m/s^2 (Fig. 14).
- monitoring of the crank angular motion to determine continuous motion activated by the assisted arm showing time evolution and values variations in term of angular velocities from -10 up to 10 rad/s (Fig. 18).
- monitoring applied force by the user on the crank to analyze the power capacity of the assisted arm in terms of time evolution and value variations from 17 up to 26 N (Fig. 13).

The limitations of the exercise running the crank can be recognized in the following main aspects:

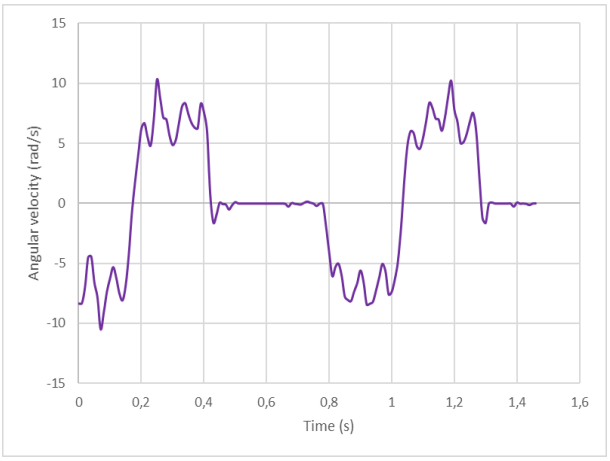
- design volume limits the portability and easy arrangement in house frames
- the size of the crank is not adjustable to the users' arm length, making it not fully suitable for all arm sizes, although it can work for a wide range
- the sensing equipment does not give full insight into the biomechanics of the assisted motion and arm muscular system contribution

Improvements can be required for home use as identified by test results and volunteer feedback in:

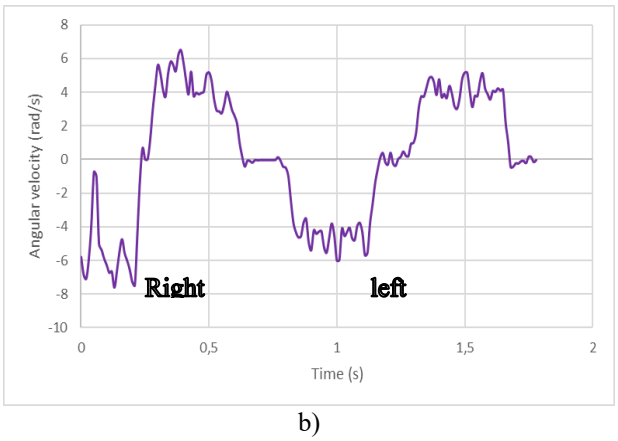
- reducing the volume and weight of the device, mainly referring to the cube frame.
- elaborating acquired data even online to permit a user to understand the outcome of the exercise.
- drafting a document with information on the safety of the elements used in the device.

Referring to safety strategies, improvements can be expected in controlled operation as function of the evolving arm conditions during exercise up to including even stop of it.

Safety should be ensured also against misuse and malfunctioning of any part of the device that can damage or be a risk for a user, up to planning an emergency stop. Safety issues can be influential on the mechanical design, electric/electronic parts, and sensing capacity of the device. Future work will be planned to attach those issues.



a)



b)

Figure 18 Acquired results in terms of angular velocity in axis y during experiment of a right-handed people of: (a) young person; (b) elder person.

Table 4 - A summary of acquired values during reported tests in Fig.13 to Fig. 18

HAND	DIRECTION OF ROTATION	MAGNITUDE	YOUNG PERSON	OLDER PERSON
RIGHT HAND	CLOCKWISE	F. MAXIMUN (N)	22.04	22.72
		ACC. MAXIMUN (m/s^2)	25.43	15.24
		ANG.VEL. MAXIMUM Ωy (rad /s)	-10.49	-7.63
		TIME (s)	0.17	0.25
	COUNTER CLOCKWISE	F. MAXIMUN (N)	20.90	22.04
		ACC. MAXIMUN (m/s^2)	21.37	11.05
		ANG.VEL. MAXIMUM Ωy (rad /s)	10.28	6.20
		TIME (s)	0.26	0.40
LEFT HAND	CLOCKWISE	F. MAXIMUN (N)	24.09	26.14
		ACC. MAXIMUN (m/s^2)	20.47	10.80
		ANG.VEL. MAXIMUM Ωy (rad /s)	-8.20	-5.9
		TIME (s)	0.26	0.41
	COUNTER CLOCKWISE	F. MAXIMUN (N)	22.04	19.76
		ACC. MAXIMUN (m/s^2)	19.70	7.74
		ANG.VEL. MAXIMUM Ωy (rad/s)	10.17	5.16
		TIME (s)	0.26	0.40

6 CONCLUSIONS

The feasibility of the new proposed device for arm exercise with features in user-oriented operation, comfort, and low cost is proven by results of lab test with a young and an older volunteer. The device design is characterized also by a portable solution with a sensored crank that can be installed on a small cubic frame for vertical and horizontal running. The reported test results are discussed in terms of the acquired data from the sensors on the rotating crank in motion and force parameters. The outcomes of the test can be recognized very satisfactory for the goal of motion assistance with such a home usage goal. Future work is planned for a consistent statistically significant campaign of test for the ultimate application in home exercising by elderly people. For this purpose, also a box will be designed to cover all the wiring of the device, leaving only access to the switch for data recording and battery recharging. This will allow safe use in the home environment.

ACKNOWLEDGMENTS

The first author wishes to gratefully acknowledge the 2023 mobility research program of Polytechnic School of the Carlos III University of Madrid that has permitted her a period of research at LARM2 in Rome in the year 2023. The study was conducted in accordance with the Declaration of Helsinki and approved by the Institutional Ethics Committee of Policlinico di Tor Vergata, Rome, with protocol code RS. 197.22 on November 15, 2022.

REFERENCES

[1] Alrabghi, L., Alnemari, R., Aloteebi, R., Alshammari, H., Ayyad, M., Al Ibrahim, M., ... , Aljuwayd, H.: Stroke types and management. International Journal of Community Medicine and Public Health, vol. 5, p.3715-3719. (2018).

[2] Chan, D.N.S., Lui L.Y.Y., So W.K.W.: Effectiveness of exercise programmes on shoulder mobility and lymphoedema after axillary lymph node dissection for breast cancer: systematic review. Journal of advanced nursing, vol. 66, no 9, p. 1902-1914, (2010).

[3] Duncan Millar, J., Mason, H., Kidd, L. What is important in supporting self-management in community stroke rehabilitation? AQ methodology study. Disability and Rehabilitation, vol. 45, no 14, p. 2307-2315. (2023).

[4] Gebreheat G, Goman A, Porter-Armstrong A. The use of home-based digital technology to support post-stroke upper limb rehabilitation: A scoping review. Clinical Rehabilitation. vol. 38, no 1, p. 60-71, (2024).

[5] Moulaei, K., Sheikhtaheri, A., Nezhad, M. S., Haghdoost, A., Gheysari, M., , Bahaadinbeigy, K. Telerehabilitation for upper limb disabilities: a scoping review on functions, outcomes, and evaluation methods. Archives of Public Health, vol. 80, no 1, p. 1-21. (2022).

[6] Klonizakis, M., Winter, E. Effects of arm-cranking exercise in cutaneous microcirculation in older, sedentary people. Microvascular Research, vol. 81, no 3, p. 331-336. (2011).

[7] Kilgour R.D., Jones D.H., Keyserlingk J.R. Effectiveness of a self-administered, home-based exercise rehabilitation program for women following a modified radical mastectomy and axillary node dissection: a preliminary study. Breast Cancer Research and Treatment vol. 109, p.285–295, (2008).

[8] Chen, J., Romero, R., Thompson, L. A. (2023). Motion Analysis of Balance Pre and Post Sensorimotor Exercises to Enhance Elderly Mobility: A Case Study. Applied Sciences, vol. 13, no 2, p. 889.

[9] Lum P.S., Burgar C.G., Shor, P.C.: Evidence for improved muscle activation patterns after retraining of reaching movements with the MIME robotic system in subjects with post-stroke hemiparesis. IEEE Transactions on Neural Systems and Rehabilitation. Engineering, vol.12, p.186–194, (2004).

[10] Mocan, B.; Mocan, M.; Fulea, M.; Murar, M.; Feier, H. Home-Based Robotic Upper Limbs Cardiac Telerehabilitation System. Int. J. Environ. Res. Public Health, vol 19, no 18, 11628. (2022).

[11] A. Keramiotou, K., Anagnostou, C., Kataxaki, E., Galanos, A., Sfikakis, P., Tektonidou, M. G.: The impact of upper limb exercise on function, daily activities and quality of life in systemic lupus erythematosus: a pilot randomised controlled trial. RMD open, 2020, vol. 6, no 1, p. e001141. (2020).

[12] B. Tsilomitrou O, Gkountas K, Evangeliou N, Dermatas E. . Wireless Motion Capture System for Upper Limb Rehabilitation. Applied System Innovation. Vol. 4, no 1, p.14. (2021).

[13] Latreche, A., Kelaiaia, R., Chemori, A., Kerboua, A.: A New Home-Based Upper- and Lower-Limb Telerehabilitation Platform with Experimental Validation. Arab J Sci Eng 48, 10825–10840 (2023).

[14] Miao, Q.; Zhang, M.; McDaid, A.J.; Peng, Y.X.; Xie, S.Q. A robot-assisted bilateral upper limb training strategy with subject-specific workspace: : A pilot study. Robotics and Autonomous Systems, vol. 124, p. 103334. (2020).

[15] Aprile, I., Germanotta, M., Cruciani, A., Loreti, S., Pecchioli, C., Cecchi, F, Carrozza, M. C. Upper limb robotic rehabilitation after stroke: a multicenter, randomized clinical trial. Journal of Neurologic Physical Therapy, vol 44. No 1. p 3-14. (2020).

[16] Fareh, R., Elsabe, A., Baziyad, M., Kawser, T., Brahmi, B., & Rahman, M. H.: Will Your Next Therapist Be a Robot? -A Review of the Advancements in Robotic Upper Extremity Rehabilitation. Sensors, vol. 23, no 11, p. 5054, (2023).

[17] Chaparro-Rico, B.D.; Cafolla, D.; Ceccarelli, M.; Castillo-Castaneda, E. NURSE-2 DoF Device for Arm Motion Guidance: Kinematic, dynamic, and FEM analysis. Applied Sciences, vol. 10, no 6, p. 2139. (2020).

[18] Skelton, D. A., Beyer, N. Exercise and injury prevention in elder people. Scandinavian journal of medicine, Science in sports, 13(1), 77-85 (2003).

[19] Klonizakis, M., Winter, E. Effects of arm-cranking exercise in cutaneous microcirculation in elder, sedentary people. Microvascular Research, 81(3), 331-336. (2011).

[20] Daigneault, J., Cooney Jr, L. M. Shoulder pain in elder people. Journal of the American Geriatrics Society, vol. 46, no 9, p. 1144-1151. (1998).

[21] Görer, B., Salah, A., Akın, H. L. (2017). An autonomous robotic exercise tutor for elderly people. Autonomous Robots, vol. 41, p. 657-678. (2017).

[22] Ferreira, L. F., Scariot, E. L., da Rosa, L. H. T. The effect of different exercise programs on sarcopenia criteria in older people: A systematic review of systematic reviews with meta-analysis. Archives of Gerontology and Geriatrics, 2023, vol. 105, p. 104868. (2023).

[23] de Mello, R. G. B., Dalla Corte, R. R., Gioscia, J., & Moriguchi, E. H.: Effects of Physical Exercise Programs on Sarcopenia Management, Dynapenia, and Physical Performance in the Elderly: A Systematic Review of Randomized Clinical Trials, vol. 2019, no 1, p. 1959486. (2019).

[24] Rantanen, T.: Promoting mobility in older people. Journal of Preventive Medicine and Public Health, 46 (Suppl 1), S50. vol. 46, no Suppl 1, p. S50. (2013)

[25] Granacher, U., Hortobágyi, T.: Exercise to Improve Mobility in Healthy Aging. Sports Med Vol.45, p.1625–1626. (2015).

[26] Costa, S. N., Ferreira, L. H. B., Bento, P. C. Effects of home-based exercise programs on mobility, muscle strength, balance, and gait in community-dwelling older adults: a systematic review and meta-analysis. J. of aging and physical activity, vol. 31, no 4, p. 693-704. (2023).

[27] Marieb, E.N, Hoehn, K.: Human anatomy & physiology. Pearson education, p.208-211, (2007).

[28] Ceccarelli, M., Sanz, S., Díaz, V., Russo, M. Design and Construction of a Prototype of an Assisting Device for Arm Exercise. Machines, Vol 12, No 2, 145. (2024).

[29] Sanz, S.; Russo, M.; Díaz, V.; M.; Ceccarelli, M. Requirements and problems for a sensored rotating device for arm exercise. Proceeding of 19th European Conference on Mechanism Science, Padova, Italy, 18–20 September 2024. No. 59, Springer Nature Switzerland AG 2024. EuCoMeS 2024, MMS 165, pp. 1–8, 2024.

[30] Ceccarelli, M.; Sanz, S.; Díaz, V. Sensorized knob for vehicle steering wheel. Italy Patent Request No.102023000016845,7 August 2023.

[31] Sanz, S.; Russo, M.; Díaz, V.; M.; Ceccarelli, M. Laboratory experiences with an intelligent robotic crank for arm exercises. Proceedings of First International Conference on Artificial Intelligence in Healthcare. Swansea, United Kingdom, 4-6 September 2024. No. 48, Springer Nature Switzerland AG 2024, AIiH 2024, LNCS 14975, pp. 1–12, 2024.

ISSN 1590-8844
International Journal of Mechanics and Control, Vol. 26, No. 02, 2025
https://doi.org/10.69076/jomac.2025.0014

INNOVATIVE THERMAL MANAGEMENT SYSTEMS FOR FUEL CELL ELECTRIC AIRCRAFT

Stefano Favre[*] Flavio Di Fede[**] Eugenio Brusa[*] Cristiana Delprete[*]

[*] Politecnico di Torino, Department of Mechanical and Aerospace Engineering

[**] Leonardo Labs, Leonardo SpA

ABSTRACT

The Thermal Management System (TMS) is a crucial component of the aircraft, particularly in case of layout exploiting a high level of electrification of propulsion systems. Specifically, use of fuel cells in aviation industry appears to be extremely challenging, due to the significant amount of waste heat produced. Therefore, the aim of this paper is introducing some technical solutions proposed by the literature for an effective thermal management of the aircraft. Particularly, the identification of most relevant heat sinks for the aviation is performed, with a specific interest for solutions exploiting the stored fuel intrinsic heat capacity. The example of a conceptual hybrid-electric, fuel cell powered, turbo-propeller driven, regional transport aircraft is then described. The Model Based System Engineering (MBSE) methodology is applied to define the system use cases and to identify the most relevant requirements. A possible system architecture is finally proposed. The paper provides some considerations over the topic of fuel-based TMS (F-TMS) to the specific case of hybrid-electric, fuel cell, regional aircraft.

Keywords: Fuel cell, Thermal management, Hybrid-electric, Aircraft, Tank

1 INTRODUCTION

During the last fifty years, the topics of environmental preservation, sustainability and pollutant emissions reduction became increasingly relevant factors in the design of all engineering products and processes [1]. Current relevance of such themes is evidenced by numerous international agreements, declarations, acts and even regulations, such as the UN Agenda 2030 of "Sustainable development goals" [2], or the European Strategic Research and Innovation Agenda (SRIA) targets for EU aviation by 2050 (Flightpath 2050) [3]. Furthermore, creation of specifically purposed joint undertakings, such as Clean Aviation [4], previously Clean Sky, undeniably proves the relevance and consistency of such themes. Amongst the various targets of the clean aviation joint undertaking, carbon neutrality and net green-house emission reduction of no less than 90% when compared to the 2020 state of the art for regional transport aviation are just some of the main objectives of this venture, while nullification of pollutants emission as well as engine noise during ground based operations are also desirable.

Contact author: Stefano Favre [1]
[1] Corso Duca degli Abruzzi, 24 – 10129 Torino, Italy
E-mail: stefano.favre@polito.it

1.1 CONTEXT AND DRIVERS

During this extended time-frame, in fact, several national and international funding programs, as well as sanctions for those companies not capable of meeting the expected environmental goals, placed the theme of sustainability progressively closer to the focus of industrial research, especially in the case of the transport sector. Electrification of propulsion systems, clearly arose as a most prominent solution for the creation of low environmental impact machines and vehicles. Amongst these, the automotive sector represents, arguably, the main driver of off-he-grid transport electrification. Plenty of studies, demonstrators, and even commercial products can be found implementing full, or at least partial, propulsion electrification via mounted electric energy storage devices in the automotive, as per the review of Rani and Jayapragash [5]. In particular,

Table I - Adopted acronyms and abbreviations.

Acronym	Meaning
BDD	Block Definition Diagram
EASA	European Aviation Safety Agency
ECS	Environmental Control System
FADEC	Full Authority Digital Engine Control
F-TMS	Fuel-based Thermal Management System
HE	Heat Exchanger
HT-PEM	High Temperature-PEM
HS	Heat Sink
IBD	Internal Block Diagram
INCOSE	INterantional COuncil of System Engineering
LT-PEM	Low Temperature-PEM
MBSE	Model-Based Systems Engineering
MT-PEM	Medium Temperature-PEM
PAX	Passengers number
PEM	Proton-exchange membrane (fuel cell)
RFLP	Requirements, Functional, Logical, Physical
ROM	Reduced Order Model
Tit.-Abs.-Key	Title-Abstract-Keywords
TLR	Technology Readiness Level
TMS	Thermal Management System

Table II - Adopted variables.

Variable	Description
$m_f(t)$	Fuel mass stored in a generic tank
$m_{f,Mtank}(t)$	Fuel mass stored in main tank
$m_{f,Rtank}(t)$	Fuel mass stored in recirculation tank
$\dot{m}_{f,brn}$	Fuel mass flow burnt by the engines
$\dot{m}_{f,rec}$	Fuel mass flow recirculated to tank
m_{HE}	Heat exchanger mass
$\dot{m}_{pump_{cool}}$	Coolant mass flow at the pump
$\dot{Q}_{HE-FC}$	Heat flow absorbed from fuel cell
$\dot{Q}_{out}$	Heat flow rejected via auxiliary ram-air cooler
$\dot{Q}_{rejected}$	Heat flow rejected through tank walls
$\dot{Q}_{waste}$	Waste heat flow
T_{cold}	Inlet temperature of cooling air
$T_f(t)$	Fuel temperature of a generic tank
T_{FC}	Fuel cell temperature
$T_{FC_{lim}}$	Fuel cell limit temperature
$T_{f,Mtank}(t)$	Fuel temperature of main tank
$T_{f,Rtank}(t)$	Fuel temperature of recirculation tank
$T_{HE_{cool,in}}$	HE inlet coolant temperature
$T_{HE_{cool,out}}$	HE outlet coolant temperature
$T_{HE_{fuel,in}}$	HE inlet fuel temperature
$T_{HE_{fuel,out}}$	HE outlet fuel temperature
T_{lim}	Limit temperature of a generic heat source
$T_{lim,HT}$	Limit temperature of a high temperature heat source
$T_{lim,LT}$	Limit temperature of a low temperature heat source
$\dot{T}_{pump_{cool,out}}$	coolant temperature at pump outlet
α	Recirculated fuel mass flow to total fuel mass flow ratio

opportunities offered by the combination of conventional and electric propulsion devices had been thorough investigated, as per the works of Castellano and Cammalleri [6], and Spano et al. [7], on hybrid-electric solutions design and optimization.

On the other hand, air-based transport was not involved in major electrification programs just until the last few decades. In fact, the introduction of significant amounts of electric devices, up to the complete electrification of the propulsion system, had always been hindered by the stringent weight and safety requirements intrinsic with the sector [8, 9]. Specifically, one of the most challenging detriments to this technological leap consists in the disadvantageous energy-to-weight ratio provided by currently available electric energy storage devices, when compared to conventional jet-fuels' specific energy of about 12 kWh/kg [10]. As of current state of the art technology, the two main representatives of such devices are the Li-ion batteries, with a specific energy of about 0.25 kWh/kg [11, 12], and the hydrogen-powered Proton-Exchange Membrane (PEM) fuel cells, with a total system energy-to-weight ratio ranging from 0.6 to 1.2 kWh/kg [13]. The difference between these values and the specific energy of conventional jet-fuel is so prominent that the resulting increase in the aircraft total mass often forces the whole system to be oversized up to the point of nullifying any environmental benefit provided by the electrification process in the first place. Indeed, some experts forecast that the suitability of electric energy storage devices for medium-to-big scale aircraft applications will not be achieved before 2050 [14, 10], assuming that current trends in average battery capacity growth are not changed, and that a specific energy of about 1.5 kWh/kg is achieved.

These considerations render the development of hybrid-electric aircraft preferable over the commitment into full electric conversions, at least in the short term. Such a compromise is vital for near future electrification since it allows to benefit from the reduced environmental impact provided by the electric powertrain while still relying on the consistency offered by conventional combustion engines. Moreover, the introduction of hydrogen-powered fuel cells in place of electro-chemical batteries appears as a more feasible solution for next-gen aircraft electrification [8], consequent

to their favourable energy-to-weight ratios, when compared to conventional lithium batteries. However, careful design and optimization of the integrated hydrogen storage devices, fuel cell stacks, and supply pipes is crucial for such an advantage to be harnessed, as evidenced in the work of Maraschi et al. [10], and Cinar et al [15]. Hence, efforts towards environmental impact reduction in near future aviation programs can reasonably be expected to likely rely on one or both of the following concepts: hybrid-electric powertrains, and hydrogen-fuel cell energy storage.

1.2 FUEL CELLS & HYDROGEN

The main advantage provided by fuel cell technology to the aerospace sector relies in the extremely high gravimetric energy density offered by hydrogen as an energy vector, possessing an outstanding net specific energy of about 33.3 kWh/kg [16], almost three time the value of typical kerosene-based jet-fuels. Conversely, however, hydrogen presents a rather poor volumetric energy density when compared to conventional fuels, requiring either to be stored at cryogenic temperatures, or under extremely high pressures of up to 700 bar. The resulting net energy-to-volume ratio of hydrogen is thus of about 3 kWh/l [16], compared to the 10 kWh/l of kerosene.

Furthermore, complex materials and designs have to be employed for the tanks, as to limit the boil-off phenomenon of liquid hydrogen [17], and the permeation of compressed hydrogen [18], leading to progressive loss of the gas through the tank walls. This results in the need for encumbering hydrogen tanks and distribution systems to be installed on-board, inevitably reducing passengers and payload capacity of a given aircraft, as well as augmenting the overall weight. Consequently, when the whole hydrogen-fuel cell system is considered, accounting for the masses of the tanks storing the hydrogen and the fuel cells converting it into electric power, a real energy-to-weight ratio of roughly 1 kWh/kg is obtained, as anticipated. However, despite these challenges, hydrogen arguably remains a preferable energy vector over batteries for the electrification of the aircraft sector, as testified by several studies from the industries [19, 20] and academia [21, 22, 23, 24] addressing more-electric aircraft development and fuel cell technology investigation. A number of demonstrators can also be found in the general aviation sector, such as the Boeing Fuel Cell Demonstrator from 2008 [25], the NASA X-57 (in its early iterations) [20], and the HY4 commercial aircraft from the H2FLY company (DLR) [26]. Commitment of the industry towards the development of larger electrified aircraft employing hydrogen-fuel cell technology is also testified by several initiatives, including the ZEROe program from Airbus [27], or the many projects from ZeroAvia [28], including the first test flight of a retrofitted Do228, small regional transport aircraft and commuter [29].

Concerning the actual fuel cells, a number of different technologies currently exist in the literature [30] supporting hydrogen conversion into electrical power. Amongst these, the Proton-Exchange Membrane fuel cells are arguably the most widespread solutions and the most frequent in the transport sector. These are further differentiated into high temperature PEM fuel cells (HT-PEM), with an operating temperature of 120 to 200 °C, and low temperature PEM fuel cells (LT-PEM), typically operating around 60 to 80 °C [30]. Between these two, the LT-PEM appear to be the favoured solutions thanks to a faster startup, higher power density, and enhanced robustness. However, despite PEMs' advantages over Li-ion batteries in terms of overall system weight, fuel cells are hindered by a much lower efficiency of the stacks compared to batteries, whose efficiencies exceed 90% [31]. PEM fuel cells, on the other hand, struggle to exceed efficiencies of about 50% under operative conditions [30, 32]. This is a crucial aspect since, for each kW of electric power being generated inside the cells, a roughly equivalent amount of waste heat gets produced as well. This phenomenon forces the need for the introduction of a system capable of effectively absorbing said waste heat, transporting it away from the source, and dissipating it into an purposefully chosen heat sink, in order to prevent the uncontrolled heating, and subsequent damage, of the fuel cell stacks. A process that is made even more difficult by the relatively low temperatures limits of about 70 to 80 °C, required by LT-PEMs. Innovations in the field of PEM membrane materials aim to ease these issues through the development of new, medium temperature, PEM fuel cells (MT-PEM), capable of operating between 100 and 120 °C with minimal damage to the membranes [33, 34, 35]. However, challenges remain.

In fact, management of such low grade high amount waste heat still represents a major challenge, with the topic of adequate fuel cell cooling being examined in many studies, as summarized in the work of Bargal et al. [36]. These challenges appear to be even more prominent in the prospect of aerospace applications, consequent to the very high powers involved with aircraft propulsion, often exceeding several MW, and the high cruising speeds of aeroplanes, causing any induced drag from the radiators to significantly hinder the aerodynamic performance. Traditional aircraft heat sources such as electronics [37], the Environmental Control System (ECS) [38], and other on-board devices, are not subject to such challenging constraints as they are typically associated with lower heat loads, rarely exceeding 50 to 100 kW of combined waste heat generation. Turbines, on the other hand, involve both very high waste heat generation and high operating temperatures, but these are almost entirely rejected into the atmosphere through the exhaust gases. This reduces the need for heat dissipation units and a coolant circuits, as the main challenge with turbines becomes the adequate screening of blades and components from extreme heat via the formation of a small air film surrounding the surfaces [39].

Finally, as the fuel cell is an electric device, care should be taken when designing the TMS as to prevent electric discharges and short circuits from propagating through the cooling circuit. Adequate dielectric coolants, based on ethylene glycol-water mixtures, shall thus be employed, along with the introduction of a deionization filter in the coolant loop [40].

1.3 THERMAL MANAGEMENT SYSTEMS

Consequently, the effective design of the Thermal Management System (TMS) is to be considered a crucial asset in any expected hydrogen fuel cell application in the aviation industry. Therefore, this paper aims at investigating, analysing, and describing several TMS solutions specifically suited for the development of hybrid-electric aircraft exploiting hydrogen-based energy storage and fuel cells energy conversion units. In the following are thus presented, first and foremost, all the most relevant solutions currently available in the scientific literature for thermal management in the aeronautical field. In an effort to conceptualize the TMS at system level, with a specific focus towards the integration of its various components, a classification and confront between relevant available heat sinks is performed. Amongst the proposed architectures, a deepening of fuel tank-heat sink solutions is specifically carried out, with the intention to fully exploit the benefits provided by the presence of conventional jet-fuel in hybrid propulsion aircraft. Finally, MBSE methodologies are applied to guide the definition of a possible design, through the use of the "V-model" diagram and the RFLP analysis, leading to a preliminary requirements analysis of the fuel-based TMS, and a possible architecture proposal, in the prospect of future numerical simulations.

2 LITERATURE SURVEY

In an effort to propose an effective tool to provide fuel cell waste heat disposal in aircraft application, an extensive analysis of current state of art of TMS solutions was carried out. A wide selection of scientific publications was identified by means of bibliographic research, providing an array of different cooling options and associated architectures. In particular, the works of Van Heerden et Al. [41], as well as Coutinho and others [42, 43, 44, 45, 46], present a brief, yet complete description of all the most relevant cooling solutions currently applied, designed or theorized in the aviation field. Subsequently, the research is specialized towards the topic of heat disposal, since the identification of a suitable heat sink for the dissipation of fuel cells, relatively low grade, high heat fluxes is a most challenging aspect. Amongst the various options, exploitation of intrinsic heat capacity of, tank stored, conventional jet-fuel is further analysed, in the prospect of usage onboard of hybrid-electric aircraft combining fuel cell powered electric propulsion and traditional turbomachinery.

2.1 METHODOLOGY

The bibliographic research is pursued with the aid of Scopus online publication database. Coherently with previous statements, the collection of relevant articles on the topic of fuel-based thermal management systems is realized through the adoption of the keywords and search criteria presented in table III.

Table III - Scopus research string criteria.

Criteria	**Specification**
Tit.-Abs.-Key	"thermal management" OR "temperature control" OR "cool*"
Tit.-Abs.-Key	"aircraft" OR "airplane" OR "aeroplane" OR "airborne" OR "aviation" OR ("aerospace" AND NOT "spacecraft")
Tit.-Abs.-Key	"heat sink" OR "heat absorb*" OR "heat exchang*" OR "heat reject*"
Tit.-Abs.-Key	"fuel" OR "tank"
Subject area	Engineering
Language	English
Database	Scopus

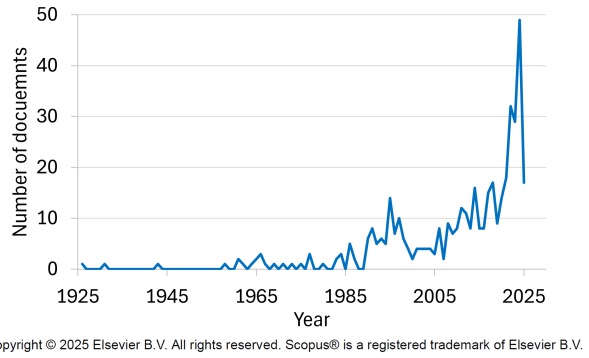
2.2 SURVEY RESULTS

The adoption of the previously described research string provides a total of 423 results specifically focused towards the use of fuel tank as an aircraft relevant heat sink. Documents are spread over a relevant time span: from the first investigations on the subject fuel-based TMS during the 60s race for increasingly faster super-sonic aircraft to the 80s and 90s challenges associated with the introduction of high power electronics in high-performance aeroplanes, till the most recent efforts towards aircraft electrification programs. Overall, the results of this research can be considered very promising for a number of reasons. Firstly, the ample selection of documents identified supports the feasibility of fuel-based thermal management systems, at the very least, from a conceptual standpoint. Second, a significant increase in the number of yearly publications over the course of the last ten to fifteen years, demonstrates the growing interest of the scientific community towards the topic of innovative TMS, as shown in Fig. 1.

Another interesting aspect to evaluate by analysing the explored collection of documents, is the presence of a percentage of conference papers (63%) doubling that of the published articles (32%). This significant difference in the document type distribution may suggest that the topic of fuel-based TMS is still matter of debate in the scientific community, still offering potential for further development over this subject. In fact, many of the proposed papers discuss the possibility to introduce such cooling tools for the management of the ever increasing thermal loads associated with the growing power of aircraft avionics and

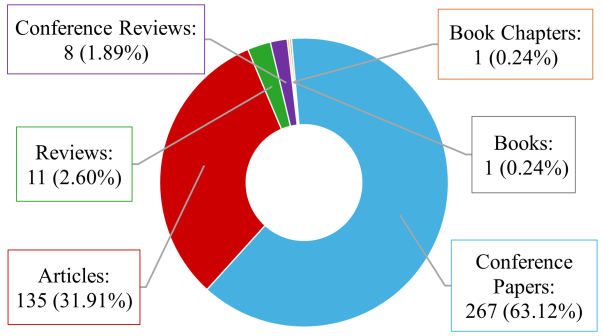
Table IV - Collection of most relevant documents on the topic of fuel-based thermal management systems, classified on their context, application, focus and solution.

Context of the research and purpose of TMS	References
Cooling in support of propulsion electrification via non-specific, or different, energy storage devices	[47], [48], [49] [50]
Cooling in support of hybrid propulsion electrification via turbo-electric architectures	[51], [52]
Cooling in support of hybrid propulsion electrification via electric batteries	[53], [54], [55], [56], [57]
Cooling in support of full propulsion electrification via hydrogen fuel cells	[58], [59], [60], [61], [62]
Medium sized aviation and regional transports (up to 150 PAX)	[63], [64]
Numerical modeling and design	[65], [66], [67], [68], [69], [70], [71], [72], [73], [74], [75], [66], [63], [64], [76], [77]
Confront between different architectures and system optimization	[57], [78], [79], [80], [81], [82], [83]
TMS integration into the whole aircraft assembly	[84], [48], [55], [56], [85]
Single tank architectures without fuel recirculation, HE on the feed-line	[51], [77], [86], [87], [88]
Single tank architectures with fuel recirculation	[73], [74], [84], [65], [56], [57], [89], [79], [52], [64], [67], [68], [85], [90], [71], [91], [92], [93], [94]
Dual tank architectures with fuel recirculation	[95], [78], [76], [80], [81], [82]
Tank array architectures with fuel recirculation	[96], [48], [70], [97], [72]



Copyright © 2025 Elsevier B.V. All rights reserved. Scopus® is a registered trademark of Elsevier B.V.

Figure 1 Number of publications per year on the topic of aviation-based, fuel tank-heat sink TMS, provided by Scopus database as of Apr 2025.



Copyright © 2025 Elsevier B.V. All rights reserved. Scopus® is a registered trademark of Elsevier B.V.

Figure 2 Publication types, and relative distribution, on the topic of aviation-based, fuel tank-heat sink TMS, provided by Scopus database as of Mar 2025.

other electronic devices. On the other hand, focus on the possibility to exploit passive heat rejection through the tank surfaces is also discussed in some papers. Finally, the presence of a number of reviews describing the use and concepts of fuel-based TMS is also a relevant factor, indicating that such a topic is already well established in the literature and, therefore, that its viability is proven. Fig. 2 shows all of the previously stated concepts.

For an easier selection and clusterization of found documents concerning the topic of fuel tank-heat sink TMS, the most relevant papers are collected and classified in Tab. IV. Articles, and conference papers are there subdivided and characterized on the basis of their intended use case, the adopted methodology and the overall focus of the research, as well as the architecture of the fuel tank assembly.

3 THERMAL MANAGEMENT SOLUTIONS FOR AVIATION

The collection of examined articles and, especially, reviews allows us to determine the presence of a number of different designs and architectures suitable for the purpose of effectively managing produced waste heat. These solutions

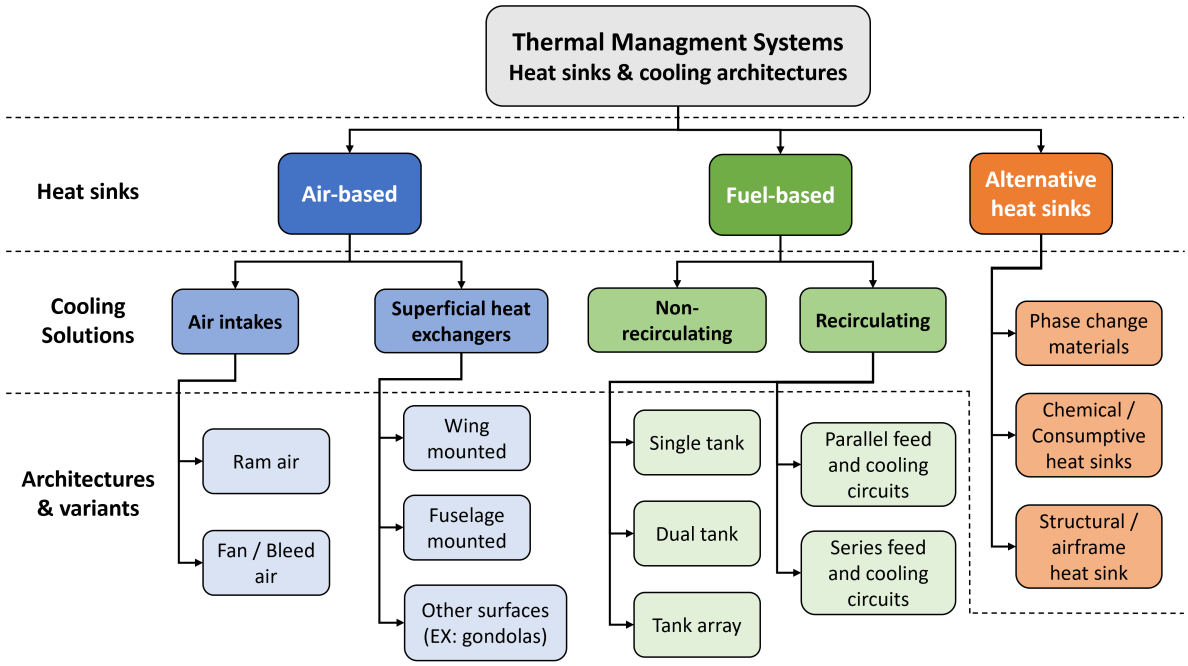


Figure 3 Classification of main thermal management systems in the aviation field, based on the adopted heat sinks.

are numerous and require a classification. There are many aspects that may be taken into account while defining the various TMS, however, one of the most relevant is the intended main heat sink of the system and, therefore, the proposed classification will be centered around this topic. For clarity's sake, we intend as a main heat sink of the TMS, the element, or component, where the waste heat produced by the heat source, a fuel cell in this case, will ultimately be transferred and collected. The adopted classification is driven by the work of Petkus and Gallington [98] and, especially, by the reviews of Van Heerden et al. [41], and Coutinho and et al. [42]. In the end, three main heat sinks could be identified: air, fuel or alternative heat sinks, which may be further specified into their own sub-categories, as shown in Fig. 3. Said specifications could relate to either: different design shapes, such as ram and superficial air cooling; opposing circuital architectures, such as recirculating and non-recirculating fuel flows; or even alternative cooling processes, such as phase change material state transitions and chemical heat sinks molecular reactions. However, it is also worth noting that, in the end, air is usually the actual final heat sink of the aircraft, since the heat absorbed by fuel is later ejected into the atmosphere via the engine fumes, while other kinds of heat sinks are also subject to heat cession to the ambient, one way or another.

In the end, all of these solutions come with a number of advantages, limitations, preferable use cases, and Technology Readiness Levels (TRL), which are here briefly summarized.

3.0.1 Air-based solutions

Air-based solutions represent the most common devices in thermal management, since the exploitation of surrounding air provides simple, yet effective, cooling, without introducing any inherent threats to the overall aircraft safety. Furthermore, since the external environment effectively acts as an ideal heat sink, not modifying its average temperature despite exchanging heat with the aircraft, air-based solutions also benefit from an unlimited heat capacity throughout the mission. On the other hand, since the heat sink is located outside of the aircraft, the overall cooling effectiveness of the system is also significantly influenced by external factors, such as the eventual presence "hot day" conditions or variations in flight altitude.

The main devices and designs employing air as an heat sink are:

1. The ram-air. These solutions supply air to internally mounted heat exchangers via purposefully shaped inlets on the aircraft surface. Ram-air designs are very common in the industry, as they provide simple and effective cooling. However, a drag penalty is also introduced by the ram structure, which hinders aircraft aerodynamics. Furthermore, ram air cannot provide cooling when the aircraft is stationary, unless a fan is mounted on the outlet duct.
2. The Bleed-air. These solutions extract a portion of the airflow compressed by the engines to employ it for cooling and cabin pressurization. The airflow is granted as long as the engines are kept spinning,

allowing cooling even when the aircraft is standing still. Nonetheless, compressor bleed-air is subject to significant heating, making it suitable only to cool high temperature components, like the turbine blades. However, in case the adopted propulsion system employs some kind of ducted fan architecture, fan bleed-air can also be extracted. Fan-air is generally subject to much smaller compression heating, making it suitable for cooling more sensible components. Bleed air preserves overall aircraft aerodynamics, but excessive bleed can significantly decrease engine performance, resulting in increases fuel consumption.

3. The superficial heat exchangers. These solutions dissipate waste heat directly into the atmosphere through the aircraft's fuselage and wings, preserving the aerodynamic performance of the aeroplane. Superficial heat exchangers offer effective cooling when the aircraft is traveling at high speeds, however, this system is made almost completely useless when stationary. Moreover, careful design is needed to prevent the heat transfer from developing flow separation on wings, the intrinsically high mass of such a distributed system needs to be addressed thoughtfully. These issues caused the superficial heat exchanger design to be employed only in some very niche applications.

In the end, ram-air designs appear as the most promising air-based solutions for fuel cells cooling, as long as the powers involved are maintained relatively low. Higher degrees of electrification are in fact expected to result in increasingly higher system induced drag. Bleed solutions do not appear to be suitable for fuel cells cooling, unless some kind of ducted fans are employed in the propulsion units. Finally, superficial heat exchangers show promise in supporting fuel cell cooling while preserving aerodynamic performance. However, tradeoffs with respect to total system mass should be evaluated carefully, while significant limitations in stationary cooling call for the integration of this solution with other systems.

3.0.2 Fuel-based solutions.

Fuel-based solutions are the second most common devices in the industry. They exploit the intrinsic heat capacity associated with the masses of fuel being stored inside tanks, leveraging on a resource that is already being hauled by the aircraft. Fuel is also an advantageous vessel for heat transport when compared to air, thanks to it being liquid and presenting favourable heat transfer coefficients. This results in lower mass flows being required and more compact heat exchangers being employed. Moreover, since the fuel is stored inside the aircraft, greater control is achieved over the heat sink, decoupling cooling from external factors such as aircraft speed, hot day conditions, and altitude.

On the other hand, flammability and potential explosive hazards are of primary concern in fuel-based TMS, requiring continuous and precise monitoring of fuel temperature and evaporation as well as the introduction of a fuel tank inerting system [99]. The total stored fuel mass is, in fact, limited by the available tank volume and mission flight requirements, causing the final heat capacity of the heat sink to also be limited. This prevents fuel from behaving like an ideal thermostat, causing its temperature to progressively rise throughout the flight. Consequently, a fuel-based TMS is capable of providing effective cooling only until the fuel temperature reaches a given threshold, which is either set by safety regulations or by the heat source's temperature limit. Reaching this threshold defines the overall system's "thermal endurance", which contributes to determine the the maximum achievable range of the aircraft.

A number of different F-TMS architectures exists, yet they will be discussed in greater detail in Sect. 3.1.

In the end, fuel-based Thermal Management Systems appear as promising solution for fuel cells cooling, as they preserve the aerodynamic performance of the aircraft and, for the most part, allow effective cooling independently of external conditions. They could be used in place, or to support, conventional ram-air cooling, especially when in stationary conditions. They are also advantaged by the fact that they are not not subject to compression heating prior entering the heat exchanger. However, the use of F-TMS for fuel cell cooling is strictly limited to the context of hybrid-propulsion electrification and clearly not suitable for full electric aircraft. Furthermore, the effectiveness and performance of fuel-based solution is progressively diminished at higher degrees of hybridization, consequent to the stored fuel mass being smaller.

3.0.3 Alternative heat sink solutions

With the term alternative heat sink solutions, we refer to all those devices employed, designed, or conceptualized, that do not directly rely on fuel, or air, to assist in the thermal management of an aircraft. These are the least common designs, are often associated with a low TRL, and are almost always combined with other, more conventional, cooling architectures. In fact, alternative heat sinks are often used to absorb peak heat loads, such as during takeoff, and later dissipate the stored heat over an extended time-span, allowing for the downsizing of other, more conventional, TMS elements. Nonetheless, alternative heat sinks can also be employed as main heat sinks for some specific low endurance use cases.

The main categories of alternative heat sinks are:

1. The phase change materials. These devices leverage on physical state transition of a material, typically fusion, to absorb heat from a heat source. Phase change materials, unlike fuel, provide the added benefit of acting as an actual thermostat. However, weight of such components can quickly become prohibitive, while the the actual materials could either be: costly, toxic or subject to cyclic degradation.

2. The chemical heat sinks. These devices absorb heat via endothermic chemical reactions, and are typically installed in modules. However, since the reactions involved in chemical heat sinks are often irreversible, such modules tend to come as consumable packages, and are not suited for long endurance cooling.
3. The structural heat sinks. These solutions simply represent the collection of all elements places in proximity of the heat source, that are capable of absorbing and storing heat from it though conduction. However, the heat capacity of structural heat sinks is often limited, making them only suitable for minimal heat loads management.

Overall, alternative heat sinks do not appear as indicated solutions for fuel cell cooling, either due to limited cooling capacity or significant added weight. Amongst them, phase change materials could arguably offer some advantages in reducing cooling requirements while considering fuel cell peak load generation, such as during take off.

In the end, looking at the results of this survey, conventional ram-air and fuel-based solutions appear as the two most promising solutions to provide fuel cell cooling in support of hybrid-electric aircraft development. Amongst these, air-based designs have already been thoroughly explored in the literature, evidencing challenges in the management of system induced drag. On the other hands, harnessing of the benefits offered by fuel-based architectures in support of fuel cell cooling still needs to be addressed. Therefore, as anticipated, this theme is further analysed in the following.

3.1 FUEL-BASED THERMAL MANAGEMENT SYSTEMS

The documents obtained via the literature analysis, described in Sect. 2 present an ample collection of theorized, conceptual, modeled, tested and applied fuel-based cooling architectures. The proposed solutions vary on a number of aspects, from the detailed numerical modeling of the tanks internal behaviour via CFD analysis to a more generic system level design of the architectures. The former allows to distinguish between two major types of fuel based solutions. The main, or terminal, fuel heat sink tend to conceive the fuel as their prevalent or unique heat sink. Heat is expected to be absorbed by the fuel, without major portion of it being transferred to the external ambient. Hence, the collection of tanks can often be assumed as an adiabatic system with respect to the environment. Such an hypothesis is very well suited for modeling of applications whose thermal conductivity to the external atmosphere is hampered by the materials adopted to build the tanks or the frame like, for example, composites and polymers.

The secondary or temporary fuel heat sink, on the other hand, do not conceive fuel as their prevalent heat sink but, rather, as complementary element. Fuel is meant to absorb heat from the heat source, only to cede it at a later stage to some other heat sink, most likely, the external environment. Two main approaches are proposed in this sense. The work of Kellermann et al. [57] for example, presents several configurations where the fuel acts as a sort of coolant for the heat source, whose purpose is to cede heat to the external ambient through the tank walls. Some of the proposed solutions even try to further enhance the process via the integration of superficial heat exchangers surrounding the tanks themselves. On the other hand, the "Hot/Cold Tank Recirculation with Tank Drains" design proposed by Doman [82], describes the possibility to exploit fuel as a secondary heat sink by having a small tank subsystem partitioned into two separated cold and hot tanks, with the later containing the exploited fuel to either be burnt in the engines or slowly cooled back to the original temperature via alternative means, such as ram air. Such a solution focuses on the possibility to use fuel as a thermal buffer in case of discontinuous, peak heat loads, with the intent of progressively ceding the majority of said heat to other heat sinks, at a later stage. For the purpose of this paper, a collection of different architectures is here presented, all suited for use both as main or temporary heat sinks, despite the latter being only truly relevant in designs allowing for fuel recirculation. In the end, about five main architectures could be identified according to: the presence or absence of a recirculation circuit, the placement of the main heat exchanger, and the compartmentation of the various tanks, as represented and discussed in the following.

3.1.1 Fuel-based TMS with submerged heat exchanger

Fuel-based TMS with submerged heat exchanger, represented in Fig. 4, are amongst the simplest possible F-TMS architectures, realized by placing the main heat exchanger directly inside the fuel tanks. Heat transfer from the heat exchanger to the heat sink occurs via natural convection, while progressive temperature increase in the tanks allows for design centered around secondary heat sink and passive heat exchanger concepts.

Overall, the main advantages of such an architecture are:

- The intrinsically reduced need for additional drag-inducing air-intakes;
- The simplicity of the design;
- The direct contact between the heat sink and the heat exchanger, reducing the need for pipings and saving weight;
- The possibility for the tank to effectively act as passive heat exchanger via progressive temperature increase in tank.

Nevertheless, the following hindrances could also be identified:

- The natural convection heat transfer mechanism is less effective when compared to forced convection, thus limiting the maximum manageable heat flow, or forcing the heat exchanger oversizing;

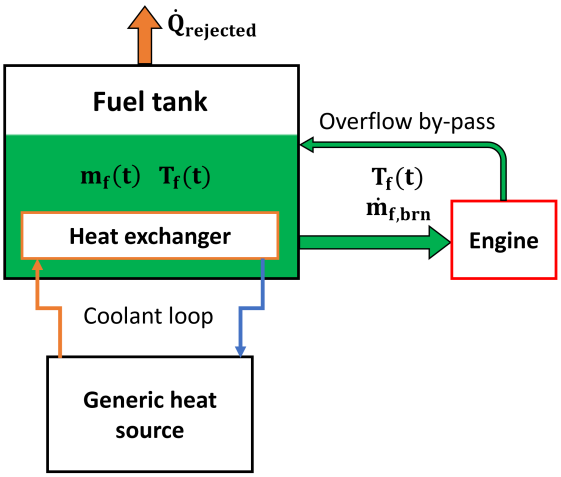


Figure 4 Fuel-based TMS with submerged heat exchanger.

- The natural convection phenomenon is not directly controllable, posing some issues in the management of high and discontinuous loads;
- The progressive temperature increase and fuel evaporation inside the tanks represent a relevant flammability hazard to be monitored and managed.

Consequently, F-TMS with submerged HE represent ideal candidates for component cooling of systems placed in proximity of aircraft fuel tanks, that are also characterized by limited heat flux production, such as the actuators or the lubrication circuit [100]. Nevertheless, the possibility to further develop the architecture for the effective management of higher heat fluxes is also proposed in some studies [57].

3.1.2 F-TMS with heat exchangers on the feed-line

F-TMS with feed-line heat exchangers, represented in Fig. 5, have the heat exchanger being placed along the supply-line to the engines, rather than inside the fuel tanks. This allows for development of forced convection heat exchange inside the heat exchanger which is beneficial for the overall efficiency of the system and the maximum achievable heat transfer. No excess of fuel mass flows is expected to be directed back to the tanks, since eventual overflows are simply bypassed directly to the entrance to the pump. For this reason, this kind of architecture is the only one that is entirely non-feasible for usage of fuel tanks as passive heat exchangers, since the temperature increase cannot occur.

Overall, the main advantages of such an architecture are:

- The reduced need for additional drag-inducing air-intakes;
- The simplicity of the design;
- The maximization of fuel heating prior injection into the combustion chamber of the engines is beneficial to the overall combustion efficiency of the aircraft, according to several studies;
- The direct consumption of heated fuel prevents fuel temperature increase inside the tanks, thus significantly reducying the safety hazard associated with the system.

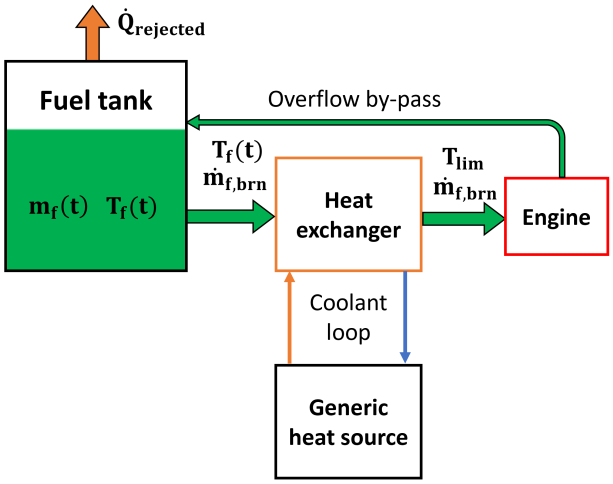


Figure 5 Fuel-based TMS with feed-line heat exchangers.

Nevertheless, the absence of a recirculation pipeline comports the impossibility to increase the fuel flow passing through the heat exchanger beyond the instantaneous needs of the engines. Therefore, the following hindrances could also be identified:

- The maximum realizable mass flows, and consequently the maximum realizable heat flux absorbtion are limited to the maximum achievable fuel flow request by the engines;
- The instantaneous fuel flow passing through the heat exchanger does not depend from the evolving needs of the heat source, yet rather from the fuel consumption curve of the mission profile. Therefore, no direct control over the cooling fuel flow is achievable, rendering mandatory the adoption of auxiliary cooling units, such as ram-air intakes for the management of excessive heat load phases;
- The impossibility to heat the fuel inside the tanks, prevents the use of the fuel-TMS as a passive heat sink.

As a consequence, this architecture is really suited for use as a simple and safe cooling system to be adopted in low heat load applications, preferably close the the engine compartment. Therefore, in fact, fuel-based TMS with feed-line heat exchangers are already very common in the industry, and frequently find application in gearbox lubricant oil cooling for turbofans driven airliners.

3.1.3 F-TMS with heat exchanger in parallel recirculation

F-TMS with heat exchanger in parallel recirculation, represented in Fig. 6, introduce the possibility to return excess fuel back to the tank via a dedicated pipeline. The heat exchanger placement does not occur along the pipeline leading to the engines yet, rather, on dedicated circuit separately located and pumped. From here the name

"recirculating-parallel", and the possibility to completely decouple the thermal circuit from the feed one. This aspect renders such an architecture particularly favourable for eventual retrofitting of already existent fuel tank arrays into integrated F-TMS. Overall, the main advantages of such an architecture are:

- The reduced need for additional drag-inducing air-intakes;
- The relative simplicity of the design, albeit the number of pumps, sensor and controls is higher than in the previous cases;
- The suitability for easy retrofit of already existent fuel tank systems.
- The parallel circuit allows to decouple thermal and engine feed management, allowing for dedicated control, monitoring and pumping for both assets;
- The dedicated cooling fuel ducts can be sized and monitored for higher fuel mass flows and, therefore, higher total absorbed heat flows, increasing the maximum cooling potential of the heat exchanger;
- The recirculating architecture allows for heat storage inside tanks, generating progressive temperature increase, which leads to potential usage of the tanks as passive heat exchangers. In the end, this translates to a generally higher thermal endurance of the aircraft.

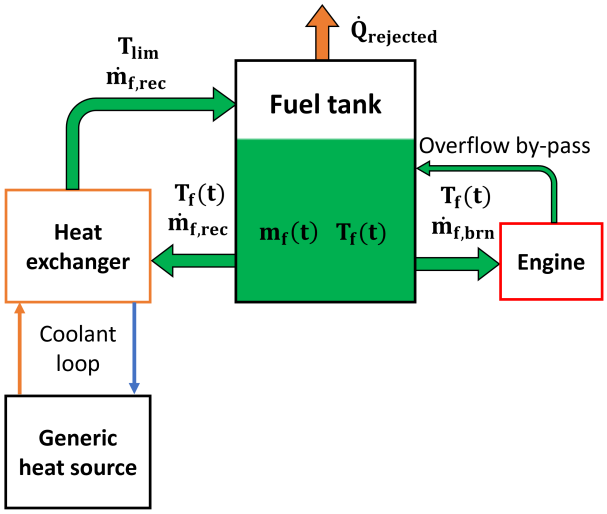


Figure 6 Fuel-based TMS with heat exchanger in parallel recirculation.

Nevertheless, the separation of the fuel heating line from the engine feed line, prevents the fluid from entering the combustion chamber at the maximum allowable temperatures. In fact, fuel sent to the engines will be at the mean temperature of the tank reservoir, which will always be lower than the temperature at the heat exchanger outlet. This aspect tends to diminish during the mission, as the mean temperature of the stored fuel rises and is thus more apparent during the initial phases of the flight. Consequently, the following hindrances could also be identified:

- The impossibility to maximize the engine-fed fuel temperature, minimizes benefit associated with combustion efficiency;
- The impossibility to maximize the engine-fed fuel temperature comports the consumption of fuel that still presents significant heat capacity to be exploited for sensible cooling. This aspect is a significant limitation to the total thermal endurance of the aircraft;
- The progressive temperature increase and fuel evaporation inside the tanks represent a relevant flammability hazard to be monitored and managed.

In the end, such an architecture is best suited for low to medium heat load management, especially in the case of elements whose activity is not directly connected to the engine functioning and may require independent or intermittent cooling. Therefore, usage of F-TMS with heat exchanger in parallel recirculation for electronic equipment cooling is currently the main application of such architectures. An example of such an architecture is provided in the Full Authority Digital Engine Control (FADEC) cooling loops described in the work of Lui et al. [97] and Ho et al. [83], while a more detailed description is proposed by Doman [82].

3.1.4 F-TMS with heat exchanger in series recirculation

F-TMS with heat exchanger in series recirculation, represented in Fig. 7, maintain the use of a dedicated pipe for thermal fuel flow return to the tank. However, in contrast with the parallel architecture, the thermal and feed lines are merged back together, with the heat exchanger being placed in series before the engine. The introduction of a valve control system downstream the heat exchanger allows for the preservation of the separate control of both flows despite the merging of the two lines. This way, the maximum required fuel mass flow amongst thermal and feed flow is provided via a single pump at the tank out-take and then passed through the heat exchanger. Fuel exiting from the heat exchanger is then split between the required amount being sent to the engines' combustion chamber, and the remaining portion, if present, being sent back to the tank. Along the return line an auxiliary air cooler could also be introduced to increase system safety or simply to extend the overall aircraft thermal endurance provided by the TMS. Overall, the main advantages of such an architecture are:

- The reduced need for additional drag-inducing air-intakes;
- The adoption of a single fuel line may reduce the number of pipes, pumps and other components associated with the design, saving weight, costs and system reliability issues;
- The feed of fuel exiting from the heat exchanger directly to the engines, allows for achievement of maximum fuel temperature and, thus, for higher improvement of combustion efficiency;

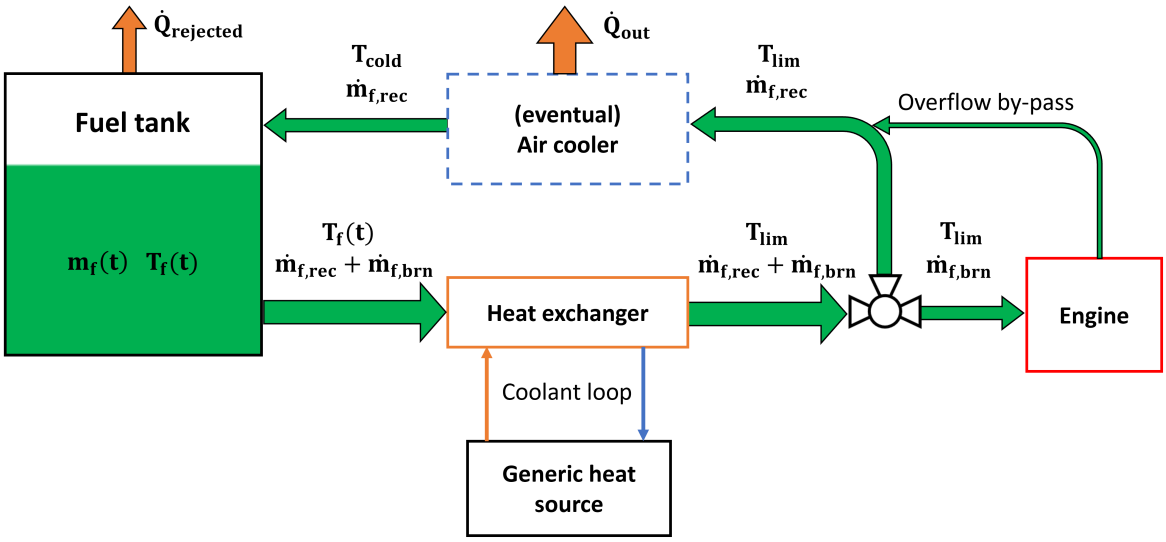


Figure 7 Fuel-based TMS with heat exchanger in series recirculation.

- The adoption of the valve control system allows for decoupling of thermal and engine fuel flow monitoring and control;
- The initial duct connecting fuel tank and heat exchanger, as well as the recirculating duct from the heat exchanger back to the tank could both be sized to account for fuel mass flows depending from the heat source needs and not the engines';
- The recirculating architecture allows for heat storage inside tanks, generating progressive temperature increase, which leads to potential usage of the tanks as passive heat exchangers similarly to the approach proposed by Kellermann et al. [57];
- The combination of recirculating architecture with series placement of both heat exchanger and engines allows for full exploitation of fuel associated thermal capacity, translating to a generally higher thermal endurance of the aircraft.

Nevertheless, the following hindrances could also be identified:

- The integrated pipeline whose flow requirements depend from more than one user, introduces the need for a reliable valve system, or other flow management device, as well as a dedicated control strategy, therefore increasing the overall system complexity;
- Integrated nature of the architecture makes it challenging to implement as an eventual retrofit, and calls for dedicated and careful design since the project phase;
- The progressive temperature increase and fuel evaporation inside the tanks represents a relevant flammability hazard to be monitored and managed.

The higher complexity of this architecture, both from a design, cost, reliability and safety point of view, relegated such a solution to advanced aircraft applications mostly, characterized by high performance requirements. In fact, challenges posed by the design always hindered its application in the market of civil transport aviation. Nevertheless, current evolution in the needs for advanced thermal management could justify the adoption of said systems.

3.1.5 F-TMS with heat exchanger in series recirculation and double tank

F-TMS with heat exchanger in series recirculation and double tank configuration, represented in Fig. 8, expand the concept of the previous design by splitting the main tank into two diverse subsystems, characterized by different purposes. The first of those components is the reservoir main tank, which is dedicated to the storage of high amounts of fuel to be kept at relatively low temperatures. Such a tank presents a single out-port from which fuel is sent to the main users, while intakes allowing for fuel return upon heating are absent. Therefore, the main tank effectively behaves like a non-recirculating F-TMS with feed-line heat exchangers and maintains its mean temperature almost unaltered along the mission. The other subsystem of the dual tank architecture is the so-called recirculating secondary tank. Characterized by a smaller capacity, said tank presents both fuel intakes and outtakes, unlike the previous one. The former allows for heated fuel in excess to reach the tank, while the latter allows for fuel extraction and supply to the various users. Therefore, this tank will be dedicated to store the hot fuel coming from the heat exchanger not being burnt in the engines. From the user point of view of the users, instead, fuel coming from both tanks will be mixed via a dedicated mixing valve, according to the current needs of the main heat sources, and then sent to the principal system heat exchanger.

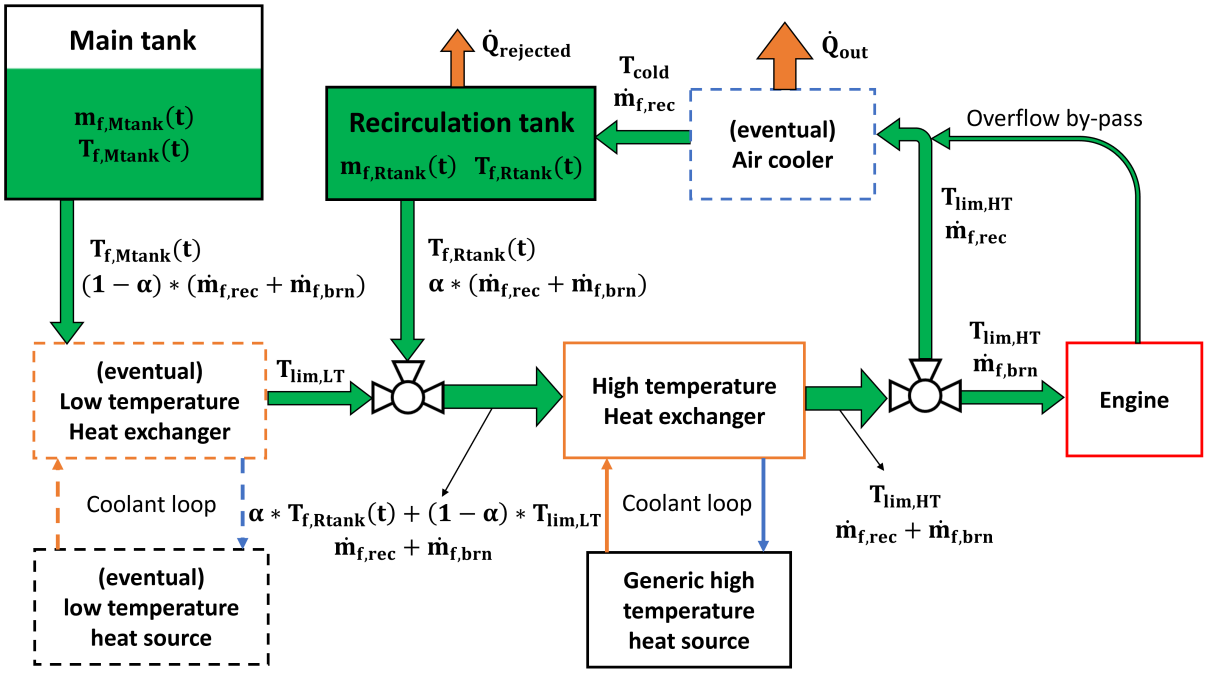


Figure 8 Fuel-based TMS with heat exchanger in series recirculation and double tank design.

The significant increase in complexity associated with the adoption of the dual tank is justified by the advantages granted by such a system, being listed below:

- The same benefits of the previous F-TMS with heat exchanger in series recirculation;
- The presence of the "low" temperature reservoir tank allows for safer cooling of sensible components, such as electronics or batteries, via access to an, almost, constant temperature heat sink;
- The separation of the tank system into a low temperature one and a high temperature one allows for higher achievable maximum fuel temperatures. In fact, by moving upstream the mixing valve all the components characterized by the lowest allowable temperature requirements, it becomes possible to cool such components only via the low temperature fuel tank. This way, the limit mean temperature of the recirculation tank can, instead, be increased, since it is no longer bounded to the requirements of sensible components. Therefore, the exploitable thermal capacity of the hauled fuel is further incremented via augmentation of maximum allowable temperatures;
- The increase in maximum allowable mean temperature of the recirculation tank permits reaching higher temperature deltas between the external environment and the fuel itself. Therefore, the mechanism of passive heat rejection through the tank walls is favoured and the overall thermal endurance of the aircraft improved.
- The lower capacity of the recirculation tank, determines the presence of a smaller associated thermal inertia when compared to a single tank system; Consequently, high fuel temperature is reached much faster in said conditions and, therefore, benefits of presenting maximum temperature delta between fuel and external air could be exploited earlier in the flight and for longer portions of the mission.

Nevertheless, the following hindrances could also be identified:

- The separation of the fuel tanks, the introduction of the mixing valve apparatus, together with the already discussed recirculating heat exchanger architecture present significant increases in complexity of the system design and control;
- The relevant increase in system complexity determines challenging increases in costs, number of components, reliability issues and need for redundancy;
- Integrated nature of the architecture makes it challenging to implement as an eventual retrofit, and calls for dedicated and careful design since the conceptual phase;
- The progressive temperature increase and fuel evaporation inside the tanks represent a relevant flammability hazard to be monitored and managed;
- The full benefits of a similar architecture are only really exploited only if the intended TMS is supposed for to provide cooling to several heat sources characterized by varying degrees of allowable maximum temperatures.

Due to the numerous challenges associated with such an architecture, no known systems are currently adopting the "F-TMS with heat exchanger in series recirculation and double tank" solution. In fact, despite numerous

studies being conducted on the topic, especially those proposed by Prof. Doman et Al. [67, 82, 81, 80, 78], investigating its benefits and even demonstrated its feasibility via experimental validation, conceptual design still is the only current application of said architecture. Nevertheless, as proposed in the aforementioned studies, it is very likely that challenges of the next generation of aircraft will justify the adoption of similar constructions on the highest performance constructions.

4 USE CASE

The previously specified literature based results are here applied to a plausible next-gen, hybrid-electric aircraft making use of fuel cell power generation units. Due to the current state of aviation based electrification programs being mostly relegated to small scale general aviation demonstrators [14], a non-better specified aircraft in the regional transport weight class is considered as the use case of this study. Said aircraft are really common constructions for use in short range air-transport and represent one of the smallest classes of available passenger aircraft. Some typical characteristics of current regional transport aircraft, such as ATR-72-600 [101], Dash 8-400 [102], Fokker F50 [103], and Do228 NXT [104], are:

- A passenger capacity ranging from 19 to 90 PAX, depending on size and configuration of the aeroplane;
- A propulsion system consisting of two separate turbo-engines, one per each semi-wing, both driving a propeller via gearbox reduction;
- A combined total mechanical power at both propellers ranging from 1.0 to 7.5 MW, depending on the overall size of the craft;
- A maximum achievable range of about 1000 to 2000 km, at full PAX payload. However, the typical mission range of said aircraft is most often comprised between 300 to 500 km during regular operation.

These specification are therefore to be associated with the following design choices, proposed to enhance project feasibility in the optic of increasing aircraft degree of electrification:

- Adoption of a hybrid propulsion system to be powered via conventional turboprop engines, coupled with electric motors, in parallel configuration, contributing to the total torque at the propeller shaft;
- Introduction of a PEM fuel cell stack, intended to convert chemical power stored inside hydrogen tanks and to supply the electric motors.

The actual degree of hybridization, however, is left undefined since, while its maximization is definitely one of the main targets of such a project, its optimal value is not so easily defined. In fact, benefits provided by systems' electrification in components efficiency and pollutants emission reduction, are easily offset by the weight increase with respect to the elements that these systems are substituting. Variations in the hybridization degree are rendered even more crucial in the case of TMS exploiting fuel as a relevant heat sink, since any reduction of fuel reserves associated with an increase in the degree of electrification, both results in higher thermal loads being generated, as well as lower exploitable heat capacity, thus significantly impacting the overall thermal endurance of the aircraft.

4.1 METHODOLOGY

Previous sentence shows how optimized design of the TMS represents one of the key assets not only in defining the overall feasibility of the project, but also in determining its effectiveness in the effort of reducing the aviation carbon footprint. Therefore, a structured design methodology is needed to guide the development of the whole aircraft system and the TMS alike. Model Based System Engineering (MBSE) approach is chosen for this purpose. Citing the INterantional COuncil of System Engineering (INCOSE) on the matter, MBSE could be described as "The formalized application of modeling to support system requirements, design, analysis, verification and validation activities beginning in the conceptual design phase and continuing throughout development and later life cycle phases."

Ample diffusion of such a methodology in the aerospace sector, as well as its demonstrated effectiveness in managing complex design development, such as an integrated fuel-based TMS, justify the adoption of the method. The associated procedure could be summarized via the so called "V-diagram", here represented in Fig. 9.

The problem is thus first identified and the project

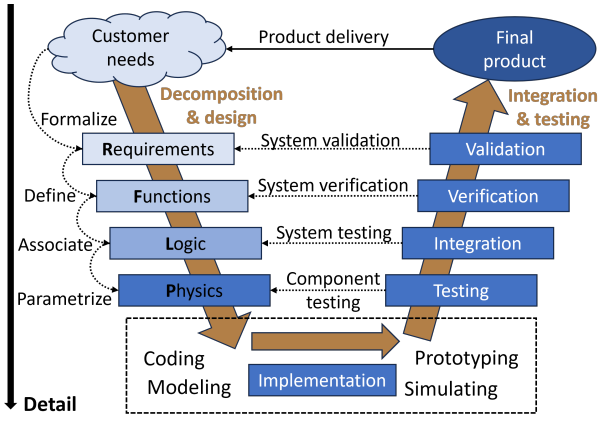


Figure 9 V-model diagram according to MBSE approach.

boundaries are defined. Then the whole system is progressively shaped via gradual decomposition into its various subsystems and components, increasing the level of detail associated with the design. At the end of the process, numerical simulations and tests of all relevant components

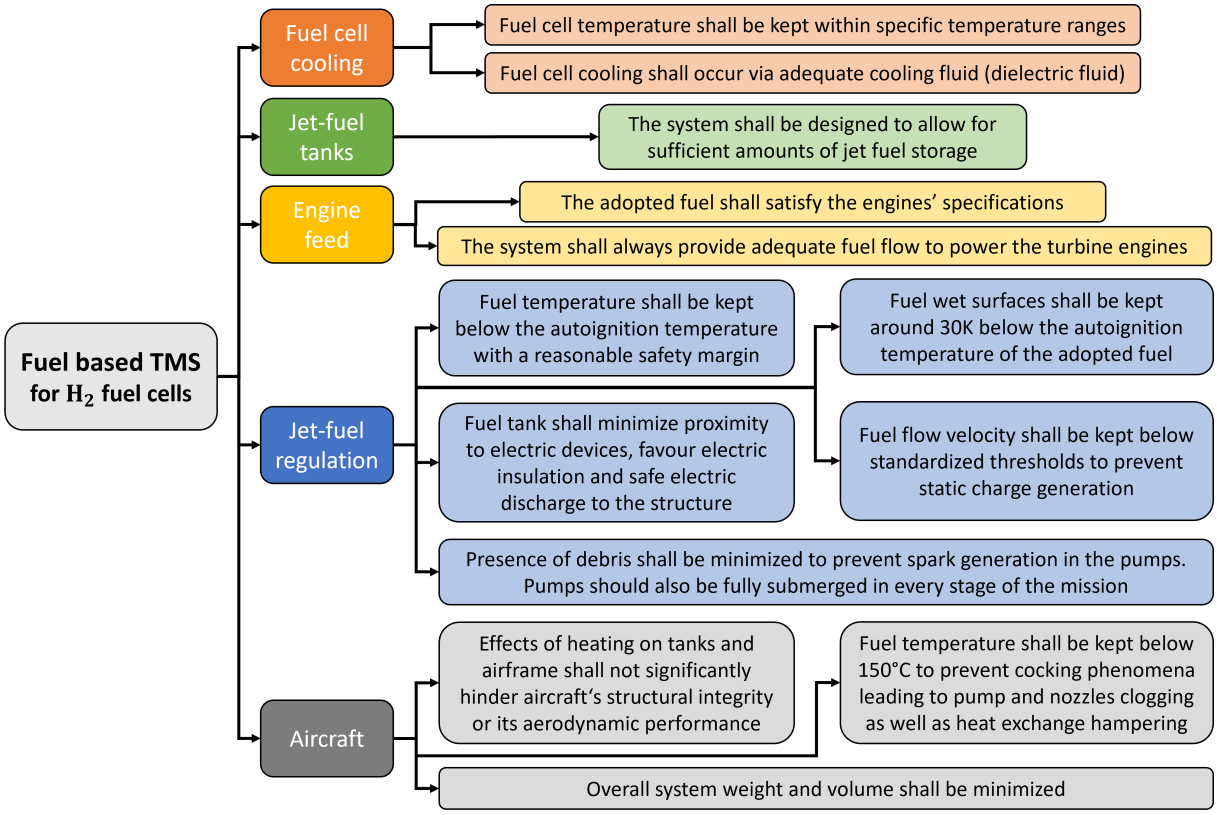


Figure 10 Main stakeholders requirements for a fuel-based thermal management system to be applied on a regional transport, twin-turboprop, parallel hybrid-electric, fuel cell powered aircraft.

are performed, completing the design phase. Later, the various components' models are progressively integrated and tested until a simulation of the global system behaviour is achieved, and the original requirements validated.
Finally, it is important to consider that, while trying to apply such a methodology, frequent iterations and revisions are suggested along the design process. This allows to verify that the final product requirements are effectively in line with the stakeholders needs as the level of detail in the modelling is increased. This is achieved by verifying that functions are properly defined and executed, that the logical elements are justified and the numerical results are in line with the expectations and coherent with the physics. An complete overview over the proposed methodology can be found in the works of Vitolo et al. [105] and Mhenni et al. [106], while the work of Pace et al. [107] provides an in depth analysis over the formalization of the system's requirements.

4.2 MBSE APPLIED TO THE USE CASE

The aforementioned methodology is therefore applied to the regional aircraft use case previously described, starting from the formalization of the intended requirements of the integrated system. Being the TMS a subsystem of the whole aircraft deliverable, the stakeholders of this study should not be identified in the final customers of the whole aircraft, yet, rather, stakeholder should be considered as the main elements that the thermal management will be expected to interface with, as well as support, satisfy and integrate. Therefore, starting from the analysis of the literature proposed architectures, it is possible to identify four main components constituting the F-TMS; those element are:

- The fuel tank, which stores the required fuel for the expected mission profile, providing it as a combustible to the engine and a heat transfer vector to the heat source. It also acts as an effective heat sink and, eventually, as a passive heat exchanger;
- The heat source, which describes the heat flux generation that will need to be managed by the integrated system;
- The engines, which define the fuel consumption profile of the aircraft, according to the mission profile, and determine the progressive depletion of fuel reserves in the tanks;
- The main heat exchanger, which is entitled with the realization of the heat transfer from the source to the fuel.
- The collection of pipes and tubes supplying the various components of the assembly represent a significant asset in the determination of the masses associated with the overall assembly and are bound to strongly influence elements placement within the aircraft. However, they are neglected

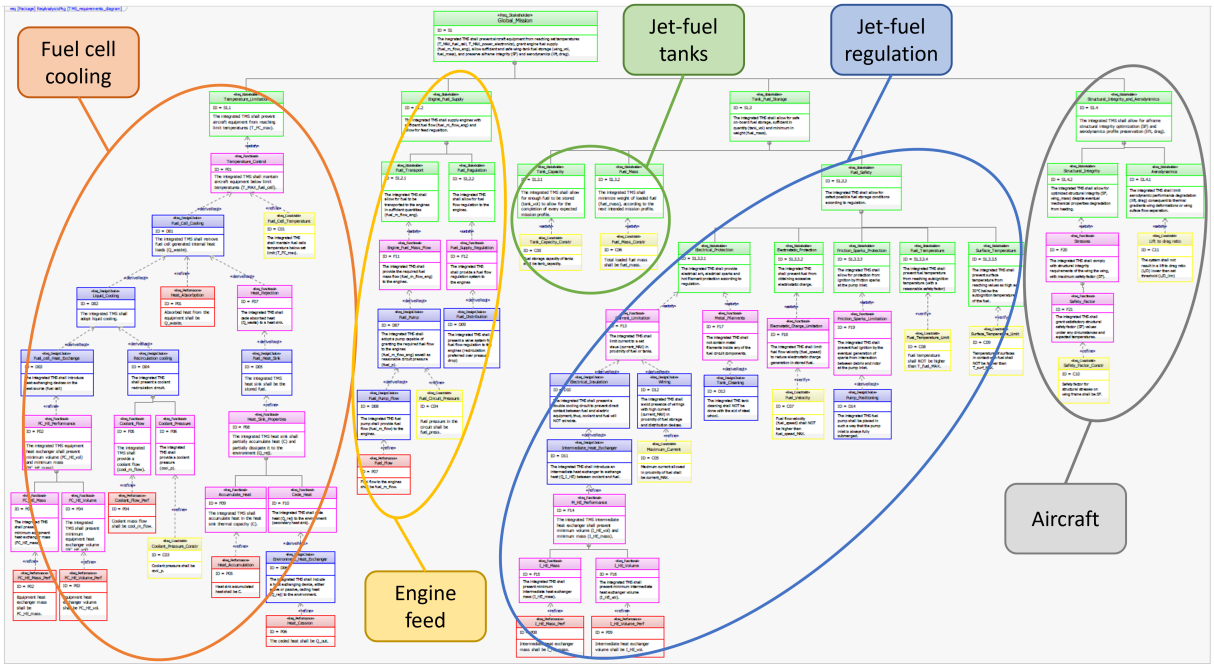


Figure 11 Preliminary requirements tree of a fuel-based TMS for hybrid-electric regional transport aircraft

for the purpose of this study, due to the preliminary nature of this study and coherently with most of the models presented in the literature, being described via lumped parameters models [57, 95, 81, 67].

Now, due to the current study being a preliminary one, and the purpose being the evaluation of the feasibility and potential of the solution from a purely thermal standpoint, the specifications of the heat exchanger, being mostly related to volume and masses constraints, could simply be translated into a global volume and mass requirement of the whole TMS. Therefore, the heat exchanger component is just integrated with the fuel cell element into a single stakeholder, contributing to the overall thermal balance as a generic resistance, describing the heat exchanger efficiency. Further analysis should investigate the properties of said elements separately in the future, with a focus towards the heat exchanger specifications.

Nevertheless, the remaining three components, clearly identify some elements which the TMS will need to interface with and that will impose some constraints and expectations on the design. Therefore, considering the use case of a regional transport aircraft, the requirements imposed by these components over the integrated F-TMS multi-functional purpose of fuel storage unit, fuel supply unit, thermal heat sink module and passive heat exchanger, were characterized as shown in Fig. 10.

However, modeling of a thermal management system subject to a progressive fuel temperature increase along the whole flight profile, comes with significant considerations on the matter of safety. Therefore, a fourth stakeholder is introduced to account for international regulations on the matter of flammability and safety while handling fuel. Specifically, the Certification Specifications for Large Aeroplanes (CS-25) [108] of the European Union Aviation Safety Agency (EASA) was taken as a reference. The most relevant guidelines, constraints and procedures expressed by said regulation on the matter of safe fuel handling, storing and heating, where thus purposefully tracked into the main requirements diagram.

Finally, some generic requirements associated with the overall interaction of the integrated F-TMS with entirety of the aircraft are also proposed. The main topics of such requirements being the limitation of system masses and volumes, the consideration of the effects of fuel heating on surrounding walls structural performance and the preservation of aircraft piping from fuel chemical precipitation and nozzle occlusion.

Both of these two other requirements are also represented in Fig. 10. Said collection of requirements is thus formalized via the use of Rational Rhapsody software and the rules of the SysML language. Some numerical values are introduced to further specify the requirements with reasonable expectations suited for an example regional transport aircraft. The previously listed stakeholder requirements are later expanded into more specific system requirements describing the various design choices, constraints and performances, leading to the formalization of the preliminary architecture; like, for example, the decision to exploit stored jet-fuel available heat capacity as a relevant heat sink for the TMS. Consequently, the waterfall of defined requirements comes to

define the whole system requirements tree that is represented in Fig. 11. A more in depth view of the contents of the requirements diagram is also provided in Fig. 15, providing details over each single requirement

Successively, the so called ”functional requirements”, which introduce the functions that the system will be expected to perform once realized, are expanded, described and explained via the creation of purposefully built functional diagrams. In particular, activity diagrams are used in this case to define the sequence of actions that the TMS will be expected to perform in response to the events occurring in the external ambient, along the surrounding and interfacing systems, as well as inside the elements of the TMS itself. For a matter of simplicity, due to the great variety of actions expected to occur, as well as to avoid the repetition of identical actions inside the same diagram, the whole activity diagram of the TMS is decomposed into several sub-models. The simplest and most common actions are thus defined into brief, non-component specific sequences, while the most elaborate functions simply recall those trivial sequences via hyperlinks, preserving the overall readability of the schemes. In order to exemplify such a concept, the amplest sequence of the model is here represented in Fig. 12, with the hyperlinks to simpler functions being evidenced by the presence of a small ”trident” mark in the bottom right corner of the connected block.

As anticipated, the fulfillment of said functions has to be performed via dedicated components which are not necessarily defined at the start of the design process. The definition of all expected system functions via MBSE approach allows for a clear and justified identification of all such required components, which are specified inside the logical diagrams of the systems. For the purpose of this study, two different diagrams where utilized, a Block Definition Diagram (BDD) and an Internal Block Diagram (IBD). The former is used to define the dependencies of the various identified components from their reference subsystems, as well as the dependencies of those subsystems from the whole TMS. The latter, instead, is used to specify the logical interfaces established amongst the various components as well as the identification of those variables that are relevant for the sizing of the components, and the associated functions. Such variables can further be classified into ”local variables” and ”global variables”. The former being dedicated to the description of a single component’s behaviour. The latter intended for the description of the whole TMS performance, its validation with respect to the design requirements, and data transfer between different models and submodels. This classification allows for proper compartmentation of the model variables, favouring flexibility in the use of the submodels, enhanced readability of codes and diagrams, and generally lower computational costs, via the minimization of the amount of variables being transferred from one model to the other and the possibility to

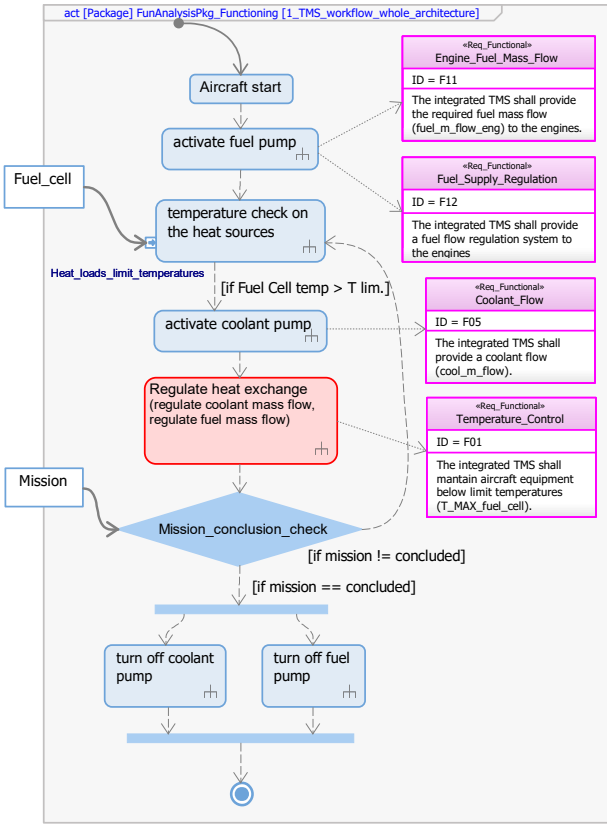


Figure 12 Activity Diagram describing the aircraft TMS activation cycle till mission conclusion

easily develop Reduced Order Models (ROM). The ”fluxes” describing how the values contained in such variables are exchanged between the various components are also defined, providing a preliminary structure to any design, sizing or testing model of interest. A representation of the developed IBD of the fuel-based TMS is shown in Fig. 13.

It is interesting to note that, in the presented Internal Block Diagram, the aircraft engines are considered as being part of the system’s heat sinks. This is due to the fact that, as stated by Manna et al. [65], any heat absorbed by the fuel being sent to the engines is effectively rejected into atmosphere through the exhaust gases. However, as the F-TMS can not influence the expected engines’ fuel consumption and requirements, it is suitable to place such components outside of the collection of elements suited for sizing and optimization of the thermal management system.

Another interesting aspect that could be extrapolated from this diagram is the necessity to interpose a secondary coolant loop between the fuel cell and the fuel heat sink, which will receive heat indirectly via an intermediate heat exchanger. This is necessary to satisfy the fuel cell side requirement for the use of a specific coolant type suitable for the component, as well as the fuel safety regulation for the limitation of fuel proximity to electricity sources.

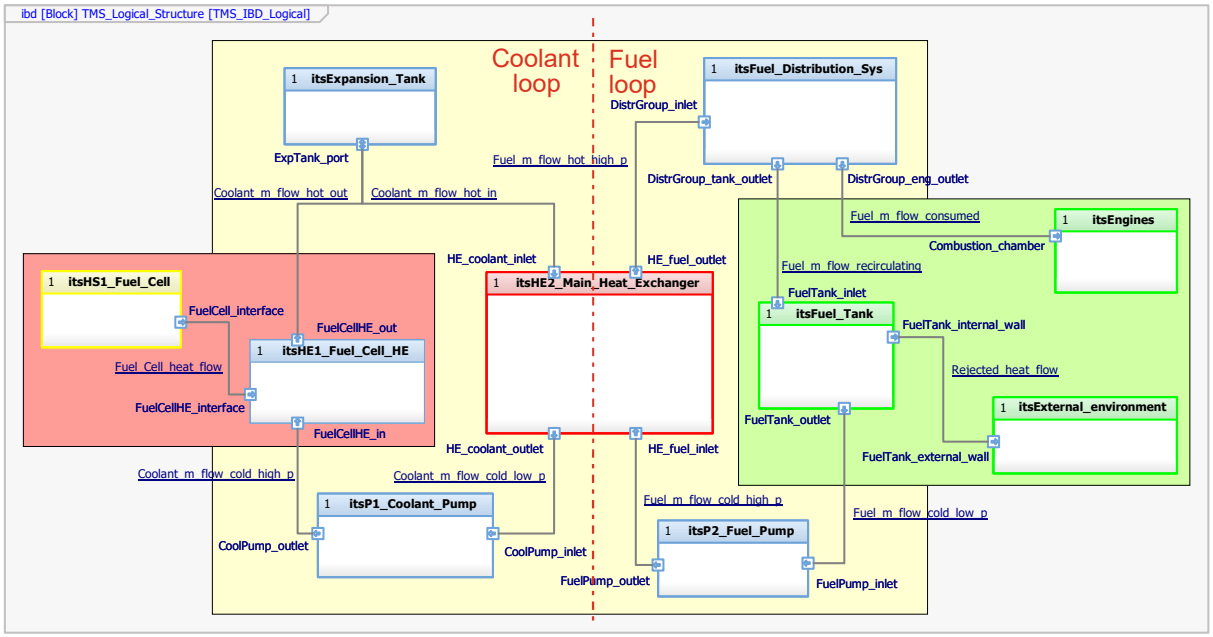


Figure 13 Internal Block Diagram of a fuel-based TMS for hybrid electric aircraft. Red square contains elements acting as heat heat sources; green square contains the heat sinks; yellow square contains elements of the TMS that require sizing and optimization, overlapping, in some cases, with with the other two squares, per the fuel cell heat exchanger, and the fuel tank.

Each logical element of the diagram is finally characterized through the definition of a series of logical variables describing the main parameters intrinsic with the modelling of said element. These parameters shall act as the main properties to be evaluated and tracked throughout the numerical simulation of the component. Some relevant examples of these variables are: the waste heat of the fuel cell $\dot{Q}_{waste}$, and its instantaneous temperature T_{FC}; the main heat exchanger temperatures $T_{HE_{cool,in}}$, $T_{HE_{cool,out}}$, $T_{HE_{fuel,in}}$, $T_{HE_{fuel,out}}$ and its associated mass m_{HE}; and also the tank stored fuel mass m_f and temperature T_f.

A series of flow variables are also defined to track parameters exchanged between the various elements of the IBD diagram via the links connecting the various proxy-ports. Most notably, the instantaneous fuel cell temperature T_{FC} and the heat extracted by the heat exchanger connecting the fuel cell to the coolant loop $\dot{Q}_{HE-FC}$; the coolant mass flow imposed by the coolant pump $\dot{m}_{pump_{cool}}$ to the fuel cell heat exchanger and its associated temperature $\dot{T}_{pump_{cool,out}}$; or the fuel mass flow sent by the fuel distribution systems to the engines $\dot{m}_{f,brn}$ and to the tanks $\dot{m}_{f,rec}$.

The last step of the descending branch of the V-model involves the translation of the IBD into a numerical simulation model. This involves the formalization of the physical correlations describing the behaviour of the various logical elements and the association of a representative numerical value to each of the defined logic variables. The actual realization and description of the numerical models is left for future investigations and will be subject of further studies by our research team. However, a few relevant numerical values can here be anticipated accordingly to the specifications of fuel cells, and regional transport aircraft, taken from the literature. These include: a limit operating temperature of the fuel cell of $T_{FC_{lim}} = 80$ °C, assuming LT-PEM; a maximum fuel cell waste heat production of $\dot{Q}_{waste} = 800$ kW, roughly equivalent to a 20% degree of electric-propulsion hybridization for a medium power regional transport aircraft. An initial tank fuel temperature of $T_f = 40$ °C, assuming the fuel to be in equilibrium with the external environment in hot day conditions.

Diversification of the presented logical model for the formalization of each of the 5 different configurations discussed in Sect. 3.1 shall also be be the subject of future analyses, along with their numerical implementation. Tradeoffs between the cooling potential and corresponding system complexity introduced by each architecture shall be addressed specifically for the intended application, via numerical simulations of the performance and confront with the requirements. Aspects such as the extracted waste heat, the system associated thermal endurance, the fuel preheating prior combustion, the passive heat rejection through the tank walls shall be compared.

In conclusion, a preliminary representation of the proposed fuel-based Thermal Management System is provided in Fig. 14. There a schematic view comprising the elements extracted from the Internal Block Diagram of Fig. 13 is

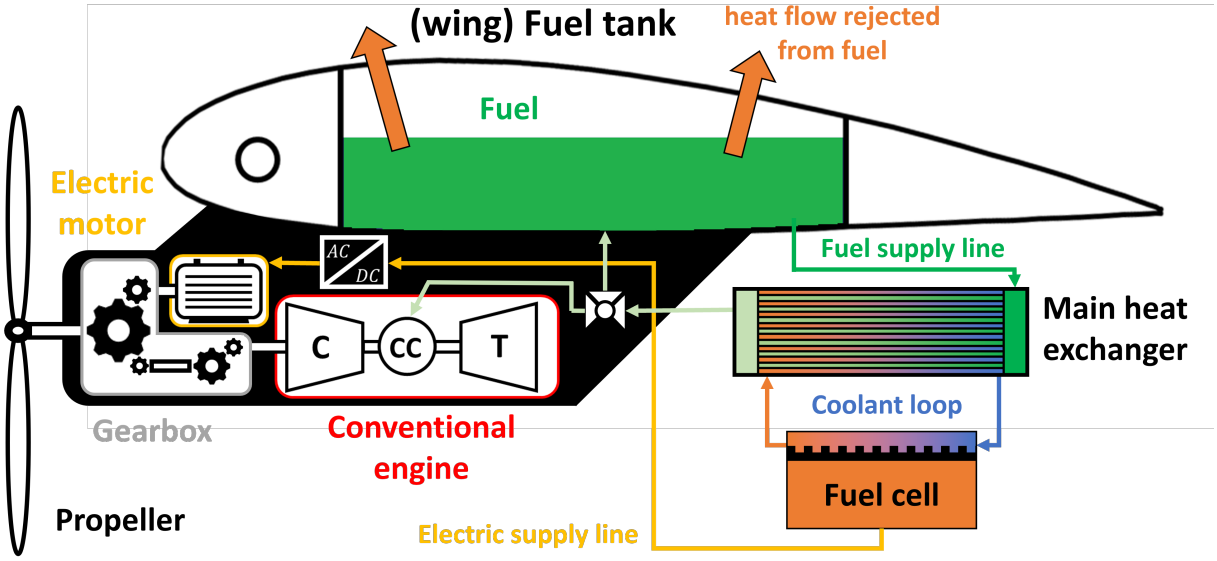


Figure 14 Fuel-based thermal management system scheme and main components for a regional transport aircraft adopting a parallel hybrid-electric propulsion supported by twin-turboprop engines and asynchronous electric motors powered trough fuel cells (not-to-scale).

provided, along with their integration into a parallel hybrid-electric propulsion configuration for a regional transport aircraft.

5 CONCLUSIONS

The results of this study evidence how the development of innovative thermal management systems for the aerospace represents a crucial asset in the design of next generation aircraft. This trend is driven by several factors, with the ever-increasing amounts of installed electric and electronic equipment being the most prominent. In particular, the adoption of fuel cells for power supply of electric motors in hybrid-electric propulsion architectures appears as a most challenging topic, mainly due to the relevant amounts of waste heat being produced by such components.

A number of different cooling solutions are presented in the literature as potential candidates for addressing this growing issue. These solutions could ultimately be classified into three separate categories, depending on the adopted reference heat sink.

- The air-based solutions. These employ external atmospheric air to provide component cooling and are, arguably, the most widespread designs due to their effectiveness, safety and simplicity;
- The Fuel-based solutions. These exploit the intrinsic thermal inertia of fuel to absorb heat from a reference heat source. Typically less prominent than air-based designs, fuel-based solution are still relatively common, thanks their convenience in cooling component that are close to the engines, and the added benefit of improved exploitation of the fuel resource. Five different F-TMS architectures are here described in detail according to the literature;
- The alternative heat sink solutions. These represents a collection of very different designs, including phase change materials and chemical heat sinks. Alternative heat sink are often limited to some niche applications, due to their reduced thermal capacity and being best suited for peak heat load management.

Amongst these three classes, air-based solutions, and especially ram-air, have been thoroughly investigated in the literature. However, issues associated with the induced drag introduced by the ram system have been shown to represent a major detriment to cooling the low temperature ($60 - 80$ °C) high waste heat production ($\varepsilon \approx 50\%$) associated with fuel cells.

The exploitation of the thermal inertia associated with fuel stored within tanks is thus suggested in this work to support fuel cell cooling in the context of hybrid-propulsion electrification for regional transport aircraft. Advantages introduced by the integration of the fuel system into the cooling loop of aircraft components are numerous. These include: a higher heat transfer coefficient compared to air, leading to lower required mass flows and more compact heat exchangers; a direct control over the supplied mass flows through the fuel pumps; an increased independence of the system from external conditions, factors, and parameters; a better exploitation of an already available resource.

Nonetheless, F-TMS also present a series of issues and challenges that need be effectively addressed for the system to perform effectively and safely. In fact, the intrinsically

limited heat capacity of stored fuel prevents this element from behaving like an ideal thermostat. Consequently, the fuel temperature is bound to increase throughout the mission up to a set limit threshold, which defines the "thermal endurance" of the system, and influences the maximum range of the aircraft. The resulting rise in fuel temperature also introduces a significant flammability hazard, which is further aggravated by the concurrent increase in fuel evaporation. This demands for both phenomena to be carefully tracked and managed, as well as for the adoption of a fuel tank inerting system.

Moreover, the adoption of a F-TMS, specifically intended for fuel cell cooling, also demands for the introduction of adequate electrical protections. These are meant to prevent electric discharges from propagating into the fuel system, leading reduced fuel cell efficiency and tank flammability hazards. The introduction of an intermediate coolant loop preventing direct contact between the jet-fuel and the fuel cells is thus required, along with the integration of a deionization filter within said loop.

Finally, the inevitable increase in system complexity when designing such an integrated architecture is addressed through the tools of the MBSE. Requirements analysis of the intended fuel-based TMS is hence proposed for the specific use case of an hybrid-electric, fuel cell powered, turbo-propeller driven, regional transport aircraft, and accounts for all major system needs expressed in the literature. A preliminary functional analysis is later conducted, leading to the formalization of the system's logical architecture, which is represented using an Internal Block Diagram. Said diagram is finally employed to define the various system parameters required for the modelling of the F-TMS and its subsequent numerical simulation.

The next phases of this study will focus on translating the proposed MBSE diagrams into an actual numerical model for the simulation of the F-TMS performance and the assessment of its feasibility. Future studies shall then expand the proposed logical framework for the formalization all five reference F-TMS architectures, and later convert them into numerical models for performance comparison.

DECLARATION OF COMPETING INTERESTS

The authors declare that they have no known competing financial interests or personal relationships that could have appeared to influence the work reported in this paper.

ACKNOWLEDGMENTS

This publication is part of the project PNRR-NGEU which has received funding from the MUR - DM352/2022 (CUP n° E12B22000560006).

REFERENCES

[1] UN General Assembly, "United nations conference on the human environment." Conference held in Stockholm, Sweden, 5-16 June 1972, June 1972.

[2] UN General Assembly, "Transforming our world: The 2030 agenda for sustainable development," September 2015. Adopted by the United Nations General Assembly, Resolution A/RES/70/1.

[3] European Commission and Directorate-General for Mobility and Transport and Directorate-General for Research and Innovation, *Flightpath 2050 – Europe's vision for aviation – Maintaining global leadership and serving society's needs*. LU: Publications Office of the European Union, 2011.

[4] Clean Aviation Joint Undertaking, "Clean aviation: Advancing sustainable aerospace innovation," 2021. European Union initiative for sustainable aviation.

[5] R. S and J. R, "Review on electric mobility: Trends, challenges and opportunities," *Results in Engineering*, vol. 23, p. 102631, 2024.

[6] A. Castellano and M. Cammalleri, "Optimal operation of power-split hybrid electric powertrain: comparison between two performance indices," *International Journal of Mechanics and Control*, vol. 23, no. 01, pp. 3–14, 2022.

[7] M. Spano, D. DelVescovo, B. Sangeorzan, D. Misul, and G. Belingardi, "Optimizing engine downsizing and driving behaviour in conventional and hybrid powertrains for autonomous driving applications," *International Journal of Mechanics and Control*, vol. 21, no. 02, pp. 1–12, 2020.

[8] H. Gesell, F. Wolters, and M. Plohr, "System analysis of turbo-electric and hybrid-electric propulsion systems on a regional aircraft," *The Aeronautical Journal*, vol. 123, pp. 1602–1617, Oct. 2019.

[9] S. Karpuk and A. Elham, "Influence of Novel Airframe Technologies on the Feasibility of Fully-Electric Regional Aviation," *Aerospace*, vol. 8, p. 163, June 2021.

[10] L. Maraschi, L. Bernabei, P. Marzioli, R. M. Galassi, P. Paolo Ciottoli, M. Valorani, and F. Piergentili, "Hybrid-electric propulsive systems sizing and performance evaluation tool for aircraft and UAV," in *2022 IEEE 9th International Workshop on Metrology for AeroSpace (MetroAeroSpace)*, pp. 43–48, IEEE, 2022.

[11] Z. P. Cano, D. Banham, S. Ye, A. Hintennach, J. Lu, M. Fowler, and Z. Chen, "Batteries and fuel cells for emerging electric vehicle markets," *Nature Energy*, vol. 3, no. 4, p. 279 – 289, 2018.

[12] A. Masias, J. Marcicki, and W. A. Paxton, "Opportunities and challenges of lithium ion batteries in automotive applications," *ACS Energy Letters*, vol. 6, no. 2, p. 621 – 630, 2021.

[13] H. Chen, T. N. Cong, W. Yang, C. Tan, Y. Li, and Y. Ding, "Progress in electrical energy storage system: A critical review," *Progress in Natural Science*, vol. 19, no. 3, pp. 291–312, 2009.

[14] C. Pornet and A. Isikveren, "Conceptual design of hybrid-electric transport aircraft," *Progress in Aerospace Sciences*, vol. 79, pp. 114–135, Nov. 2015.

[15] G. Cinar, D. N. Mavris, M. Emeneth, A. Schneegans, C. Riediger, Y. Fefermann, and A. Isikveren, "Sizing, Integration and Performance Evaluation of Hybrid Electric Propulsion Subsystem Architectures," in *55th AIAA Aerospace Sciences Meeting*, (Grapevine, Texas), American Institute of Aeronautics and Astronautics, Jan. 2017.

[16] P. Di Profio, S. Arca, F. Rossi, and M. Filipponi, "Comparison of hydrogen hydrates with existing hydrogen storage technologies: Energetic and economic evaluations," *International Journal of Hydrogen Energy*, vol. 34, no. 22, pp. 9173–9180, 2009.

[17] M. R. Usman, "Hydrogen storage methods: Review and current status," *Renewable and Sustainable Energy Reviews*, vol. 167, p. 112743, 2022.

[18] J. Condé-Wolter, M. G. Ruf, A. Liebsch, T. Lebelt, I. Koch, K. Drechsler, and M. Gude, "Hydrogen permeability of thermoplastic composites and liner systems for future mobility applications," *Composites Part A: Applied Science and Manufacturing*, vol. 167, p. 107446, 2023.

[19] N. Lapeña Rey, J. Mosquera, E. Bataller, and F. Ortí, "First fuel-cell manned aircraft," *Journal of Aircraft*, vol. 47, no. 6, pp. 1825–1835, 2010.

[20] K. V. Papathakis, O. C. Shnarr, T. M. Lavelle, N. K. Borer, T. Stoia, and S. Atreya, "Integration concept for a hybrid-electric solid-oxide fuel cell power system into the x-57 "maxwell"," in *2018 Aviation Technology, Integration, and Operations Conference*, 2018.

[21] Z. Pan, L. An, and C. Wen, "Recent advances in fuel cells based propulsion systems for unmanned aerial vehicles," *Applied Energy*, vol. 240, pp. 473–485, 2019.

[22] O. K. Keles, I. Hakyemez, M. Bagriyanik, and O. Kalenderli, "A study on power system retrofit for cessna-172s aircraft by using hydrogen fuel cell and battery hybrid," *IEEE Access*, vol. 13, p. 6089 – 6101, 2025.

[23] M. Soleymani, V. Mostafavi, M. Hebert, S. Kelouwani, and L. Boulon, "Hydrogen propulsion systems for aircraft, a review on recent advances and ongoing challenges," *International Journal of Hydrogen Energy*, vol. 91, p. 137 – 171, 2024.

[24] M. Chiara Massaro, S. Pramotton, P. Marocco, A. H. A. Monteverde, and M. Santarelli, "Optimal design of a hydrogen-powered fuel cell system for aircraft applications," *Energy Conversion and Management*, vol. 306, 2024.

[25] "Boeing fuel cell demonstrator." `https://secure.boeingimages.com/archive/Boeing-Fuel-Cell-Demonstrator-2F3XC5WZCWO.html`, 2008.

[26] "H2fly website." `https://www.h2fly.de/`.

[27] "Airbu zeroe project website." `https://www.airbus.com/en/innovation/energy-transition/hydrogen/zeroe-our-hydrogen-powered-aircraft`.

[28] "Zeroavia website." `https://zeroavia.com/`.

[29] "Zeroavia do228 flight test." `https://zeroavia.com/flight-testing/`.

[30] M. Cassir, D. Jones, A. Ringuedé, and V. Lair, "15 - electrochemical devices for energy: fuel cells and electrolytic cells," in *Handbook of Membrane Reactors* (A. Basile, ed.), vol. 2 of *Woodhead Publishing Series in Energy*, pp. 553–606, Woodhead Publishing, 2013.

[31] Z. Lin, D. Li, and Y. Zou, "Energy efficiency of lithium-ion batteries: Influential factors and long-term degradation," *Journal of Energy Storage*, vol. 74, p. 109386, 2023.

[32] H. Xu, Y. Song, H. R. Kunz, and J. M. Fenton, "Operation of pem fuel cells at 120–150°c to improve co tolerance," *Journal of Power Sources*, vol. 159, no. 2, pp. 979–986, 2006.

[33] C. H. Park, C. H. Lee, M. D. Guiver, and Y. M. Lee, "Sulfonated hydrocarbon membranes for medium-temperature and low-humidity proton

exchange membrane fuel cells (PEMFCs)," *Progress in Polymer Science*, vol. 36, pp. 1443–1498, Nov. 2011.

[34] S. Rogalsky, J.-F. Bardeau, S. Makhno, O. Tarasyuk, N. Babkina, T. Cherniavska, M. Filonenko, and K. Fatyeyeva, "New polymer electrolyte membrane for medium-temperature fuel cell applications based on cross-linked polyimide Matrimid and hydrophobic protic ionic liquid," *Materials Today Chemistry*, vol. 20, p. 100453, June 2021.

[35] J. Yang, H. Xu, J. Li, K. Gong, F. Yue, X. Han, K. Wu, P. Shao, Q. Fu, Y. Zhu, W. Xu, X. Huang, J. Xie, F. Wang, W. Yang, T. Zhang, Z. Xu, X. Feng, and B. Wang, "Oxygen- and proton-transporting open framework ionomer for medium-temperature fuel cells," *Science*, vol. 385, no. 6713, pp. 1115–1120, 2024.

[36] M. H. Bargal, M. A. Abdelkareem, Q. Tao, J. Li, J. Shi, and Y. Wang, "Liquid cooling techniques in proton exchange membrane fuel cell stacks: A detailed survey," *Alexandria Engineering Journal*, vol. 59, no. 2, pp. 635–655, 2020.

[37] M. Cencetti, E. Zeminiani, P. Maggiore, and M. Dalla Vedova, "Mbse modelling environment and multi-objective optimization of thermal control strategies for multifunctional structures," *International Journal of Mechanics and Control*, vol. 15, no. 02, pp. 37–58, 2014.

[38] P. Maggiore, M. Dalla Vedova, L. Pace, M. Tosetti, and A. Piovano, "Development of an environmental control system pack simulation model for a more electric aircraft," *International Journal of Mechanics and Control*, vol. 15, no. 02, pp. 31–35, 2014.

[39] E. Campagnoli and M. Monterossi, "Design of a new test rig facility to study the turbine thermal behaviour," *International Journal of Mechanics and Control*, vol. 19, no. 01, pp. 51–59, 2018.

[40] U. Soupremanien, S. Le Person, M. Favre-Marinet, and Y. Bultel, "Tools for designing the cooling system of a proton exchange membrane fuel cell," *Applied Thermal Engineering*, vol. 40, pp. 161–173, 2012.

[41] A. van Heerden, D. Judt, S. Jafari, C. Lawson, T. Nikolaidis, and D. Bosak, "Aircraft thermal management: Practices, technology, system architectures, future challenges, and opportunities," *Progress in Aerospace Sciences*, 2022.

[42] M. Coutinho, D. Bento, A. Souza, R. Cruz, F. Afonso, F. Lau, A. Suleman, F. R. Barbosa, R. Gandolfi, W. Affonso, F. I. Odaguil, M. F. Westin, R. J. dos Reis, and C. R. da Silva, "A review on the recent developments in thermal management systems for hybrid-electric aircraft," *Applied Thermal Engineering*, 2023.

[43] Srinath, A. Nag, P. López, Álvaro, M. Fashandi, S. Alireza, Lechat, Sylvain, di Legge, Giampiero, Nabavi, S. Ali, Nikolaidis, Theoklis, Jafari, and Soheil, "Thermal management system architecture for hydrogen-powered propulsion technologies: Practices, thematic clusters, system architectures, future challenges, and opportunities," *Energies*, vol. 15, no. 1, 2022.

[44] Y.-G. Lv, G.-P. Zhang, Q.-W. Wang, and W.-X. Chu, "Thermal management technologies used for high heat flux automobiles and aircraft: A review," *Energies*, 2022.

[45] D. Li, J. Hang, Y. Li, and S. Dong, "Fuel flowrate control for aeroengine and fuel thermal management for airborne system of aircraft—an overview," *Applied Sciences (Switzerland)*, 2022.

[46] J. WANG, Y. LI, X. LIU, C. SHEN, H. ZHANG, and K. XIONG, "Recent active thermal management technologies for the development of energy-optimized aerospace vehicles in china," *Chinese Journal of Aeronautics*, 2021.

[47] A. Link, J. Ludowicy, and M. Staggat, "ASSESSMENT OF a SERIAL COOLING CONCEPT FOR HTPEM FUEL CELL SYSTEMS FOR AVIATION APPLICATIONS," in *33rd Congress of the International Council of the Aeronautical Sciences, ICAS 2022*, 2022.

[48] A. van Heerden, D. Judt, C. Lawson, S. Jafari, T. Nikolaidis, and D. Bosak, "Framework for integrated dynamic thermal simulation of future civil transport aircraft," in *AIAA Scitech 2020 Forum*, 2020.

[49] R. H. Jansen, C. Bowman, A. Jankovsky, R. Dyson, and J. Felder, "Overview of NASA electrified aircraft propulsion research for large subsonic transports," in *53rd AIAA/SAE/ASEE Joint Propulsion Conference, 2017*, 2017.

[50] N. Morioka, H. Saito, N. Takahashi, M. Seta, and H. Oyori, "Thermal management system concept with an autonomous air-cooled system," in *SAE Technical Papers*, 2014.

[51] N. Heersema and R. Jansen, "Thermal management system trade study for SUSAN electrofan aircraft," in *AIAA Science and Technology Forum and Exposition, AIAA SciTech Forum 2022*, 2022.

[52] J. Kim, K. Kwon, S. Roy, E. Garcia, and D. Mavris, "Megawatt-class turboelectric distributed propulsion, power, and thermal systems for aircraft," in *AIAA Aerospace Sciences Meeting, 2018*, 2018.

[53] E. Adler, B. Brelje, and J. Martins, "Thermal management system optimization for a parallel hybrid aircraft considering mission fuel burn," *Aerospace*, 2022.

[54] T. Hendricks, C. Tarau, and R. Dyson, "Hybrid electric aircraft thermal management: Now, new visions and future concepts and formulation," in *InterSociety Conference on Thermal and Thermomechanical Phenomena in Electronic Systems, ITHERM*, 2021.

[55] P. Abolmoali, A. Donovan, S. Patnaik, P. McCarthy, D. Dierker, N. Jones, and R. Buettner, "Integrated propulsive and thermal management system design for optimal hybrid electric aircraft performance," in *2020 AIAA/IEEE Electric Aircraft Technologies Symposium, EATS 2020*, 2020.

[56] I. Roumeliotis, L. Castro, S. Jafari, V. Pachidis, L. de Riberolles, O. Broca, and D. Unlu, "Integrated systems simulation for assessing fuel thermal management capabilities for hybrid-electric rotorcraft," in *Proceedings of the ASME Turbo Expo*, 2020.

[57] H. Kellermann, A. Habermann, P. Vratny, and M. Hornung, "Assessment of fuel as alternative heat sink for future aircraft," *Applied Thermal Engineering*, 2020.

[58] S. Wright and J. Dr, "FUEL CELLS AND NOVEL THERMAL MANAGEMENT ADVANCEMENTS REQUIRED FOR AVIATION," in *33rd Congress of the International Council of the Aeronautical Sciences, ICAS 2022*, 2022.

[59] E. Waddington, J. Merret, and P. Ansell, "Impact of LH2 fuel cell-electric propulsion on aircraft configuration and integration," in *AIAA Aviation and Aeronautics Forum and Exposition, AIAA AVIATION Forum 2021*, 2021.

[60] E. Vredenborg and F. Thielecke, "Thermal management investigations for fuel cell systems on-board commercial aircraft," in *SAE Technical Papers*, 2013.

[61] G. Romeo, G. Correa, F. Borello, E. Cestino, M. Asce, and M. Santarelli, "Air cooling of a two-seater fuel cell-powered aircraft: Dynamic modeling and comparison with experimental data," *Journal of Aerospace Engineering*, 2012.

[62] G. Romeo, E. Cestino, F. Borello, and G. Correa, "Engineering method for air-cooling design of two-seat propeller-driven aircraft powered by fuel cells," *Journal of Aerospace Engineering*, 2011.

[63] J. Roland and M. Rumpfkeil, "Wing fuel-tank heat-sink calculation for conceptual aircraft design," *Journal of Aircraft*, 2017.

[64] G. A. L. C Zilio, G. Pernigotto, F. Chiacchio, P. Borrelli, and E. D'Errico, "Cfd analysis of aircraft fuel tanks thermal behaviour," in *Journal of Physics: Conference Series (JPCS)*, 2017.

[65] R. Manna, N. Ravikumar, S. Harrison, and K. Boulama, "Aircraft fuel thermal management system and flight thermal endurance," *Transactions of the Canadian Society for Mechanical Engineering*, 2022.

[66] J. Jasa, C. Mader, and J. Martins, "Trajectory optimization of a supersonic aircraft with a thermal fuel management system," in *2018 Multidisciplinary Analysis and Optimization Conference*, 2018.

[67] D. Doman, "Optimal cruise altitude for aircraft thermal management," *Journal of Guidance, Control, and Dynamics*, 2015.

[68] B. German, "Tank heating model for aircraft fuel thermal systems with recirculation," *Journal of Propulsion and Power*, 2012.

[69] B. German, M. Daskilewicz, and J. Doty, "Using interactive visualizations to assess aircraft thermal management system modeling approaches," in *11th AIAA Aviation Technology, Integration,and Operations (ATIO) Conference, including the AIAA Balloon Systems Conference and 19th AIAA Lighter-Than-Air Technology Conference*, 2011.

[70] Y. Zhang, G. Lin, Y. Tu, and X. Mao, "Conceptual design and dynamic simulation of thermal management for fighter aircraft fuel system," in *AIAA Modeling and Simulation Technologies Conference 2010*, 2010.

[71] F. Issacci, J. L. Farr Jr., A. Wassel, and V. Van Griethuysen, "Integrated thermal management analysis tool," in *Proceedings of the Intersociety Energy Conversion Engineering Conference*, 1996.

[72] S. J. Black, "X-29 FUEL/AUXILIARY OIL SYSTEMS THERMAL MANAGEMENT.," in *Proceedings - Society of Automotive Engineers*, 1986.

[73] Y. Suat, A. Özkan, and E. Sirkeci, "1d modelling of thermal management of a jet trainer aircraft," in *SAE Technical Papers*, 2023.

[74] Y. Liu, G. Lin, J. Guo, and J. Zhu, "Dynamic prediction of fuel temperature in aircraft fuel tanks based on surrogate," *Applied Thermal Engineering*, 2022.

[75] Y. Feng, Y. Liu, Y. Cao, K. Gong, S. Liu, and J. Qin, "Thermal management evaluation for advanced aero-engines using catalytic steam reforming of hydrocarbon fuels," *Energy*, 2020.

[76] S. Qian, C. Nan, and Y. Yu, "Analysis of aircraft integrated thermal management using fuel as heat sink," in *AUS 2016 - 2016 IEEE/CSAA International Conference on Aircraft Utility Systems*, 2016.

[77] L. Peng, S. Dong, and D. Guo, "A dynamic node thermal analysis method of fuel tank based on sinda/fluint software," in *AUS 2016 - 2016 IEEE/CSAA International Conference on Aircraft Utility Systems*, 2016.

[78] D. Doman, "Fuel flow topology and control for extending aircraft thermal endurance," in *Journal of Thermophysics and Heat Transfer*, 2018.

[79] M. Oppenheimer, D. Sigthorsson, and D. Doman, "Extending aircraft thermal endurance by fuel pump sizing," in *AIAA Guidance, Navigation, and Control Conference, 2018*, 2018.

[80] D. Doman, "Fuel flow control for extending aircraft thermal endurance part II: Closed loop control," in *2016 AIAA Guidance, Navigation, and Control Conference*, 2016.

[81] D. Doman, "Fuel flow control for extending aircraft thermal endurance part i: Underlying principles," in *2016 AIAA Guidance, Navigation, and Control Conference*, 2016.

[82] D. Doman, "Rapid mission planning for aircraft thermal management," in *AIAA Guidance, Navigation, and Control Conference, 2013*, 2015.

[83] Y.-H. Ho, T. Lin, B. Hill, and G. Tibbs, "Thermal benefits of advanced integrated fuel system using JP-8+100 fuel," in *World Aviation Congress, 1997*, 1997.

[84] R. Wang, S. Dong, H. Jiang, P. Li, and H. Zhang, "Parameter-matching algorithm and optimization of integrated thermal management system of aircraft," *Aerospace*, 2022.

[85] M. Bodie, "Power thermal management system design for enhanced performance in an aircraft vehicle," in *SAE Technical Papers*, 2010.

[86] N. Seki, N. Morioka, H. Saito, and H. Oyori, "A study of air/fuel integrated thermal management system," in *SAE Technical Papers*, 2015.

[87] M. Glickstein, V. Van Griethuysen, and E. Hodge, "Integration of high heat sink fuels in aircraft thermal management systems," in *American Society of Mechanical Engineers, International Gas Turbine Institute, Turbo Expo (Publication) IGTI*, 2003.

[88] R. Trebosc, "SST concorde air conditioning system," in *SAE Technical Papers*, 1967.

[89] M. Oppenheimer, D. Sigthorsson, and D. Doman, "Control of fuel thermal management systems with transport delays," in *AIAA Scitech 2019 Forum*, 2019.

[90] J. Letlow and L. Jenkins, "Development of an integrated environmental control system," in *SAE Technical Papers*, 1998.

[91] W. Harrison III, K. Binns, S. Anderson, and R. Morris, "High heat sink fuels for improved aircraft thermal management," in *SAE Technical Papers*, 1993.

[92] R. Hitzigrath, "Improving aircraft fuel-thermal management," in *SAE Technical Papers*, 1993.

[93] S. Iya, "Thermal management of advanced aircraft secondary power systems," in *SAE Technical Papers*, 1990.

[94] W. A. Hudson and M. L. Levin, "INTEGRATED AIRCRAFT FUEL THERMAL MANAGEMENT.," in *Proceedings - Society of Automotive Engineers*, 1986.

[95] G. Huang, D. Doman, M. Rothenberger, B. Hencey, M. DeSimio, A. Tipton, and D. Sigthorsson, "Dimensional analysis, modeling, and experimental validation of an aircraft fuel thermal management system," *Journal of Thermophysics and Heat Transfer*, 2019.

[96] D. Sigthorsson, M. Oppenheimer, and D. Doman, "N-tank thermal management system framework for thermal endurance enhancement," in *AIAA Science and Technology Forum and Exposition, AIAA SciTech Forum 2022*, 2022.

[97] C. Lui, C. Lee, and E. Schwan, "Integrated environmental control system and liquid cooling system for f/a-18 e/f aircraft," in *SAE Technical Papers*, 1995.

[98] E. P. Petkus and R. W. Gallington, "HALE thermal balance," in *AIAA/ASME/SAE/ASEE 23rd Joint Propulsion Conference, 1987*, 1987.

[99] X. Peng, H. Wang, L. Huang, G. Liu, C. Wang, and S. Feng, "Performance of an oxygen-consuming inerting system for an aircraft fuel tank with rp-3 aviation fuel in flight," *Aerospace Science and Technology*, vol. 123, p. 107446, 2022.

[100] D. Li, S. Dong, J. Wang, and Y. Li, "Modeling and simulation of system-level temperature for airliner hydraulic system in a full flight mission profile," in *IET Conf Publ*, vol. 2018, pp. 338–343, Institution of Engineering and Technology, 2018.

[101] "Atr 72-600 tecnical data sheet." https://www.atr-aircraft.com/wp-content/uploads/2020/07/Factsheets_-_ATR_72-600.pdf.

[102] "Dash 8-400 tecnical data sheet." https://dehavillandfield.com/wp-content/uploads/2022/08/Dash8_Spec_Sheet_web.pdf.

[103] "Fokker 50 tecnical data sheet." https://www.fokkerservicesgroup.com/media/3vcjom4m/fsg_fokker-50.pdf.

[104] "Do 228 tecnical data sheet." https://www.ga-ats.com/fileadmin/GAE_General/Downloads/Do228_NXT_Datasheet.pdf.

[105] F. Vitolo, A. Rega, C. Di Marino, A. Pasquariello, A. Zanella, and S. Patalano, "Mobile robots and cobots integration: A preliminary design of a mechatronic interface by using mbse approach," *Applied Sciences (Switzerland)*, vol. 12, no. 1, 2022.

[106] F. Mhenni, J.-Y. Choley, O. Penas, R. Plateaux, and M. Hammadi, "A sysml-based methodology for mechatronic systems architectural design," *Advanced Engineering Informatics*, vol. 28, no. 3, pp. 218–231, 2014. Multiview Modeling for Mechatronic Design.

[107] L. Pace, M. Dalla Vedova, and P. Maggiore, "Model-based definition of requirements to support system verification," *International Journal of Mechanics and Control*, vol. 18, no. 02, pp. 135–141, 2017.

[108] European Union Aviation Safety Agency (EASA), "Certification specifications for large aeroplanes (cs-25)," January 2024. Part of the EASA certification process for large aircraft.

APPENDIX

A Complete representation of the F-TMS requirements diagram is provided in the following, Fig. 15.

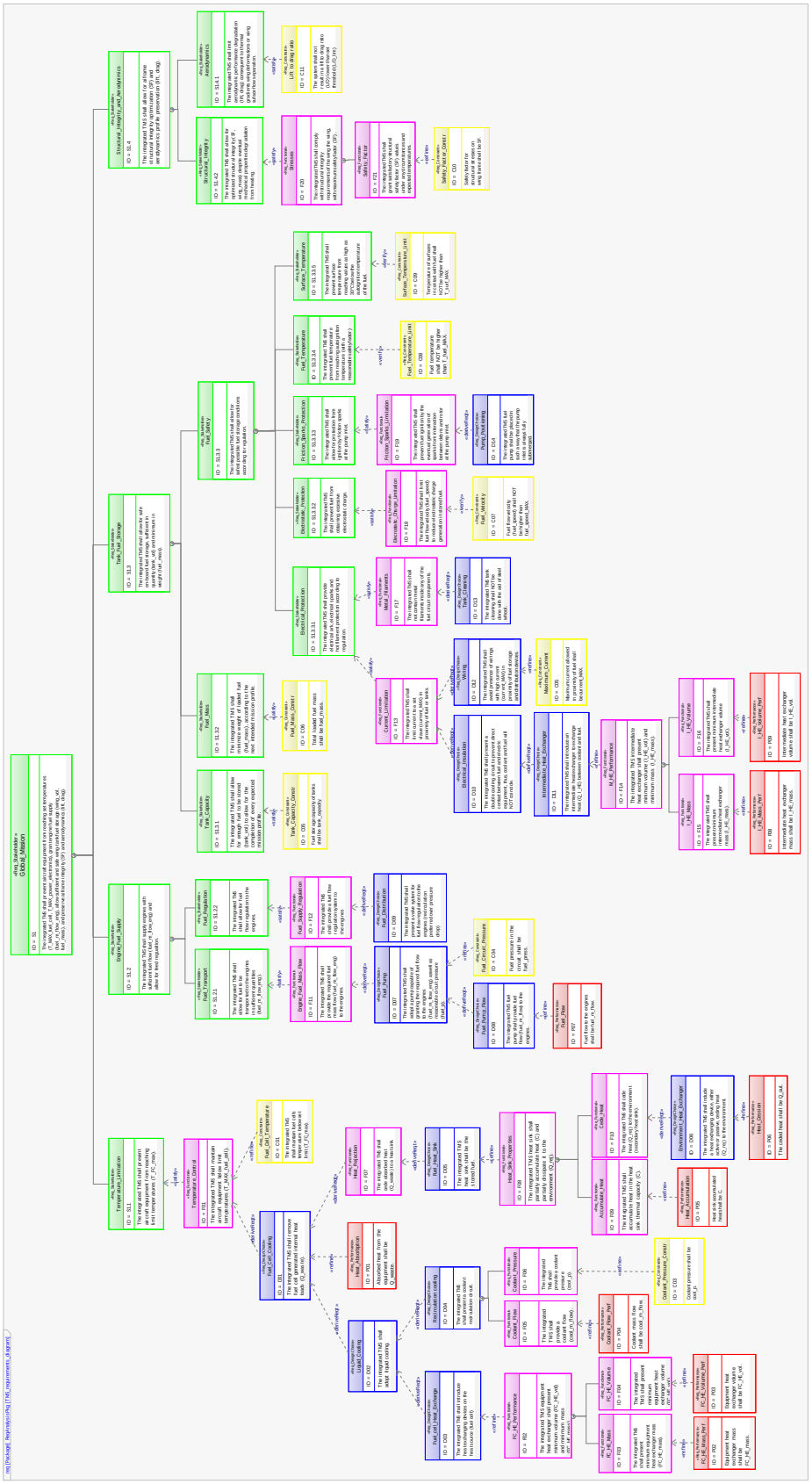


Figure 15 Complete requirement diagram of a F-TMS for fuel cell cooling on hybrid-electric regional transport aircraft.

ISSN 1590-8844
International Journal of Mechanics and Control, Vol. 26, No. 01, 2025
https://doi.org/10.69076/jomac.2025.0015

IS LIGHTING BASED ON PHOTOPIC REQUIREMENTS IN ASSEMBLY WORKSTATIONS ALSO OPTIMAL FOR NON-VISUAL PERFORMANCE IN A HUMAN-CENTRIC PERSPECTIVE? A CASE STUDY IN THE AUTOMOTIVE SECTOR

Antonio Carlin* Valerio Roberto Maria Lo Verso**

* Department of Management and Production Engineering, Politecnico di Torino, Torino, RESLOG, Italy

** Department of Energy 'Galileo Ferraris', Politecnico di Torino, TEBE Research Group, Torino, Italy

ABSTRACT

The article explores how assembly stations in the automotive components industry are structured using Lean Production principles to minimize setup times, reduce travel distances, and ensure ergonomic arrangements of tools and materials. With the integration of Industry 4.0 technologies, companies are increasingly digitizing production processes through systematic data collection, enhancing efficiency. A key factor in optimizing workstations is proper lighting, which is also central to the emerging Industry 5.0 paradigm that prioritizes human well-being alongside productivity. The study focuses on experimental lighting analyses conducted at a plant near Turin, Italy, operated by a multinational automotive company. Researchers examined both the visual and non-visual effects of light within U- and L-shaped work cells, taking measurements at the work surfaces and eye level of the operators. To compare objective findings with subjective experience, questionnaires were administered to the workers. Results showed that the lighting met regulatory standards and provided good support for circadian rhythms. However, some employees expressed concerns about glare and wanted more control over the luminous flux and positioning of the lighting systems. The findings suggest that enhancing lighting flexibility can improve visual ergonomics and support the transition toward more adaptive and worker-centred smart workstations aligned with Industry 5.0 principles.

Keywords: Industry 4.0, Industry 5.0, Workstation 4.0, integrative lighting, Lean production

1 INTRODUCTION

Car manufacturers use specialized component suppliers to produce their cars. They can produce not only individual components, but increasingly complete modules to be assembled directly on assembly lines. Therefore, automotive component suppliers adopt Just-in-Time (JIT) and Just-in-Sequence (JIS) principles in their factories, thanks to the Lean approach developed by Toyota Motor Company to synchronize the production with the strict schedules of car manufacturers.

Contact author: Antonio Carlin[1], Valerio R.M. Lo Verso[2]

[1]Politecnico di Torino, Torino, RESLOG, Italy
[2]Politecnico di Torino, TEBE Research Group, Torino, Italy
E-mail: antonio.carlin@polito.it, valerio.loverso@polito.it

The need to apply JIT and JIS has provided a strong impetus for the organization of work according to the model of lean cell production, which, thanks to their configuration and compliance with the principles of workplace ergonomics [1], allow productions to be quickly modified and adapted to customer requirements. Since 2012, with the new factory concept developed by the European Union with the introduction of Industry 4.0, cell-based production has been able to further benefit from the digitization and interconnection of production processes, improving control over the complexities of supply chains [2] and reducing the uncertainty of lead times for car manufacturers. In fact, Industry 4.0 integrates machines and devices with sensors and related software to better predict, control, and plan business [3]; besides, it acts as an enabler of lean manufacturing [4-5], thus activating increased product quality and efficiency of production processes [6].

In this regard, Cohen et al. [7] proposed a system named Workstation-Operator Interaction 4.0 (WOI 4.0) to enhance the human-machine interaction to improve operator performance, safety, wellbeing, and satisfaction, along with the production measure. In general, the manufacturing sector faces considerable challenges in a dynamic and competitive environment, and process improvement is a crucial tool to enhance competitiveness in the market and maintain long-term sustainability [8].

1.1 FROM INDUSTRY 4.0 TO INDUSTRY 5.0: A HUMAN-CENTRIC APPROACH FOR THE WELL-BEING OF WORKERS

The Industry 4.0 model emphasized the transformation of factories into intelligent structures (smart factories'). This was possible thanks to the introduction of IoT (Internet of Things) and interconnection through cloud servers, developing new business models strongly focused on efficiency and productivity. However, Bortolini et al. [9] stress that humans are one of the most adaptable elements in assembly and manufacturing systems. These must be designed to support and guide workers, rather than replacing them, by incorporating new technologies, improving their skills, and addressing any limitations they may have [10-12]. Similarly, the literature review carried out by Valette et al. [13] revealed the "great interest in human-centricity in today's industrial research". Technology is meant to be a resource to increase production efficiency, without replacing human workers, but supporting their overall wellbeing [14-15]. A 'human-centred approach' is the key factor to pursue, rather than a 'technology centre' approach: Grabowska et al. [16] evolved the concept 'Cyber-Physical Systems (CPS)' into a new 'Human Cyber-Physical Systems (H CPS)'. However, Reiman et al. [17] highlight the immaturity of Industry 4.0 from the perspective of human factors and ergonomics, as the "new technologies may also have unexpected effects in processes and cause problems to the workers". Therefore, it is essential to define and introduce clear criteria for human-centred design, increasingly relying on the integration of digital work tools [18]. In this new scenario, dominated by strong digitization and automation, the need to introduce an improvement in the cooperation between humans and machines in factories led to the creation of yet another new business model that goes by the name of "Industry 5.0" [19-20]. With this new business model, it is finally possible to speak of a "Collaborative Industry," with the ultimate goal of providing added value to production through the creation of customized products that meet consumers' needs. Therefore, since cooperation and customization are the key factors for the transition from today's Industry 4.0 toward the factory model of the future 5.0, the role of humans becomes an indispensable and determining element in production processes, in the creation of Quality in products, and in their customization [21]. Equally essential, according to recent indications from the European Community, the well-being of workers must be placed at the centre of production processes [22-23]. It was considered important to analyse the workstations of the VALEO plant in Santena (Turin) as their switches, multifunction steering wheels, touchscreen displays, and switch units are assembled for the main manufacturers of luxury cars and supercars. Assembly activities require highly professional staff with enhanced manual skills, since they carry out assembly that cannot be delegated to robots. Therefore, they represent an interesting example of a work activity in which the human factor becomes fundamental due to the high customizations introduced, also in line with the framework proposed by Industry 5.0 [24]. In addition to the electronic version a hardcopy of the complete paper including diagrams with annotations must be supplied.

1.2 TYPICAL WORKSTATION LAYOUTS IN ASSEMBLY ACTIVITIES

Within the industry involved in assembling products for the automotive sector, production by work cells is widespread. The use of this type of layout is one of the most important aspects of Lean Production. Usually, the cell layout is organized around the assembly of one product or the assembly of similar products. With this type of production layout, it is possible to increase flexibility and productivity by reducing lead time, raising Product Quality, contain equipment, and reduce the stock of semi-finished products. Depending on the configuration, workstations may feature seated or standing operators. In cell production, the most frequently used configurations are 'U'-shaped, but 'L'-shaped or 'I'-shaped layouts are also used (Figure 1). The former allows the feeding points of the components to assembly to be brought closer to the output points of the finished products, while the latter allows the use of surface area to be reduced by arranging two separate, specular cells. The workstations 4.0 analysed in this work are equipped with mechanical equipment designed ad hoc by the Valeo Group R&D team and can be replaced in about 10 minutes. The workstations 4.0 are completed by some monitors that help the operators in correctly carrying out the assembly with photographs, examples and work instructions. The assembly lines that are made up of these workstations are also configured, according to the principles of lean production, to allow operation by one or more operators at the same time, to guarantee maximum flexibility.

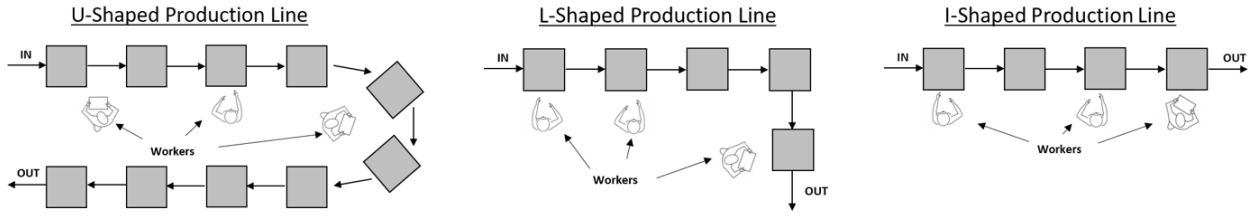


Figure 1 Typical configurations of cells.

1.3 POTENTIAL OF LIGHTING FOR THE WELL-BEING OF WORKERS IN INDUSTRIAL BUILDINGS

The International Ergonomics Association approved a definition of Visual Ergonomics, as "*the multidisciplinary science concerned with understanding human visual processes and the interactions between humans and other elements of a system. Visual ergonomics applies theories, knowledge and methods to the design and assessment of systems, optimizing human well-being and overall system performance. Relevant topics include, among others: the visual environment, such as lighting; visually demanding work and other tasks; visual function and performance; visual comfort and safety; optical corrections and other assistive tools*" [25]. In a letter to the Editor of Applied Ergonomics, Toomingas [26] reports that visual conditions can be problematic, leading to decreased performance and negative emotional reactions. This can decrease wellbeing and cause health problems, not only in the visual system, but also in other parts of the body such as neck and shoulders. On the other hand, well-adapted visual conditions can enhance system performance, health and wellbeing, and positive emotions. Models, knowledge, and methods of visual ergonomics are therefore necessary to understand how humans and elements of a system interact with each other and how systems should be designed to be optimal [27]. In recent literature, visual ergonomics encompasses the integration of the so-called visual and non-visual effects of light: the former are related to the aspects concerned with vision (performance, comfort, wellbeing etc.), the latter to aspects determining the non-forming vision effects that impact on circadian entrainment and thus on mood, alertness, sleepiness, cognitive processes, etc. According to the Industry 5.0 vision outlined by the European Commission [22-23], it is crucial to put humans back at the centre of production activities and use modern technologies to facilitate them in carrying out their tasks, such as, for example, collaborative robots (cobots). In this frame, several ergonomic devices have already been adopted to accommodate the needs of operators including, for example, by electrically adjusting the height of workbenches or tilt worktops, along with solutions for ergonomic positioning of components to be assembled. Which raises some questions: since light plays a key role in assembly activities, why, to date, isn't the same importance also attributed to lighting systems? Besides, when choosing workbench lighting, are the light sources selected also considering melanopic effects on users? Are lighting systems conceived to optimize the vertical illuminance (both photopic and melanopic) at eye-level? Visual and non-visual effects of light are addressed in more detail in the following subsections.

1.3.1 Visual effects of light

Among interventions aimed at increasing the visual ergonomics, Hemphälä and Eklund [28] evaluated the visual environment in mail sorting facilities through a before-after design (modifying the embedded lighting systems of the sorting racks) through field illuminance measurements and questionnaires. Twenty-seven participants reported that work conditions improved after the intervention, with reduced visual strain and mail sorting time. better general mood, less work induced stress. Gugliermetti et al. [29] explored sustainable lighting strategies in industrial settings by integrating natural and artificial light sources to optimize energy efficiency while maintaining visual comfort through hybrid lighting solutions tailored for industrial applications. Leccese et al. [30] analysed the lighting of some workstations used for diagnostic radiology by comparing adjustable and non-adjustable lighting settings through field measurements and questionnaire to 16 radiologists. The LED adjustable lighting resulted in reduced visual fatigue reported by the participants. Aarts et al. [31] studied the effect of lighting on errors performed by the nursing staff of different age in reading medication labels under nine lighting conditions, including three illuminances (100 lx, 500 lx, and 1000 lx) and three correlated color temperatures CCT (3000 K, 4000 K, and 6500 K). They observed a higher number of errors for older participants, with the highest impact of light conditions for the smallest font size (2.5 pt) and insufficient visual acuity of the participants. Dianat et al. [32] explored the association between objective and subjective assessments of environmental ergonomic factors including noise, lighting, and heat, through a field study in three manufacturing plants, collecting data from 130 workstations. They found that recommended noise, illuminance, and temperature levels were not met in about half of the workstations surveyed, which was consistent with the low satisfaction expressed by the operators. Similarly, Hsieh et al. [33] assessed how different lighting environments can affect people's concentration and working performance, comparing two lighting setups (task lighting and general lighting) and two attention task times (15 and 30 min, respectively). The concentration level of 60 participants was evaluated by measuring electroencephalogram (EEG) signal and cortisol secretion. Their findings indicated that concentration is influenced by the lighting conditions, with improved task performance in an environment with focused lighting for a 15-minute task duration, accompanied by activated cortisol secretion. In a different study, Juslen et al. [34] analysed the effect of illuminance on speed and percentage of errors of workers in assembling electronic devices in a factory in Holland, by comparing two horizontal illuminances at the workplace, 1200 lx or 800 lx (with a corresponding vertical illuminance of 600 lx or 400 lx, respectively). They observed a higher speed of production (+2.9% in summer and +3.1% in winter) for the 1200-lx setting. Instead, no significant effect of the illuminance on the percentage of errors was detected. In industrial spaces, Juslan and Tenner [35] showed that improving lighting conditions at work surfaces resulted in increasing visual performance, comfort, and ambience, interpersonal relationships, biological clock, stimulation, job satisfaction and problem solving. Another crucial aspect is the possibility for users to have personal controls. Studies carried out in office spaces have shown that when users can adjust the illuminance level on their desks, this has a positive effect on their satisfaction with the environmental conditions, lighting quantity and quality,

mood, improved motivation and vigilance, with an indirect positive effect on their productivity [36-37]. Moreover, Despenic et al. [38] observed through two field studies that individuals chose different illuminance levels for the same task and provided a method for modelling their lighting preference profiles based on characteristics as activeness, dominance, lighting tolerance, and dimming level preference.

1.3.2 Non-visual effects of light

Visual ergonomics impacts on human factors through the interaction between the ambient lighting and the occupants of an indoor space. A body of literature research has demonstrated how lighting can affect the physiological, biological, and cognitive psychological aspects of humans, such as alertness, mood, working performance, hormone secretion, sleep, and circadian rhythms [39-54]. These impacts are significantly influenced by factors such as light spectral power distribution, intensity, duration, and individual circadian phases. The CIE S 026/E:2018 [55] introduced spectral sensitivity functions and metrics to assess how light affects the five photoreceptor types in the human retina that drive non-visual responses. Two metrics were introduced to quantitatively assess the non-visual effects of light: (i) the melanopic Equivalent Daylight Illuminance (mel-EDI), in [lx] to quantify the magnitude of the effects; and (ii) the melanopic Daylight Efficacy Ratio (mel-DER), which represents the melanopic content (mel-EDI) of each lx of photopic illuminance. In the second independent expert symposium organized by the CIE in Manchester in 2019 [56-57], guidelines were proposed under the motto "proper light at proper time," recommending mel-EDI $\geq$ 250 lx during the day, reducing to less than 10 lx three hours before bed, and less than 1 lx at night. Similar thresholds are proposed in the WELL Building Standard [58], developed by the International WELL Building Institute, which addresses both visual and circadian systems to promote health-focused lighting in buildings. The standard operates on a point-based system, making it a useful framework for integrative lighting analysis but is not tailored specifically for industrial buildings. It is worth stressing that while mel-EDI offers insights into non-visual light effects, no formal international standards exist.

Recently, several manufactures have developed the so-called tunable white LED luminaires, able to mimic daylight (the reference circadian light, particularly the skylight with a CCT of 6500K). In this regard, Cajochen et al. [59] tested a tunable LED lighting system on visual comfort, circadian physiology, daytime alertness, mood, cognitive performance, and sleep, by exposing 49 participants to a comparative test with a conventional LED light in laboratory conditions. The participants reported better visual comfort, felt more alert and happier in the morning and evening under daylight LED than conventional LED, while the diurnal melatonin profile, vigilance and working memory performance were not significantly different. In industrial buildings, particular attention has been paid to night-shift workers, who are exposed to peculiar ambient work conditions that may result in reduced cognitive performance, sleepiness, and higher possibility for human error and related incidents, due to the disruption of their circadian rhythms [60-62].

Some studies investigated whether blue-enriched white light was a practical strategy to decrease sleepiness and improve cognitive performance during night shifts. Motamedzadeh et al. [63] conducted a study through a before-after interventional design by surveying 30 control room staff members of a petrochemical industry. Every participant was exposed to two new lighting conditions (17000 K and 6500 K blue enriched white light), each lasting for a week. Through Karolinska Sleepiness Scale (KSS) and melatonin assessment using salivary and Eliza technique, their results showed that participants' sleepiness and melatonin rhythm significantly declined when they were exposed to blue-enriched white light, with positive effects on reducing memory or omission errors, and on increasing the reaction time during the attention task. Similar results were also obtained by Sletten et al. [64], while Riz à Porta et al. [65]) analysed four million behavioural responses from 1437 security officers at an international airport, comparing night shift and morning shift workers, finding no performance differences between the two shifts.

1.3.3 Integrative lighting (human-centric lighting): integration of visual and non-visual effects of light

The concept of "integrative lighting" was introduced by the International Commission on Illumination [55] to promote the balanced use of light to support both visual (photopic) and non-visual (melanopic) effects in building design. This approach, also known as "human-centric lighting" [66], combines electric and natural light to create health-supportive environments. Metrics like melanopic Equivalent Daylight Illuminance (mel-EDI) help quantify light's impact on the non-visual system. While integrative lighting has been widely investigated in offices [67-75], and classrooms [76-80], it has received less attention in industrial buildings. One of the few examples is the study by Van de Putte et al. [81]: they demonstrated that integrative lighting improved sleep and alertness in shift workers compared to standard lighting. Despite growing awareness of its benefits, current design standards still focus mainly on visual and energy efficiency requirements, often neglecting non-visual effects. There is a clear need for further guidelines to address both photopic and melanopic aspects, particularly in industrial settings where performance, attention, and safety are critical.

1.4 RESEARCH GOALS

According to the Industry 5.0 vision outlined by the European Commission [22-23], it is important to put humans back at the centre of production activities and use modern technologies to facilitate them in carrying out their activities, such as, for example, collaborative robots (cobots). In this frame, several ergonomic devices have already been adopted in recent times to accommodate the needs of operators including, for example, by electrically adjusting the height of workbenches or tilt worktops, along with solutions for ergonomic positioning of work equipment and components to be assembled. The question then arises: since light plays a fundamental role during assembly activities, why, to date, isn't the same importance also attributed to lighting systems? Besides, when choosing workbench lighting, aren't the light sources selected considering both photopic and melanopic effects on users?

The authors of the present paper already explored in the past the topic of 'factory of the future', assessing the enhancement of wellbeing of the workers by optimizing daylight amount in management offices, production/services area, and warehouse [82-83]. In this frame, the current paper presents results from a study on integrative lighting conditions in the manufacturing area of an actual factory located in the suburbs of Turin, in northern Italy (latitude: 45°N). Both electric lighting and daylighting conditions were taken into consideration, particularly focusing on lighting conditions that are produced at a sample of representative workstations, both U-shaped and L-shaped. The study therefore aims at bridging a research gap, which is the verification of the extent to which human-centric lighting (integrative lighting) conditions are achieved in real settings of industrial buildings, designed to meet photopic requirements. Such a gap is analysed in a real case-study, which is an industry in the automotive sector. In more detail, the research was conducted with the following objectives:

a) to analyse the photopic illuminance on workstations (benches and monitors) and the circadian illuminance (mel-EDI) at the eyes of the operators working at the workstations (on benches and while reading monitors) and verify if this could meet the recommendations reported in the CIE documents or in the WELL protocol
b) to investigate how the lighting conditions were perceived by the workers.

2 CASE STUDY: INDUSTRY OF ASSEMBLING INTERIOR COMPONENTS FOR LUXURY CARS NEAR TURIN (ITALY)

The study was carried out at an industrial plant, which hosts 27 assembly lines, focusing on six lines selected as the most significant from the point of view of lighting comfort analysis.

The main activity consists of assembling interior components for luxury cars ranging from infotainment controls, centre tunnels with automatic transmission, touchscreen displays, and multi-function steering wheels.
There are three shifts as follows: (i) first shift: 06:00 - 14:00; (ii) second shift: 14:00 - 22:00; and (iii) middle shift: 08:00 -16:45.
The production department staff consists of about 30 operators, ten of which employed in component receiving and storage, assembly line feeding, and finished product handling management.

2.1 CHARACTERISTICS OF THE BUILDING AND OF THE LEAN PRODUCTION LINE

The building where assembly is carried out has a rectangular area of about 1400 m^2 with a shed roof facing north-east (Figure 2). Therefore, the rectangular manufacturing area has a glazed full-height façade facing South-West SE and receives daylight mainly through the rooflighting systems (shed). The building, although inaugurated in 1974, has numerous features aimed at the well-being of the operators, with particular attention to the natural lighting of the working environment.
Furthermore, its shed roof configuration offers the possibility of integrating smart green technologies, including solar thermal collectors and photovoltaic panels, that can further contribute to the internal comfort of the operators while saving energy [84-86].
Each production line was designed according to the principles of lean production to make it possible to alternate the assembly of quantities of products belonging to the same type, but different in shape as they belong to cars of different brands. This is possible because each line is designed in a simple way, adopting layouts where it is very easy to quickly change the equipment.



Figure 2 Image of the industrial building used in the study.

In addition, for each assembly line, the work surfaces and positions of components and equipment are placed based on ergonomics principles so as not to fatigue operators and allowing assemblies with a high-quality standard throughout the work shift. Six production lines were selected across the manufacturing area, whose configurations and types of products assembled are reported in Table I.

Table I - configurations and types of products assembled in the production lines analysed in the study

Production Line	Layout configuration	Types of products
I016	L-Shaped	Instrument panel for climate, speed, lights and infotainment services control
I024	L-Shaped	Touch-screen display
I028	U-Shaped	Automatic transmission selector
I034	L-Shaped	Buttons for automatic seat memorization
I037	L-Shaped	Multi-function steering wheels, paddle-shift, etc.
I041	L-Shaped	Central tunnels with automatic transmission controls

2.2 LIGHTING CHARACTERISTICS OF WORKSTATIONS

The lighting concept of the manufacturing area relies on the combination of two systems: an arrays of pendant downlight LED lighting systems (suspended at a height of 6.74 m above the finished floor) provides general lighting to the area, especially for circulation spaces, whilst the most important contribution for the assembly tasks is provided by LED systems embedded in the structures of the cells, mounted at a height of 1.90 m above the finished floor. These are downlight systems with a diffuser to guarantee the minimum illuminance levels on the assembly benches without any glare for the workers. Figure 3 shows an example of one of the production lines that were investigated.

3 METHOD

The study relied on a combination of approaches: (i) experimental field measurements, to quantify the lighting levels at workstations where users perform their task, with respect to both visual (photopic illuminances and quantities) and non-visual effects (melanopic illuminances) of light; (ii) a short questionnaire to collect the individual perceptions of the lighting conditions as expressed by the users working at the workstations considered.



Figure 3 Image of the production line I016 (L-shaped).

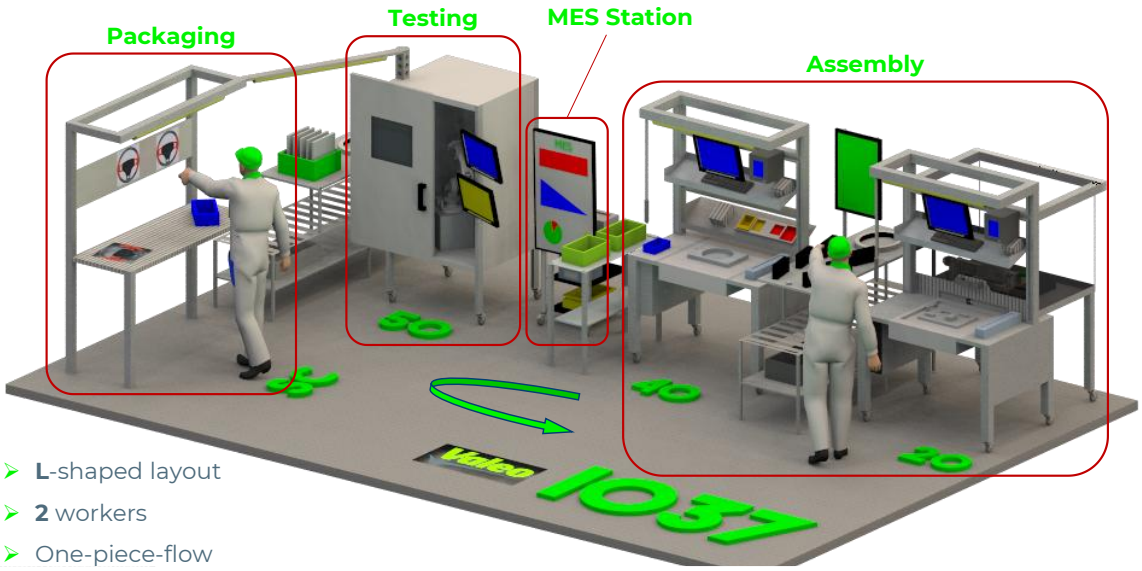


Figure 4 Schematic visualizations of two L-shaped cells, where benches, monitors and embedded lighting systems are highlighted, as well as the various tasks carried out by the workers. NOTE: MES = Manufacturing Execution System.

3.1. MEASUREMENTS

In an integrative lighting perspective, both photopic and melanopic quantities were measured. Photopic quantities were: illuminance (E), Colour Rendering Index (CRI), and Correlated Colour Temperature (CCT). The melanopic equivalent daylight illuminance (mel-EDI) was the melanopic quantity measured. All the quantities were acquired by using a spectrophotometer Gigahertz BTS256-EF (measurement range: 360–830 nm; measurement sensitivity: 10 nm; error: ±2.2%). Measurements were taken on two types of surfaces:

- *task areas*, namely: (i) benches, where workers perform tasks such as mounting, assembling, and controlling the quality of object of various size; on each bench, four measurements were taken, according to a square grid of 25 cm of size, and then assuming the average value; and (ii) monitors used by workers to read/input information on a screen: in this case, one measure was taken, positioning the instrument on the vertical (or tilted) surface of the screen. Differently, three measures were taken for the totems (e-WS), to account for the different quantity of light received due to their extension in size
- *eye-level*, positioning the instrument at a height of 1.6 m above the floor, pointing at benches and monitors, to reproduce the actual view directions of workers while performing their task.

Figure 4 shows the surfaces where measures were taken for two workstations (I-024 and I-037, L-based cells).

3.1.1. Requirements for photopic quantities

Regarding photopic quantities, the European Standard EN-12464-1:2021 [87] was taken as reference. The main parameters specified by the standard for various task activities are: (i) maintained average illuminance Em and illuminance uniformity U0; (ii) limiting unified glare rating RUGL; and (iii) colour rendering index CRI (or Ra), namely:

- rough assembly (e.g., large transformers):
  $E_m \geq 300$ lx, $U_0 \geq 0.60$ modified $E_m \geq 500$ lx
  $R_{UGL} \leq 25$ CRI = $R_a \geq 80$
- medium assembly (e.g., switchboards):
  $E_m \geq 500$ lx, $U_0 \geq 0.60$ modified $E_m \geq 750$ lx
  $R_{UGL} \leq 22$ CRI = $R_a \geq 80$
- fine assembly (e.g., IT equipment, computers):
  $E_m \geq 750$ lx, $U_0 \geq 0.70$ modified $E_m \geq 1000$ lx
  $R_{UGL} \leq 19$ CRI = $R_a \geq 80$
- precision assembly (e.g., printed circuit boards):
  $E_m \geq 1000$ lx, $U_0 \geq 0.70$ modified $E_m \geq 1500$ lx
  $R_{UGL} \leq 16$ CRI = $R_a \geq 80$

The ‘modified’ minimum illuminance is a 1-step increase in the minimum E_m that can be applied under any of the following conditions: critical visual work; errors costly to rectify; great importance attributed to accuracy, higher productivity or increased concentration; unusually small size or low contrast of task details; unusually long-time task; low daylight provision; visual capacity of workers below normal.

3.1.2. Recommendations for melanopic quantities

Concerning the melanopic daylight illuminance (m-EDI), it was decided to refer to the two documents currently present in the literature: (i) the earlier mentioned documents from the CIE, which sets to maintain at least 250 lx of mel-EDI during daytime; (ii) the recommendations expressed in the WELL Building Standard, version 2. Both approaches converge on a minimum value of mel-EDI of 250 lx. The WELL protocol offers two options, granting different points for different targets achieved:

- mel-EDI ≥ 250 lx (consistently with the CIE recommendation) to receive 3 points
- mel-EDI ≥ 136 lx to receive 1 point.

3.2. QUESTIONNAIRE

A short questionnaire was specifically designed to investigate how the workers perceived the lighting conditions available at the various benches and monitors where they perform their tasks. The questionnaire was distributed among 11 workers and consisted of three sections (plus one section to collect free comments). Section A, on lighting conditions generally perceived at the workstation as a whole; the section contained two types of questions:

- Q1: «*overall, how do you rate the quantity of light at this workstation*?». The users could express their judgment using a 5-point scale, where: 1 = too low; 2 = low; 3 = adequate; 4= high; 5 = too high
- Q2 to Q5: the users could express their agreement on different statement, using a 4-point scale, where: 1 = totally disagree; 2 = partially disagree; 3= partially agree; 4 = totally agree; the questions were:
- Q2: «*overall, the lighting quantity at my workstation is adequate*»
- Q3: «*overall, lighting conditions at my workstation create a stimulating environment*»
- Q4: «*overall, lighting conditions at my workstation favour my concentration*»
- Q5: «*overall, lighting conditions at my workstation create a comfortable environment*».

Section B, on lighting conditions perceived regarding specific benches and monitors used to carry out the work activity (mounting, assembly, control, using a monitor – reading or inputting information on screen).

Like in Section A, the users were asked to express their agreement using a 4-point scale, where: 1 = totally disagree; 2 = partially disagree; 3= partially agree; 4 = totally agree; the following questions were asked:

- Q6: «*in this moment, lighting conditions facilitate carrying out my task*»
- Q7: «*in this moment, I perceive glare while I'm carrying out my task*».

Above questions were repeated for all the benches and monitors positioned at the workstation.

Section C, to collect information on the workers, such as gender, age, height, and the duration time of the shift («For how many hours through your shift have you worked today»?).

Comments: the participants were asked to highlight criticalities concerned with the lighting conditions that may not have been covered by the questionnaire items, as well as to express their desires for an improved and more 'visually ergonomic' workstation.

The full questionnaire is reported in Appendix A.

4 RESULTS

The following images (Figures 5-12) report the experimental results that were collected at the various workstations analysed in the study. Both the measurements and the subjective judgments expressed by the workers are shown.

It should be noted that the M/E is an alternative, more concise, symbol for the melanopic daylight efficacy ratio mel-DER. In all these figures, the symbols visualized have the following meanings:

E photopic illuminance [lx]
M mel-EDI = melanopic daylight equivalent illuminance [lx]
M/E mel-DER = melanopic daylight efficacy ratio [-]
R_a CRI = colour rendering index [-]
CCT correlated colour temperature [K].

4.1. SYNTHETIC RESULTS: VISUAL EFFECTS OF LIGHT ON BENCHES

Figure 13 reports the average illuminance levels measured at the various workplanes. The values measured at monitors are not reported as these are self-illuminated. Illuminance was found to be above 500 lx (corresponding to medium assembly activities) on all the benches analysed; this was an expected result, as the lighting systems embedded in the cells is specifically sized to meet with this standard requirement; it can also be noted, though, that the measured illuminances are also above the 750-lx threshold (corresponding to fine assembly activities) at all workstations, excluding two cases (I028_evening and I034, in both cases on bench C, where complex tasks are carried out, such as assembling steering wheels). Moreover, all workstations also meet the minimum 1000-lx requirement, apart from two other cases (benches A and F in workstation I037 at evening, i.e. in electric lighting only), which can be associated with precision assembly activities, but also as 'modified' increased illuminances for rough and fine assembly.

4.2. SYNTHETIC RESULTS: VISUAL AND NON-VISUAL EFFECTS OF LIGHT AT EYE-LEVEL

The quantities measured at eye-level are reported in Figures 14-15: mel-EDI and mel-DER (Figure 14), and correlated colour temperature CCT (Figure 15).

The following main considerations can be drawn:

- non-visual effects of light: eye-level mel-EDI showed a wide range of values, from 53 lx to 1525 lx, with an average value of 601 lx and a standard deviation SD = 394.3 lx; referring to the target values set by CIE and in the WELL protocol, it is worth noting that 71.9% of the view directions towards benches or monitors showed values mel-EDI ≥ 250 lx (3-point WELL criterion) , with 86.0% of values mel-EDI ≥ 136 lx (1-point WELL criterion); for the same view directions, mel-DER was found to be in the range 0.58-0.89, with an average value of 0.67 (SD = 0.07)
- CCT values were in the range 3902-5600 K, with an average value of 4469 K (SD = 394.6 K); overall, the colour temperature resulting from the various spectral power distributions (electric light, daylight when present, light reflected off the workstations surfaces for the various view directions considered) is mainly in the neutral range (3300 K ≤ CCT ≤ 5300 K); the higher values above 5300 K are those of the cold light emitted by the e-WS monitors.

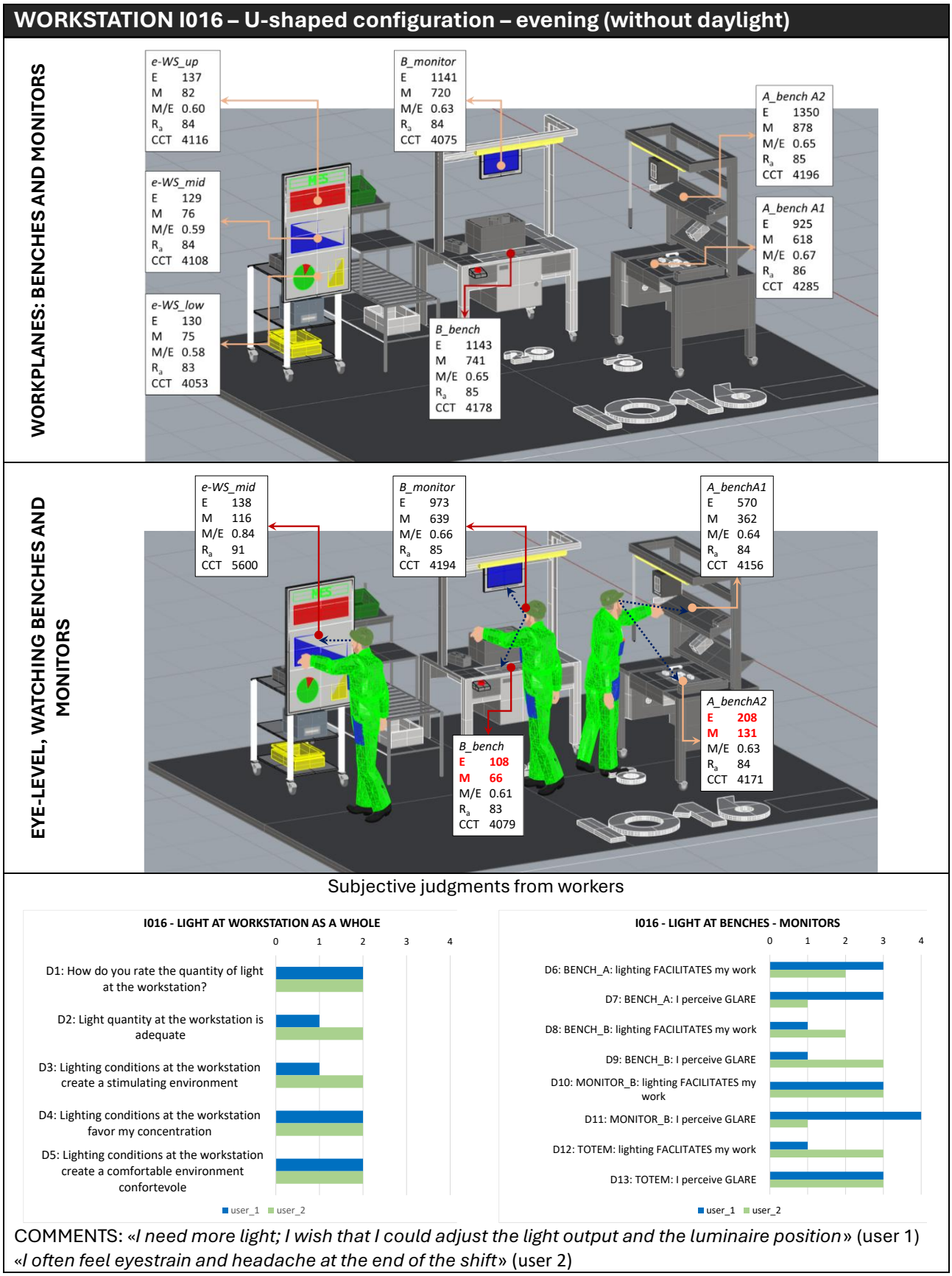
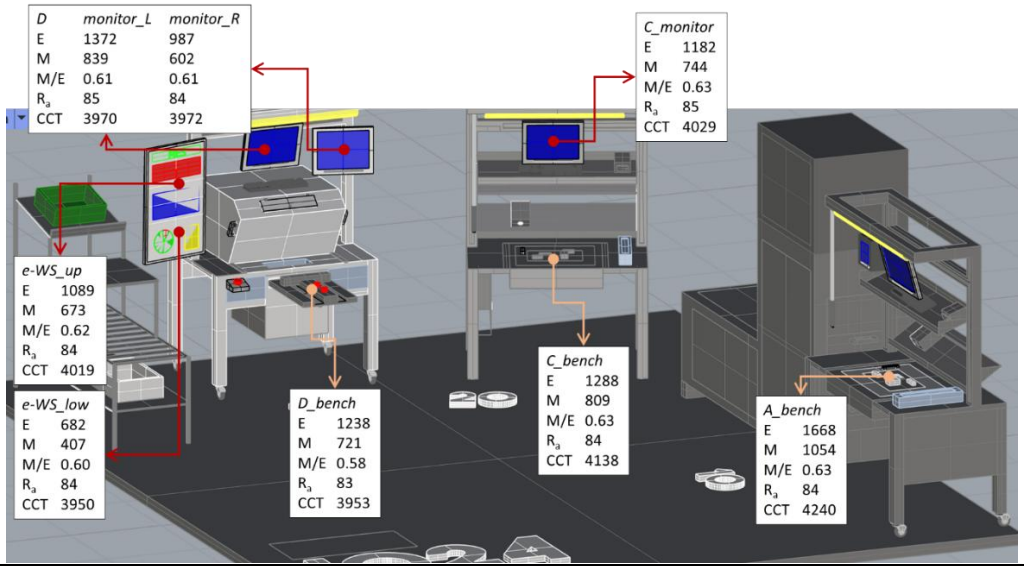


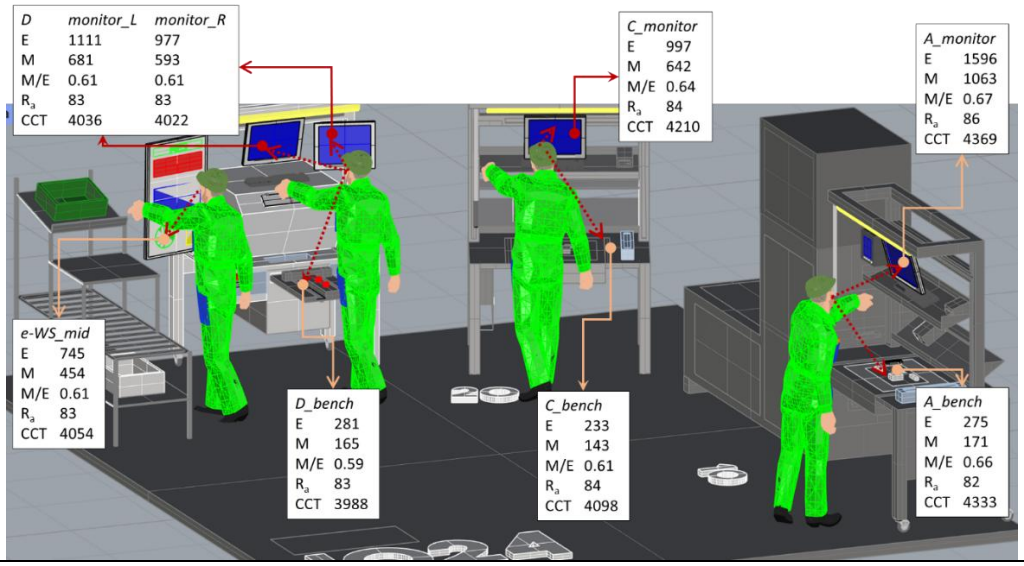
Figure 5 Lighting measurements and subjective judgments for workstation I016 (L-shaped).

WORKSTATION I024 – L-shaped configuration – evening (without daylight)

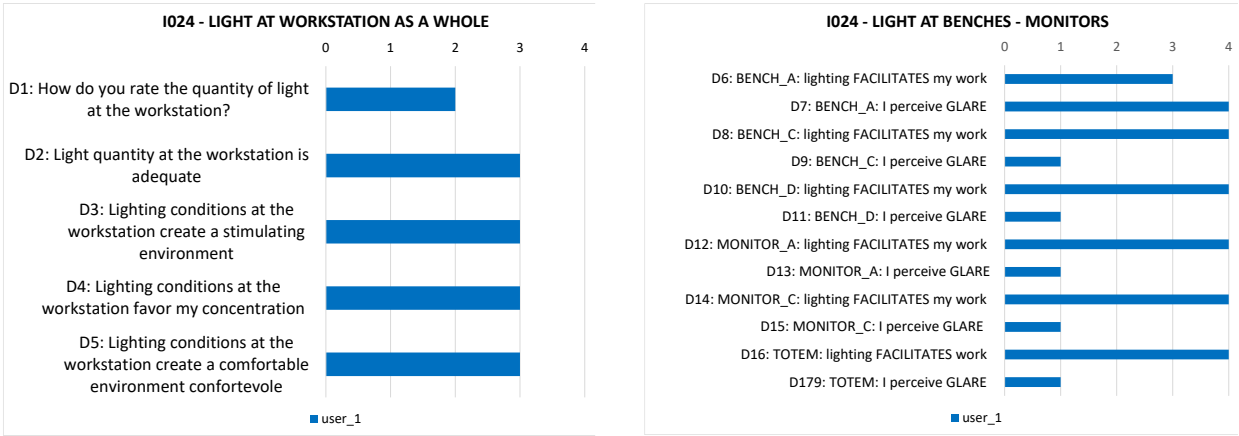
WORKPLANES: BENCHES AND MONITORS



EYE-LEVEL, WATCHING BENCHES AND MONITORS



Subjective judgments from workers



COMMENTS: «*Lighting conditions are sometimes glaring, especially when I'm reading the monitors*»

Figure 6 Lighting measurements and subjective judgments for workstation I024 (L-shaped).

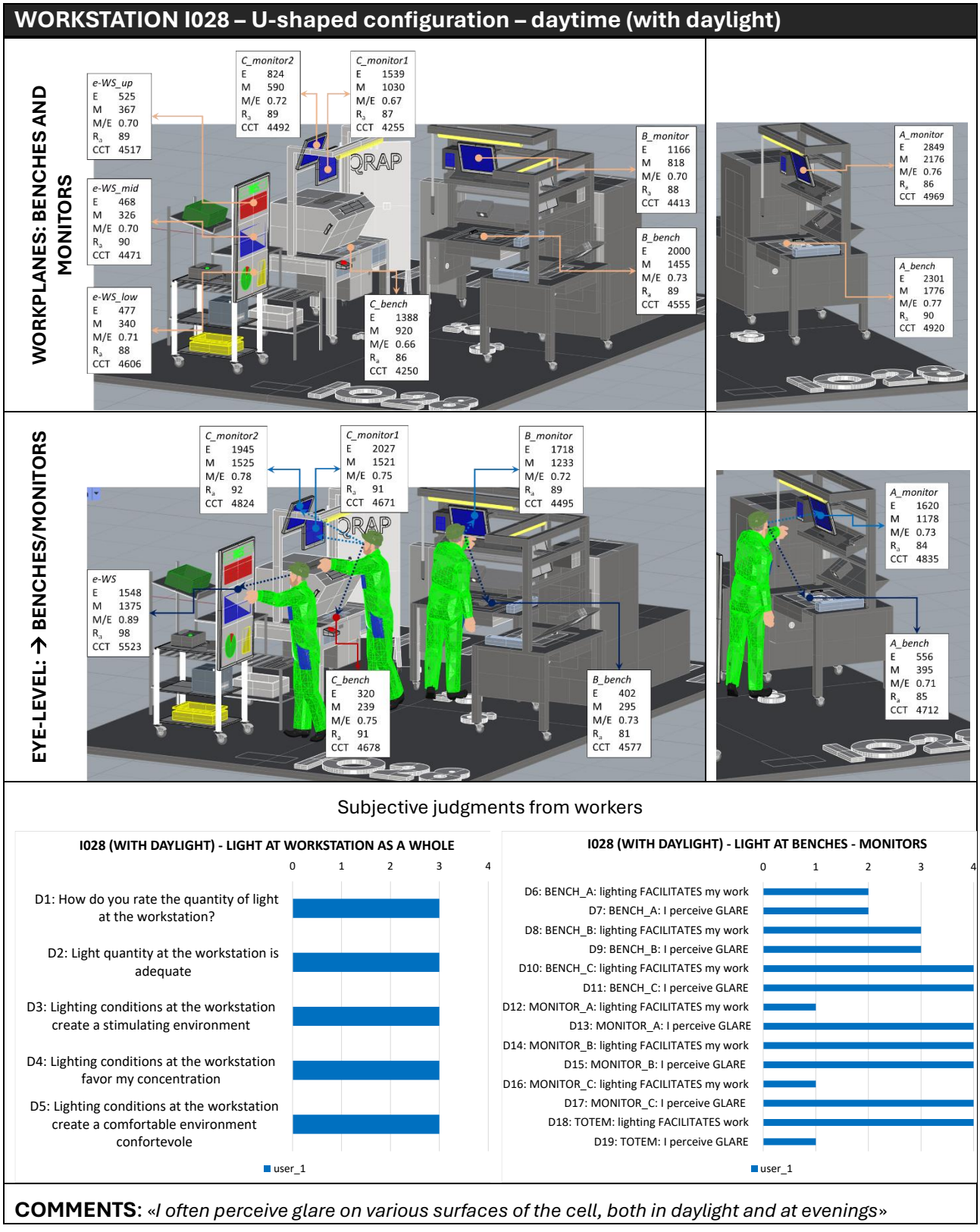


Figure 7 Lighting measurements and subjective judgments for workstation I028 (U-shaped, with daylighting).

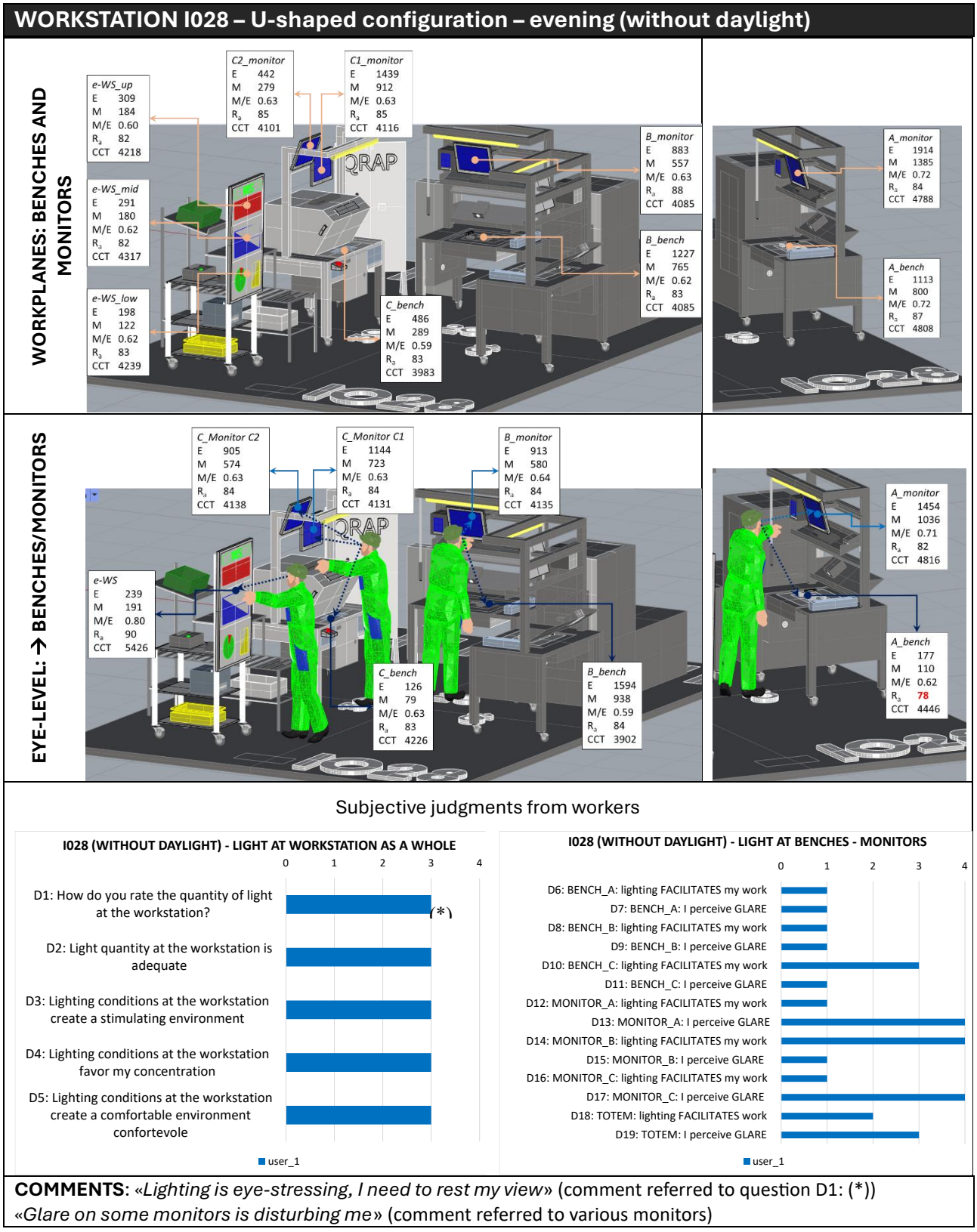


Figure 8 Lighting measurements and subjective judgments for workstation I028 (U-shaped, without daylighting).

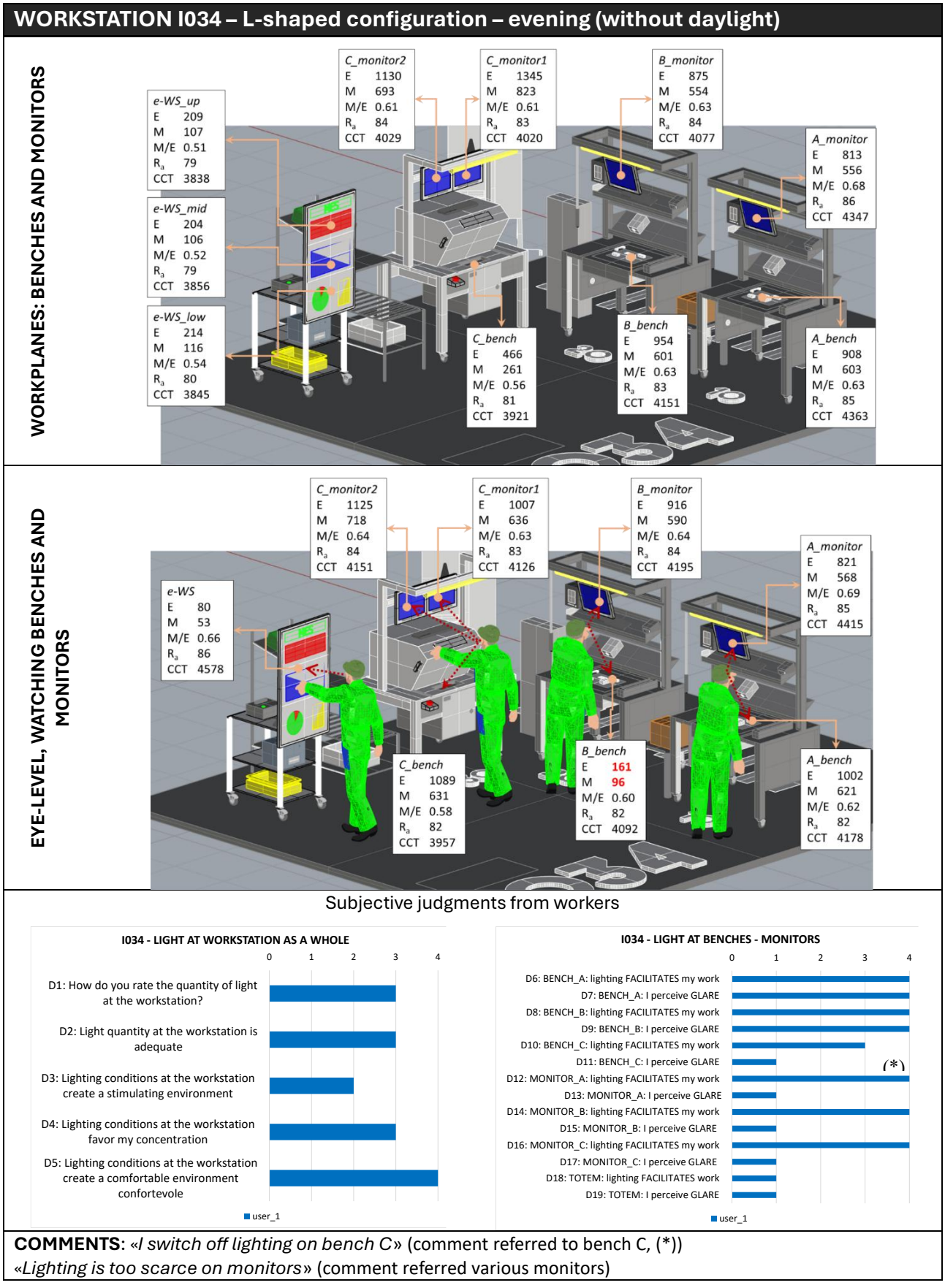
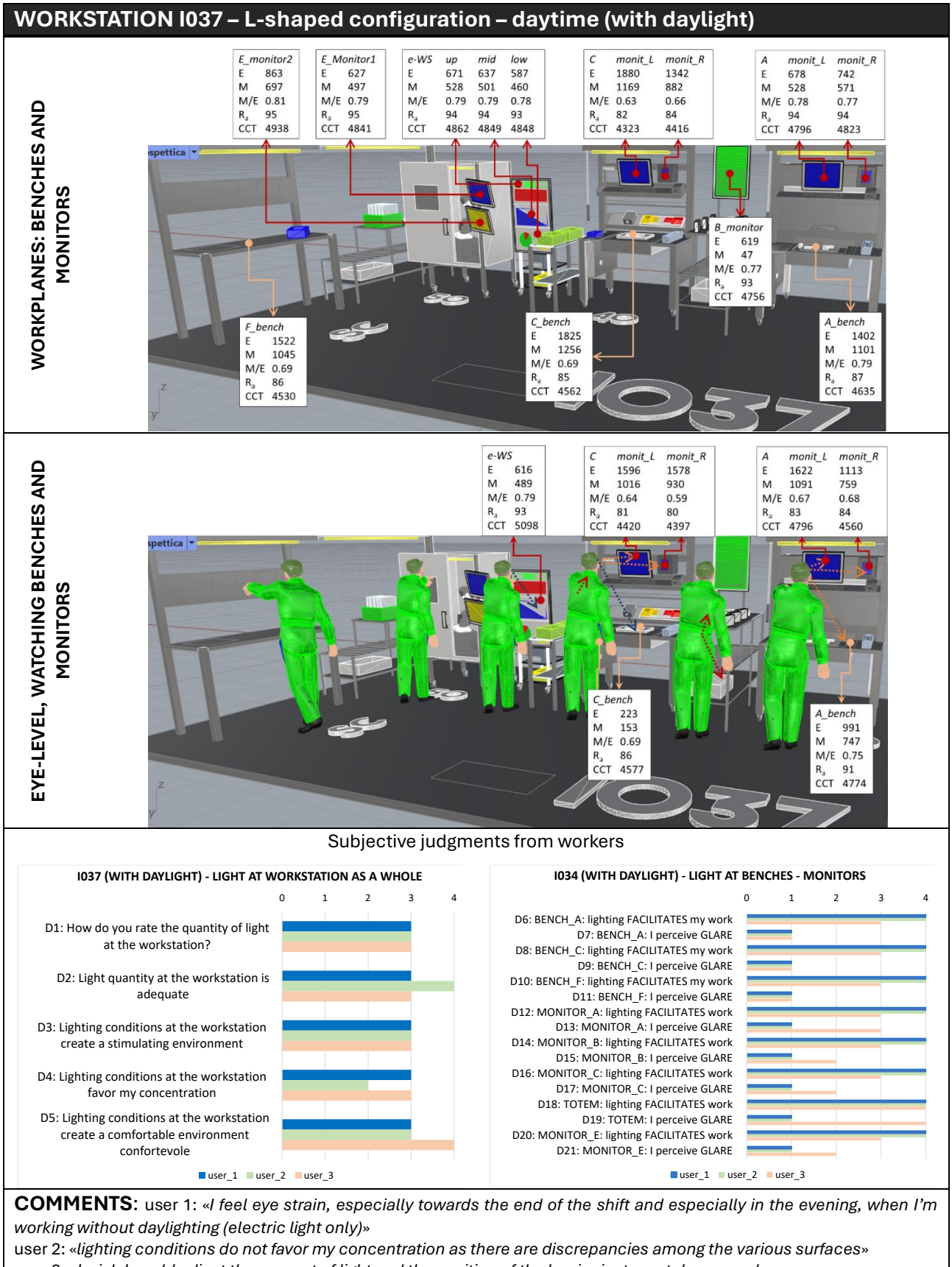


Figure 9 Lighting measurements and subjective judgments for workstation I034 (L-shaped). NOTE: the e-WS was off.



COMMENTS: user 1: «*I feel eye strain, especially towards the end of the shift and especially in the evening, when I'm working without daylighting (electric light only)*»
user 2: «*lighting conditions do not favor my concentration as there are discrepancies among the various surfaces*»
user 3: «*I wish I could adjust the amount of light and the position of the luminaire to match my needs*»

Figure 10 Lighting measurements and subjective judgments for workstation I037 (L-shaped), with daylight.

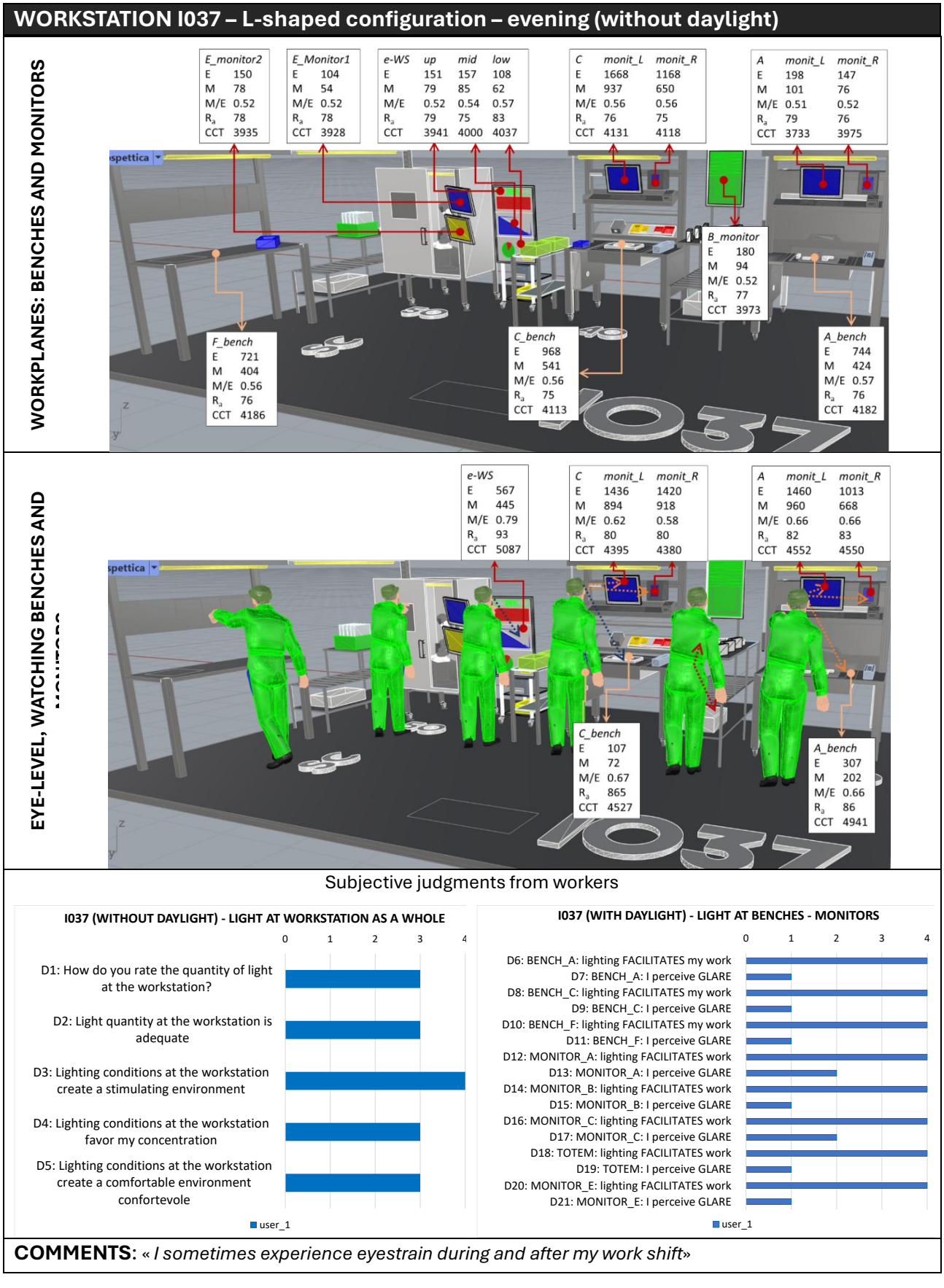


Figure 11 Lighting measurements and subjective judgments for workstation I037 (L-shaped), without daylight.

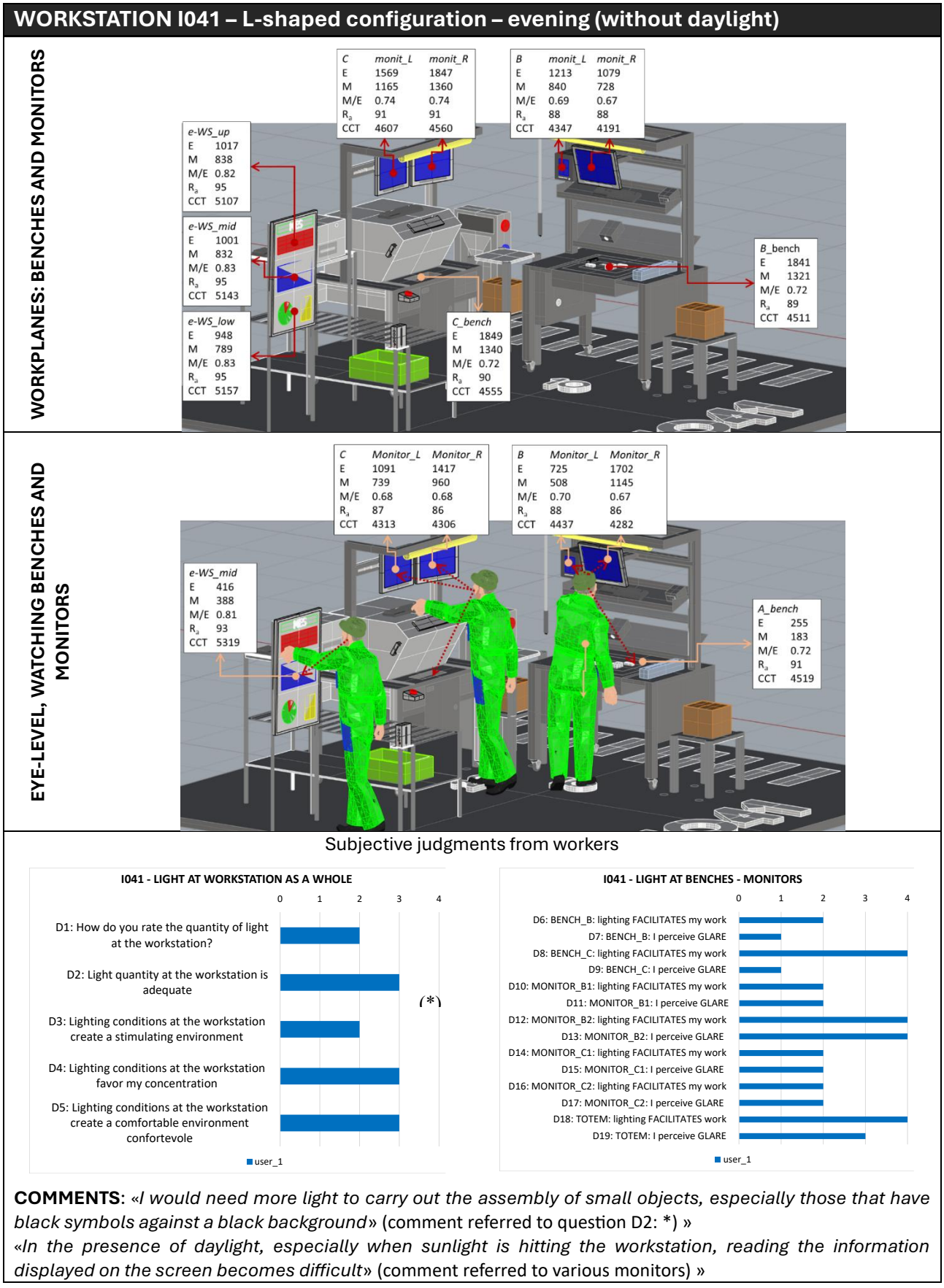


Figure 12 Lighting measurements and subjective judgments for workstation I041 (L-shaped).

4.3. EFFECT OF DAYLIGHT

For two workstations (namely I028 and I037), measurements were repeated during daytime, in the presence of daylight, and in the evening, in electric light only. The following considerations can be drawn by comparing data:

For illuminance values on benches:

- workstation I028: the average illuminance on the 3 benches (A, B, C) was 1896 lx in daylit conditions and 952 lx in electrical lighting conditions only, thus with a relative increment of +99.2% due to daylight
- workstation I037: the average illuminance on the 3 benches (A, B, C) was 1583 lx in daylit conditions and 844 lx in electrical lighting conditions only (relative increment of +87.5% due to daylight)
- at both workstations, illuminance values on the various benches were over 1300 lx, which is consistent with the strictest illuminance requirements of precision assembly ($E \geq 1000$ lx)

For mel-EDI and mel-DER:

- workstation I028: the average mel-EDI for all the view directions was 970 lx in daylit conditions and 527 lx in electrical lighting conditions only, thus with a relative increment of +83.9% due to daylight; the corresponding average m-DER increased from 0.66 to 0.76 in daylight condition (15.4%)
- workstation I037: the average mel-EDI for all the view directions was 741 lx in daylit conditions and 580 lx in electrical lighting conditions only (relative increment of +27.7% due to daylight); the corresponding average m-DER increased from 0.66 to 0.69 in daylight condition (+4.0%)
- at both workstations, thanks to the increment in the mel-EDI values at eye-level, all view directions comply with the 1-point WELL criterion as well as, apart from one case, with the 3-point WELL criterion

For CCT:

- workstation I028: the average CCT for all view directions increased from 4403 K in daylit conditions to 4789 K (+8.8%)
- workstation I037: a different trend was observed, as the average CCT for all the view directions remains unchanged (4628 K in daylit conditions and 4633 K in electrical lighting conditions only).

To summarize, the presence of daylight increased the light levels at the two workstations considered, but more significantly for the illuminance values on the benches and to a lower extent for the vertical planes at eye-level (mel-EDI, mel-DER, CCT).

4.4. SUBJECTIVE EVALUATIONS

Eleven workers answered the questionnaires, five men and six women, whose age was in the range 31-57 years (average: 49.3 years; SD: 6.86 years). The height of the participants ranged from 153 cm to 180 cm (average: 168.4; SD: 9.8 cm). Splitting the sample and analysing separately the groups of men and women, some differences emerged: men had a lower age (average: 47.2 years; SD: 10.1 years) than woman (average: 51.2 years; SD: 2.1 years); as for the height, men showed a higher height, with an average of 176.8 cm (SD: 3.42 cm) than women (average: 161.3 cm; SD: 7.34 cm). As for the question «*For how many hours through your shift have you worked today?*», 9 workers answered that they had been working for more than 6 hours, while one woman for 2-4 hours and one man for less than 2 hours. Therefore, most operators filled in the survey towards the end of their shift. Figs. 16-17 summarize the subjective judgments expressed by the sample of workers.

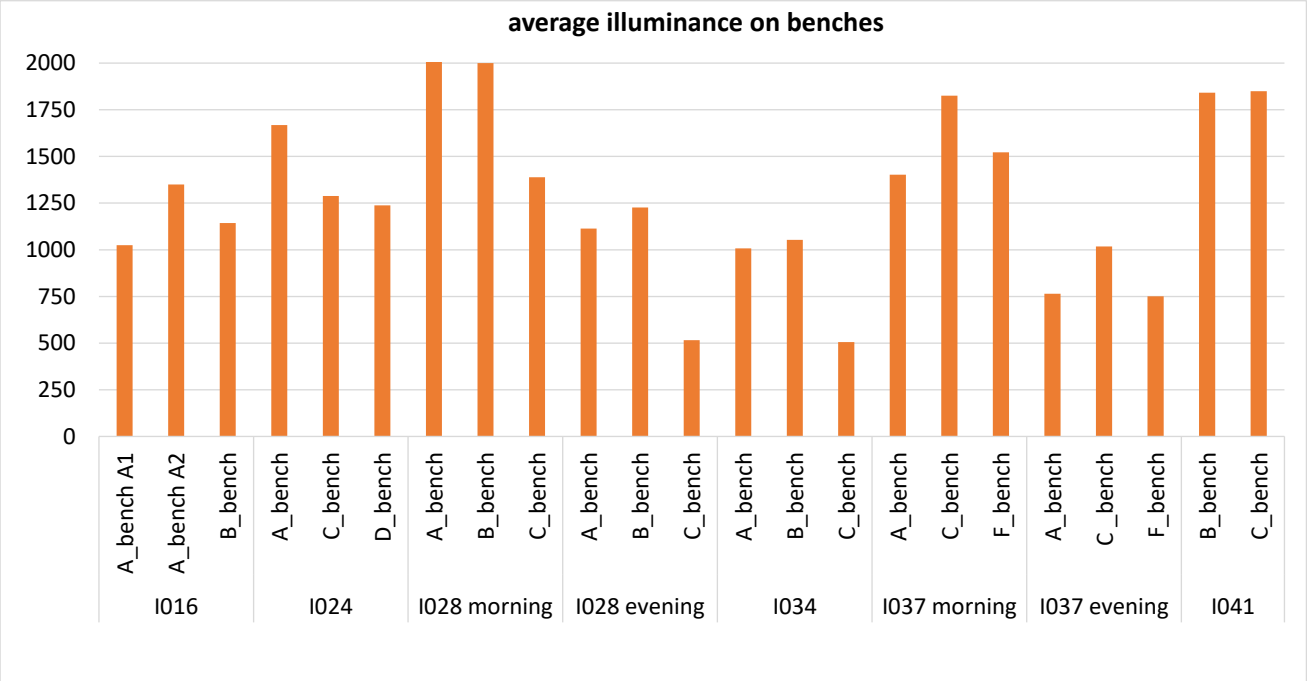
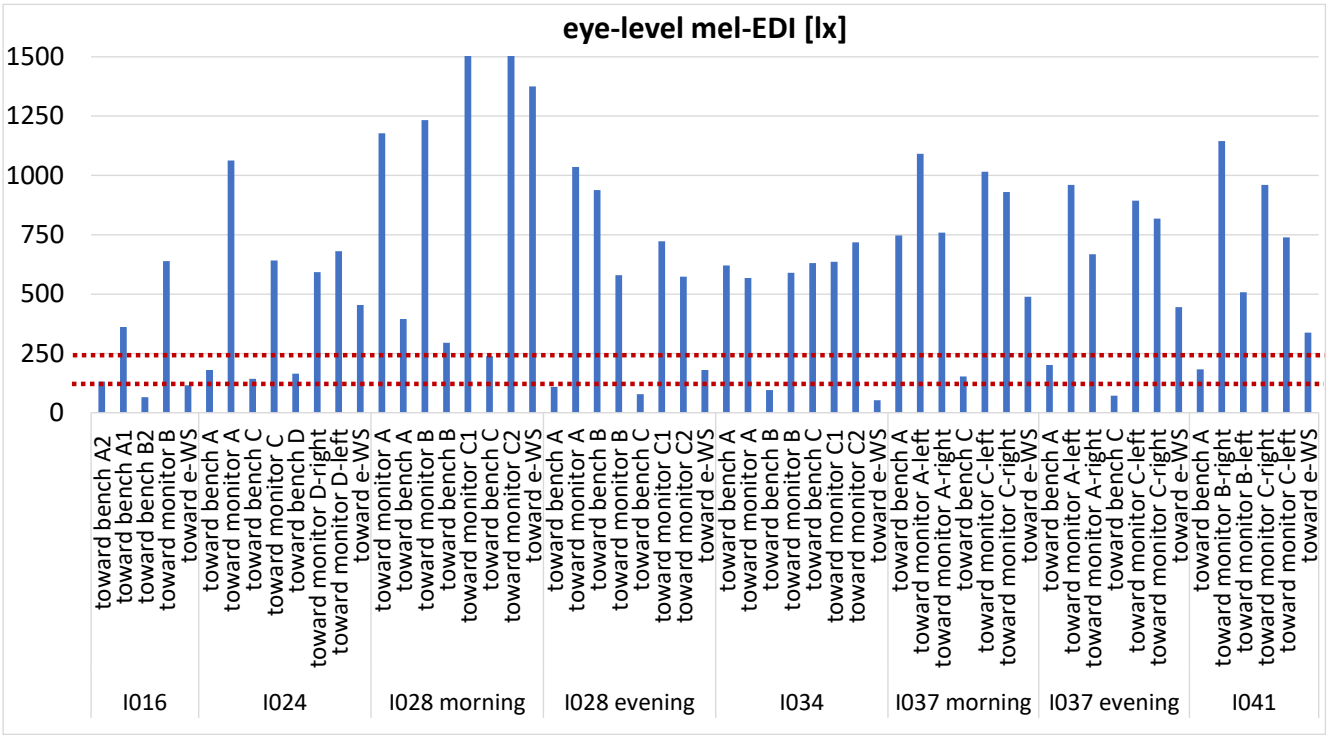


Figure 13 Average illuminance values measured on the various benches analysed.



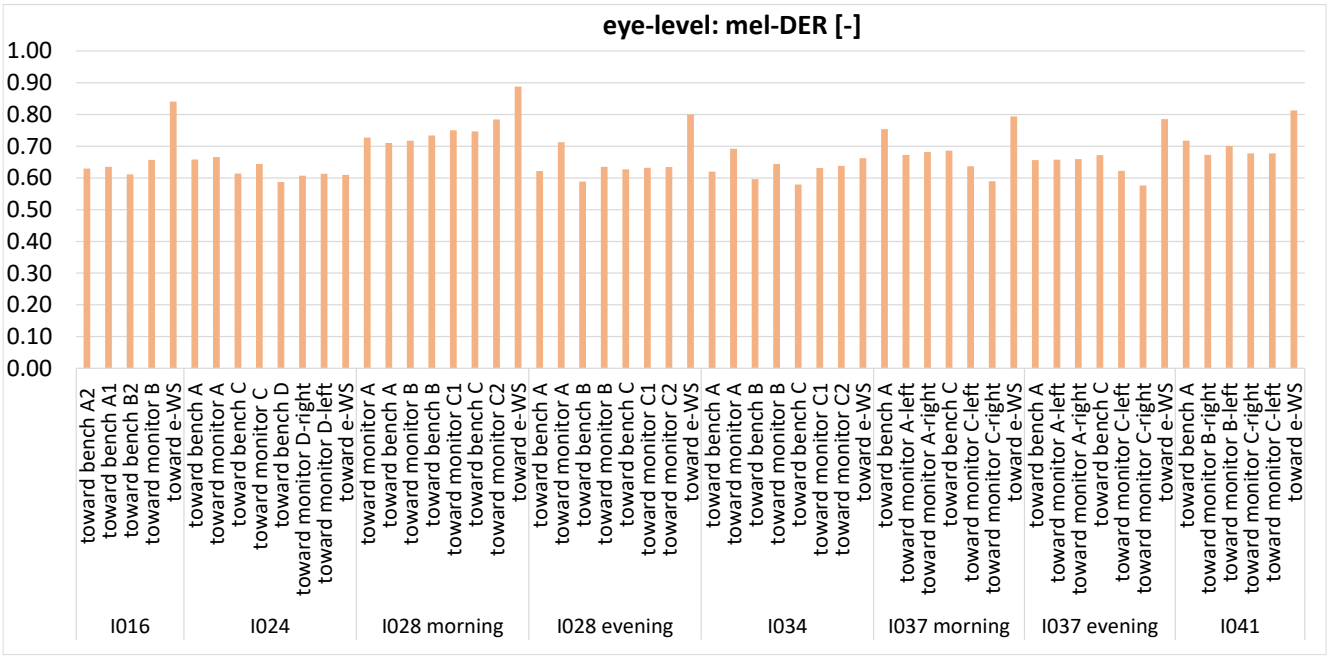


Figure 14 Melanopic results from measurements at eye-level: mel-EDI and mel-DER.

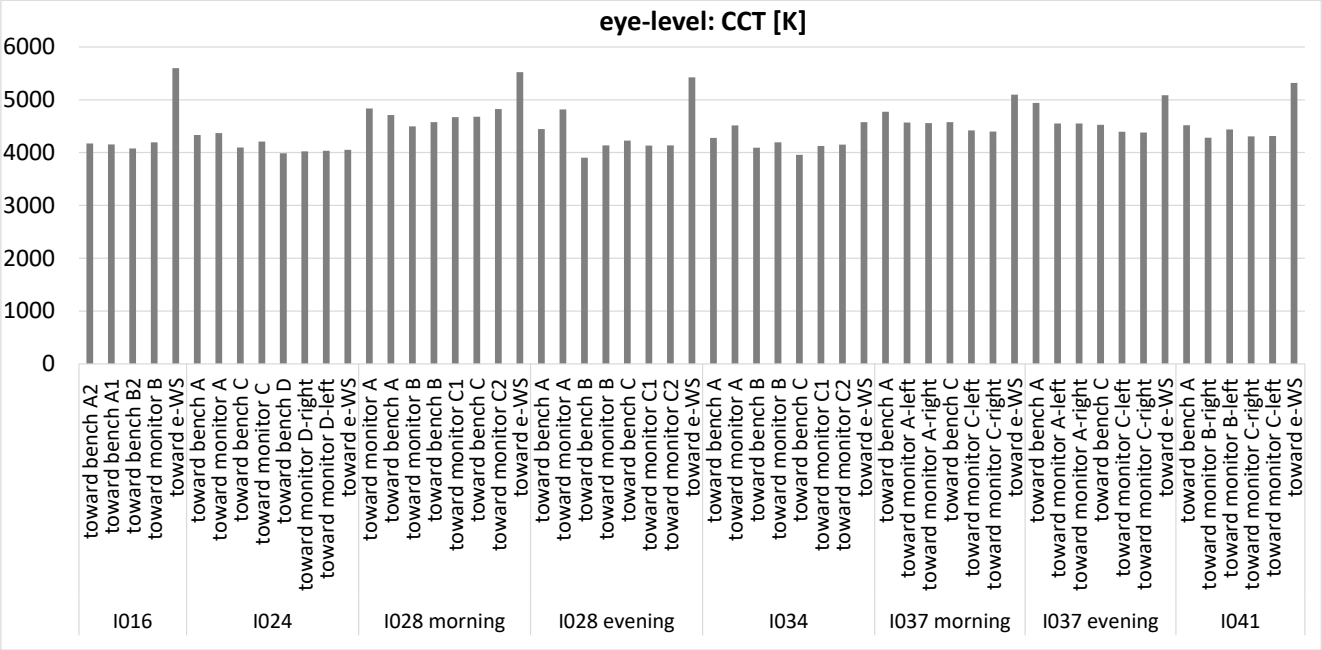


Figure 15 Photopic results from measurements at eye-level: correlated colour temperature CCT.

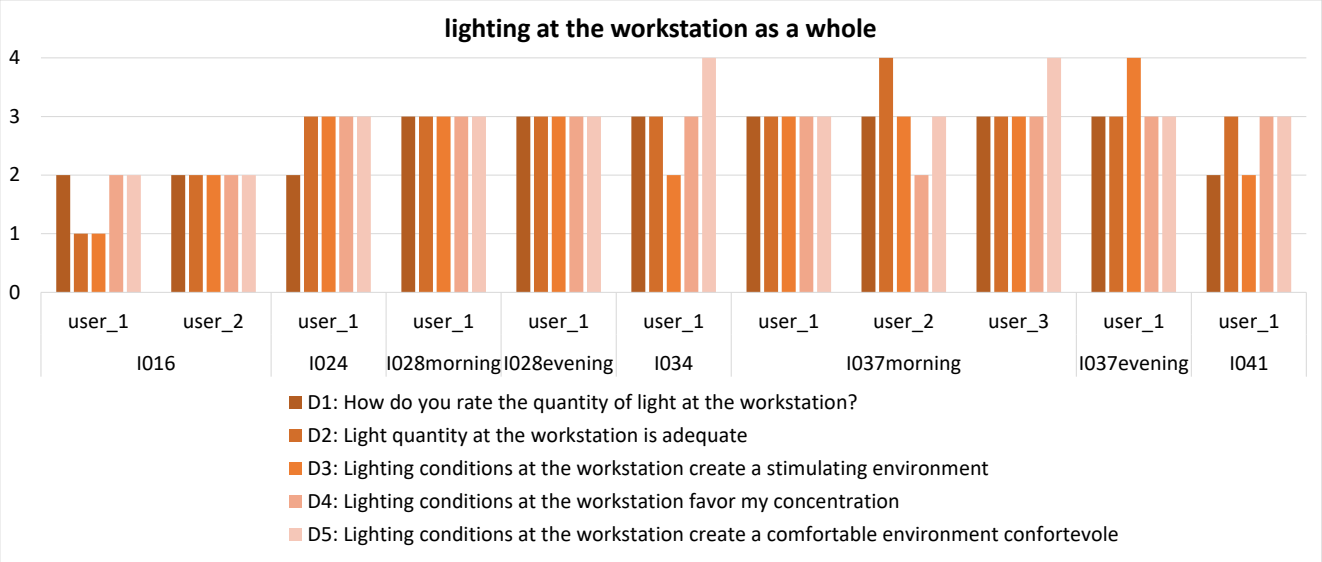


Figure 16 Synthesis of subjective judgments expressed by the workers on the lighting conditions globally perceived at the workstation.

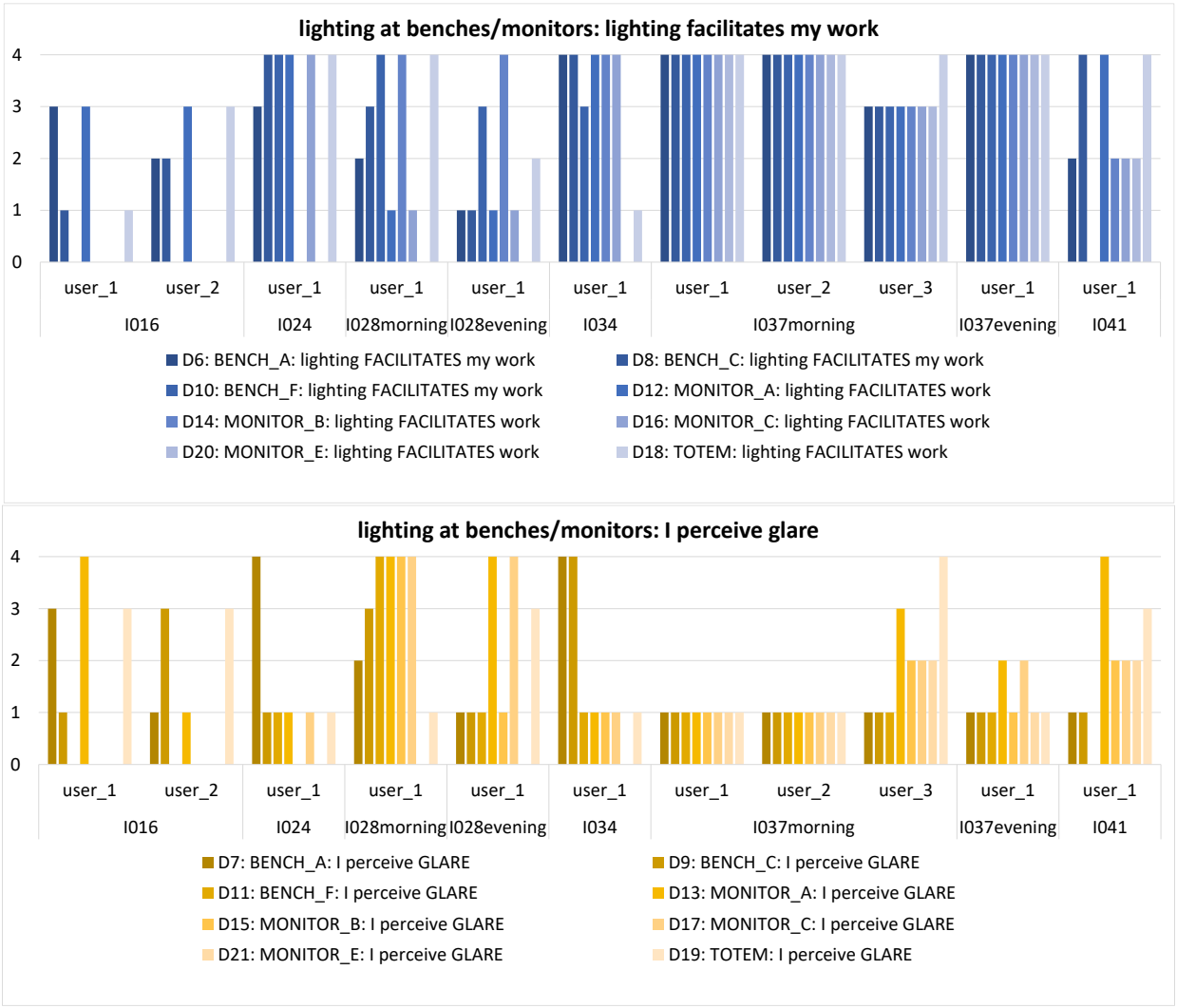


Figure 17 Synthesis of subjective judgments expressed by the workers on the lighting conditions perceived at specific benches and monitors.

Besides the subjective scores, interesting findings emerged from the open comments. The following considerations can be drawn from the results shown in the figures:

- for lighting conditions on the workstation as a whole: the workers expressed satisfaction with the overall lighting conditions for most workstations, with an average scores ≥ 3 (questions D1-D5); slightly lower score were expressed by the worker of workstations I024 (average score of 2.80), particularly for the quantity of light, and by the worker of workstation I041 (average score of 2.60), who reported a low quantity of light and a low stimulating lighting scenario; however, the lowest scores were expressed by the 2 workers of workstation I016 (average score: 1.60 and 1.80, respectively), with lowest scores on the quantity of light and on the stimulating ambient light. Particularly, these workers complained about the fatigue and eyestrain they perceive and would like to have a flexible lighting system
- for the lighting conditions at each specific bench/monitor, regarding the questions on «lighting facilitates my work»: a lower number of high scores was observed compared to the assessment on the whole workstations. Four workstations received high scores (average score ≥ 3). Average scores < 3 were observed for workstations I016 (average: 2.33 for both workers), consistently with the low scores expressed on the overall workstation, and I041 (average score: 2.67). The lowest scores were expressed for workstation I028 during the evening (average: 1.83), while the scores resulted higher (average: 2.50) but still not satisfactory during the daytime, thanks to the presence of daylight; however, complaints about eyestrain were expressed by the evening worker and on glare during the daytime (see next point)
- for the lighting conditions at each specific bench/monitor, regarding the questions on «I perceive glare»: complaints about glare were raised for some surfaces (bench/monitors) at workstations I016 (however, the average score was 2.67), I024 (average: 1.60), I034 (average: 2.00), and I041 (average: 2.00). The most critical workstation was I028, especially during daytime: complaints about glare concerned all the surfaces, thus resulting in a quite high average score of 3.50

- some complaints about the lighting systems were expressed in terms of visual fatigue and eyestrain, especially by the evening workers (electric light only)
- a higher flexibility of the lighting systems available at the workstations is demanded, for what concerns both the amount and the color of the light emitted and the position of the luminaire; both aspects should be adjusted and controlled by each worker in a customized way.

5 DISCUSSION

The photopic illuminances measured on benches were compliant with the minimum requirements set by the reference European standard EN 12464-1:2021 for medium precision tasks ($E_{wp} \geq 500$ lx), and for most benches also for fine and high-precision tasks ($E_{wp} \geq 750$ lx and $E_{wp} \geq 1000$ lx, respectively). This is an expected result, as the lighting systems were designed just to guarantee compliance with the minimum maintained illuminance requirements of the standard, along with avoidance of glare. Accordingly, the various benches are equipped with embedded anti-glare lighting systems. For this reason, glare measurements were excluded from the analyses. Even though the compliance of illuminance values is a somewhat expected result, this is not always the case. There is literature evidence of non-compliant illuminance values at workstation workplanes. For instance, Giovannini et al. [75] observed through field measurements some illuminance values below standard in office spaces with fluorescent luminaires in Turin (Italy), while Lo Verso et al. [88-89] found several incompliances regarding both daylighting and electric lighting in health care spaces and in university classrooms, and Almarez and Nawang [90] highlighted that only 3 out of 23 classrooms were compliant with the standard illuminance value of 300 lx in a high school in the Philippines. Examples of non-compliant illuminances in industrial buildings were not found, but it is also possible that the company management did not disclose such data for publication.

On the circadian lighting side, 71.9% of view directions towards benches and monitors showed mel-EDI $\geq$ 250 lx, thus meeting the CIE recommendation and the 3-point WELL criterion. The percentage increased to 86.0% when focusing on mel-EDI values $\geq$ 136 lx, as per the 1-point WELL criterion. For the same view directions, an average CCT of around 4500 K was detected. Considering that the lighting systems were designed to comply with photopic requirements and not specifically with circadian recommendations, this can be considered a very good result. Such performance seems to be due to a combination of the following factors: (i) illuminance values significantly higher than 500 lx for most workstations; (ii) mel-DER values in the range 0.59-0.89; (iii) presence of daylight, which contributes to increasing both photopic and melanopic quantities. Conversely, it is worth noting that the melanopic performance is not linked to lighting systems with cold CCT (above 5300 K), as light reaching the eyes of the operator is mostly in the neutral range. However, several melanopic non-compliances remain, and are equally distributed among the various types of surfaces that workers observe during their task (benches, monitors, e-WS - totems). Possible solutions may involve the use of new generation lighting systems, including tunable white luminaires, able to modify their spectral power distribution (SPD) during the day to mimic the dynamic variation of the SPD of daylight (sunlight and skylight). Besides, it is possible to consider the installation of dedicated task lights with a cold CCT to be used at the best operator convenience, following up the study from Figueiro et al. [91], who optimized the lighting systems to support visual and non-visual lighting design without increasing discomfort glare or lighting power density. They considered four ceiling lighting setups, incorporating various combinations of direct and indirect lighting, plus one additional design that employed blue task lighting (with a high mel-DER value), all providing participants with an equally high level of circadian-effective lighting. They found out that most participants preferred the task lighting over the ceiling-mounted lighting. Similarly, in the industrial sector, it would be worth developing lighting systems embedded in the assembly workstation, able to optimize the photometric curve to favour the melanopic illuminance at eye-level, as well as the light output and the variation of the colour temperature. Concerning similar studies, Van de Putte et al. [81] exposed 80 shift workers in an assembly plant to integrative lighting with mel-EDI of 192 lux, characterized by bright light with a high fraction of short wavelengths. Their results indicated improved sleep efficiency, reduced sleep latency, and enhanced alertness during the morning shift compared to the control group. Kindt et al. [92] exposed 71 shift workers in a truck factory to a Human-Centric Lighting (HCL) condition with a vertical mel-EDI of 250 lx and a CCT of 5000 K. Compared to the control group (44 lx, 4000 K), the HCL group showed significant improvements in sleep quality and attention, with lower amounts of errors. Nie et al. [93] engaged three subjects in 38 consecutive days of shift work in a semi-isolated, controlled environment with dynamic daylight-like lighting. The lighting system featured tunable illuminance (226 to 678 photopic lx, and 170 to 650 melanopic lx, simulating daylight dynamics), CCT (2680 to 7314 K), demonstrating stable circadian rhythms, improved alertness at night hours and cognitive performance, with a maintained mood status, through proper tuning of the lighting systems. Similar results were also obtained by He and Yan [94]. Zauner and Plischke [95] applied non-visual lighting design principles in an industrial production line to support the circadian health of night shift workers. They designed a new luminaire that allows for a large melanopic stimulus range between 412 and 73 lx mel-EDI vertically at eye level, while maintaining a neutral white illuminance at task level between 1250 and 900 lx. Their findings demonstrated that the designed lighting system successfully increased night-time alertness, with workers reporting better adaptation to night shifts. It seems that different approaches can be applied to enhance non-visual effects of light and circadian entrainment: tunable systems, modified spectral power distribution (and CCT), increased melanopic illuminance levels over 250 lx, in combination with increased photopic illuminance on workplanes.

In the case-study used in the research, the lighting systems embedded in the cells were not tunable, with a constant neutral CCT. However, they produced good circadian light levels at the workers' eyes by increasing the illuminance level, which resulted in mel-EDI values over 250 lx at most view directions. Clearly, increased illuminance level may lead to increased energy consumption, but it's also true that the lighting systems are embedded in the bench structure, thus minimizing the distance between the source and the workplanes. On the other hand, glare issues may arise and need to be addressed through an optimized design of the luminaire photometry and position. About the view directions considered for melanopic measurement, it is worth noting that no formal indication is specified in the CIE documents, nor in the WELL protocol. It is evident that a user can assume different view observation while performing a task, particularly when working in production cells in an industrial setting. However, to the best of the Authors' knowledge, there is currently no established rule governing the selection of weighting factors to achieve a balance among different view observations that an occupant may encounter while working. Consequently, it was decided to adhere to the actual working conditions and to refer to the main directions that workers assume towards benches and monitors. It seems that more research is needed on this aspect, as well as about how to apply the circadian recommendations in industrial workspaces, especially considering how strategic the comfort and wellbeing of the workers and the human-machine interaction has become in the industry 5.0 protocol.

Another aspect of interest emerged from the comments expressed by the workers involved in the survey: most of them expressed satisfaction with the lighting conditions, but complaints about low lighting levels on certain benches or monitors were expressed, as well as glare issues; wishes were expressed about having the possibility of controlling several aspects:

1) dimming the light output; this suggests the possibility of installing lighting systems with higher light output and let the workers dim it based on their preferences; for instance, Safranek et al. [96] monitored five patient rooms in a neonatal intensive care unit (NICU) where an automatic tunable lighting system was installed, with manual override options, and found that giving occupants control over the lighting system resulted in optimized light levels without a considerable increase in energy use
2) changing the colour of the light emitted by the lighting systems, in terms of correlated colour temperature; this can also be beneficial in melanopic terms, as highlighted above
3) adjusting the position of the lighting systems: this involves both vertical and horizontal shifting and possible tilt; this wish was particularly expressed by the group of women involved in the study, who had an average height lower than the counterparts of men (161.3 cm versus 176.8 cm): the lower height may expose the group of women to higher discomfort (in terms of glare, for instance). The electric lighting luminaires are embedded in the structure of the cells and thus in a fixed position, but it seems that more flexibility is desired in this aspect
4) having supplementary lighting systems close to the least lit surfaces, shaded by the specific shape of the equipment.

It is worth noting that beneficial effects of controlling lights are well documented in the literature (for instance in Kompier et al. [97]), as already shown in the introduction section, particularly for what concerns the possibility of adjusting the workplane illuminance [37-38; 98-99].

In the building used as case-study, the operators work on different shifts, from 6 am until 10 pm, which means that there isn't an overnight shift. Workers in factories are exposed to longer periods of electric lighting, in the absence of daylight, than other categories of workers (such as in office or educational buildings). The quantity and the spectral quality of electric lighting becomes a key factor in their wellbeing and performance, like it is for night-shift workers. In this regard, it is worth stressing that most current circadian lighting recommendations (like those from WELL Building Standard or guidelines inspired by CIE and academic research) are designed around the "typical" daytime worker, i.e., people active during the day and sleeping at night. These standards aim to strengthen the natural light-dark cycle, supporting high melanopic stimulation in the morning (bright, blue-enriched light) to boost alertness, and low stimulation in the evening (warm, dim light) to promote melatonin secretion and healthy sleep. On the other hand, shift workers are an entirely different case, as their activity-rest rhythms are inverted or irregular (e.g., awake and working at night, trying to sleep during daylight). Non-visual needs for them are not yet clearly defined in the standards, so simply applying 'normal' circadian lighting strategies could increase circadian disruption, lead to worse sleep quality, higher risk of health problems (e.g., metabolic disorders, cardiovascular issues). It seems therefore that need for targeted, evidence-based lighting recommendations that address their specific chronobiological risks, able to clarify the following aspects: addressing how to artificially shift circadian rhythms using light timing, intensity, spectrum; how to protect shift workers from "wrong-time" light exposure (like bright light when they need to sleep after work); and how designing dynamic lighting profiles for night workers, different from daytime workers.

5.1. MERITS AND LIMITS

The innovation of the study lies in analysing integrative lighting conditions in an actual industrial building as one of the vectors to rely on for the transition from Industry 4.0 to Industry 5.0 paradigms. The study therefore combined the Industry 5.0 principles with human-centric lighting. Among non-residential buildings, the integrative lighting approach has been explored in office, educational, and healthcare buildings, but to a significantly lower extent to industrial and manufacturing spaces. The study from Van de Putte et al. (2022) is one of the few studies what specifically analysed circadian lighting conditions in an industrial setting. The present study aimed at bridging this gap, by assessing and verifying if the proposed melanopic recommendations in terms of mel-EDI values could be met in an existing industrial context. Besides the merits, there are some limitations that need to be acknowledged.

The first limitation is the fact the survey was conducted in a single automotive manufacturing plant. It would have been useful to carry out, for example, experimental testing in other companies in the automotive industry that perform assemblies that require the presence of highly skilled operators, so that comparisons could be made. In justification of this lack, it should be mentioned that it is difficult to get authorizations for lighting tests in production environments since the analyses/field campaigns and surveys interrupt the activities of employees or be limited by the secrecy policies of certain processes. Another limitation concerns the low number of participants in the subjective questionnaires (n=11): this was due to the number of workers who worked at the workstations selected for the study, all of them involved in the questionnaire. Considering the reduced sample of participants, no statistical analyses were performed to sustain the measurements results: however, the subjective assessments were useful to highlight some trends, such as the occurrence of glare perceived at various workstations during tasks, especially (but not only) when the workers assumed a view direction towards the suspended monitors. Besides the subjective scores, useful information was collected from the open comments: in short, these highlighted inadequate light levels and glare problems in some cases, and raised some interesting requests, such as the need to adjust the light output, in terms of light intensity and spectral power distribution, and the position of the lighting systems. Besides, dedicated task lights in the proximity of the worst lit work surfaces were also desired. To summarize, the need for more flexibility in the lighting systems emerged.

6 CONCLUSIONS

The study focused on experimental integrative lighting analyses that were carried out at a plant of a multinational company operating in the luxury automotive sector, under natural and electric light, in central and evening shifts, on U- and L-shaped conformed work cells. The analyses consisted of campaigns of experimental measurements on the work surfaces of the benches and at eye-level of the operators, measuring both visual and non-visual effects of light. In addition, questionnaires were administered to workers to compare subjective perceptions with measured data. Both photopic illuminances on benches and monitors of sample workstations and eye-level melanopic quantities (mel-EDI and mel-DER) were measured in-the-field to verify if photopic and circadian recommendation can be met in actual industrial settings, typically designed to comply with photopic targets, especially in terms of workplane photopic illuminance. As industries evolve from Industry 4.0 to Industry 5.0, the focus increasingly shifts towards the wellbeing of workers, through a human-centred approach. In this new industrial paradigm, lighting emerges as a critical factor in supporting operators' well-being, directly impacting not only their health but also their overall work performance. Proper lighting is essential to ensure optimal working conditions, as it influences both visual comfort and the non-visual effects of light on the human body.

The main findings from the experimental study results indicated that:

- visual effects of light: all workstations were generally well lit and met current standards in terms of average maintained illuminance, as one could expect considering that lighting systems are designed to meet such criterion as for the standard EN 12464-1:2021 non-visual effects of light: eye-level mel-EDI measurements ranged from 53 lx to 1525 lx, with an average of 601 lx (SD: 394.3 lx); with regard to the target set by the CIE and the WELL protocol, 71.9% of view directions toward benches or monitors showed mel-EDI $\geq$ 250 lx, meeting the 3-point WELL criterion; while 86.0% of them showed mel-EDI $\geq$ 136 lx, meeting the 1-point WELL criterion. Although current lighting systems are designed to meet photopic standards (which primarily address visual requirements), melanopic measurements reveal important nuances. These measurements assess how lighting affects non-visual functions, such as circadian rhythms, which are crucial for maintaining energy levels, alertness, and sleep quality. Despite compliance with photopic guidelines, some lighting environments may still fail to fully support the broader spectrum of human health needs, particularly in terms of circadian regulation
- feedback from workers indicates general satisfaction with the lighting conditions, yet many expressed a desire for improvements. Specifically, they emphasized the need for more flexible and adjustable lighting systems that could be customized to suit individual preferences and work requirements. Such flexibility could allow workers to adjust light intensity or quality based on the task at hand or personal comfort, fostering a more adaptive and health-supportive work environment.

This highlights the growing need for further research into integrative, human-centric lighting, which seeks to harmonize both visual and non-visual effects of light. Integrative lighting accounts for not only the brightness and colour of light but also its impact on human circadian rhythms and overall well-being. While significant progress has been made in understanding and applying this concept in tertiary environments such as offices, schools, and hospitals, there has been limited attention paid to industrial spaces. Yet, industrial environments stand to benefit greatly from human-centric lighting solutions, as they are often characterized by long working hours and conditions that demand sustained attention and alertness. To fully embrace the potential of Industry 5.0, where technology and human-centric design converge, it is crucial to expand the application of integrative lighting principles to industrial settings. By doing so, industries can create environments that not only enhance productivity but also prioritize the health and well-being of their workers, ensuring a more sustainable and human-focused approach to industrial design. For this reason, the authors plan to evaluate in the future the possibility for each operator to independently set the lighting of the various workstations and to memorize them automatically, so that every time an employee logs in to the work cell, the settings saved are loaded and the cell sets the customized lighting conditions [7, 28, 100].

This option would also allow as successive assemblies of different products which may require specific lighting levels for each operator, the different needs to be satisfied in an extremely fast way, precisely according to the flexibility, productivity [7, 37-38, 101] and speed established by the lean approach.

ACKNOWLEDGMENTS

The authors wish to express their sincere gratitude to Valeo ISC Italia (Santena plant), and notably to Davide Cino, for supporting the research.

REFERENCES

[1] Vilda F.G., Fabra J.A.Y. and Torrents A.S. A human-centered approach for lean factory design, *ScienceDirect Procedia Manufacturing*, Vol 41, pp. 445-454, 2019.

[2] Cagliano A.C., Carlin A. and Rafele, C. Understanding Supply Chain Complexity with Performance Measurement. *Proc. of the 13th IFAC Symposium on Information Control Problems in Manufacturing*, Vol. 13, pp. 1126-1131, Moscow (Russia), June 3-5, 2009.

[3] Martin R., Lin S.W., Miller B., Durand J., Joshi R., Didier P., Chigani A., Torenbeek R., Duggal D., Bleakley G., et al. *Industrial Internet Reference Architecture Technical Report; Technical Report*. Industrial Internet Consortium: Boston, MA, USA, 2015.

[4] Sanders A., Elangeswaran C. and Wulfsberg J.. Industry 4.0 implies Lean Manufacturing: Research activities in industry 4.0 function as enablers for Lean manufacturing. *Journal of Industrial Engineering and Management*, Vol. 9, pp. 811-833, 2016.

[5] Kolberg D., Knobloch J. and Zuhlke D. Towards a Lean automation interface for workstations, *International Journal of Production Research*, Vol. 55, pp. 2845-2856, 2017.

[6] Tortorella G.L., Fetterman D., Giglio R., Borges G.A. Implementation of industry 4.0 and Lean production in Brazilian manufacturing companies. *International Journal of Production Research*, Vol. 56, No. 8, pp. 2975-2987, 2017.

[7] Cohen Y., Golan M., Singer G. and Faccio M. Workstation-Operator Interaction in 4.0 Era: WOI 4.0. IFAC (International Federation of Automatic Control), IFAC PapersOnLine Vol. 51, No. 11, pp. 399–404, 2018.

[8] Prifti V. and Nebiu S. Optimization of work processes in a production company in Albania. *International Journal of Mechanics and Control*, Vol. 25, No. 01, pp. 15-20, 2024.

[9] Bortolini M., Faccio M., Galizia F.G., Gamberi M. and Pilati F. Adaptive Automation Assembly in the Industry 4.0 Era: A reference Framework and Full-Scale Prototype. *Applied Sciences*, Vol. 11, paper number 125, 2021.

[10] Belhadj I., Aicha M., Hammadi M. and Aifaoui N. Human-robot interoperability for end of life disassembly lines of mechatronic products. *International Journal of Mechanics and Control*, Vol. 25, No. 02, pp. 3-8, 2024.

[11] Allagui A., Belhadj I., Plateaux R., Hammadi M., Penas O. and Aifaoui N. Design for selective assembly and disassembly process optimization. *International Journal of Mechanics and Control*, Vol. 25, No. 02, pp. 9-14, 2024.

[12] Raparelli T., Eula G., Mazza L., Ivanov A., Pietrafesa F., Mala R. and Pontin M. A preliminar prototype of an industrial exoskeleton for the operator's trunk support. *International Journal of Mechanics and Control*, Vol. 23, No. 02, pp. 37-52, 2022.

[13] Valette E., El-Haouzi H.B. and Demesure G. Industry 5.0 and its technologies: A systematic literature review upon the human place into IoT-and CPS-based industrial systems. *Computers & Industrial Engineering*, Vol. 184, paper number 109426, 2023.

[14] Nahavandi S. Industry 5.0. A Human-Centric Solution. *Sustainability*, Vol. 11, paper number 4371, 2019.

[15] Longo F., Padovano A. and Umbrello S. Value-oriented and ethical technology engineering in Industry 5.0: A human-centric perspective for the design of the factory of the future. *Applied Sciences*, Vol. 10, paper number 4182, 2020.

[16] Grabowska S., Saniuk S. and Gajdzik B. Industry 5.0: improving humanization and sustainability of Industry 4.0. *Scientometrics*, 127, 117–3144, 2022.

[17] Reiman A., Kaivooja J., Parviainen E., Takala E. and Lauraeus, T. Human factors and ergonomics in manufacturing in the industry 4.0 context – A scoping review. *Technology in Society*, Vol. 65, No. 101572, 2021.

[18] Tegtmeier P., Weber C., Sommer S., Tisch A. and Wischniewski S. Criteria and Guidelines for Human Centered Work Design in a Digitally Transformed World of Work: Findings from a Formal Consensus Process. *International Journal of Environmental Research and Public Health*, Vol. 19, No. 23, paper number 15506, 2022.

[19] Gualtieri L., Palomba I., Merati F.A. Rauch, E. and Vidoni R. Design of Human-Centered Collaborative Assembly Workstations for the Improvement of Operators' Physical Ergonomics and Production Efficiency: A Case Study. *Sustainability*, Vol. 12, paper number 12093606, 2020.

[20] Xu X., Lu Y., Vogel-Heuser B. and Wang L. Industry 4.0 and Industry 5.0 – Inception, conception and perception. *Journal of Manufacturing Systems*, Vol. 61, pp. 530-535, 2021.

[21] Ozkeser B. Lean Innovation Approach in Industry 5.0. *Proc. of The Eurasia Proceedings of Science, Technology, Engineering & Mathematics (EPSTEM)*, 2, 422-428, International Conference on Research in Education and Science (ICRES), April 28-May1, 2018, Marmaris, Turkey.

[22] European Commission. *Industry 5.0*. Publications Office of the European Union, Luxembourg, 2021.

[23] European Commission. *The European Pillar of social rights action plan*. Publications Office of the European Union, Luxembourg, 2021.

[24] Pizoń J., Witczak M., Gola A. and Świć A. Challenges of Human-Centered Manufacturing in the Aspect of Industry 5.0 Assumptions. *IFAC PapersOnLine*, Vol. 56, No. 2, pp. 156–161, 2023.

[25] IEA (International Ergonomics Association) website. Definition of Visual Ergonomics: https://iea.cc/member/visual-ergonomics/, last access: May16, 2025.

[26] Toomingas A. Letter to the Editor. A definition of visual ergonomics. *Applied Ergonomics*, Vol. 45, pp. 1263-1264, 2014.

[27] Mattoni B., Gori P. and Bisegna F. A step towards the optimization of the indoor luminous environment by genetic algorithms. *Indoor and Built Environment*, Vol. 26, No. 5, pp. 590-607, 2017.

[28] Hemphälä H. and Eklund J. A visual ergonomics intervention in mail sorting facilities: Effects on eyes, muscles and productivity. *Applied Ergonomics*, Vol. 43, pp. 217-229, 2012.

[29] Gugliermetti F., Bisegna F. and Ferri S. Sustainable lighting design by hybrid solutions in industrial places. International *Proc. of Conference 'Light and Lighting'*, Budapest, Hungary, May 27-29, 2009, pp. 200-208.

[30] Leccese F., Salvadori G., Montagnani C., Ciconi A. and Rocca M. Lighting assessment of ergonomic workstation for radio diagnostic reporting. *International Journal of Industrial Ergonomics*, vol. 57, pp. 42-54, 2017.

[31] Aarts M.P.J., Craenmehr G., Rosemann A.L.P., van Loenen E.J. and Kort H.S.M. Light for patient safety: Impact of light on reading errors of medication labels. *International Journal of Industrial Ergonomics*, Vol. 71, pp. 145-154, 2019.

[32] Dianat I., Vahedi A. and Dehnavi S. Association between objective and subjective assessments of environmental ergonomic factors in manufacturing plants. *International Journal of Industrial Ergonomics*, Vol. 54, pp. 26-31, 2016.

[33] Hsieh M.C., Zhang Y.Q., Dong R., Lee Y.C., Yu Ni C. Use of EEG signals, cortisol secretion, and task performance to evaluate the effects of different lighting environments on concentration level in a sustained attention task. *International Journal of Industrial Ergonomics*, Vol. 92, paper number 103371, 2022.

[34] Juslén H.T., Wouters M.C.H.M. and Tenner A.D. Lighting level and productivity: a field study in the electronics industry. *Ergonomics*, Vol. 50, No. 4 pp. 615-624, 2007.

[35] Juslen H. and Tenner A. Mechanisms involved in enhancing human performance by changing the lighting in industrial workplace. *International Journal of Industrial Ergonomics*, Vol. 35, pp. 843-855, 2005.

[36] Veitch J., Donnelly C., Galasiu A., Newsham G., Sander D. and Arsenault C. IRC Research Report 299: *Office Occupants? Evaluations of an Individually controllable Lighting Systems*. National Research Council Canada, Institute for Research in Construction, Ottawa, Canada, 2010.

[37] O'Brien W. and Gunay H.B. The contextual factors contributing to occupants' adaptive comfort behaviors in offices e A review and proposed modeling framework. *Building and Environment*, Vol. 77, pp. 77-87, 2014.

[38] Despenic M., Chraibi S., Lashina T. and Rosemann A. Lighting preference profiles of users in an open office environment. *Building and Environment*, Vol. 116, pp. 89-107, 2017.

[39] Boyce P.R. *Human factors in lighting*. CRC Press, London (UK), 2003.

[40] Cajochen C. Alerting effects of light. *Sleep Medicine Reviews*, Vol. 11, No. 6, pp. 453-464, 2007.

[41] Lockley S.W. *Circadian Rhythms: Influence of Light in Humans*. In L. R. Squire (Ed.) Encyclopedia of Neuroscience (5th ed.), pp. 971-988, 2010.

[42] de Kort Y., Smolders K. Effects of dynamic lighting on office workers: First results of a field study with monthly alternating settings. *Lighting Research & Technology*, Vol. 42, No. 3, pp. 345-360, 2010.

[43] Wei M., Houser K.W., Orland B., Lang D.H., Ram N., Sliwinski M.J. and Bose M. Field study of office worker responses to fluorescent lighting of different CCT and lumen output. *Journal of Environmental Psychology*, Vol. 39, pp. 62-76, 2014.

[44] Borisuit A., Linhart F., Scartezzini J.-L. and Münch M. Effects of realistic office daylighting and electric lighting conditions on visual comfort, alertness and mood. *Lighting Research & Technology*, Vol. 47, No. 2, pp. 192-209, 2015.

[45] Wang Q., Xu H., Zhang F. and Wang Z. Influence of color temperature on comfort and preference for LED indoor lighting. *Optik*, Vol. 129, pp. 21-29, 2017.

[46] Amundadottir M.L., Rockcastle S., Sarey Khanie M., Andersen M. A human-centric approach to assess daylight in buildings for non-visual health potential, visual interest and gaze behavior. *Building and Environment*, Vol. 113, pp. 5-21, 2017.

[47] Kazemi R., Choobineh A., Taheri S., Rastipishe P. Comparing task performance, visual comfort and alertness under different lighting sources: An experimental study. *EXCLI Journal*, Vol. 17, pp. 1018-1029, 2018.

[48] Burattini C., Piccardi L., Curcio G., Ferlazzo F., Giannini A.M. and Bisegna F. Cold LED lighting affects visual but not acoustic vigilance. *Building and Environment*, Vol. 151, pp. 148-155, 2019.

[49] Chao W.C., Hong L.Y., Hsieh M.-C., Wang E.M.Y., Yang C.C., and Su L.C. Effect of correlated colour temperature and illuminance levels on user's visual perception under LED lighting in Taiwan. *Ergonomics*, vol. 63, No. 2, pp. 175-190, 2020.

[50] Zhang R., Yang Y., Fang Q., Liu Y., Zhu X., Wang M. and Su, L. Effect of Indoors Artificial Lighting Conditions on Computer-Based Learning Performance. *International Journal of Environmental Research and Public Health*, Vol. 17, pp. 2537, 2020.

[51] Wolska A., Sawicki D. and Tafil-Klawe M. *Visual and non-visual effects of light. Working environment and well-being*. CRC Press, Boca Raton, 2020.

[52] Ngarambe J., Kim I. and Yun G.Y. Influences of Spectral Power Distribution on Circadian Energy, Visual Comfort and Work Performance. *Sustainability*, Vol. 13, pp. 4852, 2021.

[53] Wirz-Justice J., Skene D.J. and Münch M. The relevance of daylight for humans. *Biochemical Pharmacology*, Vol. 191, pp. 114304, 2021.

[54] Li, Y. Fang W., Qiu H., Wang J. The non-visual effects of correlated color temperature on the alertness, cognition, and mood of fatigued individuals during the afternoon. *International Journal of Industrial Ergonomics*, Vol. 101, paper number 103589, 2024.

[55] CIE (Commission Internationale de l'Eclairage). CIE System for Metrology of Optical Radiation for ipRGC-Influenced Responses to Light. Publication CIE S 026/E:2018, CIE Central Bureau: Vienna, Austria, 2018.

[56] Brown T.M. Melanopic illuminance defines the magnitude of human circadian light responses under a wide range of conditions. *Journal of Pineal Research*, Vol. 69, paper number 12655, 2020.

[57] CIE (Commission Internationale de l'Eclairage). CIE Position Statement on Integrative Lighting Recommending Proper Light at the Proper Time, 3rd edition, CIE Central Bureau, Vienna, Austria, 2024.

[58] IWBI (International WELL Building Institute). WELL Building Standard v2. Version Q2 2024, NY, USA,2024, last access May 16, 2025.

[59] Cajochen C., Freyburger M., Basishvili T., Garbazza C., Rudzik F., Renz C., Kobayashi K., Shirakawa Y., Stefani O. and Weibel J. Effect of daylight LED on visual comfort, melatonin, mood, waking performance and sleep. *Lighting Research and Technology*, Vol 51, pp. 1044-1062, 2019.

[60] Geiger-Brown J., Rogers V.E., Trinkoff A.M., Kane R.L., Barker Bausell R. and Scharf S.M. Sleep, Sleepiness, Fatigue, and Performance of 12-Hour-Shift Nurses. *Chronobiology International*, Vol. 29, No. 2, 2021.

[61] Haidarimoghadam R., Kazemi R., Motamedzadeh M., Golmohamadi R., Soltanian A. and Zoghipaydar M.R. The effects of consecutive night shifts and shift length on cognitive performance and sleepiness: a field study, International *Journal of Occupational Safety and Ergonomics*, Vol. 23, No. 2, pp. 251-258, 2017.

[62] Esmaily A., Jambarsang S., Mohammadian F. and Houshang Mehrparvar A. Effect of shift work on working memory, attention and response time in nurses. *International Journal of Occupational Safety and Ergonomics*, Vol. 28, No. 2, pp. 1085-1090, 2022.

[63] Motamedzadeh M., Golmohammadi R., Kazemi R. and Heidarimoghadam R. The effect of blue-enriched white light on cognitive performances and sleepiness of night-shift workers: A field study. *Physiological Behaviour*, Vol. 17, pp. 208-214, 2017.

[64] Sletten T.L., Ftouni S., Nicholas C.L., Magee M., Grunstein R.R., Ferguson S., Kennaway D.J, O'Brien D., Lockley S.W. and Rajaratnam S.M.W. Randomised controlled trial of the efficacy of a blue-enriched light intervention to improve alertness and performance in night shift workers. *Occupational and Environmental Medicine,* 74(11), 792-801, 2017.

[65] Riz à Porta R., Michel S., Sterchi Y., Sauer J. and Schwaninger A. Night work, circadian rhythm, and cognitive performance: A field study with airport security screeners. *International Journal of Industrial Ergonomics*, Vol. 104, paper number 103638, 2024.

[66] ISO/CIE International Standards Organization and Commission Internationale de l'Eclairage. *ISO/CIE TR 21783; Light and Lighting—Integrative Lighting—Non-Visual Effects*. Geneva, Switzerland, 2022.

[67] Safranek S., Collier J., Wilkerson A. and Davis R. Energy impact of human health and wellness lighting recommendations for office and classroom applications. *Energy and Buildings*, Vol. 226, paper number 110365, 2020.

[68] Figueiro M., Steverson B., Heerwagen J., Yucel R., Roohan C., Sahin L., et al. Light entrainment and alertness: A case study in offices. *Lighting Research and Technology*, Vol. 52, No. 6, pp. 736-750, 2020.

[69] Zeng Y., Sun H., Lin B. and Zhang, Q. Non-visual effects of office light environment: Field evaluation, model comparison, and spectral analysis. *Building and Environment*, Vol. 197, paper number 107859, 2021.

[70] Zeng, Y., Sun, H. and Lin, B. Optimized lighting energy consumption for non-visual effects: A case study in office spaces based on field test and simulation. *Building and Environment*, Vol. 205, paper number 108238, 2021.

[71] Fostervold K. and Eilertsen D. Implementing integrative lighting in conventional office luminaires: Effects on melatonin secretion and sleepiness. *Lighting Research and Technology*, Vol. 54, No. 8, pp. 778-797, 2022.

[72] Hosseini S.N. and Ansari I.S. A daylight assessment on visual and nonvisual effects of light shelves: A human-centered simulation-based approach. *Journal of Daylighting*, Vol. 9, pp. 28-47, 2022.

[73] Gentile N., Lee E.S., Osterhaus W., Altomonte S., Amorim C., Ciampi G., et al. Evaluation of integrated daylighting and electric lighting design projects: Lessons learned from international case studies. *Energy and Buildings*, Vol. 268, paper number 112191, 2022.

[74] Bellia L., Fragliasso F., Seraceni M., Sodano G. Integrative lighting design: How to optimize visual and non-visual effects in a cell office. *Journal of Daylighting*, Vol. 10, pp. 192-203, 2023.

[75] Giovannini L., Lo Verso V.R.M., Valetti L., Daltrozo J.G., Pellegrino A. Analysis of integrative lighting through field measurements and annual daylight simulations in offices. *Lighting Research and Technology*, published online first, Vol. XX, pp. 1–30, 2025.

[76] Acosta I., Campano M.A., Leslie R. and Radetsky L. Daylighting design for healthy environments: Analysis of educational spaces for optimal circadian stimulus. *Solar Energy*, Vol. 193, pp. 584-596, 2019.

[77] Eitland E., Klingensmith L., MacNaughton P., Cedeno Laurent J., Spengler J., Bernstein A. and Allen J.G. *Schools for health: Foundations for student success*. Healthy Buildings Team at Harvard T.H. Chan School of Public Health, Boston, MA, USA, 2021.

[78] Ezpeleta S., Orduna-Hospital E., Aporta J., Luesma M.J., Pinilla I. and Sánchez-Cano A. Evaluation of visual and nonvisual levels of daylight from spectral power distributions considering orientation and seasonality. *Applied Sciences*, Vol. 11, paper number 5996, 2021.

[79] Lo Verso V.R.M., Giovannini L., Valetti L. and Pellegrino, A. Integrative lighting in classrooms: Preliminary results from simulations and field measurements. *Buildings*, Vol. 13, paper number 2128, 2023.

[80] Alkhatatbeh B. *Harmonizing visual and non-visual light effects for energy-efficient classrooms' designs*. PhD Thesis, The Pennsylvania State University, The Graduate School, 2023.

[81] Van de Putte E., Kindt S., Bracke P., Stevens M., Vansteenkiste M., Vandevivere L. and Ryckaert W.R. The influence of integrative lighting on sleep and cognitive functioning of shift workers during the morning shift in an assembly plant. *Applied Ergonomics*, Vol. 99, paper number 103618, 2022.

[82] Lo Verso V.R.M., Invernizzi S., Carlin A. and Polato A. Towards the factory of the future: A new concept based on optimized daylighting for comfort and energy saving. Proc. of IEEE 15th International Conference on Environment and Electrical Engineering, EEEIC 2015, pp. 701–706, paper number 7165250, 2015.

[83] Carlin A., Lo Verso V.R.M., Invernizzi S., Polato A. Optimised daylighting for comfort and energy saving for the factory of the future. *International Journal of Mechanics and Control*, Vol. 18, No. 1, 15-29, 2016.

[84] Todeschi V., Mutani G., Baima L. and Nigra M. Smart solutions for sustainable cities—the re-coding experience for harnessing the potential of urban rooftops. *Applied Sciences*, Vol. 10, No. 20, paper number 7112, 2020.

[85] Mutani G. and Todeschi V. Roof-integrated green technologies, energy saving and outdoor thermal comfort: Insights from a case study in urban environments. *International Journal of Sustainable Development and Planning*, Vol. 16, No. 1, pp. 13-23, 2021.

[86] Mustafaraj G., Dhoska K, Spaho E, Sulejmani A. and Koça O. Applied energy efficiency measures in industrial building by using EnergyPlus software. *International Journal of Mechanics and Control*, Vol. 25, No. 01, pp. 37-44, 2024.

[87] CEN (Comité Européen de Normalisation). Light and lighting—Lighting of workplaces—Part 1: Indoor workplaces. European Standard 12464-1:2021, Brussels, Belgium, 2021.

[88] Lo Verso V.R.M., Caffaro F. and Aghemo C. Luminous environment in healthcare buildings for user satisfaction and comfort: An objective and subjective field study. *Indoor and Built Environment*, Vol. 25, No.5, pp. 809-825, 2016.

[89] Lo Verso V.R.M., Giuliani F., Caffaro F., Basile F., Peron F., Dalla Mora T., et al. Questionnaires and simulations to assess daylighting in Italian university classrooms for IEQ and energy issues. *Energy and Buildings*, Vol. 252, paper number 111433, 2021.

[90] Almarez D. and Nawang A.A. Evaluation of compliance with the lighting standards for school workspace. *Liceo Journal of Higher Education Research*, Vol. 16, No. 2, pp. 42-63, 2020.

[91] Figueiro M.G., Bullough J.D., Thayer A., Nagare R. and Rea M.S. Supporting visual and non-visual lighting design without increasing discomfort glare or lighting power density. *Lighting Research and Technology*, Vol. 57, No. 1, pp. 5-27, 2025.

[92] Kindt S., Van de Putte E., Bracke P., Vandevivere L. and Ryckaert W. Human Centric Lighting: The impact of light on sleep and attention of factory shift workers. *European Journal of Public Health*, Vol. 30, No. 5, pp. v696, 2020.

[93] Nie J., Zhou T., Chen Z., Dang W., Jiao F., Zhan J., et al. The effects of dynamic daylight-like light on the rhythm, cognition, and mood of irregular shift workers in closed environment. *Scientifc Reports*, Vol. 11, paper number 13059, 2021.

[94] He S. and Yan Y. Impact of advance light exposure on assembly-line workers' subjective work alertness and sleep quality. *Lighting Research & Technology*, Vol. 55, No. 2, pp. 221–236, 2023.

[95] Zauner J. and Plischke H. Designing Light for Night Shift Workers: Application of Nonvisual Lighting Design Principles in an Industrial Production Line. *Applied Sciences*, Vol. 11, paper number 10896, 2021.

[96] Safranek S., Wilkerson A., Irvin L. and Casey C. Using occupant interaction with advanced lighting systems to understand opportunities for energy optimization: Control data from a hospital NICU. *Energy and Buildings*, Vol. 251, paper number 111357, 2021.

[97] Kompier M.E., Smolders K.C.H.J. and de Kort Y.A.W. A systematic literature review on the rationale for and effects of dynamic light scenarios. *Building and Environment*, Vol. 186, paper number 107326, 2020.

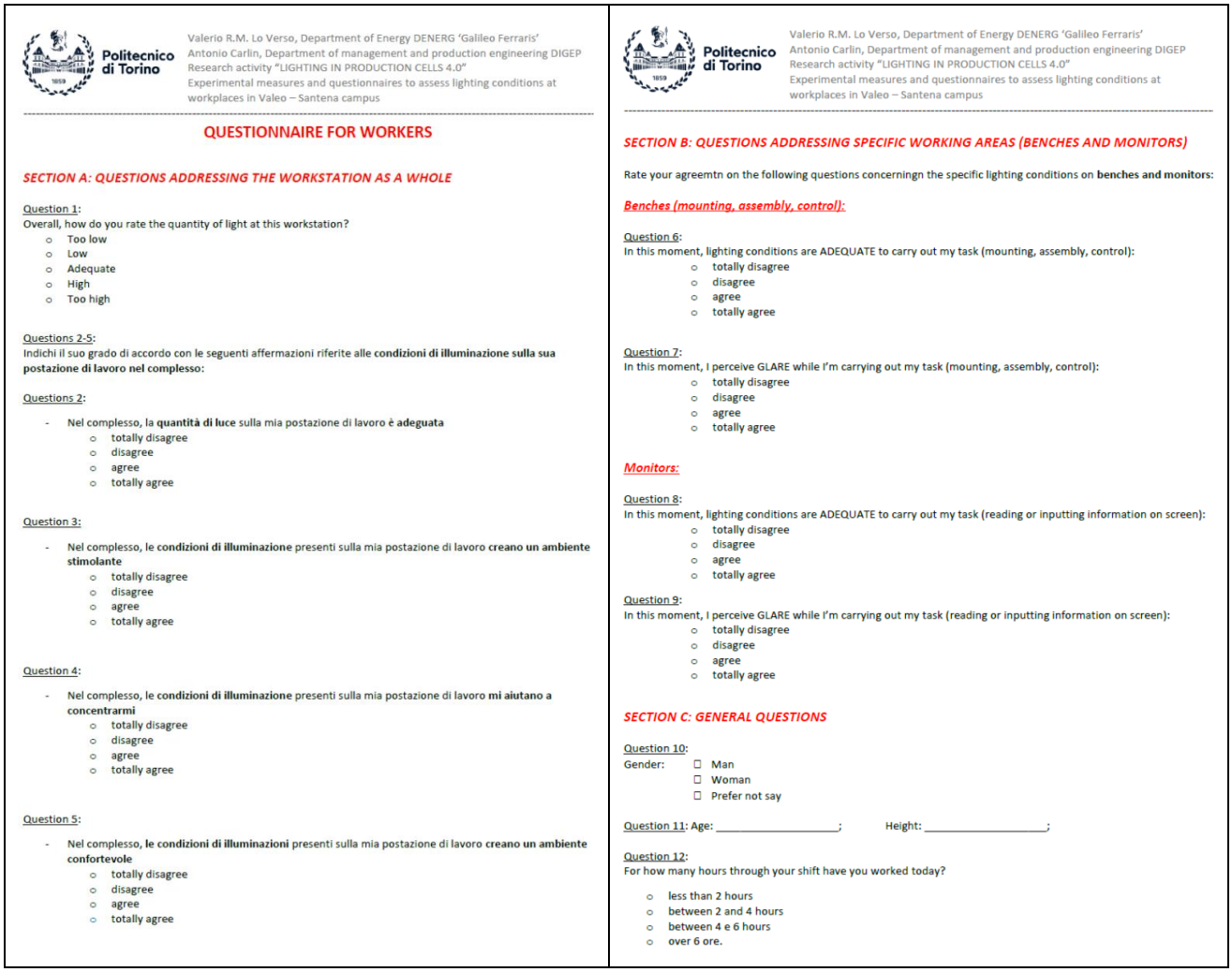
[98] Veitch J.A., Stokkermans G.M.M. and Newsham G.R. Linking lighting appraisals to work behaviors. *Environment and Behavior*, Vol. 45, No. 2, 198-214, 2013.

[99] Rockcastle S. and Mahic A. Simulating the annual energy demand to meet non-visual health recommendations from a luminaire level lighting control system. *Energy and Buildings*, Vol. 303, paper number 113772, 2024.

[100] Moore T., Carter D. and Slater A. A study of opinion in offices with and without user-controlled lighting. *Lighting Research and Technology*, Vol. 36, No. 2, 131-146, 2004.

[101] Boyce P., Veitch J., Newsham G., Myer M. and Hunter C. Lighting quality and office work: Two field simulation experiments. *Lighting Research and Technology*, Vol. 38, No. 3, pp. 191-223, 2006.

APPENDIX A: QUESTIONNAIRE SUBMITTED TO WORKERS



Politecnico di Torino

Valerio R.M. Lo Verso, Department of Energy DENERG 'Galileo Ferraris'
Antonio Carlin, Department of management and production engineering DIGEP
Research activity "LIGHTING IN PRODUCTION CELLS 4.0"
Experimental measures and questionnaires to assess lighting conditions at workplaces in Valeo – Santena campus

QUESTIONNAIRE FOR WORKERS

SECTION A: QUESTIONS ADDRESSING THE WORKSTATION AS A WHOLE

Question 1:
Overall, how do you rate the quantity of light at this workstation?
- Too low
- Low
- Adequate
- High
- Too high

Questions 2-5:
Indichi il suo grado di accordo con le seguenti affermazioni riferite alle **condizioni di illuminazione sulla sua postazione di lavoro nel complesso:**

Questions 2:
- Nel complesso, la **quantità di luce** sulla mia postazione di lavoro è **adeguata**
  - totally disagree
  - disagree
  - agree
  - totally agree

Question 3:
- Nel complesso, le **condizioni di illuminazione** presenti sulla mia postazione di lavoro **creano un ambiente stimolante**
  - totally disagree
  - disagree
  - agree
  - totally agree

Question 4:
- Nel complesso, le **condizioni di illuminazione** presenti sulla mia postazione di lavoro **mi aiutano a concentrarmi**
  - totally disagree
  - disagree
  - agree
  - totally agree

Question 5:
- Nel complesso, **le condizioni di illuminazioni** presenti sulla mia postazione di lavoro **creano un ambiente confortevole**
  - totally disagree
  - disagree
  - agree
  - totally agree

Politecnico di Torino

Valerio R.M. Lo Verso, Department of Energy DENERG 'Galileo Ferraris'
Antonio Carlin, Department of management and production engineering DIGEP
Research activity "LIGHTING IN PRODUCTION CELLS 4.0"
Experimental measures and questionnaires to assess lighting conditions at workplaces in Valeo – Santena campus

SECTION B: QUESTIONS ADDRESSING SPECIFIC WORKING AREAS (BENCHES AND MONITORS)

Rate your agreemtn on the following questions concerningn the specific lighting conditions on **benches and monitors**:

Benches (mounting, assembly, control):

Question 6:
In this moment, lighting conditions are ADEQUATE to carry out my task (mounting, assembly, control):
- totally disagree
- disagree
- agree
- totally agree

Question 7:
In this moment, I perceive GLARE while I'm carrying out my task (mounting, assembly, control):
- totally disagree
- disagree
- agree
- totally agree

Monitors:

Question 8:
In this moment, lighting conditions are ADEQUATE to carry out my task (reading or inputting information on screen):
- totally disagree
- disagree
- agree
- totally agree

Question 9:
In this moment, I perceive GLARE while I'm carrying out my task (reading or inputting information on screen):
- totally disagree
- disagree
- agree
- totally agree

SECTION C: GENERAL QUESTIONS

Question 10:
Gender:
- ☐ Man
- ☐ Woman
- ☐ Prefer not say

Question 11: Age: _____; Height: _____;

Question 12:
For how many hours through your shift have you worked today?
- less than 2 hours
- between 2 and 4 hours
- between 4 e 6 hours
- over 6 ore.

ISSN 1590-8844
International Journal of Mechanics and Control, Vol. 26, No. 01, 2025
https://doi.org/10.69076/jomac.2025.0016

VIBRATION PROTECTION SYSTEM OF CONSTANT ACCELERATION OF THE OPERATOR'S SEAT

M S Korytov*, V S Shcherbakov*, and I E Kashapova*

* The Siberian State Automobile and Highway University

ABSTRACT

Heavy equipment vehicles operators are exposed to harmful levels of vibration in their daily work. In this regard, antivibration systems for operators' seats are of great importance as the last stage of vibration protection. The objective of the research is to develop a mathematical model of the antivibration system of the operator's seat, providing a given acceleration of the vibration isolated mass. The input parameters in the algorithm of the mathematical model of the proposed antivibration system were the local coordinate of the seat displacement from its own zero position and its first derivative. The seat acceleration in the fixed coordinate system was set discretely and had three values. The local coordinate was returned to the specified range. The model is implemented as a Simulink block diagram. Besides, some results obtained at the low-frequency harmonic vibrations of the seat base are presented. A comparison is made with a traditional viscoelastic antivibration system. The seat acceleration amplitudes, the seat coordinates in the fixed coordinate system and the local coordinates of the antivibration mechanism have been used as the comparison parameters. Systems with low stiffness coefficients are the most effective among the traditional antivibration systems. The intended application of the developed model is to evaluate and compare the effectiveness of various antivibration systems.

Keywords: vibration protection, isolation, acceleration, displacement.

1 INTRODUCTION

Among the adverse workplace factors, mechanical vibrations and shocks are among the most dangerous types of impacts that workers are usually exposed to. This problem is especially relevant for operators of heavy equipment vehicles [1, 2], in particular, construction, road and lifting vehicles [3, 4]. Vibrations are mainly transmitted to the operator through the car seat and cabin floor [5, 6]. Heavy equipment vehicles actively interact with the supporting surface and operating environments. Moreover, not only an asphalted road but also a dirt road and off-roads often act as the supporting surface [7, 8]. This causes low-frequency vibration effects and impacts during transportation of materials, work with soil, single-piece cargoes, etc. [9, 10].

Contact author: M S Korytov[1], V S Shcherbakov[1], I E Kashapova[1]

[1]Mira Pr. 5, Omsk 644080 Russian Federation.

E-mail: kms142@mail.ru

Drivers and passengers of heavy vehicles are also exposed to vibration effects while driving [11, 12]. At the same time, the low frequency range is most important from the point of view of ensuring the comfort of the operator and passengers. The transmission points of vibrations, shocks and impacts are located at the points where the machine cab is connected to the base chassis, as well as the operator's seat to the cabin [5, 6]. Relatively simple antivibration mounts are generally installed at the attachment points of cabins, while the design of antivibration seat systems can be much more complex. Antivibration seat systems, being the last stage of the operator protection, are becoming extremely important. Passive and active vibration isolation systems are used for operator's seats. Passive vibration isolation systems do not use external energy supply and often have a simpler design than active ones. In active systems, electromechanical effects and corresponding transducers are typically used, which makes it possible to limit not only simple but also complex spatial vibrations of multi-mass systems [13] and spatial vibrations of the vibration isolated mass around several axes of rotation [14]. Active antivibration systems also provide, if necessary, to take into account flexible connections between

the elements of mechanical systems [15]. The extensive capabilities of active vibration isolation systems are partially compensated by their disadvantages in the form of relatively high complexity and cost, which reduces the reliability of such systems. Despite this, electromagnetic vibration protection systems are already widely used, in particular in the seats of drivers and passengers of heavy vehicles [16].

2 THE RESEARCH OBJECTIVE

Mathematical modeling is widely used in the development of new and improved designs of antivibration systems for road vehicles operators' seats. It is mathematical modeling which is the key stage in conducting any scientific research, since it makes possible to consider a variety of options for combining the parameters and helps to avoid high costs of resources for direct field study of a complex subject matter. The idea of this research is to find a mathematical description and possibility of conducting a study of such a vibration isolation system of the operator's seat, which would have the perfect properties in terms of minimizing the impacts on the vibration-protected mass of the operator. The efficiency criterion of the vibration protection system is the absolute acceleration of the vibration-protected mass, which should not exceed the maximum set value of $a_{\max}$. It is necessary to develop the mathematical model and its software implementation ensuring the vertical movement of the seat with the operator at the absolute acceleration being equal to $\pm\, a_{\max}$, with specified movements of the seat base, i.e. the operator's cabin. Standard impacts have been considered as a typical example: harmonic vibrations of the base with the amplitude A_{mp} and frequency f. We studied the simulation case when the absolute acceleration of the seat with the operator in the fixed coordinate system with any movements of the seat base, equals to the following values $\left[-a_{\max};\ 0;\ a_{\max}\right]$. This compensates for the local deformation of the vibration protection mechanism.

3 MATERIALS AND METHODS

The developed mathematical model is a vibration isolation system of constant accelerations. It is assumed that any parameters of the dynamical system under consideration can be measured and their values are known at any given time. The current values of a number of parameters are necessary both for modeling and implementing the proposed system. The second assumption has been made that vibrations of the seat with the operator do not affect the movements of the seat base, i.e. the dynamic system of the seat with kinematic excitation of its base vibrations has been examined. The third assumption was that the drive of the proposed antivibration system of constant accelerations is capable of providing the absolute set acceleration of the seat at the current time, regardless of the seat weight, its current coordinates and velocity. Therefore, the acceleration of the seat in the fixed coordinate system has been directly set in the model. The practical implementation of the vibration isolation system of constant accelerations has not been examined in this article, but the principles of its performance allow it to be classified as an active vibration isolation system. It can be implemented on the basis of the electromechanical or hydraulic elements and corresponding sensors. The measured parameters of the dynamic system of the seat with a movable base, necessary for the mathematical description of the vibration isolation system of constant accelerations, are the local coordinate of the antivibration mechanism displacement from its own mid or zero position y_1 and its first time derivative

$$\dot{y}_1 = \frac{dy_1}{dt} \tag{1}$$

In addition to the above-mentioned parameters, the current values of the seat absolute coordinate in the fixed coordinate system y, and/or its derivatives $\dot{y}$ and $\ddot{y}$ can also be required for the practical implementation.

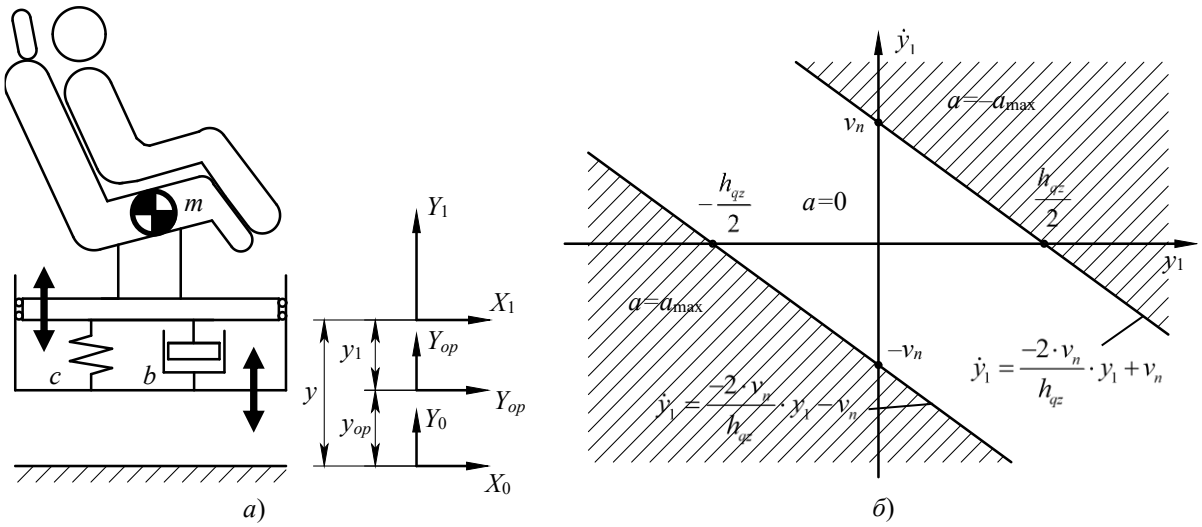
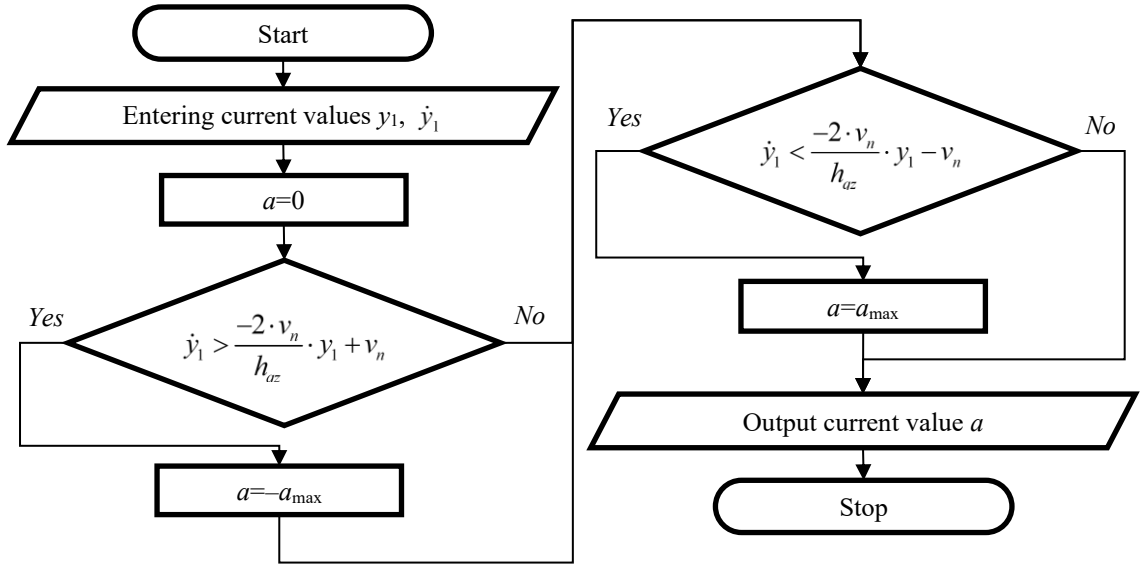
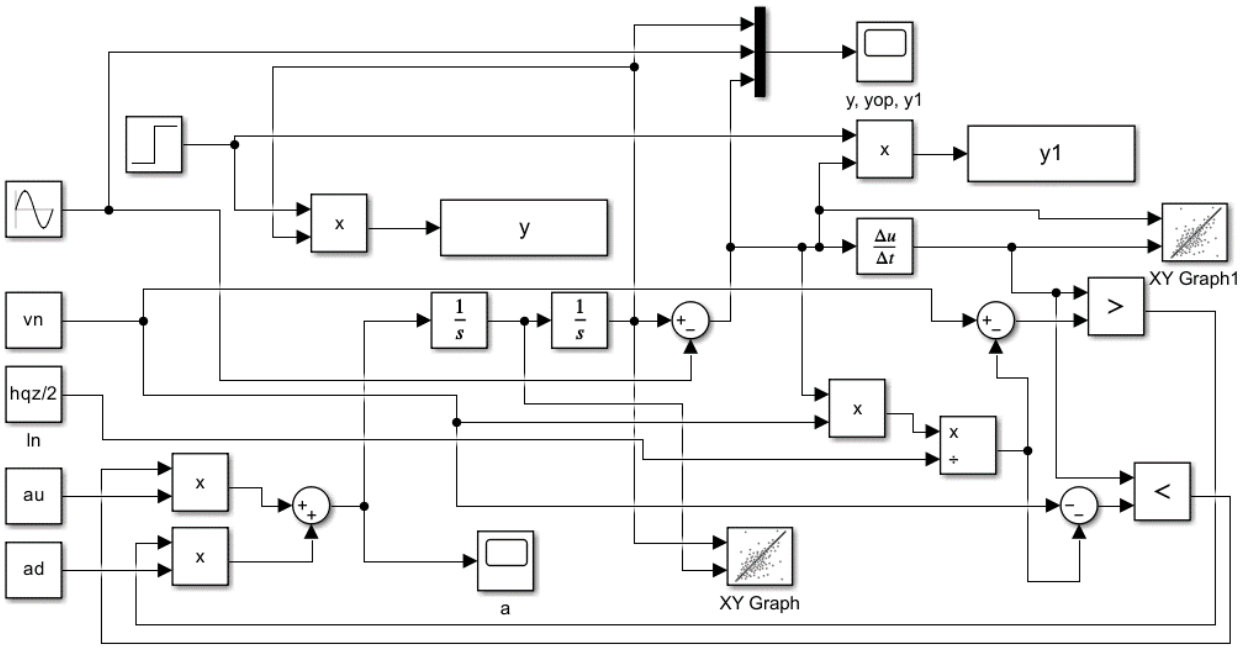


Figure 1 Linear coordinates of the dynamic seat system (a) and the proposed scheme for the discrete setting of the absolute seat acceleration, depending on the values combinations the seat local coordinate and its first derivative.



a)



b)

Figure 2 A block diagram of the algorithm for calculating the current value of the absolute seat acceleration (a) and a mathematical model of the vibration protection system of constant accelerations in the form of a Simulink block diagram (b).

The coordinates y and y_1 are related by the following dependence:

$$y_1 = y - y_{op}, \quad (2)$$

where y_{op} is the displacement of the coordinate system X_{op} Y_{op} connected to the seat base relative to the fixed coordinate system X_0 Y_0 (Fig. 1(a)). The accepted scheme for setting the value of the seat absolute acceleration a, depending on the values combinations of the seat local coordinate y_1 and its first derivative $\dot{y}_1$ is shown in Fig. 1(b).

The scheme implements the principle of discrete setting the absolute acceleration of the seat, which can take three values: $a \in [-a_{max};\ 0;\ a_{max}]$. The scheme has been formed in such a way as to provide the following values of the absolute acceleration function of the seat at a number of characteristic points of the values combination of two arguments:

1. If the local coordinate y1 (deformation) of the vibration protection mechanism of the seat is within a certain range

$y_1 \in \left[-h_{qz}/2;\ \ h_{qz}/2\right]$ and the rate of its change is zero, then the absolute acceleration of the seat should be zero.

2. If the rate of change of the local coordinate of the vibration protection mechanism of the seat is within a certain range of insensitivity $\dot{y}_1 \in \left[-v_n;\ \ v_n\right]$ and the local coordinate y_1 is zero, then the absolute acceleration of the seat should be zero.

3. If the local coordinate y_1 is greater than a certain positive value $(h_{qz}/2)$ and its velocity is greater than or equal to zero (the local coordinate y_1 increases, i.e. the base shifts down relative to the seat), then the absolute acceleration of the seat should be negative.

4. If the local coordinate y_1 is lower than a certain negative value $(-h_{qz}/2)$ and its velocity is lower than or equal to zero (the local coordinate y_1 decreases, i.e. the base shifts up relative to the seat), then the absolute acceleration of the seat should be positive.

The scheme implementation ensures returning the local coordinate value to the range of $y_1 \in \left[-h_{qz}/2;\ \ h_{qz}/2\right]$ when it goes beyond the specified range. Where, h_{qz} is the size of a section similar to the section of quasi-zero stiffness in the known vibration protection systems [6]. In this case, the absolute accelerations of the seat with the operator in the fixed coordinate system $X_0\ Y_0$ should not exceed $a_{\max}$.

The equations of the inclined lines in Fig. 1(b) have the following form:

$$\dot{y}_1 = \frac{-2 \cdot v_n}{h_{qz}} \cdot y_1 \pm v_n . \tag{3}$$

The positive sign in formula (3) corresponds to the upper straight line, while the negative sign corresponds to the lower one. The algorithm for calculating the current value of the absolute seat acceleration a as a function of the current values y_1 and $\dot{y}_1$ is presented in Fig. 2(a). The mathematical model implementing the specified algorithm is shown in Fig. 2(b) as a Simulink MATLAB block diagram. In addition to the comparison and mathematical blocks, it contains two *Integrator* (1/s) blocks that calculate the velocity $\dot{y}$ and displacement y of the seat in the fixed coordinate system based on the current values of its absolute acceleration a. In constants blocks of the model, the absolute upward and downward accelerations of the seat took the following values: au=+$a_{\max}$, ad= –$a_{\max}$, respectively.

In the case under consideration of piecewise constants, instantaneously changing values of the absolute seat acceleration a, its current velocity and displacement have been calculated using the following analytical dependencies:

$$\dot{y} = \dot{y}_0 + t \cdot a\ ;\ y = y_0 + t \cdot \dot{y}_0 + \frac{a \cdot t^2}{2}\ , \tag{4}$$

where $\dot{y}_0$, y_0 are the absolute velocity and displacement of the seat at the initial time of a separate time interval at which acceleration is $a = \ddot{y}$=const .

The base harmonic vibrations have been set in the *Sine Wave* block as a sinusoidal function:

$$y_{op} = A_{mp} \cdot \sin\left(t \cdot w\right), \tag{5}$$

where $w = 2 \cdot \pi \cdot f$.

The described vibration protection system of constant accelerations has been compared, as an example, with a traditional antivibration system which includes the elastic and damping elements. It also had one translational degree of freedom relative to the seat base. For the traditional system, the amplitude of the absolute seat coordinate $y_{\max}$, the amplitude of the local coordinate $y_{1\max}$ and the amplitude of the absolute acceleration $a_{\max}$ have been calculated using the analytical dependencies given in [6].

4 EXPERIMENTAL RESULTS

Figure 3(a), (b) shows the time dependences of the coordinates y, y_1, y_{op} of the vibration protection system of constant accelerations, obtained at low-frequency harmonic vibrations of the seat base. Figure 3(b) is an enlarged fragment of Fig. 3(a) for the time period from 40 to 50 seconds. This is a steady oscillation mode. The parameters of the vibration protection system and base vibrations as an example took the following values: the boundary local velocity is v_n=0.005 m/s, the size of the dead zone or quasi-zero stiffness is h_{qz}=0.07 m, the absolute acceleration of the seat is $a_{\max}$=1 m/s^2, the amplitude of the seat base vibrations is A_{mp}=0.06 m, the vibration frequency of the seat base is f=1 Hz. The maximum time step for numerical integration of the Simulink model was 10^{-4} s, which ensured high simulation accuracy. Figure 3(c) shows the functional dependences of the amplitude $y_{\max}$ of the absolute seat coordinate in the fixed coordinate system and the amplitude of the local coordinate $y_{1\max}$ on the stiffness coefficient of the traditional antivibration system c. The horizontal lines indicate the same amplitudes for the proposed vibration protection system for comparison. Figure 3(d) shows the functional dependences of the amplitude $a_{\max}$ of the absolute seat acceleration in the fixed coordinate system on the stiffness coefficient of the traditional vibration protection system c. The horizontal lines indicate the same amplitude $a_{\max}$ for the proposed vibration protection system for comparison. When studying the traditional antivibration system, its parameters took the following values: the operator and seat weight is m=100 kg, the resistance coefficient is b=50 N/(m/s). The stiffness coefficient c varied within $c \in \left[10;\ \ 20000\right]$ N/m, at 10 N/m intervals. Figure 3(e) shows the functional dependences $y_{\max}$ and $y_{1\max}$ on the amplitude of harmonic vibrations of the seat base A_{mp}. Fig. 3(f) shows the functional dependencies of $a_{\max}$ on A_{mp}. The horizontal lines also indicate the corresponding function values for the proposed vibration protection system. The argument value A_{mp} varied within $A_{mp} \in \left[0.0025;\ \ 0.15\right]$ m, at 0.0025 m intervals. When A_{mp} was varied, the stiffness coefficient of the traditional system took a relatively small value of c=1000 N/m. This value brings the traditional system closer to the effect of quasi-zero stiffness. Such antivibration systems are considered effective in protecting against low-frequency vibrations, which is partially confirmed by the data in Fig. 3(c, d).

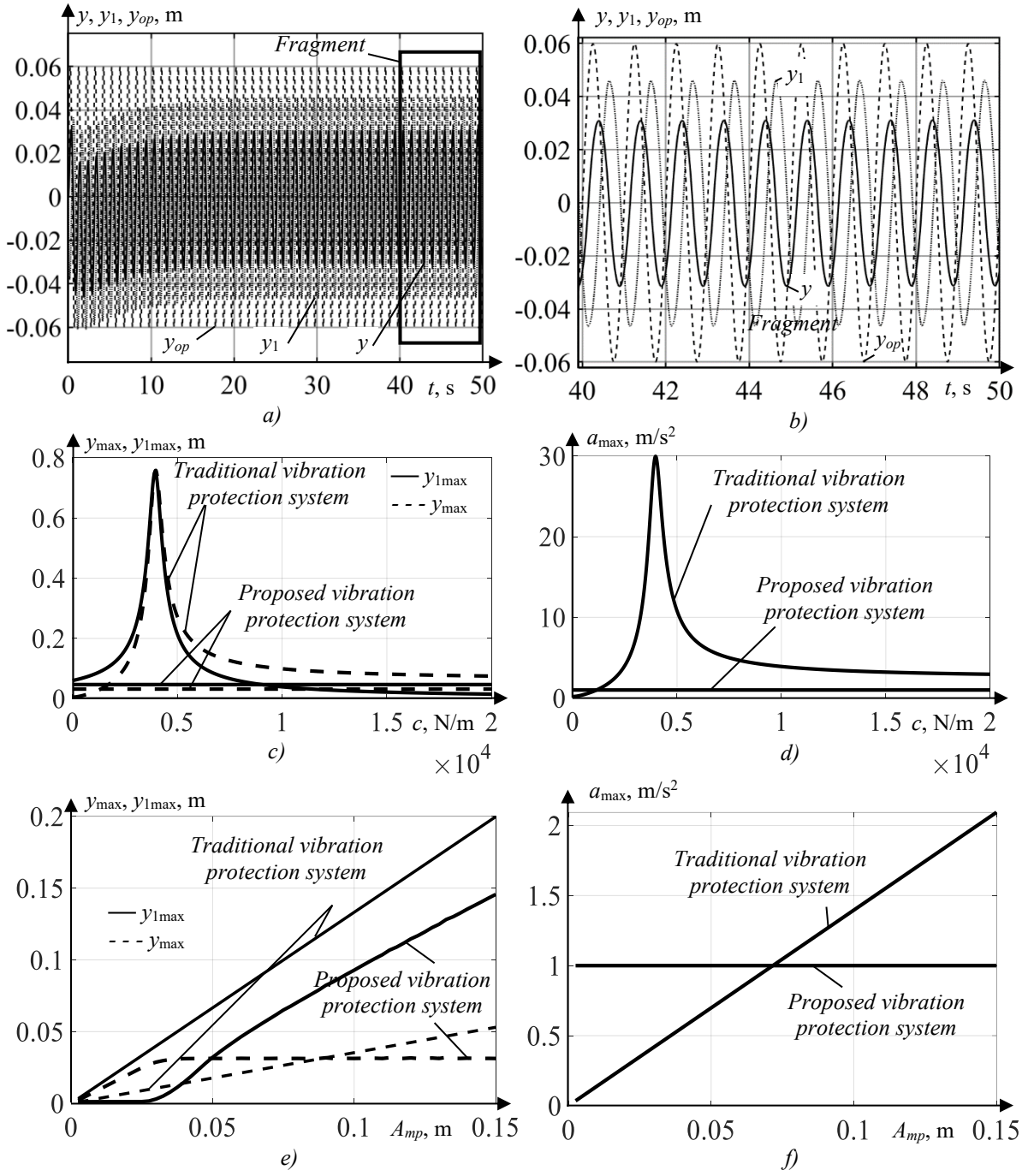


Figure 3. Simulation results: (a) and (b) are the time dependences of the linear coordinates of the proposed vibration protection system; (c) and (d) are the dependences of the coordinates and acceleration amplitudes on the stiffness coefficient of the traditional system; (e) and (f) are the dependences of the coordinate and acceleration amplitudes on the amplitude of the seat base vibrations for the proposed and traditional systems.

5 DISCUSSION OF A POSSIBLE EXPERIMENTAL VERIFICATION OF THE MODEL ACCURACY.

Physical implementation of the proposed vibration protection system in the form of an experimental stand, in the future of development of the described research topic, will be necessary to assess the accuracy of the mathematical model of the proposed system. It will require the use of the following equipment, as one of the possible options. This is an electrodynamic vibration stand that provides sinusoidal vibrations of the vibration table with a given frequency. A hydraulic system in the form of a double-acting hydraulic cylinder with a hydraulic motor, a hydraulic motor drive (electric motor) and a hydraulic distributor with direct electromagnetic control. An elastic element in the form of a

compression spring. Acceleration sensors (accelerometers), as well as displacement sensors. A recording hardware complex and a control personal computer. Finally, a vibration-protected object in the form of a seat with an operator or a dummy replacing the operator. A hydraulic drive can be proposed first of all, since it has a very high response speed. But it is also possible to use a pneumatic drive and other types of drives in the system and the stand. The movement of the stand objects must be limited by vertical guides. The objects will form a chain: vibration table - hydraulic cylinder - spring - seat. Monitoring the length of the spring using a length sensor will allow the control signal to be generated for the hydraulic distributor using a tracking algorithm. Tracking movements of the hydraulic cylinder rod in dynamics will ensure a spring length close to the specified one, taking three discrete values. This will ensure a constant force acting on the seat and a constant specified acceleration of the seat, taking three discrete values in the described mathematical model. Signals from the acceleration sensors installed on the vibration table and the seat will be used not for the hydraulic cylinder control system, but for the data collection system, which will allow an assessment of the actual accelerations of the seat and its base.

6 CONCLUSIONS

The conducted research is considered by the authors as an attempt to build a mathematical model of the vibration protection system, ideal in terms of limiting the seat acceleration. The analysis of simulation data shows that the proposed vibration protection system of constant accelerations in most simulation cases provides significantly lower oscillation amplitudes of both the absolute coordinate of the seat and the local coordinate of the antivibration mechanism deviation from the zero position. The maximum value of the seat absolute acceleration of the proposed vibration protection system is equal to a given relatively small value of 1 m/s^2 in the case under study.

When the stiffness coefficient is varied, the amplitude of the seat absolute acceleration in the traditional antivibration system is significantly higher than that in the proposed vibration protection system, with the exception of traditional systems with a low stiffness coefficient less than 1150 N/m. Furthermore, the absolute coordinate amplitude of the seat with the operator in the traditional vibration protection system is less than that in the proposed one, but only at the low values of the stiffness coefficient, less than 1343 N/m. Nevertheless, the local coordinate amplitude of the displacement of the vibration protection mechanism from its own zero position in the traditional antivibration system is less than that in the proposed one, only with relatively high values of the stiffness coefficient, over 9,000 N/m. However, with high rigidity, the acceleration amplitude of the traditional system is significantly higher than that of the proposed one. Therefore, summarizing the results obtained by varying the stiffness coefficient of the traditional antivibration system and comparing it with the proposed vibration protection system of constant accelerations, the following conclusions were made. The traditional antivibration system can be more effective than the proposed one for selected indicators, but not in all three indicators at once at the low and high values of the stiffness coefficient. The three minimized parameters include the amplitudes of the absolute coordinate, local coordinate and absolute acceleration. While the traditional vibration protection systems with the effect of quasi-zero stiffness and those close to them give lower amplitudes of the absolute seat coordinate and acceleration, still they have an amplitude of the local coordinate significantly higher than that of the proposed system. Besides, as the stiffness of the traditional system approaches zero, the uncontrolled drift of the local coordinate can increase, in particular, under the different from harmonic influences. This will require the vibration protection system with quasi-zero stiffness of sections limiting uncontrolled movements in the static power characteristic [6]. However, the presence of the above-mentioned sections, in turn, can potentially have a significant, including negative impact on the indicators used for evaluation in this research, for example, to increase the maximum acceleration of the seat. It is beyond the scope of this paper and requires separate research. It should be noted that the partial advantage of the traditional vibration protection system with the effect of quasi-zero stiffness over the proposed system under the ideal harmonic influences can not be present with other, including more complex, types of impacts. When varying the amplitude of the seat base vibrations, the proposed vibration protection system always surpasses the traditional antivibration system, even close to quasi-zero, according to the criterion of minimizing the local coordinate. While with an increase in the amplitude of the seat base vibrations, it predominates in all three comparison parameters. The field of application of the proposed vibration protection system of constant accelerations can be as follows: it can be used to compare the efficiency of the traditional and promising vibration protection systems, including those with quasi-zero stiffness or close to them, as well as with piecewise linear or nonlinear static force characteristics. It is assumed that the proposed vibration protection system of constant accelerations will have the most significant advantages under the low-frequency influence with a high amplitude and strong impacts.

REFERENCES

[1] de la Hoz-Torres M.L., Aguilar A.J., Ruiz D.P., Martínez-Aires M.D. Whole Body Vibration Exposure Transmitted to Drivers of Heavy Equipment Vehicles: A Comparative Case According to the Short- and Long-Term Exposure Assessment Methodologies Defined in ISO 2631-1 and ISO 2631-5. *International Journal of Environmental Research and Public Health*, Vol. 19, No. 9, pp. 5206, 2022.

[2] Jiang, R., Rui, X., Zhu, W., Wei, M., Zhu, H., Gu, L. Vibration Reduction of Tracked Vehicle-Seat-Occupant System Based on Two-Stage Magnetorheological Suspension. *Proceedings of the*

2nd International Conference on Mechanical System Dynamics. ICMSD 2023. *Lecture Notes in Mechanical Engineering*, 2024.

[3] Korchagin P., Teterina I., Korchagina E. Road roller operator's vibroprotection system improvement. *Journal of Physics: Conference Series*, Vol. 1791, pp. 012012, 2021.

[4] Robinah N., Safiki A., Thomas O., Annette B. Impact of road infrastructure equipment on the environment and surroundings. *Global journal of environmental science and management-GJESM*, Vol. 8, No. 2, pp. 251-264, 2022.

[5] Seong-Hwan Kim, Dal-Seong Yoon, Gi-Woo Kim, et al. Road traveling test for vibration control of a wheel loader cabin installed with magnetorheological mount. *Journal of Intelligent Material Systems and Structures*, pp. 1045389X20953900, 2020.

[6] Korytov M.S., Shcherbakov V.S., Kashapova I.E. Investigation of dynamic characteristics of the vibration isolation system for operators' seats. *International Journal of Mechanics and Control*, Vol. 24, No. 02, pp. 19-26, 2023.

[7] Peng H., Yanchun Y., Weijia X., et al. Vibration modelling and testing of off-road vehicle incorporating coupled roll and pitch vibrations. *Biosystems Engineering*, Vol. 240, pp. 111-122, 2024.

[8] Hu K., Zhang W., Li K, et al. Vibration analysis and optimization of tracked tractor frame based on modal programming method. *Journal of Chinese Agricultural Mechanization*, Vol. 42, No. 8, pp. 121-126, 2021.

[9] Galdin N.S., Semenova I.A., Galdin V.N. Analysis of the striker stroke impact on the hydropneumatic impact devices energy performance. *Journal of Physics: Conference Series*, Vol. 1260, No. 11, pp. 112010, 2019.

[10] Lynas D., Burgess-Limerick R. Whole-body vibration associated with dozer operation at an Australian surface coal mine. *Annals of work exposures and health*, Vol. 63, No. 8, pp. 881-889, 2019.

[11] Vella A., Vigliani A., Tota A., Lisitano D. Experimental Ride Comfort Analysis of an Electric Light Vehicle in Urban Scenario. *SAE Technical Paper*, No. 01, pp. 1086, 2020.

[12] Theunissen J., Tota A., Gruber P., Dhaens M., Sorniotti A. Preview-based techniques for vehicle suspension control: a state-of-the-art review. *Annual Reviews in Control*, Vol. 51, pp. 206-235, 2021.

[13] Tashakori, S., Fakhar, M., Suppression of Torsional Vibrations in Drilling Systems by Using the Optimization-Based Adaptive Back-Stepping Controller, ISSN 1590-8844. *International Journal of Mechanics and Control*, Vol. 20, No. 01, pp. 106-110, 2019.

[14] Duong, Q.K, Hubinsky, P., Shaping Nurbs Curve Based on Genetic Algorithms for Vibration Reduction, ISSN 1590-8844. *International Journal of Mechanics and Control*, Vol. 18, No. 02, pp. 85-90, 2017.

[15] Barjuei, E.S., Gasparetto, A., Predictive Control of Spatial Flexible Mechanisms, ISSN 1590-8844. *International Journal of Mechanics and Control*, Vol. 16, No. 01, pp. 85-96, 2015.

[16] Xie P., Che Y., Liu Z. and Wang G., Research on Vibration Reduction Performance of Electromagnetic Active Seat Suspension Based on Sliding Mode Control. *Sensors*, Vol. 22, pp. 5916, 2022.

ISSN 1590-8844
International Journal of Mechanics and Control, Vol. 26, No. 01, 2025

https://doi.org/10.69076/jomac.2025.0017

CARDIOVASCULAR AND METABOLIC ENGAGEMENT AFTER AN ENDURANCE RACE IN PILOTS DRIVING MOTORBOATS ELECTRICALLY POWERED BY GREEN ENERGY

Andrea Manuello Bertetto[1], Filippo Tocco[2,10], Gaia Bellomi[2], Livio Mulargia[2], Michele Ruggiu[2,10], Marco Palmas[2,10], Myosotis Massidda[2], Giovanna Ghiani[2], Fernanda Velluzzi[2], Salvatore Melis[2,10], Andrea Fois[3], Antonio Hector Dell'Osa[4], Angelo Cerina[5], Ugo Bertelli[6], Mauro Giovanni Carta[7], Pietro Roberto Bianco[8], Alberto Concu[9,10]

[1]Department of Mechanical and Aerospace Engineering, Politecnico di Torino, Turin, Italy
[2]Department of Medical Sciences and Public Health, Sports Medicine and Nutrition Units, University of Cagliari, Italy
[3]Nomadyca Ltd, Remote Biosignals Acquisition Unit, Mulago Hospital, Kampala, Uganda
[4]Laboratorio de Electrónica Aplicada y Biomedicina, Universidad Nacional de Tierra del Fuego, Ushuaia, Argentina
[5]Acquaforte Thalasso & Spa Medical Team, Forte Village Resort, Santa Margherita di Pula, Cagliari, Italy
[6]Blue Matrix Asd, Cagliari, Italy
[7]Department of Medical Sciences and Public Health, Psychiatric and Psychosomatics Unit, University of Cagliari, Italy
[8]Hewlett-Packard Enterprise, Sofia, Business Park, Mladost 4, Bulgaria
[9]AC Technologies Ltd, Bioimpedance Devices Manufacturing, Cagliari, Italy
[10]Sporting Life&Medicine Lab, Sardegna Ricerche, Agency for Research, Innovation and Technology Development, Italy

ABSTRACT

During the Sardinia Innovative Boat Week, held in Olbia, Italy, in September 2024, several teams of students and university researchers, competed with self-built prototypes in a motorboats endurance race, i.e. the a Ton's Race, lasting 4 hours and dedicated to electrically powered boats. Just before and after the race, 5 pilots: 4 males and 1 female ageing 28.8 ± 17.7 years, were engaged for several non-invasive anthropometric, psychometric, metabolic and cardiovascular tests (these latter by an Authors self-built electrical impedance cardiograph) through which was found post-race falling in the body mass (-0.6 kg) with statistically significant reduction in ventricle preload (-21%) and heart rate (-13%), and increases in ventricle ejection velocity (23%), after load (12%), heart mechanical efficiency (23%). Experimental results outline for the first time a biomechanical functional model of the main adaptations of the organs recruited in this new and green motor boats sports activity.

Keywords: motor boat races, electrical powered engines, electrical impedance cardiography, bioenergetics

1 INTRODUCTION

During the Sardinia Innovative Boat Week held in Olbia, Italy, in September 2024, several teams of students and university researchers, coming from various European countries, met in this pleasant seaside location with the common goal of concentrating scientific skills, technologies and human resources, giving life to a competitive event: a race dedicated to electric boats.

Contact authors: Alberto Concu[1], Andrea Manuello Bertetto[2]

[1]AC Technologies Ltd, Via Pais 12-09128 Cagliari, Italy
[2] Politecnico di Torino, DIMEAS, Corso Duca degli Abruzzi 2424-10129 Torino, Italy
E-mail: aconcu44@gmail.com, andrea.manuello@polito.it

This sport-technological event was typically characterized by its efficiency for which electric mobility is proposed as one of the best systems to achieve a substantial balance.
This event held in Olbia, linking the competitions between prototypes of motor boats, built by young engineers from prestigious universities with a strong push towards increasingly stringent objectives aimed at reducing the environmental impact of the transport system, paid a growing focus on greater energy to meet the pressing need to implement the ecological transition also at sea, has certainly proved to be a winning idea.
In fact, conceived by laboratories and spin-offs of international academic origin and mostly piloted by researchers and university students, these revolutionary boats were the expression of a vision of the future, in which environmental protection and innovation must be inseparable.

In addition to all of what above, it should not be overlooked that sport's performances at sea with these characteristics certainly require a high level of physical and mental efforts from the pilots, also in considering what observed in previous experiments concerning of staying at sea for several hours on small boats. In fact, in a previous study [1] it has been shown that in sailors exposed 2.5 hours in the sea with a wind speed of 24 $km\ h^{-1}$ and an air temperature of 7 $°C$, there was a significant reduction of body mass, mainly caused by water loss, together with a fall in the blood electrolytes concentrations.
Furthermore, previous anxiety-related conditions, which these motorboat pilots may have been interested, could have affected neurovegetative homeostasis during the race with performance effects mainly of cardiometabolic nature. In this sense, possible increases in cortisol release when driving boats powered by fossil fuel engines should not be overlooked, as this type of engine produces loud noises and strong mechanical vibrations, both of which are known to give rise to increases in the blood concentration of this hormone with cardiovascular excitatory activity [2, 3, 4].
Taking advantage of this exceptional event where a large number of pilots of electric motor boats find themselves all together competing in endurance nautical performances, the goal of better knowing which body systems adjustments occur in athletes dedicate to performing long lasting motor boat races in the sea, electrically powered, is the goal to be achieved here. In this aim, in a group of pilots voluntarily engaged the after race changes in anthropometric, hemodynamic and metabolic variables were compared with those occurred before race.

2 METHODS

2.1 SUBJECTS

Boat's pilots engaged in this study were 5 of which 4 males and one female, ageing 28.8 ± 17.7 years (lower age: 16 years, higher age: 60 years); their height and body mass were respectively 172 ± 3.5 cm and 67.1 ± 5.9 kg. Just before experimental engagement, for each chosen pilot a team's physician proceeded to an anamnestic interview from which was ascertained his suitability for this research. They were then informed about the experimental procedure and all declared their informed consent.

2.2 THE BOATS

All engaged pilots competed in the Uniclass Category, of which a boat is shown in figure 1, being catamaran hulls with a maximum weight of 250 kg of which 90 kg including pilot size. The hull dimensions were: length 5.5 m, width 2.5 m with 40 cm over water. The organization of the motorboat event provided innovative ready-to-use hulls, i.e. the so called Uniclass Category, for the races upon request. These catamarans are the result of an innovative design and boat construction technology characterized by standards of lightness and strength.
They are made with an owned combination of carbon fibres and hemp that ensures a robust structure and lightweight in vessels. All teams were required to install their propulsion units and control systems on these hulls and competing using only clean energy sources such as electrical batteries. The electrical motors developed by the various teams were powered with voltages ranging between 48 V and 96 V.



Figure 1 Typical boat Uniclass prepared by one of the crews participating in the Olbia's competition with its pilot positioned in the cockpit while preparing to start an endurance race. A rechargeable battery bank is positioned behind the cockpit.

2.3 EXPERIMENTAL PROTOCOL

All the 5 chosen pilots were tested just before (T1) and after (T2) being they engaged in a Ton's Race, lasting 4 hours, travelling in a circular motion several times in the stretch of sea in front of the port of Olbia, in Italy.

2.3.1 Clinical and functional evaluations

By a portable electronic scale (INN-117, Innoliving Ltd, Italy) and a common wall tape measure, in both T1 and T2 tests were recorded from each subject, while standing barefoot, the height in cm and the body mass (BM) in kg [5].
Furthermore, after having carried out the anthropometric measurements and while the pilots were seated, the following clinical-functional measurements were also not invasively made on them:

- systolic (SABP) and diastolic (DABP) arterial blood pressures measurement, in *Torr*, using a commercial automatic cuff sphygmomanometer (Omron m3, Netherlands), from both which the mean arterial blood pressure was also calculated as: MABP = DAP + 1/3 (SAP + DAP) [6, 7];
- peak of the expiratory flow (PEF) production, in $l\ min^{-1}$, using a special graduated cylinder inserted through mouth in which the subject produced a maximum air outflow (Mini-Wright, Clement-Carke Int. UK) [8];
- maximum force expression during the handgrip maneuver (HGM), measured in kg, carried out with the dominant hand, using a dedicated, commercial device (Gripx, Vatmaster Consulting, Germany) [9];
- urine specific density (SDU) measured by means of reactive strips (Combi Screen, Germany) [10];
- body temperature (BT), measured in $°C$, by an electronic thermometer for tympanic assessments (Gima, Italy) [11].

2.3.2 Cardiodynamic evaluations

By means of a self-built portable electrical impedance cardiograph (EIC), already validated and tested [12, 13, 14], which was supplied by an autonomous power bank, both beat-to-beat thoracic electrical impedance (Zt) and electrocardiogram (ECG) tracks were assessed from each engaged subject. Their thorax was connected to the EIC through 4 couples of disposable electrodes positioned within the ideal truncated cone having the lower base lying on the plane of the xiphoid process and the upper base on the plane of the roots of the neck muscles [15]. The two external pairs of electrodes injected into the thorax an alternating mono frequency (65 *KHz* which eliminates the capacitive reactance [16]) current (It) of constant intensity (1 *mA*), while the 5 cm more internal pairs detected the resulting drop in the applied electrical potential difference (ΔVt) [17]. By applying the Ohm's law, the software implemented in the EIC returned the corresponding Zt as:

$$Zt = \Delta Vt : It \tag{1}$$

By utilizing a free LabChart reader (ADInstruments USA) for data acquisition and data analysis, from the instrumental

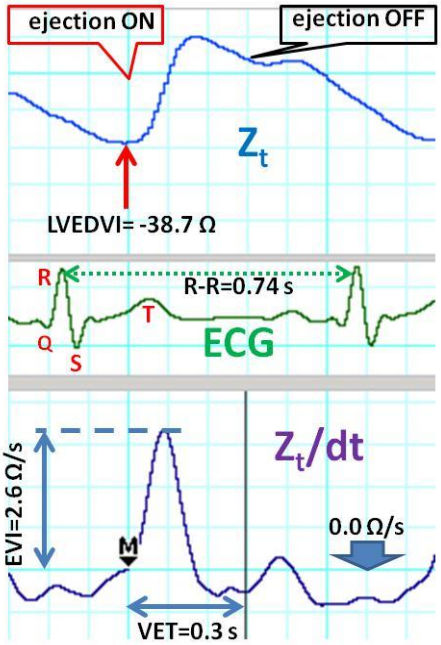


Figure 2 Within a typical heart beat of a tested pilot, from top to bottom, tracks show changes in thoracic electrical bioimpedance (Zt), electrocardiogram (ECG) and mathematical first derivative of the thoracic electrical bioimpedance (Zt/dt). LVEDVI: index of the inverse left ventricle end diastolic volume, R-R: between ECG's R waves time interval, EVI: left ventricle ejection velocity peak index, VET: left ventricle ejection time. M: graphic marker indicating the precise time in which started the left ventricle ejection, Q-R-S: left ventricle ECG depolarizing waves, T: left ventricle repolarising wave.

tracks of the Zt, its first derivative Zt/dt and ECG, the following cardiodynamic variables were beat-to-beat acquired as shown in figure 2:

- the index of the inverse value of the left ventricle end diastolic volume (LVEDVI), represented in the impedance track of figure 2 as the minimum value assumed by Zt, in Ω^{-1}, since it has been found that this Zt value inversely correlates with the left ventricle pre-load [18];
- left ventricle index of peak ejection velocity (EVI), measured in $\Omega\ s^{-1}$ as the maximum amplitude in the Zt/dt track (third track from top in figure 2) since it has been found that this electrical variable overlaps the track of blood flow velocity in the aorta artery, assessed with the Doppler technique and measured in $m\ s^{-1}$ [19];
- left ventricle ejection time (VET), measured in *s* in the Zt/dt track as the time interval between the start of the EVI and its after-peak mathematical minimum value since it has been found that these two time points respectively correspond to the first and second sound of the cardiac phonocardiogram or the opening and closing in the aortic valve [20].

Since it is known that the ejection fraction of the ventricle volume during the systole depends on: the ventricle hydraulic volume (HVV), its pre-load, its ejection velocity peak and the corresponding ejection time, so the following equation could be proposed to evaluate the left ventricle stroke volume (SV) by substituting measurable impedance derived variables to the hydraulic ones as:

$$SV = HVV \text{ x } LVEDVI \text{ x } EVI \text{ x } VET \tag{2}$$

Equation (2) allows to calculating the beat-to-beat SV provided that the HVV must be known. This limitation has been overcome by the experimental observation that this volume is comparable to that of the volume of the thoracic electrically participating tissues (VEPT) expressed in cm^3 [21], and that the latter can be obtained from an experimentally acquired nomogram, through the body weight, height and the gender of the subject concerned [17]. So, the transfer equation from electrical to hemodynamic variables for the beat-to-beat measurement of SV can be quantitatively formulated as follows [22]:

$$\begin{aligned} SV = (VEPT)\ x\ (LVEDVI)\ x\ (EVI)\ x\ (VET) &= \\ (\text{cm}^3)\ \text{x}\ \ (\Omega^{-1})\ \ \text{x}\ (\Omega\ \text{s}^{-1})\ \text{x}\ (\text{s}) &= \text{cm}^3 \end{aligned} \tag{3}$$

Equation (3) had been previously validate by comparing SV obtained in this way with that detected with other standardized methods [23]. Moreover, it has been utilized this non invasive technique also in acquiring cardiodynamic variables in racing car pilots [24]. Both during the T1 and T2 tests, while measuring the arterial blood pressures, each pilot kept sitting 2 minutes during which the beat-to-beat Zt and ECG tracks were assessed, from which, subsequently, 10 heartbeats were analyzed in temporal succession starting from the beginning of the second minute of acquisition. This time delay was set to distance the period of acquisition

of the haemodynamic variables from that during which the measurement of arterial blood pressures was carried out in such a way of avoiding mental troubles influences in the analyzed heart beats.

Moreover, from the figure 2 (second track from top) it can be obtained the value of the heart rate per minute (HR) concerning a given heart beat as dividing 60 to the measured R-R time interval. For instance, in the heart rate analyzed in figure 2, by dividing 60 to 0.74 was obtained an HR of 81 beats per minute.

Additional hemodynamic variables that were obtained from data collected in figure 2 are those following:

- cardiac output per minute (CO) as the product SV x HR, measured in $l\ min^{-1}$;
- total peripheral vascular resistance index (PVR) obtained by dividing the (MABP) at rest to the CO, measured in $Torr\ l^{-1}\ min^{-1}$;
- rate-pressure product (RPP) obtained by multiplying the SABP by the HR, measured in $Torr\ beats^{-1}\ min^{-1}$ and considered as an indirect index of myocardial oxygen consumption or heart's energy cost [25];
- mechanical work index of the left ventricle (LVMW) as the product of MABP and SV, measured as *Torr ml* [26];
- left ventricle mechanical efficiency index (LVME) obtained as the ratio between LVMW and RPP and measured as $ml\ beats\ min^{-1}$ [26].

Furthermore, EVI was chosen here as a good index of myocardial contractility.

2.3.3 Psychometric evaluations

In the aim of verify possible conditioning of the hemodynamic variables of interest by previous states of anxiety, at the time of their engagement the pilots were administered a specific questionnaire: the Generalized Anxiety Disorder 7-item (GAD-7) [27], shown in table I, in which a total score for the chosen seven items ranges from 0 to 21. In the GAD-7 a score from 0 to 4 implies minimal anxiety, from 5 to 9 indicates mild anxiety, from 10 to 14 indicates moderate anxiety while from 15 to 21implies a condition of severe anxiety.

3 RESULTS

Table IIa shows changes in BM occurring in each tested pilot when he landed after 4 hours competing in the motorboat Ton's Race (T2), compared to the same measurements assessed before the race (T1). It can be shown that the after race BM was reduced on average of 600 *g* or quasi 1%.

However, applying the statistic Student's *t* test for paired data between T1 and T2 values and considering a $P<0.05$ as statistically significant (MedCalc statistical package, Belgium), despite an important loss of the average value in the BM, this anthropometric variable did not reached an after-race statistically significant difference ($P=0.867$). Moreover, this table shows that, after race, MABP increased on average of about 8 *Torr* or quasi 10% respect the value assesses before race. The table also shows that the measured tympanic BT never fell under 36°C while still maintaining values always below 37°C.

Table I - GAD-7 Anxiety questionnaire

Over the last two weeks, how often have you been bothered by the following problems?	Not at all	Several days	More than half the days	Nearly every day
1. Feeling nervous, anxious, or on edge	0	1	2	3
2. Not being able to stop or control worrying	0	1	2	3
3. Worrying too much about different things	0	1	2	3
4. Trouble relaxing	0	1	2	3
5. Being so restless that it is hard to sit still	0	1	2	3
6. Becoming easily annoyed or irritable	0	1	2	3
7. Feeling afraid, as if something awful might happen	0	1	2	3

Table IIa - Subjects clinical and functional variables before (T1) and after (T2) race

Sub.	BM (*kg*)		MABP (*Torr*)		BT (*°C*)	
	T1	T2	T1	T2	T1	T2
(A)	70.3	68.9	78.3	88.7	36.1	36.5
(B)	61.7	60.8	91	93.3	36.1	36.4
(C)	70.2	68.6	90	90	36.9	36.1
(D*)	60	61.4	83.3	78.7	36.4	36.7
(E)	73.3	72.6	84	117	36.2	36.1
M.	*67.1*	*66.5*	*85.3*	*93.5*	*36.3*	*36.4*
±SD	*5.9*	*5.1*	*5.2*	*14.2*	*0.34*	*0.26*
Δ		*-0.6*		*8.2*		*0.1*

Sub.: subjects; BM: body mass; MABP: mean arterial blood pressure; BT: body temperature; M.: mean; ±SD: standard deviation; Δ: T1-T2; *: woman

Table IIb - Subjects clinical and functional variables before (T1) and after (T2) race

Sub.	SDU_{urine} (*Abs. Units*)		HGM (*kg*)		PEF ($l\ min^{-1}$)	
	T1	T2	T1	T2	T1	T2
(A)	1025	1010	50.5	45.4	640	740
(B)	1025	1005	56.8	53.3	550	570
(C)	1020	1010	42.8	43.2	570	580
(D*)	1005	1010	39	35.7	250	390
(E)	1015	1010	51.2	46.5	610	630
M	*1018*	*1009*	*48.1*	*44.8*	*524*	*582*
±SD	*8.4*	*2.2*	*7.1*	*6.3*	*157*	*127*
Δ		*-9*		*-3.3*		*58*

Sub.: subjects; SDU: specific density units; HGM: handgrip maneuver; PEF: peak of expiratory flow; (Abs. Units): Absolute Units; M: mean; ±SD: standard deviation; Δ: T2-T1; *: woman

Table III - GAD-7 questionnaire results

Sub.	Not at All (0)	Several Days (1)	More than half The days (2)	Nearly every Day (3)	Total
(A)	2	5			5[b]
(B)	3	2	2		6[b]
(C)	4	3			3[a]
(D*)	3	3	1		5[b]
(E)	1	1	3	2	13[c]

Sub.: subjects; [a]minimal anxiety; [b]mild anxiety; [c]moderate anxiety; *: woman

However, neither MABP nor BT averaged values differences between before and after race reached the statistical significance. Table IIb shows that while the T2 averaged value of PEF increased 58 $l\ min^{-1}$ or +11% with respect to the T1, on the contrary, both SDU and HGM reduced their averaged values after performing the race. In fact, the former variable was lowered of 9 *Units*, i.e. quasi 1%, and the second one fell on average of more than 3 kg or almost – 7% the pre race value. However, in the variables shown in this table, statistical comparisons among T1 and T2 conditions by the Student's *t* test appeared as significant only concerning the after race reduction in the SDU (P=0.0491). In table III the anxiety scores, i.e. the GAD-7, reached by each pilot over the last two weeks before the green motor boating races, are reported. In the pre-race period only one of they came from a minimal level of anxiety, three had experienced mild anxiety while the latter was as moderately anxious. Concerning hemodynamic data acquired when assessing, beat-by beat, 2 minutes of EIC tracks from each subject both at T1 and T2 experimental conditions , it has been chosen to analyse,

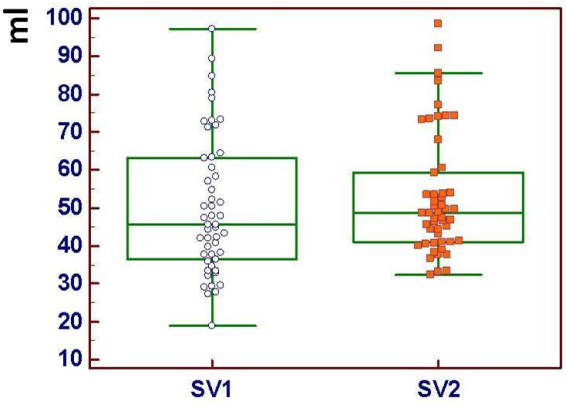


Figure 3 Box and whiskers representation shows left ventricle stroke volume distribution among all tested subjects respectively before (SV1) and after (SV2) boat's performances. Fifty heart beats were considered in both former (empty blue circles) and second (full orange squares) cardiovascular tests. The orange squares outside the graphs are outlier values.

by means of the free LabChart software, the first 10 heart beats which followed one another immediately after the start of the second minute recording. In the aim of compare for each chosen haemodinamic variable data from T1 versus T2 conditions to establish possible differences statistically significant, for each variable were pooled the data of all the values acquired from each subject in each of the two experimental conditions therefore, constituting, for a given variable, two groups of data each of 50 values in order to compare them statistically. Firstly, it has been tested the degree of normality of each data distribution using the D'Agostino-Pearson test for normal distribution [28], establishing in this way that almost all of the data distributions rejected the parametric condition.

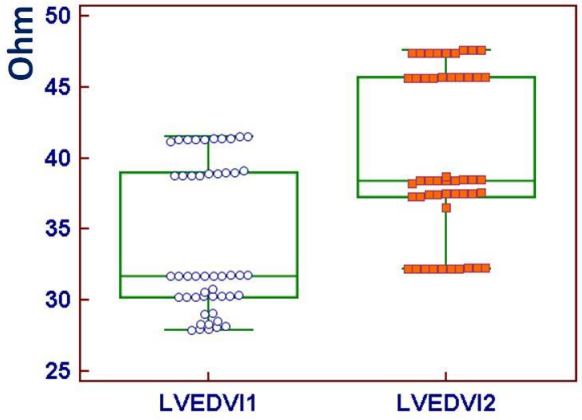


Figure 4 Box and whiskers representation shows inverse left ventricle end diastolic volume index distribution among all tested subjects respectively before (LVEVI1) and after (LVEVI2) boat's performances. Fifty heart beats were considered in both former (empty blue circles) and second (full orange squares) cardiovascular tests.

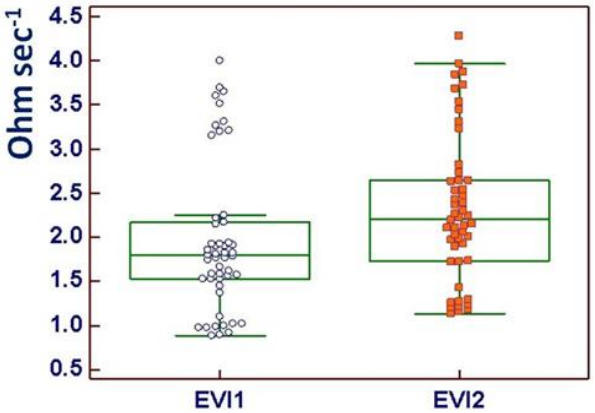


Figure 5 Box and whiskers representation shows left ventricle peak ejection velocity index distribution among all tested subjects respectively before (EVI1) and after (EVI2) boat's performances. Fifty heart beats were considered in both former (empty blue circles) and second (full orange squares) cardiovascular tests. The orange squares outside the graphs are outlier values.

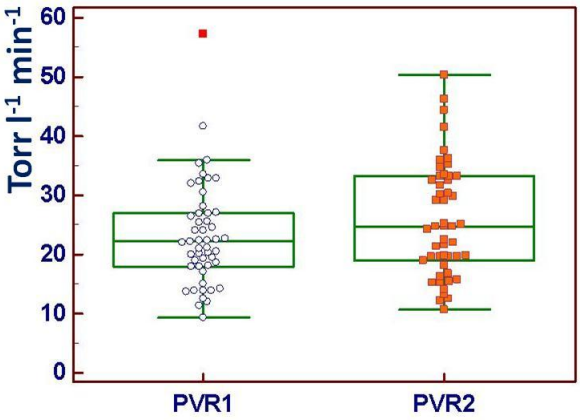


Figure 6 Box and whiskers representation shows left ventricle total peripheral vascular resistance index distribution among all tested subjects respectively before (PVR1) and after (PVR2) boat's performances. Fifty heart beats were considered in both former (empty blue circles) and second (full orange squares) cardiovascular tests. The orange squares outside the graphs are outlier values.

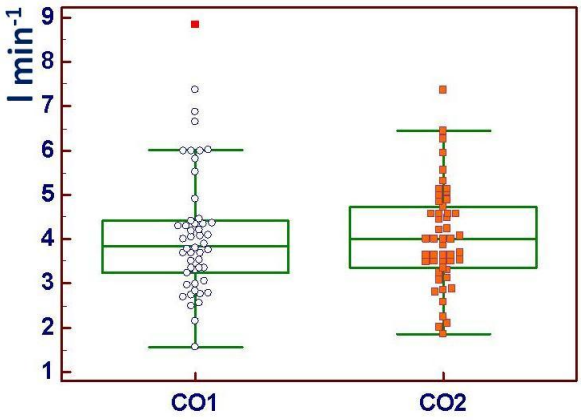


Figure 8 Box and whiskers representation show left ventricle cardiac output per minute distribution among all tested subjects respectively before (CO1) and after (CO2) boat's performances. Fifty heart beats were considered in the former (empty blue circles) and second (full orange squares) cardiovascular tests. The orange squares outside the graphs are outlier values.

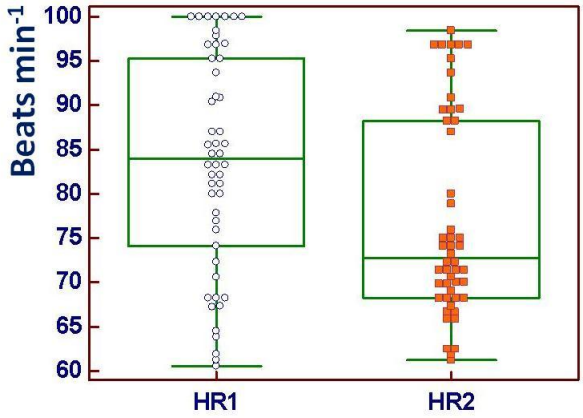


Figure 7 Box and whiskers representation show heart rate per minute distribution among all tested subjects respectively before (HR1) and after (HR2) boat's performances. Fifty heart beats were considered in the former (empty blue circles) and second (full orange squares) cardiovascular tests.

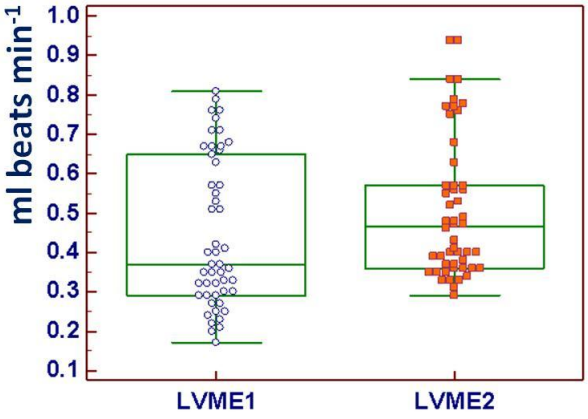


Figure 9 Box and whiskers representation show left ventricle mechanical efficiency index distribution among all tested subjects respectively before (LVME1) and after (LVME2) boat's performances. Fifty heart beats were considered in both former (empty blue circles) and second (full orange squares) cardiovascular tests. The orange squares outside the graphs are outlier values.

Whereby, for the comparison between the data collected in T1 and T2 it has been chosen to use the non-parametric Wilcoxon test for paired data [28]. So, data were graphically represented by the box and whisker plot method which displays a statistical summary of a variable in terms of median, quartiles and extreme values [29, 30]. Graphs in figures from 3 to 9 concern the two box and whisker plots for each data distribution assessed in T1 and T2, respectively for: SV, LVEDVI, EVI, PVR, HR, CO, LVME. About the SV, from graphs in figure 3 it can be easily shown that despite the interquartile box values of SV2 (from 42.0 to 59.4 *ml*) entirely falls within that of V1 (36.5 to 63.2 *ml*), however the VS2 median (48.7 *ml*) enhanced the VS1 one (45.6 *ml*) of 6.8%. Nevertheless, the statistical significance for this comparison was not reached, even if only by a little.

Graphs in figure 4 show the LVEDVI distribution assessed during both T1 and T2 tests. It can be shown that LVEDVI distribution in T2 was positioned much higher than in T1. In fact, the interquartile range of this variable assessed after race shows values from 37.3 to 45.7 Ω while before race these were from 30.2 to 39.0 Ω. Moreover, the LVEDVI2 median (38.4 Ω) was about 21% higher than in the LVEDVI1 (31.7 Ω) distribution, and for this reason this difference was statistically significant ($P<0.0001$). As previously specified in the methods at paragraph 2.3.2, the variations of the end-diastolic ventricular volume must be interpreted as reciprocal values with respect to those shown in the figure which represent the variations of the thoracic

bioimpedance. Therefore, the data in this figure agree with a significant decrease in the ventricular preload which occurred after the race. Now considering the left ventricle ejection velocity peak (EVI), its data distribution in T2 versus T1 (figure 5) shows that the T2 interquartile range was noticeably higher (from 1.73 to 2.65 $\Omega\ s^{-1}$) than in T1 (from 1.53 to 2.17 $\Omega\ s^{-1}$) and the median after race (2.21 $\Omega\ s^{-1}$) was +23.5% than that before race (1.79 $\Omega\ s^{-1}$), so the difference among these two distribution was statistically significant (P<0.0001). The total peripheral vascular resistance index (PVR in figure 6), assessed during the T2 showed an interquartile range (from 19.0 to 33.2 *Torr* l^{-1} *min*$^{-1}$) that was a little bit higher than during T1 (from 18.0 to 26.9 *Torr*$^{-1}$ l^{-1} *min*$^{-1}$). However, even if the post-race median (24.7 *Torr* l^{-1} *min*$^{-1}$) of the PVR was higher than 12% of in the pre-race one (22.1 *Torr* l^{-1} *min*$^{-1}$), this difference had a P=0.05 or borderline for statistical significance. Heart rate per minute (HR) distribution assessed during the two experimental conditions is shown in figure 7.

Interquartile ranges of this variable show a partial superimposition when comparing T1 (from 74.2 to 95.2 *beats min*$^{-1}$) versus T2 (from 68.2 to 88.2 *beats min*$^{-1}$) data distribution, and the median in T2 (72.7 beats min^{-1}) was 13.2% lower than the one in T1 (83.8 *beats min*$^{-1}$) for which its distribution in T2 was significantly lower than in T1 (P=0.008). Cardiac output per minute (CO) shows in figure 8 that interquartiles of both T1 (from 3.24 to 4.42 *l min*$^{-1}$) and T2 (from 3.35 to 4.74 *l min*$^{-1}$) data were practically overlapped as well as their medians: respectively of 3.84 and 4.00 l min^{-1}. In fact, this comparison did not reach statistical significance (P=0.685). In figure 9 are shown box and whisker plots for data distributions concerning the left ventricle mechanical efficiency index before (LVME1) and after the race (LVME2). Despite interquartile range of T2 (from 0.36 to 0.57 *ml beats min*$^{-1}$) was entirely contained within the one of T1 (from 0.29 to 0.65 *ml beats min*$^{-1}$), the T2's median value (0.47 *ml beats min*$^{-1}$) was 27% higher in comparison to that of the T1 (0.37 *ml beats min*$^{-1}$), and this post-race higher median value than before one was statistically significant (P=0.0026).

5 DISCUSSION

As shows table IIa, after race the averaged BM was reduced of 0.6 kg with respect that measured before one. This after-race BM fall could be attributed to a reduction in the body's water content. In fact, Lewis *et al*. [1] had been shown that in sailors exposed from 2 to 3 hours in the sea with a speed wind and a low air temperature, there was a significant reduction of body mass mainly caused by water loss, and this occurred despite not increases in the urine specific density as also occurred in these electric boat's pilots when submitted to the T2 (see table IIb). Cardiodynamic behaviours shown by the variables of interest, along the assessed 10 heart bears in each engaged pilot, indicate a quasi 7% increase in the SV median shown during T2 when compared that in T1. However, probably due to the small number of pilots which it could be able to recruit in the midst of the frenetic activities of several teams involved in the races, this difference did not reach the statistical significance (P = 0.56 or neat to what expected for reaching this goal). It must be considered that beat-to-beat SV values result from both central cardiac and peripheral vascular variables. The central/heart-depending variables are in turn due to homeometric or heterometric nature events [31].

The formers depend on intrinsic electromechanical properties of the heart, i.e. the ventricle contractility here achieved by the peak ventricular ejection velocity index (EVI), the second one, also defined as the ventricle pre-load, being related with heterometric mechanisms concerning changes in ventricular diastolic volume, based on the Frank-Starling law [31], up to reach the end diastolic ventricular volume. Moreover, to obtain the systolic ejection flow of the left ventricle also contributes the hydraulic resistance that this blood outflow must overcome to carry the blood towards the vascular periphery, i.e. the so-called total peripheral vascular resistance (PVR) also defined as the ventricular after-load, i.e. as PVR fall the LVEDV increases contributing to enhancing SV and vice versa [7].

Taking into account as stated above, assessed data concerning the left ventricle pre-load, i.e. the LVEDV behaviour as defined figure 4, since its interquartile box in T2 is positioned almost totally above that obtained in T1 giving rise to a statistically significant increase in the median corresponding to T2 compared to that corresponding to T1, this means an high and statically significant reduction in the post race of this cardiodynamic variable. So, as a consequence of the prolonged competition in driving electrical motorboats, there was a significant reduction in left ventricular pre-load and therefore a strong reduction in the central contribution of the heterometric type to the size of the subsequent SV. What above observed can be considered as an expected event probably caused by the poor activation, along the 4 hours of the race, of the so-called muscle pump mainly carried out by the calves rhythmic contractions on the lower limbs veins when walking. In fact, it has been found that the left ventricle pre-load is closely related to the pressure gradient from post-caval vein towards the right atrium which, in turn, depends on the frequency and intensity of lower leg veins squeezing made by *triceps surae* muscles contractions. When occurring, this latter event gives rise to an increase in left ventricle blood filling up to reaching the LVEDV and consequently its contribution to an adequate SV on heterometric basis [7]. It is therefore reasonable to deduce that during the race, due to a prolonged stay in a sitting posture, this gave rise to a scarcely intense and not periodic contractile activity of the pump muscles on the leg veins which, in this way, resulted in the lesser LVEDV here observed [32]. Furthermore, this prolonged postural condition of the pilots might have give rise to transient

conditions of relative insufficiency of the venous valves of the legs which could have been maintained even while pilots were performing T2 [33]. However, to support the SV despite the lessening of the LVEDV contribution, in these pilots gave a help the increase in activity of the central homeometric mechanism in terms of a significant increase in myocardial contractility of sympathetic origin [34]. This, increasing the systolic shortening speed of the myocardial fibres, as shown here by the increase in EVI, compensates in this way the function of SV in contributing to have CO values as requested by body organs activities. In fact, as show graphs in figure 8, this latter variable did not fall after the race despite a significant reduction in HR shown in graphs of figure 7. Furthermore, in order to help support the blood flow from the heart to the vascular periphery, during the T2 performance it has been assessed an increase in PVR (figure 6), statistically considerable as almost significant, which gave rise to the detected increase in MABP of 8 *Torr* with respect to the pre-race condition (see table IIa).
Unfortunately, this increase in blood pressure was not supported by the achievement of statistical significance. Graphs in figure 9 highlight an important occurrence that happened in these experiments, i.e. the mechanical efficiency of the heart's left ventricle (LVME), measured in the pilots recruited after they had finished the race with electrical motor boats, was 27% higher than that detected before the race. This bioenergetic variable, although obtained indirectly as a ratio between the LVMW and the clinical indicator of its energy expenditure in terms of its O_2 consumption, i.e. the RPP, was still statistically significant and, therefore, allows to deduce that the psycho-physical activity, delivered during long lasting driving marine vehicles powered by electrical energy originating from green sources, could result in making more efficient aerobic energy substrates for the heart mechanical work delivery. Finally, after a demanding power boating performance such as the Ton's Race in Olbia, the nautical pilots tested here did not show any signs of significant decay in muscular strength nor in respiratory capacity as well as in thermal homeostasis as shown in Tables IIa and IIb by the HGM, PEF and BT tests respectively. Furthermore, it may be that, on the basis of the significant reduction in HR shown as an average of all pilots after the motorboat test, the condition of mild/moderate anxiety manifested in the days preceding this performance from 4 of the 5 pilots here recruited (see the results of the GAD-7 questionnaire in table III), as observed in previous experiments [35], this demanding psycho-physical task could have played a therapeutic role in terms of reducing the previously existing level of anxiety. Therefore it follows that in future research and with adapting numbers of recruited subjects, it is commendable to measure this parameter both before and after a race with electrically power motor boats. In fact, a post-race decrease in anxiety levels in pilots of these boats would be possible given the current data set that agrees with a generalized decrease in orthosympathetic tone.

CONCLUSIONS

Although, to the knowledge of these Authors, there are currently no other experiments regarding the cardio-metabolic adaptations induced by an endurance race with boats electrically powered, there is still a sufficiently robust literature on the people in which the harmful effects that occur when racing with land vehicles powered by endothermic engines, have been studied.
In fact, especially in the context of racing with cars, i.e. formula 1, NASCAR, IndyCar and WEC, the use of internal combustion engines gives rise to well-documented damage in pilots due to the excess concentrations of carbon monoxide (CO) as well as very high temperatures in the restricted cockpit environment together with several organ damage associated with the excess of noise and mechanical vibrations, especially generated by this type of engine [2]. However, the emerging worldwide production for racing series of electric cars, the so-called "Formula E Car Series", by totally eliminating the production of CO, with great advantages also for the natural environment, generate far less heat and emit both little noise and vibrations. It can therefore be reasonably stated that electric vehicles are predicted to greatly reduce driving stress in athletes who dedicate themselves to piloting competitive marine vehicles since this has been clearly demonstrated by the results of this experiment.
In fact, metabolic and cardiodynamic condition which appeared in these 5 pilots after a long lasting physical performance as was that of driving a motor boat engaged in a Ton's Race lasting 4 hours, can be largely assimilated to what is observed after a long-lasting kayaking where, together with a reduction in the percentage of body fat mass [5], there is generally a shift from chronotropic to inotropic control in the cardiovascular beat-to-beat activity. The shown post-race reduction in HR and increase in EVI, both statistically significant, confirm this adaptation which is also in agreement with a likely improvement, in these athletes, in aerobic metabolism which could also justify the observed statistically significant increase in their cardiac mechanical efficiency, and this without any post-race stress of hyperthermic or hypovolemic type, as shown, in turn, by the maintenance of normal values of tympanic temperature (table IIa) and specific urine density (table IIb).
Finally, both the post-race maintenance of a good capacity for producing muscle strength and a good functionality of bronchial flow, as shown in the values of HGM and PEF (table IIb) acquired in the T2 assessments along with a probable anxiolytic action, as the reduced post-race HR seems to accompany, highlight the possibility of using motorboat sports activities based on electric motors powered by green energy, aimed at improving one's physical exercise based on aerobics energy substrates from a health-related quality of life perspective.

STUDY LIMITATIONS

Probably, the most evident limitation of this study is given by the limited number of subjects tested and, within them, also by the wide age range. In fact, this experimentation was carried out, as they say, "directly on the field" without a prior schedule, and so it suffered from a lot of obstacles in the search for pilots who, despite their heavy commitments in preparing for the race, had also to dedicate time to undergo the proposed experimental protocol.
However, given the experimental results acquired here which, in any case, promise that the line of research undertaken can provide important indications on this new sporting specialty, Authors of this work intend to proceed as soon as possible to resume the experimentation with a protocol that includes a larger sample of subjects which would be subdivided into two groups: the one drawing electrically powered boats and the other drawing fossil fuel powered boats, so as to better define what has been acquired here.

REFERENCES

[1] Lewis E.J., Fraser S.J., Thomas S.G. and Wells G.D., Changes in hydration status of elite Olympic class sailors in different climates and the effects of different fluid replacement beverages. *J Int Soc Sports Nutr*. Vol. 10, No. 1, pp.1-11, 2013.

[2] Reid M.B. and Lightfoot J.T., The Physiology of Auto Racing. *Med Sci Sports Exerc*. Vol. 51, No. 12, pp. 2548-2562, 2019.

[3] Jemni M., Marina M., Delextrat A., Tanner A., Basset F.A., Gu Y., Hu Q., Zhou H., Mkaouer B. and Konukman F., Salivary endocrine response following a maximal incremental cycling protocol with local vibration. *PLoS One*. Vol. 15, No. 9 pp. e0238051, 2020.

[4] Michaud D.S., Thomson E.M., van Oosterhout P. and McNamee J.P., Hair cortisol as a viable tool for the assessment of an association between environmental noise exposure and chronic stress. *J Acoust Soc Am*. Vol. 152, No. 2, pp. 866-876, 2022.

[5] Tocco F., Massidda M., Ghiani G., Palmas M., Ruggiu M., Velluzzi F., Solinas R., Masala A., Fois A., Melis L., Manuello Bertetto A., dell'Osa A.H., Cerina A., Cappagli C., Melis S., Loi V., Marcello R. and Concu A., Biomechanical and cardiometabolic changes in skilled kayaker after 41 days of cruising around the island of Sardinia: a case study (part 1). *International Journal of Mechanics and Control*. Vol. 25, No. 02, pp. 113-119, 2024.

[6] Pan F., Chen F., Liu C., Yang Z., Liu Z. and Zheng D., Quantitative Comparison of Korotkoff Sound Waveform Characteristics: Effects of Static Cuff Pressures and Stethoscope Positions. *Ann Biomed Eng*. Vol. 46, No. 11, pp. 1736-1744, 2018.

[7] Campagna M., Lecca L.I., Velluzzi F., Serra C., Bianco P., Manuello Bertetto A., Dell'Osa A.H., Fanni B., De Pau A., Fois A., Melis L., Kalb A., Marcello R., Melis S., Concu A. and Tocco F., A mechatronic simulator of an aircraft cockpit to study, by a virtual flight test, cardiovascular fitness in airline pilots banned to fly since covid-19 lockdown. *International Journal of Mechanics and Control*. Vol. 23, No, 2, pp. 85-99, 2022.

[8] Karaaslan B.G., Ucgun H., Kaya M., Cengiz G.N., Ozturk S., Barut O., Korkut Z., Aydemir S., Meric Z., Topcu B., Kulli H.D., Cokuğras H. and Kiykim A., Breath of relief: Transforming pediatric asthma care with telemedicine-guided exercises. *Clin Transl Allergy*. Vol. 15, No. 3, pp. e70049, 2025.

[9] Melo G.L.R., Espírito Santo R.C, Dubey V.P. and Agostinis-Sobrinho C., Handgrip strength measurement protocols in individuals with Down syndrome: a systematic review and meta-regression. *Ann Med*. Vol. 57, No. 1, pp. 2453077, 2025.

[10] Wu W.C., Concu A., Solinas R., Meloni L., Manuello-Bertetto A., Fois A., Loviselli A., Deledda A. and Velluzzi F., Metabolic power and energy cost of mechanical work carried out by a sailor engaged in a solo ocean race: a case study. *International Journal of Mechanics and Control*. Vol. 19, No. 02, pp.19-32, 2018.

[11] Velluzzi F., Fois A., Dell'Osa A.H., Tocco F., Manuello Bertetto A., Serra C., Melis L., Bertelli U. and Concu A., Mechatronic face mask anti COVID-19 to remotely record cardiorespiratory variables in farm's workers engaged in jobs at high risk of infection. *International Journal of Mechanics and Control*. Vol. 22, No. 01, pp. 61-76, 2021.

[12] Tocco F., Crisafulli A., Marongiu E., Milia R., Kalb A. and Concu A., A portable device to assess underwater changes of cardiodynamic variables by impedance cardiography. *J Phys.: Conf. Ser.* Vol. 407, pp. 012026, 2012.

[13] Marongiu E., Crisafulli A., Ghiani G., Olla S., Roberto S., Pinna M., Pusceddu M., Palazzolo M., Sanna I., Concu A. and Tocco F., Cardiovascular Responses during free-diving in the sea. *Int J Sports Med*. Vol. 36, pp. 297-301, 2015.

[14] Tocco F., Mattana D.V., Solinas R., Velluzzi F., Usai P, Fois A., Melis L., Bianco P., Serra C., Manuello Bertetto A., Dell'Osa A.H., Pereira A.F., Cerina A., Loviselli L., Marcello R., Melis S. and Concu A., Cardiometabolic benefits from a coastal sailing in a radical cystectomy patient remotely controlled by an internet of thing mechatronic tool: a case study. *International Journal of Mechanics and Control*. Vol. 24, No. 02, pp. 39-61, 2023.

[15] Tocco F., Solinas R., Velluzzi F., Massidda M., Mattana D.V., Fois A., Melis L., Manuello Bertetto A., Bonisoli E†., Venturini S., Bianco P., Dell'Osa A.H., Pereira A.F., Melis S., Cerina A., Loviselli L., Marcello R. and Concu A., A mechatronic tool for revealing inverse relationships among heart's stroke

volume and head's linear acceleration induced by moored boats rolling in elderly sailors with unchanged body sizes: a non-drug anti-hypertensive advantage?. *International Journal of Mechanics and Control*. Vol. 25, No. 01, pp. 133-142, 2024.

[16] Dell'Osa A.H., Battacone G., Pulina G., Fois A., Tocco F., Loviselli A., Concu A. and Velluzzi F., Electrical impedance for easily discover undeclared freeze-thaw cycles in slaughtered bovine meat. *J Electr Bioimp*. Vol. 12, pp. 3-10, 2021.

[17] Bernstein D.P., A new stroke volume equation for thoracic electrical bioimpedance: theory and rationale. *Crit Care Med*. Vol. 14, No. 10, pp.904-909, 1986.

[18] Okutani H., Fujinami T. and Nakamura K., Studies on mean thoracic impedance (Zo). *Proc. of the 5th International Conference on Electrical Bioimpedance*, Tokyo, Japan, pp. 31-34, 1981.

[19] Goli V.D., Teague S.M., Prasad R., Harvey J., Voyles W.F., Olson E.G., Schechter E. and Thadani U., Noninvasive evaluation of aortic stenosis severity utilizing Doppler ultrasound and electrical bioimpedance. *J Am Coll Cardiol*. Vol. 11, pp. 66-71, 1988.

[20] Crisafulli A., Melis F., Orrù V., Lener R., Lai C. and Concu A., Non invasive assessment of systolic time intervals during exercise by means of impedance cardiography technique. *Sports Med Train and Rehab*. Vol. 10, pp.13-27, 2001.

[21] Sramek B.B., (1981) Noninvasive technique for measurement of cardiac output by means of electrical impedance. *Proc. of the 5th International Conference on Electrical Bioimpedance*, Tokyo, Japan, pp. 39-42, 1981.

[22] Concu A., Respiratory and cardiac effect of passive limb movements in man. *Pflug Arch Eur J Physiol*. Vol. 412, pp. 548-550, 1988.

[23] Concu A. and Marcello C., Stroke volume response to progressive exercise in athletes engaged in different training modes. *Eur J Appl Physiol*. Vol. 66, pp. 11-17, 1993.

[24] Mallows R.J. and Newman D.G., Cardiovascular data acquisition in a dynamic motion environment. *Aviat Space Environ Med*. Vol. 79, No. 4, pp. 416-419, 2008.

[25] Schenone C.V., Ashley Cain M., Schenone A.L., Smith T., Tsalatsanis A., Louis J.M. and Crousillat D.R., Changes in rate-pressure product associated with pregnancy. *Am J Obstet Gynecol MFM*. Vol. 6, No. 4, pp. 101338, 2024.

[26] Ciuti C., Marcello C. and Concu A., Competitive sports activities improve cardiocirculatory performance in insulin-dependent diabetics. *Sports Med Train and Rehab.* Vol. 5, pp. 173-187, 1994.

[27] Riglea T., Wellman R.J., Sylvestre M.P., Sabiston C. and O'Loughlin J., Factor structure and measurement invariance of the GAD-7 across time, sex, and language in young adults. *J Affect Disord*. Vol. 375, pp. 359-365, 2025.

[28] Kecik M., Kropp M., Thumann G., Pajic B., Guber J. and Guber I., Intradevice Repeatability and Interdevice Comparison of Two Specular Microscopy Devices in a Real-Life Setting: Tomey EM-4000 and Nidek CEM-530. *Medicina (Kaunas)*. Vo. 60, No. 7, pp. 1110, 2024.

[29] Krzywinski M. and Altman N., Visualizing Samples with Box Plots. *Nature Methods*. Vol. 11, pp. 119-120, 2014.

[30] Sarais G., Crisafulli A., Concu D., Fois A., Raweh A. and Concu A., Hydroxytyrosol but not resveratrol ingestion induced an acute increment of post exercise blood flow in brachial artery. *Health*. Vol. 8, pp. 1766-1777, 2016.

[31] Guyton A.C. and Hall J.E., *Textbook of medical physiology.* 10th edition, W.B. Saunders Company, USA, 2007.

[32] Dawson E.A., Shave R., Whyte G., Ball D., Selmer C., Jans Ø., Secher N.H. and George K.P. Preload maintenance and the left ventricular response to prolonged exercise in men. *Exp Physiol*. Vol. 92. No. 2, pp. 383-90, 2007.

[33] Nicolini G., Manuello A., Capone A., Marongiu G., Dell'Osa A.H., Fois A., Velluzzi F. and Concu A., Possible assessment of calf venous pump efficiency by computational fluid dynamics approach. *Front Physiol*. Vol. 11, No. 1003, pp. 1-17, 2020.

[34] Orani G.P. and Decandia M., Role of the heart and peripheral resistance in the reflex effect of group I afferent fibers on blood pressure. *Cardioscience*. Vol. 5, No. 1, pp. 25-30, 1994.

[35] Tocco F., Crisafulli A., Milia R., Marongiu E., Mura R., Roberto S., Todde F., Concu D., Melis S., Velluzzi F., Loviselli A., Concu A. and Melis F. Nervous facilitation in cardiodynamic response of exercising athletes to superimposed mental tasks: implications in depressive disorder. *Clin Pract Epidemiol Ment Health*. Vol. 23, pp. 166-173, 2015.

ISSN 1590-8844
International Journal of Mechanics and Control, Vol. 26, No. 01, 2025
https://doi.org/10.69076/jomac.2025.0018

SOLAR THERMAL ENERGY, CASE STUDY - REGIONAL INSTITUTE OF PUBLIC HEALTH

Drita Qerimi[1], Gazmend Shala[2], Arlinda Alimehaj Rrecaj[3]

[1] UBT, Faculty of Mechatronics Engineering p.n., 10000 Pristine, Kosovo

[2] Termovent Mechanical Engineer, Miradi e Eperme, 12000 Fushë Kosovë, Kosovo

[3] University of Pristina, Faculty of Mechanical Engineering, Traffic and Transport Department, 10000 Pristina, Kosovo

ABSTRACT

In recent years, there has been an increase in the production capacities from RES such as: hydro power plants, wind energy, solar energy, but in Kosovo still the energy produced from lignite continues to dominate as a source primary energy with 77.7%, which, on the one hand enables a security of long-term electricity production, but remains a problem of impact on the environment due to the emission of greenhouse gases and pollutants others. The present chapter discusses mathematical model, simulation program that allows to accurately calculate the yield of a solar thermal system, measurement of active energy and Economic assessment for Regional Institute of Public Health RIPH. Kosovo has an average solar energy potential with the average sun duration for the city of Pristine is 5.44 [h], while the average horizontal irradiation is 3.79 [kWh/m^2] per day. In this paper, the first step is analysing and mapping of appropriate surfaces for installation of solar thermal collectors. To realize the demand for sanitary hot water for RIPH, need total gross surface area: 116.64 [m^2], with 48 collectors located under corner 33°.

Keywords: renewable energy, solar thermal energy, domestic hot water, saving electricity, CO_2 reduction

1 INTRODUCTION

The solar system that studied is in University Clinical Center of Pristine, Kosovo. The Solar Domestic Water Heating (SDWH) system is providing sanitary hot water for Regional Institute of Public Health, the first part Solar 1 is a Laboratory, a second part Solar 2 serves for the Faculty of medicine, in the following the analyse for Solar 1 is presented Fig.1 shows the roof of the Institute, this roof is more suitable for the installation of solar collectors because doesn't have any obstructions, this part is sufficient space for installation the collectors to meet the demand for sanitary hot water. Based on the daily demand for sanitary hot water the number of collectors that will be placed is calculated. Photovoltaic solar panels, and those for heating water, achieve maximum performance when the sun's rays fall perpendicular to their surface [17]. Figure 1 shows the free surface is 375.15 [m^2]. Whereas, according to the calculations the roof surface required for installed solar panels is 116.64 m^2.

Contact author: Arlinda Alimehaj Rrecaj

E-mail: arlinda.alimehaj@uni-pr.edu



Figure 1 Regional Institute of Public Health.

2 THE DOMESTIC HOT WATER CALCULATION FOR REGIONAL INSTITUTE OF PUBLIC HEALTH

This clinic is located at the University Clinical Center of Pristine, with Latitude 42.64° and Longitude 21.15°. The following should be noted when calculating the hot water demand: Hot Water Demand calculations at other temperatures (T) should be adjusted for the 60°C reference temperature and for the purposes of making this adjustment, the following assumptions and observations should be made:

a) The equation assumes that the cold-water temperature (inlet water temperature) is 12 °C and a linear relationship 48 °C is the difference between 60 °C and 12 °C.
b) For buildings with seasonal variations in hot water demand such are Hotels, game Lodges and similar premises, the demand may be adjusted by an annual occupancy rate of factor of not less than 70%, [12].
c) In calculating demand, is assumed that the daily hot water demand is constant, throughout the year.
d) In calculating demand for domestic residential houses, the number of persons is taken to be equal to the number of bedrooms x 1.2, [14].
e) In calculating the heat load of the solar water heating system, heat losses in the hot water distribution system are considered.

Since, Solar-only systems cannot guarantee a high enough hot water temperature at the draw-off points as required by EN 806-2 (60°C), and many national regulations within Europe, special attention should be paid to the bacteria Legionella.

In the context of Legionella control the factors that need special consideration for solar hot water systems are: [15].

- The use of storage tanks with frequently changing water temperatures in the range of 10°C to 80°C, so that part of the tank and water is within the temperature range favorable to the growth of Legionella species.
- The use of a storage tank that frequently and for long periods is at a temperature level above 65°C and, as such, disinfects the Legionella and biofilms within the tank.
- The use of non-solar heat sources that may thermally disinfect the hot water.

For an instantaneous solar water heater, a warning should be attached at a clearly visible location on the solar-only system with the following text:

- *"When no hot water has been used for more than 2 weeks, the system must be flushed for 5 minutes at a draw-off point other than a shower!"*
- *"Flush the system when not used for more than 2 weeks!"*

For all solar-only systems not fulfilling the recommendations before, the solar-only system should be dimensioned such that:

- The temperature of 65°C is reached at the top of the store and 50°C at its bottom, for one hour, once a month, with a probability of 99%, and
- The temperature of 60°C is reached at the top of the store and 45°C at its bottom, for one hour, once a week, with a probability of 90%.

In the pursuit of sustainable development and reduction of environmental impact, energy efficiency has become a paramount concern in the design and operation of buildings and their mechanical systems [18]. To calculate the demand for sanitary hot water for these institutions it is necessary to calculate the monthly average radiation incident on the collector, for this, in this work, the method **Isotropic Sky** was used [2]. Using the isotropic diffuse assumption, the monthly average radiation incident on the collector can be estimated. A collector is to be installed in Pristine, Regional Institute of Public Health, with latitude L = 42º64'N at a slope of 33^0 to the south. The monthly mean solar radiation on an unshaded tilted surface can be expressed as:

$$\overline{H_T} = \overline{H}\left(1 - \frac{\overline{H_d}}{\overline{H}}\right)\cdot \overline{R}_b + \frac{\overline{H_d}}{\overline{H}}\cdot\left(\frac{1+\cos\beta}{2}\right)\cdot\overline{H} + \overline{H}\cdot\rho_g\left(\frac{1-\cos\beta}{2}\right) \quad (1)$$

$\overline{H}$ - Monthly average total insolation on a terrestrial horizontal surface (MJ/m^2-d), Table 1. -The ground reflectance is 0.2 for all months except December and March ($\rho_g = 0.4$) and January and February ($\rho_g = 0.7$) [2].

$\overline{H_0}$ - monthly average daily total insolation on an extraterrestrial horizontal surface, calculated with interpolation from [2] for each month as a function of latitude, together with the recommended dates of each month.

Table I - Horizontal Irradiation [kW·h/m^2]

Month	*Daily*	Monthly
Jan	1.64	50.90
Feb	2.44	68.44
Mar	3.41	105.68
Apr	4.31	129.37
May	5.24	162.60
Jun	6.18	185.65
Jul	6.44	199.69
Aug	5.70	176.83
Sep	4.15	124.51
Oct	2.80	87.03
Nov	1.75	52.68
Dec	1.38	42.90
Annual	3.79	1386.32

The monthly average clearness index, $\overline{K_T}$, is defined as:

$$\overline{K_T} = \frac{\overline{H}}{\overline{H_0}} \quad (2)$$

The amount of insolation on a terrestrial surface at a given location and time depends on the orientation and slope of the surface. In the case of flat-plate collectors installed at a certain fixed angle, system designers need to have data about the solar radiation on the surface of the collector.

For $h_{ss} \leq 81.4^\circ$ and $0.3 \leq \overline{K_T} \leq 0.8$

$$\frac{\overline{H_d}}{\overline{H}} = 1.391 - 3.560\overline{K_T} + 4.189\overline{K_T}^2 - 2.137\overline{K_T^3} \quad (3)$$

and for $h_{ss} > 81.4^\circ$ and $0.3 \leq \overline{K_T} \leq 0.8$

$$\frac{\overline{H_d}}{\overline{H}} = 1.311 - 3.022\overline{K_T} + 3.427\overline{K_T}^2 - 1.821\overline{K_T^3} \quad (4)$$

With the monthly average daily total radiation $\overline{H}$ and the monthly average daily diffuse radiation $\overline{H_D}$ known, the monthly average beam radiation on a horizontal surface can be calculated by:

$$\overline{H_B} = \overline{H} - \overline{H_D} \quad (5)$$

The ratio of the average daily beam radiation on the tilted surface to that on a horizontal surface for the month is $\overline{R_b}$

$$\overline{R_b} = \frac{\cos(L-\beta)\cdot\cos(\delta)\cdot\sin(h'_{ss}) + \left(\frac{\pi}{180}\right)\cdot(h'_{ss})\cdot\sin(L-\beta)\cdot\sin(\delta)}{\cos(L)\cdot\cos(\delta)\cdot\sin(h_{ss}) + \left(\frac{\pi}{180}\right)h_{ss}\cdot\sin(L)\cdot\sin(\delta)} \quad (6)$$

Where:

L Local longitude,
δ Declination,
h_{ss} Hour angle at sunset [2],

$h_{ss}^{'}$ Hour angle for the tilted surface for the mean day of the month, which is given by:

$$h_{ss}^{'} = \min\begin{bmatrix}\cos^{-1}(-\tan L \cdot \tan\delta)\\ \cos^{-1}(-\tan(L-\beta)\tan\delta)\end{bmatrix} \quad (7)$$

where ''min'' means the smaller of the two items in the brackets. The results for Average daily total radiation for 12 months on the tilted surface for Regional Institute of Public Health presented in Table 2. Energy quantities are in mega joules per square meter. It is difficult to put limits of accuracy on them, they are probably no better than ±10%.
In this clinic was installed a solar thermal system, financed by the World Bank, with a total of 48 collectors divided into two parts, this system serves for laboratory part (Solare 1) and the Faculty of Medicine (Solare 2), where: Solare 1
G = 4000 [l] – the volume of the boiler,
T_{min} = 12 [°C] – the temperature in boiler entry (water supply),
T_{max} = 50 [°C] – the temperature at the exit of the boiler,
Cp = 1.16 [Wh/kgK] - specific capacity of water [15],
h = 0.81 – utilization coefficient [6],
p = 2.23 [m²] – effective area of the collector,
q = 4.746 [kWh/m²day] – the capacity of sunlight [1].

$$Q = \frac{G \cdot C_p(T_{max} - T_{min})}{1000} = 176.32[kWh/day] \quad (8)$$

Collector area:

$$S = \frac{Q}{q \cdot h} = 45.87[m^2] \quad (9)$$

The number of collector is 21

$$n = \frac{S}{p} = 21\,[colector] \quad (10)$$

3 CALCULATION WITH SOFTWARE T*SOL 2018

T*SOL is the simulation program that allows to accurately calculate the yield of a solar thermal system dynamically over the annual cycle, [5]. For evaluation or design of solar systems (with components collector, collector loop, heat exchanger and tanks), many parameters must be studied and experimented. However, this is not always possible due to different weather types and the difficulty of data gathering and certainty.
That's why simulation presents various interesting options for design and simulation of physical behavior, there will be always errors and uncertainties, because solar energy systems are transient in nature. Therefore, simulation and experimentation are complementary. However, modelling assumptions should be valid to avoid big uncertainties. To design or optimize a solar system with T*SOL, the following steps must be followed:

a) Calculation of Energy Balance
A thermal energy balance is generated to calculate status and temperature changes during a simulation period. Mathematically, this means the numerical solution of a differential equation [5].
Temperature difference = Total of all input and output energies/Total of all heat capacities.
Energy input can be (depending on the component):
- Irradiation,
- Heat supply to the heat exchanger,
- Heat transfer by mass flow due to consumption or circulation,
- Intermixture of storage tank layers.

Energy output can be:
- Heat losses by radiation from the collector (quadratic transmission coefficient),
- Heat losses at the insulation of the collector, the piping (collector loop or circulation), the valves, or the storage tanks,
- Heat transfer to the heat exchanger,
- Heat transfer by mass flow due to consumption or circulation,
- Intermixture of storage tank layers.

The heat capacities of the following components are considered:
- Collector
- Piping of the collector loop
- Storage tank content

Table II- Results for RIPH with L = 42º64' N

Parameters Object		$\overline{H}$ [MJ/m²]	$\overline{H}_0$ [MJ/m²]	$\overline{K}_T$	$\overline{H_d}/\overline{H}$	$\overline{R}_b$	h_{ss} [°]	$h_{ss}^{'}$ [°]	$\overline{H}_T$ [MJ/m²]
Regional Institute of Public Health	Jan	5.911	13.663	0.433	0.462	2.254	69.394	86.278	10.014
	Feb	8.798	18.769	0.469	0.423	1.796	77.771	87.761	13.038
	Mar	12.27	26.186	0.469	0.46	1.409	87.772	89.589	14.923
	Apr	15.52	33.861	0.458	0.47	1.119	98.783	91.614	16.156
	May	18.88	39.436	0.479	0.45	0.95	108.26	93.313	17.977
	Jun	22.28	41.7	0.534	0.397	0.883	113.11	94.152	20.352
	Jul	23.19	40.494	0.573	0.362	0.912	110.908	93.774	21.583
	Aug	20.53	35.819	0.573	0.362	1.041	102.727	92.329	20.801
	Sep	14.94	28.744	0.52	0.41	1.281	92.043	90.377	17.166
	Oct	10.11	20.922	0.483	0.408	1.654	81.04	88.354	13.856
	Nov	6.322	14.763	0.428	0.467	2.117	71.61	86.664	9.951
	Dec	4.982	12.116	0.411	0.487	2.422	66.933	85.855	8.583

b) Calculation of Irradiation
In the supplied climate files, irradiation to the horizontal plane is given in watts per square meter of active solar surface. The program converts this to the tilted surface during the simulation and multiplies it by the total active solar surface. This model considers the anisotropy factor for circumsolar radiation and the ground reflection factor (= 0.2). Irradiation on the collector area (active solar surface) is calculated from the radiation strength (W/m²) on the horizontal plane: the height of the sun and the solar azimuth is determined on the basis of the date, time, and latitude.

c) Calculating Collector Thermal Losses
The energy absorbed by the collector and output to the collector loop less heating losses is calculated as follows:

$$P = G_{dir} \cdot \eta_{\circ} \cdot f_{IAM} + f_{IAMdiff} \cdot G_{diff} \cdot \eta_{\circ} - k_{\circ} \cdot (T_{cm} - T_A) - k_q \cdot (T_{cm} - T_A)^2 \quad (11)$$

with :

G_{dir}	Part of solar irradiation striking surface
G_{diff}	Diffuse solar irradiation striking a tilted surface
T_{cm}	Average temperature in the collector
T_A	Air temperature
f_{IAM}	Incident angle modifier.
k_0	Heat transfer coefficient (in W/m²/K)
kq	Heat transfer coefficient (in W/m²/K²).

d) Calculation of Primary Energy Consumption
Consumption values, efficiencies, solar fractions, and other parameters can be calculated from the temperatures and the energy flows of the system. In this case, district heating is calculated from the energy transferred to the auxiliary heating at the heat exchanger via the heat equivalent and the efficiency of the auxiliary heating.

e) Calculation of CO_2 Emissions
The CO_2 emissions saved by the solar system are calculated in the results summary. For this, it is necessary to know which type of primary energy is saved by the solar system.

f) Calculating Efficiency and the Solar Fraction
The collector loop efficiency is defined as follows:

$$Collector\ Loop\ Efficiency = \frac{Energy\ output\ from\ the\ collector\ loop\ via\ the\ heat\ exchangeer}{Energy\ irradiated\ onto\ the\ collector\ area\ (active\ solar\ surface)}$$

The system efficiency is defined as follows:

$$System\ efficiency = \frac{Energy\ output\ from\ the\ solar\ system}{Energy\ irradiation\ on\ to\ the\ collector\ area(active\ solar\ surface)}$$

The solar fraction is defined as follows:

$$Solar\ fraction = \frac{Energy\ supplied\ to\ the\ standby\ tank\ from\ the\ solar\ system}{Total\ energy\ supplied\ to\ the\ standby\ tank(Solar\ system + auxiliary\ heating)}$$

3.1 MODELING AND SIMULATION OF SOLAR WATER HEATING SYSTEMS

Based on the calculations we have 21 collectors but in the clinic there are installed 2·24 = 48 collectors, with a total of 6 modules with 8 collectors.

3.1.1 Simulation

Based on the calculations made for the volume of the boiler and number of collectors, the following system is obtained.

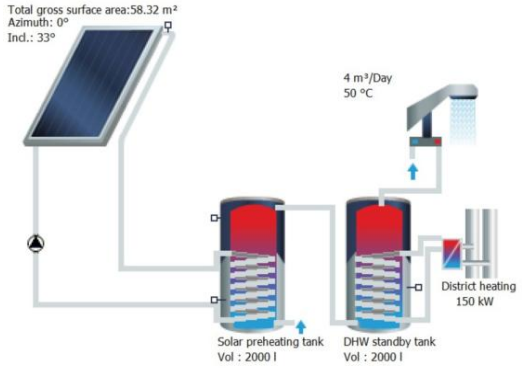


Figure 2 The DHW system for Regional Institute of Public.

In the following are presented the simulations with this software for some institutions. Tab. 3 shows the basis data for this station. As a general conclusion it can be suggested that for sanitary hot water temperature for 50˚C: the total solar fraction for Regional Institute of Public is 60%, the solar contribution is 40819 kWh, the CO_2 emissions is 9925 kg, and the Savings District heating is 45947 kWh.

4 THE F-CHART METHOD

This and the following sections outline the f-chart method for estimating the annual thermal performance of active heating systems for buildings (using either liquid or air as the working fluid) where the minimum temperature of energy delivery is near 20°C. The f-chart method provides a means for estimating the fraction of a total heating load that will be supplied by solar energy for a given solar heating system. The primary design variable is collector area: secondary variables are collector type, storage capacity, fluid flow rates, and load and collector heat exchanger sizes.
The two dimensionless groups are:[2]

$$\boldsymbol{X = F_R \cdot U_L \cdot \frac{F_R'}{F_R} \cdot (T_{ref} - T_a) \cdot \Delta t \cdot \frac{A_C}{L}} \quad (12)$$

$$\boldsymbol{Y = F_R \cdot (\tau\alpha)_n \cdot \frac{F_R'}{F_R} \cdot \frac{\overline{(\tau\alpha)}}{(\tau\alpha)_n} \cdot \overline{H_T} \cdot N \cdot \frac{A_C}{L}} \quad (13)$$

where:

A_C	Collector area (m^2)
F_R'	Collector heat exchanger efficiency factor [%]
F_R	Collector heat removal factor [%]
U_L	Collector overall loss coefficient (W/m²/°C)
Δt	Total number of seconds in month
$\overline{T}_a$	Monthly average ambient temperature (°C) [10]
T_{ref}	Empirically derived reference temperature (100°C)
L	Monthly total heating load for space heating and hot water (J)
$\overline{H}_T$	Monthly average daily radiation incident on collector surface per unit area (J/m²)
N	Days in month
$\tau\alpha$	Monthly average transmittance – absorptance product.

Table IV shows the results of these calculations.

Table III- The results of studied parameters

Parameters Object		Solar contribution to DHW [kWh]	DHW solar fraction [%]	CO2 emissions avoided [kg]	E-SL to tank [kWh]	Energy from Auxiliary heating [kWh]	Savings District heating [kWh]
Regional Institute of Public Health – Solar 1	Months	50°C	50°C	50°C	50°C	50°C	50°C
	Jan	2042	32	474	2043	4336	2196
	Feb	2357	37	547	2329	4067	2534
	Mar	3408	52	792	3413	3142	3665
	Apr	3792	64	887	3861	2133	4109
	May	4202	74	1038	4254	1500	4806
	Jun	4339	82	1096	4470	965	5075
	Jul	4664	93	1185	4794	349	5487
	Aug	4517	92	1148	4608	369	5314
	Sep	3854	76	953	3941	1241	4413
	Oct	3621	61	865	3606	2272	4006
	Nov	2447	39	572	2432	3861	2647
	Dec	1577	32	366	1562	3426	1696
	Year	**40819**	**60**	**9925**	**41315**	**27660**	**45947**

Table IV- Monthly and Annual Performance

Mon	T [°C]	H_T [MJ/m^2]	L [GJ]	Xc	Y	f	fL [GJ]
Jan	0.2	10.014	22.47	4.775	0.627	0.285	6.356
Feb	2.5	13.038	20.30	4.548	0.816	0.43	8.725
Mar	6.6	14.923	22.47	4.145	0.934	0.526	11.83
Apr	11.1	16.156	21.75	3.702	1.011	0.596	12.97
May	15.64	17.977	22.47	3.255	1.125	0.686	15.41
Jun	19.72	20.352	21.75	2.854	1.274	0.787	17.11
Jul	22.21	21.583	22.47	2.609	1.351	0.839	18.85
Aug	22.15	20.801	22.47	2.615	1.302	0.814	18.30
Sep	16.32	17.166	21.75	3.189	1.075	0.661	14.36
Oct	11.54	13.856	22.47	3.659	0.867	0.508	11.43
Nov	6.26	9.951	21.75	4.178	0.623	0.311	67.62
Dec	1.2	8.583	22.47	4.676	0.537	0.221	49.64
Year		184.401	264.6				147.1

The fraction of the annual heating load supplied by solar energy is determined by repeating the calculation of X, Y and *f* for each month and summing the results as indicated by:

$$\boldsymbol{F} = \frac{\sum \boldsymbol{f_i} \cdot \boldsymbol{L_i}}{\sum \boldsymbol{L_i}} \tag{14}$$

When this process is repeated for all 12 months the annual solar contribution is estimated to be 55.6%

5 THE MAIN SYSTEM COMPONENTS

The system was designed to generate hot water for DHW use. The main components of the solar hot water heating system at the Regional Institute of Public Health (Fig. 3) are:

Closed-Loop System – The system is designed as a standard closed loop system, where a pump circulates a water/propylene glycol mixture through the collectors and an external heat exchanger.

Infectious Diseases Clinic – A total of six modules were installed at the Clinic, with two parts: **Solar I** of three modules plumbed in series, three set of eight panels are plumbed in parallel, same in **Solar II** of three modules plumbed in series, three set of eight panels are plumbed in parallel**.** ***Preheat Tank*** – There are two preheat tanks in this system (with 2*2000 liters), that heated water from the solar thermal collectors and preheat the domestic hot water before it is supplied to the auxiliary tanks. As shown in Figure 3, the preheat tanks are heated solely by the collector array. ***Auxiliary Tank – Regional Institute of Public Health*** system uses a standard Auxiliary Tank with 2000 liter (Type KODSAN KCD, the diameter 1260 [mm] and the height 2230 [mm] [3]). Pre-heated water from the preheat tanks is fed to the auxiliary tank where it is heated to the hot water delivery set point, if necessary, and supplied to the facility. In the winter season this tank heated from District Heating.

External Heat Exchanger – An external heat exchanger transfers heat from the solar collectors to the pre-heat tanks.
Solar Pump Station – Circulation pumps circulate water through the solar thermal loop and the external heat exchanger. A separate set of pumps circulate fluid from the pre-heat tanks to external heat exchangers.
Solar Controller – Under normal operations at the Bean Center, the circulating pumps serving the solar collectors and the solar storage tanks are started when the collector temperature exceeds the solar tank storage and stopped when the collector temperature is less than the solar storage tank.
Installed Costs – The installed system cost of the 48-panel system at the Regional Institute of Public Heal this **42816 [€]** (for both Solar I and Solar II). A photo of the 48-panel, installation at the Regional Institute of Public Health is provided in Figure 3. The presence of dirt or dust causes losses of solar panels efficiency up to 40% [16].



Figure 3 Regional Institute of Public System Installation (collectors, Preheat Tank, Auxiliary Tank, Controller).

5.1 STUDIED SYSTEM SCHEME IN AUTOCAD

With the application of software AutoCAD all components of Solar Hot Water System (Solar 1 and Solar 2) at the Regional Institute of Public Health are drawn in Figure 3. It should be mentioned that the entire system uses renewable energy, only pump and controller is electrical equipment. In this station the measurements are registered 24 hours every 5 minutes beginning May to September.
It is worth mentioning that in this station there is mainly energy exchange during the 24 hours, and very rare the expression N/A. The maximum value in this station is 1100 [Wh], on 31 July, which is shown in Fig. 6.
In the Regional Institute of Public Health, there is an exchange of energy almost 24 hours, for this reason the solar contribution value is higher.
In the following, an annual overview of the Regional Institute of Public Health was made.
Annual solar contribution, money saves and CO_2, reduction was calculated as follows:

- Annual solar contribution data
- Money saves depend on the fuel, in this case electricity:
- CO_2 reduction
- Annual solar contribution Tab. 1 [kWh]
- Boiler efficiency 0.95
- Unit price of electricity 0.079 [€/kWh]
- CO_2 emission per kWh electric 0.219 [kgCO_2/kWh]

$$E_X = 2191\text{kWh} \cdot \frac{1}{0.95} \cdot 0.0779\text{euro/kWh} = 179.662\text{euro}$$

Table V shows the amount saved by using solar energy for water heating is 3347.158 [€], but the maintenance of the system was not included in this value. The system reduced CO_2 emission by 9409.854 [kg], which is an important amount of reduced CO_2 in the atmosphere.

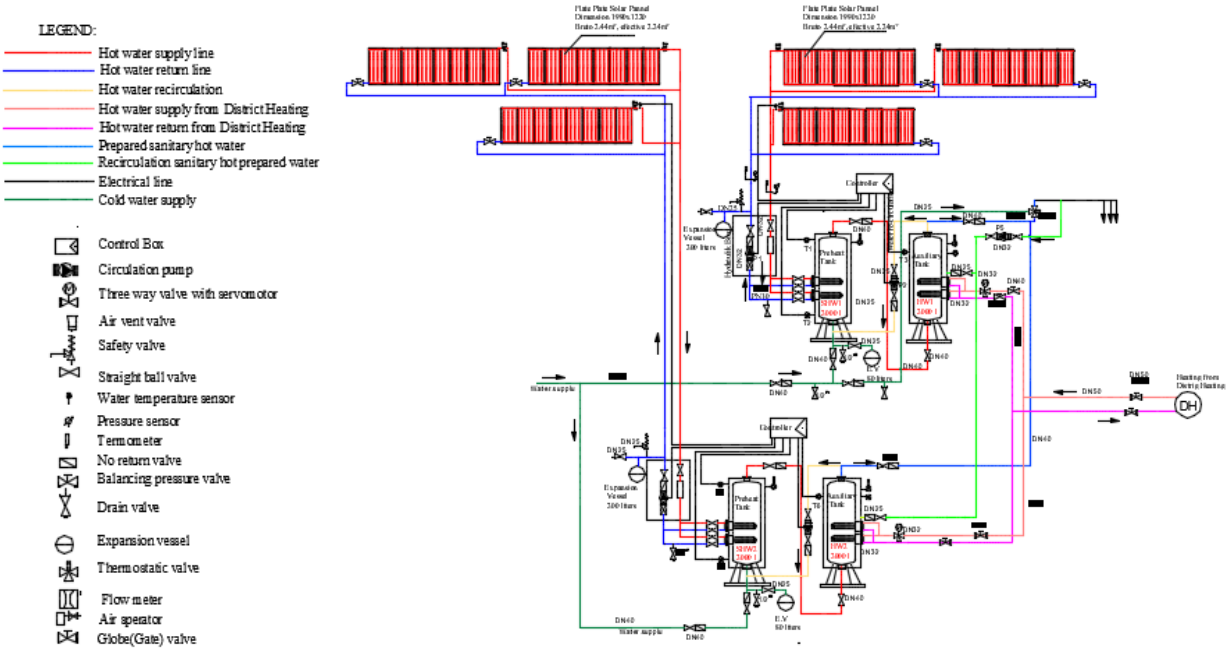


Figure 4 Schematic Solar Hot Water System at the Regional Institute of Public Health.

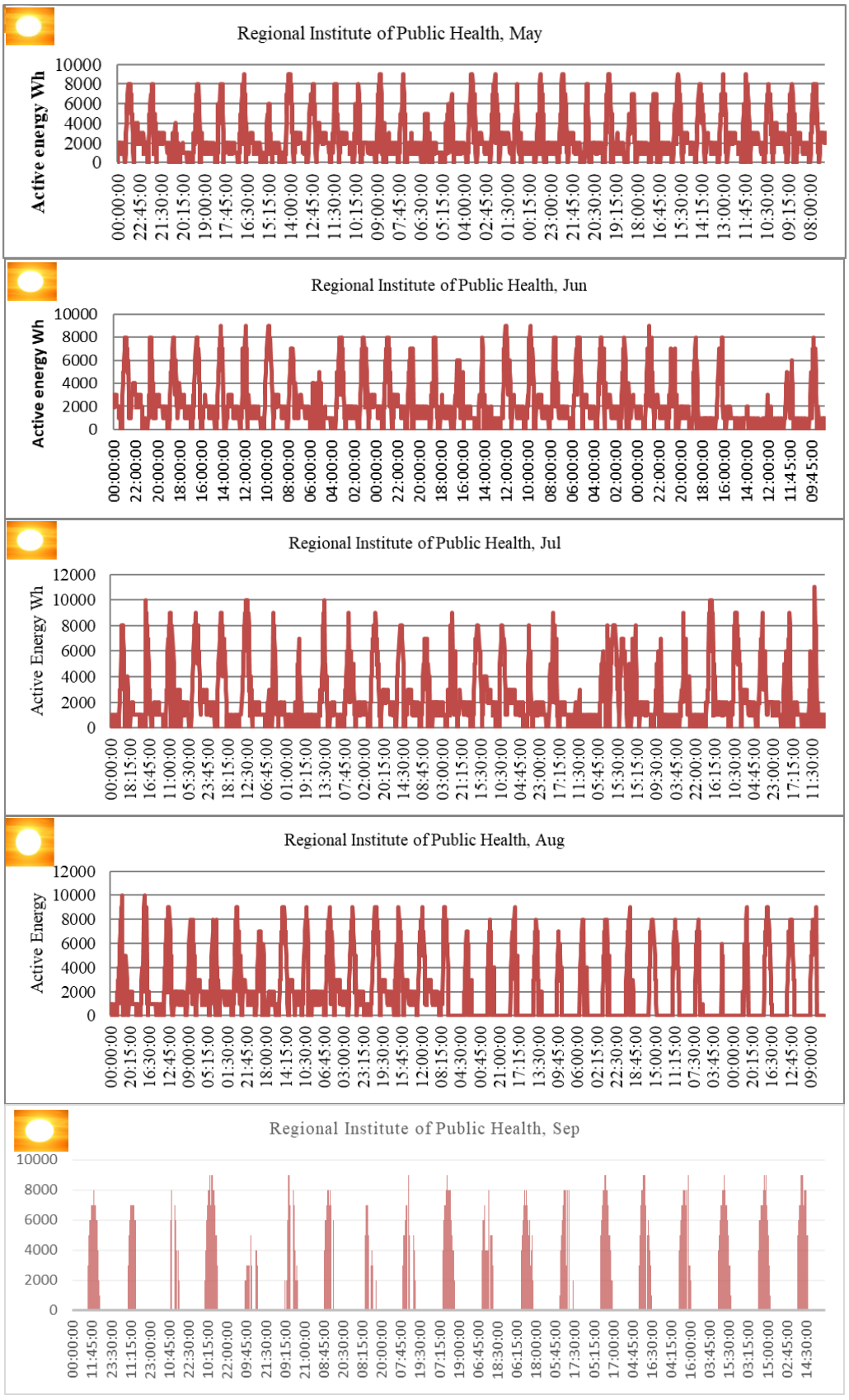


Figure 5 Solar Hot Water System – Active Energy measured from May to September.

Table V- Monitored Regional Institute of Public Health

Months	Solar contribution [kWh]	Annual money saves [€]	Annual CO_2 reduction [kg]
Jan	2042	167.44	470.73
Feb	2357	193.274	543.35
Mar	3408	279.456	785.63
Apr	3792	310.944	874.15
May	4202	344.564	968.67
Jun	4339	355.798	1000.25
Jul	4664	382.448	1075.17
Aug	4517	370.394	1041.28
Sep	3854	316.028	888.44
Oct	3621	296.922	834.73
Nov	2447	200.654	564.09
Dec	1577	129.314	363.54
Annual	40819	3347.158	9409.854

6 ECONOMIC ASSESSMENTS FOR RIPH

In the investigation of the economic benefits of utilizing solar energy instead of conventional sources of energy, it is mandatory to take into consideration all the economic parameters of such an investment. It is assumed that the cost of the solar water heater is paid at the beginning and the value for RIPH for this clinic is 21408 [€]. The life span of the solar water heater is taken to be 20 years (starting from 2018 to 2038), the thermal performance degradation of the system is assumed to be 1% per year [11], unit price of electricity in Kosovo is 0.0779 €/kWh. Based on results obtained in Table III for cumulative cash flow analysis.

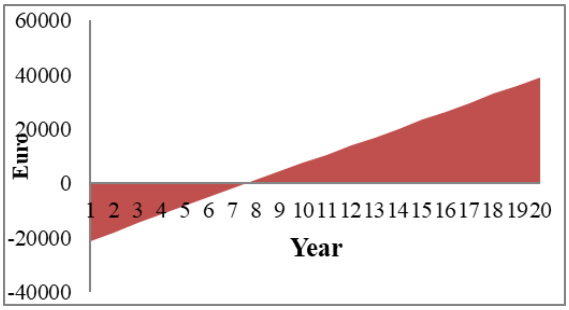


Figure 5 The result of cumulative cash flow analysis for the city of Regional Institute of Public Health

For this clinic, the annual energy needs covered by a solar water heater are founded 65% of the annual water heating use. Moreover, the cumulative cash flow analysis result is shown in Fig. 5. The simple and equity payback periods are 7.6 years.

7 CONCLUSIONS

This paper investigates solar thermal energy for one system that install in one social institution in Pristina, which increases the quality of life, thus serves with hot sanitary water. Improving the performance and utilization of solar thermal systems will increase solar energy harvesting and reduce the dependency on fossil-based energy sources.

This review article focuses on:

- Environmental characteristics for Pristina:
  - Global horizontal radiation 1351 [kWh/m^2]
  - Insolation 5.44 [h]
  - Air temperature 11.3 [°C]
- RIPH located at 42.64°0" N and 21.15°0" E.
- Appropriate roof space to put the collectors 375.15 [m^2].
- The number of collectors is 24.
- The result of simulation with TSOL software:
  - Solar fraction for Pristine is 60%
  - Solar contribution is 40819 [kWh]
  - CO_2 emissions avoided are 9925 [kg]
  - Savings District heating is 45947 [kWh].
- The f-chart method is used step by step based on the Duffie and Beckman to calculate Monthly and Annual Performance for RIPH:
  - Estimated annual solar contribution 40861.1 [kWh]
  - The fraction of the annual heating load supplied by solar energy is 55.6%.
- Active energy - In this station the measurements are registered 24 hours every 5 minutes beginning May to September. It is worth mentioning that in this station there is mainly energy exchange during the 24 hours, and very rare the expression N/A.
- Monitored Regional Institute of Public Health:
  - the amount saved by using solar energy for water heating is 3347.158 [€]
  - the system reduced CO_2, emission avoided is 9409.854 [kg]

Significantly increasing the use of renewable energy is an urgent task for the time being. The use of solar thermal energy in Kosovo is being used mainly in social institutions, which aims to increase the quality of life and conserve energy. The return of the investment is made after 7.6 years, but the protection of the environment is important when it is known that Kosovo has a high level of pollution, especially in the winter season.

CONFLICTS OF INTEREST

The authors declare no conflict of interest.

REFERENCES

[1] D. Qerimi, C. Dimitrieska, S. Vasilevska, A. Alimehaj. *Modeling of the Solar Thermal Energy Use in Urban Areas*, 2020.

[2] J. Duffie, W. Beckman, *Solar Engineering of Thermal Processes*, Fourth Edition.

[3] Kodsan - Product catalogue ,2017.

[4] Renewable 2023 Global Status Report - REN21.

[5] T*SOL® Pro Version 5.5 Design and Simulation of thermal solar systems.

[6] Test Report, Thermal Performance of a Solar Collector 2012.

[7] *Urban development plan "Pristina 2012-2022"*, September 2013.

[8] Dinçer and C. Zamfirescu, *Sustainable Energy Systems and Applications*, LLC 2011.

[9] Energy regulatory office, annual report 2023. Prishtina March 2024.

[10] Instituti hidrometeorologjik i Kosoves.

[11] *Solar Heat Worldwide*, Edition 2024.

[12] J. Twidell and T. Weir. Renewable Energy Resources. A. Ramos, I. Guarracino, A. Mellor, D. Alvarez, P. Childs, J. Nicholas, E. Daukes, N. Markides. *Solar-Thermal and Hybrid Photovoltaic-Thermal Systems for Renewable Heating*: May, 2017.

[13] N.Sahiti, M. Pireci, B. Verselaj, *Burimet e ripërtritshme te energjisë*.

[14] Code of practice – The CEN/TR 16355 technical report of CEN/TC 164/WG 2 on Legionella applied to solar hot water systems.

[15] P. Iodice, A. Amoresano, G. Langella, Thermodynamic analysis of screw expanders at part-load working conditions: energy losses, fluid leakage and overall efficiency, *International Journal of Mechanics and Control*, Vol. 24, No. 1, pp. 89-96, 2023.

[16] M. Cristodaro, S. Fortuna, A. Greco, A. C. Petrolino, G. Carbone, Design of solar panels cleaning device - Cleanator, *International Journal of Mechanics and Control*, Vol. 23, No. 01, pp. 35-44, 2022.

[17] S. Poçari, L. Lamani, M. Alcani, A. Hoxha, Implementation of PID position control for a photovoltaic system using mathematical model and LabVIEW, *International Journal of Mechanics and Control*, Vol. 25, No. 01, pp. 9-14, 2024.

[18] G. Mustafaraj, K. Dhoska, A. Sulejmani, O. Koça, E. Spaho, Applied energy efficiency measures in industrial building by using EnergyPlus software, *International Journal of Mechanics and Control*, Vol. 25, No. 01, pp. 37-44, 2024.

ISSN 1590-8844
International Journal of Mechanics and Control, Vol. 26, No. 01, 2025
https://doi.org/10.69076/jomac.20XX.00YY

TEMPLATE FOR PREPARING PAPERS FOR PUBLISHING IN INTERNATIONAL JOURNAL OF MECHANICS AND CONTROL

Author1* Author2**

* affiliation Author1

** affiliation Author2

ABSTRACT

This is a brief guide to prepare papers in a better style for publishing in International Journal of Mechanics and Control (JoMaC). It gives details of the preferred style in a template format to ease paper presentation. The abstract must be able to indicate the principal authors' contribution to the argument containing the chosen method and the obtained results. (max 200 words)

Keywords: keywords list (max 5 words)

1 TITLE OF SECTION (E.G. INTRODUCTION)

This sample article is to show you how to prepare papers in a standard style for publishing in International Journal of Mechanics and Control.
It offers you a template for paper layout, and describes points you should notice before you submit your papers.

2 PREPARATION OF PAPERS

2.1 SUBMISSION OF PAPERS

The papers should be submitted in the form of an electronic document, either in Microsoft Word format (Word'97 version or earlier).
In addition to the electronic version a hardcopy of the complete paper including diagrams with annotations must be supplied. The final format of the papers will be A4 page size with a two column layout. The text will be Times New Roman font size 10.

Contact author: author1[1], author2[2]

[1]Address of author1.
[2]Address of author2 if different from author1's address
E-mail: author1@univ1.com , author2@univ2.com

2.2 DETAILS OF PAPER LAYOUT

2.2.1 Style of Writing

The language is English and with UK/European spelling. The papers should be written in the third person. Related work conducted elsewhere may be criticised but not the individuals conducting the work. The paper should be comprehensible both to specialists in the appropriate field and to those with a general understanding of the subject.
Company names or advertising, direct or indirect, is not permitted and product names will only be included at the discretion of the editor. Abbreviations should be spelt out in full the first time they appear and their abbreviated form included in brackets immediately after. Words used in a special context should appear in inverted single quotation mark the first time they appear. Papers are accepted also on the basis that they may be edited for style and language.

2.2.2 Paper length

Paper length is free, but should normally not exceed 10000 words and twenty illustrations.

2.2.3 Diagrams and figures

Figures and Tables will either be entered in one column or two columns and should be 80 mm or 160 mm wide respectively. A minimum line width of 1 point is required at actual size. Captions and annotations should be in 10 point with the first letter only capitalised *at actual size* (see Figure 1, Figure 2, Table VII and Table VIII).

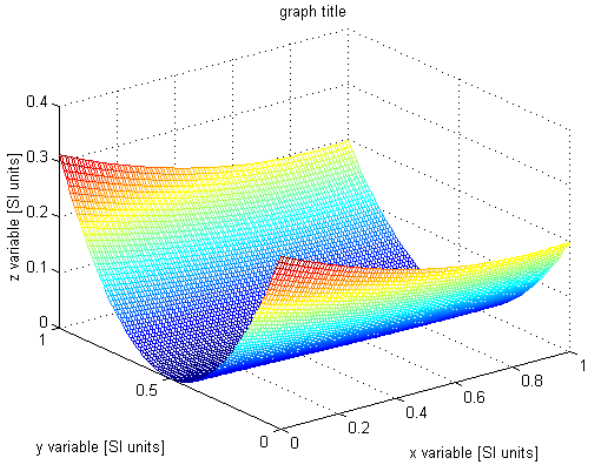


Figure 1 Simple chart.

Table VII - Experimental values

Robot Arm Velocity (rad/s)	Motor Torque (Nm)
0.123	10.123
1.456	20.234
2.789	30.345
3.012	40.456

2.2.4 Photographs and illustrations

Authors could wish to publish in full colour photographs and illustrations. Photographs and illustrations should be included in the electronic document and a copy of their original sent. Illustrations in full colour …

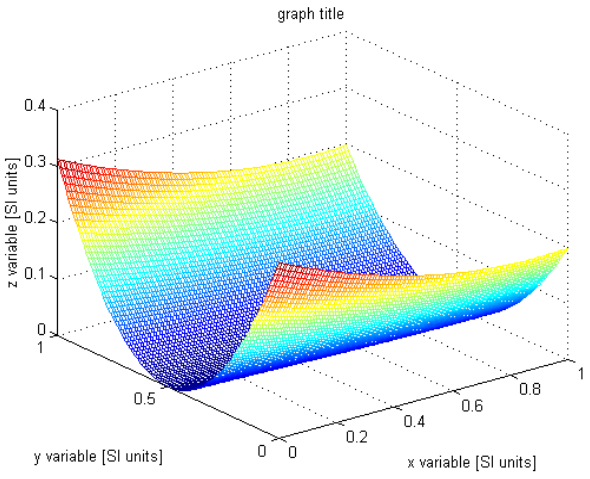


Figure 2 Simple chart.

2.2.5 Equations

Each equation should occur on a new line with uniform spacing from adjacent text as indicated in this template. The equations, where they are referred to in the text, should be numbered sequentially and their identifier enclosed in parenthesis, right justified. The symbols, where referred to in the text, should be italicised.

- point 1
- point 2
- point 3

1. numbered point 1
2. numbered point 2
3. numbered point 3

$$W(d) = G(A_0, \sigma, d) = \frac{1}{T}\int_0^{+\infty} A_0 \cdot e^{-\frac{d^2}{2\sigma^2}} dt \quad (1)$$

3 COPYRIGHT

Authors will be asked to sign a copyright transfer form prior to JoMaC publishing of their paper. Reproduction of any part of the publication is not allowed elsewhere without permission from JoMaC whose prior publication must be cited. The understanding is that they have been neither previously published nor submitted concurrently to any other publisher.

4 PEER REVIEW

Papers for publication in JoMaC will first undergo review by anonymous, impartial specialists in the appropriate field. Based on the comments of the referees the Editor will decide on acceptance, revision or rejection. The authors will be provided with copies of the reviewers' remarks to aid in revision and improvement where appropriate.

5 REFERENCES (DESCRIPTION)

The papers in the reference list must be cited in the text. In the text the citation should appear in square brackets [ ], as in, for example, "the red fox has been shown to jump the black cat [3] but not when...". In the Reference list the font should be Times New Roman with 10 point size. Author's first names should be terminated by a 'full stop'. The reference number should be enclosed in brackets.

The book titles should be in *italics*, followed by a 'full stop'. Proceedings or journal titles should be in *italics.* For instance:

Table VIII - Experimental values

Robot Arm Velocity (rad/s)	Motor Torque (Nm)	Motor Torque (Nm)	Motor Torque (Nm)
0.123	10.123	10.123	10.123
1.456	20.234	20.234	20.234
2.789	30.345	30.345	30.345
3.012	40.456	40.456	40.456

REFERENCES (EXAMPLE)

[1] Smith J., Jones A.B. and Brown J., *The title of the book*. 1st edition, Publisher, 2001.

[2] Smith J., Jones A.B. and Brown J., The title of the paper. *Proc. of* C*onference Name*, where it took place, Vol. 1, paper number, pp. 1-11, 2001.

[3] Smith J., Jones A.B. and Brown J., The title of the paper. *Journal Name*, Vol. 1, No. 1, pp. 1-11, 2001.

[4] Smith J., Jones A.B. and Brown J., *Patent title*, U.S. Patent number, 2001.

International Journal of Mechanics and Control – JoMaC
Published by ASTRA M B S.R.L.

TRANSFER OF COPYRIGHT AGREEMENT

NOTE: Authors/copyright holders are asked to complete this form signing section A, B or C and mail it to the editor office with the manuscript or as soon afterwards as possible.	*Editorial Secretary address:* Andrea Manuello Bertetto Matteo D. L. Dalla Vedova, Simone Venturini, Alessandro Aimasso *Dept. of Mechanical and Aerospace Engineering* *Politecnico di Torino* *C.so Duca degli Abruzzi, 24 – 10129 Torino – Italy* *e_mail: jomac@polito.it* *fax n.: +39.011.090.6999*

The article title:

By:_____

To be Published in ***International Journal of Mechanics and Control JoMaC***
Official legal Turin court registration Number 5320 (5 May 2000) - reg. Tribunale di Torino N. 5390 del 5 maggio 2000

A Copyright to the above article is hereby transferred to the JoMaC, effective upon acceptance for publication. However the following rights are reserved by the author(s)/copyright holder(s):
1. All proprietary rights other than copyright, such as patent rights;
2. The right to use, free or charge, all or part of this article in future works of their own, such as books and lectures;
3. The right to reproduce the article for their own purposes provided the copies are not offered for sale.

To be signed below by all authors or, if signed by only one author on behalf of all co-authors, the statement A2 below must be signed.

A1. All authors:

SIGNATURE_____DATE_____ SIGNATURE_____DATE_____

PRINTED NAME_____ PRINTED NAME_____

SIGNATURE_____DATE_____ SIGNATURE_____DATE_____

PRINTED NAME_____ PRINTED NAME_____

A2. One author on behalf of all co-authors:
"I represent and warrant that I am authorised to execute this transfer of copyright on behalf of all the authors of the article referred to above"

PRINTED NAME_____

SIGNATURE_____ TITLE_____ DATE_____

B. The above article was written as part of duties as an employee or otherwise as a work made for hire. As an authorised representative of the employer or other proprietor. I hereby transfer copyright to the above article to *International Journal of Mechanics and Control* effective upon publication. However, the following rights are reserved:
1. All proprietary rights other than copyright, such as patent rights;
2. The right to use, free or charge, all or part of this article in future works of their own, such as books and lectures;
3. The right to reproduce the article for their own purposes provided the copies are not offered for sale.

PRINTED NAME_____

SIGNATURE_____ TITLE_____ DATE_____

C. I certify that the above article has been written in the course of employment by the United States Government so that no copyright exists, or by the United Kingdom Government (Crown Copyright), thus there is no transfer of copyright.

PRINTED NAME_____

SIGNATURE_____ TITLE_____ DATE_____

CONTENTS - Special Issue of the International Journal of Mechanics and Control (JoMaC) dedicated to the 5th International Conf. on IFToMM Italy (IFIT 2024)

01 **Preface for the Special Issue of the International Journal of Mechanics and Control (Jomac) dedicated to the 5th International Conference of the IFToMM Italy, IFIT 2024**
M. C. Valigi, C. Visconte

03 **Synthesis of Oldham chain based six-bar dwell mechanisms for three-pose rigid-body guidance**
G. Figliolini, C. Lanni, L. Tomassi

13 **Performance and efficiency PF a hybrid self-propelled cable logging carriage: an experimental study**
S. Leitner, L. Maccioni, G. Carabin, R. Spinelli, R. Vidoni

23 **Obstacle avoidance methods for differential drive robots**
F. Neri, G. Palmieri, D. Costa, M. Callegari

37 **Regularized dynamic parameter identification for the Mitsubishi RV-5AS-D-S01 robot**
D. Dona', P. Boscariol, M. Bottin, B. Lenzo, G. Rosati

49 **A hands-free human-machine interface for electric wheelchair control based on face and torso movements**
L. Baglieri, D. Matsuura, T. Kobayashi, G. Quaglia

57 **Force-optimized monolithic PneuNets soft actuators: design, simulation and characterization**
M. Tiboni, D. Loda

67 **Improving accuracy and robustness in robot kinematic calibration using a single draw-wire encoder: a comparative analysis**
G. Boschetti, T. Sinico

79 **Design and characterization of a new soft robotic tendon driven gripper for precision grasping**
S. Logozzo, M. C. Valigi

CONTENTS – Regular Issue

87 **An innovative prototype of an automatic device for moving fingers and wrist during fMRI analysis**
G. Eula

103 **Modeling a subject wearing an industrial trunk support exoskeleton**
G. Eula

119 **Simplified model for dynamic analysis of robotic manipulators**
A. Cesaro, M. Bottin, M. Tonan, A. Doria, G. Rosati

129 **Design and testing of Almaty Ankle Exoskeleton V.2**
N. Zhetenbayev, M. Ceccarelli, M. Russo

145 **Design and testing a sensored rotating crank for arm exercises of elderly people**
S. Sanz, M. Russo, M. Garrosa, M. Ceccarelli

159 **Innovative thermal management systems for fuel cell electric aircraft**
S. Favre, F. Di Fede, E. Brusa, C. Delprete

185 **Is lighting based on photopic requirements in assembly workstations also optimal for non-visual performance in a human-centric perspective? A case study in the automotive sector**
A. Carlin, V. R. M. Lo Verso

213 **Vibration protection system of constant acceleration of the operator's seat**
M. S. Korytov, V. S. Shcherbakov, I. E. Kashapova

221 **Cardiovascular and metabolic engagement after an endurance race in pilots driving motorboats electrically powered by green energy**
A. Manuello Bertetto, F. Tocco, G. Bellomi, L. Mulargia, M. Ruggiu, M. Palmas, M. Massidda, G. Ghiani, F. Velluzzi, S. Melis, A. Fois, A. H. Dell'Osa, A. Cerina, U. Bertelli, M. G. Carta, P. R. Bianco, A. Concu

231 **Solar thermal energy, case study - Regional Institute of Public Health**
D. Qerimi, G. Shala, A. Alimehaj Rrecaj

NEWS FROM THE JOMAC EDITORIAL BOARD:

Starting from the June 2024 issue, JoMaC provides an Open Access service to our authors.
You are invited to visit the JoMaC website (http://www.jomac.it) for further details.